University of Surrey

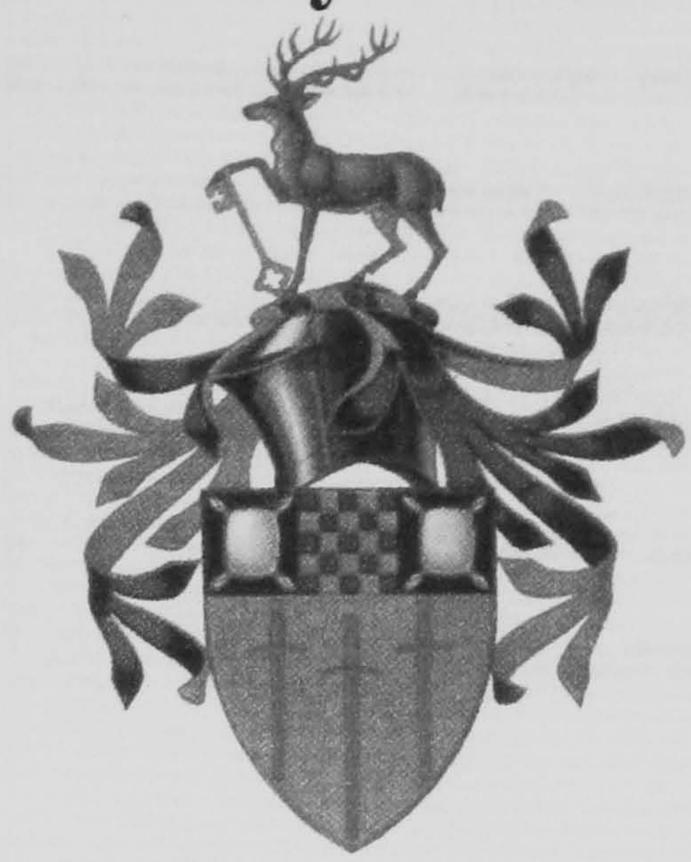

School of Engineering

The use of a polarimetric sensor to detect matrix cracking damage in composite laminates

Hongrui Wang

A thesis submitted for the degree of doctor of philosophy

November 2003

Abstract

An optical system based on a polarimetric sensor has been demonstrated to be successful for detecting matrix crack development during quasi-static loading when embedded in a cross-ply laminate. Unlike previous studies, the transparent nature of the coupons used here makes it possible to determine the time when cracks pass the sensor. Using this method, it has been possible to show a clear one-to-one relationship between a step-change of optical output and the time when the cracks pass the sensor.

The response of polarimetric sensors of different configurations, both free and embedded in laminates, have been obtained. Experiments with sensors of different configurations embedded in cross-ply laminates show that these sensors could detect cracking in large composite structures.

With regard to crack detection, there is a step-change in optical signal when a transverse crack passes the embedded sensor. Using band pass FFT filter techniques, it has been shown that the moment that cracks pass the sensor can be determined. This FFT filtering crack detection technique is likely to be useful in real time crack detection in engineering applications.

Further experiments on detecting transverse cracks in double cross-ply laminates have shown that cracks can be detected both under quasi-static loading and four-point bending tests. However, one of the limitations of the sensor is that it cannot detect cracks that occur in the 90° ply not adjacent to the sensor.

Attempts at modelling aspects of the behaviour of the embedded sensors have been made. Firstly, the values of the parameters which connect strain to phase change of the sensor have been obtained. Secondly, the optical response of embedded sensors has been analysed and the effect of twist on the sensitivity of embedded sensors have been

obtained. Thirdly, it has been shown that the interaction between the sensor and cracks that pass adjacent to the sensor would be expected to produce a decrease in the sensitivity of the sensors, which has been confirmed by the experimental evidence. However, the theoretical modelling has not been able to explain the change in intensity when a crack passed the sensor.

Papers published and conferences attended

H.Wang, S.L.Ogin, A.M.Thorne, G.T.Reed and M.Ussorio, "Crack detection around a hole in a cross-ply laminate using an embedded polarimetric fibre optic sensor", in "Proceedings of ICCM-14, The Fourteenth International Conference on Composite Materials" – San Diego, (USA), July, 2004.

H. Wang, S.L. Ogin, A.M.Thorne and G.T. Reed, "Use of a polarimetric sensor for damage detection in cross-ply composite laminate", in "Proceedings of ECCM-10, The Tenth European Conference on Composite Materials" –Brussels Brugge , (Belgium), June 2002.

H. Wang, S.L. Ogin, A.M.Thorne and G.T. Reed, "Matrix Crack Detection by An Embedded Polarimetric Sensor", in"The 9th Annual Congress of the UK Chinese Materials Association", Oxford (U.K.), May, 2002

M.Ussorio, H.Wang, S.L.Ogin, A.M.Thorne and G.T.Reed, "Flexural modulus reduction due to matrix cracking damage in a GFRP cross-ply laminate", in "Proceedings of ICCM-14, The Fourteenth International Conference on Composite Materials" – San Diego, (USA), July, 2004.

M.Ussorio, H. Wang, S.L.Ogin, A.M.Thorne and G.T.Reed, "Use of fibre Bragg gratings for damage detection in cross-ply laminates", in "Proceedings of Advancing with Composites 2003", Milan, (Italy), May, 2003, pp. 21-29.

M.Ussorio, H. Wang, S.L.Ogin, A.M.Thorne and G.T.Reed, "Matrix cracking behaviour of GFRP cross-ply laminate under bending", in "Proceedings of Advancing with Composites 2003", Milan, (Italy), May, 2003, pp. 21-29.

E.N.Barton, S.L.Ogin, A.M.Thorne, G.T.Reed and H. Wang , "Use of a polarimetric sensor to detect the fatigue crack growth of matrix cracks in a cross-ply composite laminate", in "Proceedings of ICCM-13, Thirteenth International Conference on Composite Materials" – Beijing (China), June 2001

Acknowledgements

I would like to express my sincere gratitude to my project supervisors **Dr. Steve Ogin, Mr. Tony Thorne** and **Prof. Graham Reed**, for their supervision, support and encouragement during this period of research.

I would also thank Mr. Mauro Ussurio, Mr. Reg. Whittingham, Mr Tom Lawton members of the Composite Materials Research Group, and the school secretarial staff for their friendly advice and assistance.

On a more personal note, I wish to acknowledge my wife, who has taken care of the family throughout these years and has made it possible for me to focus on the project.

Contents

Chapter 1. Introduction

There is a world-wide interest in materials research to incorporating intelligence into engineering materials, enabling them to sense the external stimuli and alter their properties to adapt to the changes in the environment. One example is the use of fibre optical sensors to detect damage in composite materials. Since composite materials are used in more and more complex structures, it is very important to develop a technology which can probe the internal integrity of a structure, especially for those structures that cannot be monitored by conventional methods. Optical sensors are a versatile technology and many types of sensors have potential application in many areas. In this area, some of the early work on damage detection concentrated on the losses induced in the optical fibre due to fibre failure or bending losses induced in an area of damage. More recent approaches have made use of a wide variety of sensors e.g. Bragg grating sensors, optical time domain reflectometry, optical coherence domain reflectometry, Michelson interferometric sensors and polarimetric sensors (Sirkis, 1993; Kwon, 1997; Tsuda, 1999; Murukeshan, 1999). Damage detection is crucial for safety and reliability of composite materials and it is of great importance for industries such as aerospace, marine and civil engineering. It has been widely recognised that fibre optic sensor technology is a non-destructive technology that can be used to monitor internal changes in composite structures.

This work focuses on using a polarimetric optic sensor with Hi-Bi PANDA fibres to detect damage (transverse cracks) in a relatively simple cross-ply laminate. Compared to other types of fibre optic sensors available, the fibre optic polarimetric sensor (FOPS) has its own unique advantages. Such a sensor typically employs a single high-birefringence fibre for detection and provides information on the integrated strain over the sensing region. Thus a single sensor covering the area of interest can be used for global health monitoring. The polarimetric sensor is not only sensitive to the

measurands, but also can be designed to be insensitive to external stimuli (Gaumont et al, 1998; Araujo et al, 2001) and can be appropriately configured in order to ensure ease of installation and assembly.

The aim of this project is to investigate the use of a fibre optic sensor (a polarimetric sensor) to detect initial cracking damage in a simple glass fibre reinforced laminate under load. Other types of damage (for example, cracks initiated around a circular hole in a cross-ply coupon, detection of cracks in four point bending) have also been considered.

The structure of the thesis is as follows. A literature review in Chapter 2 is followed by a description of various background theories involved in the present study in Chapter 3. A description of the materials and experimental procedures, both optical and mechanical, is presented in Chapter 4.

Chapter 5 deals with the general characteristics of the polarimetric sensor. The light path arrangement described in the experimental procedure in Chapter 4 is demonstrated to be well understood. Genuine optical fringes can only be obtained by bending the lead-out fibre properly and an optimisation of the bend diameter and number of loops of the lead-out fibre has been carried out. The polarization state of polarised light in the fibre core has been analysed and compared with the experimental results. In addition, the response of polarimetric sensors of different structures and different embedding conditions (free sensor, sensor embedded in unidirectional laminate, sensor embedded in cross-ply laminate) have been described here. Results on the application of the polarimetric sensor in fatigue tests, and the temperature response of the sensor, are also presented.

In Chapter 6, results on different types of damage detection development (e.g. transverse cracks in cross-ply coupons with and without circular holes) are presented.

The experimental results show that there is a clear one to one relationship between the step-changes of the optical output and the instant that the cracks pass the sensor.

In Chapter 7, a method employing FFT filter analysis is developed which shows that it would be possible to detect transverse cracks in a composite structure in real time using the polarimetric sensor. Further crack detection experiments are described in Chapter 8 using polarimetric sensors in double cross-ply coupons tested in tension and four-point bending tests.

In Chapter 9, the results of experiments to determine the strain-optical parameters of the optical fibre utilised in the present work are described and the sensitivity of a bare fibre polarimetric sensor made of the Hi-Bi PANDA fibre has been measured experimentally.

These results are used in Chapter 10 where various theoretical considerations are presented. The sensitivities of embedded sensors, and the interaction between embedded sensors and cracks which pass the sensor in an adjacent ply, are discussed. For example, a model has been developed for the sensitivity of a polarimetric sensor embedded in a cross-ply laminate including the effect of the initial orientation of the optical axes of the sensor at the reference splice relative to the composite axes and the total twist angle of the sensor to the second splice.

Finally, Chapter 11 summarises the conclusions of this thesis and presents suggestions for further work in this area.

Chapter 2. Literature Review

2.1 Introduction

This literature review provides the background of previous work on fibre optic sensors in materials, particularly with regard to damage and its detection. It will focus on two major areas: (a) detection of different types of damage in composite materials using fibre optic sensors; (b) background theory of polarimetric sensors and their application. Each of these areas is a large field in itself and the intention of this review is to provide an overview of these topics.

2.2 Fibre optic sensor types

Optical fibres are dielectric waveguiding devices used to confine and guide light. In the past few decades, the optical fibre as an information carrier in communication systems, has been fully developed. However, optical fibres can be more than mere signal carriers. Any disturbance of the fibre alters the characteristics of the guided light; such alterations can be monitored and related to the magnitude of the disturbing influence. This is the concept of fibre optic sensors first put forward by Butter and Hocker(1978).

The principal advantages which fibre optic sensors possess over conventional sensors are as follows:

- small size and low weight;
- immunity to electromagnetic interference (EMI);
- simultaneous sensing of more than one parameter;
- good corrosion resistance in a range of environments;
- high sensitivity;
- high fatigue life;
- very wide operating temperature range;
- non-conductive;

- fast response times.

The major disadvantages associated with using fibre optic sensors are:

- it may be necessary to isolate the sensor from unwanted parameters;
- availability of optical sources;
- cost and availability of suitable instrumentation;

Comparing the advantages with disadvantages, in many circumstances the advantages will outweigh the disadvantages.

There are various types of sensors based on the modulation of different characteristics of light such as intensity, wavelength, phase or polarisation. For example, Figure 2.1, shows a variety of interferometric fibre optic sensors and associated applications.

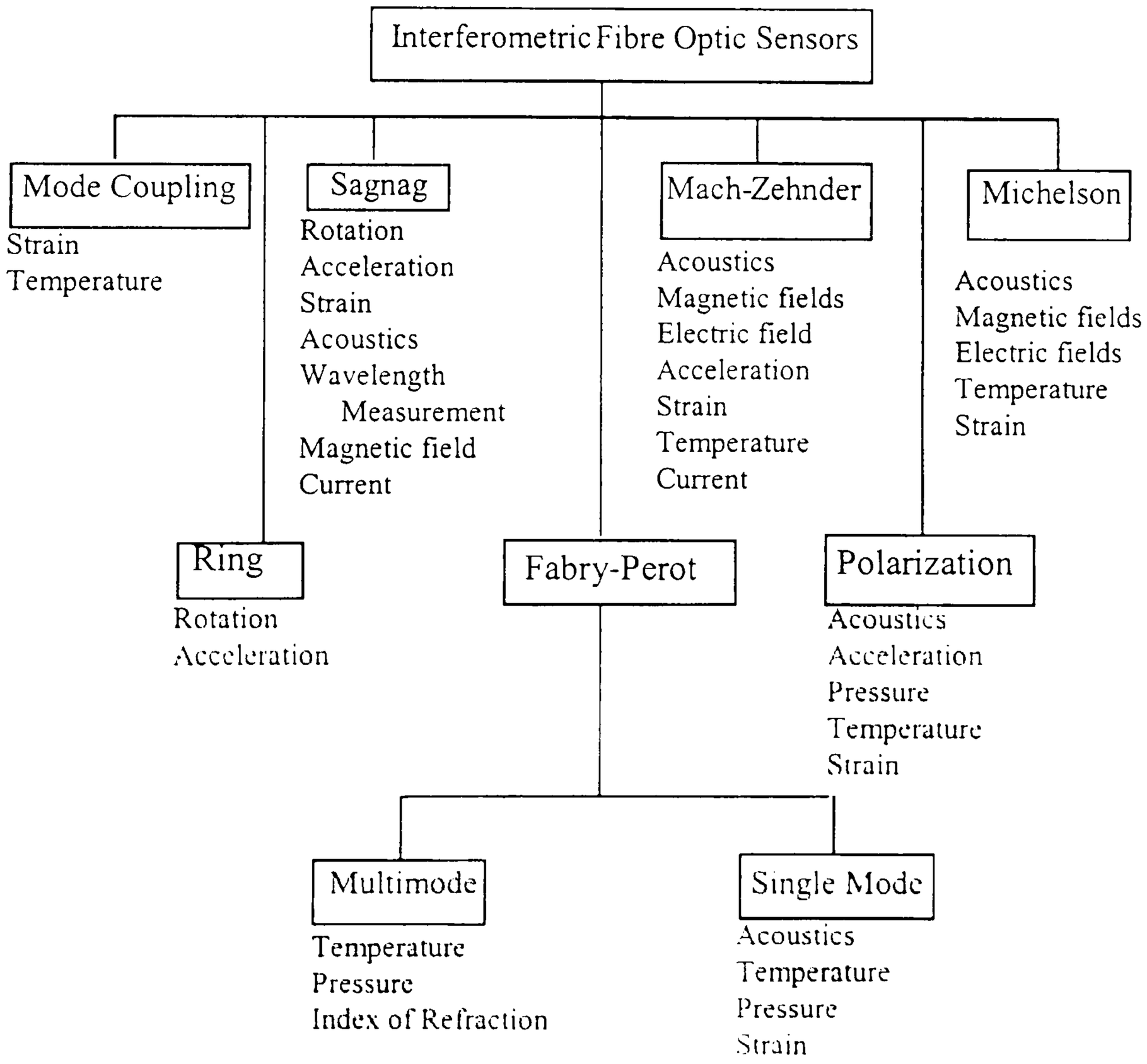

Figure 2.1 A schematic diagram showing a variety of interferometric fibre optic sensors and associated applications (After Udd, 1991).

In recent years, the research and development of fibre optic sensors has gradually moved from the laboratory to engineering applications. A number of different studies on bridges (Tennyson et al, 2001; George et al, 2001), aircraft (Guemes et al. 2001). space vehicles (Lunia et al, 2000), watercraft (Wang et al, 2001), industry robots (Fernandez et al, 2001; Garcia-Ramos et al, 2003), medical apparatus (Gunther et al. 2001), and chemical composition (Zhang et al, 1999; Johnson et al, 2000; Lee et al. 2002) have been documented.

Of particular interest here are composite materials incorporating fibre optic sensors. Composite materials are designed so that they have better properties of weight, stiffness, strength, durability, etc. than traditional engineering materials. This design concept is passive, that is, the properties are not controllable in use. Optic fibre sensors, which act as a functional element within a composite material, have been developed since the 1980s. This type of composite material falls into the category of "smart composites."

2.3 Damage detection with fibre optic sensors

Damage monitoring with fibre optic sensors is of intense interest in the field of composite materials, though still at an early state of development. Since the geometrically small types of damage, such as matrix cracks and debonding, are often too small to be detected by quick inspections of composite materials, current design guidelines use design allowable limits so that composites are used in the range where these types of damage do not occur. However, damage tolerant design, which allows such types of damage, is very important to allow composites to be used under a wider range of strain, and hence real-time damage monitoring is an attractive method to assure the health of composite structures. Fibre optic sensors are potentially a very good way to monitor damage initiation and development. Essentially, they are of two types for damage detection: intensity-modulated sensors and interferometric sensors.

2.3.1 Intensity modulated sensors

Sensors based on the fracture of optical fibres are the simplest and cheapest sensors for damage detection. Optical power loss indicates the damage initiation when the

embedded optical fibres are broken due to the external strain (Hale, 1992). This sensing technique is not very sensitive and can only be regarded as the so-called 'final function' of fibre optic sensors.

Micro-bend sensors also depend on optical power loss, this time caused by the local deformation of the optical fibres. For example, Bocherens et al (2000) embedded a network of multi-mode polyimide-coated fibres in a radome sandwich material. Based upon the hypothesis that an impact was able to induce a permanent local bend into the structure and thus on the optical fibre, a technique, optical time domain reflectometry (OTDR), was used. In a basic optical time domain reflectometer, a laser diode launched very short optical pulses into the fibre under test. The light reflected back from the fibre to the optical time domain reflectometer was detected by a fast photodetector. The round trip delay time of the light was related to a specific location of the reflector/back scatter along the fibre. So, taking into account the value of the mean refractive index, distance measurement could be performed. A reference OTDR measurement was made before the impact tests in order to locate any potential defect due to fibre embedding or to composite cure. This state was compared to a second measurement signal after impact. The subtraction between these two signals (before and after the impact) allowed the detection and the accurate location of defects. However, there are some drawbacks of this technique: it does not deal with the detection of impacts in real time and it is only sensitive to permanent damage.

Another application example of an OTDR is the detection of cracks by a 'zig-zag' sensor attached to the surface at the bottom of a concrete bridge deck (Leung, 2001). Before the formation of cracks, the backscattered signal vs. time followed a relatively smooth curve (the upper line in Figure 2.2a). In the straight portions of the fibre, the signal power reduced gradually due to optical absorption and scattering. In the curved portion (where the fibre changes in direction), bending loss might occur depending on the radius of curvature. When a crack opened in the structure, a fibre intersecting the crack at an angle other than 90° had to bend to stay continuous (Figure 2.2a, inset). The sudden bending of an optical fibre at the crack resulted in a sharp drop in the optical signal (Figure 2.2b, lower line). From the time values on the OTDR record corresponding to the sharp signal drops, the location of each crack in the structure could be deduced and from the magnitude of each drop, the crack opening could be

determined. The proposed technique does not require prior knowledge of the crack location. Moreover, a single fibre can be employed to detect and monitor a number of cracks. A good application of the sensor is in the monitoring of flexural cracks in bridges, which may form at arbitrary locations along the deck. However, there are still some shortcomings of this technology. Only cracks that pass the fibre can be detected. An internal crack within the structure that does not reach the surface cannot be found.

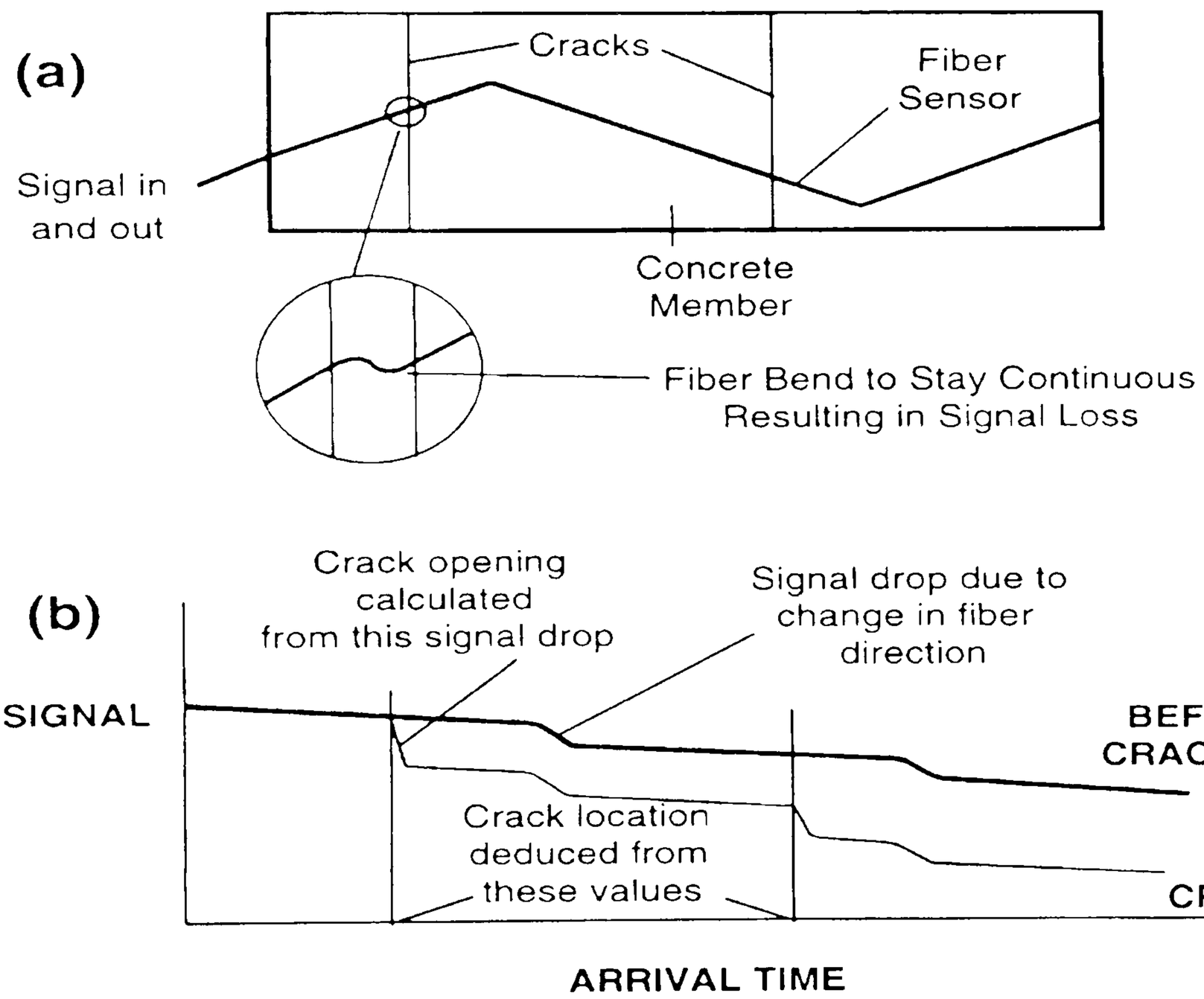

Figure 2.2. Crack detection by OTDR technology, (from Leung, 2001).

Other workers (Badcock and Fernando, 1995; Lee et al, 2001) utilised another type of intensity-based fibre optic sensor. They embedded, or surface mounted, two lengths of optical fibres with a reasonable gap between two cleaved ends. The output intensity changed when the gap changed due to strain in the host and hence damage could be detected. The whole system can be composed of inexpensive components and real-time monitoring, but the sensor is a "point" sensor and it cannot detect damage that has little effect on the distance between two cleaved fibre ends.

2.3.2 Interferometric sensors

Interferometric sensors are usually more sensitive to strains than intensity modulated sensors and can be used to detect damage at a higher sensitivity. There are a large number of sensors based on interferometry: the Michelson interferometric sensors, the Fabry-Perot interferometric sensors, the Bragg grating sensors and the polarimetric sensors. The first three types of sensors have very high sensitivity to axial strain, and they can detect minor changes of stiffness of host material due to damage. The polarimetric sensors can detect damage because they have high transverse strain sensitivity.

Kwon et al (1997) embedded a Michelson interferometric sensor in the 0° ply of a $[90_4/0_4]_s$ cross-ply CFRP laminate which was then tested in four-point bending to determine simultaneously the internal strain and failure points (for example, matrix cracks). When a single-mode optical fibre is deformed, the phase of light propagating in the optical fibre is shifted. The phase shift depends on the three dimensional strains in the optical core. In the case of homogeneous optical fibre, the optical phase shifts linearly with the longitudinal strain in the optical core. The experimental set-up is shown in Figure 2.3. A 2X2 coupler was used to launch the laser light into the sensing fibre and reference fibre. A piezo-electric transducer (PZT sensor) was bonded to the top surface of the laminate as a secondary crack detector and as a trigger so that the fibre optical signal during damage formation could be examined within the first few hundred milliseconds of crack formation. An electric strain gage was attached to the surface of the composite beam to compare the measured strain with the internal strain from the Michelson sensor. The signals from the strain gage, PZT and optical sensors were continuously acquired and stored in a PC. An example of the data is shown in Figure 2.4. Figure 2.4(a) shows top surface strain measured by an electrical strain gage and internal strain (the strain where the fibre optic sensor was embedded) obtained from fibre optical signal is shown in Figure 2.4(b). The sine wave variation of the output optical intensity with increasing strain was disrupted by the formation of matrix cracks. The optical failure signal was obtained by discarding the sinusoidal wave due to static deformation using a digital filter (see Figure 2.4(c)). High pass filtering the optical signal showed that there was almost a one-to-one correlation between the crack formation detected by the PZT sensor and by the filtered optical

signal (see Figure 2.4(c) and 2.4(d)), although the detection of the cracking by the PZT sensor is, of course, another indirect technique. Though this technology can detect damage in real time, the reference fibre, required by interferometric sensors for practical purposes, makes the sensor physically larger and may limit the number of applications.

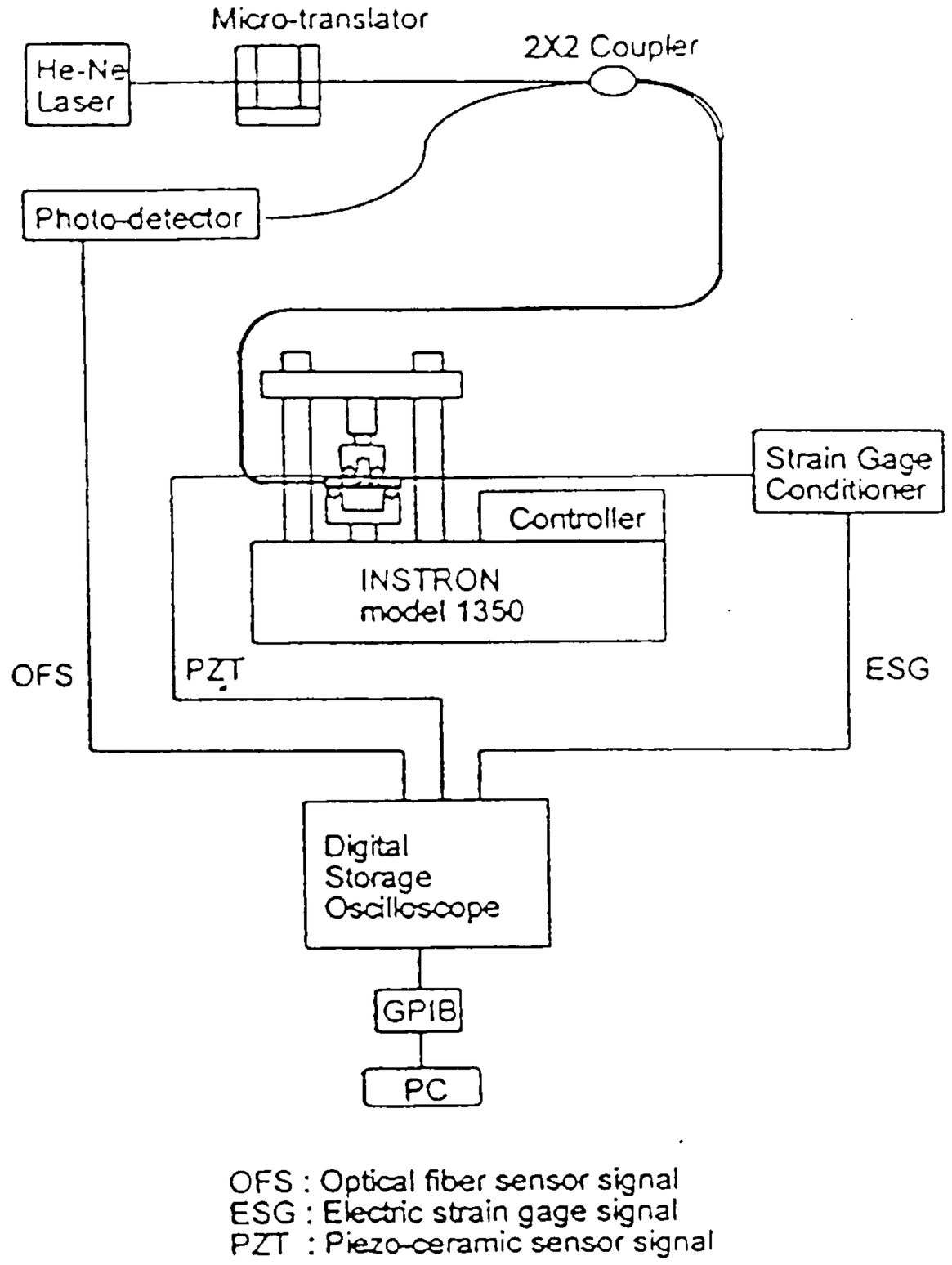

Figure. 2.3 Experimental set-up from Kwon et al (1997) for simultaneous strain measurement and damage detection.

Tsuda et al (1999) used a similar approach to that of Kwon and colleagues. In the work of Tsuda et al, a Michelson interferometric sensor was surface-mounted onto a unidirectionally reinforced CFRP laminate for damage monitoring and an acoustic emission (AE) sensor was used as a second method of damage detection. The laminate was subjected to a quasi-static tensile load parallel to the reinforcing fibres or to an impact test. The authors noted that the interference signal changed discontinuously when there was some kind of damage in the host material, such as matrix cracking and fibre breaking, which was detected by the AE sensor. By examining the frequency component of the optical output, it was concluded that the

high-frequency interference signal with high amplitude occurred when the monitored material was damaged. Using a high pass digital filter, the damage signal from the sensor was extracted and this signal with high intensity showed a good agreement with damage events detected using the AE method.

EFPI (extrinsic Fabry-Perot interferometer) sensors are also used in damage detection (Levin et al, 1997; Chang et al, 1998; Hong et al, 2001). The sensor consists of a hollow glass tube capped over the end of a single mode input/output fibre, as shown in Figure 2.5(a). A gold coated fibre, placed inside the glass tube facing the single-mode fibre, functions as a Fresnel reflector and forms an air gap that acts as a low-finesse EFPI cavity. The first reflection at the glass-air interface acts as the reference reflection signal for the interferometer. The second reflection from the surface of the gold deposited mirror generates the sensing reflection signal. These two form an interferometer and the phase change of the optical output is proportional to the change of the air cavity length. In a similar way to Tusda et al (1999), Hong et al (2001) monitored the frequency change of the optical output. It was found that when impact or excessive loads were applied to the composite structure, if no damage happened, only a sensor signal below the frequency range of 20 kHz could be seen. However, for the case of structural failure, stress wave emission induced by matrix cracks or reinforcing fibre breakage could be observed in the 20 kHz-200 kHz frequency range. Hong et al (2001) embedded an EFPI sensor (see Figure 2.5(a)) into a cross-ply laminate and launched laser light from a laser diode source into it. Using some advanced signal processing tools, such as Short Time Fourier Transform (STFT) and Wavelet Transform (WT), a time-frequency analysis of the optical output was carried out to identify the moment of damage (see Figure 2.5(c) for matrix cracking detection and fibre breakage detection). In Figure 2.5(c), S shows the raw sensor signal, the details D1, D2 and D3 represent approximately 200 kHz, 100-200 kHz and 1-100 kHz signal range respectively. Damage information is shown in the D1-D3 high frequency components, especially in the D2 and D3 frequency range. Based on the experimental results, a frequency threshold of 25 kHz was set in the real-time failure detection system (see Figure 2.5(b)). This, it was claimed, was the first real-time damage detection system available for an engineering application. A serious disadvantage is that the sensor system is a localised one, which means cracks or damage cannot be far away for the EFPI sensor.

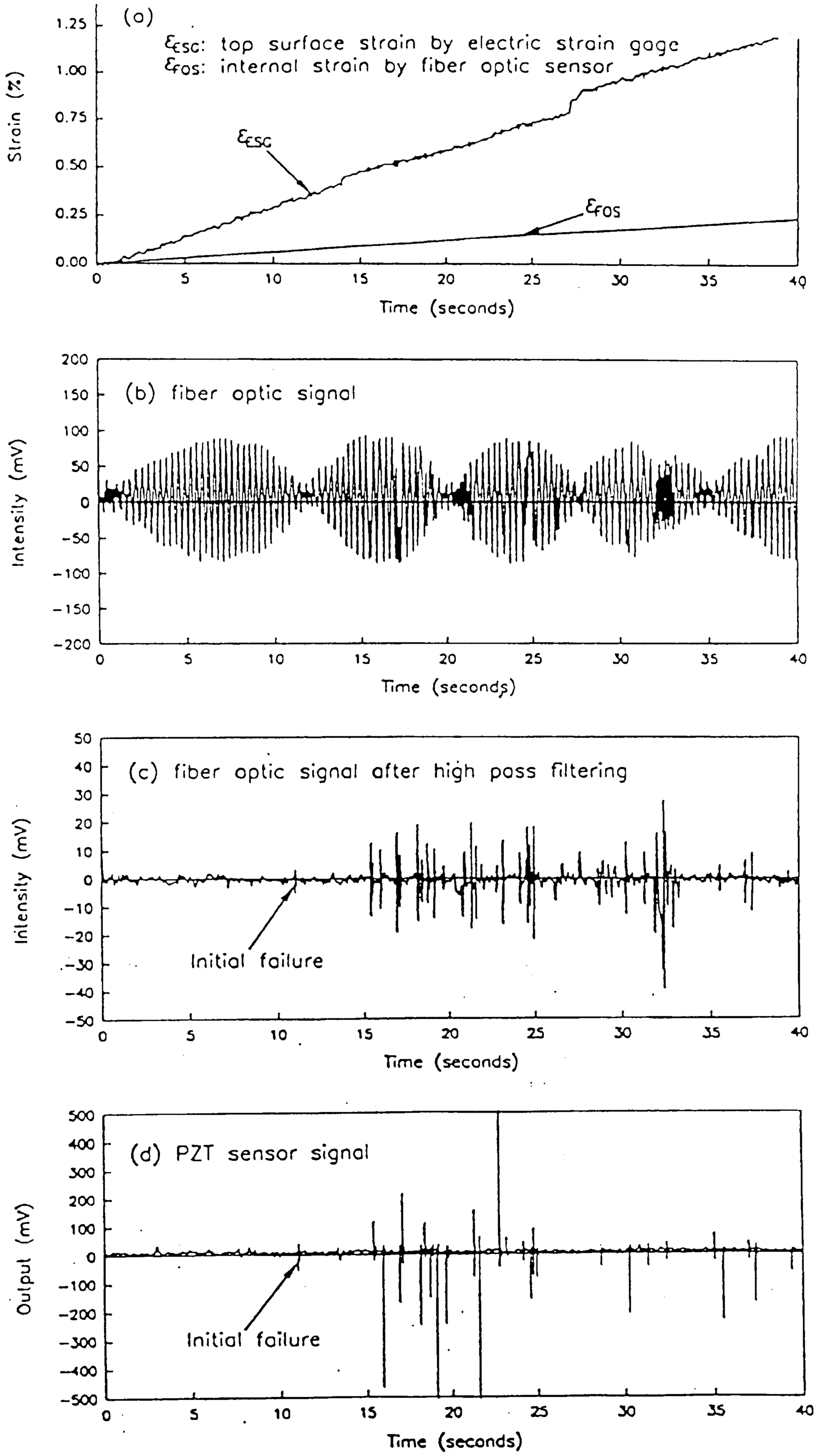

Figure 2.4 Experimental results using strain gages, fibre optic and PZT sensors (from Kwon et al, 1997).

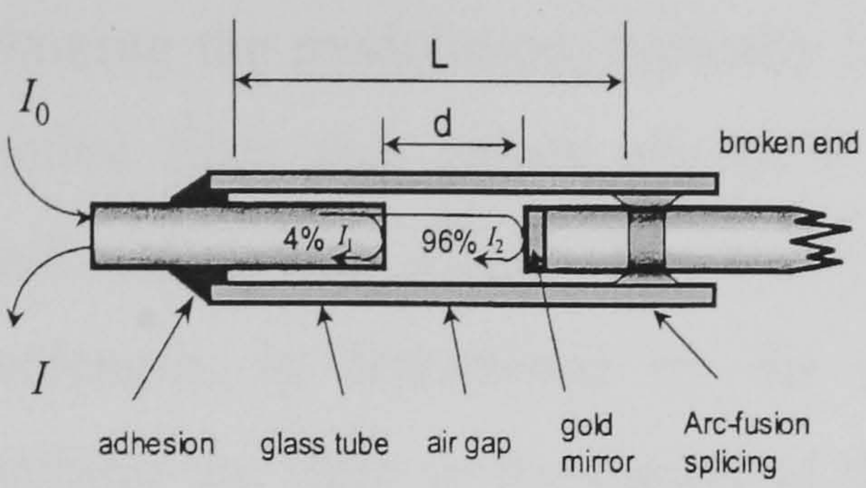

a. Schematic diagram of EFPI sensor

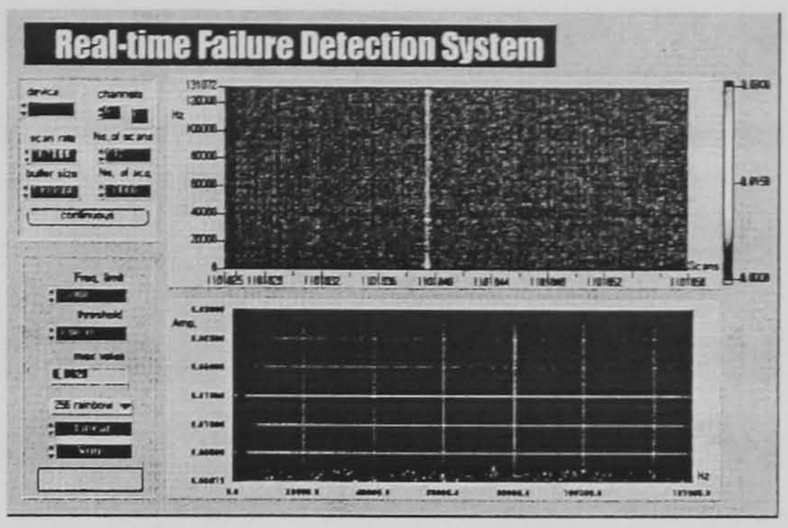

Matrix cracking

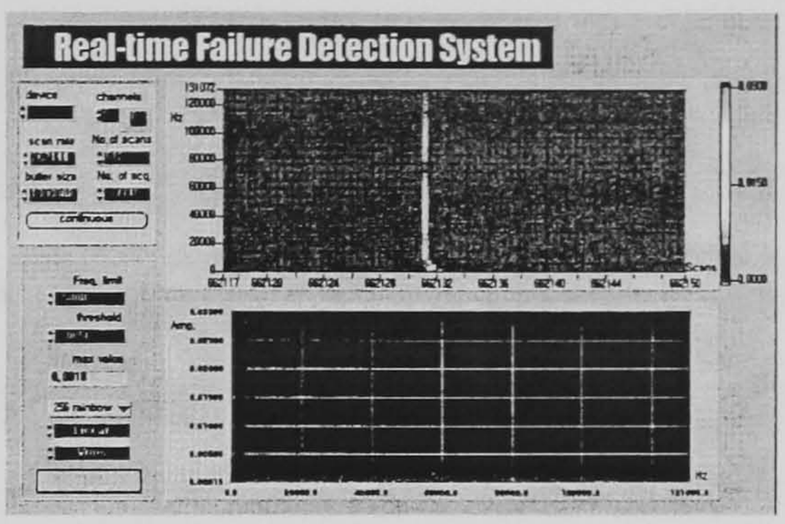

Fiber breakage

b. failure signal detected by real-time failure detection system

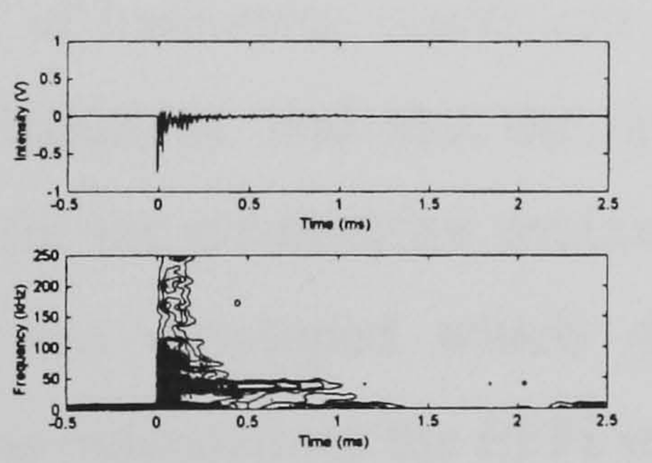

Short Time Fourier Transform

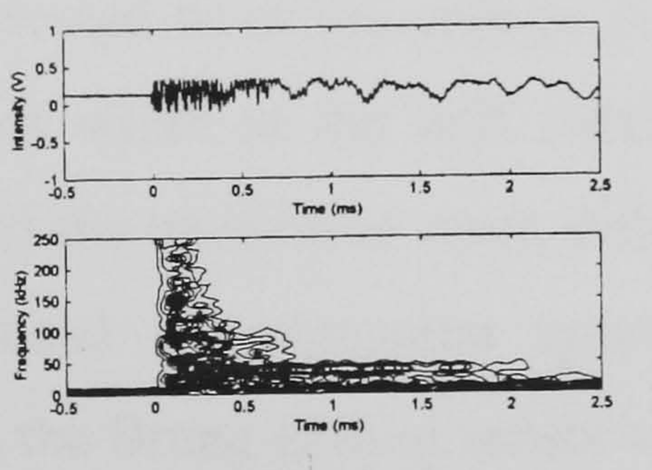

Short Time Fourier Transform

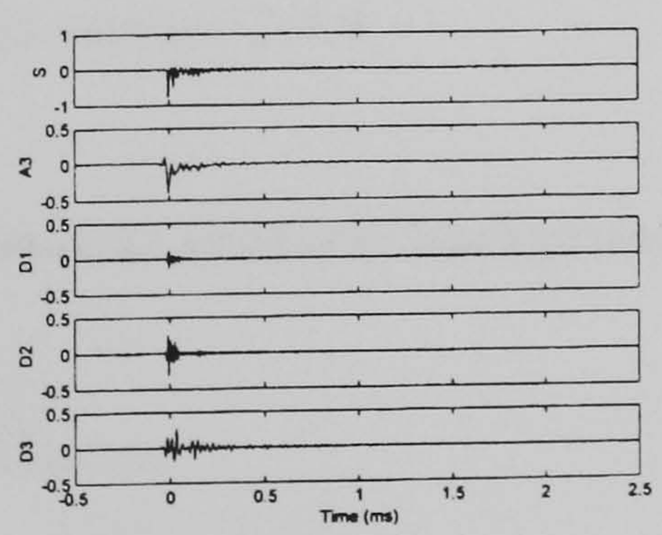

Wavelet Transform

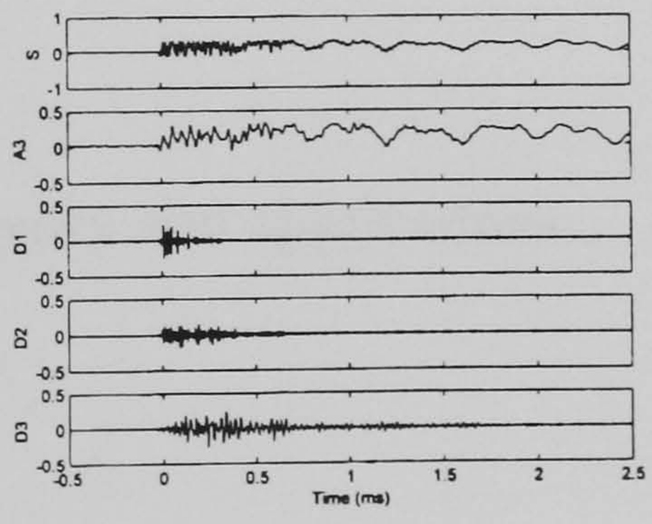

Wavelet Transform

c. Matric cracking signal by EFPI and its STFT and WT

d. Fibre fracture signal by EFPI and its STFT and WT

Figure 2.5 Experimental setup and results using an EFPI sensor for damage detection, from Hong et al (2001).

The Bragg grating sensor, which is currently the subject of intense research. has also been used to detect damage in composite materials. A fibre Bragg grating is a periodic modulation of the index of refraction in the core of an optical fibre. The region containing the modulation, typically limited in length to a centimetre or less, acts as selective filter that passes all but a narrow band of light when illuminated by a broadband optical source. The centre wavelength of the reflected band, the Bragg wavelength, is determined by the periodicity of the modulation. Since axially stretching the fibre in the region of the modulation affects the periodicity, the fibre grating lends itself naturally to strain or temperature sensing as the Bragg wavelength shifts linearly with the applied axial strain. The Bragg grating sensor is one of the candidates for damage detection because they are very sensitive to non-uniform strain distribution along the entire length of the gratings as well. Yoji et al (2000) embedded an uncoated, small diameter Bragg grating sensor at the 0/90 interface of a cross-ply laminate to detect cracks developed in the 90° ply. The results showed that the occurrence of transverse cracks can be detected from the change in the form of the reflection spectrum, and that the spectrum width at the half maximum is a good parameter for the quantitative evaluation of the transverse crack density in real time. A model was developed which reproduced the measured spectrum very well. However, as indicated for the EFPI sensor, the Bragg grating sensor is a 'point' sensor, e.g. it only has a sensing length equivalent to its length which is normally 10 mm.

A sensor with a much longer length capable of monitoring damage can be obtained employing a polarimetric sensor. Damage detection with polarimetric sensors will be discussed in section 2.4.4.

2.4 Polarimetric sensors: background theory and applications

2.4.1 Introduction

Basically, the operation of polarimetric sensors falls into two categories. In the first, changes in a physical field alter the birefringence in the fibre core directly or indirectly (for example, a free sensor under thermal stress or an embedded sensor under strain). In the second, a physical field changes the polarisation state in the fibre directly (examples are electrical current sensors (Lee et al, 1998), or magnetic field

sensors (Rashleigh, 1981)). The polarimetric sensor used in these experiments falls into the first category.

The basic structure of an optical fibre contains three parts: coating, cladding and core. The refractive index of the optical core is higher than that of the cladding so that the light launched into the core can be maintained within the core. The core and the cladding are usually made of silica glass and are very vulnerable. They are protected by the coating. A well-controlled state of polarisation of the light along the fibre path can be obtained by adding Stress Applying Parts (SAP) into the cladding of single mode fibres. Based on the stress applied to the core, the fibres are divided into Hi-Bi fibres and Lo-Bi fibres. In addition, the shape of the SAP determines whether the Hi-Bi fibres are classified as Bow-tie fibres, Panda fibres, side-pit fibres, etc. Figure 2.6 shows a Panda fibre embedded in a cross-ply composite coupon. As a consequence of the birefringence induced by the SAP, two orthogonal polarisation modes are produced in the fibre that propagate at different velocities. The phase shift between these two orthogonal polarisation modes can be easily influenced by the physical field. Hence, the external disturbance can be calculated from the optical output (Rashleigh, 1983). This is the basis of the polarimetric sensor.

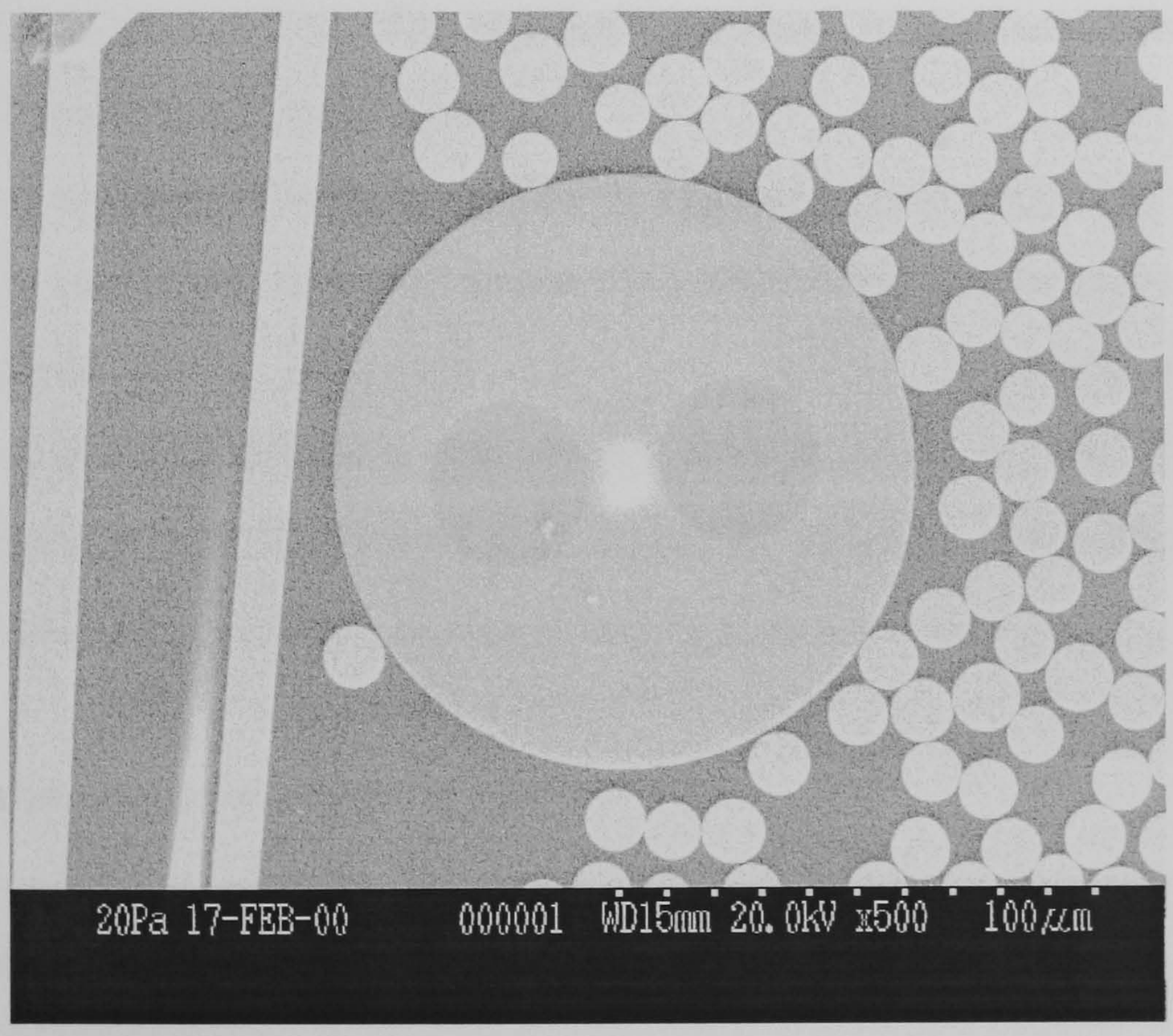

Figure 2.6 A cross-section image of a Panda fibre embedded in a cross-ply composite coupon (Barton, 2000).

Compared to other types of fibre optic sensors available, the fibre optic polarimetric sensor (FOPS) has its own unique advantages. Such a sensor typically employs a single high-birefringence fibre for detection and provides information on the integrated effect over the sensing region. Thus a single sensor covering the area of interest can be used for global health monitoring. Other advantages of FOPS are:

1. Compared with 'point sensors', the Hi-Bi fibre is sensitive to perturbations over its entire length. So data from damage at various sites can be recorded. This gives a better indication of damage than conventional point-based sensors.
2. They can be surface mounted or internally embedded in the structures and no reference fibre is needed, hence, the polarimetric sensor can have minimum effect on the structures.
3. Compared with the Michelson or EFPI sensor, the polarimetric sensor has a simpler configuration.

Polarimetric sensors also have some disadvantages:

1. The sensitivity of a polarimetric sensor is about a factor of 100 lower than a standard interferometric sensor which is based on the change of light path (Hadjiprocopiou et al, 1996). The reduced sensitivity of the sensor makes it less suitable for 'point' strain measurement.
2. A number of external disturbances (like change of temperature) can change the birefringence inside the core and hence the polarimetric sensor can be prone to both transverse strain sensitivity error and thermal apparent strain error (Rashleigh, 1983). Sometimes this makes interpretation of the experimental results difficult; indeed, the sensor is often better suited to measuring transverse strains than axial strains due to its high transverse strain sensitivity.

2.4.2 Configurations of polarimetric sensors

The configuration of polarimetric sensors can be divided into two types: non-localised and localised.

2.4.2.1 Non-localised polarimetric sensor

An example of a non-localised polarimetric sensor is shown in figure 2.7. Circularly polarised laser light (or lineally polarised light) is launched into the core to excite the orthogonal modes of the fibre equally. External perturbation of interest (e.g., strain, temperature, pressure, etc.) will change the birefringence of the core and the phase difference of the two polarisation modes propagating inside the core. The light output from the fibre passes through a Polarisation Beam Splitter (PBS) that separates the output beam into two beams with orthogonal polarisation. The output powers (intensities) detected by the photodetectors are sine square functions of birefringence.

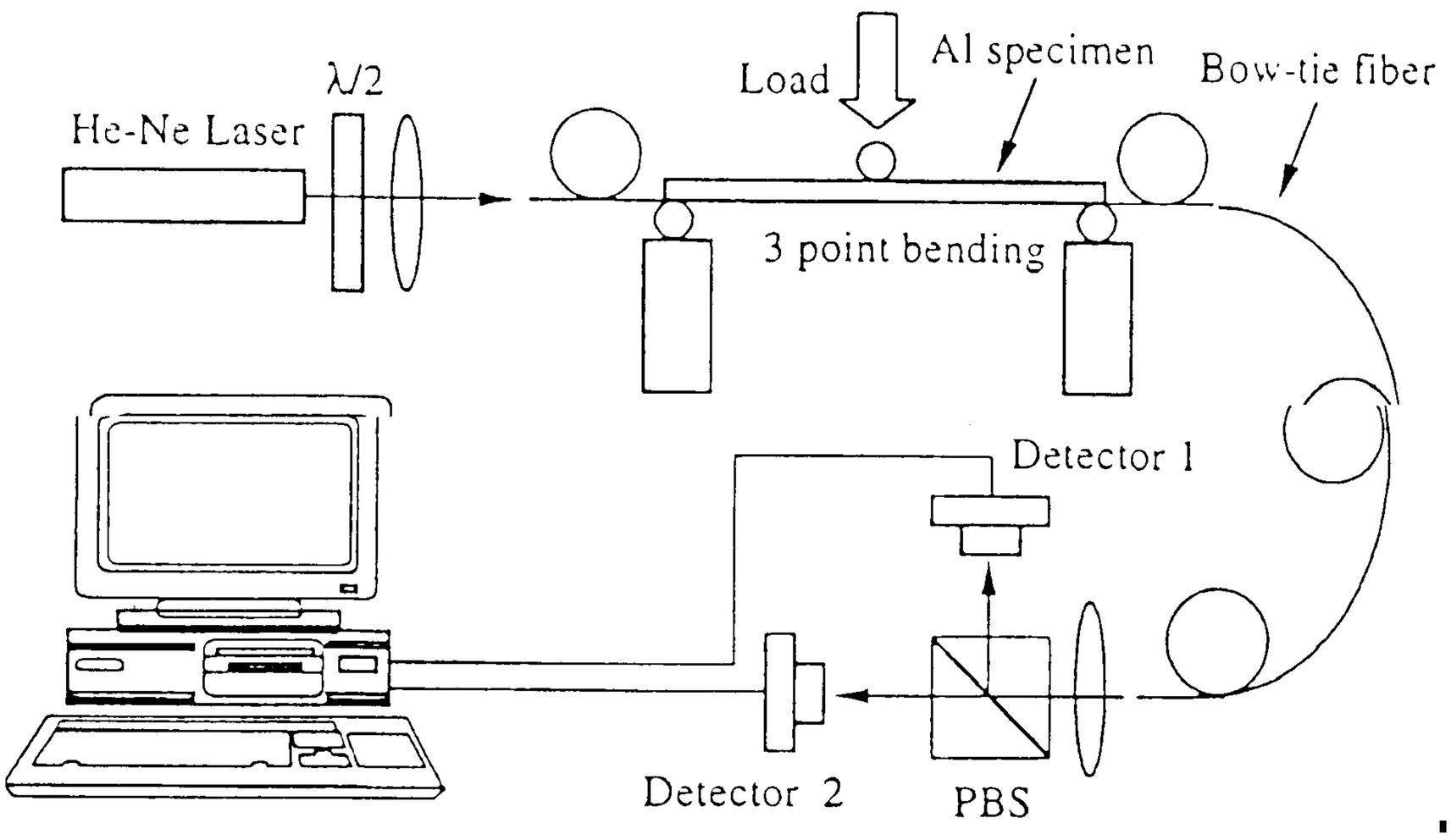

Figure 2.7 An example of experimental setup of non-localized polarimetric sensors (Ma et al. 2001).

The advantage of this type of configuration is that the complicated splicing of the fibre is avoided. A disadvantage is that all of the fibre is subject to external disturbance, especially the lead-in point and lead-out point where the external field is not homogenous when the sensor is embedded. This may make understanding of the results problematic.

2.4.2.2 Localised polarimetric sensor

In the localised polarimetric strain sensor, a restricted region along a Hi-Bi fibre is made strain sensitive. The sensors can have two 45° splices (transmissive) or one 45°

splice and an end mirror (reflective), as shown in Figure 2.8. In Figure 2.8(a), linearly polarised light is launched into one axis of the fibre. At the first 45° splice. the incoming light splits and excites both modes equally. At the second 45° splice, the two modes rejoin and interfere with each other. In Figure 2.8(b), polarised light is reflected back from the mirror end and the gauge length is double the distance between the 45° fusion splice and the mirror end. In this configuration, only one 45° splice is need, but an optical coupler is also needed. By eliminating one of the modes with a polariser or bending the lead-out fibre (Varnham and Payne, 1984), fringes due to the external disturbance can be seen.

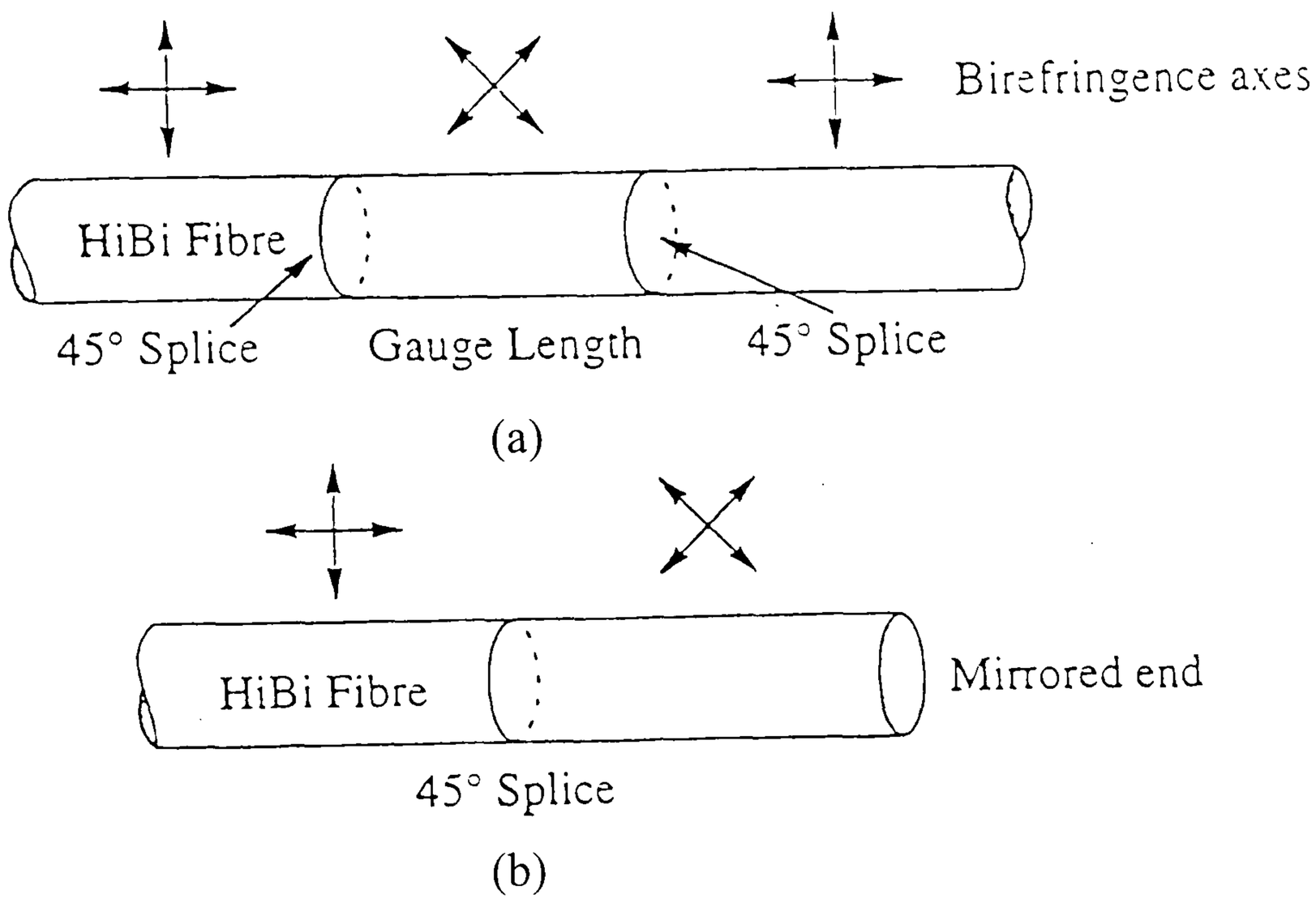

Figure 2.8 Schematic diagram of localised polarimetric sensor.
(a) transmissive and (b) reflective

A practical experimental polarimetric sensor arrangement using the configuration shown in Figure 2.8(b) is shown in Figure 2.9.

The localised polarimetric sensor incorporates 45° splices, which require special equipment to produce. The advantage of the configuration is that information over a desired length can be obtained.

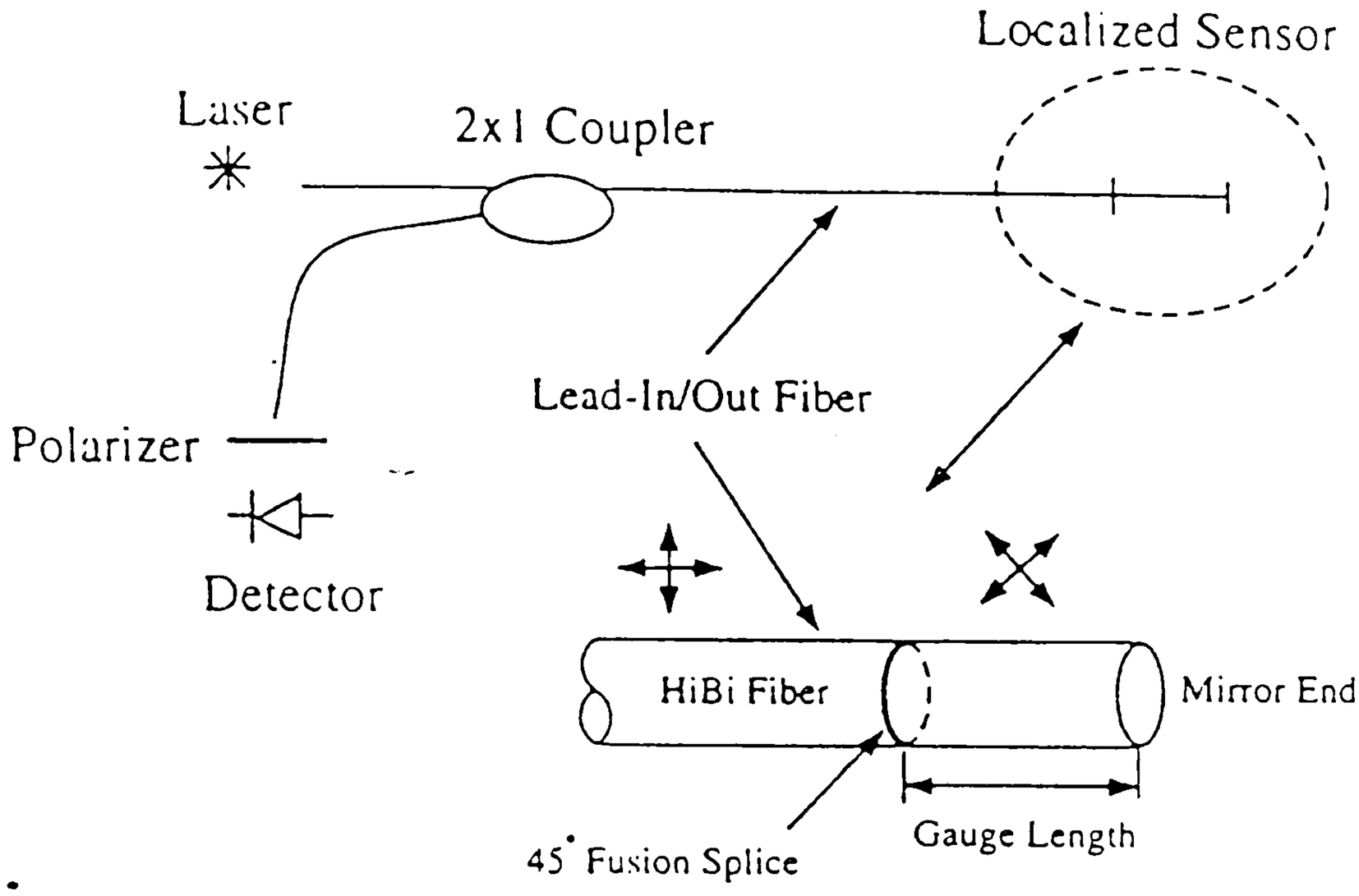

Figure 2.9 Experimental setup of a localised polarimetric sensor, Lo et al (1995).

2.4.3 Theoretical model for polarimetric sensors

For all fibre optical sensors, including polarimetric sensors, analysis of the optical output from a fibre optic sensor involves one basic question: what is the sensor actually measuring? The answer to this question falls into two parts.

The first part needs to relate the mechanical state in the host to that in the optical core. If the sensor is free or surface mounted, there is no complex interaction between the sensor and the host material and the answer is relatively straightforward. If the sensor is embedded into the host material with or without a coating, it is much more complicated. Some workers (Pak et al, 1992; Liu et al , 1993; Yuan et al, 1998) have tried to solve the problem. All the results show that the strain in the core is not the same as in the host. For example, Graham et al (2000) pointed out that sharp, narrow, strain 'spikes' due to structural imperfections in host materials (represented by $\varepsilon_z^m(R,z)$)are poorly transferred to the fibre sensor core (where the strain field is represented by $\varepsilon_z^f(r_f,z)$ in Figure 2.10. A sensor in a generally orthotropic material presents an even greater degree of complexity. For this problem, Kollar and Steenkiste (1998) have developed closed form expressions that relate the strains

inside an orthotropic material to the strains inside the sensor based on elasticity theory.

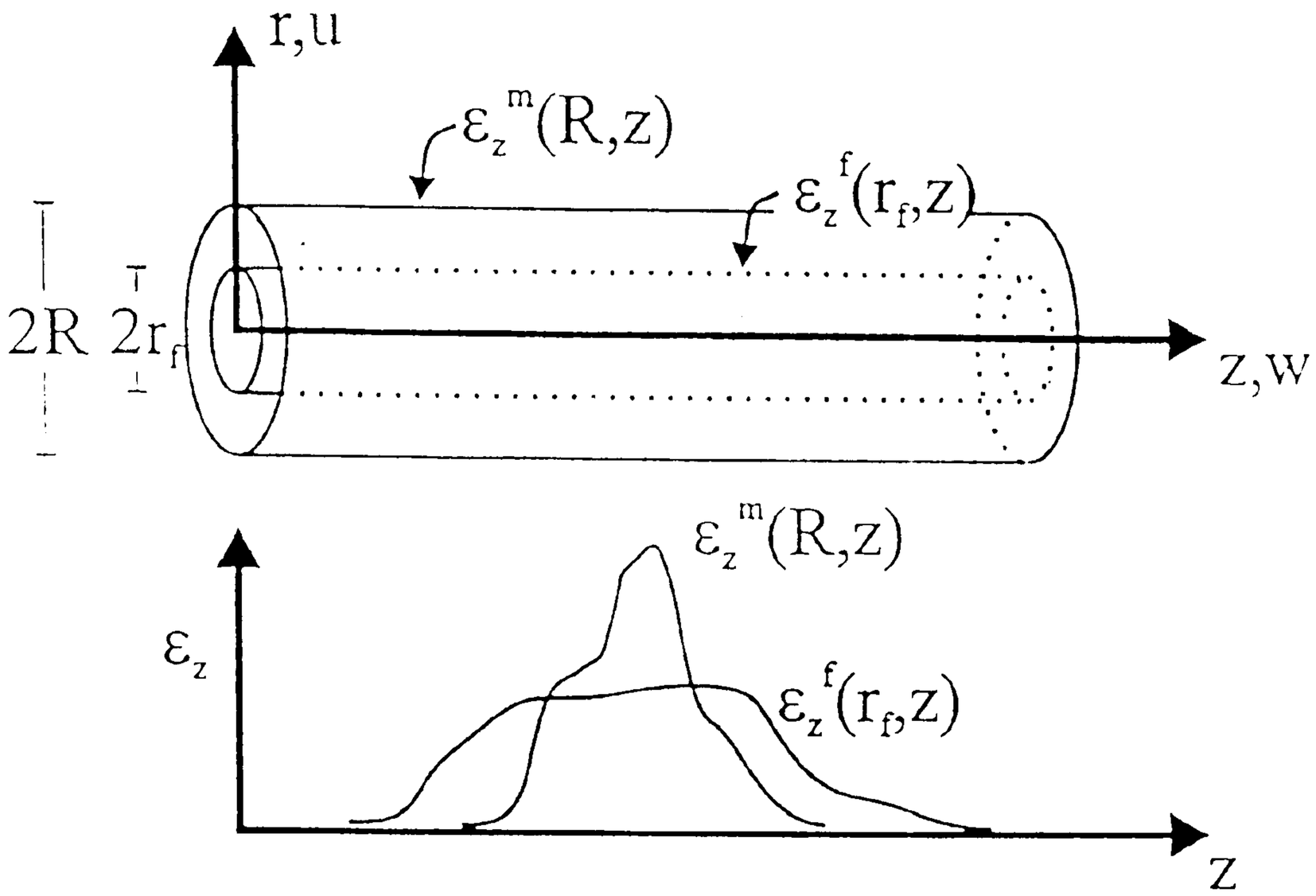

Figure 2.10 Strain transfer from host to sensor, Graham et al (2000).

The second part of the answer to the question about what sensors actually measure needs to relate the strain in the optical fibre to the physical quantity recorded, such as optical intensity. When the sensor is free or surface mounted, Butter and Hocker's model (1978) provides a solution to the problem. The strain in the optical fibre changes the refractive index of the fibre by the strain-optical effect. The change of refractive index (and light path) changes the relative phase of coherent light propagating inside the core. In an interferometric sensor, when the light in the sensing fibre interferes with the optical output from a reference fibre, fringes can be seen. As polarimetric sensors use high birefringence fibres (or low birefringence fibres) which have two orthogonal optical axes, the light in the two modes can be made to interfere with each other, so no reference fibre is needed.

However, when polarimetric sensors are embedded in a host, there is a complex interaction between host and sensor. Sirkis et al (Sirkis, 1993; Sirkis and Lo et al, 1994) developed a phase-strain-temperature model for polarimetric sensors based on the assumption that a set of residual strains exist in the fibre core and that these strains

lead to a residual state of birefringence. The primary strain state (transferred from the host material) inside the core changes the refractive index via the strain-optical effect, thus changing the phase of light in the core. This model has been used successfully for a number of different cases (Barry and Huang, 1998; Lo et al, 1995).

The model above does not consider the effect of shear around the core. Another model, by Calero et al (1994), describes the effect of shear force around the core. In this model, the birefringence axes of the core are not only determined by the host material properties, geometry and boundary conditions on the fibre, but also by the original birefringence properties of the fibre. When the optical birefringence axes are not aligned with the mechanical principal axes in the host, a shear strain will be present, causing the original birefringence axis to rotate. In their paper, Calero et al showed that Sirkis's model is one of the special cases when the optical axes and mechanical primary axis are aligned. However, the Calero et al model was developed for the special case when embedded sensors are under compression and no universal relationship between strain and optical output was given, as in the Sirkis' model.

2.4.4 Applications of polarimetric sensors

Polarimetric sensors can detect various physical fields, for example temperature (Rasmussen and Scholl, 1997), strain (Asundi et al, 1998) and pressure (Passy et al, 1992; Norbert et al, 1998). The sensitivities of some types of Hi-Bi fibres are listed in Table 2.1 (Domanski et al, 1994). The sensitivities are expressed in terms of a phase shift per unit length of fibre, for either temperature or pressure.

Table 2.1. Temperature and pressure sensitivities of HB fibres (Domansi et al, 1994)

	York HB	Andrew E-type	Side hole	Panda	3M HB
Wave length (nm)	820	820	820	633	633
Temperature sensitivity (rad/°C·m)	-4.75	-0.97	-0.5	-5.23	-2.83
Pressure sensitivity (rad/MPa·m)	9.23	0.65	-34	9.5	4.8

For temperature measurements, Rasmussen and Scholl (1997) coiled a single-mode fibre on a cylindrical former with a high thermal expansion coefficient. The birefringence introduced by bending and stress was a function of temperature and a temperature change of 0.006 K could be detected using the sensor.

When polarimetric sensors are employed to detect other physical fields, thermal drift is unwanted and there are several methods to desensitise the polarimetric sensor to temperature.

The first method is to introduce a reference fibre that is free of thermal disturbance, when it is practically possible.

The second method is to build a novel configuration of sensor that is intrinsically temperature stable, as devised by Wong and Poole (1992). They introduced a new fibre structure which gives zero stress birefringence, by balancing the stresses generated in the core of an elliptical-core fibre with stresses generated by the inclusion of stress-applying sectors in the cladding. A temperature sensitivity as small as 0.0025 rad/°C/cm, over a range of 30°C-210°C, was obtained in this way.

The third method is to introduce additional birefringence. Based on the Johns matrices formalism (Johns, 1941), a simple temperature compensation can be introduced (Bock et al, 1989). An additional section of the Hi-Bi fibre is added so that the reference and sensing fibres should have the same length but their birefringence axes are crossed, i.e. the fast axis of the sensing section should be aligned with slow axis of the reference section. Provided that both sections are at the same temperature, the phase shift caused by the different velocity of light components in the modes of the reference section (caused by a temperature change) is compensated by an opposite phase shift in the sensing section. The structure of the sensor is shown in Figure 2.11. Experimental results without the reference section (solid diamonds) show the expected sinusoidal output with increasing temperature. When the reference section is added, the temperature sensitivity is reduced (open squares).

The sensitivity of a polarimetric sensor under a diametrical load changes with the

relative angle between the load direction and the primary optical axes in the fibre (Lo and Sirkis, 1995). Even so, some other researchers have used polarimetric sensors to measure pressure. For example, Bock et al (1990) showed that polarimetric sensors could be used at depth in the sea to measure high hydrostatic pressure and Ansari et al (1995) used a polarimetric sensor to measure the magnitude of dynamic compressive loads.

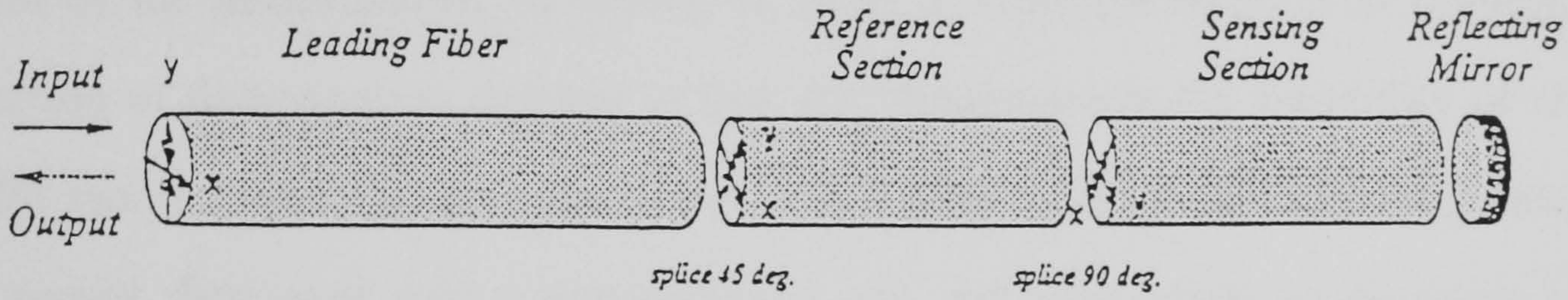

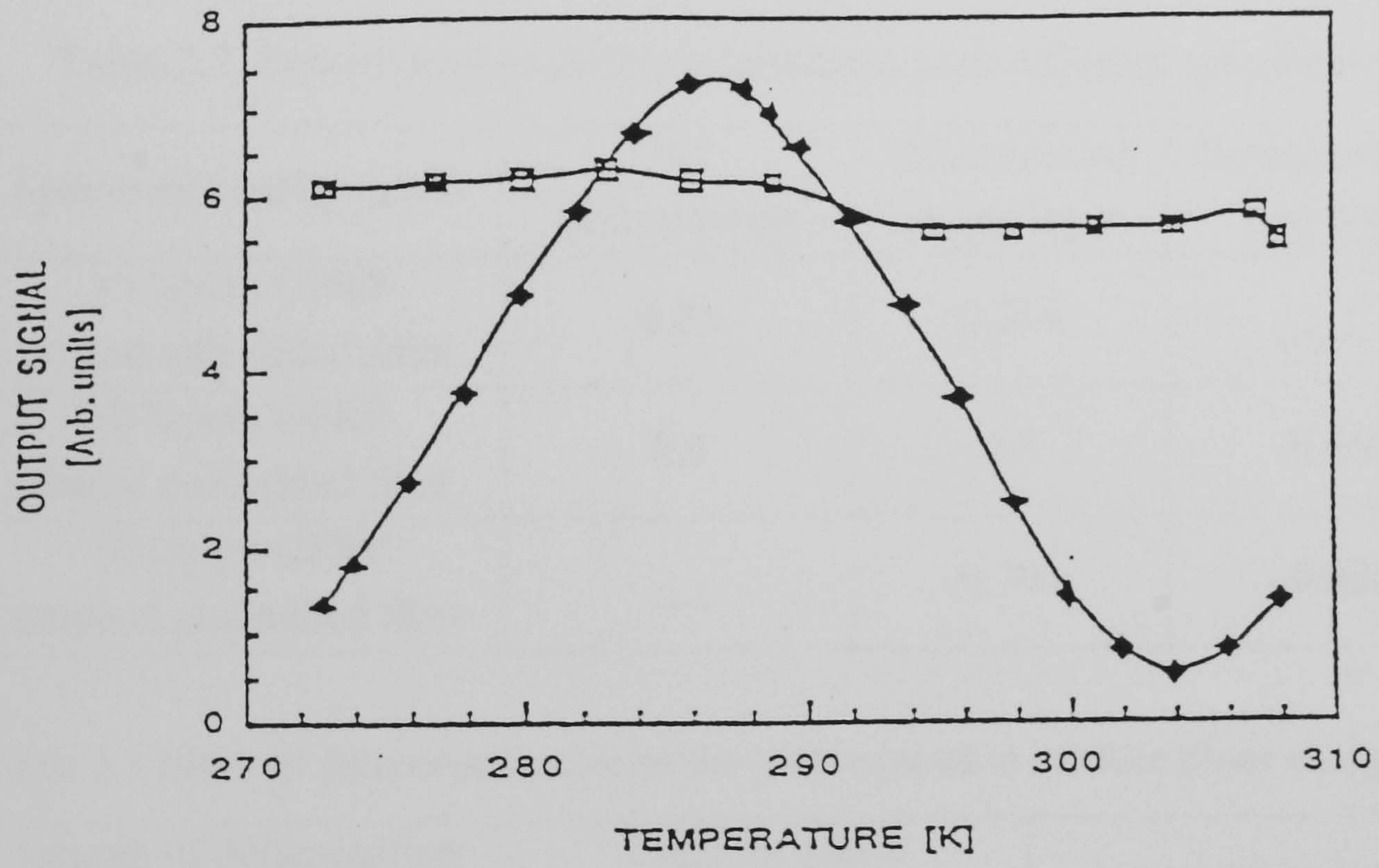

Figure 2.11 Temperature compensation scheme of a polarimetric sensor in a reflective configuration and experiment results (Bock et al, 1989).

Polarimetric sensors used to measure strain either surface mounted (Hadjiprocopiou et al, 1995) or embedded (Barry and Huang, 1998, Sirkis and Lo, 1994), can be traced back to Rashleigh (1983). Based on the change of strain sensitivity, Asundi et al (1996), Murukeshan et al (2000), Ma et al (2001) have used polarimetric sensors for global health/damage detection. They showed that by monitoring the sensor

sensitivity, it is possible to predict the amount of structural damage, as shown in Table 2.2 (Asundi, 1998). In the table, the sensitivities of the sensor reduce with the introduction of delaminations and the extent of the delaminations. The change in sensitivity was attributed to the fact that there was a change in the properties of composite material, such as flexural stiffness due to the presence of delamination. They also suggested that the change in sensitivity of the sensor could be related to the extent of the delamination, as shown in Table 2.3 (Murukeshan et al (1999)). The detection of delamination damage in this way demonstrates the feasibility of on-line health monitoring of composites using such a sensor, although the configuration of the sensor they used was a non-localised one and care needs to be taken in the interpretation of the results.

Table 2.2. Sensitivities of different laminates with different specifications

Specimen configuration	No delamination	Delamination in one layer	Delamination in two layers
10 layers CFRP coated embedded fibre	0.25	0.214	—
10 layers GFRP coated embedded fibre	0.6	0.5	0.462
10 layers GFRP stripped embedded fibre	—	0.795	0.625

Table 2.3 Effect of delamination size on the load required to produce phase change of π

Length of delamination (mm)	Load for phase change of π (kg)	% reduction in load
0	37.3	0.00
10	31.6	16.18
20	29.2	22.55
30	26.9	28.65

Barton et al (2000, 2001) attempted to detect the fatigue growth of transverse cracks in cross-ply laminates based on the high transverse strain sensitivity of the polarimetric sensor. Due to the transparent nature of the glass fibre reinforced laminate, it was possible to observe the propagation of the cracks and their interaction

with the sensor. When the cracks passed the sensor, a dramatic change of the optical output was observed and with the aid of a Fast Fourier Transform, which can be used to help to pick out signals within a particular frequency range, a connection was made between signal changes and the growth of a crack passing the sensor. However, although a number of examples of this change in signal were found, insufficient data was collected to establish this technique for fatigue crack detection. In addition, the detection of cracks in quasi-static loading was not investigated and there was an incomplete understanding of the behaviour of the sensor.

2.5 Conclusions

Based on the literature review the following conclusions have been reached:

Composite damage detection technology using fibre optic sensors has great engineering value and is the subject of intense research. The Michelson sensor, EFPI sensor, the Bragg grating sensor, the polarimetric sensor and some optical intensity modulated sensors, have all been used to detect damage in composite structures. Based on their ultra high sensitivity, the Michelson sensor, the EFPI sensor and the Bragg grating sensor can detect the minor stiffness changes or stress waves in the host structure caused by damage, as shown by the authors. However, as the Michelson sensor is a two-fibre interferometer, and the Bragg grating sensor and the EFPI sensor are 'point' sensors, these natural shortcomings may inhibit their practical applications.

Compared with other types of fibre optic sensor, polarimetric sensors are less sensitive and are prone to transverse strain and thermal stress error, but they are simply configured and no reference fibres are needed. Most useful of all, the sensors are integrating sensors, and they can detect the external disturbances along the fibre or between the 45° splices, which means that the sensors have great potential to detect damage, such as transverse cracks, in composite structures, whether small or large.

The aim of this thesis is to show that transverse cracks in composite laminates can be detected in tensile loading using a polarimetric sensor embedded at the 0/90 interface of a cross-ply laminate. This literature review has highlighted some important areas to study. It is necessary to provide a better understanding, both theoretically and

experimentally, of the behaviour of polarimetric sensors embedded in composite laminates so that the question of the interaction between the sensor and matrix cracking damage can be addressed. The literature review has also shown that it would be valuable to establish an unambiguous relationship between the occurrence of matrix cracks and changes in optical output and this can be achieved using transparent GFRP coupons.

In the next chapter, various background theories relevant to the work in this thesis are presented, including polarimetric fibre optics, crack propagation in cross-ply laminates and the interaction between the embedded sensor and the host material.

Chapter 3. Relevant Background Theories

3.1 Introduction

The topics in this chapter have been included to briefly introduce and review most of the background theory which is relevant to this work, specifically: polarisation optics, polarimetric sensors and matrix cracking in a cross-ply laminate. The descriptions included here are intended to provide a summary of the various topics mentioned, and not to cover all the theoretical background in detail. The full development of the theories can be found in the references to the source literature given in the course of this chapter.

The first section, section 3.2, gives an overall introduction to fibre optic sensor. This is followed by an introduction to Hi-Bi fibre (Section 3.3) and a theoretical model of the polarimetric sensor (Section 3.4). The strain state around an embedded sensor is described in Section 3.5. Finally there is an introduction to matrix crack propagation in cross-ply laminates in section 3.6.

3.2 An introduction to fibre optic sensors

Fibre optic sensors are essentially a means whereby light guided within an optical fibre can be modified in response to an external physical, chemical, biological, biomedical or similar influence. Light from an optical source is launched into a fibre via a stable coupling mechanism and guided to the point at which the measurement is to take place. At this point either the light can be allowed to exit the fibre and be modulated in a separate zone before being re-launched into either the same or a different fibre - these are called extrinsic sensors - or the light can continue within the fibre and be modulated in response to the measurand whilst still being guided - these are known as intrinsic sensors.

The fact that the fibre itself can respond to an external influence immediately indicates that the lead-in and lead-out optical fibre may also be accidentally responsive to external influences. This gives rise to the possibility for interference with the sensed signal along the fibre path. The need for lead (lead-in and lead-out) insensitivity and transmission line neutrality is an important prerequisite for a practical sensor. An optical sensor system must be carefully designed to meet this demand.

The final detected output from fibre optic sensors is influenced by many parameters along the way and it is important to analysis how these arise. In general, the detected signal can be represented as follows (Dakin et al, 1988):

Electrical output = SP * D * FT * M * Q * FR * S

where SP represents the operations performed by signal processing within the detection electronics, D represents the signal generated by the photodetector in response to the optical input to the detector, FT represents the transmission function of the fibre linking the sensor to the detector, M represents the modulation function applied to the optical signal as it passes through the modulator, Q represents the quantity to be measured as interpreted through the modulation characteristics of the modulator, FR represents the transmission function of the fibre linking the source to the modulator and S represents the output from the source itself coupled to the fibre.

Accordingly, the optical sensor system should have the following components:

- modulators: the means by which light can be modulated in response to the physical measurands;
- optical sources for sensors;
- optical signal detector system;
- the optical fibres that link different components of the system;

- fibre optic components such as lens, 1/4λ plate, etc;
- a signal processing system.

3.3 An introduction to the polarisation-maintaining fibre

3.3.1 Polarisation optics

Light is a transverse electromagnetic wave but only cases where the electric field vector resides in a fixed plane are considered here. This plane is referred to as the plane of vibration and the light is said to be plane polarised or simply referred to as p-state light. The following section describes the superposition of the orthogonal plane polarised light waves of the same frequency. Consider two perpendicular harmonic optical fields given by:

$$\begin{aligned} E_x(z,t) &= E_{0x}\cos(kz-\omega t) \\ \hat{E}_y(z,t) &= E_{0y}\cos(kz-\omega t+\varepsilon) \end{aligned} \qquad 3.1$$

where E is the electric amplitude vector, k is propagation number and ω is the angular frequency. The waves move in the positive z-direction and have a relative phase difference ε. The plane of vibration of $E_x(z, t)$ corresponds to the xz-plane, while $E_y(z, t)$ resides in the yz-plane. The resulting disturbance varies with ε and is given by:

$$\hat{E}(z,t) = \hat{E}_x(z,t) + \hat{E}_y(z,t) \qquad 3.2$$

In the specific instance when $\varepsilon = m\cdot\pi$ $(m=0, \pm1, \pm2, \ldots)$, the resulting wave is linearly polarised light. When $\varepsilon = m\cdot\pi + \pi/2$ $(m=0, \pm1, \pm2, \ldots)$ and $E_{0x}=E_{0y}$, the resultant is circularly polarised light. A schematic demonstration of linearly and circularly polarised light is shown in Figure 3.1(a) and Figure 3.1(b). A more general superposition yields elliptical light where the endpoint of the field vector sweeps out

an ellipse as E changes in magnitude and direction. After some manipulation of the equations above to remove the explicit dependence on $(kz-\omega t)$, we get:

$$(\frac{E_y}{E_{0y}})^2 + (\frac{E_x}{E_{0x}})^2 - 2(\frac{E_y}{E_{0y}})(\frac{E_x}{E_{0x}})\cos\varepsilon = \sin^2\varepsilon \qquad 3.3$$

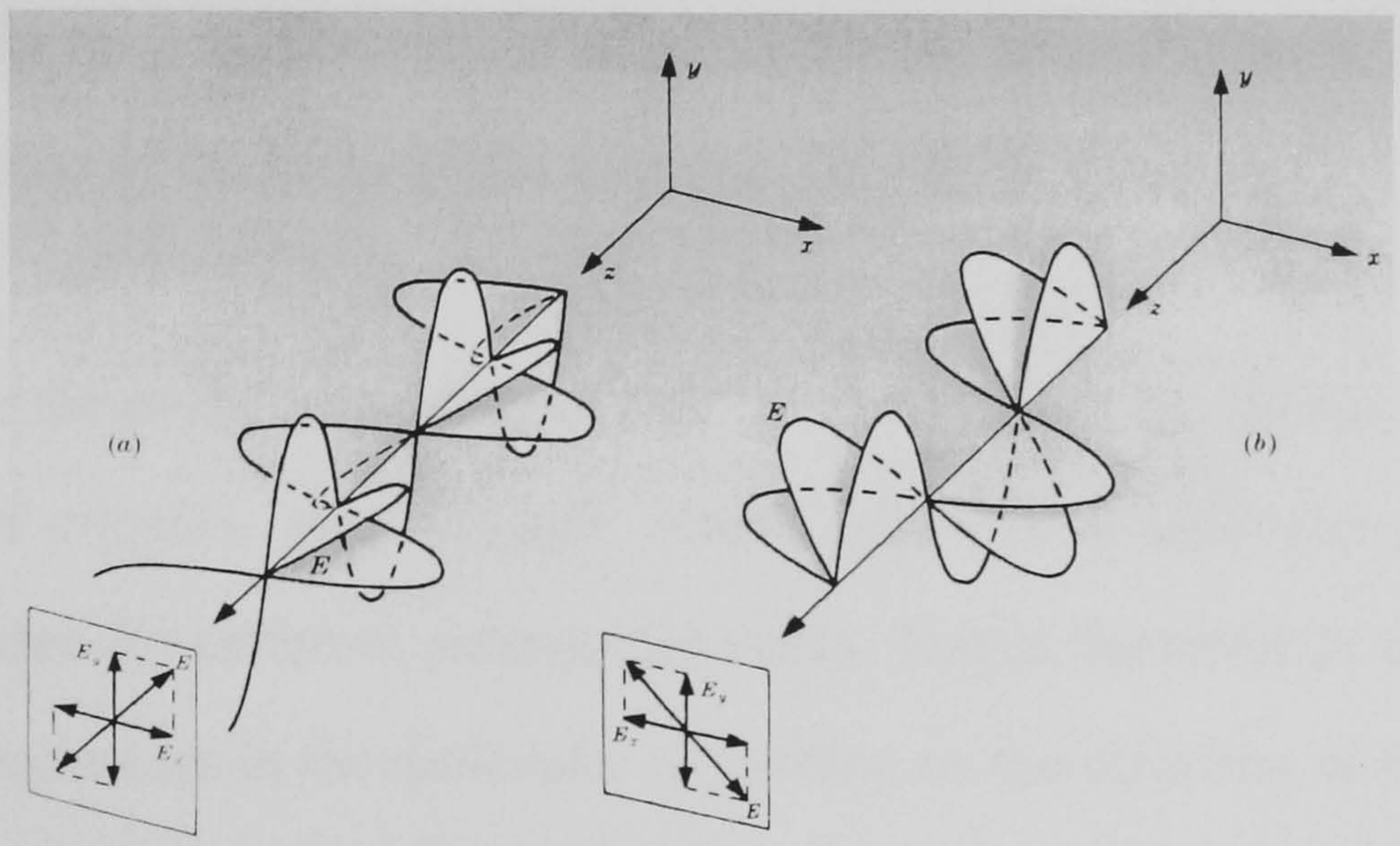

(a) Linear polarisation

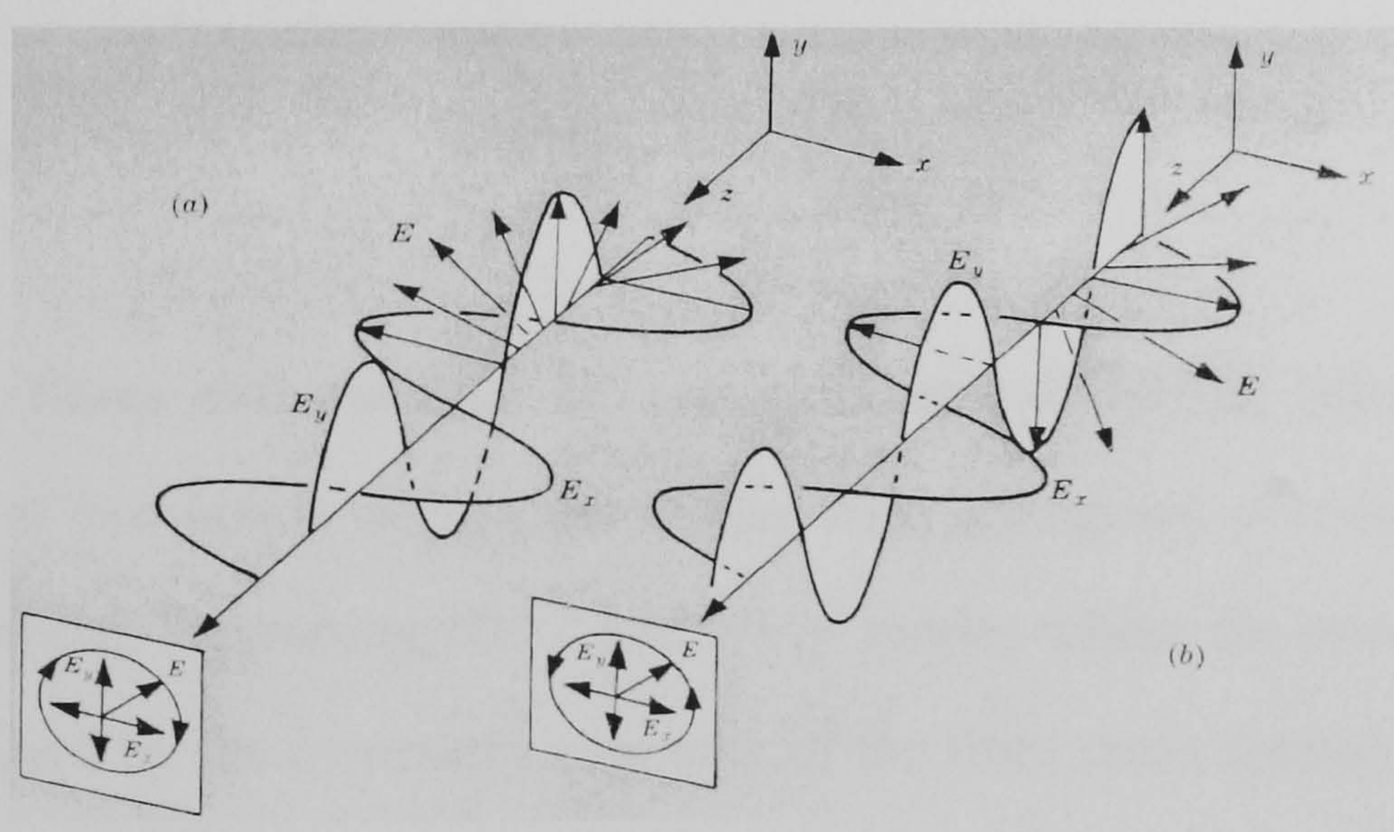

(b) circular polarisation

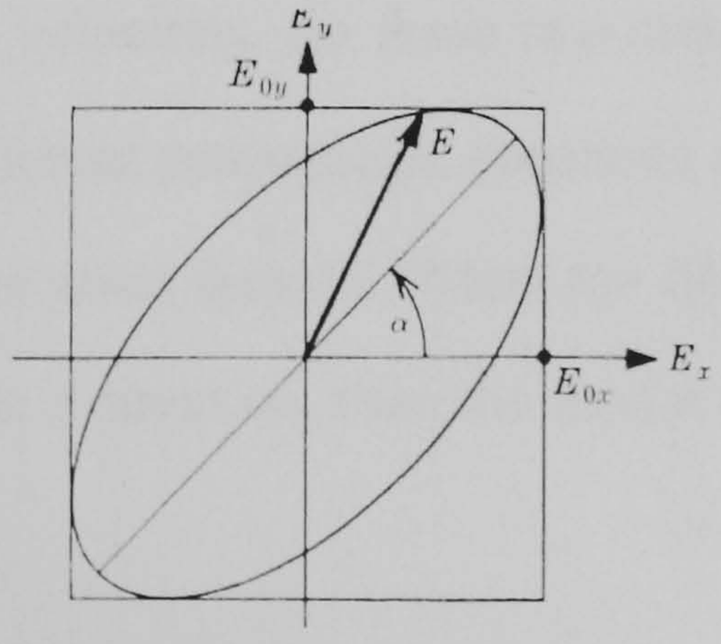

(c) Elliptical polarisation

Figure 3.1 Some polarisation states of light (Hecht, 1975)

This is the equation of an ellipse tilted at an angle α to the E_x-axis, as shown in the Figure 3.1(c). The value of α can be computed from the equation

$$\tan 2\alpha = \frac{2E_{0x}E_{0y}}{E_{0x}^2 - E_{0y}^2}\cos\varepsilon \qquad 3.4$$

This can only be true, however, if ε is constant in time or at least, is changing only slowly in a time of the order of the response time of the detector.

Control over the polarisation state of light can be affected by utilising the polarisation properties of crystals. Most crystals exhibit polarisation anisotropy, i.e. a different refractive index for different polarisation states. This is the result of different electron vibration frequencies in the molecules depending on the direction of light with respect to the crystal axes (Senior, 1992).

3.3.2 Mode birefringence

Single-mode fibres with nominal circular symmetry about the core axes allow the propagation of two nearly degenerate modes with orthogonal polarisations. They are therefore bimodal, supporting HE_{11}^x and HE_{11}^y modes where the principal axes x and y are determined by the symmetry elements of the fibre cross section. Thus the fibres behave as a birefringence medium due to the difference in the effective refractive indices, and hence phase velocities, for these two orthogonally polarised modes. The modes therefore have different propagation constants β_x and β_y which are dictated by the anisotropy of the fibre cross section. When the fibre cross section is independent of the fibre length L in the z direction, then the modal birefringence B_F for the fibre is given by:

$$B_F = \frac{(\beta_x - \beta_y)}{(2\pi/\lambda)} \qquad 3.5$$

where λ is the optical wavelength, β_x and β_y are propagation constants of x and y axes respectively. Light polarised along one of the principal axes will retain its polarisation for all lengths of the fibre.

If both modes in the fibre are excited by input polarised light, they will change in phase relative to each other as they propagate. The final phase difference between the two modes depends on the fibre length L in the z direction and is given by:

$$\Phi(z) = (\beta_x - \beta_y)L \qquad 3.6$$

assuming that the phase coherence of the two mode components is maintained.

The polarisation state in the core is generally elliptical and varies periodically along the fibre. This situation is illustrated in Figure 3.2 where the incident linear polarisation which is at 45° with respect to the x axis becomes circular polarisation at $\phi=\pi/2$, and linear again at $\phi=\pi$. The process continues through another circular polarisation at $\phi=3\pi/2$ before returning to the initial linear polarisation at $\phi=2\pi$. The characteristic length L_b corresponding to this process is known as the beat length. It is given by:

$$L_B = \frac{\lambda}{B_F} \qquad 3.7$$

In fact, beat length L_B can be derived from the following equation directly.

$$\Phi(z) = 2\pi = (\beta_x - \beta_y)L_B \qquad 3.8$$

and L_B can be written as:

$$L_B = \frac{2\pi}{\beta_x - \beta_y} \qquad 3.9$$

The radially distributed intensity depends on the polarisation of the transmitted light. There is a series of bright and dark bands with a period corresponding to the beat length which can be seen from one side of the fibre by naked eyes, as shown in Figure 3.2.

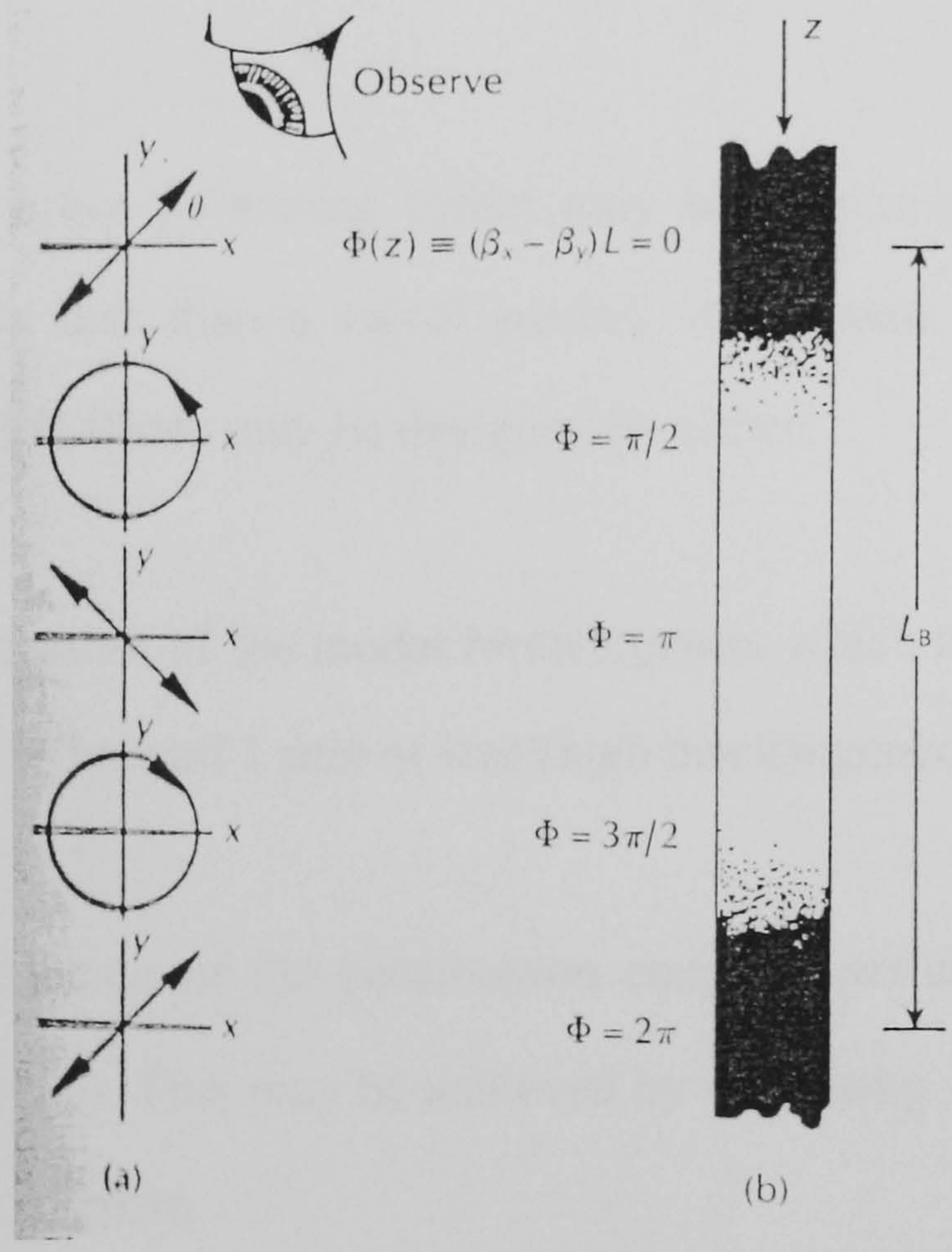

Figure 3.2 An illustration of the beat length in a single mode optical fibre (Senior, 1992)

(a) The polarisation states over the beat length within the fibre.

(b) The light intensity distribution over the beat length within the fibre.

3.3.3 Polarisation-maintaining fibres

In practice, fibres cannot be made as perfect cylindrical structures so that various perturbations along the fibre length such as strain or variations in the fibre geometry and composition lead to coupling of energy from one polarisation to the other. These perturbations are difficult to eradicate as they may easily occur in the fibre manufacture and cabling. The energy transfer is at a maximum when the perturbations have a period Λ, corresponding to the beat length, and defined by:

$$\Lambda = \frac{\lambda}{B_F} \qquad 3.10$$

However, the cross polarizing effect may be minimized when the period of the perturbations is less than a cutoff period, Λ_c (around 1 mm). Hence polarisation maintaining (PM) fibres may be designed by either:

(a). the maximization of the modal birefringence, which may be achieved by reducing the beat length to around 1 mm or less (high birefringence); or

(b). the minimisation of the polarisation coupling perturbations with a period of Λ (low birefringence). This may be achieved by increasing Λ_c, giving a large beat length of around 50m or more.

Techniques have been developed to produce both high and low birefringence fibres. Birefringence occurs when the circular symmetry in single-mode fibres is broken which can result from the effect of geometrical shape or stress. Alternatively, to design low birefringence fibres, it is necessary to reduce the possible perturbations within the fibre manufacture.

The various types of PM fibre, classified in terms of their linear polarisation maintenance, are shown in Figure 3.3. In addition, a selection of the most common structures is illustrated in Figure 3.4.

In Figure 3.3, Hi-Bi fibres are separated into two types which are generally referred to as two-polarisation fibres and single-polarisation fibres. In the latter case, in order to allow only one polarisation mode to propagate through the fibre, a cutoff condition is imposed on the other mode by utilising the difference in bending loss between two polarisation modes.

In Figure 3.4, (a) and (b) employ geometrical shape birefringence, whilst (c), (d), (e) and (f) utilise various stress effects. The residual birefringence within conventional single-mode fibres can be compensated by twisting the fibre after manufacture to produce Lo-Bi fibre, as shown in (g).

Some characteristics of polarisation-maintaining fibres are shown below:

Table 3.1: Characteristics of polarisation-maintaining fibres (Dakin, 1988)

Fibre type	Modal birefringence B ($\times 10^{-4}$)	Polarisation-holding parameter ($\times 10^{-6}$ /m)	Minimum loss (dB/km)	Minimum loss wavelength (μm)
Elliptical core	4.0	10	2.5	1.3
Bow tie	4.8	1	<1	1.55
PANDA	3.15	0.16	0.22	1.55

3.4 The polarimetric sensor

The polarimetric sensors used in the present study employ Hi-Bi fibres. The sensor utilises relative phase shift between two orthogonally polarised light in one Hi-Bi

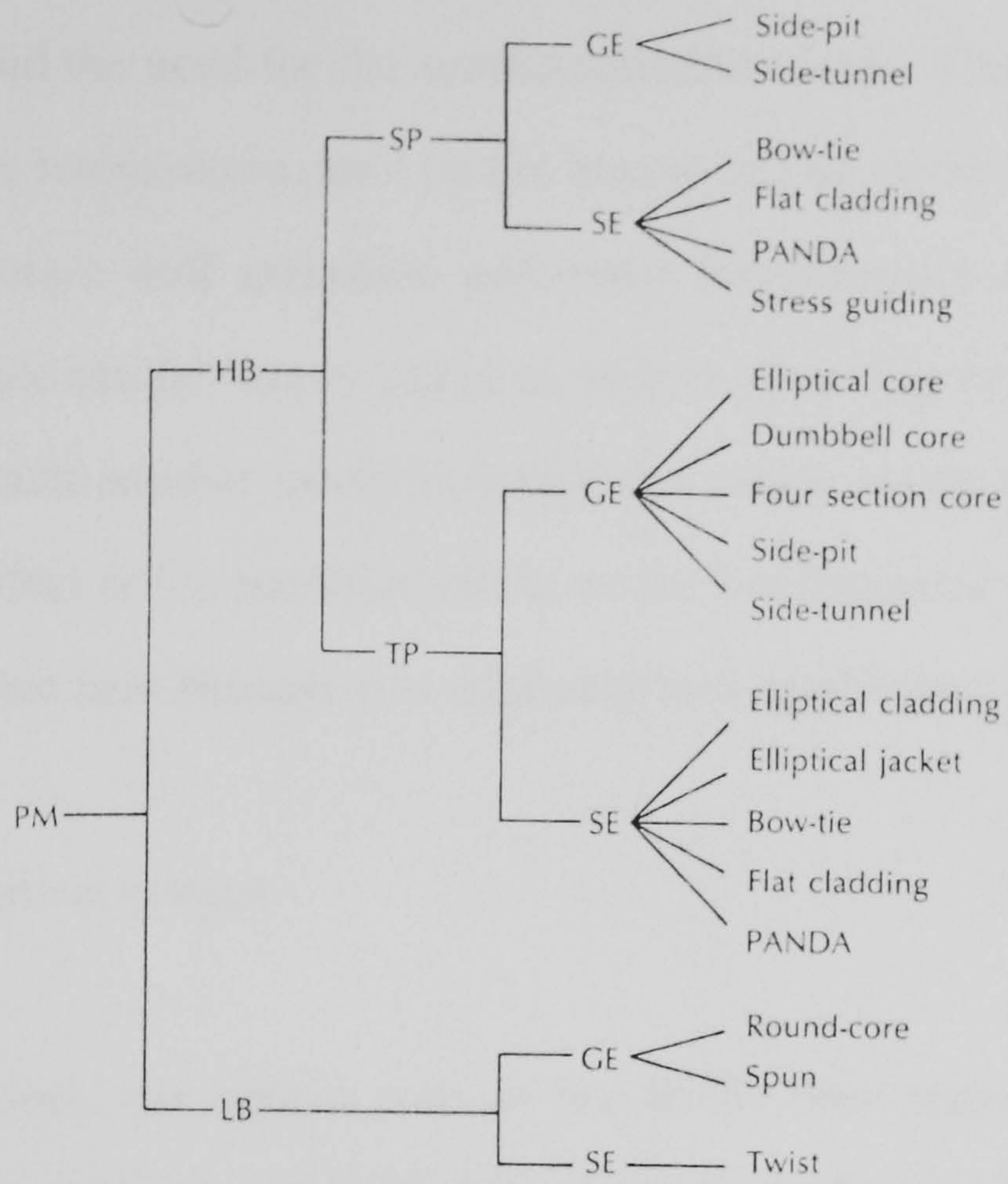

Figure 3.3 Polarisation maintaining fibre types classified from linear polarisation maintenance view point. PM: polarisation maintaining; HB: high-birefringence; LB: low-birefringence; SP: single-polarisation; TP: two-polarisation; GE: geometrical effect; SE: stress effect. (Senior, 1992).

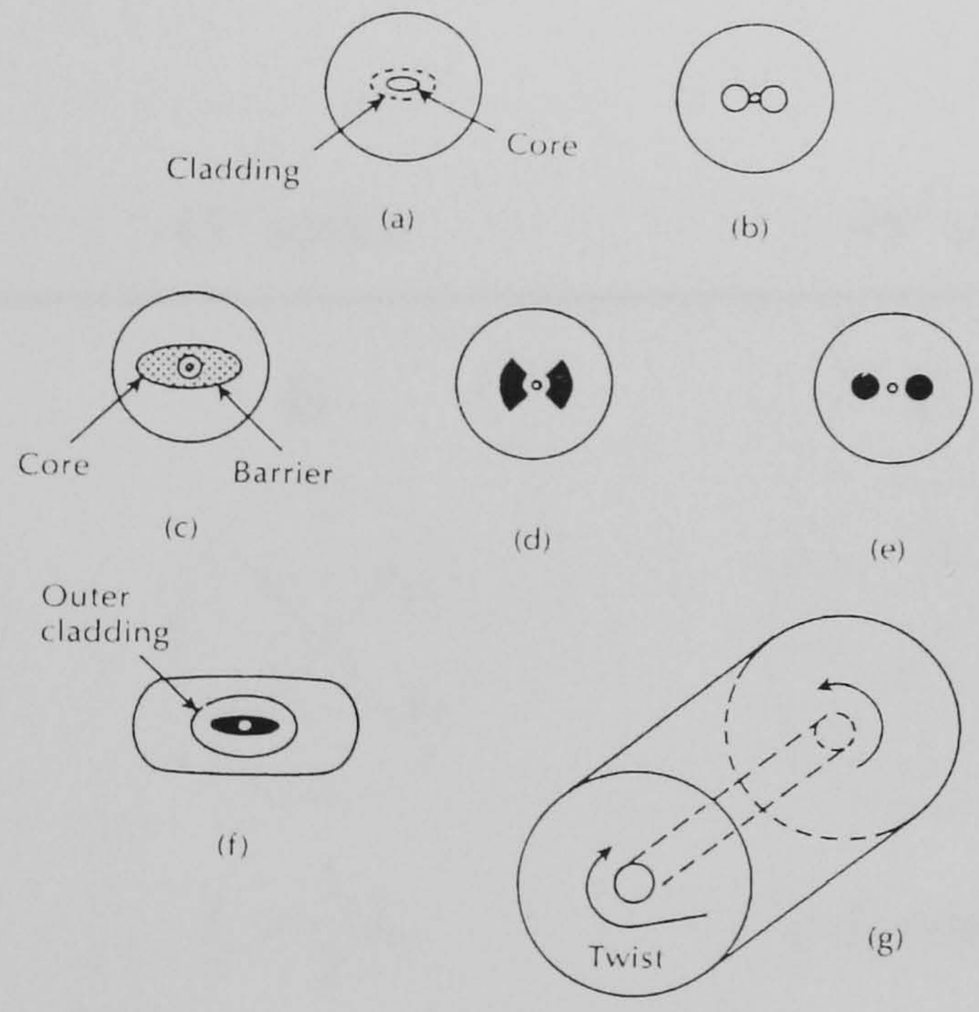

Figure 3.4 Polarisation maintaining fibre structure (a) elliptical core; (b) side-pit fibre; (c) elliptical stress-cladding; (d) bow-tie stress regions; (e) circular-stress regions (PANDA fibre); (f) flat fibre; (g) twisted fibre (Senior, 1992).

fibre and hence, avoid the need for the second reference fibre. The effect of external influence (e.g. strain, temperature, etc.) on the sensor can be studied in two ways. For example, external strain will introduce additional birefringence into the core and different birefringence can be simply added as vectors according to Rashleigh (1983). Sirkis et al (1993) built another model in which the strains inside the core are added first, and then the effect of the modified strain on the birefringence is considered. The latter model is adopted here because it is relatively well established.

3.4.1 Visibility of optical fringes

In polarimetric sensors, the optical core of the Hi-Bi fibre transmits orthogonally polarised components of light with different velocities. A change of strain state in the host material will affect the strain state in the fibre core and hence the relative phase of the orthogonally polarised optical signals. The interference of these signals results in a dynamic change in the output signal, which can be used for damage detection. A schematic diagram of the polarimetric sensor used in the present study is shown in Figure 3.5.

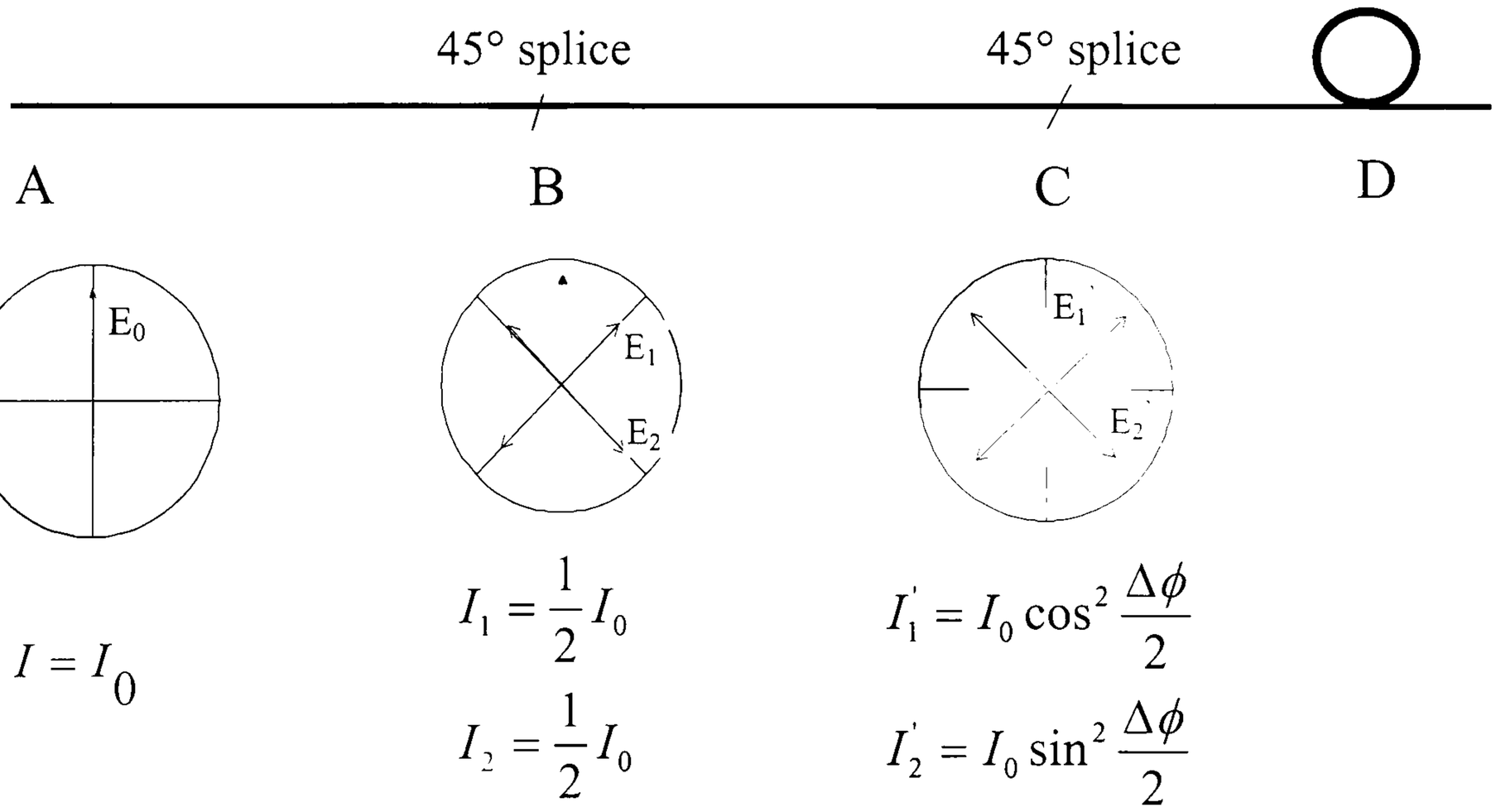

Figure 3.5 A schematic diagram for a polarimetric sensor.

As shown in Section 2.4.2, there are several ways to manufacture polarimetric sensors. The configuration adopted here has some advantages over other structures: the gauge length of the sensor, or the length of fibre that is sensitive to external disturbance, can be selected. This will be discussed later in Chapter 6.

For the sensor in Figure 3.5, linearly polarised laser light of 633 nm wavelength is launched into one of the axes of the PANDA fibre at point *A*. The splices at point *B* and *C* provide the localisation of the sensor and are achieved by rotating the axes of the fibre through 45° relative to the orientation in the lead-in/out sections of the optical fibre, lengths *AB* and *CD*, respectively. As both polarised modes are present in the fibre length *BC*, they will recombine and interfere when they pass through a similar 45° splice at point *C*. The fibre length that lies between points *B* and *C* is called the gauge length of the fibre. There are thus two interference phenomena in each of the two axes of the Hi-Bi fibre at point *C*. If the optical intensity was measured at a point between *C* and *D*, before the bending of lead-out fibre at point *D*, no interference fringes can be recorded. This is determined by the principle of energy conversation. No energy is lost between point *A* and *C* if the light attenuation due to the optical fibre and joint loss due to splices are ignored. A polarisation insensitive detector can only record the intensity from a laser source under this condition. Fringes can only be recorded if the two modes in the fibre are separated by a polarisation splitter (as shown in Figure 2.7(a)), an analyser or if one of the two modes is removed by bending (coiling) the fibre at point *D*. In the present study, the lead-out fibre is bent with an appropriate bend radius and a required number of loops to eliminate one of the two modes. This is very simple, no expensive polarisation splitter crystal or complicated adjustment of light path is needed. Most importantly, clear fringes (which will be shown in Chapter 5) can be obtained in this way.

This method of using a coiled length of fibre to eliminate the light from one axis of the lead-out fibre works as follows (Varnham, 1984; Simpson, 1983). Suppose one of the polarised states, the x-mode, propagates in the core along the x-axis with a

effective index n_{xcore} and the other, the y-mode, has an associated effective index of n_{ycore}, where $n_{xcore} > n_{ycore}$. Both modes may exist in the fibre if their refractive indices are higher than that of the cladding, i.e. $n_{x,ycore} > n_{x,ycladd}$ (see Figure 3.6(a)). The fibre bend introduces additional stresses and alters the effective indices $n_{x,ycore}$ and $n_{x,ycladding}$. By an adequate combination of the bend diameter and the number of loops, the effective index of one mode in the core becomes equal to the effective index in the cladding, i.e. $n_{ycore*} = n_{xcladding*}$ (Figure 3.6(b)). For this case, one of the modes in the core will escape from the core to the cladding and will not propagate along the fibre. Thus, when the fibre is bent, a differential bend loss occurs that can be enhanced by a judicious choice of the bend radius and the operation wavelength to give a large polarisation extinction ratio. However, bending the fibre also produces a small transfer of power from one mode to the other mode (mode coupling). By choosing a larger loop diameter and increasing the number of loops, the polarisation that is dominated by the attenuation of one of the modes in the core, not by the polarisation cross coupling, can be realised.

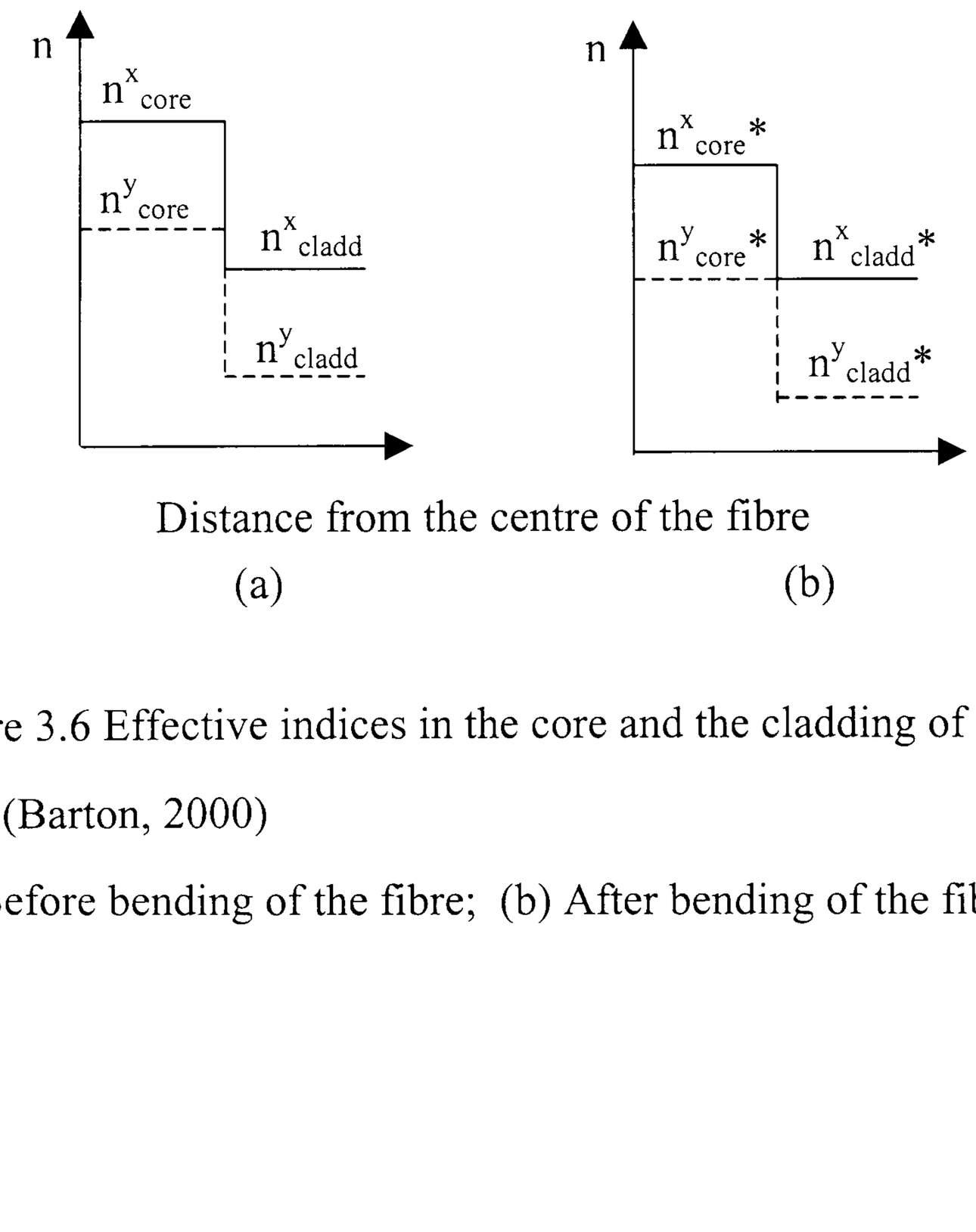

Figure 3.6 Effective indices in the core and the cladding of an optical fibre (Barton, 2000)

(a) Before bending of the fibre; (b) After bending of the fibre.

With regard to strain measurements, an applied strain will change the birefringence and the two optical path lengths within the sensor gauge length *BC*, thus changing the relative phase of the two polarisation modes in the fibre. The splice at point *B* excites both modes in the fibre length *BC*, so each mode in the fibre is analogous to the case of two-beam interferometry. When the splice at point *B* is 45°, the light intensities in the *x*- mode and *y*-mode between fibre length *BC* are:

$$I_x = I_y = \frac{1}{2} I_0 \tag{3.11}$$

where I_x, I_y and I_0 are light intensities in *x* mode, *y* mode and the initial input light intensity.

At point *C*, the fibre is rotated 45° and the light in both modes will resplit. Because the light in both modes originated from the same linearly polarised light and have a relative phase difference, $\Delta\varphi$, they will interfere with each other at point *C* and the light intensity in the *x* and *y* mode in the fibre length *CD* is:

$$\begin{aligned} I_x^{CD} &= I_x^{'} + I_y^{'} + 2\sqrt{I_x^{'} I_y^{'}} \cos\Delta\varphi = \frac{1}{4} I_0 + \frac{1}{4} I_0 + \frac{1}{2} I_0 \cos\Delta\varphi \\ &= I_0 \cos^2 \frac{\Delta\varphi}{2} \\ I_y^{CD} &= I_x^{'} + I_y^{'} + 2\sqrt{I_x^{'} I_y^{'}} \cos(\Delta\varphi + \pi) = \frac{1}{4} I_0 + \frac{1}{4} I_0 + \frac{1}{2} I_0 \cos(\Delta\varphi + \pi) \\ &= I_0 \cos^2 (\frac{\Delta\varphi}{2} + \frac{\pi}{2}) \\ &= I_0 \sin^2 \frac{\Delta\varphi}{2} \end{aligned} \tag{3.12}$$

When one of the modes is removed by bending, as discussed above, fringes due to the change of relative phase difference in the sensor gauge length can be obtained.

Introducing 45° splices at point *B* and *C* is a special case. In a more general situation, the light intensity in the *x* and *y* modes in the fibre length *CD* can be written as (Born. 1970):

$$I_{x,y} = \frac{I_0}{2}[1 + V_{VIS}\cos(\Delta\varphi)] \qquad 3.13$$

where I is the sensor output power, I_0 is the initially launched light intensity, $\Delta\varphi$ is the relative phase difference between the two polarisation modes and V_{VIS} is the visibility of the light modulation. The depth of modulation, or visibility of the observed polarimetric response, is limited by the accuracy of the orientations of the fibres in the splices and can vary from zero to unity. The visibility, V_{VIS}, is given by

$$V_{VIS} = \frac{I_{\max} - I_{\min}}{I_{\max} + I_{\min}} = \gamma \frac{\sin 2\alpha \sin 2\delta}{1 + \cos 2\alpha \cos 2\delta} \qquad 3.14$$

where α and δ are the angles in the splices at point *B* and *C* with respect to the fibre axes, and γ represents the correlation function between the polarisation modes. This is a function of the length of the fibre, the polarisation dispersion of the fibre and the spectral half-width of the source. The interfering waves in this case are the polarisation modes. Figure 3.7 shows the optical output of the polarimetric sensor (equation 3.14), with the visibility for three different splicing angles such as: $\alpha=\delta=70°$, $\alpha=\delta=60°$ and $\alpha=\delta=45°$. So maximum visibility is obtained for $\alpha=\delta=45°$, for which $V_{VIS} = \gamma$. In the absence of mode coupling between the two polarisation states, and if a monochromatic source is used, then $\gamma = 1$ and, therefore the visibility V_{VIS} equals unity. In this case, equation 3.13 is identical to equation 3.12.

In the discussions below, a phase shift of 2π is referred to as a fringe and the number of fringes is determined by the strain state around the sensor. By observing and monitoring the number of fringes, the strain in host structures can be determined.

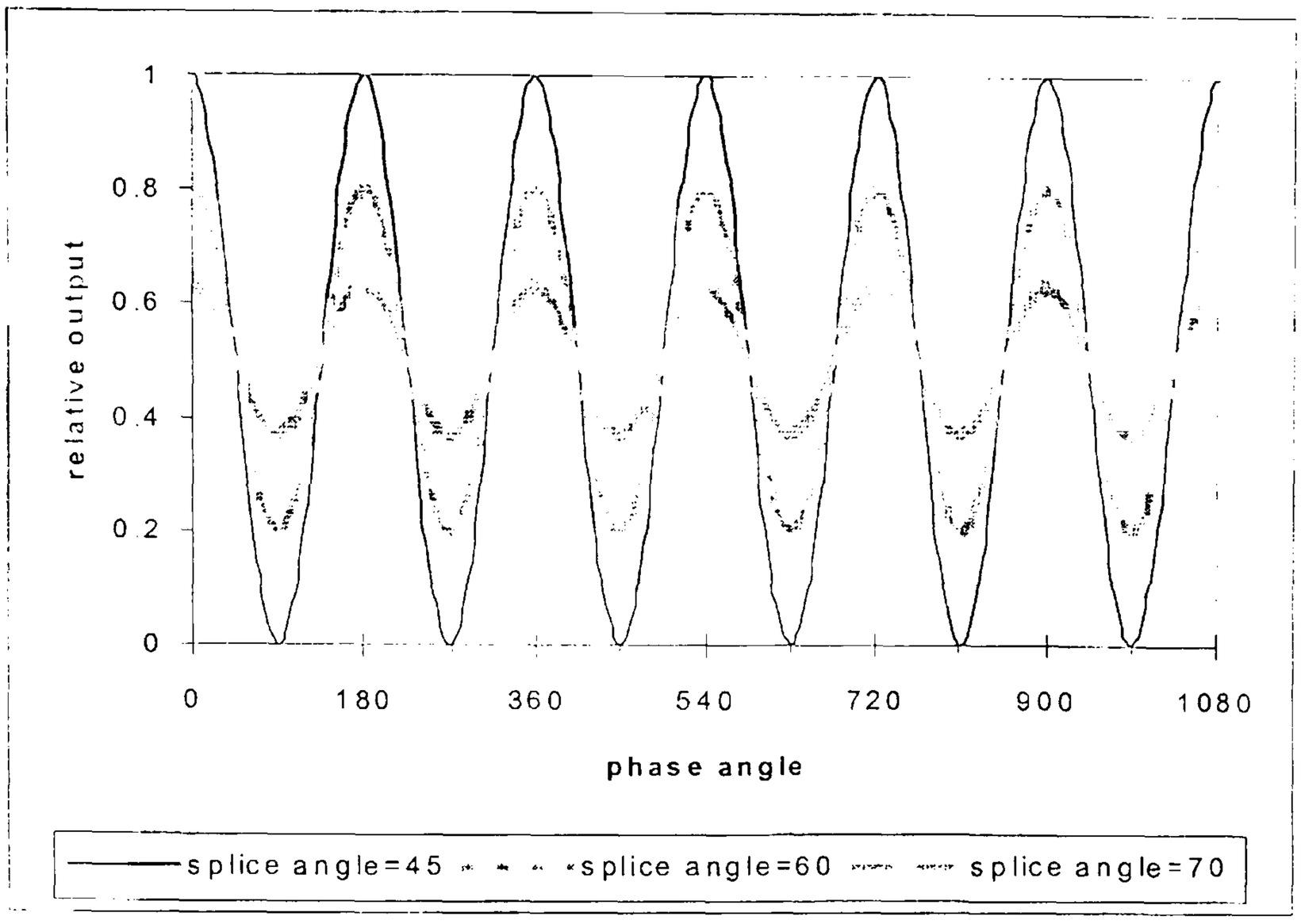

Figure 3.7 Polarimetric sensor output response for different splice angles, (Born, 1970).

3.4.2 Strain sensitivity of a polarimetric sensor

The relationship between optical output fringes, or optical phase change, $\Delta\varphi$, and the applied three-dimensional strain for a polarimetric sensor was introduced in the phase-strain model of Sirkis and Lo (1994). They assumed that a fictitious set of residual strains exist in the fibre core and that these strains lead to a residual state of birefringence which is independent of the original birefringence state inside the core. The general equation for the phase retardation, φ, as a function of strain is given by (Sirkis, 1993):

$$\varphi = \frac{2\pi}{\lambda} \int_L n(\varepsilon_{ij})(1+\varepsilon_{11})dL \qquad 3.15$$

where φ is the phase retardation at a given strain, λ is the wavelength of light used, $n(\varepsilon_{ij})$ is the refractive index as a function of strain in the core, ε_{11} is the fibre strain in

the direction along the fibre and L is the gauge length. Assume for the moment that the optical fibre was used to fabricate the sensor has two distinct optical axes with different indices, and that these different refractive indices are made different solely by a manufacturing induced residue strain state. Under these assumptions, the total phase retardation experienced by the light components propagation along the fast and slow optical axes is described by:

$$\varphi_2 = \frac{2\pi}{\lambda}\int_L n_2(\varepsilon_{ij}+\varepsilon_{ij}^r)(1+\varepsilon_{11})dL$$
$$\varphi_3 = \frac{2\pi}{\lambda}\int_L n_3(\varepsilon_{ij}+\varepsilon_{ij}^r)(1+\varepsilon_{11})dL \qquad 3.16$$

where ε_{ij}^r is the residual strain induced during manufacture of the optical fibre. φ_2 and φ_3 are phase retardation in the x and y mode in the core, which are designated as 2 and 3 in the following discussion.

The phase retardation due to the residual strain state only in the fast and slow axes is:

$$\varphi_{02} = \frac{2\pi}{\lambda}\int_L n_2(\varepsilon_{ii}^r)dL$$
$$\varphi_{03} = \frac{2\pi}{\lambda}\int_L n_3(\varepsilon_{ii}^r)dL \qquad 3.17$$

So the phase retardation difference between the residual strain state and the external load induced strain field is given by:

$$\Delta\varphi_2 = \frac{2\pi}{\lambda}\left(\int_L n_2(\varepsilon_{ij}+\varepsilon_{ij}^r)(1+\varepsilon_{11})dL - \int_L n_2(\varepsilon_{ii}^r)dL\right)$$
$$\Delta\varphi_3 = \frac{2\pi}{\lambda}\left(\int_L n_3(\varepsilon_{ij}+\varepsilon_{ij}^r)(1+\varepsilon_{11})dL - \int_L n_3(\varepsilon_{ii}^r)dL\right) \qquad 3.18$$

Hence the phase difference of the light in the fast and slow axes is

$$\Delta\varphi = \Delta\varphi_2 - \Delta\varphi_3 = \frac{2\pi}{\lambda}\int_L \{[n_2(\varepsilon_{ij}+\varepsilon_{ij}^r) - n_3(\varepsilon_{ij}+\varepsilon_{ij}^r)](1+\varepsilon_{11}) - B\}dL) \qquad 3.19$$

where $B = n_{2(}\varepsilon_{ij}{}^{r}{}_{)} - n_{3(}\varepsilon_{ij}{}^{r}{}_{)}$ is the modal birefringence specified by a fibre manufacturer. The refractive indices as a function of strain can be obtained from a standard strain optic relation (Sirkis, 1994) where the refractive indices are related to the total strain in the core of the fibre (which is a linear combination of the externally applied and residual strains) by strain optic coefficients, P_{ij}.

$$\begin{bmatrix} 1/n_1{}^2 - 1/n_0{}^2 \\ 1/n_2{}^2 - 1/n_0{}^2 \\ 1/n_3{}^2 - 1/n_0{}^2 \\ 1/n_4{}^2 - 1/n_0{}^2 \\ 1/n_5{}^2 - 1/n_0{}^2 \\ 1/n_6{}^2 - 1/n_0{}^2 \end{bmatrix} = \begin{bmatrix} P_{11} & P_{12} & P_{12} & 0 & 0 & 0 \\ P_{12} & P_{11} & P_{12} & 0 & 0 & 0 \\ P_{12} & P_{12} & P_{11} & 0 & 0 & 0 \\ 0 & 0 & 0 & P_{44} & 0 & 0 \\ 0 & 0 & 0 & 0 & P_{44} & 0 \\ 0 & 0 & 0 & 0 & 0 & P_{44} \end{bmatrix} \times \begin{bmatrix} \varepsilon_{11} + \varepsilon_{11}{}^{r} \\ \varepsilon_{22} + \varepsilon_{22}{}^{r} \\ \varepsilon_{33} + \varepsilon_{33}{}^{r} \\ \varepsilon_{44} + \varepsilon_{44}{}^{r} \\ \varepsilon_{55} + \varepsilon_{55}{}^{r} \\ \varepsilon_{66} + \varepsilon_{66}{}^{r} \end{bmatrix} \qquad 3.20$$

Here n_0 is the refractive index of non-strained silica and n_1 to n_6 are the refractive indices as a function of strain in the core of the fibre. The linearised equations for the refractive indices can be found by expanding $1/n_{22}$ and $1/n_{32}$ in the above matrix in a Taylor series about $\varepsilon_{ij}{}^{r}$ and neglecting the higher order terms (Sirkis, 1993).

$$n_2(\varepsilon_{ij}+\varepsilon_{ij}^r) = n_2^r[1 - \frac{1}{2}(n_2^r)^2(P_{12}\varepsilon_{11} + P_{11}\varepsilon_{22} + P_{12}\varepsilon_{33}] \qquad 3.21$$

$$n_3(\varepsilon_{ij}+\varepsilon_{ij}^r) = n_3^r[1 - \frac{1}{2}(n_3^r)^2(P_{12}\varepsilon_{11} + P_{12}\varepsilon_{22} + P_{11}\varepsilon_{33}]$$

The final form of the phase-strain model for a polarimetric sensor is found by substituting Equations 3.21 into Equation 3.19:

$$\Delta\varphi = \frac{2\pi}{\lambda}\int_L [K_1\varepsilon_{11} + K_2\varepsilon_{22} + K_3\varepsilon_{33}]dL \qquad 3.22$$

where $\Delta\varphi$ is the relative phase change between two polarisation modes caused by three-dimensional strain; λ is the wavelength of light in vacuum; ε_{11}, ε_{22} and ε_{33} are the three normal strains; L is the gauge length of the sensor; K_1, K_2 and K_3 are dimensionless coefficients which determine the contribution of each component of the normal strains to $\Delta\varphi$, and

$$\begin{aligned} K_1 &= B + \frac{1}{2}[(n_3^r)^3 - (n_2^r)^3]P_{12} \\ K_2 &= \frac{1}{2}[(n_3^r)^3 P_{12} - (n_2^r)^3 P_{11}] \\ K_3 &= \frac{1}{2}[(n_3^r)^3 P_{11} - (n_2^r)^3 P_{12}] \end{aligned} \qquad 3.23$$

Equation 3.22 shows that the polarimetric sensor response is totally determined by the strain state around the core. External effects, such as load, thermal effect or impact will induce additional strain into the core, hence optical fringes reflecting the external influence can be obtained.

The residual refractive indices, n_{2r} and n_{3r} required are difficult to individually determine. However by a uni-axial tension and a diametrical compression test, the K values can be experimentally determined. The K values for some Hi-Bi fibres are shown in the following table (Sirkis, 1994).

Table 3.2 Model parameters for Bow-Tie, E-core and Lo-Bi fibres

	K_1	K_2	K_3
Bow-Tie	-0.197	-0.714	-0.618
E-Core	-0.223	-0.722	-0.730
Lo-Bi	-0.233	-0.771	-0.771

It is interesting to find that for all of the fibres, K_2 and K_3 values are about 3 or 4 times bigger than that of K_1. This means that the polarimetric sensor is much more sensitive to transverse strain than to longitudinal strain. Hence it is likely to be possible to detect the passing cracks in a cross-ply laminate which will induce large lateral strain changes around the sensor.

3.5 Interaction between polarimetric sensors and host materials

In the model discussed above, ε_{11}, ε_{22} and ε_{33} are three normal strains in the optical fibre core. It is important to note that the strains in the core and strains in the host material are different. The diameters of embedded optical fibres are about 15 times larger than that of the reinforcing glass fibre. If the host material, e.g. the glass fibre reinforced composite, is taken to be homogeneous, the optical fibre is a large inclusion with a higher elastic modulus than the surrounding material. Such a large inclusion will change the local strain state significantly and cannot be neglected. Researchers have explored this interaction in several different ways (Sirkis, 1993; Kim, 1993; Kollar et al, 1998). Some specific elasticity solutions for cylindrical inclusions (optical fibres) embedded in transversely isotropic host are described by Sirkis (1993).

The strain states in the fibre core for the cases shown in Figure 3.8 can be found by following the standard theory of elasticity solution methods for transversely isotropic hosts of infinite extent with circular isotropic elastic inclusions (optical sensors). The continuity of radial stresses and displacements are enforced at the fibre-host interface. The axial strain in the fibre is taken to be equal to the corresponding strain component in the host following the plain strain assumption. For brevity, the strain states are simply listed here.

In case (a):

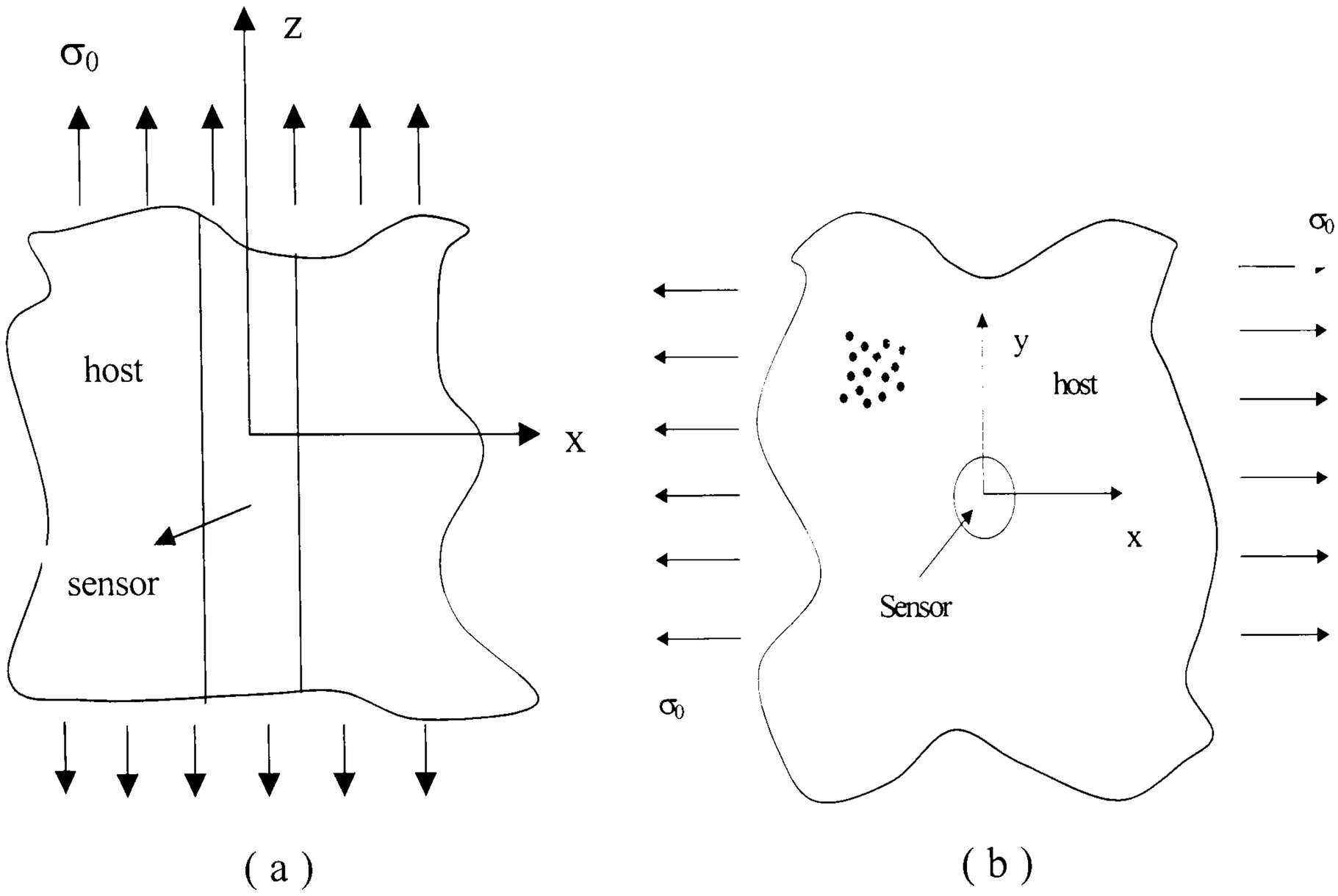

Figure 3.8 Optical fibre embedded in a transversely isotropic laminate subjected to (a) longitudinal tensile loading and (b) transverse tensile loading (Sirkis, 1993).

$$\varepsilon_z = \frac{(C_{22} + C_{23})}{C_{11}(C_{22} + C_{23}) - 2C_{12}^2}\sigma_0$$
$$\varepsilon_x = \varepsilon_y = \frac{C_{12}(C_{23} - C_{22}) - \lambda_f(C_{23} + C_{22})}{[2(\lambda_f + G_f) - (C_{23} - C_{22})][C_{11}(C_{22} + C_{23}) - 2C_{12}^2]}\sigma_0 \qquad 3.24$$

in case (b):

$$\varepsilon_z = \frac{2C_{12}}{C_{11}(C_{22} + C_{23}) - 2C_{12}^2}\sigma_0$$
$$\varepsilon_x = A_1 + A_2 \qquad 3.25$$
$$\varepsilon_y = A_1 - A_2$$

where

$$A_1 = \frac{C_{12}^2 - \lambda_f C_{12} - C_{11}C_{22}}{[2(\lambda_f + G_f) + (C_{22} - C_{23})][C_{11}(C_{22} + C_{23}) - 2C_{12}^2]}\sigma_0$$

$$A_2 = \frac{C_{22}\mathrm{X}_h - 2C_{23} + C_{22}}{(C_{23} - C_{22})[\mathrm{X}_h(2G_f + C_{22} + C_{23}) - (3C_{23} - C_{22} - 2G_f]}\sigma_0 \qquad 3.26$$

$$\mathrm{X}_h = \frac{3 - \nu_{23} - 4\nu_{12}\nu_{21}}{1 + \nu_{23}}$$

and

$$C_{12} = \frac{1 - \nu_{23}\nu_{32}}{E_1 E_3 \Delta}$$

$$C_{12} = \frac{\nu_{21} + \nu_{31}\nu_{23}}{E_2 E_3 \Delta}$$

$$C_{22} = \frac{1 - \nu_{13}\nu_{31}}{E_1 E_3 \Delta} \qquad 3.27$$

$$C_{23} = \frac{\nu_{32} + \nu_{12}\nu_{31}}{E_1 E_2 \Delta}$$

$$\Delta = \frac{1 - \nu_{12}\nu_{21} - \nu_{23}\nu_{32} - \nu_{31}\nu_{13} - 2\nu_{21}\nu_{32}\nu_{13}}{E_1 E_2 E_3}$$

where E_i (i = 1, 2 and 3) is the Young's modulus of the host, ν_{ij} (i = 1,2,3, j = 1,2,3) is the Poisson's ratio of the host. Subtitle 1, 2 and 3 correspond to the z, x and y axes in Figure 3.8. λ_f and G_f are lame constants for the fibre. This model is used later in the analysis of the response of polarimetric sensors embedded in unidirectional coupons.

3.6 Matrix cracks in cross-ply GFRP laminates

The main aim of the present study is to detect damage in a cross-ply laminate with an embedded polarimetric sensor. However, it is first necessary to understand the behaviour of this type of damage.

Laminated composites are typically produced from a combination of unidirectional layers, so that properties such as laminate stiffness depend on the orientation of adjacent plies. For undamaged composite laminates, laminated plate theory (LPT) or

approximate Rule-of-mixture expressions can be used to predict the laminate stiffness from those of the individual layers. Under mechanical loading, matrix cracking is the predominant mechanism in the initial stage of degradation of cross-ply composite laminates. The matrix crack density increases as a consequence of increasing applied strain or an increasing number of fatigue cycles, with a consequent change in such laminate properties such as Young's modulus, Poisson's ratio and the residual strain after unloading (Garret et al, 1977; Boniface, 1997; Crocker et al, 1997, Bassam, 1998).

When a crack propagates across the whole width of a coupon, residual thermal strains around the crack are released, and the compliance of the coupon will also increase due to the development of the crack. A detailed theoretical background is presented below.

The majority of continuous fibre polymer matrix composite laminates are cured at elevated temperatures. Cooling to room temperature produces a balanced system of curing stresses on a macroscale between the layers of a laminate. The magnitudes of the macroscopic curing stresses generated in the different layers of a laminate depend upon the laminate elastic moduli and coefficients of thermal expansion. Any damage which locally reduces the balanced macroscopic curing stresses, or releases stored elastic energy can lead to a change in laminate dimensions.

The geometry of a 0/90 cross-ply laminate is defined in Figure 3.9. The laminate has a central 90° ply of thickness *2d* on either side of which is a longitudinal ply of thickness *b*. The laminate has a width *W*. The plies have moduli E_1 and E_2 parallel and perpendicular to the fibres respectively and a transverse shear modulus G_T. For the uncracked laminate the Role-of-Mixtures expression for the modulus parallel to the loading direction is:

$$E_0 = (bE_1 + dE_2)/(b + d) \qquad 3.28$$

To analyse the stress distribution in a laminate where the transverse ply is cracked, a shear-lag model is widely used (Garrett and Bailey, 1978; Ogin et al, 1985; Boniface et al, 1991). In this approach, load is shed back into the transverse ply from the longitudinal ply by shear of the transverse ply. The longitudinal displacement profile across the transverse ply is assumed to be parabolic and the longitudinal displacement across the longitudinal ply is assumed to be constant.

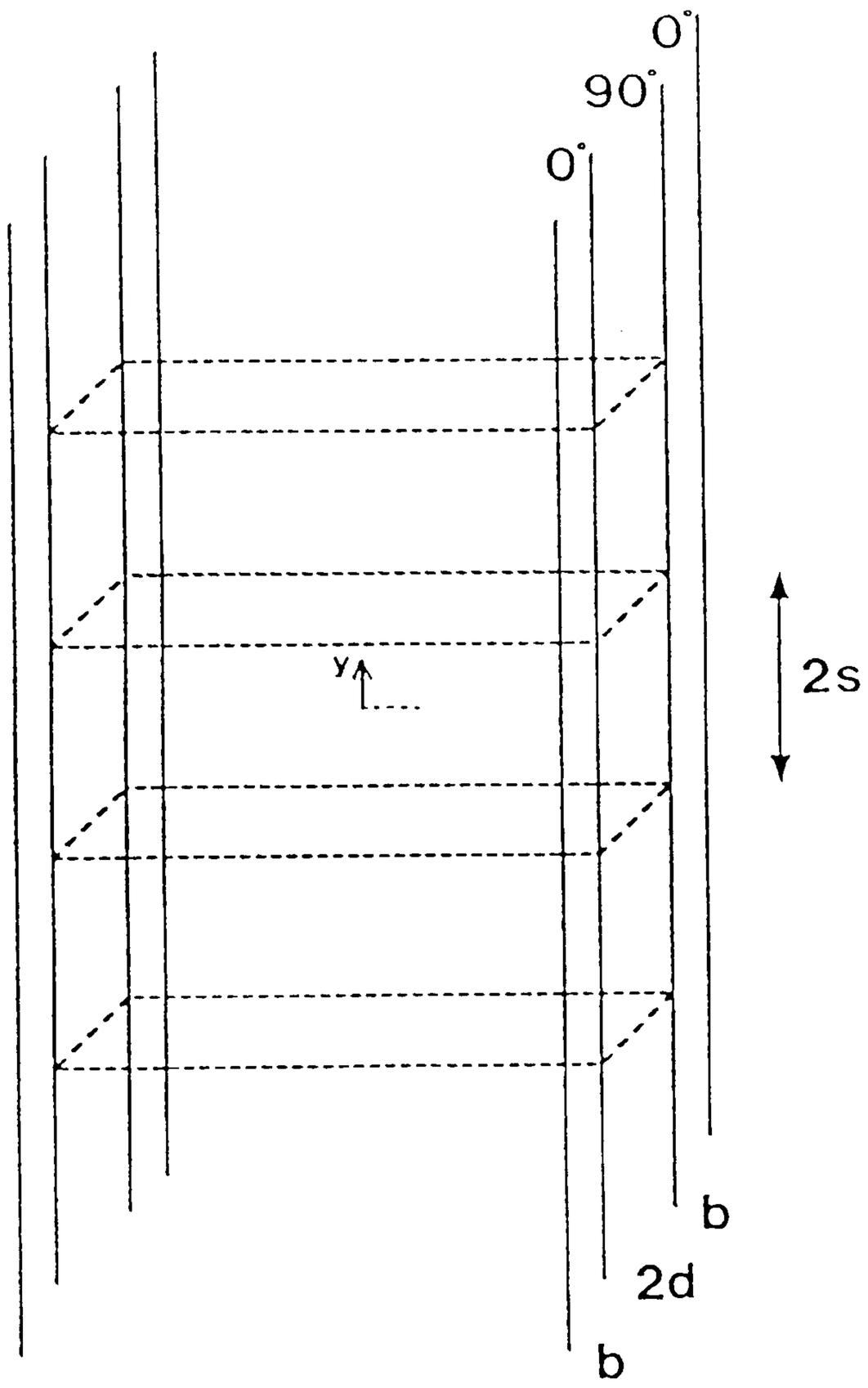

Figure 3.9 Geometry of a cross-ply laminate containing an array of cracks with a spacing of *2s* apart. The origin of the coordinates ($y = 0$) is midway between the cracks.

Using a *x*-*y* co-ordinate system with its origin at the middle of the transverse ply midway between two cracks spaced *2s* (see Figure 3.9), then the longitudinal stresses in the longitudinal and transverse plies are given by σ_1 and σ_2 respectively, where

$$\sigma_1 = \sigma(1+\frac{d}{b}) - \frac{d}{b}(\sigma\frac{E_2}{E_0} + \sigma^T)(1-\frac{\cosh(\lambda y)}{\cosh(\lambda s)})$$
$$\sigma_2 = (\sigma\frac{E_2}{E_0} + \sigma^T)(1-\frac{\cosh(\lambda y)}{\cosh(\lambda s)}) \qquad 3.29$$

and σ^T is the residual thermal stress in the laminate ply.

The variation of shear stress in the transverse ply is described by:

$$\tau = \lambda x(\sigma\frac{E_2}{E_0} + \sigma^T)\frac{\sinh(\lambda y)}{\cosh(\lambda s)}) \qquad 3.30$$

The shear stress in the longitudinal plies is assumed to be zero. In equation 3.30, σ and σ^T are the stresses applied to the laminate and the thermal residual stress in the transverse ply respectively, this thermal stress arises from the mismatch in coefficients of thermal expansion of the 0° and 90° plies during cooling. The thermal stress can be determined using a simple force balance approach, where (Bailey et al, 1979):

$$\sigma^T = -\frac{bE_1E_2\Delta\alpha\Delta T}{bE_1 + dE_2} \qquad 3.31$$

The quantity of λ is given by :

$$\lambda^2 = \frac{\alpha G^T(b+d)E_0}{d^2bE_1E_2} \qquad 3.32$$

Usually α is taken to be 3 (assuming a parabolic variation of the longitudinal displacements in the transverse ply), but it can vary and depend on the assumptions

about the displacements in the transverse ply and G^T is the transverse shear modulus of the laminate.

Equations 3.29 can be used to deduce an expression for the reduced modulus (and hence increased compliance) of a cross-ply laminate between two cracks, spaced $2s$ apart. This is found by writing an expression for the mean strain, ε:

$$\varepsilon = \frac{\sigma}{E} = \frac{1}{s}\int_0^s \frac{\sigma_1}{E_1} dy \qquad 3.33$$

where E is the reduced modulus. By substituting σ_1 from equation 3.29, integrating and rearranging, equation 3.33 becomes:

$$E = \frac{E_0}{1 + \frac{1}{\lambda s}\frac{dE_2}{bE_1}\tanh(\lambda s)} \qquad 3.34$$

When the cracks occur during mechanical loading, the length of the laminate will increase a small amount as a consequence of the reduction in the elastic modulus. Hence, there are two contributions to the laminate dimensional changes: there is an extension as a result of the increased compliance of the system and there is an extension associated with the relaxation of the residual thermal stress.

As shown in Figure 3.10, before the formation of crack C, the displacement between cracks A and B is given by:

$$\delta = 2\int_0^s \frac{\sigma_1}{E_1} dy \qquad 3.35$$

Substituting equation 3.29 gives:

$$\delta_\sigma = 2\int_0^{\infty} \frac{1}{E_1}[\sigma(1+\frac{d}{b}) - \sigma\frac{E_2}{E_0}\frac{d}{b}(1-\frac{\cosh(\lambda y)}{\cosh(\lambda s)})]dy \qquad 3.36$$

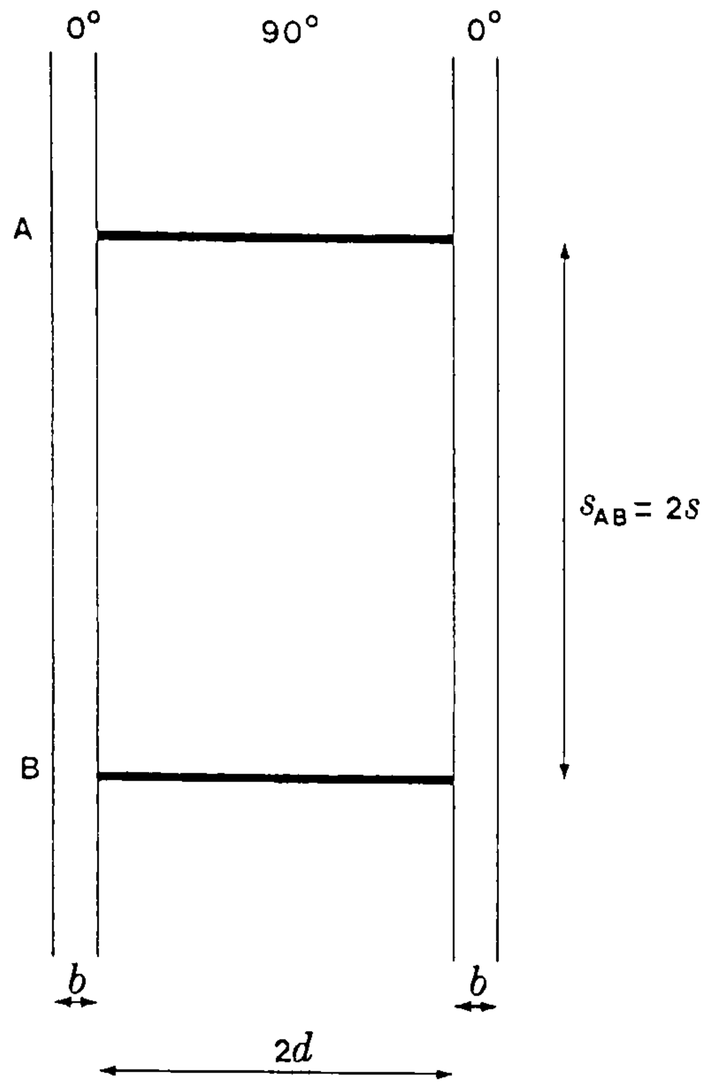

Figure 3.10 Geometry of cross-ply laminate (edge view).

After the formation of crack *C* the displacement between cracks *A* and *B* is given by (as shown in Figure 3.11):

$$\delta_\sigma^{'} = 4\int_0^{\frac{1}{2}s} \frac{1}{E_1}[\sigma(1+\frac{d}{b} - \sigma\frac{E_2}{E_0}\frac{d}{b}(1-\frac{\cosh(\lambda y)}{\cosh(\frac{1}{2}\lambda s)})]dy \qquad 3.37$$

Hence the displacement as a result of the increased compliance of the laminate after the formation of crack *C* is given by

$$\Delta^\sigma = \delta_\sigma^{'} - \delta_\sigma = \frac{1}{E_1}\sigma\frac{E_2}{E_0}\frac{d}{b}[\frac{4}{\lambda}\tanh(\frac{1}{2}\lambda s) - \frac{2}{\lambda}\tanh(\lambda s)] \qquad 3.38$$

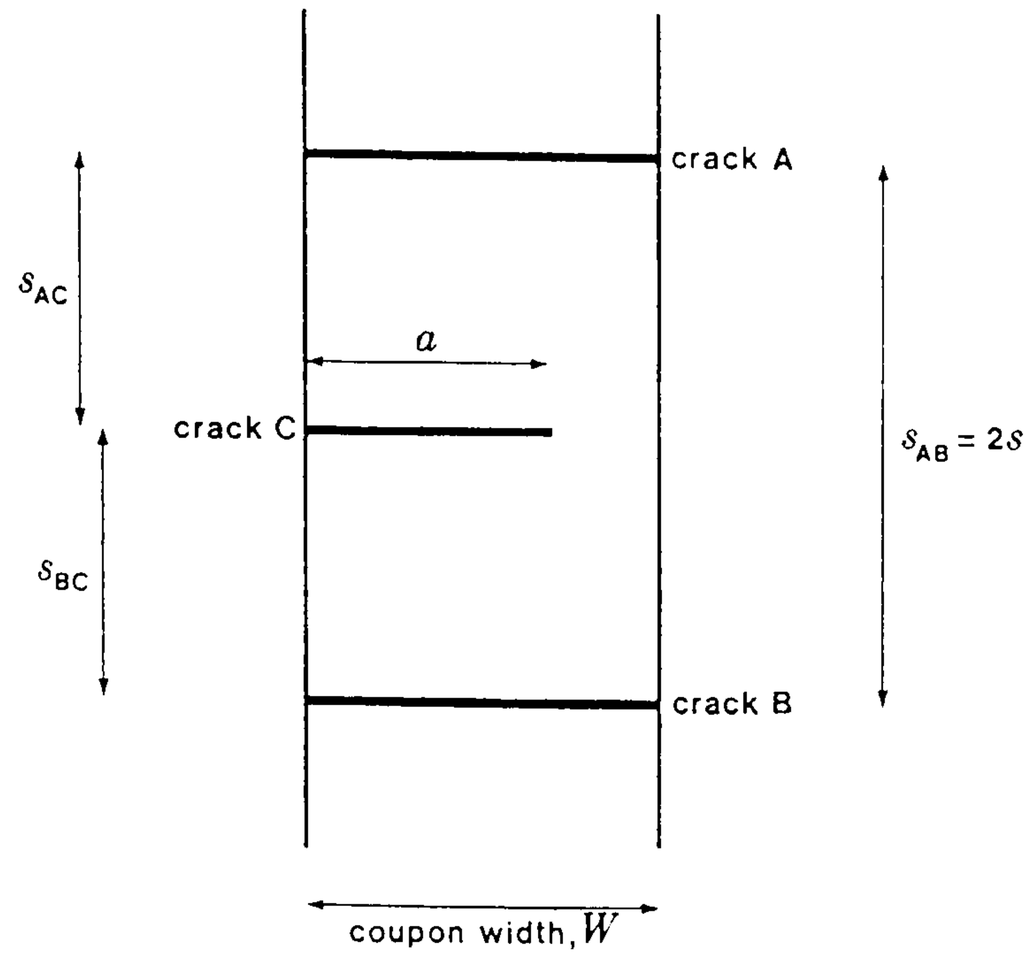

Figure 3.11 Formation of a transverse ply crack C between two existing cracks A and B spaced 2s apart.

The extra displacement as a result of the release of the residual thermal stresses may be calculated in a similar way. Before the formation of crack *C*, the displacement between crack *A* and *B*, associated with the thermal residual stress in the transverse ply, σ_T, is :

$$\delta_T = -2\int_0^s \frac{1}{E_1}\sigma^T \frac{d}{b}[1-\frac{\cosh(\lambda y)}{\cosh(\lambda s)}]dy \qquad 3.39$$

After the formation of crack *C*, the displacement between cracks *A* and *B* is:

$$\delta_T^{'} = -4\int_0^{\frac{1}{2}s} \frac{1}{E_1}\sigma^T \frac{d}{b}[1-\frac{\cosh(\lambda y)}{\cosh(\frac{1}{2}\lambda s)}]dy \qquad 3.40$$

Hence the displacement due to the relaxation of the residual thermal stresses is given by:

$$\Delta^T = \delta_T^{'} - \delta_T = \frac{1}{E_1}\sigma^T \frac{d}{b}[\frac{4}{\lambda}\tanh(\frac{1}{2}\lambda s) - \frac{2}{\lambda}\tanh(\lambda s)] \qquad 3.41$$

Hence, the overall displacement due to the propagation of crack C between two cracks spaced *2s* apart is given by:

$$\Delta = \Delta^{\sigma} + \Delta^{t} \qquad 3.42$$

Hence, the effect of cracks on the properties of a coupon, e.g. the reduction of modulus and the increase of coupon length, is reasonably well understood. The strain state around the edges of a transverse crack is much less well understood.

With the aid of an aramid fibre strain sensor embedded near a 0/90 interface in a transparent cross-ply GFRP laminate, the enhancement of strain in the vicinity of a transverse ply crack has been measured directly (Arjyal et al, 1998). The results show a large strain magnification in the crack plane for the cracks with a factor of 4 to 7 (Figure 3.12). In the figure, every peak indicates one crack and is labelled according

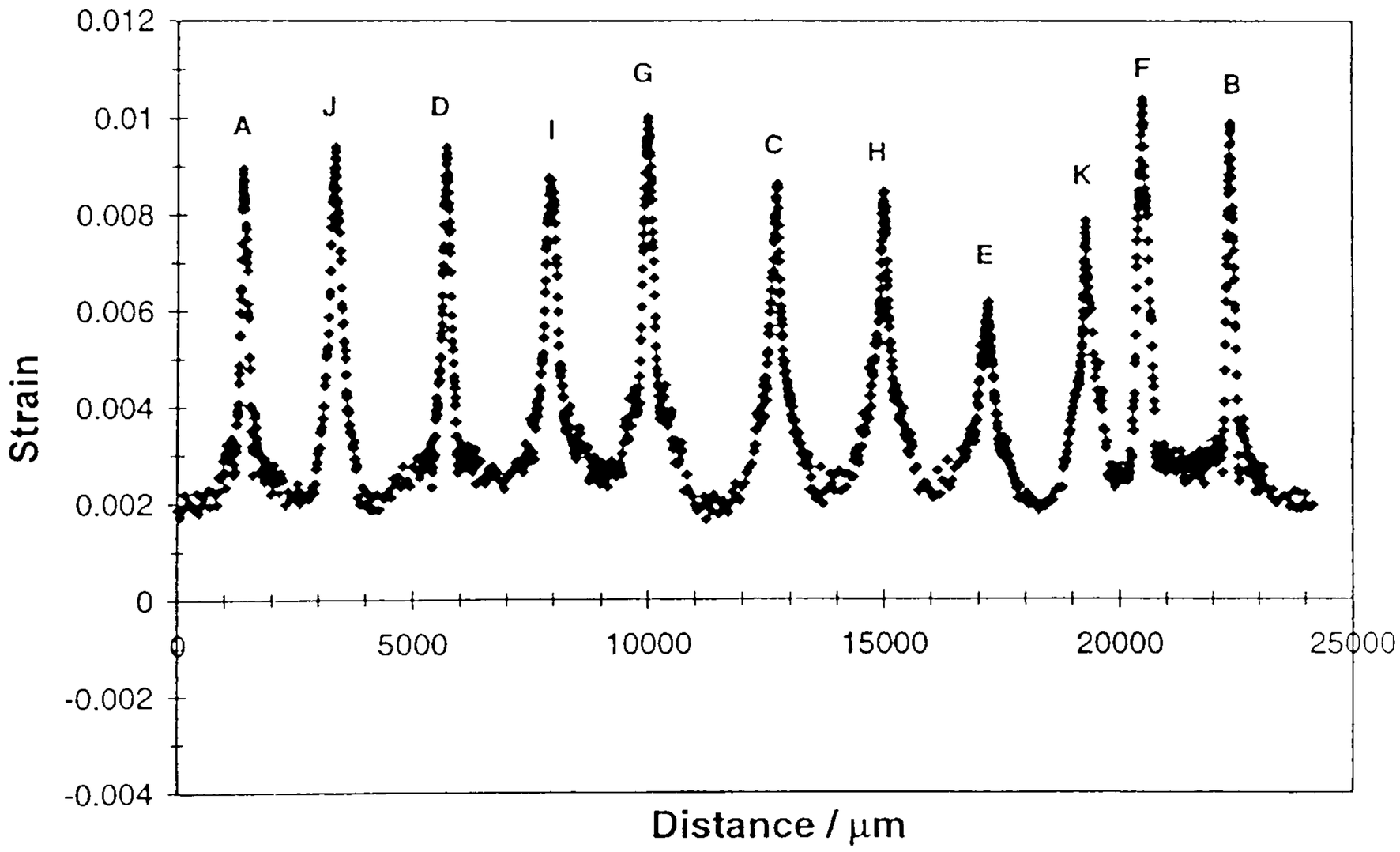

Figure 3.12 Strain distribution in the embedded Kevlar 49 fibre sensor on the basis of Raman spectroscopy within the 20mm gauge length at the point of transverse crack saturation. (Arjyal et al, 1998).

to the occurrence sequence of the crack development. The strain magnification factor measured using the aramid fibre reduces with increasing distance between the sensor and the 0/90 interface, falling from about 6 at a distance of about 10 μm from the interface to about 2 at a distance of 25 μm from the interface, as shown in Figure 3.13.

In Chapter 6, the response of a polarimetric sensor embedded at the 0/90 interface in a cross-ply laminate to the growth of such cracks will be discussed.

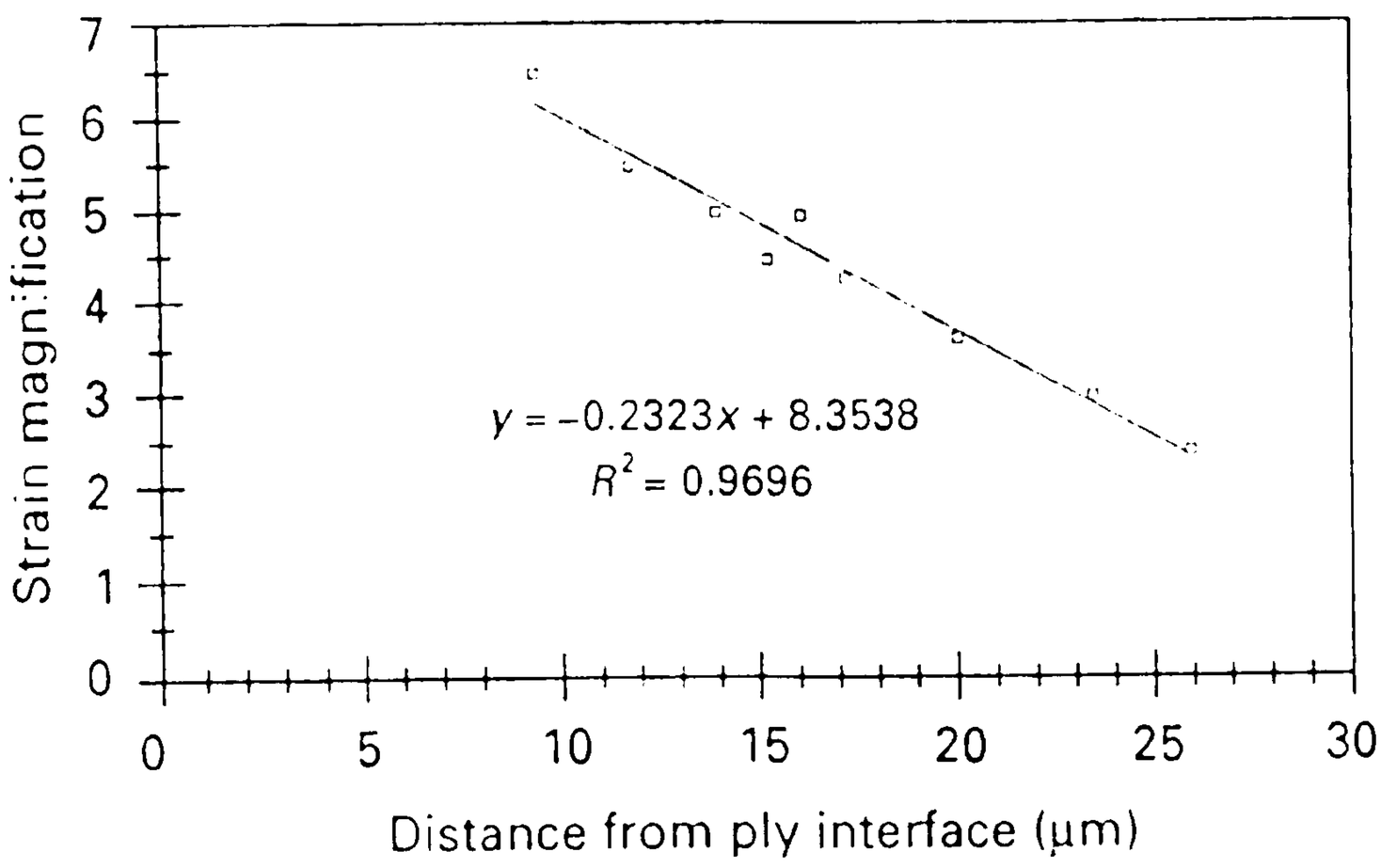

Figure 3.13 Strain magnification as a function of distance from the 0/90 interface for various transverse ply cracks. The solid line is a least-squares fit to the experimental data, (Arjyal et al, 1998).

The following chapter outlines the materials and manufacturing methods used in this work, together with the procedures used to characterise the sensors and the mechanical test methods employed to test the coupons with embedded sensors.

Chapter 4. Materials and experimental procedures

4.1 Introduction

Materials manufacturing and mechanical test methods used in the experimental study of the polarimetric sensor embedded in composites are described in this chapter, beginning with the manufacturing procedure for the unidirectional and cross-ply GFRP composites with embedded optical fibres in section 4.2. The fabrication of the sensors will be described in section 4.3. Section 4.4 introduces the mechanical test methods for the coupons with embedded polarimetric sensors and the light path arrangement. In section 4.5, the test methods for the polarimetric sensors are described. Finally, the data processing method is introduced in section 4.6.

4.2 Manufacture of composite materials with embedded fibre optic sensors

Cross-ply $(0/90)_s$ glass/epoxy laminates were fabricated with embedded optical sensors, using a filament winding/wet lay-up technique (Boniface, 1991). For the unidirectional coupons, the optical fibres were glued into the grooves of an additional frame perpendicular to the reinforcing fibres first and then the glass fibres of the 0° ply were wound parallel to the optical fibres, leaving sufficient optical fibre exposed at both ends for connections to the rest of the light path to be made. The glass fibres were wound at a controlled speed in order to gain a final ply thickness of approximately 0.5 mm. For the cross-ply laminate, the reinforcing glass fibres were wound on a square steel frame first (90° ply) and then the steel frame was turned 90° and the optical fibres were glued on top of the wound fibres into the grooves of an additional frame perpendicular to the reinforcing fibres. After that, the glass fibres of 0° ply were wound parallel to the sensors. For the double cross-ply laminate, the procedure varied with the different position of the embedded sensors. When the

layout of the laminate was 0/sensor/90/90/0/90/90/0, the three layers of reinforcing fibres, i.e. the inner 0° ply and the two adjacent 90° plies were wound first, then the sensor was glued into the grooves of an additional frame. The outer layer of 0° ply was wound last. When the layout of the laminate was 0/90/90/sensor/0/90/90/0, the central 0° ply was wound first, and the sensor were glued into the grooves of an additional frame. The remaining plies, the two 90° plies first, and then the 0° ply, were then wound.

After winding, the wound frames were impregnated with an epoxy resin (Epikote 828 (100 g), with curing agent Nadic Methyl Anhydride (NMA) (60 g) and accelerator K61B (4 ml). Prior to the impregnation, a vacuum was used to eliminate air bubbles entrapped in the epoxy resin. Wetting of the fibres was achieved by warming the uncured laminate with the use of a hot plate inside a vacuum chamber for approximately 20 min.

Plain rectangular test coupons, about 230 mm in length and 20 mm wide, were cut from laminates which were approximately 250 mm×200 mm, using a water-lubricated diamond saw with a nominal 600-grade grit finish. For most experiments, the coupons were cut so that the fibre optic sensor was located approximately in the centre of the coupon (see Figure 4.1). Experiments on coupons with a circular hole required the coupons to be cut in such a way that the sensors were off-set from the centre of the coupons, and about 3 to 5 mm away from the hole edge. Coupons were cut out before post-curing at 150°C for 3 hours. After post-curing, aluminium alloy end tabs, 20 mm long and 20 mm wide, were bonded to the coupon to avoid damage to the surface plies in the testing machine grips during loading. Adhesion was promoted by lightly abrading the surface of the coupon and etching the end tabs in a solution of sodium dichromate and sulphuric acid. A glue seat for an extensometer was also applied onto the coupon before mechanical testing to ensure that the

extensometer knife edge remained in a fixed position on the coupon's surface during testing.

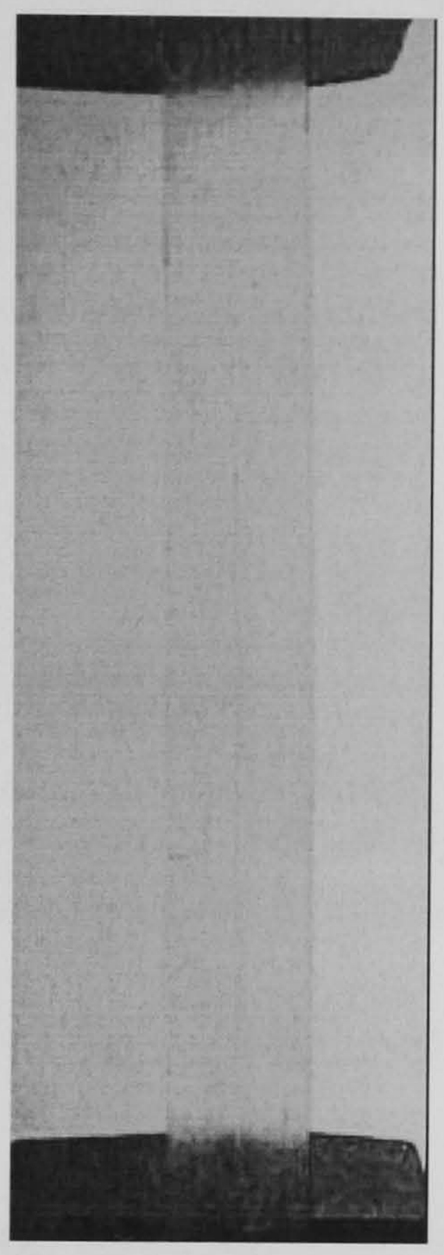

Figure 4.1 An example of a transparent coupon, with a fibre optic sensor in the middle, in the grips of the fatigue machine. The width of the coupon is 20 mm.

4.3 Manufacture of polarimetric sensors

Polarimetric sensors are attractive because of their simple construction, as described in Section 3.4. For these experiments, polarimetric sensors with two 45° splices, and with bending of the lead-out fibre, were made.

The sensors were made of a single mode, polarisation maintaining fibre (Hi-Bi PANDA fibre obtained from Fujikura Europe Ltd, diameter of the bare fibre without coating is 125 μm, diameter of the core is 3.5 μm, diameters of the stress rods are 16.5μm, Beat length (L_B) is 1.2 mm (λ = 0.63 μm)). A protective nylon coating and inner silicone coating were removed from the fibre (the length depends on the structure of the sensor) by a coating stripper and a lens tissue soaked with high purity alcohol (to clean the stripped bare fibre). As shown in Figure 3.5, the gauge length of the sensor (i.e. fibre length BC) was achieved by a rotation of the axes of the fibre through two 45° splices in the sensing section relative to the orientation in the lead-

Figure 4.2 The Fijikura splicer (FSM-20PM) employed in the experiments.

in/out sections of the optical fibre. Splicing and rotation of the fibres were carried out using a Fujikura fusion splicer (Model: FSM-20PM; see Figure 4.2). The splice involved using V-grooves to align the fibres to be joined at any necessary angles. The automatic alignment procedure of the fusion splicer was used to ensure that the connection between the two fibres was optimised. The final joining was completed by spark fusion.

For characterising the fibre under tension, three configurations of free polarimetric sensor were fabricated, as shown in Figure 4.3 (details of the test rig are described in Section 4.5.2). In the figure, thicker lines represent optical fibres with coatings (inner coating and outer coating), thinner lines represent stripped bare fibres (without any coating). The sensor with the structure shown in Figure 4.3(a) had two 45° splices within the grips of the tension rig and was connected with the other part of the light path by two 0° splices. In figure 4.3(b), the bare fibres were connected within the grips by one 0° splice and the sensor was joined to the light path by two 45° splices outside the grips. A 90° splice, positioned exactly at the central point between the two grips, was used to join the two bare fibres for the sensor shown in Figure 4.3(c). The

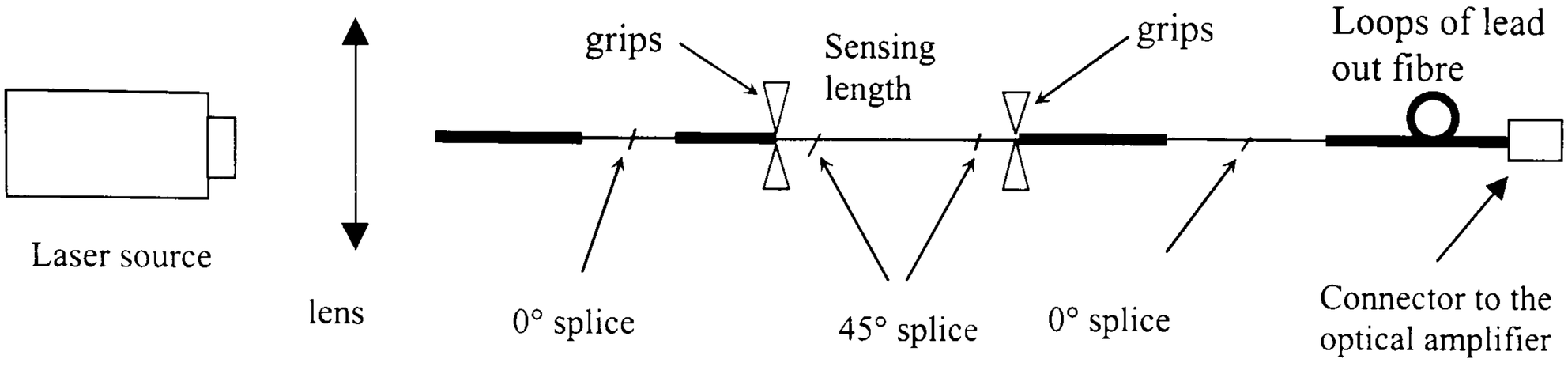

Figure 4.3 Different structures of free sensors.
(a) 45° splices within grips;
(b) 45° splices outside grips, 0° splices within grips;
(c) 45° splices outside grips, 90° splices within grips.

sensor was connected to the other part of the light path by two 45° splices outside the grips. The gauge length between the two grips was 185 mm and the gauge length of the sensor between two 45° splices in Figure 4.3(a) was about 100 mm (see Section 4.5 for better details).

For testing embedded sensors, two configurations of the polarimetric sensor were embedded into the coupons, as shown schematically in Figure 4.4. Again, as in Figure 4.3, the thicker lines represent optical fibres with coatings (inner coating and outer coating), and the thinner lines represent stripped fibres (without any coating). In the

first type, the 45° splices were embedded within the coupon, with gauge lengths (the distance between the splices) in the range from 50 to 100 mm (Figure 4.4(a)). In the second type, the 45° splices were outside the coupons. This latter configuration resembles a situation in which the gauge length of the sensor is unlimited. For this latter configuration, an additional 0° splice was used to join the two pieces of stripped fibres (Figure 4.4(b)).

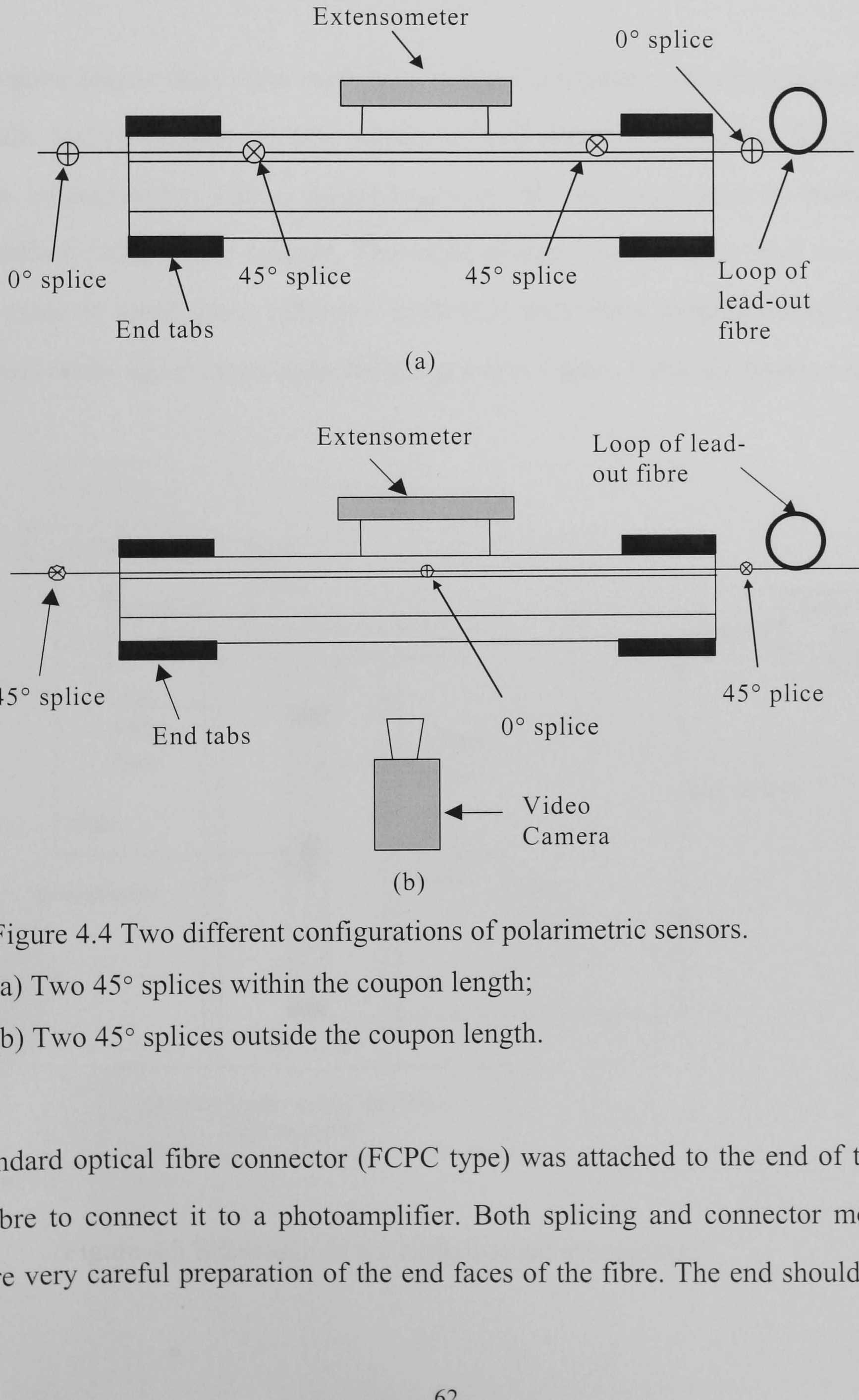

Figure 4.4 Two different configurations of polarimetric sensors.

(a) Two 45° splices within the coupon length;

(b) Two 45° splices outside the coupon length.

A standard optical fibre connector (FCPC type) was attached to the end of the lead-out fibre to connect it to a photoamplifier. Both splicing and connector mountings require very careful preparation of the end faces of the fibre. The end should be both

perpendicular to the axis of the fibre and have a surface that is optically flat. This was achieved by using a high precision Fujikura cleaver (CT-07) and polishing the fibre end with a single mode one-piece FC connector kit.

4.4 Mechanical test methods for coupon testing

4.4.1 Quasi-static loading

Quasi-static tensile tests were performed using a computer controlled Instron servo-hydraulic testing machine (8000), usually in load control mode (ramp function). An Instron extensometer with a gauge-length of 50 mm was used to monitor the longitudinal strain of the coupon. The extensometer knife edges rested on grooved seats, made of cured epoxy adhesive, to prevent them from slipping during the tests. Load and strain signals were recorded using a data logger, while the damage state was

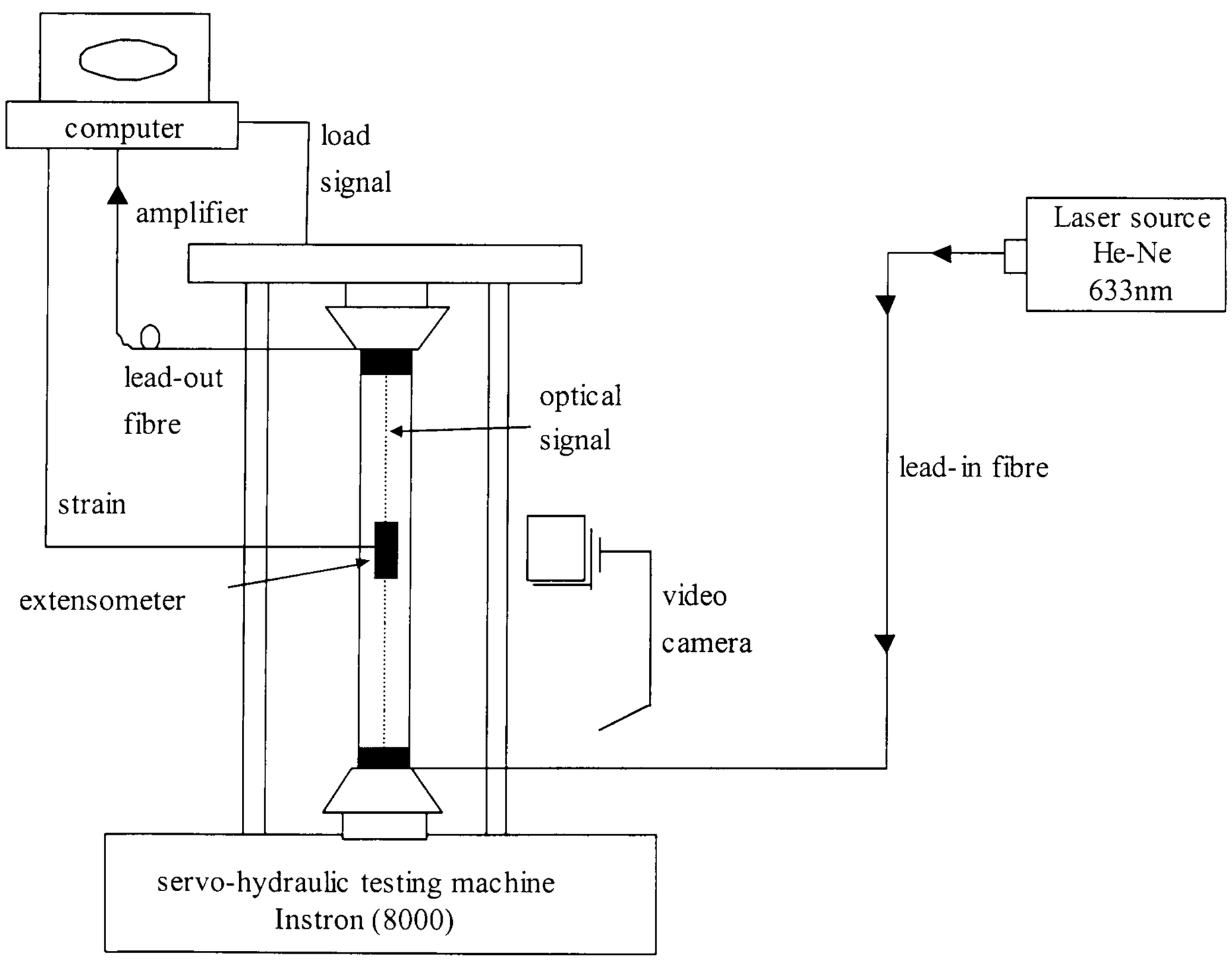

Figure 4.5 Schematic of the experimental arrangement.

monitored directly using a video camera (see Chapter 6). The data-sampling rate (the volume of data the computer records per second) could vary from 0.1 kHz to 1.667 kHz, and the optimum rate for each test was determined to ensure a reasonable file size (below 20 MB) and clear fringes (see Section 5.5). A schematic experimental arrangement for a test in simple tension is shown in Figure 4.5.

Initially, the development of transverse ply cracks was deduced from videos taken with an analogue video camera which were subsequently converted into digital format. Pictures derived from the digital video were then examined to show the occurrence and propagation of the cracks. A digital timer placed beside the coupon showed exactly the moment that the cracks passed the embedded sensor. It should be noted that the mechanical test and the timer were started manually, and hence there is a small difference in the time shown on the timer and the time recorded by the computer. By gently tapping the extensometer at the beginning of the test, strain spikes were introduced into the recorded strain signal, so that the time difference between the timer and the computer data-logger could be obtained. For example, in Figure 4.6(a), the time of the second tap recorded by the computer is 9.4s, whereas in Figure 4.6(b) the time of the second tap shown on the digital timer is 9.88s. Hence, there is a known time difference between the computer recordings and the visual recordings, of 0.48s.

In subsequent tests, a digital video recorder was used which made the additional digital timer unnecessary, although synchronisation using the tapping routine was still required.

4.4.2 Fatigue loading

Tension-tension fatigue tests were carried out using an Instron servo-hydraulic testing machine (8000) at a frequency in a range from 1 to 10 Hz and stress ratio, R, (R = minimum stress/maximum stress) of 0.1, using a sinusoidal waveform. The test

machine was used usually in load control mode. Most tests were in tension-tension mode and quasi-static tensile tests were carried out first to determine the stiffness of each coupon from which fatigue test parameters were calculated to give the required stress and strain levels for the coupons. A similar procedure was adapted for tests carried out in four-point bending.

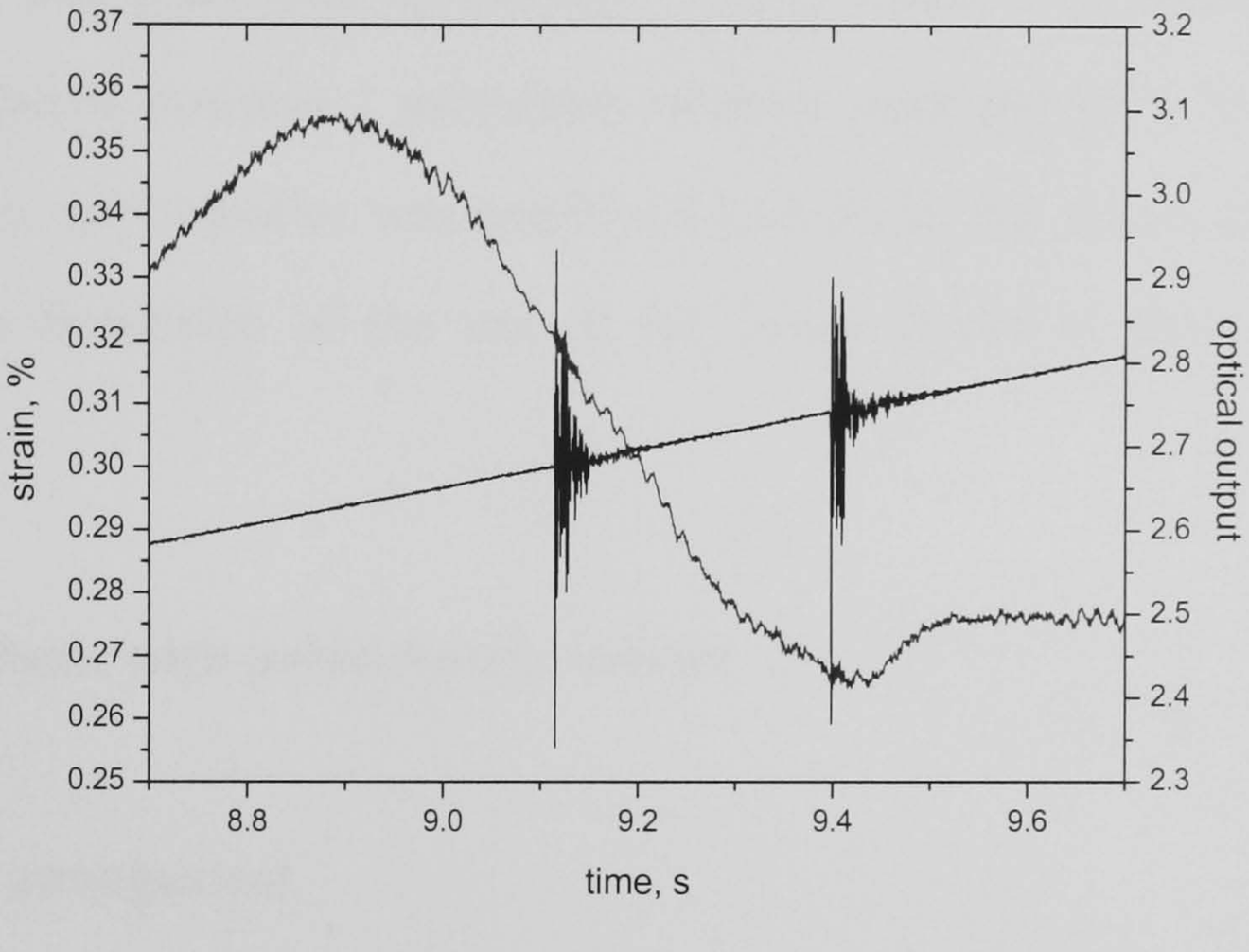

(a)

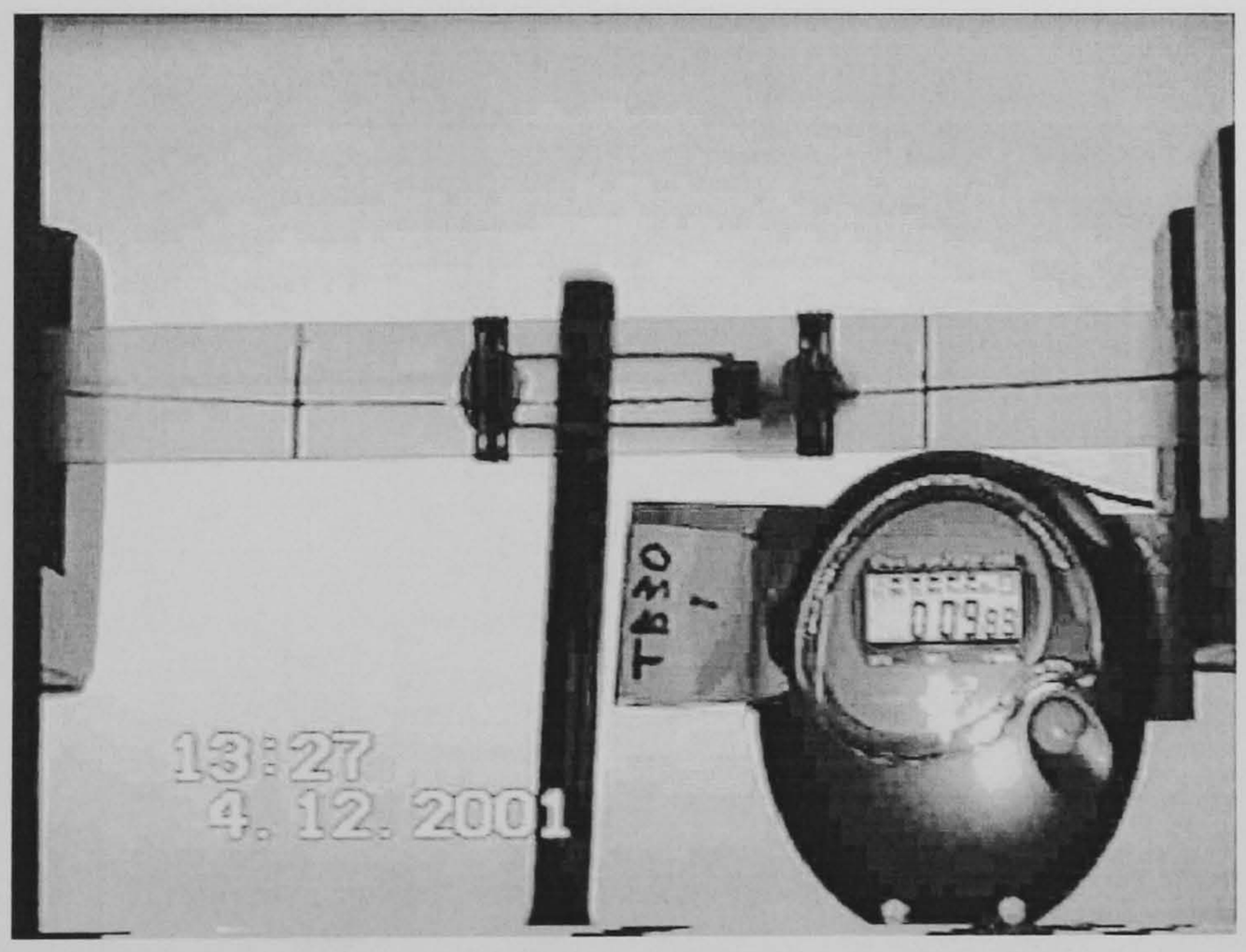

(b)

Figure 4.6 Synchronization of the timer and the fatigue machine.

(a) Two strain spikes introduced by tapping the extensometer twice;

(b) Still picture from the digital video file of the second tap.

4.4.3 Four-point bending test

For the four-point bending tests, a special rig was constructed to fit into the grips of the fatigue machine. The experimental arrangement is shown in Figure 4.7. The distance between the inner rollers is 85 mm and the distance between the outer rollers is 185 mm. For the fatigue tests in four-point bending, the frequency was 1 Hz and the test machine was controlled by position control mode with position ratio, R, (R = minimum relative position / maximum relative position) of 0.33 and a saw-tooth waveform. An extensometer was employed to monitor the strain, as shown in Figure 4.7. Detailed discussion of the use of the extensometer in these tests is given in Section 8.3.

4.5 Test methods with polarimetric sensors

4.5.1 Optical arrangement

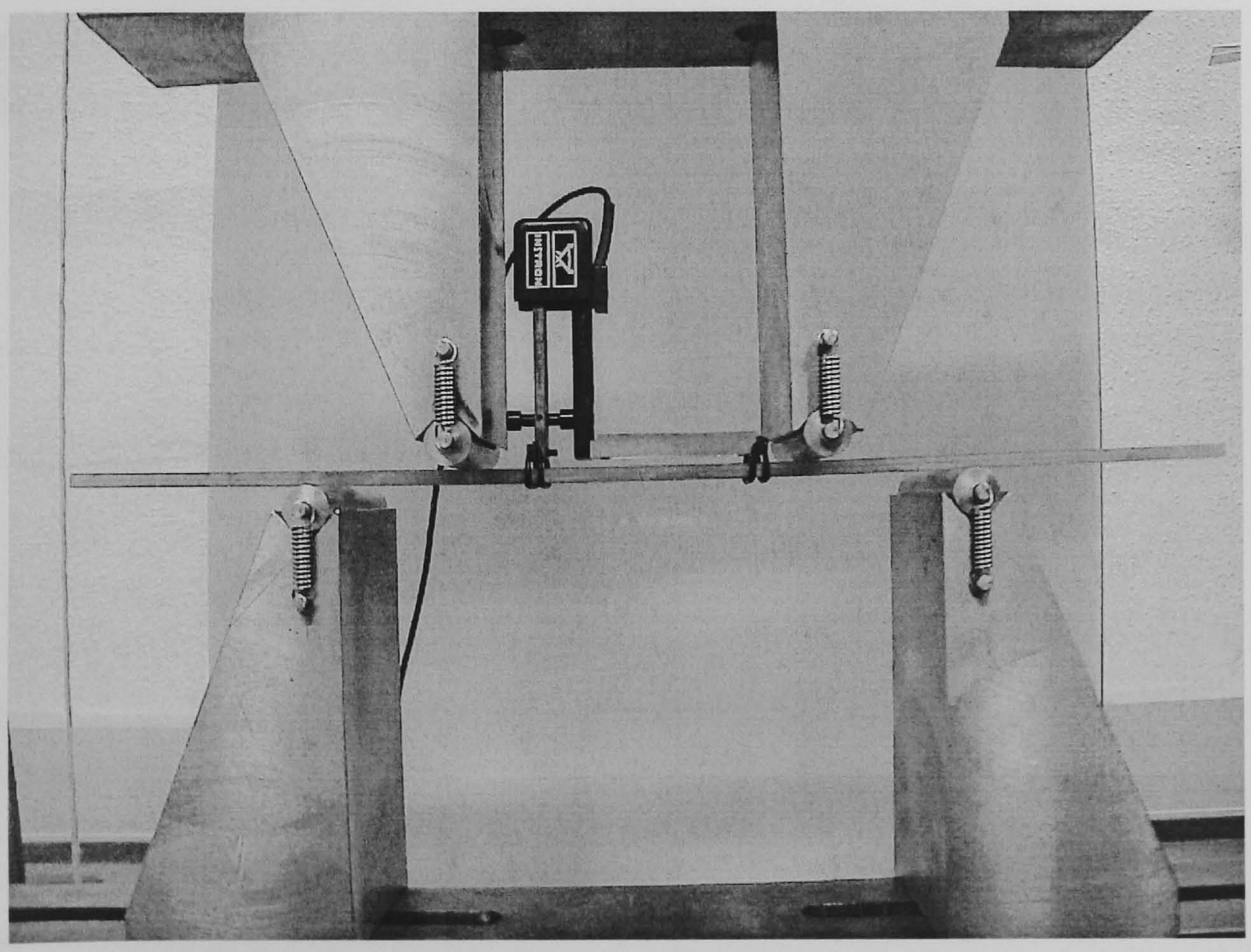

Figure 4.7 Experimental setup of four point bending test.

Linearly polarised light from a He-Ne gas laser source (part B in Figure 4.8), 633 nm operational wavelength, was launched into the fibre core fibre through a Newport F-91 series precision fibre coupler (part C in Figure 4.8). As discussed in Section 3.4, the incoming light needs to excite exactly one of the two modes in the core. This was achieved as follows (note that the supporting background theory for this procedure is discussed in Section 5.2):

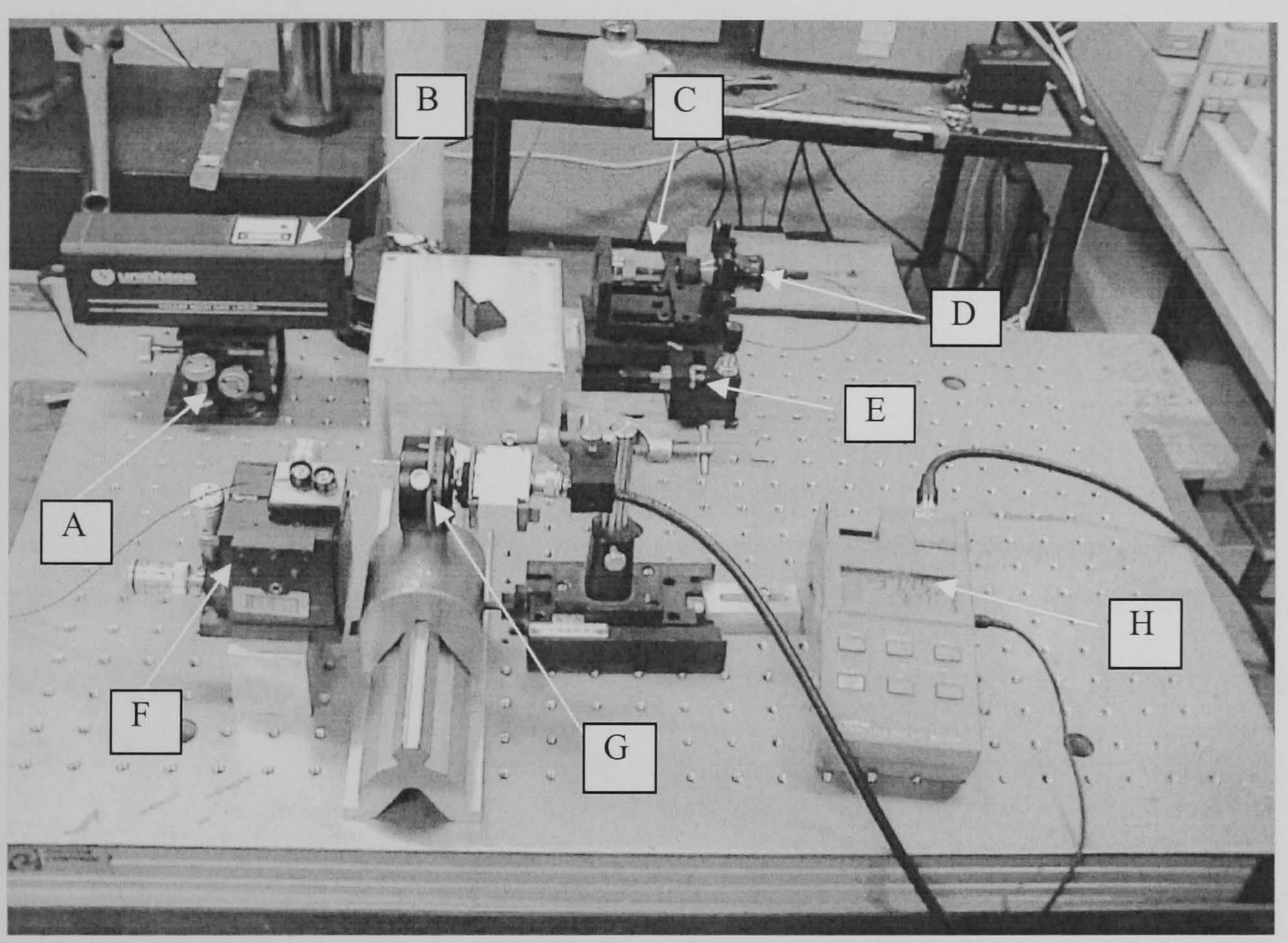

(a)

(b)

Figure 4.8 Optical path arrangement of polarimetric sensors.
(a) Experimental arrangement;
(b) Schematic of the experimental arrangement.
Key to labelled devices:
A. Micro-translator holding laser source. B. He-Ne laser source
C. Optical coupler. D. Optical chuck. E. Micro-translator holding lead-in fibre.
F. Micro-translator holding lead-out fibre. G. Optical analyser.
H. Portable optical meter

(1). The relative position of the laser source and the cleaved end of the optical fibre was adjusted to ensure that light coupled from the laser source into the fibre core was maximised. This was achieved by adjusting the micro-translators of both the laser source (part A in Figure 4.8) and the fibre holder (part E in Figure 4.8), carefully, and monitoring the output using a portable optical meter (part H in Figure 4.8).

(2). The other end of the fibre was stripped, cleaved and held by another micro-translator (part F in Figure 4.8). A polarising analyser (part G in Figure 4.8) was placed in front of this fibre end and the detector of a portable power meter (part H in Figure 4.8) was positioned behind the analyser. The micro-translator was adjusted to ensure that maximum light was launched into the detector.

(3). When the polarising analyser (part G in Figure 4.8) was rotated through 360°, a sine wave form of the optical output was recorded, as expected, because the incoming light from the laser was linearly polarised in one plane. The analyser was then rotated to one of the angles at which maximum light intensity could be obtained.

(4). Finally, the optical fibre at the laser end was rotated using an optical chuck (part D in Figure 4.8). An approximately sine squared (or cosine squared) wave form of the optical output was recorded (see Figure 4.9). The fibre was now rotated to one of the angles where the maximum light intensity was obtained. At this angle, the incoming linearly polarized light excited exactly one of the two modes in the optical fibre core.

For optical fringes to be detected using the polarimetric sensor, separation and elimination of one of the orthogonal modes of the optical signal, produced by interference at the second splice, is required. This was achieved by bending the lead-out part of the optical fibre, which induced the loss of one of the modes through the cladding (see Section 3.4.1). The appropriate bend radius and number of loops were determined experimentally by repeating quasi-static tests on the same sensor

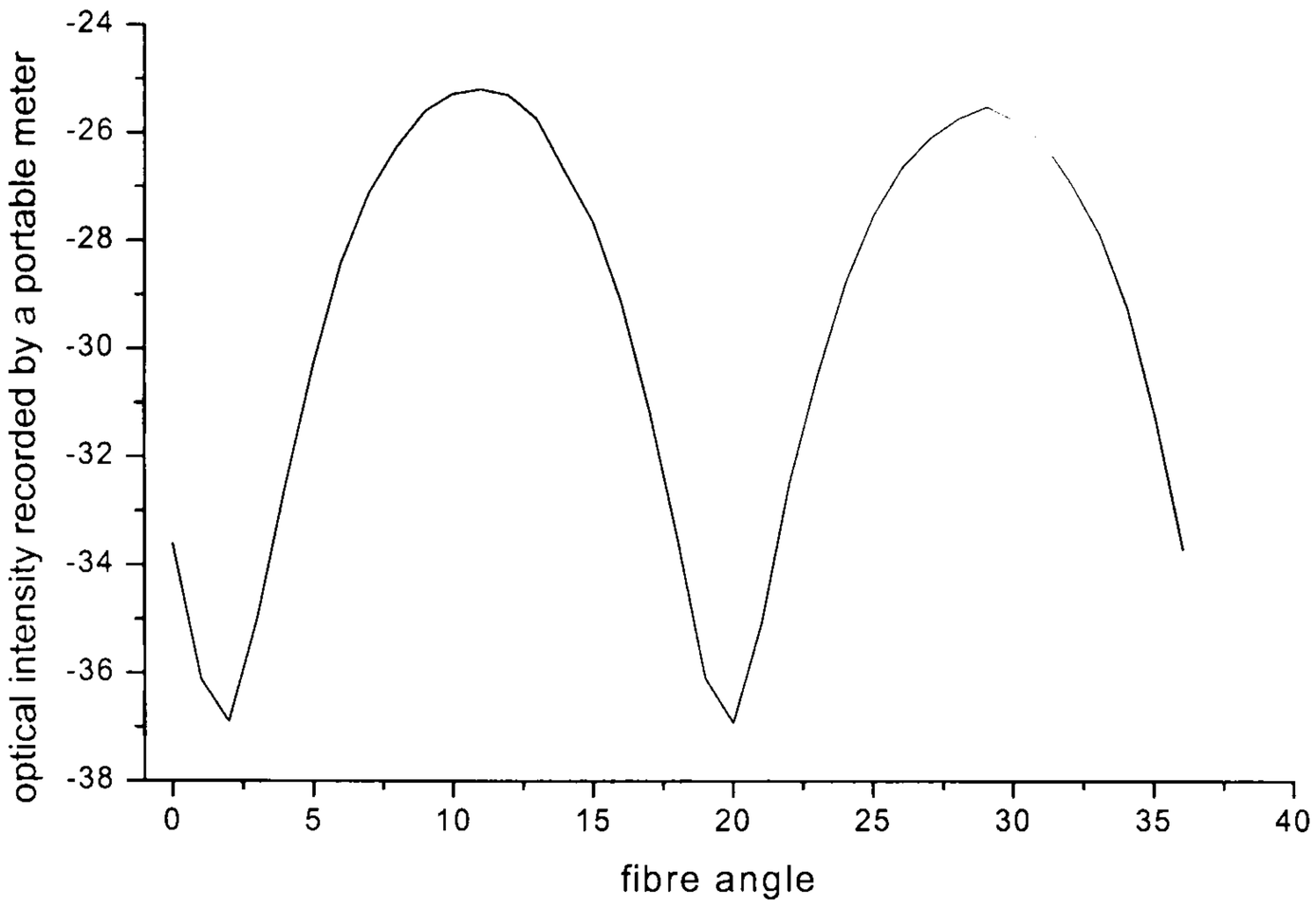

Figure 4.9 Changes of optical output with when light is launched into the fibre at different angles.

embedded in an unidirectional coupon between strain of 0% and 0.3%, using different bend radii and different numbers of loops of the lead-out optical fibre. Detailed results are discussed in Section 5.3. The optimum bend of the lead-out fibre was determined to be: loop diameter, 9.5 mm; number of loops, 8. All experiments using polarimetric sensors employed this optimum configuration.

After separation of the modes, the lead-out fibre was connected to the photo amplifier, which was an in-house manufactured transconductance amplifier with a pin photodiode (BPW87) as the active device. The optical output was converted to a voltage and recorded simultaneously with the load and strain signals by the Instron servo-hydraulic controller. The data sampling rate varied from 0.1 kHz to 1.667 kHz. Demodulation techniques or filters were not used during data acquisition.

4.5.2 Tension test of free sensor

Tension tests and transverse compression tests of free sensors were carried out to determine strain-optical coefficients of the polarimetric sensor (see Chapter 9). 'Free sensor' here means a polarimetric sensor that is not embedded in a coupon. The

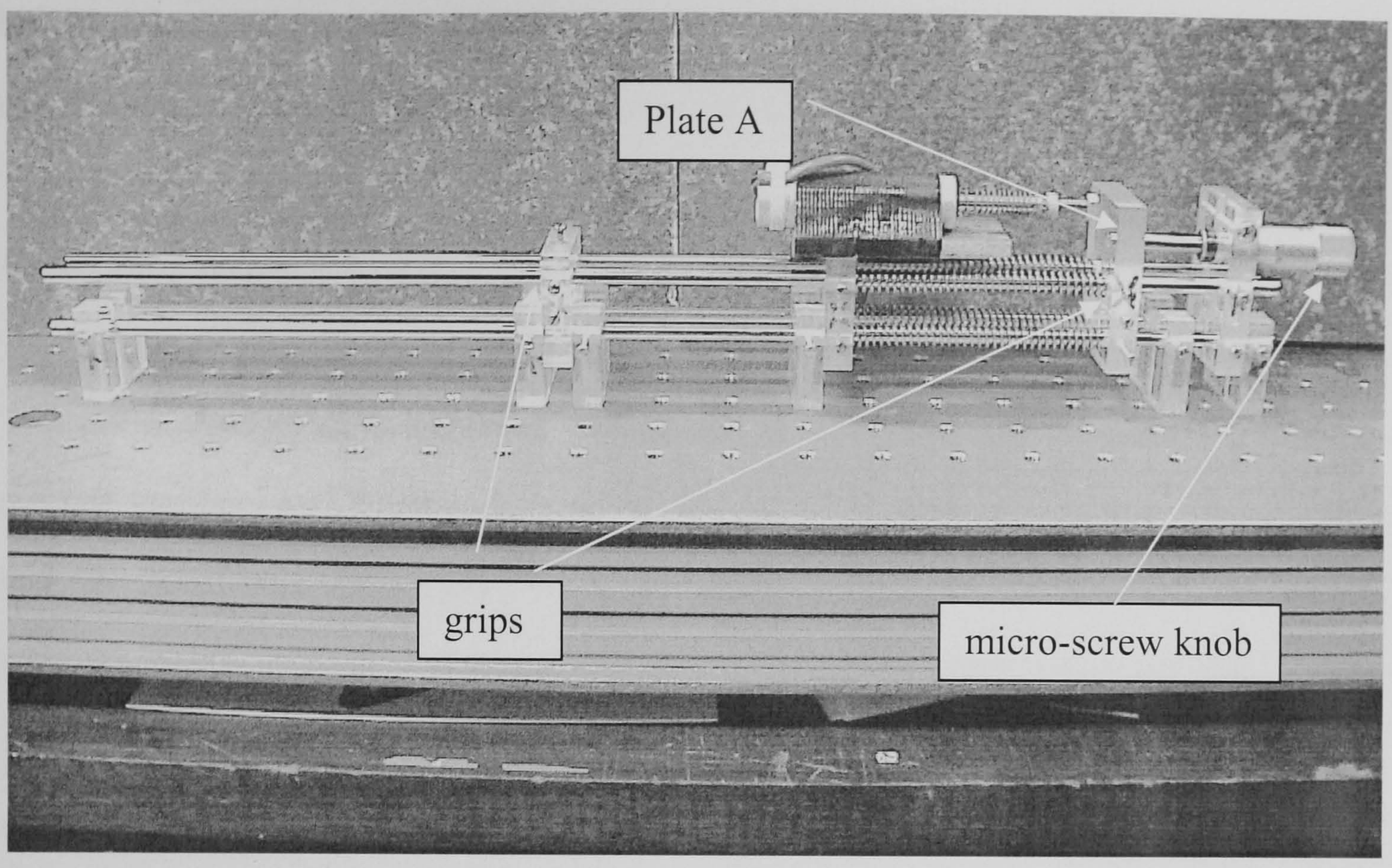

(a)

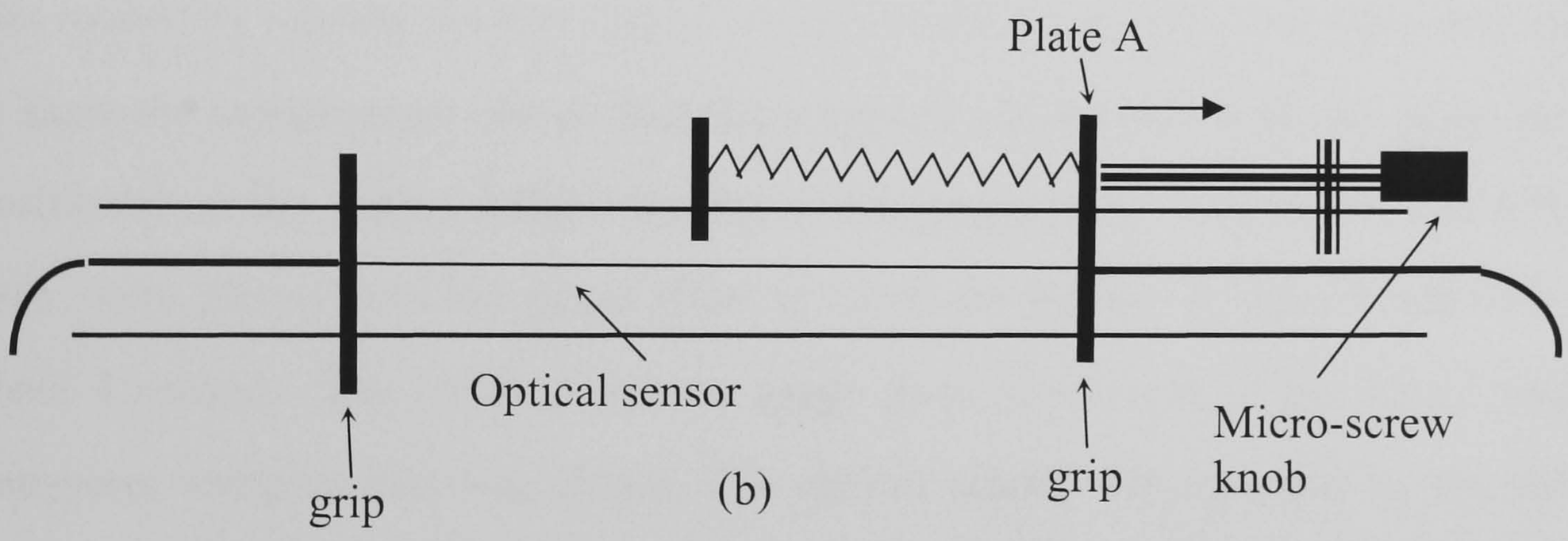

(b)

Figure 4.10 Free sensor tension rig.
(a) Experimental arrangement;
(b) Schematic of the experimental arrangement.

manufacture of the sensor was the same as described in Section 4.3 and the sensor was stripped, and had two 45° splices at various distances apart. . The tensile tests were carried out in a specially made tension rig (see Figure 4.10). The sensor was fastened to the frame by two grips. The grips could move along the frame to allow different gripped gauge lengths of the sensor. Displacement of the sensor was introduced by withdrawing plate A using a micro-screw knob at a manually controlled speed. Strain on the sensor was calculated by dividing the displacement of the plate

by the length of the bare fibre between the two grips. The two 45° splices in the experiments were either within the grips or outside them.

4.5.3 Compression tests of the bare polarimetric sensor

Transverse compressions tests of bare polarimetric sensors were carried out using manual loading. The experimental setup is shown in Figure 4.11. Three gauge plates and an optical bench were used in the experiments to ensure a flat surface during the tests. Two optical chucks, marked at angles of 15°, were used to grip the fibre and to control the rotation of the sensor. Before the sensor was removed from the splicer, at which point the fibres were straight and without any twist, two marks were made on both end of the fibre to minimise the twist of the sensor during the tests. The sensor was rotated by rotating the two chucks simultaneously. A dummy bare fibre was used to share the compression load so that the weights could be placed on the gauge plate positioned on the sensor without tipping of the gauge plate. Ten weights, of 475 g each, were placed onto the gauge plate by hand one by one at regular intervals of about 4 seconds. The width of the top gauge plate (the length of the sensor under transverse compression) was 20mm. The optical output was recorded by the data-logger as a function of time and the resulting fringe profile was stepped because of the manual nature of the tests.

4.5.4 Temperature response of the polarimetric sensor

The temperature response of the polarimetric sensor was characterised by testing the response of the sensor to temperatures in the range from 20 °C to 120 °C. Figure 4.12 shows the schematic experimental arrangement. In these tests, a polarimetric sensor with a gauge length of 1 m was put into an oven and the sensor was connected to the laser light path by two 45° splices as usual. The splices, however, were put into the oven to make sure that the whole length of the sensor was experiencing the same change of temperature. The optical fibre was looped within the oven to eliminate non-

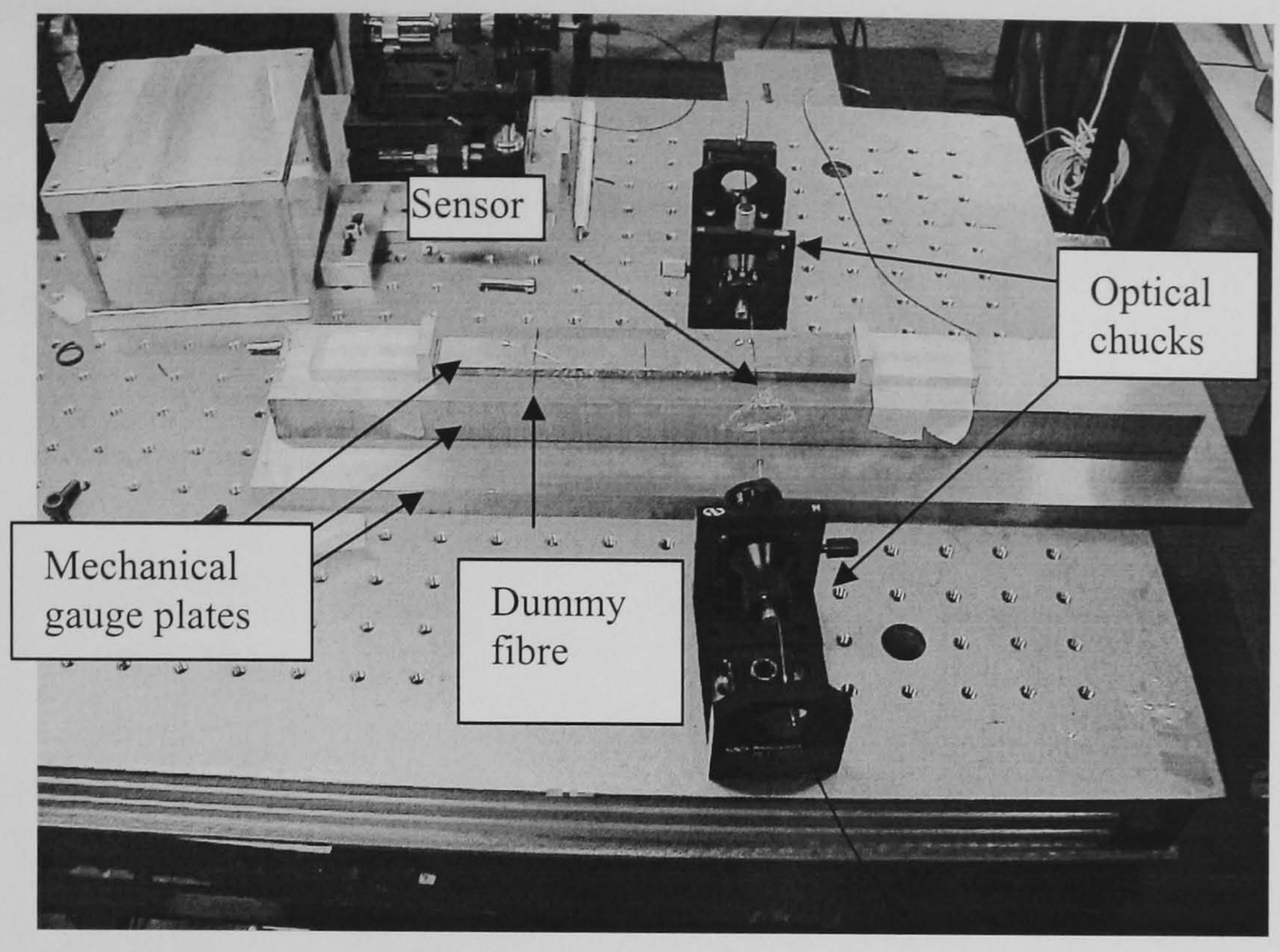

(a)

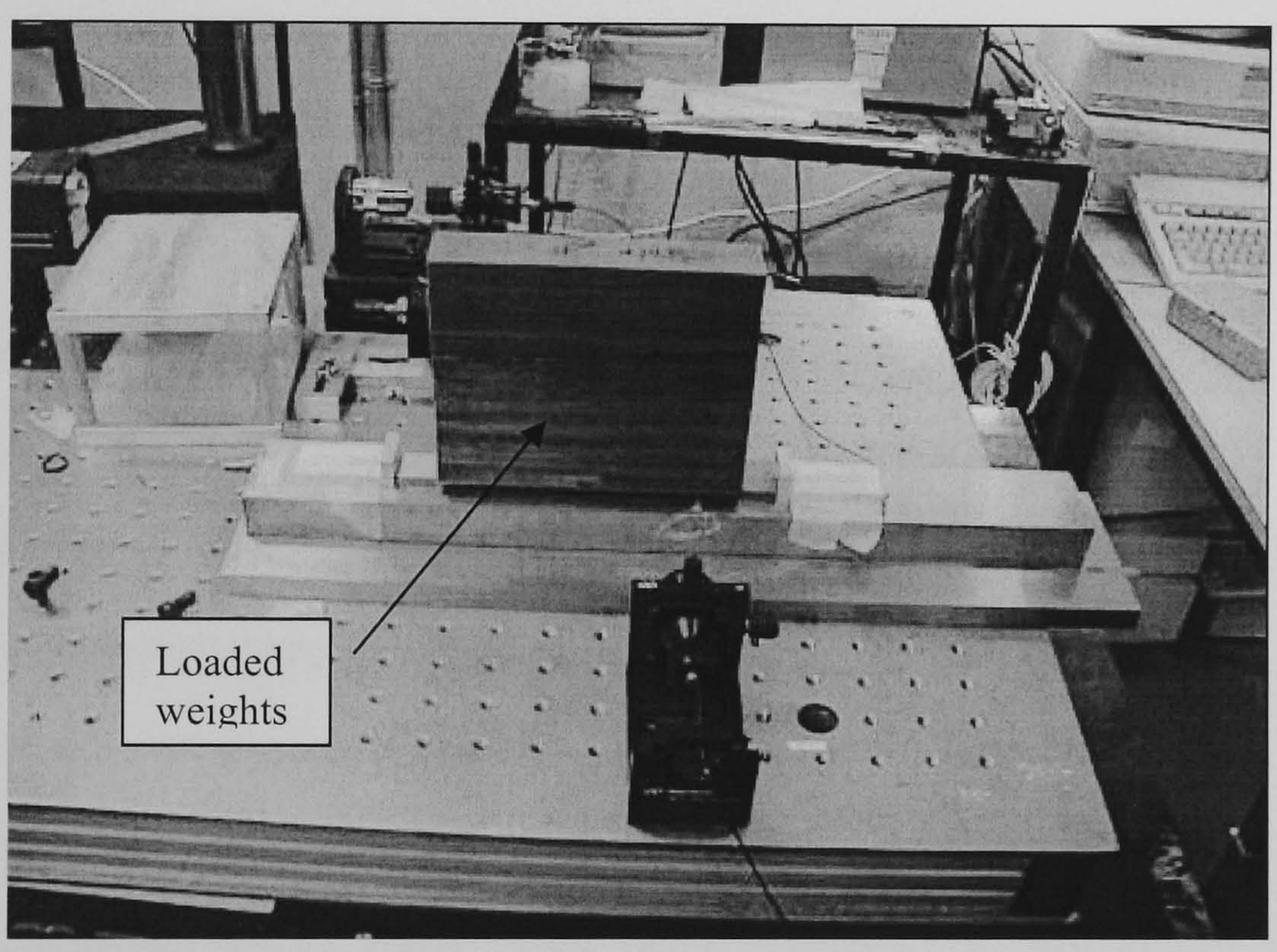

(b)

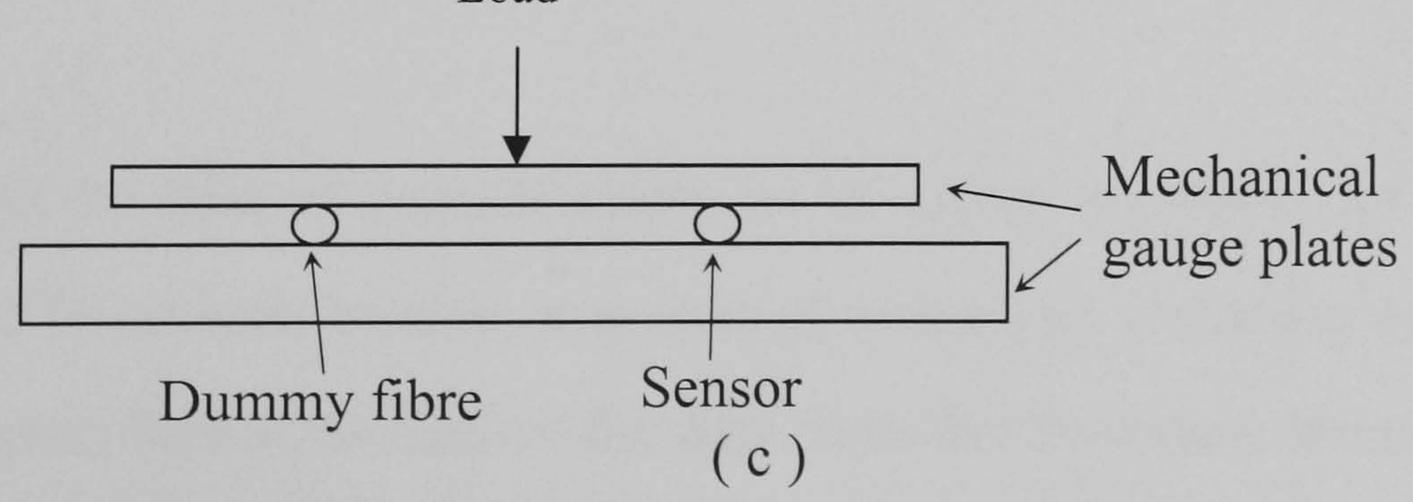

(c)

Figure 4.11 Experimental set up of compression tests of bare polarimetric sensor.
(a) Before loading the weights; (b). After the weights has been loaded;
(c) Schematic of experimental arrangement.

uniform thermal effects and a thermometer was positioned near the optical fibre to measure the temperature around the sensor. The temperature signal and optical signal were recorded by the computer simultaneously. The results of these tests are described in Section 5.7.

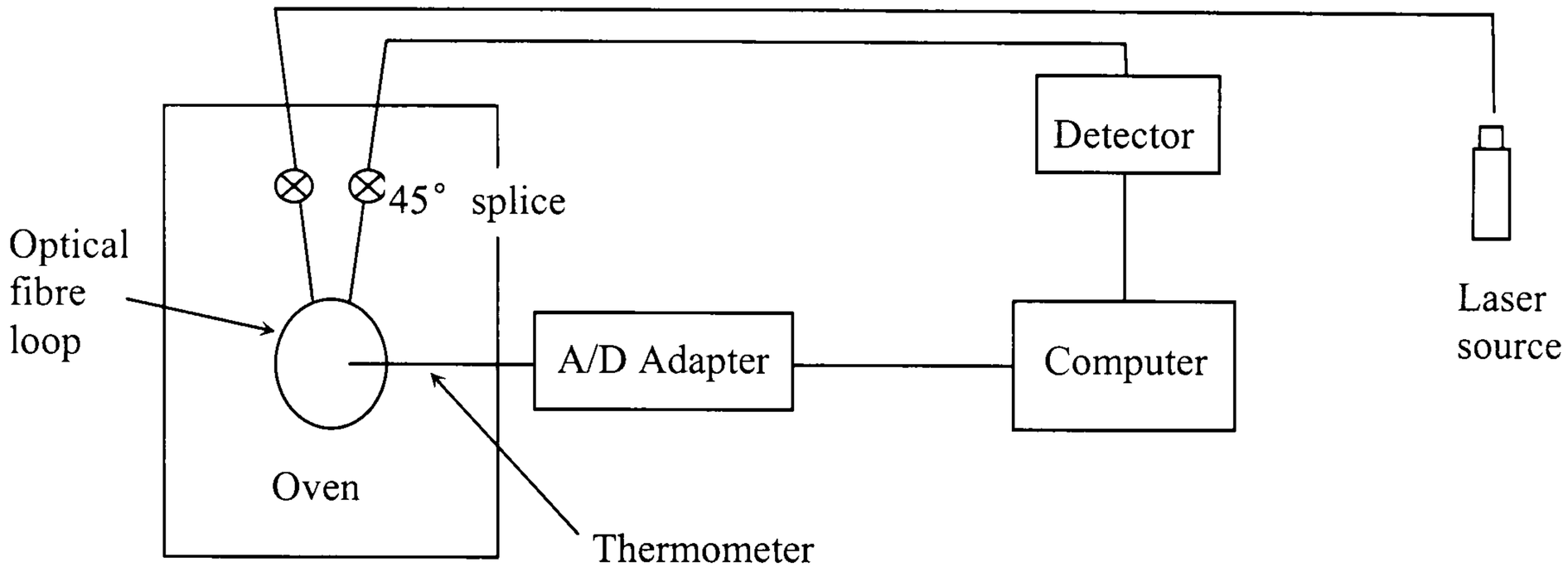

Figure 4.12 Experimental arrangement for the temperature tests on polarimetric sensors.

4.6 Data processing method

The optical output recorded in the tests with the sensors was usually in the form of a sinusoidal variation (more specifically $\sin^2$ or $\cos^2$). However, a sudden change in the signal was seen when a crack passed the sensor (see Chapter 6). As will be seen, in some of the tests, it was necessary for the recorded data to be filtered using a Fast Fourier Transform (FFT) filter. This was achieved by employing the computer software ORIGIN® 6.0 in the following steps (see ORIGIN manual, 1999):

Firstly, the set of data of interest needs to be input; secondly, the Fast Fourier Transform (FFT) analysis window was opened to analysis frequency composition of the optical signal; finally, to convert the data from the frequency domain to the time domain, the data of interest was multiplied by a FFT filter function.

The type of filter used here was a FFT band pass filter, which is one of four common types of frequency filters shown schematically in Figure 4.12: (a) low pass, (b) high pass, (c) band reject and (d) band pass. The purpose of these filters is to allow some frequencies to pass unaltered, while completely blocking other frequencies. The low pass filter means that only frequencies lower than a defined frequency can pass, while the high pass means only frequencies higher than a defined frequency can pass. In a band reject filter, all the frequencies between two defined frequencies are rejected. The band pass means only frequencies between defined frequencies can pass.

In the present study, a standard Fourier Frequency analysis was carried out initially to find out if there were any frequencies changes in the optical output as the cracks passed the sensor (using ORIGIN® 6.0). Then the FFT band pass filter was used to pick out the time when the frequency changes occurred together with the video

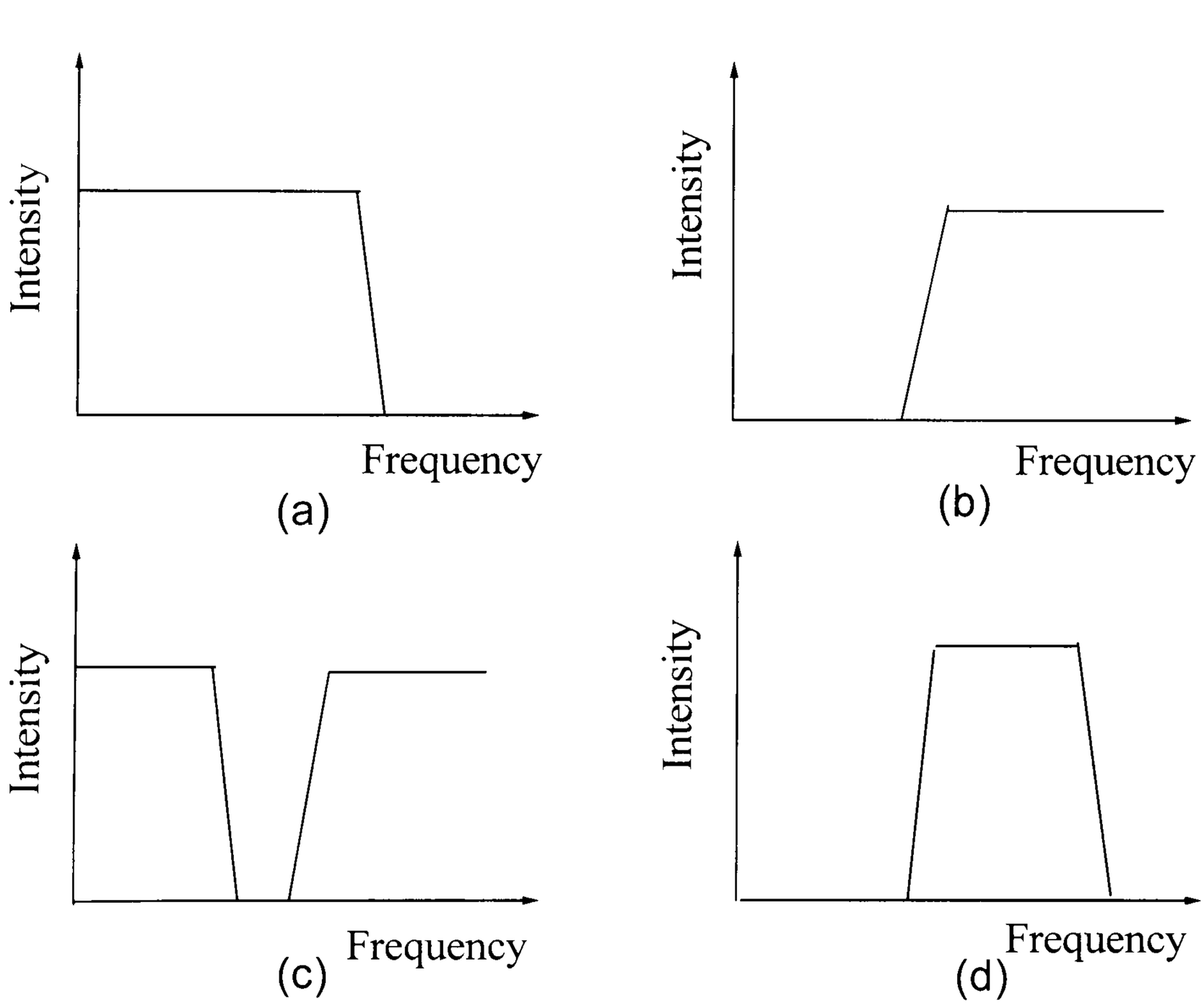

Figure 4.13 The four common frequency responses.

(a) low pass; (b) high pass; (c) band reject; (d) band pass.

recording showing developments of the cracks.

4.7 Concluding comments

In this chapter, the optical and mechanical testing arrangements have been described. In the next chapter, results on the general characteristics of the polarimetric sensor will be presented.

Chapter 5. General characteristics of the polarimetric sensor

5.1 Introduction

Before the polarimetric sensors could be used to detect damage (e.g transverse cracks in a GFRP laminate), the fundamental behaviour of the polarimetric sensor needed to be investigated. In this chapter, the results of these tests are described.

5.2 Optimisation of the light path arrangement

The light path was arranged as described in Section 4.5.1. The reason why the light path was arranged in such a way is discussed here.

The linearly polarised light from the laser source can be expressed as:

$$\hat{E} = \hat{E}_0 \cos(\hat{k} \cdot \hat{r} + \omega t + \varphi_0) \qquad 5.1$$

Here $\hat{E}$ is the electric amplitude vector, $\hat{E}_0$ is the maximum amplitude of the electric amplitude vector, $\hat{k}$ is the propagation vector, $\hat{r}$ is the space vector, ω is the angular frequency and φ_0 is the initial phase.

In general cases, the light is launched into the optical core at a random angle to the x-axis of the core, so that both modes in the core are excited, but unequally, as shown in Figure 5.1(a). The light waves in the x -and y- mode can be expressed as:

$$\begin{aligned} E_x &= E_0 \cos\theta \cos(kx + \omega t + \varphi_0) \\ E_y &= E_0 \sin\theta \cos(ky + \omega t + \varphi_0) \end{aligned} \qquad 5.2$$

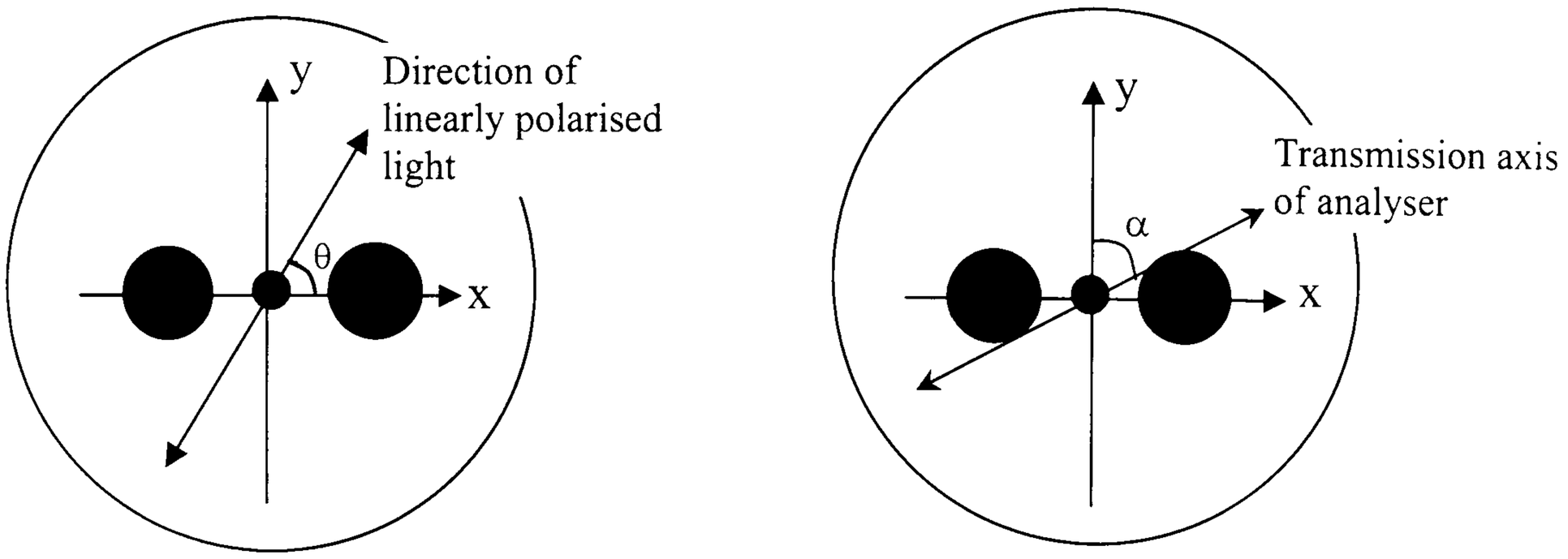

(a) (b)

Figure 5.1 (a) Relative orientation of linearly polarised light and axes of fibre core.
(b) Relative orientation of linearly transmission axis of analyser and axes of fibre core.

where θ is the angle between the x-axis (mode) of the fibre and the direction of the polarisation of the incoming light.

The light intensity in both modes can be expressed as:

$$I_x = I_0 \cos^2 \theta$$
$$I_y = I_0 \sin^2 \theta \qquad 5.3$$

where I_0 is the initial light intensity that is launched into the optical fibre core, I_x and I_y are light intensities in x- and y-axis in the core respectively.

The different propagation speeds of the light wave in the two modes give rise to a phase difference, $\Delta\varphi$, when the light waves arrive at the far end of the fibre. Hence, the polarisation state of the light emerging from the fibre is elliptically polarised. However this elliptical polarisation can be treated as a vector addition of the polarised light in the x- and y-modes, which can be handled separately.

Assuming that the transmission axis of the analyser is oriented at a random angle, α, to the x-mode direction, as shown in Figure 5.1(b), then the electric vector components of both modes along the transmission axis are:

$$\begin{aligned} E_x' &= E_x \sin\alpha = E_0 \cos\theta \sin\alpha \cos(kx + \omega t + \varphi_1) \\ E_y' &= E_y \cos\alpha = E_0 \sin\theta \cos\alpha \cos(ky + \omega t + \varphi_1 + \Delta\varphi) \end{aligned} \qquad 5.4$$

The light intensity that can pass through the analyser is:

$$I = I_x' + I_y' = I_0 \cos^2\theta \sin^2\alpha + I_0 \cos\theta^2 \sin^2\alpha = [\cos^2\theta - \cos^2\alpha \cos(2\theta)]I_0 \qquad 5.5$$

When the analyser is rotated, the value that changes in equation 5.5 is the angle α. According to equation 5.5, the maximum light intensity recorded by the detector arises when $\alpha = 0$ or π ($cos2\theta>0$) and the minimum light is transmitted at $\alpha = \pi/2$ or $3\pi/2$ ($cos2\theta>0$). Hence, once the analyser is rotated to the angle where maximum light intensity is obtained, the transmission axis of the analyser is now aligned with one of the mode axes in the core, for example, the x-axis.

Once the analyser transmission axis and x-axis in the core are aligned, the light intensity recorded by the detector is:

$$I_x = I_0 \cos^2\theta \qquad 5.6$$

When the optic fibre is rotated, which means θ changes from 0 to 2π, a cosine squared optical output is obtained, as shown in Figure 4.9, which is reproduced as Figure 5.2 here. The optic fibre can now be set to the angle at which the maximum light intensity is obtained, so that the incoming light excites exactly one of the two optical modes in the fibre core.

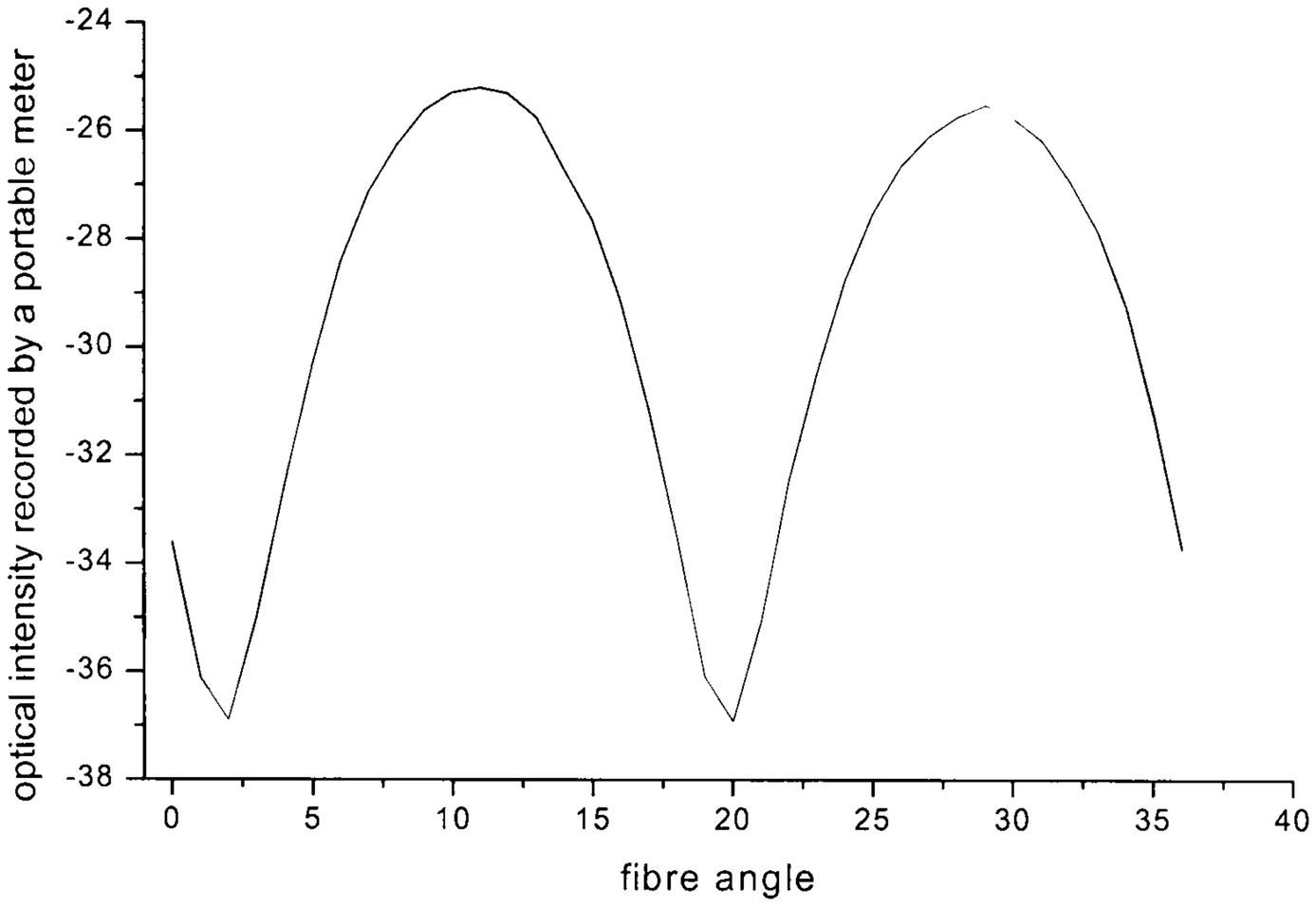

Figure 5.2 Changes of optical output with when light is launched into the fibre at different angles.

5.3 Optimisation of the bending of the lead-out fibre

As described in Chapters 3 and 4, bending the lead-out fibre of the polarimetric sensor removes one of the two orthogonal optical modes and fringes and enables the change of strain in the sensor core to be seen. The determination of the optimum combination of bend diameter and number of loops is described in this section.

As expressed in equation 3.12, the optical output light intensity for both modes of the lead-out fibre can be expressed as:

$$I_x = I_0 \cos^2 \frac{\Delta\varphi}{2} \qquad 5.7$$

$$I_y = I_0 \sin^2 \frac{\Delta\varphi}{2}$$

where I_x, I_y and I_0 are the light intensities in x-mode, y-mode and the initial input light intensity respectively and $\Delta\varphi$ is the phase difference between the two modes induced by an external stimulus within the gauge length of the sensor.

If there is no bending of the lead-out fibre, hence no loss of light, the measured optical output will be:

$$I = I_x + I_y = I_0 \sin^2 \frac{\Delta\varphi}{2} + I_0 \cos^2 \frac{\Delta\varphi}{2} = I_0 \qquad 5.8$$

In other words, the sensor output intensity would be constant and no optical fringes could be seen nor any strain changes in the sensor core would be detected.

When the lead-out fibre is bent, the change of refractive index in the cladding causes some light in the core to leak out. Assuming that a fraction a% of the light intensity in mode x is retained and b% of the light intensity in mode y is retained to be recorded by the detector, then the optical output is:

$$I = a \cdot I_1 + b \cdot I_2 = I_0 (a \cos^2 \frac{\Delta\varphi}{2} + b \sin^2 \frac{\Delta\varphi}{2}) = I_0 [a + (b - a) \sin^2 \frac{\Delta\varphi}{2}] \qquad 5.9$$

In most cases, $a \neq b$, so when $\Delta\phi$ changes with strain, temperature etc., optical fringes will always be seen, even though bending of the sensor has not been optimised.

During tests to optimise the sensor, the optical output obtained for a selection of different combinations of bend diameter and number of loops are shown in Figures 5.3 to 5.6. All the results were obtained from the same polarimetric sensor embedded in a unidirectional laminate under consecutive tests. The coupon was not removed from the grips during the tests.

Figure 5.3, for example, shows the light intensity (i.e. optical output) when the coupon was loaded from a strain of about 0.125% to about 0.4% in about 40 seconds, and then similarly unloaded. In this example, not extra bending of the lead-out fibre was added to the natural bend of the fibre that occurred where the optic fibre emerged

from the coupon. The light intensity shows no obvious fringes with strain. Any fringes of small amplitude (due to the small difference of a and b in Equation 5.9) are presumably buried by the noise of the laser source.

For the test shown in Figure 5.4, 22 loops of 22.5 mm bend diameter were employed. Some noise from the laser source can still be seen, although the fringes due to $\Delta\varphi$ are reasonably clear in this figure. Unsurprisingly, the mean light intensity recorded decreased from Figure 5.3 to Figure 5.4. The fringes are much better defined in Figure 5.5, where 2 loops with a bend diameter of 9.5 mm were employed.

A systematic study of different number of loops and different bend diameters showed that the clearest fringes were obtained with 8 loops and a bend diameter of 9.5 mm (Figure 5.6) although other combination of loop number and bend diameter could give clear fringes as well. For example, a single loop bent to a diameter of 3 mm also gave clear fringes. However, small bend diameters sometimes cause the fibre to break and hence, the bend configuration of 8 loops with a diameter of 9.5 mm has been used in all tests.

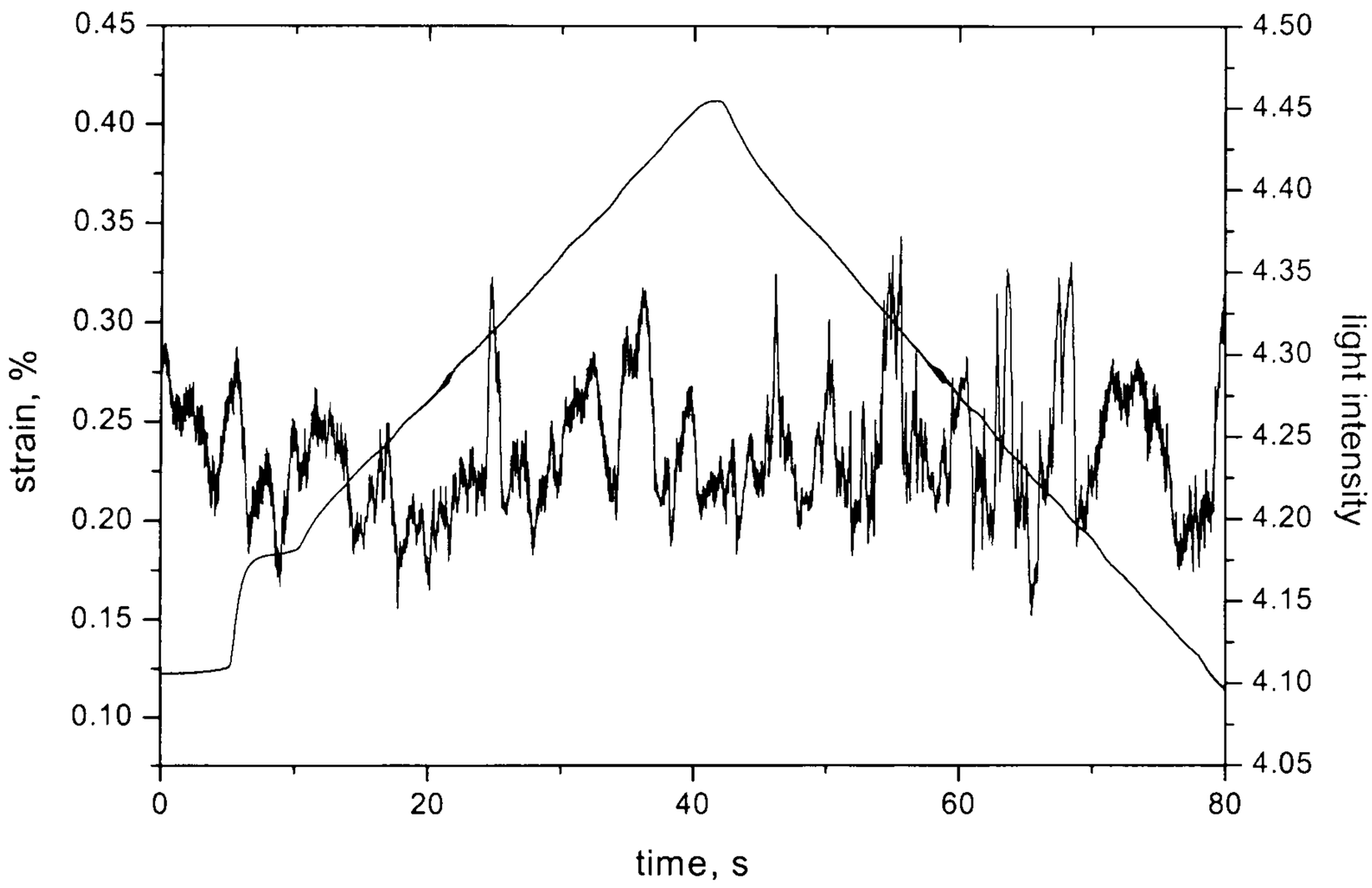

Figure 5.3 Response of strain and optical signal of an embedded polarimetric sensor without bend of lead-out fibre.

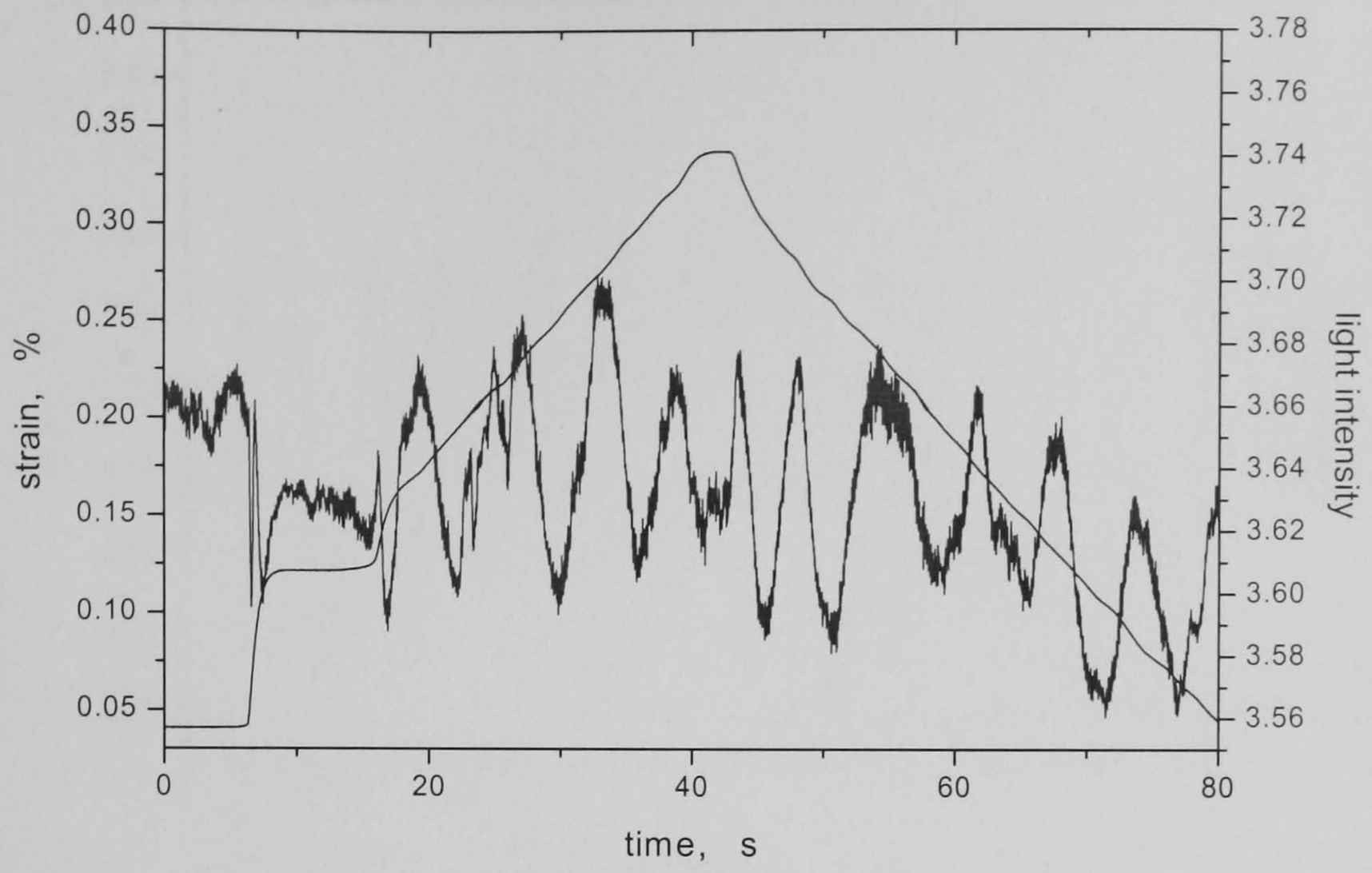

Figure 5.4 Response of strain and optical signal of an embedded polarimetric sensor when lead-out fibre is bent. Bend configuration: 22 loops with a diameter of 22.5mm.

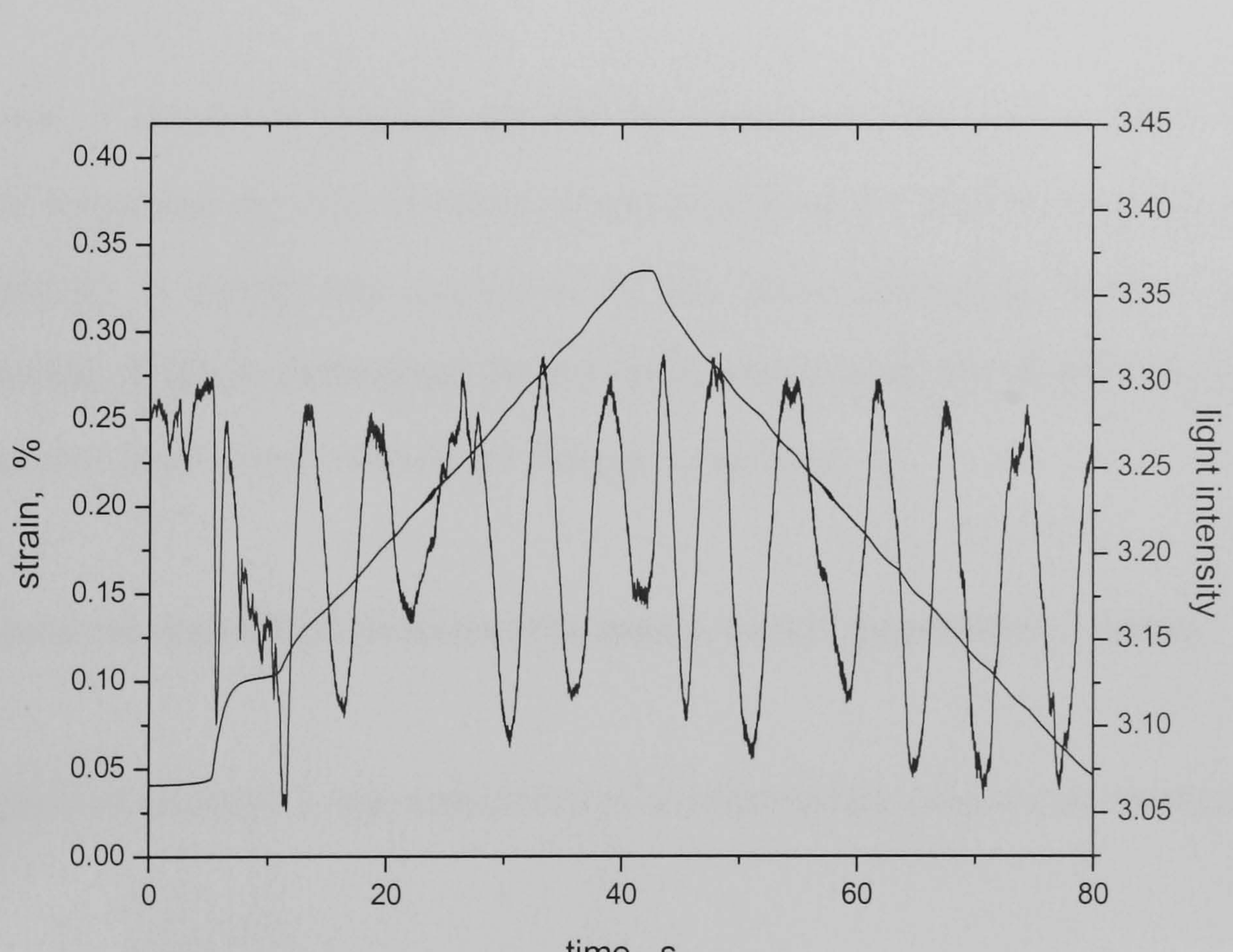

Figure 5.5 Response of optical signal plotted against strain of an embedded polarimetric sensor when lead-out fibre is bent. Bend configuration: 2 loops with a diameter of 9.5mm.

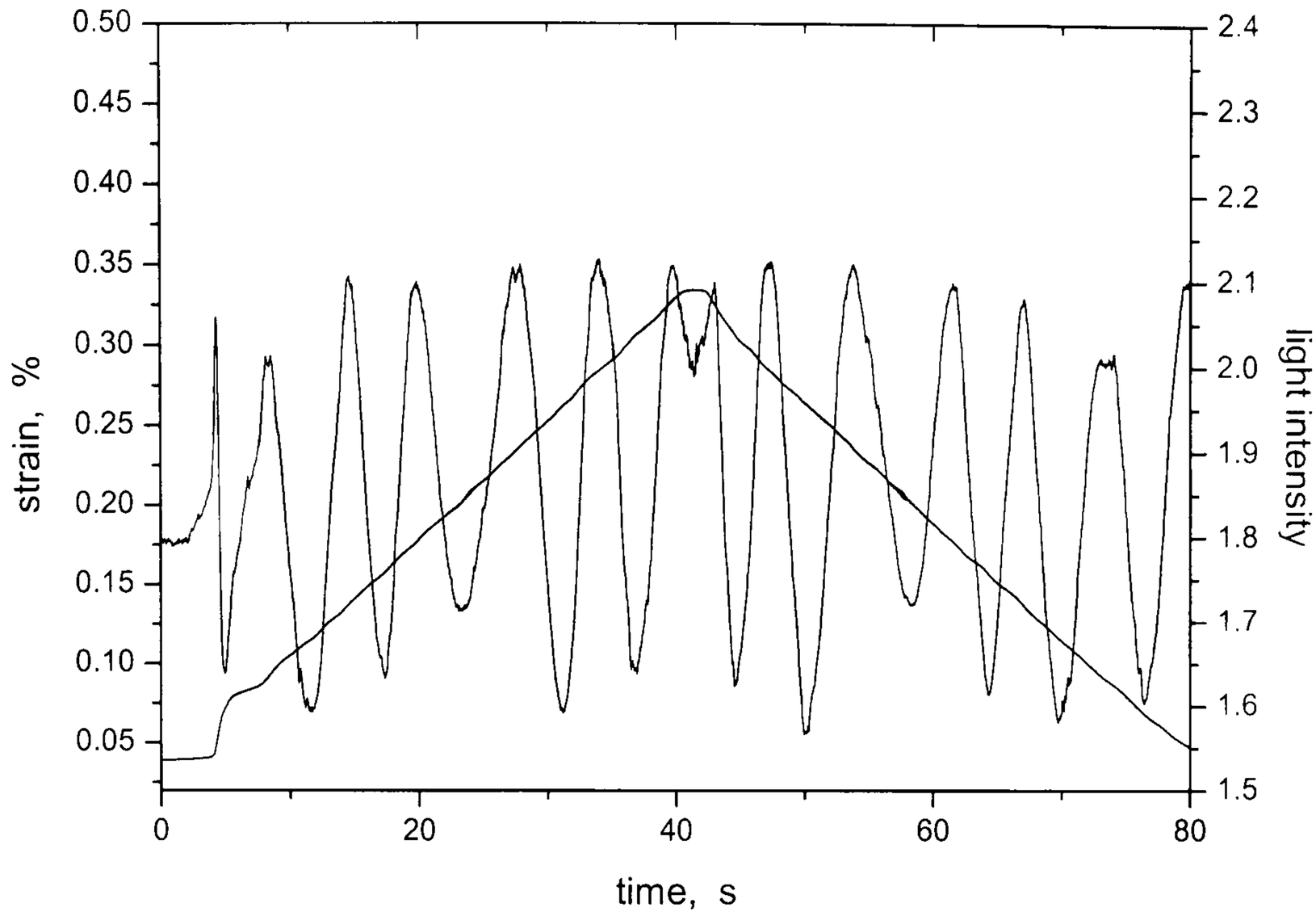

Figure 5.6 Response of optical signal plotted against strain of an embedded polarimetric sensor when lead-out fibre is bent. Bend configuration: 8 loops with a diameter of 9.5mm.

As an aside, it should be pointed out that the bending of the lead-out fibre (i.e. the number of loops and the loop diameter) does not change the sensitivity of the sensors. The sensitivity is completely controlled by the phase difference between the two optical modes, which is determined by the strain state around the sensor. The bending of the lead-out fibre simply allows the fringes to be seen.

5.4 Response of embedded polarimetric sensor under quasi-static loading

As discussed in Chapter 3, the sensitivity of a polarimetric sensor can be represented as:

$$\Delta\varphi = \frac{2\pi}{\lambda}\int_L [K_1\varepsilon_{11} + K_2\varepsilon_{22} + K_3\varepsilon_{33}]dL \qquad 5.10$$

where $\Delta\varphi$ is the relative phase change between the two polarisation modes caused by a three-dimensional strain; λ is the wavelength of light in vacuum; ε_{11}, ε_{22} and ε_{33} are the three normal strains in the fibre core; L is the gauge length of the sensor and K_1. K_2 and K_3 are dimensionless strain-optical coefficients which determine the contribution of each component of the normal strains to the relative phase change, $\Delta\varphi$.

Equation 5.10 shows that the response of the polarimetric sensor depends totally on the strain state around the core. External effects (such as load, thermal effect or impact) will induce additional strain into the core, so that optical fringes reflecting the external influence can be obtained. When the strain field along the sensor is homogenous and independent of the longitudinal direction of the sensor (for example, a polarimetric sensor embedded in a unidirectional coupon), then equation 5.10 can be rewritten as:

$$\Delta\varphi = \frac{2\pi}{\lambda} L(K_1\varepsilon_{11} + K_2\varepsilon_{22} + K_3\varepsilon_{33}) \qquad 5.11$$

In this case, when a polarimetric sensor is embedded in a unidirectional coupon, the relationship between the normal strains in the core of optical sensor and the normal strains in the host coupon is:

$$\begin{aligned} \varepsilon_{11} &= \varepsilon_1 \\ \varepsilon_{22} &= -\nu'\varepsilon_1 \\ \varepsilon_{33} &= -\nu'\varepsilon_1 \end{aligned} \qquad 5.12$$

where ε_1 is the longitudinal strain in the coupon and ν' is the effective Poisson's ratio for the sensor that includes the interaction between the host coupon and the embedded sensor.

Substituting equation 5.12 into equation 5.11,

$$\Delta\varphi = \frac{2\pi L}{\lambda}\varepsilon_1(K_1 - \nu' K_2 - \nu' K_3) = C\varepsilon_1 \qquad 5.13$$

where C is a constant. Equation 5.13 shows that when a polarimetric sensor is embedded in a unidirectional laminate, there is a linearly relationship between the longitudinal strain applied to the coupon and the optical output phase change. This means that when the strain varies with time, the fringes induced by the change of strain will vary with time as well. When the optical signals are plotted against strain, and hence the effect of time is removed, the fringes should be the same for all strain rates. Or, to put it another way, if the optical phase change is plotted against strain, it should be a straight line and the slope of the straight line is the constant C in equation 5.13. Figures 5.7 to 5.10 illustrate these effects.

Figure 5.7 shows recorded data (optical output and strain measured using an extensometer for a simple tension test) for a test using a number of different strain rates when the optical signals and the strain signals are plotted against time. There was no change in strain for about the first 8 seconds, the strain was then increased very rapidly to about 0.14% and held constant for about 20 seconds. The strain was then increased rapidly to about 0.18%, and then more slowly, and uniformly, to about 0.34% at 40 seconds, before being reduced slowly to its original value. Figure 5.8 is a magnification of part of Figure 5.7 for the time range between 6 s and 31 s. The strain rate is the highest from 8 s to 10 s, and the optical fringes during this time are close together. When the strain rate is reduced, e.g between 20 s and 22 s, the optical fringes become wider. The fringes become even wider under the lowest strain rate from 23 s to 30 s. It is worth pointing out that during the time 15 s to 18 s, when there was no strain change, there was no optical phase change (and hence no fringes) as well, even though there were strains acting on the sensor. Hence, another way to view the model expressed by equation 5.10 is that the model describes the dependence of change of optical phase difference on the change of strain state in the fibre core.

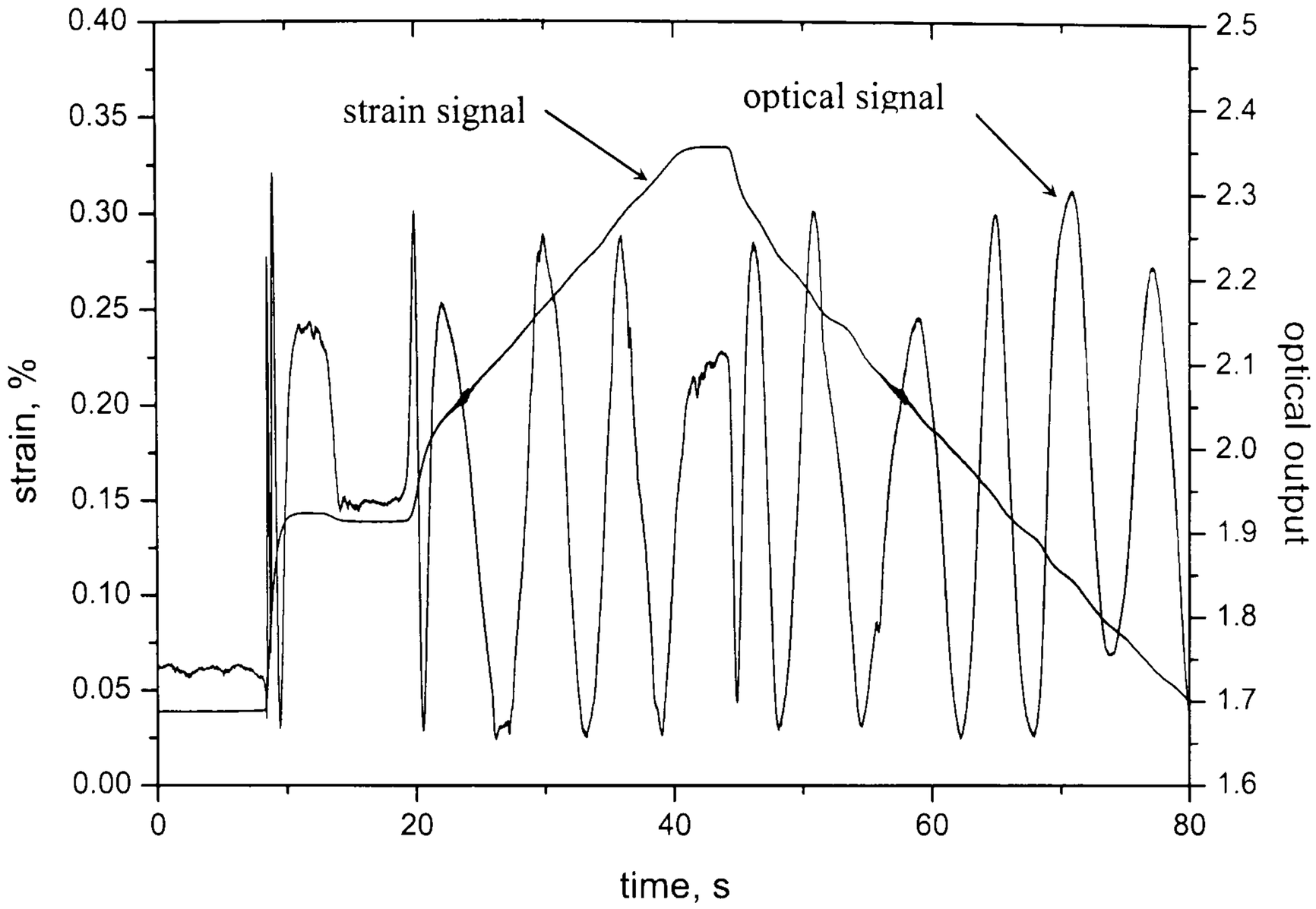

Figure 5.7 Original data recorded from a polarimetric sensor embedded in a unidirectional laminate.

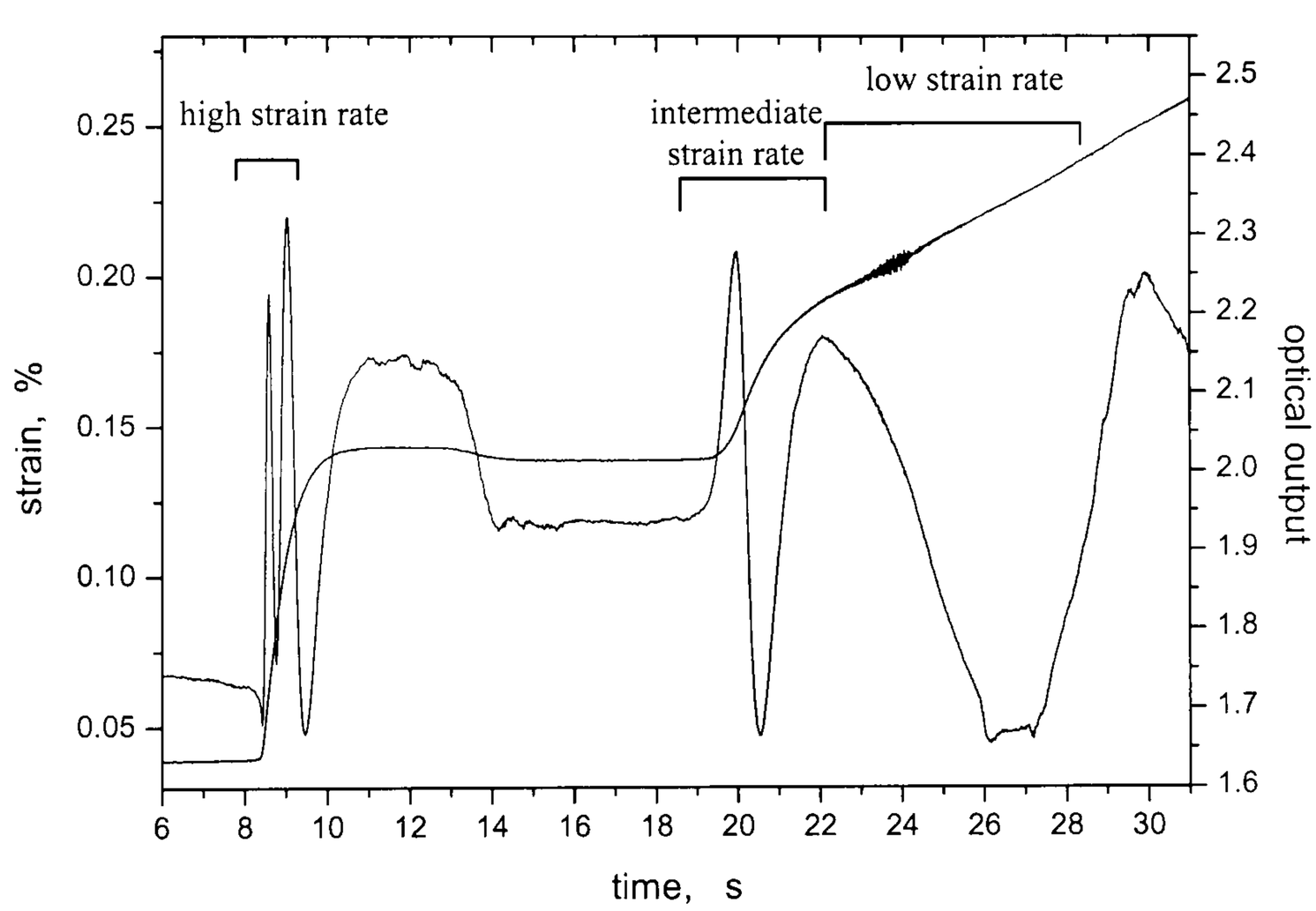

Figure 5.8 Polarimetric sensor behaviour at different strain rates (partial magnification of Figure 5.7).

The optical fringes in Figure 5.7 and Figure 5.8 look a little confused. However, when the optical output is plotted against strain, as shown in Figure 5.9, the fringes are much clearer due to the removal of the time dependence. The fringes are reproducible, almost perfectly, for both increasing and decreasing strain (this reproducibility is

more obvious when the coupon is tested under fatigue loading, see Section 5.6). When optical phase change is plotted against strain, the straight line predicted by equation 5.13 can be obtained, as shown in Figure 5.10. The phase change in Figure 5.10 is obtained by simply counting the number of peaks in the optical output, given that the phase difference represented by two consecutive peaks is 2π.

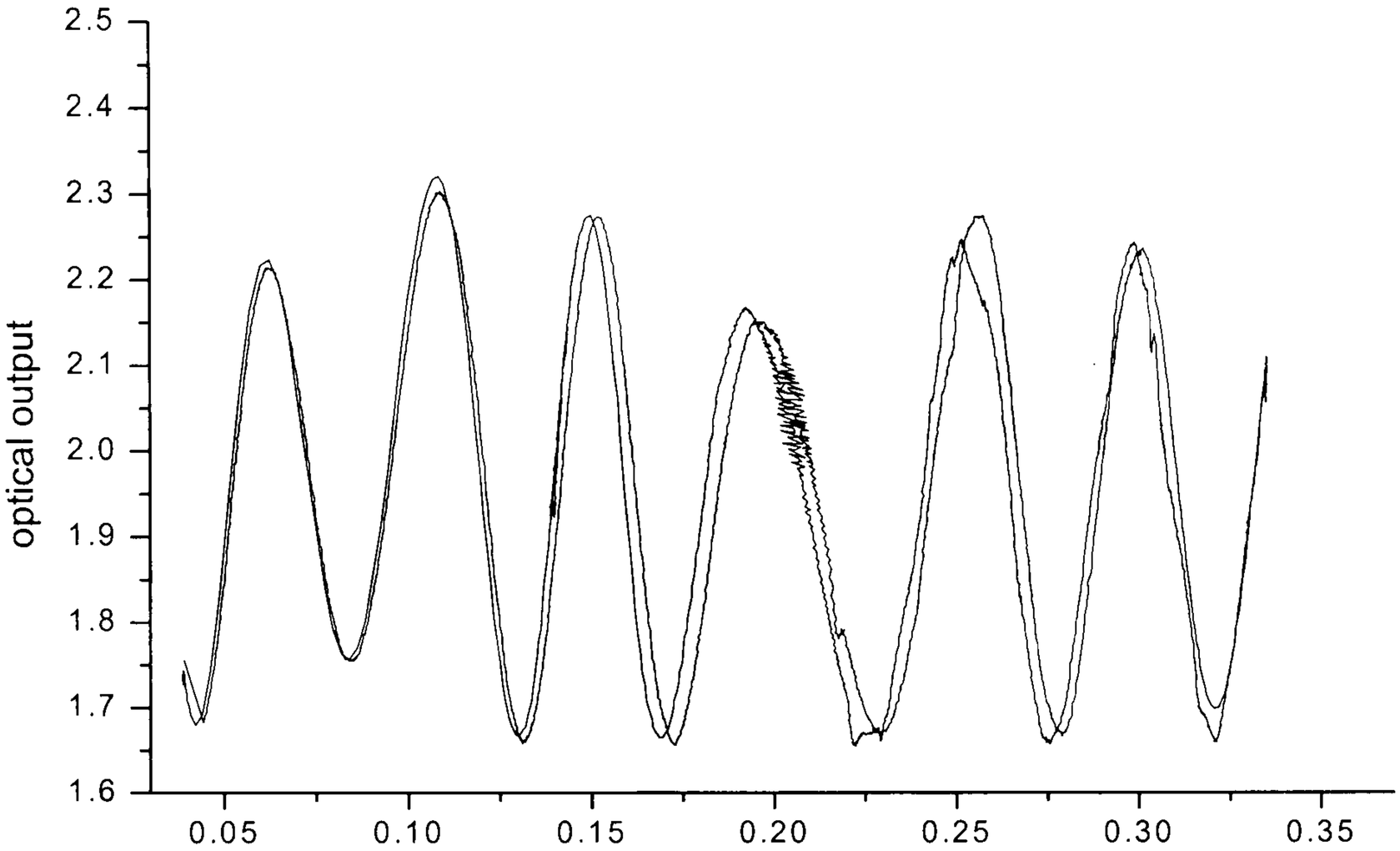

Figure 5.9 Optical fringes of Figure 5.9 when optical signal is plotted against strain.

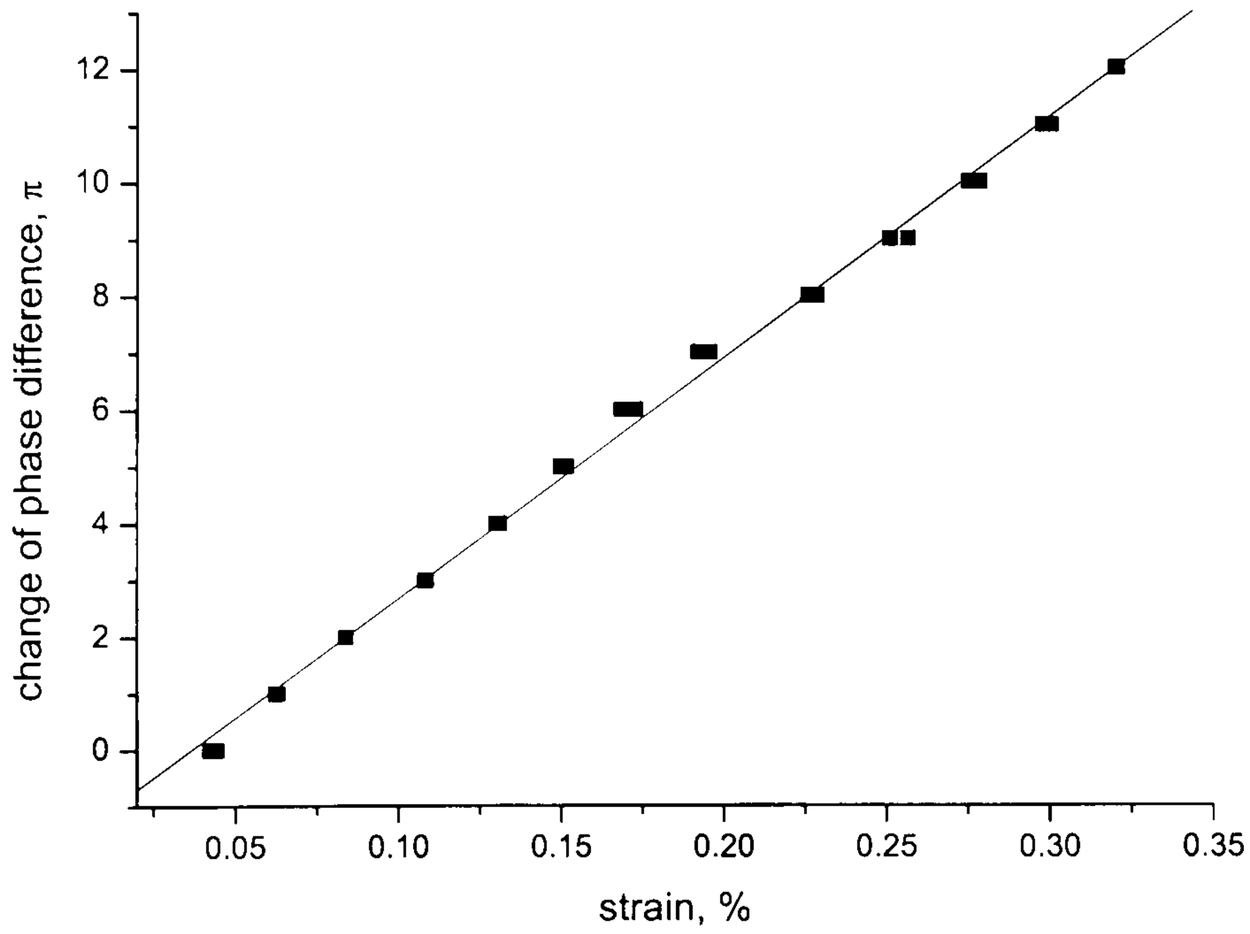

Figure 5.10 Change of optical phase against strain of the data set in Figure 5.8.

5.5 Effect of the orientation of the incoming polarised light in relation to the fibre birefringence axes

If the lead-in fibre is oriented so that the incoming light (point *A* in Figure 5.11) excites both modes in the fibre core, the fringes are more complicated. When the light is launched into the optical core at a random angle θ (as shown in Section at point A in Figure 5.11) to the slow *x*-axis of the core, both modes in the core are excited. The light wave in the *x* and y mode can be expressed as:

$$\begin{aligned} E_x &= E_0 \cos\theta \cos(kx + \omega t + \varphi_0) \\ E_y &= E_0 \sin\theta \cos(ky + \omega t + \varphi_0) \end{aligned} \qquad 5.14$$

where φ_0 is the initial phase. When the light in both modes reaches point *B* (see Figure 5.11), the phase of light in the fast y-mode has advanced over that in the *x*- mode by an amount:

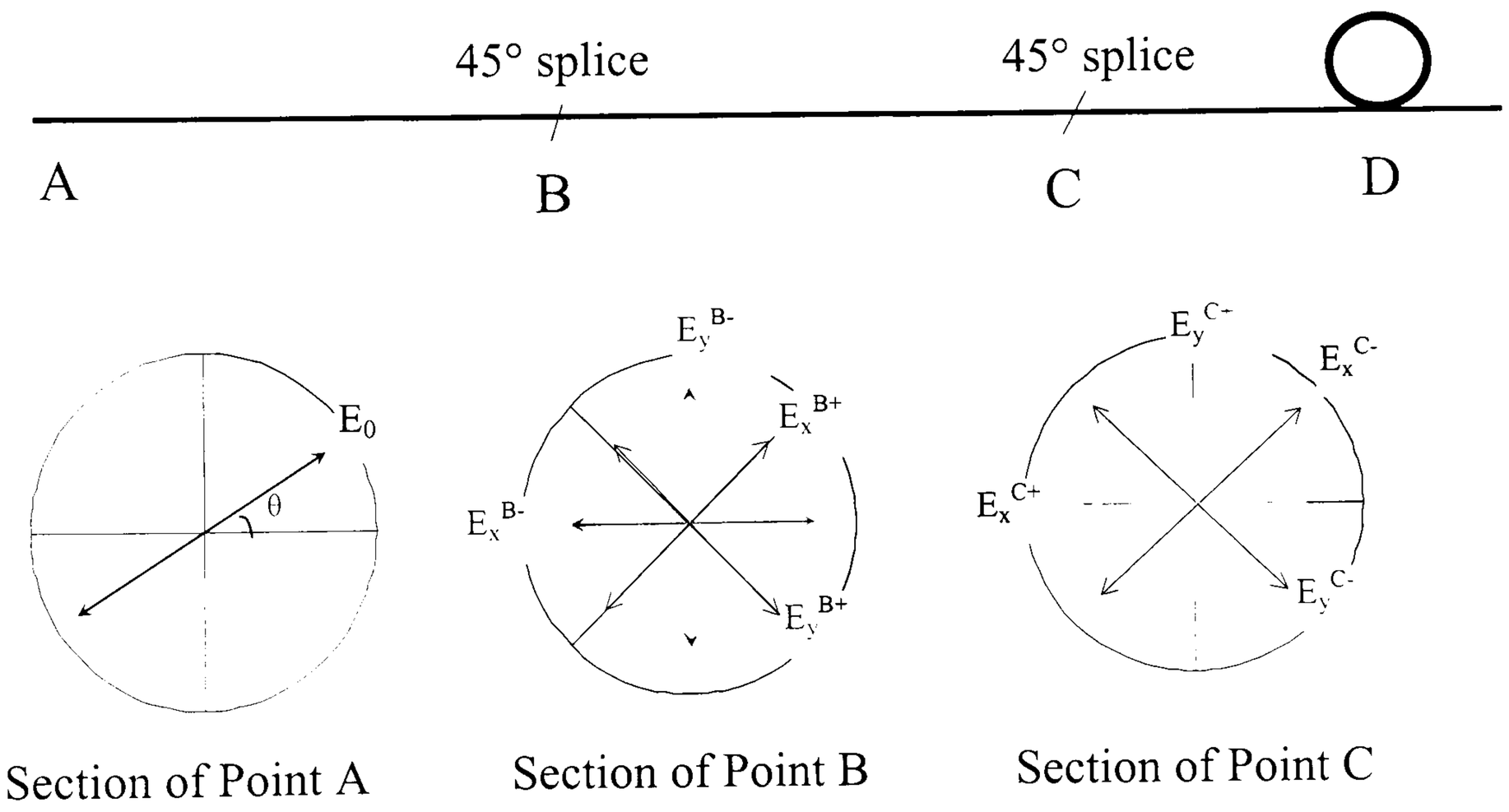

Figure 5.11 A schematic diagram for a polarimetric sensor.

$$\Delta\varphi = 2\pi \frac{L_{AB}}{L_B} \tag{5.15}$$

where L_B is the beat length of the fibre and L_{AB} is the distance from point A to the first 45° splice at point B. The lightwaves in the x- and y-modes can be expressed as:

$$\begin{aligned} E^{x}_{B^-} &= E_0 \cos\theta \cos(kx + \omega t + \varphi_1) \\ E^{y}_{B^-} &= E_0 \sin\theta \cos(ky + \omega t + \varphi_1 + \Delta\varphi) \end{aligned} \tag{5.16}$$

After point B, where there is a 45° splice, both lightwaves will split and the light in the x-mode and y-mode can be expressed as:

$$\begin{aligned} E^{x}_{B^+} &= \frac{\sqrt{2}}{2} E_0 \cos\theta \cos(kx + \omega t + \varphi_1) - \frac{\sqrt{2}}{2} E_0 \sin\theta \cos(kx + \omega t + \varphi_1 + \Delta\varphi) \\ E^{y}_{B^+} &= \frac{\sqrt{2}}{2} E_0 \cos\theta \cos(ky + \omega t + \varphi_1) + \frac{\sqrt{2}}{2} E_0 \sin\theta \cos(ky + \omega t + \varphi_1 + \Delta\varphi) \end{aligned} \tag{5.17}$$

Over the gauge length of the sensor, L_{BC}, another phase difference, $\Delta\varphi'$, is induced due to both any external strain effect and the mode birefringence. Before point C, the light in both modes can be expressed as:

$$\begin{aligned} E^{x}_{C^-} &= \frac{\sqrt{2}}{2} E_0 \cos\theta \cos(kx + \omega t + \varphi_2) - \frac{\sqrt{2}}{2} E_0 \sin\theta \cos(kx + \omega t + \varphi_2 + \Delta\varphi) \\ E^{y}_{C^-} &= \frac{\sqrt{2}}{2} E_0 \cos\theta \cos(ky + \omega t + \varphi_2 + \Delta\varphi') \\ &+ \frac{\sqrt{2}}{2} E_0 \sin\theta \cos(ky + \omega t + \varphi_2 + \Delta\varphi + \Delta\varphi') \end{aligned} \tag{5.18}$$

After another 45° splice at point C, the light in both modes become:

$$E_{C^-}^{x} = \frac{1}{2}E_0\cos\theta\cos(kx+\omega t+\varphi_2) - \frac{1}{2}E_0\sin\theta\cos(kx+\omega t+\varphi_2+\Delta\varphi)$$
$$+\frac{1}{2}E_0\cos\theta\cos(kx+\omega t+\varphi_2+\Delta\varphi') + \frac{1}{2}E_0\sin\theta\cos(kx+\omega t+\varphi_2+\Delta\varphi+\Delta\varphi') \quad 5.19$$
$$E_{C^-}^{y} = \frac{1}{2}E_0\cos\theta\cos(ky+\omega t+\varphi_2+\Delta\varphi') + \frac{1}{2}E_0\sin\theta\cos(ky+\omega t+\varphi_2+\Delta\varphi)$$
$$-\frac{1}{2}E_0\cos\theta\cos(ky+\omega t+\varphi_2) + \frac{1}{2}E_0\sin\theta\cos(ky+\omega t+\varphi_2+\Delta\varphi)$$

Hence, the light in one mode, for example, the x-mode, is the interference of four coherent lightwaves of different amplitude and phase. Detailed discussion is quite complex and only some special cases are presented here. When $\theta = 0°$ and all light is launched at the lead-in fibre into the x-mode, the electric vector in this mode is:

$$E_{C^+}^{x}\Big|_{\theta=0^0} = \frac{1}{2}E_0\cos(kx+\omega t+\varphi_2) + \frac{1}{2}E_0\cos(kx+\omega t+\varphi_2+\Delta\varphi') \quad 5.20$$

and the light intensity in the x-mode is:

$$I_{C^+}^{x}\Big|_{\theta=0\circ} = I_1 + I_2 + 2\sqrt{I_1 I_2}\cos\Delta\varphi' = \frac{1}{4}I_0 + \frac{1}{4}I_0 + \frac{1}{2}I_0\cos\Delta\varphi' = I_0\cos^2\frac{\Delta\varphi'}{2} \quad 5.21$$

When $\theta = 90°$ and all light is coupled into the y-mode, the electric vector in the x-mode is:

$$E_{C^+}^{x}\Big|_{\theta=90^0} = \frac{1}{2}E_0\cos(kx+\omega t+\varphi_2+\Delta\varphi+\Delta\varphi') \quad 5.22$$
$$+\frac{1}{2}E_0\cos(kx+\omega t+\varphi_2+\Delta\varphi+\pi)$$

and the light intensity in the x mode is:

$$I_{C^+}^{x}\Big|_{\theta=90^\circ} = I_1 + I_2 + 2\sqrt{I_1 I_2}\cos(\Delta\varphi'-\pi) = \frac{1}{4}I_0 + \frac{1}{4}I_0 + \frac{1}{2}I_0\cos(\Delta\varphi'-\pi)$$
$$= I_0 \sin^2\frac{\Delta\varphi'}{2} \qquad 5.23$$

Equation 5.21 and 5.23 correspond to equation 3.12. The equations suggest that when the lead-in fibre is rotated through 90°, the optical fringes are inverted. The results of such an experiment are shown in Figure 5.12 where the lead-in fibre has been rotated in 15° intervals from 0° to 90°. Comparison of Figure 5.12(a), Figure 5.12(g) and Figure 5.12(h) shows that the fringes are indeed inverted when the lead-in fibre is rotated by 90°. There is little difference in the fringes when the linearly polarised light is about 15° off the *x*- or *y*- axis (Figure 5.12(a) and Figure 5.12(b), Figure 5.12(f) and Figure 5.12(g)). Hence, the demands of the light path arrangement are not high when the sensor is used to monitor strain or damage. In other words, the input light at point *A* in Figure 5.11 could be as much as 15° off-axis without unduly affecting the results. This result agrees with Calero et al (1994).

5.6 Response of polarimetric sensor under cyclic loading

In order to complete the study of the basic mechanical response of the sensor, some tests were carried out under cyclic loading and these results are described in this section. All the tests were carried out under load control mode with sensors embedded in unidirectional composites. Sinusoidal wave forms with stress ratio R=0.1 (R = minimum stress/maximum stress) were employed. The cyclic frequencies adopted were 1 Hz and 10 Hz. The data sampling rate was changed with frequency to ensure there were at least 100 data points in one set of fringes.

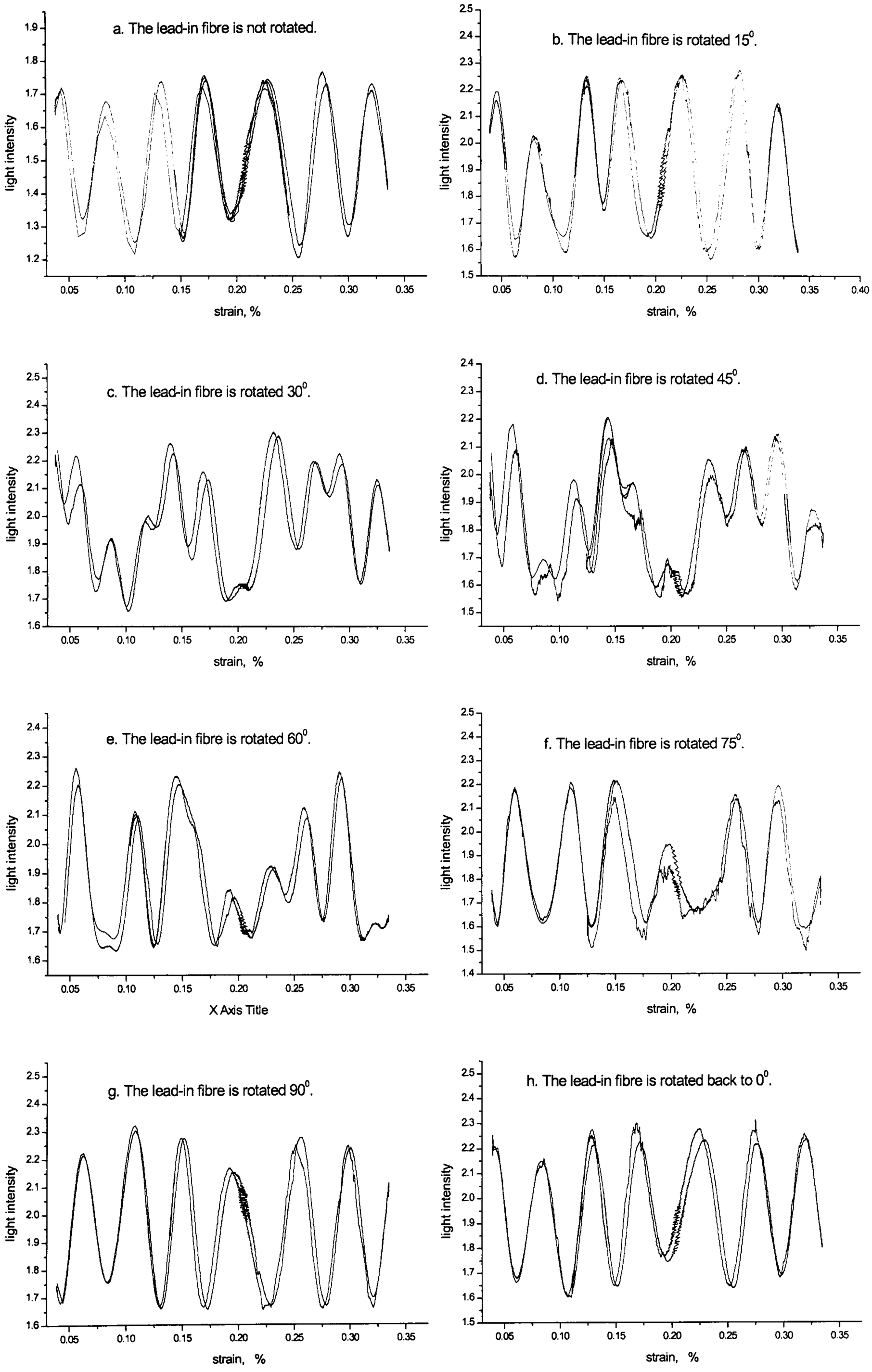

Figure 5.12 Change of optical fringes when lead-in fibre is rotated.

The results shown in Figure 5.13 to 5.16 are for frequencies of 1 Hz and 10 Hz. Figure 5.13 shows the strain recorded by the extensometer and the optical output as a function of time, for tests at 1 Hz and Figure 5.14 is a magnification of part of these results. Figure 5.15 and 5.16 show similar results for a cycling frequency of 10 Hz. Comparison between Figure 5.14 and 5.16 shows that although the fringes are less well defined in Figure 5.16, the sensitivity of the sensor (i.e. the number of fringes for a given strain) has not changed. This demonstrates that the response of the sensor is fast and makes it possible for the polarimetric sensor to monitor strain (and possibly damage) under cyclic loading. Indeed, it is likely that the sensor is limited here by the response of the detector and the sampling frequency, rather than by the intrinsic speed of response of the sensor.

Returning to Figure 5.9, only one cycle of load was performed in that test, and the fringes redraw themselves only once on unloading. Under cyclic loading, many cycles of load are performed and the fringes repeat many times. However, due to the instability in time of the optical output intensity of the laser source during cyclic loading, the fringes move vertically along the *y*-axis (i.e. light intensity axis; see Figure 5.17 and 5.18). Hence, cyclic test results show thick fringes, although the individual fringes have the same shape as those under quasi-static load. Figure 5.17 and 5.18 show the optical output as a function of strain over many cycles and the drift of the optical output intensity, due to output drift of the laser source, is apparent.

At higher cycling frequencies, the sampling rate of the data must be high enough in order to obtain true fringes. For example the fringes shown in Figure 5.19 (where the sampling rate is 100 Hz) are misleading when compared to the true fringes in Figure 5.14 (where the sampling rate is 1000 Hz).

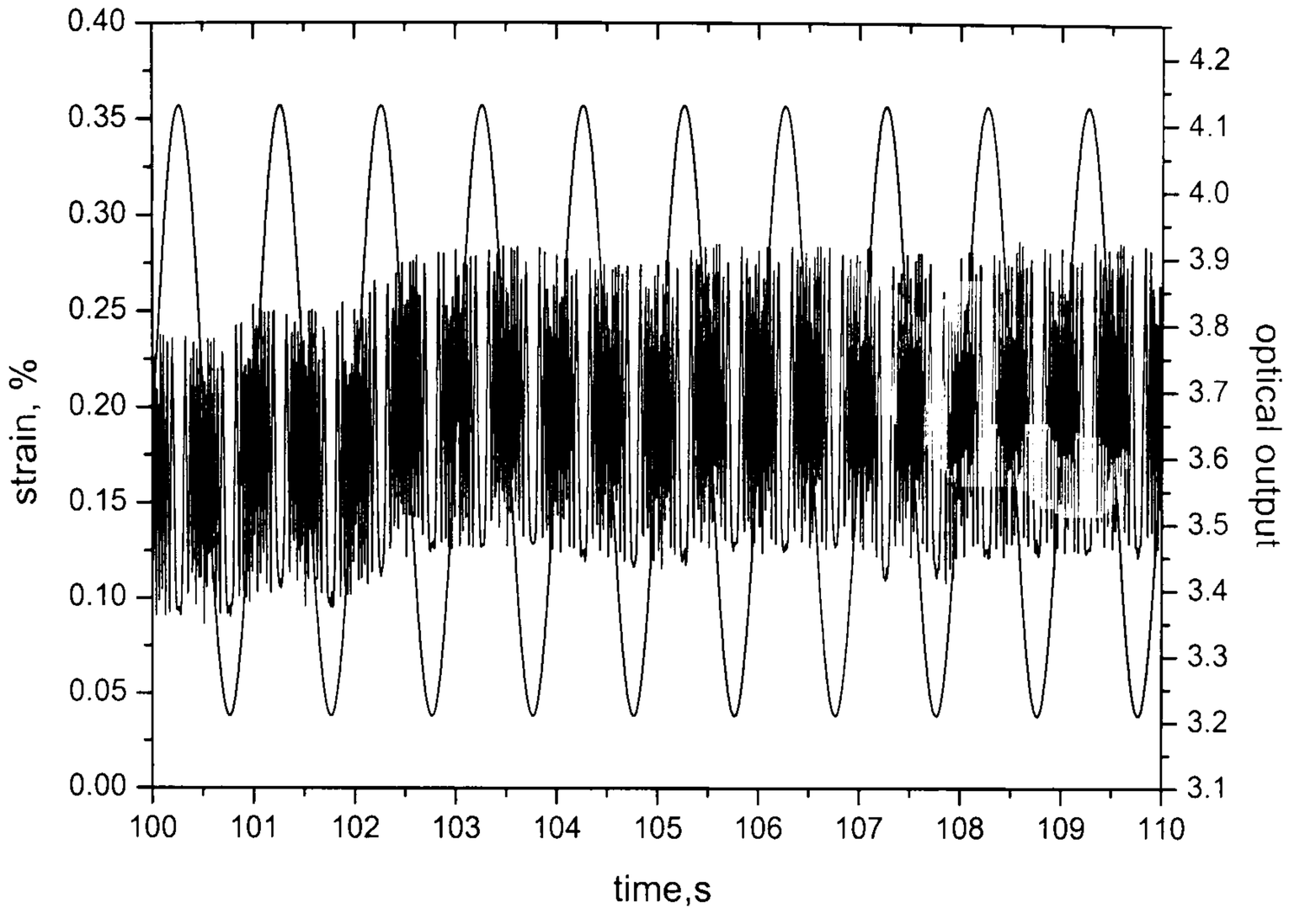

Figure 5.13 Strain signal and optical signals of an embedded polarimetric sensor under fatigue test (frequency=1 Hz, sampling rate=1kHz).

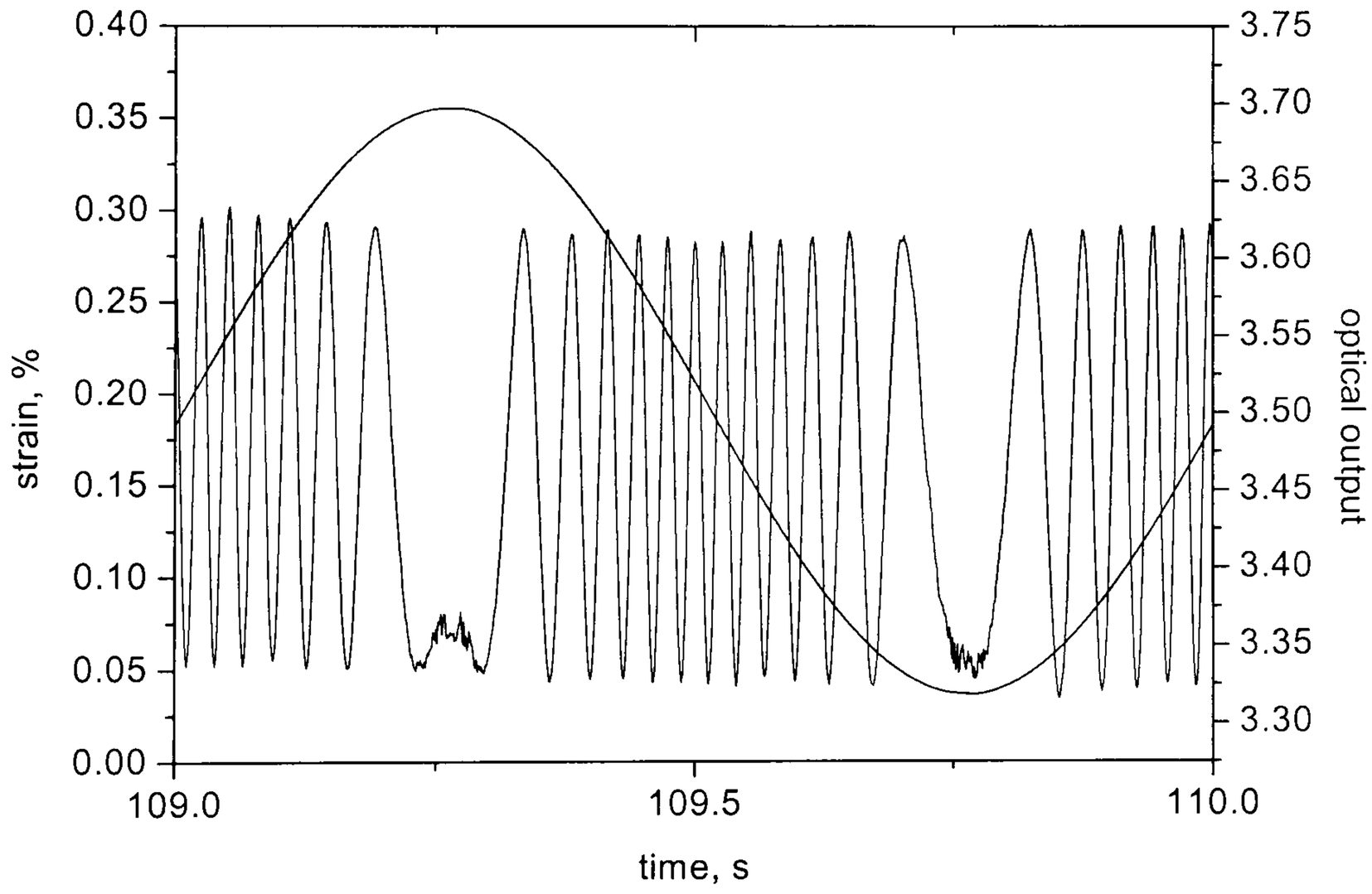

Figure 5.14 Partial magnification of Figure 5.13 in time range from 109s to 110s (frequency=1 Hz, sampling rate=1kHz).

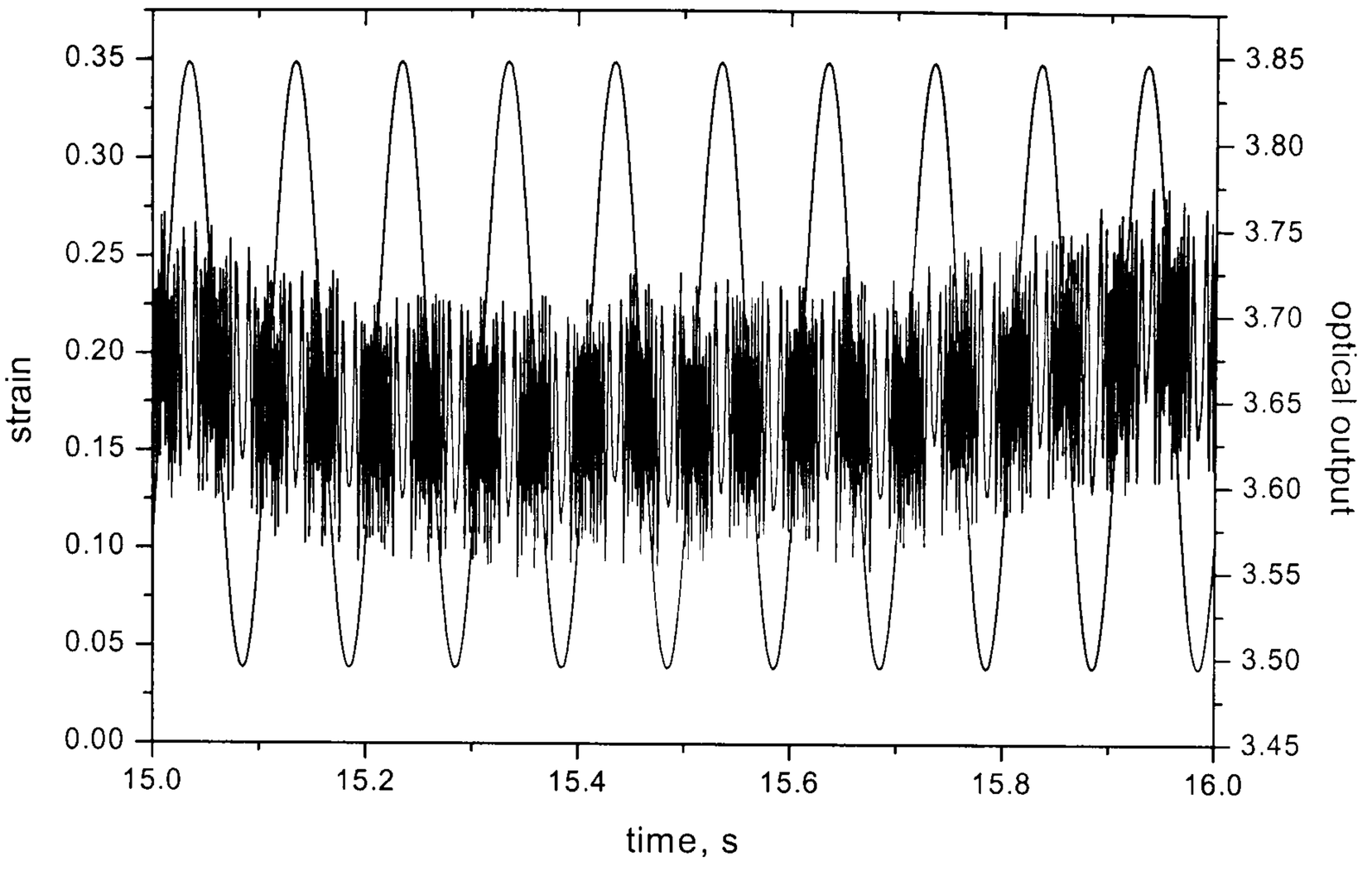

Figure 5.15 Strain signal and optical signals of an embedded polarimetric sensor under fatigue test (frequency=10 Hz, sampling rate=1kHz).

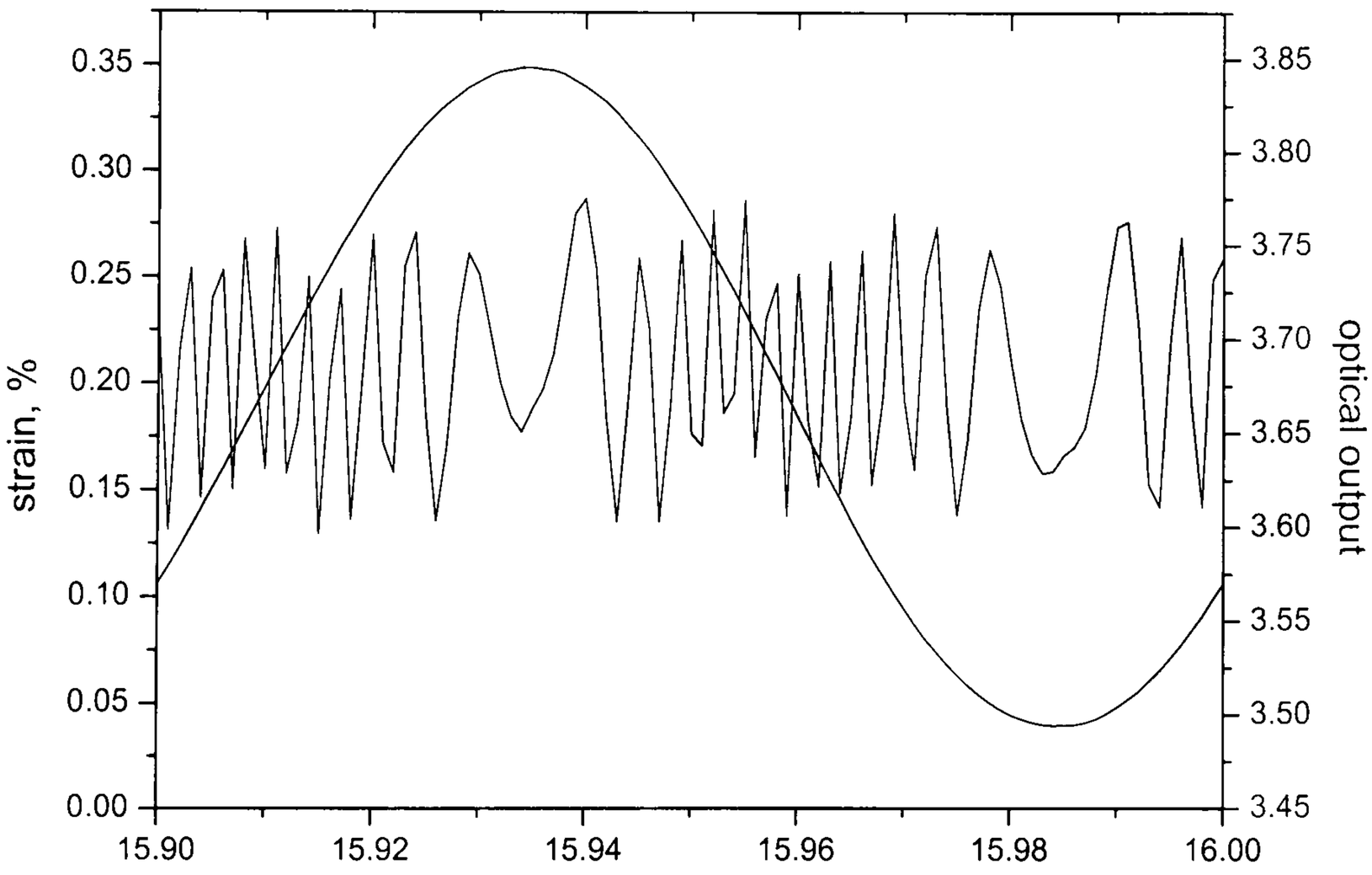

Figure 5.16 Partial magnification of Figure 5.15 in time range from 15.9s to 16s (frequency=10 Hz, sampling rate=1kHz).

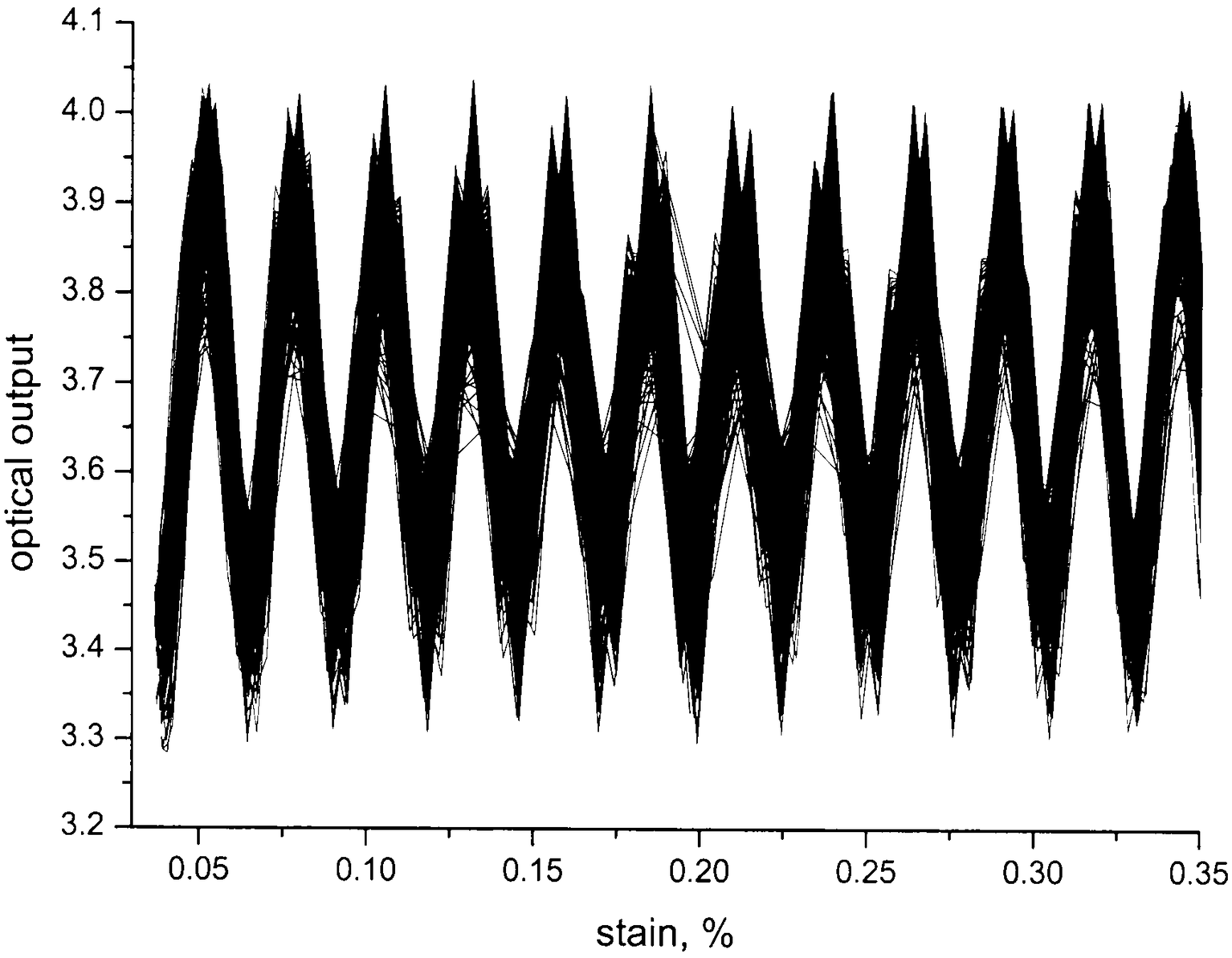

Figure 5.17 Optical fringes of an embedded polarimetric sensor under fatigue test (frequency=1 Hz, sampling rate=1kHz).

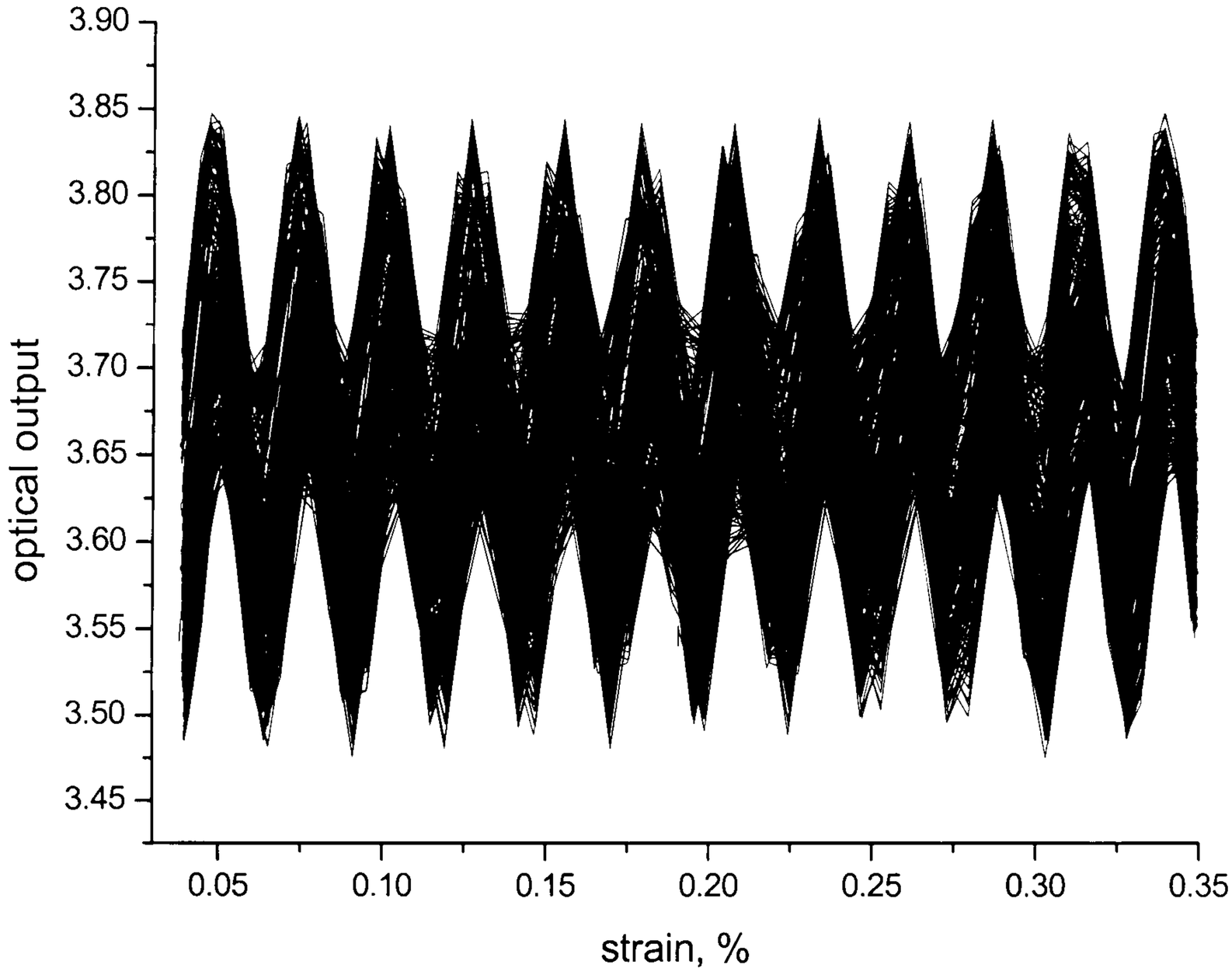

Figure 5.18 Optical fringes of an embedded polarimetric sensor under fatigue test (frequency=10 Hz, sampling rate=1kHz).

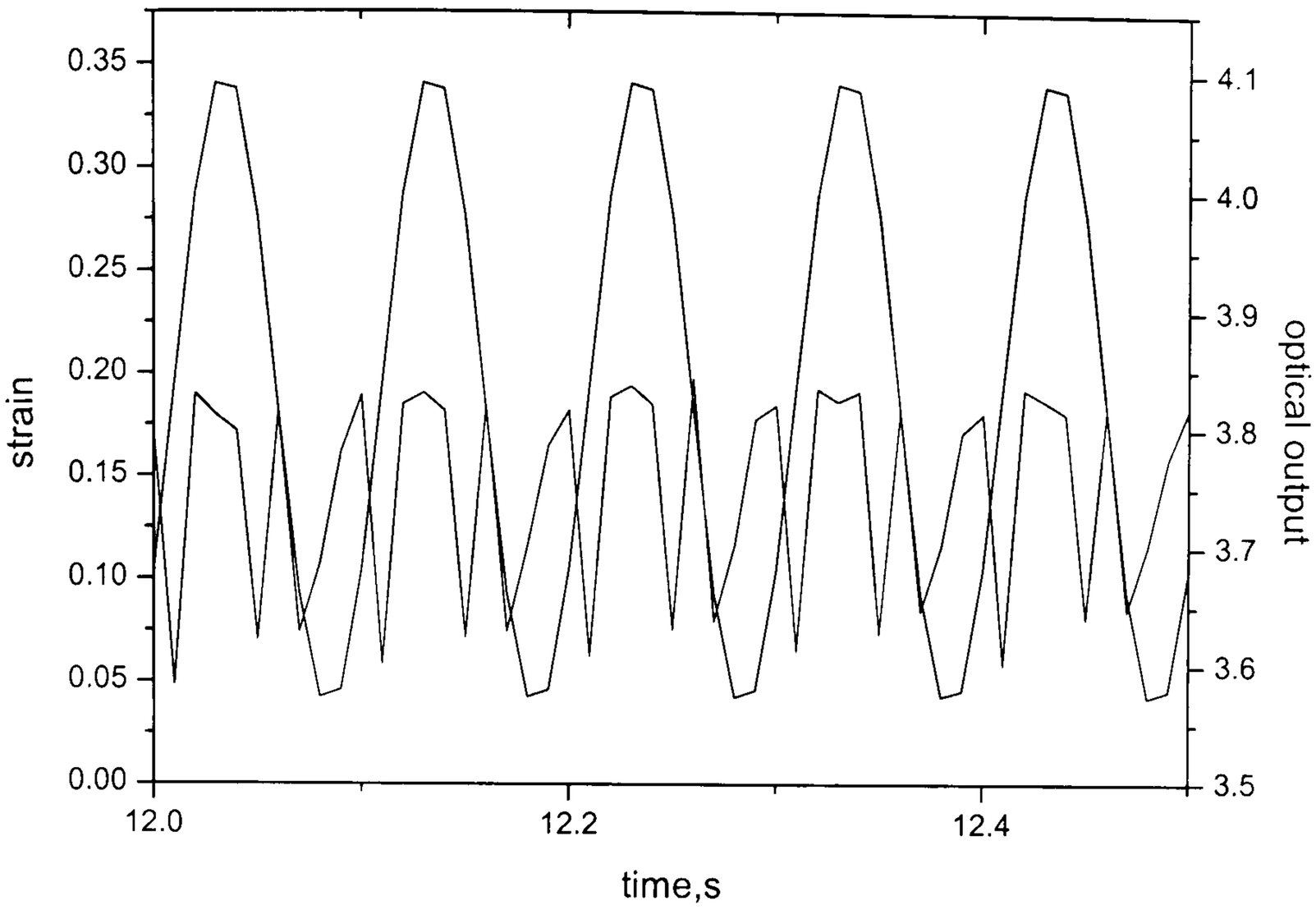

Figure 5.19 Optical fringes of an embedded polarimetric sensor under fatigue test (frequency=1 Hz, sampling rate=0.1kHz).

Figure 5.20 shows the response of an embedded polarimetric sensor under cyclic loading during a test in which the sensor fractured at a transverse ply crack. This result is included to show the surprising robustness of the sensor. The initial, single optical fringe at low strain (from 0% to about 0.06%) was caused by loading the specimen to the mean load before the cyclic test started. The specimen was cycled between 0.06% and 0.125% strain at a frequency of 5 Hz in load control. The fringes superimposed each cycle, but at slightly different optical output values (due to drift of the laser output power), to become a dark thick band, in a similar way to the results in Figure 5.17 and Figure 5.18. After about 360 cycles of the cyclic test, the sensor broke at a strain of about 0.38%, and there was an immediate drop in optical output, although the cyclic testing was continued. Despite fracture of the sensor, the fringes were still visible, but the sensitivity of the sensor was slightly reduced. Since the gap between the two broken ends of the sensor increased with applied strain, it is not surprising that, with the consequent loss of light, the fringes also become less visible at higher strains, as Figure 5.20 shows.

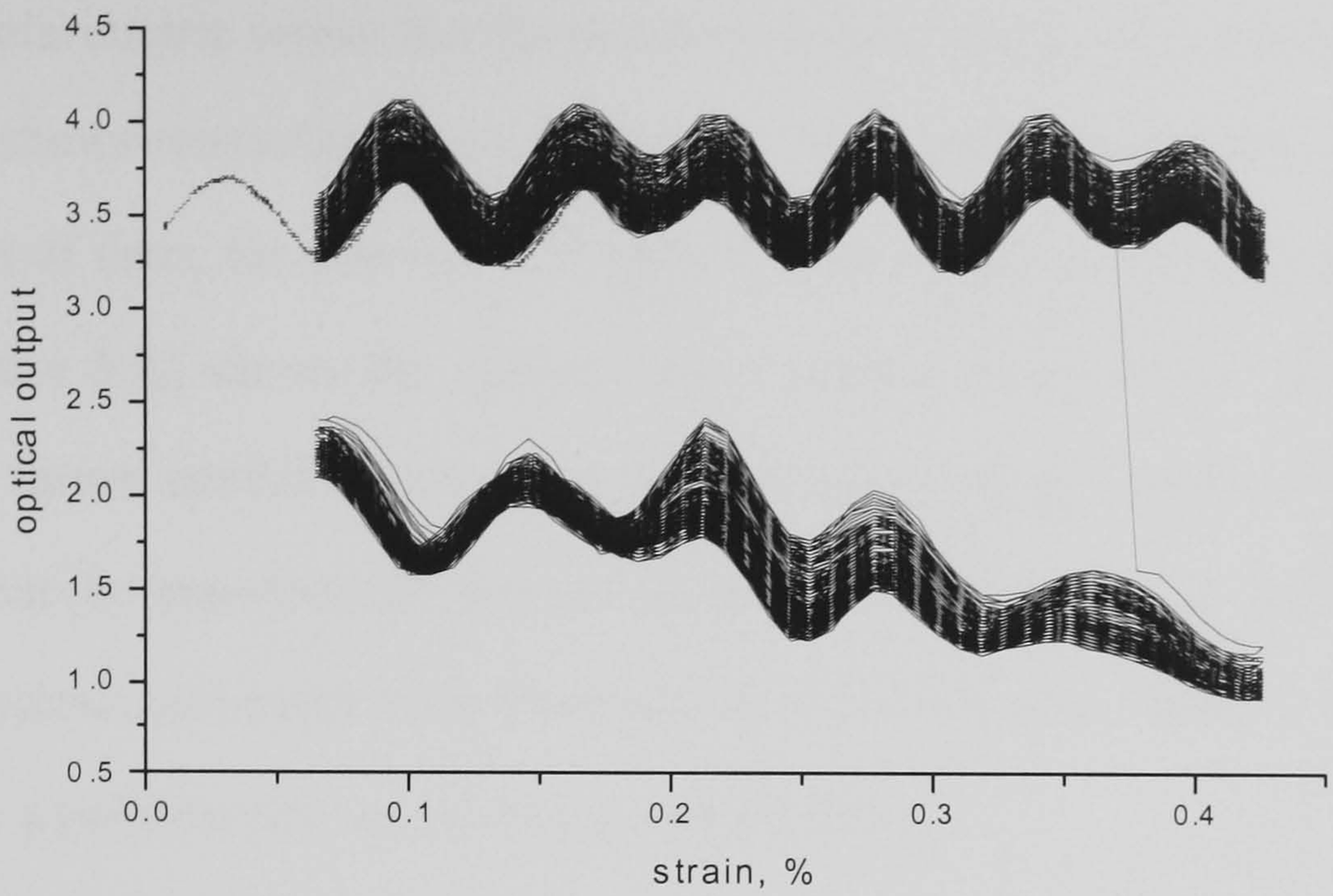

Figure 5.20 Response of embedded polarimetric sensor under fatigure after it is broken at a transverse crack.

This section on the cyclic behaviour of the sensor was included to help demonstrate that the sensor response is well understood. Attempts were made to use the good, cyclic response of the sensor to monitor the fatigue growth of matrix cracks, but it was found that the changes during fatigue were too subtle to be detected and hence most of the work was focused on quasi-static crack development.

In the next section, the response of the sensor to temperature changes is quantified, an investigation which was required to establish the significance of any temperature changes during the quasi-static tests.

5.7 Thermal response of the polarimetric sensor

As described in Section 3.3, the birefringence of a polarimetric fibre is induced by the difference of the thermal coefficient of expansion between the cladding and the SAPs. When the temperature changes, the stress induced by the SAPs will change as well,

and the resulting change in birefringence is expressed as optical fringes. In other words, the polarimetric sensor has the potential to be a temperature sensor.

Figure 5.21 shows temperature as a function of time and optical output (oscillations) as a function of time, for a sensor of length 0.75 m heated in an oven from 20 °C to 130 °C. Figure 5.22 shows the optical output plotted as a function of temperature. Figure 5.23 shows similar results for a sensor with a gauge length of 0.3 m. These tests show that the experimental thermal sensitivity of the sensor is 4.9±0.2 rad/°C/m, which is in good agreement with Domansi et al (1994), who found a value of 5.23 rad/°C/m for a polarimetric sensor using a Panda fibre.

A sensitivity of about 5 rad/°C/m is not very large and shows that the polarimetric sensor is not very sensitive to temperature. Hence, it has been demonstrated that, for all of the testing undertaken on coupons in present study, the thermal contribution to the measured phase shifts can be neglected as the experimental durations varied from 1 to 5 minutes in a temperature controlled room.

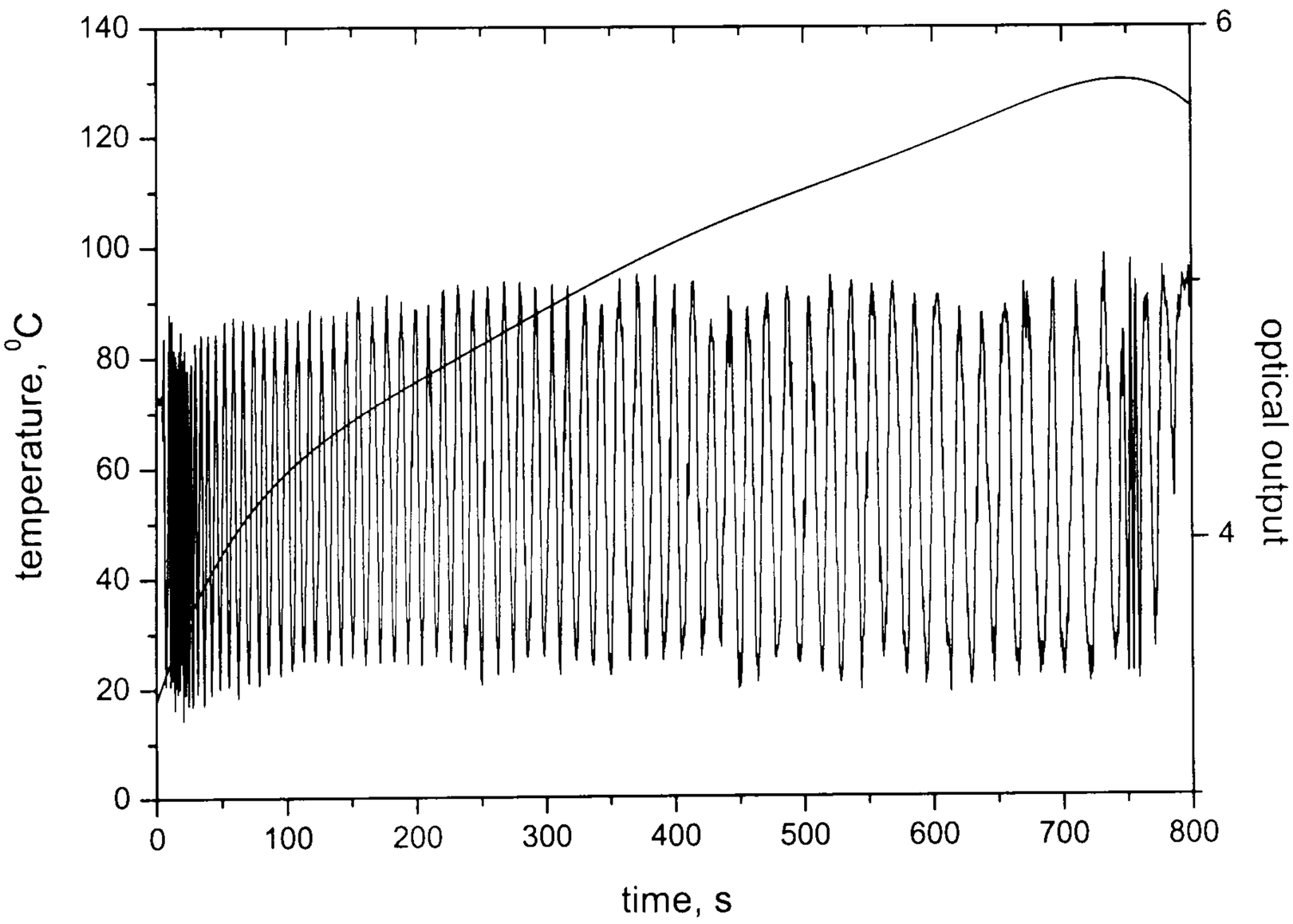

Figure 5.21 Thermal response of polarimetric sensor with a length of 0.75 m.

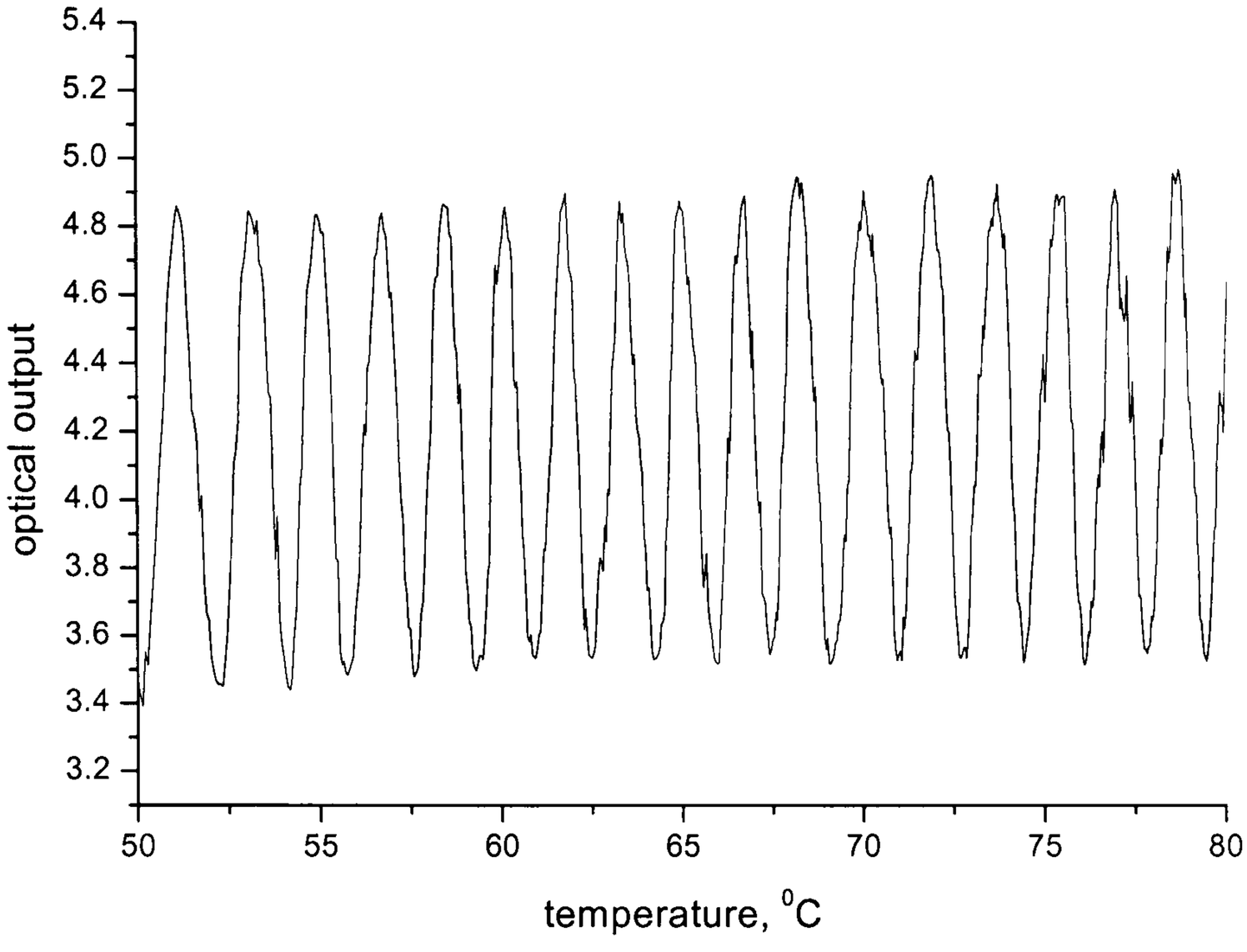

Figure 5.22 Thermal response of polarimetric sensor with a length of 0.75 m when optical output is plotted against temperature.

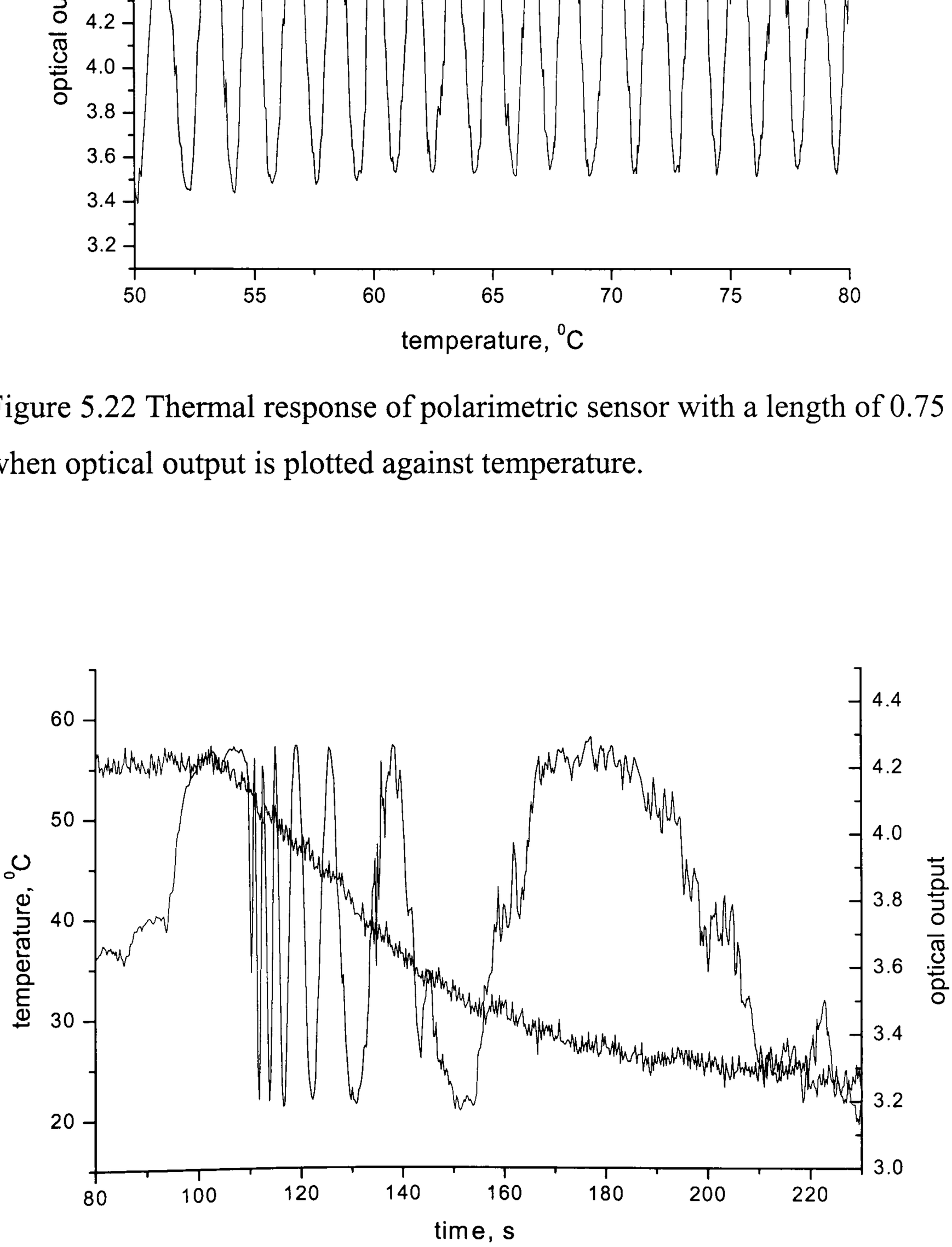

Figure 5.23 Thermal response of polarimetric sensor with a length of 0.30 m.

5.8 Conclusion

In this chapter, various basic aspects of the behaviour of a polarimetric sensor have been discussed.

The optical arrangement employed has been explained and demonstrated to be understood both theoretically and experimentally. The bend diameter and number of loops of the lead-out fibre have been optimised and clear optical fringes due to changes of strain have been obtained. The polarisation state of light in the fibre core has been discussed in relation to the experimental results. In particular, it has been demonstrated that the demands of the light path arrangement are not high when the sensor is used to monitor strain or damage. The polarised light launched into the optical core can be as much as 15° off-axis without unduly affecting the results. Further tests have shown that polarimetric sensors can be employed to monitor strain under cyclic loading and in order to obtain true fringes, the sampling rate of the data must be high enough. Finally, the experimental results show that the polarimetric sensor is not very sensitive to the temperature.

In summary, in this chapter the fundamental understanding of the polarimetric sensor has been established and the sensor can now be used to detect damage in composite materials.

Chapter 6. Transverse crack detection by embedded polarimetric sensors

6.1 Introduction

In this chapter, the results of experiments using polarimetric sensors to detect damage development are described, specifically the development of matrix cracks in a cross-ply composite laminate. Unlike previous studies, the transparent nature of the composites used in this work enables the moment at which the cracks interact with the sensor to be observed directly. The experiments with an embedded sensor focus on detecting transverse cracks during quasi-static loading. Two different configurations of polarimetric sensors have been embedded. The response of the load signal, strain signal and optical signal to crack development are presented in Section 6.2 and 6.3 respectively. In further work, which is presented in Section 6.4, a circular hole was drilled in a cross-ply coupon with thicker 0° plies and 90° plies to establish the effect of cracks that pass the sensor and cracks that do not pass the sensor.

6.2 Detection of transverse cracks by a polarimetric sensor with two 45° splices embedded in the coupon

It is well known that when a cross-ply laminate is under tension, transverse cracks will occur in the 90° ply at a strain of about 0.4%. For a specimen with a 1 mm thick 90° ply, the position where a crack might occur is not controlled. With reference to Figure 4.4(a), the cracks can occur within the extensometer gauge length and between the two 45° splices, outside the extensometer gauge length and between the two 45° splices, or outside the extensometer and outside the two 45° splices. It has been found

that cracks occurring at different positions will induce different responses of load, strain and optical signals.

6.2.1 Cracks occurring within the extensometer gauge length and between the two 45° splices

If a crack occurs in the transverse ply of a cross-ply laminate, the laminate will extend by a small amount (Boniface, 1991). There are two contributions to this extension: there is an extension as a result of the increased compliance of the system but there is also an extension associated with the relaxation of the thermal stress arising from the mismatch in coefficients of thermal expansion of the 0° and 90° plies during cooling. Figure 6.1 shows the results of cracks development in a cross-ply specimen in this condition. In the figure and figures that follow, the positions of the embedded sensor and the two 45° splices are marked by dark lines on the coupon. In Figure 6.1(a), a period of 1.5 seconds is shown during which the load is increasing from approximately 8.325 *kN* to 8.360 *kN*. The testing machine is operated under load control and the demand signal is the gradually increasing load. Figure 6.1(a) also shows the strain recorded by the extensometer, which increases from about 0.4542% to 0.4582%. Fluctuations in both the load and strain signals occur at a time of about 33.7 seconds and these, as will be seen, correspond to the development of a transverse crack. Figure 6.1(b) shows the strain signal again, over the same time period, but plotted here with the optical output, which varies from 2.53 to 2.38 (arbitrary units). In Figure 6.1(c), consecutive digital images of the coupon are shown with an indicated time of 34.08 seconds. Synchronization of timescale of the data-logger and the timer shows that the data-logger has a 0.4 seconds delay compared to the time shown in Figure 6.1(c). Consequently, it is proven that the fluctuations in the load, strain and optical output correspond to the development of the crack.

The changes in the recorded outputs can be explained as follows. In this case, the cracks occurred within the extensometer gauge length and the small extension was

recorded by the extensometer as an immediate, step-like change of strain, as shown in Figure 6.1(a). This small increase in length (corresponding to a strain of about 20 $\mu\varepsilon$, equivalent to about 1 μm over the 50 mm gauge length) caused the load on the sample to drop suddenly. Due to the fast response ability of the servo-hydraulic test machine which was in load-control, the machine increased the load to match the demand load

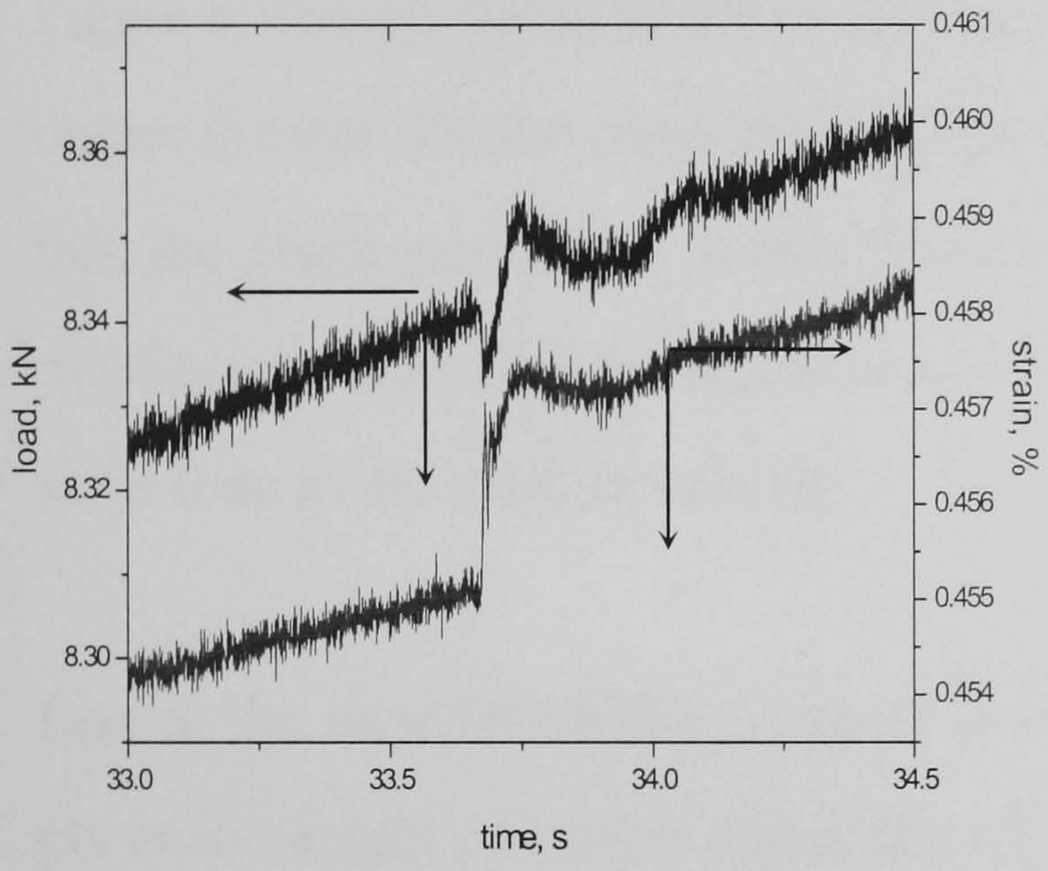

(a)

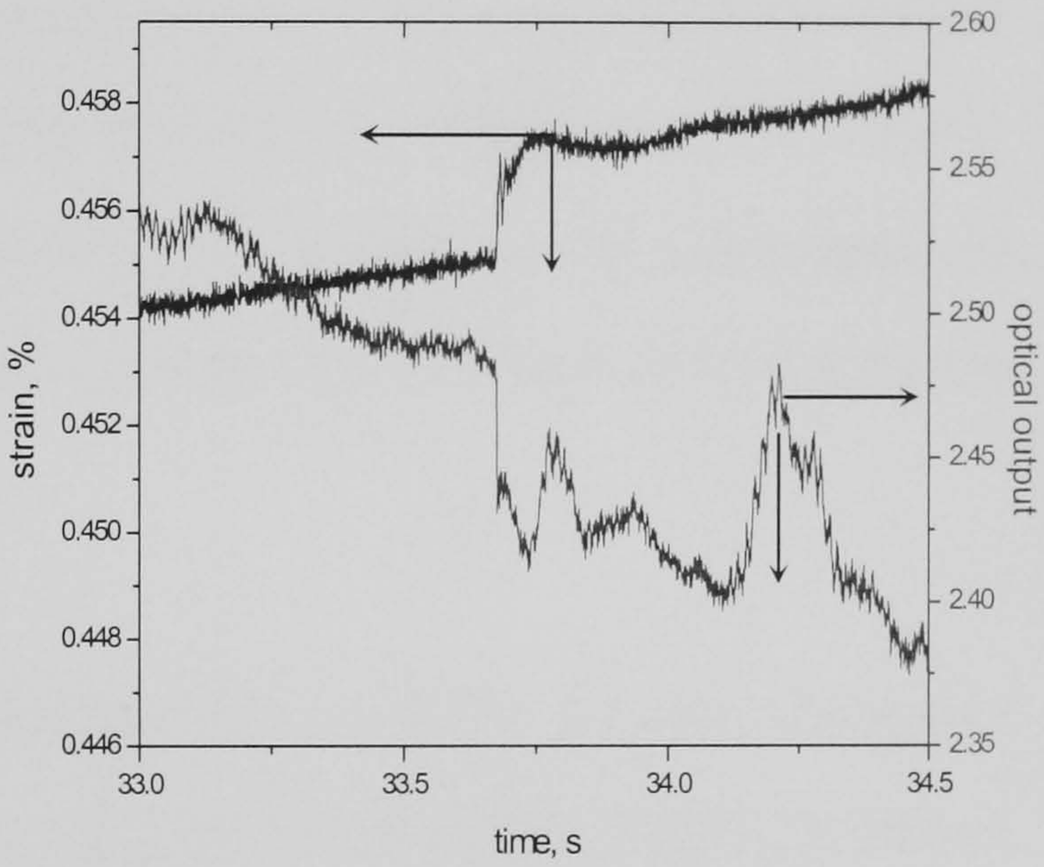

(b)

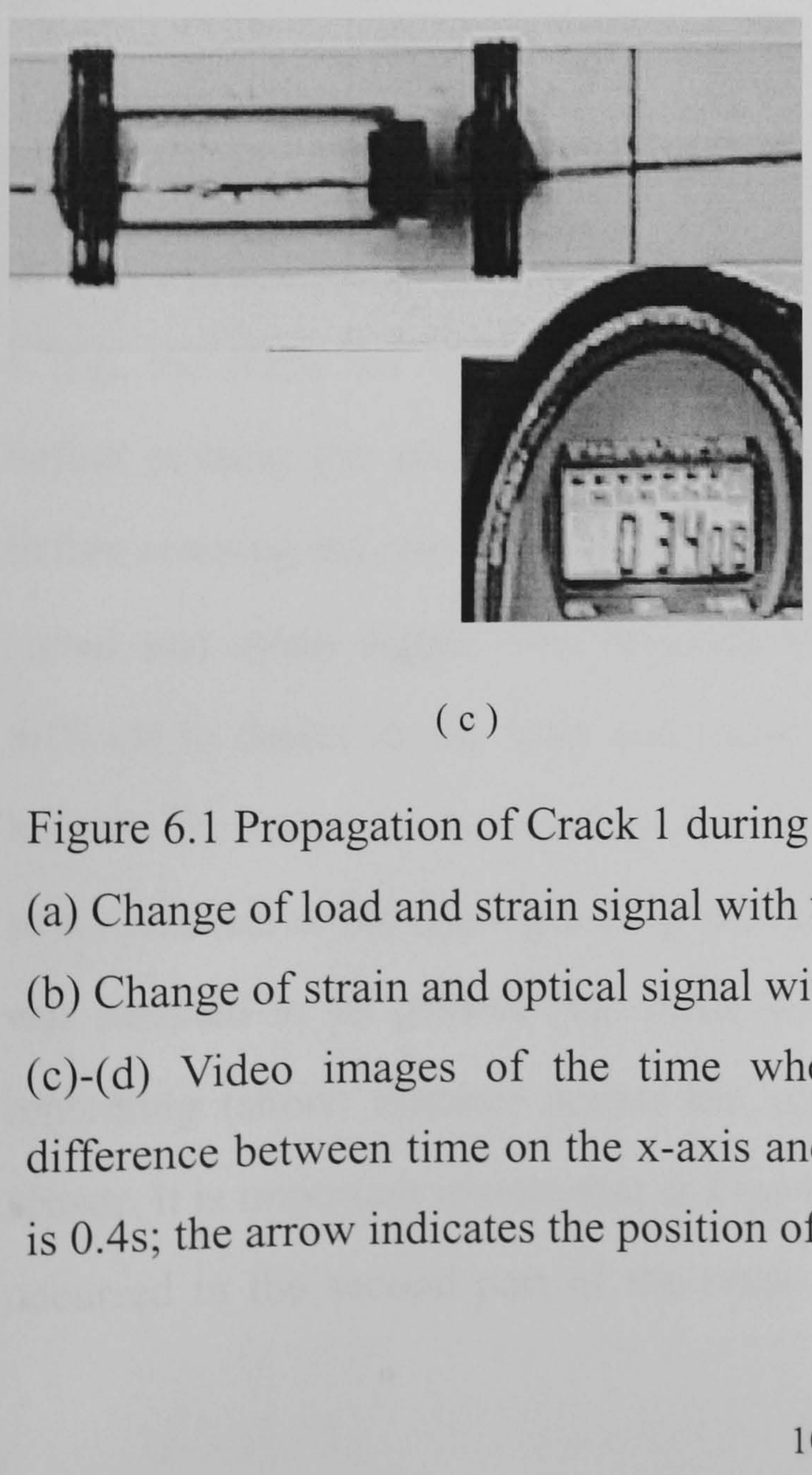

(c)

(d)

Figure 6.1 Propagation of Crack 1 during time 33-35s.

(a) Change of load and strain signal with time.

(b) Change of strain and optical signal with time.

(c)-(d) Video images of the time when the crack passed the sensor. (The difference between time on the x-axis and time shown on the clock in the picture is 0.4s; the arrow indicates the position of the crack which is difficult to see here.)

curve in the load controlled test immediately. In doing that, the testing machine slightly overloaded the coupon, and then recovered to the correct demand load within about 0.25 seconds. Hence, the load fluctuations shown in Figure 6.1(a) were a consequence of the servo-loop controlling the load. Checking the optical signals over this time range closely, a sudden change of optical output is found which is coincident with the sudden change in strain, as shown in Figure 6.1(b). The irregular fringes in Figure 6.1(b) are due to noises in the laser source, but the sudden change in the optical output is clear. Digital photographs taken from the video recording show the moment that the crack passed the sensor (Figure 6.1(c)). These photographs confirmed, as mentioned above, that the discontinuous optical signal change occurred at exactly the same time as the crack developed.

Due to the unpredictability of crack development in cross-ply laminates, transverse ply cracks might propagate across the whole width of coupons immediately, as shown in Figure 6.1 (Crack 1), or propagate in several steps, as shown in Figure 6.2 (Crack 2).

Figure 6.2 shows results similar to those in Figure 6.1, but this time for a crack (Crack 2) which propagated in stages. In Figure 6.2(c), Crack 2 has not yet formed. In Figure 6.2(d), the crack has propagated half-way across the coupon and indeed has stopped before passing the sensor. The crack remained here for a short time (about 0.1s) before crossing the rest of the coupon. Figure 6.2(a) shows the fluctuations of the load signal and strain signal. The interrupted growth of the crack over 0.1 seconds is difficult to detect in the load and strain signals, but an attempt has been made to indicate the stages of the crack growth in Figure 6.2(b). At (i), the sharp increase in strain was due to the crack growing over half-way across the coupon. At (ii), the crack was arrested in its growth (for about 0.1 seconds) and at (iii), the crack grew the remaining (short) distance across the coupon, when it also passed the fibre optic sensor. It is important to note that in Figure 6.2(b), the sudden change of optical signal occurred in the second part of the crack growth when the crack passed the sensor.

Such results suggest strongly that the change of optical output is triggered by the passing crack, but further experiments are required to confirm these observations (see Section 6.4).

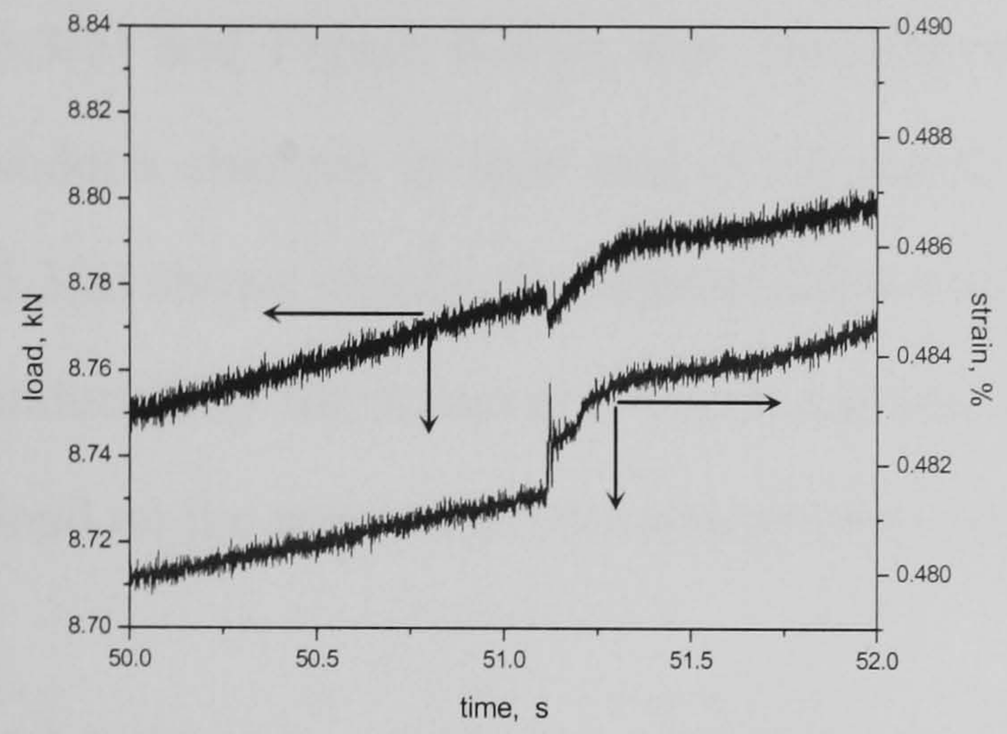

(a)

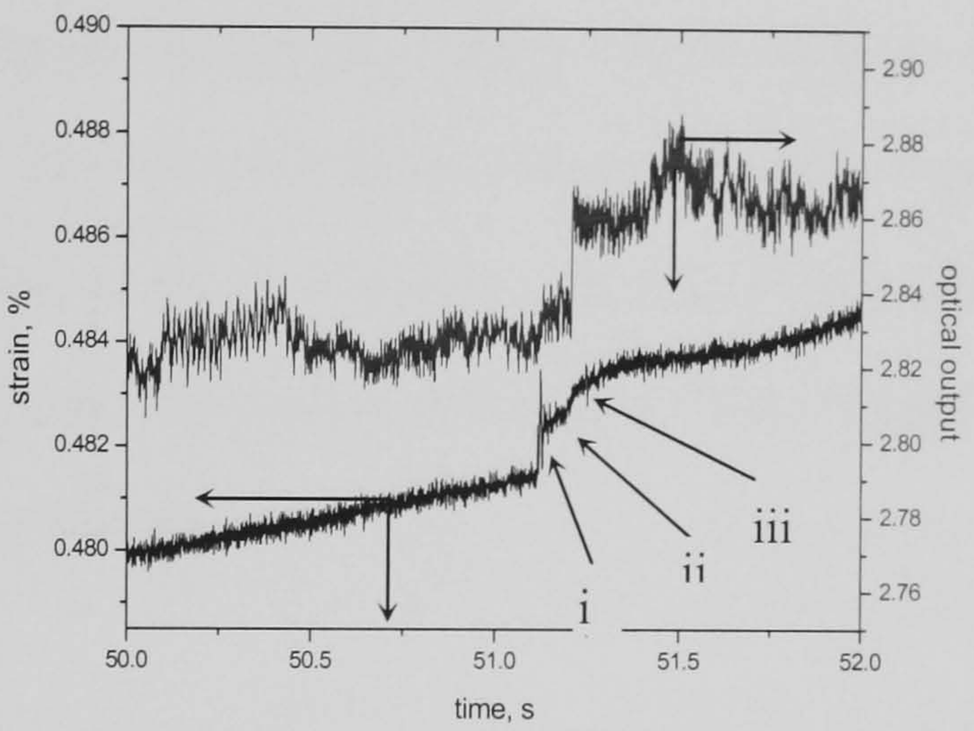

(b)

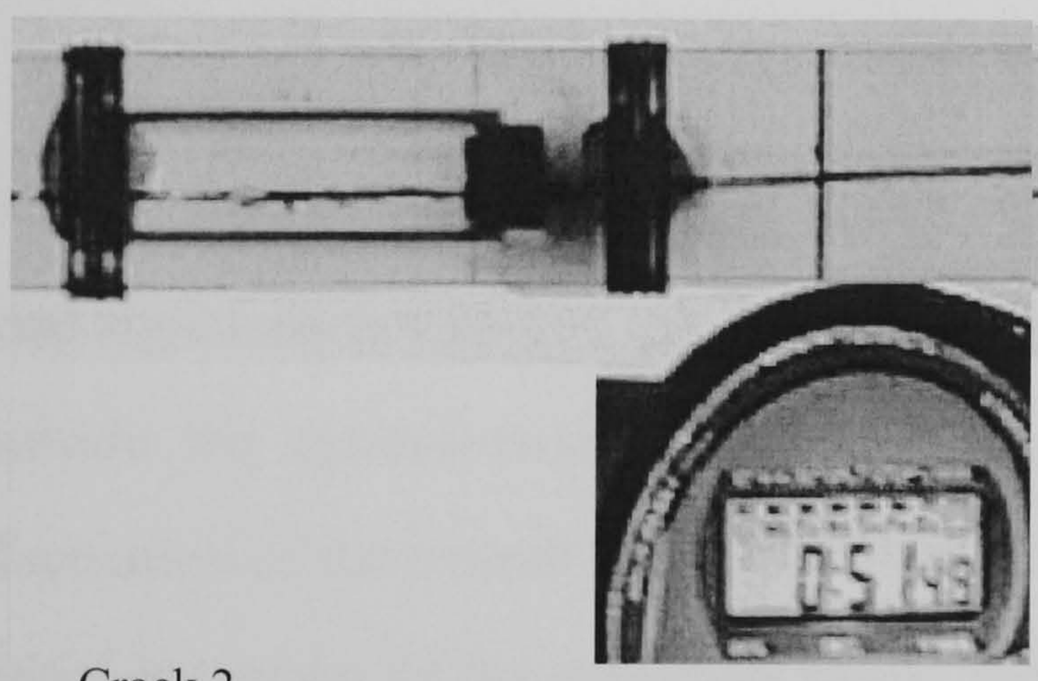

(c)

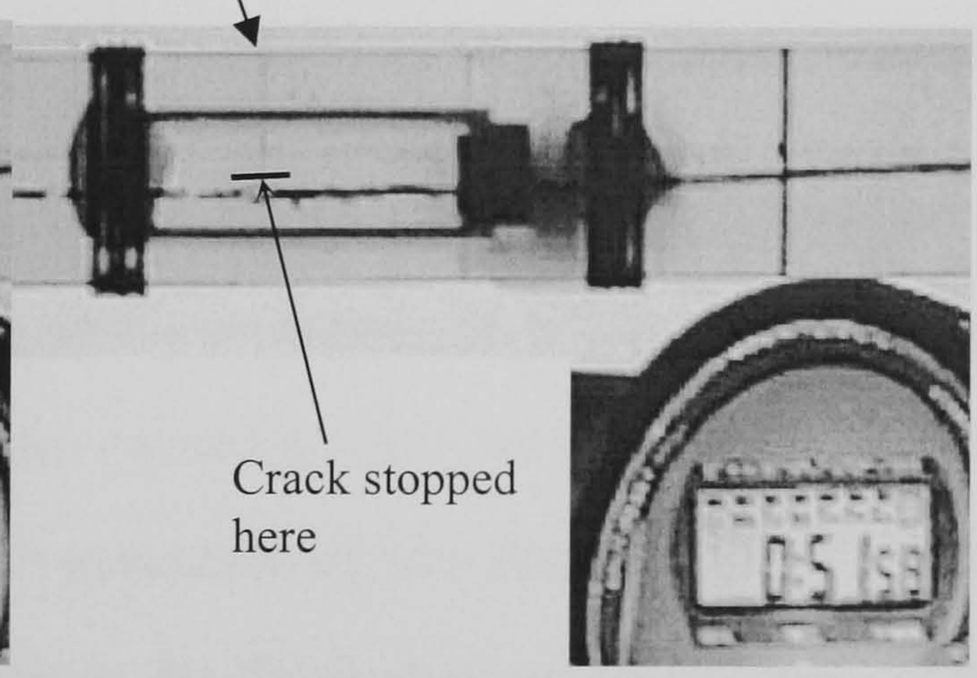

(d)

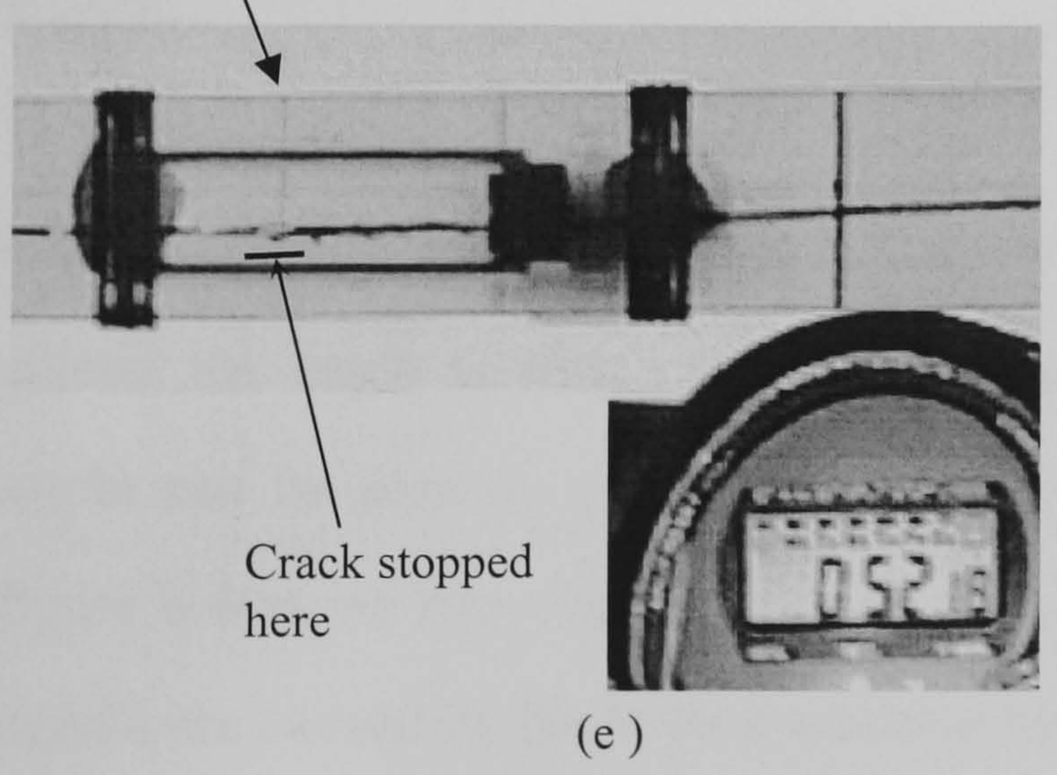

(e)

Figure 6.2 Propagation of Crack 2 during time 51-53 s.

(a) Change of load and strain signal with time.

(b) Change of strain and optical signal with time.

(c)-(e) Video images of crack development. (The difference between the time on the x-axis and time shown on the clock in the picture is 0.4s.)

Figure 6.3 shows one further example of crack development within the extensometer gauge length and between the two 45° splices. The crack (Crack 3) grew across the full width of the coupon at a time of about 165.2 seconds. It can be seen from Figure 6.3(a) and Figure 6.3(b), that the step-change in optical output corresponds to the sudden changes in load and strain output due to crack development. Indeed, Figure 6.3(a) shows clearly the superposition of two strain fluctuations: the strain fluctuation induced by the transverse crack and the strain fluctuation induced by the change of load on the specimen (the overall strain fluctuation).

6.2.2 Cracks occurring outside the extensometer gauge length and between the two 45° splices

When cracks propagate across the whole width of the coupon quickly, fluctuations of load signal always happen, as shown in Figure 6.1(a). However, when a crack occurs outside the extensometer gauge length, the extensometer can only pick up the fluctuation of the overall strain of the sample generated by the change of load, not the initial extension of the specimen which induces the fluctuation of load signal on the coupon.

When a crack occurs outside the extensometer gauge length, and within the two 45° splices, the crack is within the sensor gauge length, so the step-change of optical output can be seen as expected. Figure 6.4 shows such an example (Crack 4). In Figure 6.4(a), no step-change in strain is seen, and the fluctuations in strain and load signals are caused by the testing machine restoring the load to the demand value after the crack has developed. Figure 6.4(b) shows that the step-change in optical output occurs at the same time as the fluctuations in strain, which in turn corresponds to the time when the crack developed (Figure 6.4(c)). The video recording shows that the crack passed the sensor at about 61.56 seconds. The recorded optical output shows a

step-change at 61.16 seconds, which, given the time difference of 0.4 seconds between data-logger and video recording, is the same time.

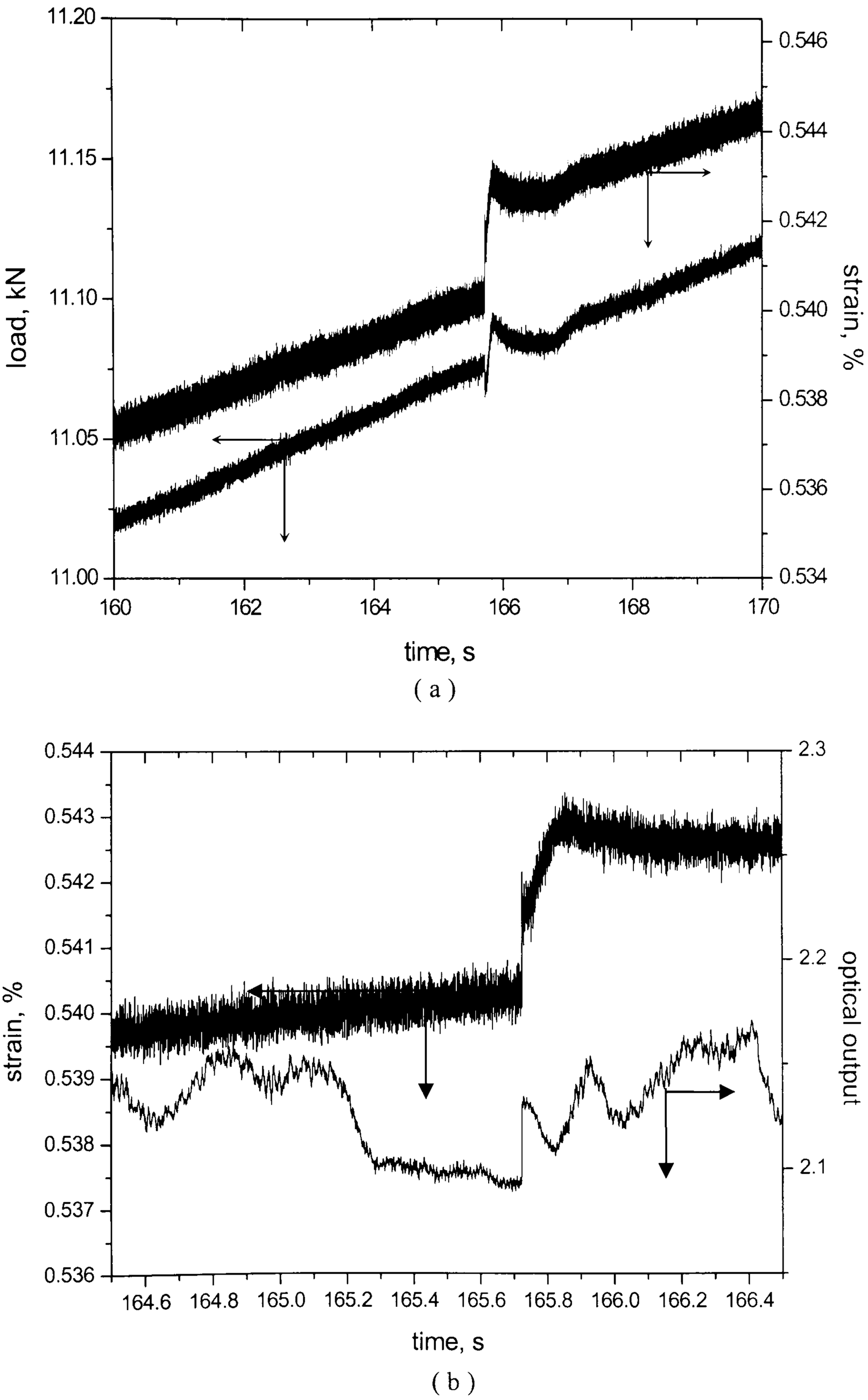

Figure.6.3 Propagation of Crack 3 within the extensometer gauge length.

(a) Change of load and strain signal with time.

(b) Change of strain and optical signal with time.

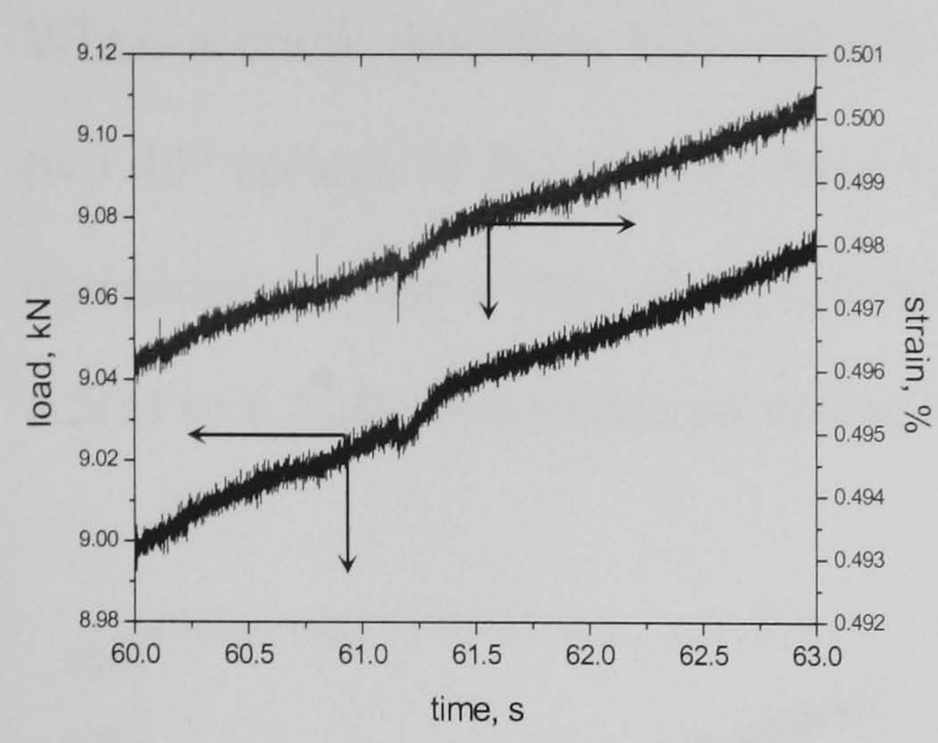

(a)

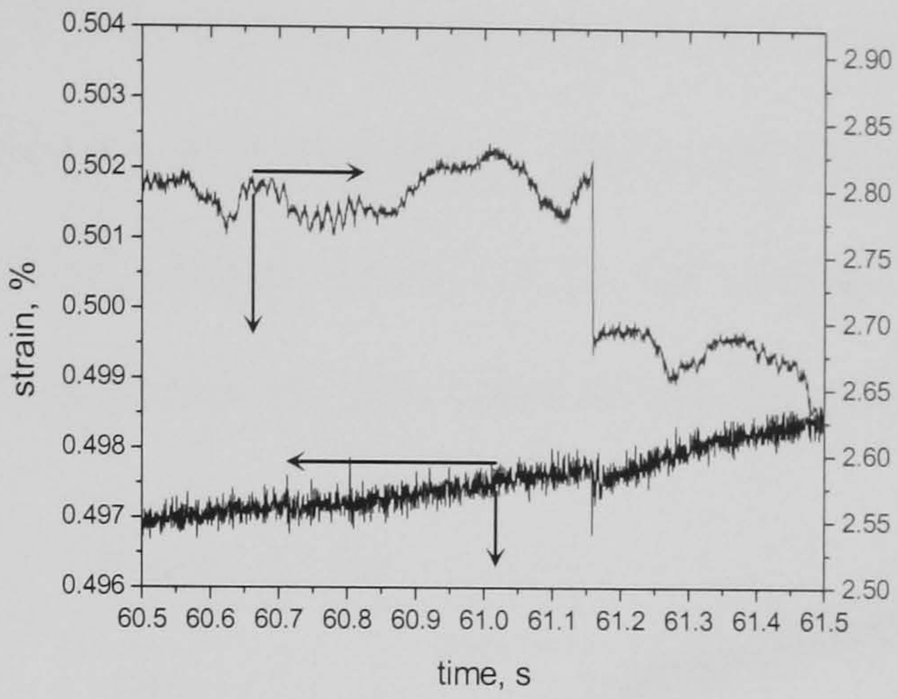

(b)

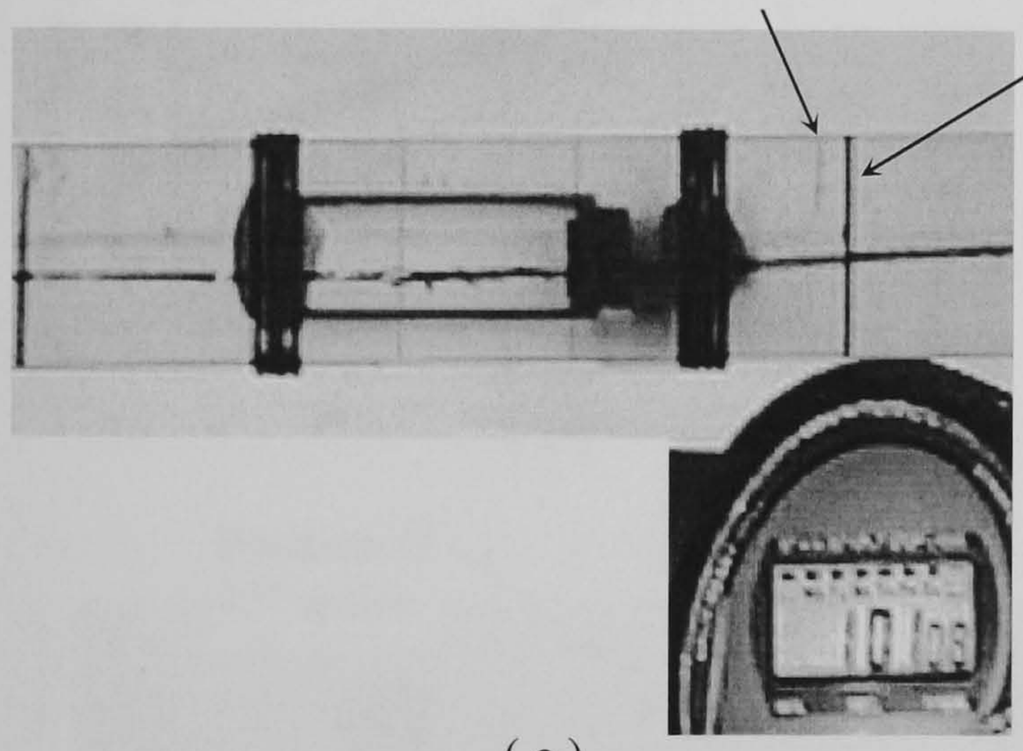

(c)

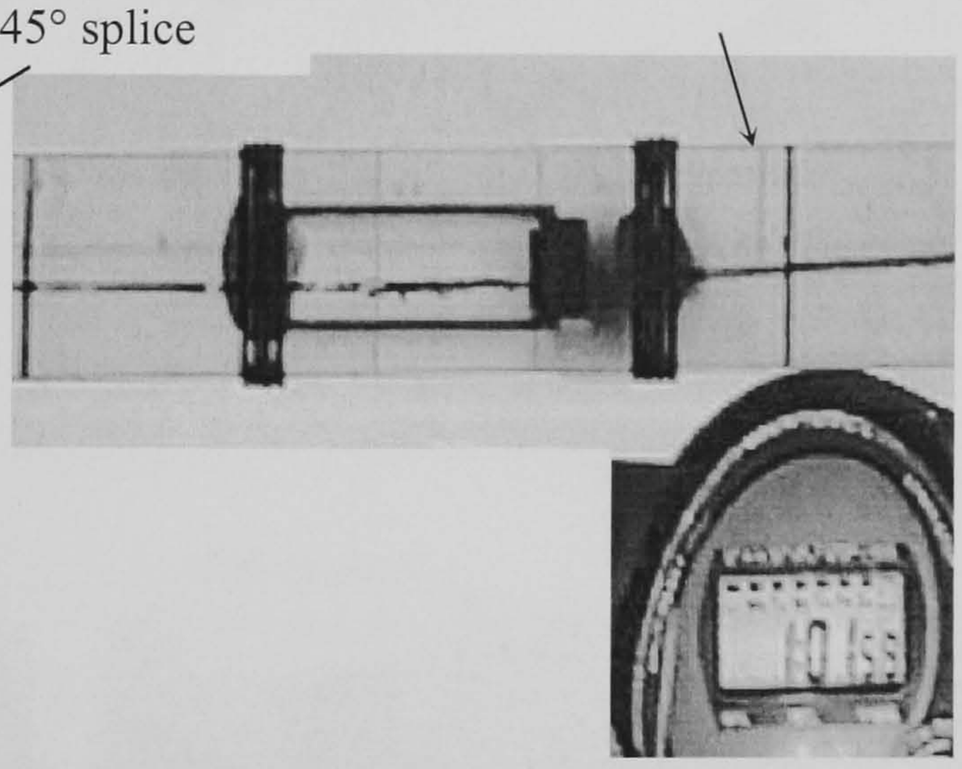

(d)

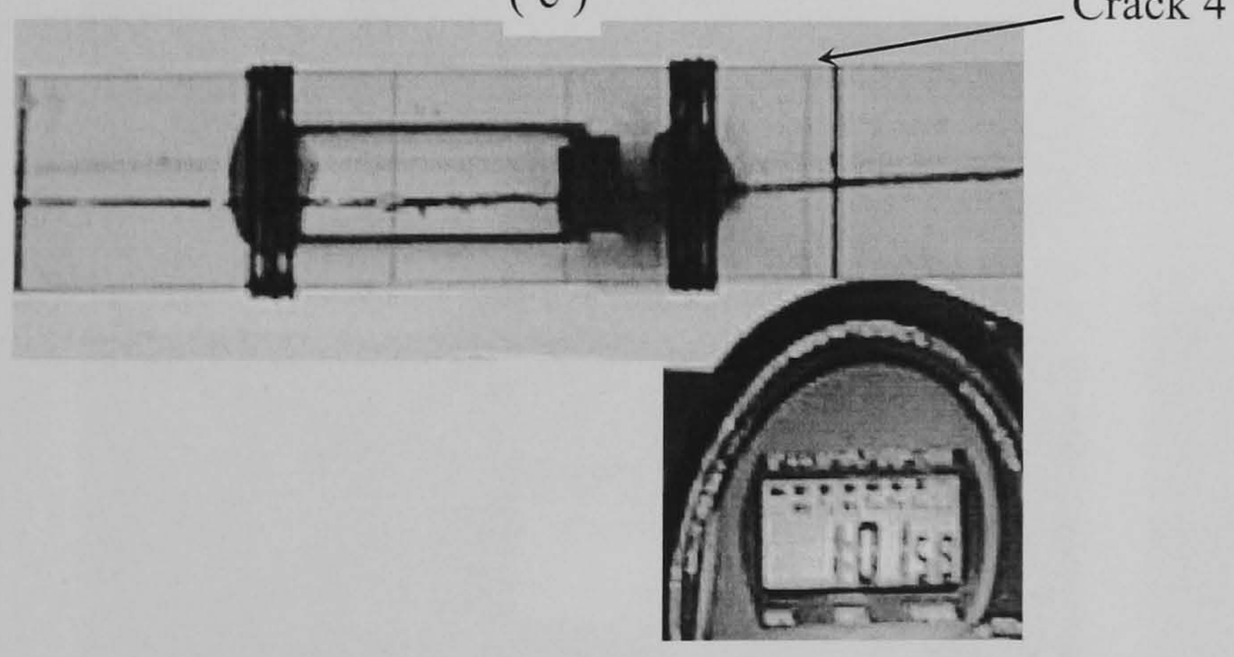

(e)

Figure 6.4 Propagation of Crack 4 during time 61-62s.

(a) Change of load and strain signal with time.

(b) Change of strain and optical signal with time.

(c)-(e) Video images of crack development. (The difference between time on the x-axis and time shown on the clock in the picture is 0.4s; the arrow indicates the position of the crack.)

6.2.3 Cracks occurring outside the extensometer and outside the two 45° splices

When a crack develops both outside the extensometer gauge length and outside the two 45° splices of the sensor, there is neither a step-change in strain recorded by the extensometer nor a step-change in the optical output recorded by the sensor. Figure 6.5(a) to 6.5(d) shows such an example. In this case, the load and strain fluctuations at

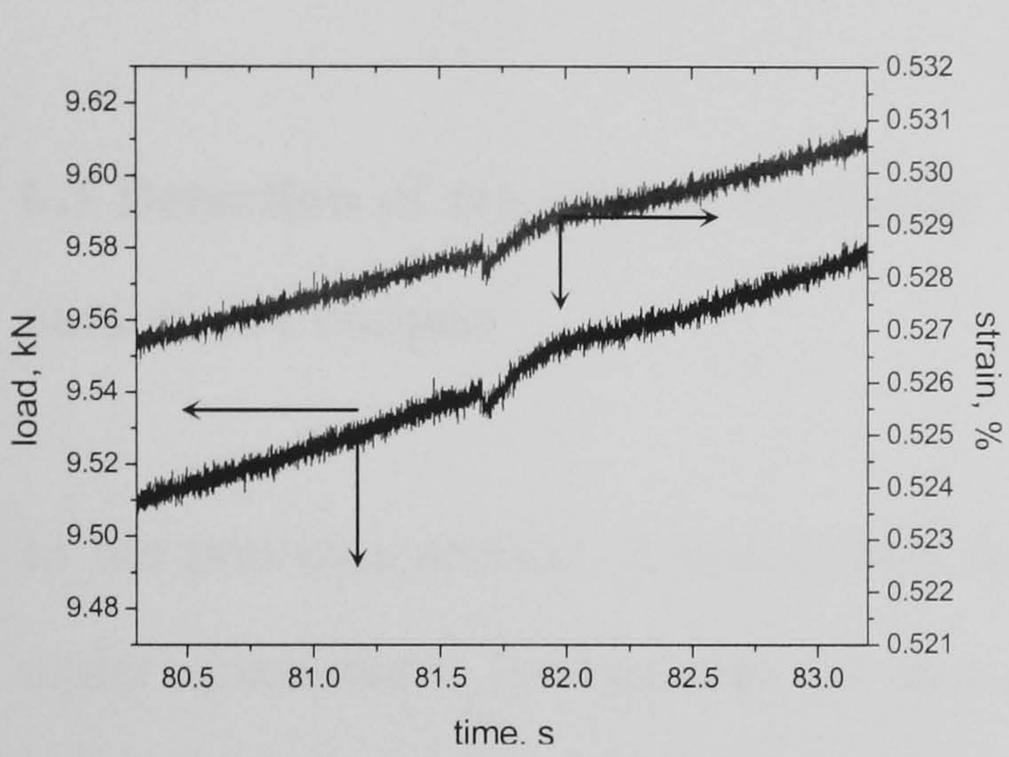

(a)

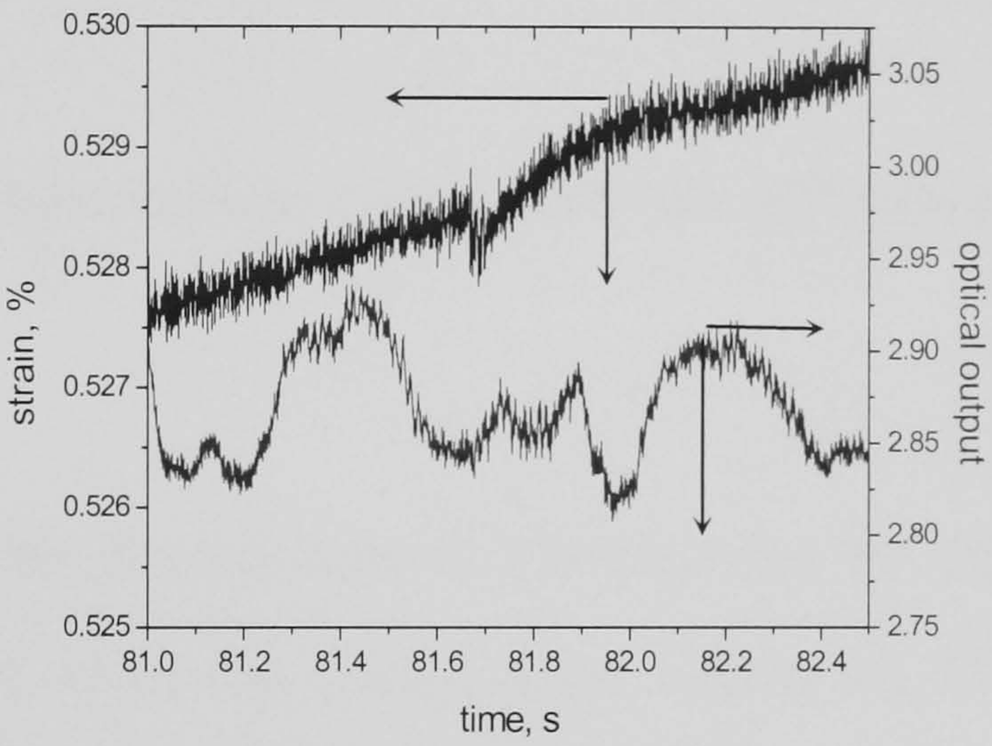

(b)

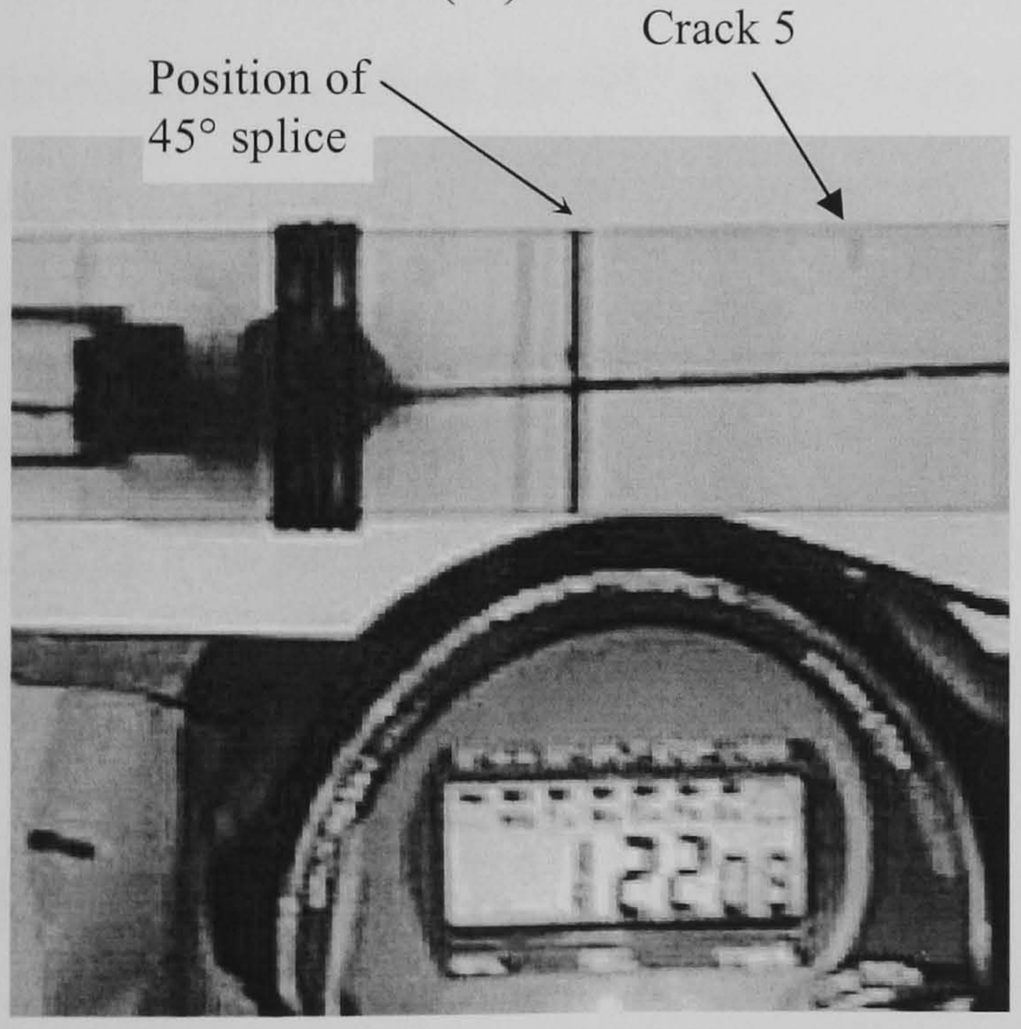

(c)

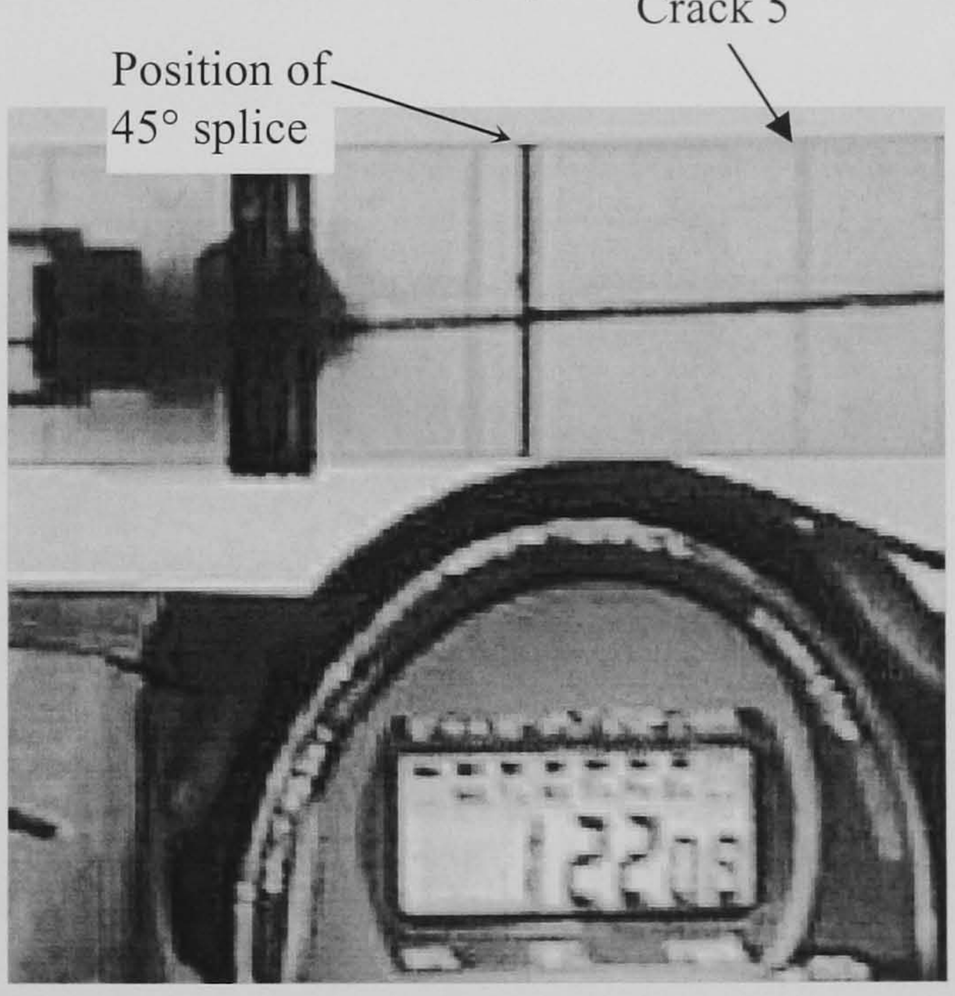

(d)

Figure 6.5 Propagation of Crack 5 outside gauge length of the embedded sensor
(a) Change of load and strain signal with time.
(b) Change of strain and optical signal with time.
(c)-(d) Video images of the time when the crack passed the sensor. (The difference between time on the x-axis and time shown on the clock in the picture is 0.4s; the arrow indicates the position of the crack.)

about 81.7 seconds suggest that a crack has formed (Figure 6.5(a)), although the lack

of a step-change in the strain suggests that the crack has developed outside the extensometer gauge length. Figure 6.5(b) shows that there is also no step-change in the optical output, suggesting that the crack developed outside the 45° splices of the sensor. This is confirmed by the video images in Figure 6.5(c) and (d) which show that the crack developed at 81.68 seconds (i.e., 82.08 less 0.4 seconds) about 20 mm beyond the 45° splice. The position of this splice is indicated by a black line on the specimen.

6.3 Detection of transverse cracks by a polarimetric sensor with two 45° splices outside the coupon

In the previous section, it was shown that the development of cracks in the 90° ply under quasi-static loading can be detected when the cracks occur within the 45° splices of the embedded polarimetric sensor. This suggested that cracks could be detected even when the 45° splices were far apart. This was confirmed in a series of experiments with the 45° splices of the sensor located outside the end tabs of the coupon; and the structure of this type of sensor is shown in Figure 4.4(b). Now, the complete length of the coupon is within the gauge length of the sensor, so all the cracks that develop in the coupon should be detected by the embedded sensor. Again, an extensometer was used to monitor the strain signal.

6.3.1 Detection of cracks occurring within the extensometer gauge length

When a crack develops within the extensometer gauge length, the response of load, strain and optical signals, as shown in Figure 6.6(a) and 6.6(b), are exactly the same as those discussed in Section 6.2.1. This is because the crack has developed within both the extensometer and sensor gauge lengths. An example is shown in Figure 6.6 (Crack 6) at 69.67 seconds, indicated by strain and optical output step-changes in

Figures 6.6(a) and(b), corresponds to the crack which is shown in the video images (Figure 6.6(c) and (d)) that has developed at the same time.

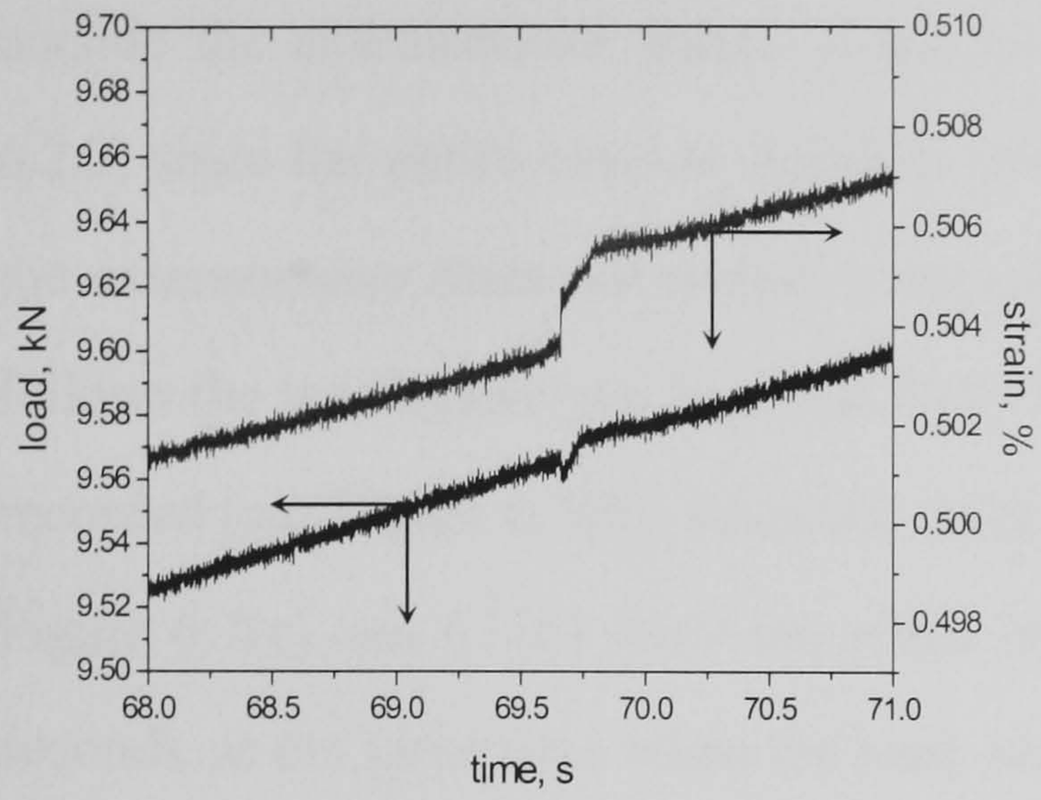

(a)

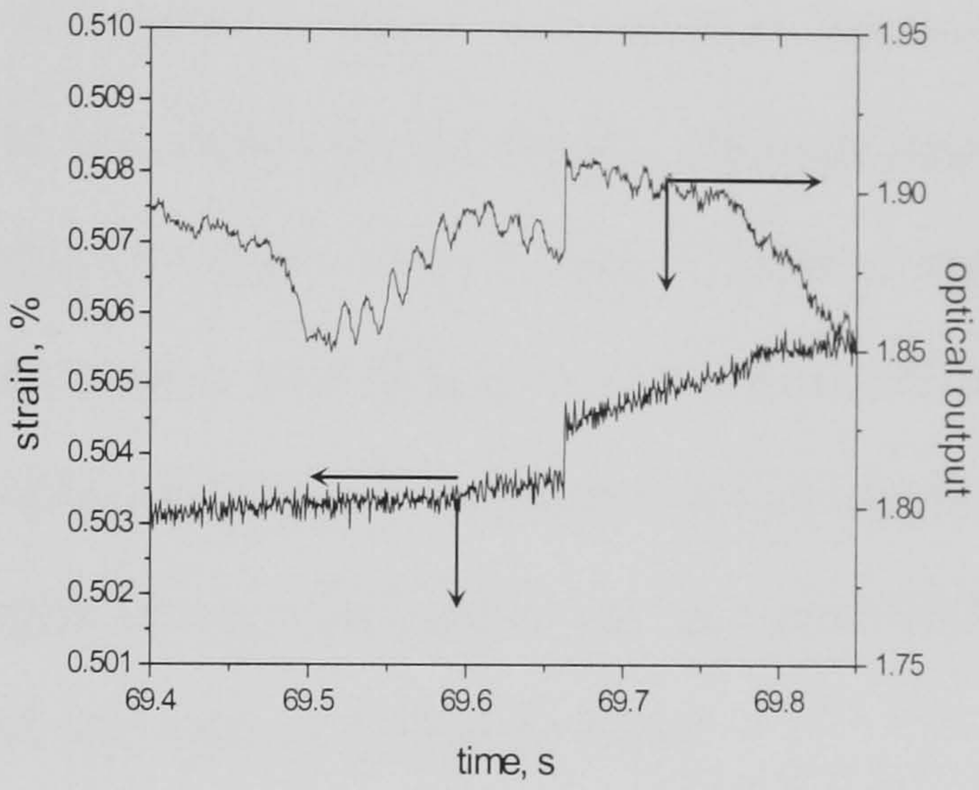

(b)

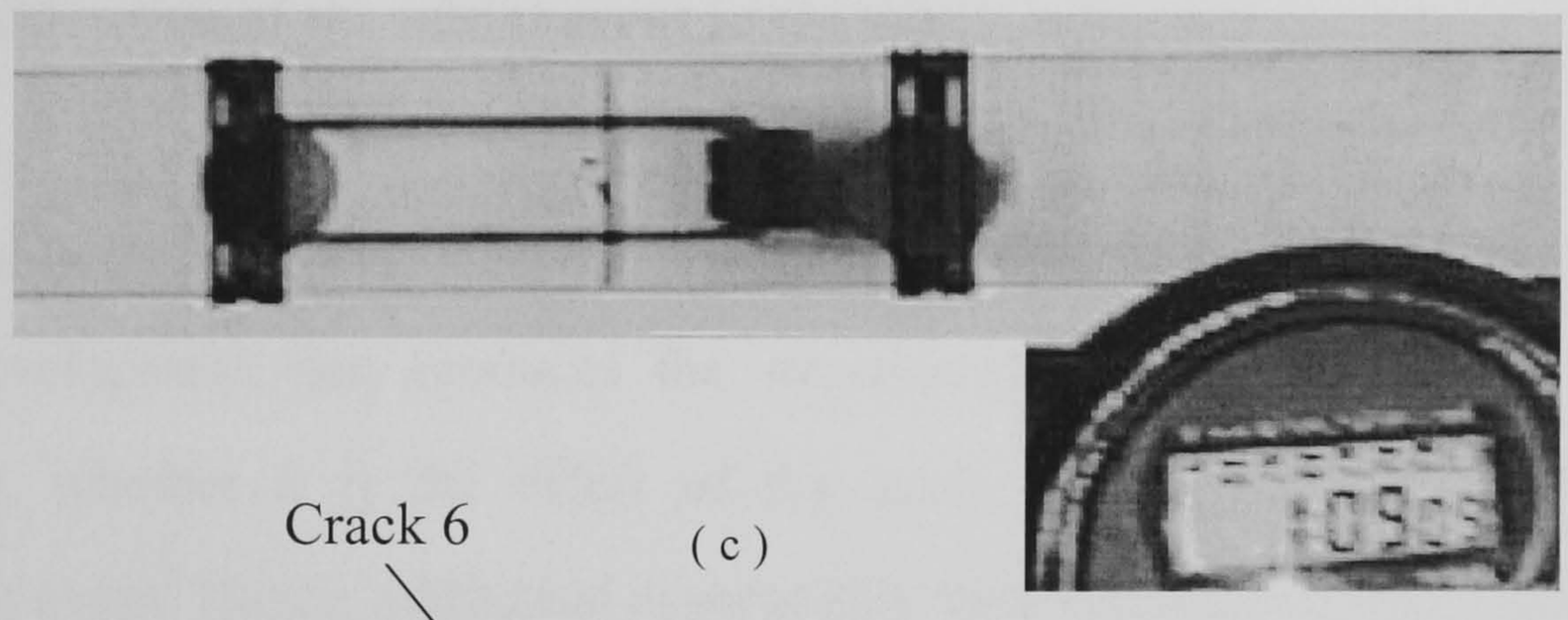

(c)

(d)

Figure.6.6 Propagation of Crack 6 within the extensometer gauge length.

(a) Change of load and strain signal with time.

(b) Change of strain and optical signal with time.

(c) and (d) Video images of the time when the crack passed the sensor. (The difference between time on the x-axis and time shown on the clock in the picture is 0.55s; the arrow indicates the position of the crack.)

6.3.2 Detection of cracks occurring outside the extensometer gauge length

In this case, the fluctuations of load, strain and optical signal when cracks occur outside the extensometer gauge length are the same as those described in Section 6.2.2, since the entire coupon length is within the sensor gauge length. As expected, the extensometer does not record a step-change in strain when Crack 7 formed but follows the load signal (see Figure 6.7(a)). However, a step-change in optical output is recorded (see Figure 6.7(b)) since the crack developed within the sensor gauge length. Figure 6.7(c) and 6.7(d) show the video images of crack development, at about 94.3 seconds, at the same time when the load, strain and optical signal fluctuate.

6.4 Identification of the initial event in the crack detection

In the experiments described so far, it is difficult to establish whether it is the effect of crack development that produces the step-change in the optical output or, more precisely, whether it is the effect of the crack passing the sensor which is the important event. Hence, additional experiments were required to verify this point.

In the experiments described in this section, a circular hole was drilled at the centre of cross-ply coupons which had polarimetric sensors embedded on one side of the hole. The hole acts as a strain concentrator, and when cracks initiate from the hole, they either grow on the sensor side, or on the side which does not contain the sensor. Hence, the importance of cracks passing the sensor, or not, can be established.

6.4.1 Experimental arrangement to detect cracks around a circular hole

In these experiments, coupons with thicker 0° plies were used with the aim of minimising the risk of splitting the 0° plies when the coupons were drilled. The thickness of the 90° ply was 2 mm, and the thickness of both 0° plies were 1 mm. A circular hole with a diameter of 8 mm was drilled at the centre of the coupon using a

portable drill. Polarimetric sensors with 45° splices typically 100 mm apart (i.e. the splices are inside the coupon gauge length) were embedded into the 0° ply, near the

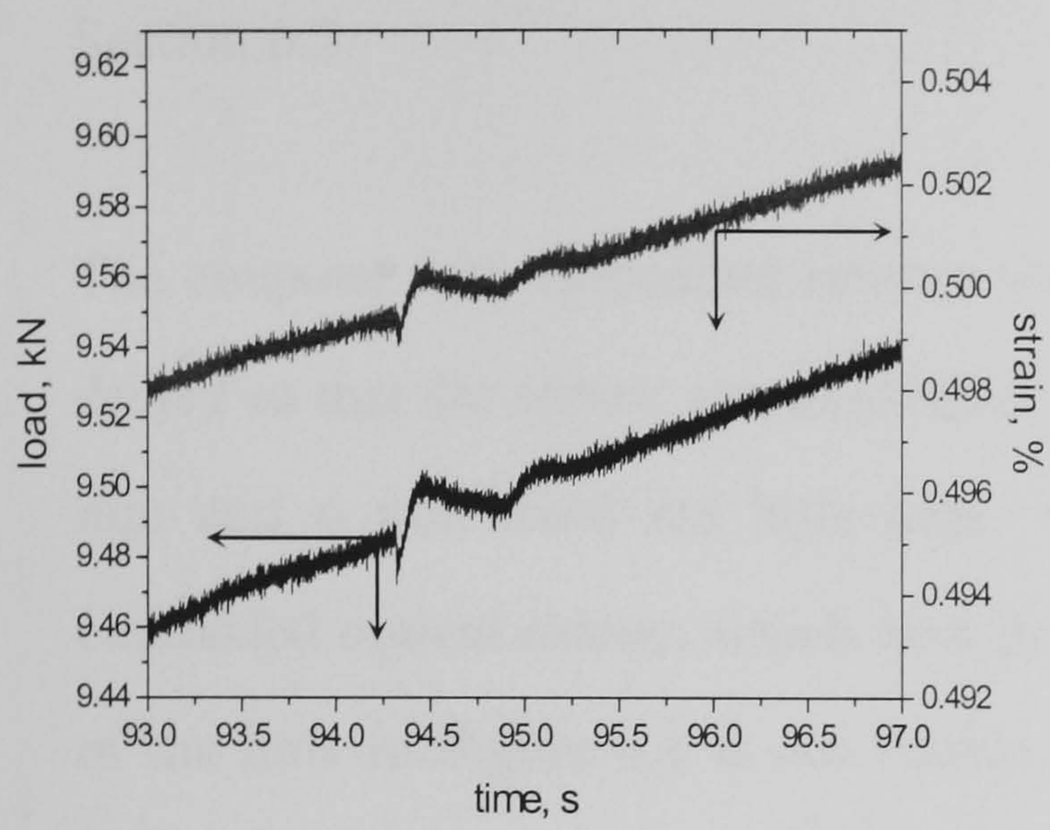

(a)

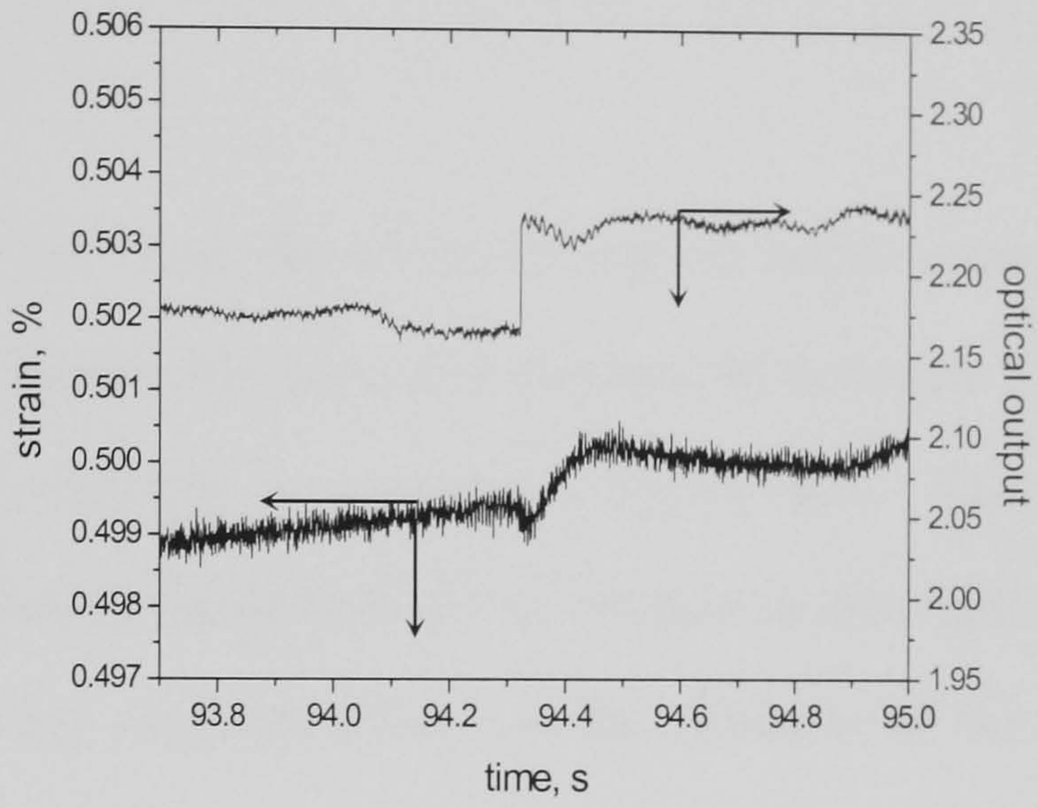

(b)

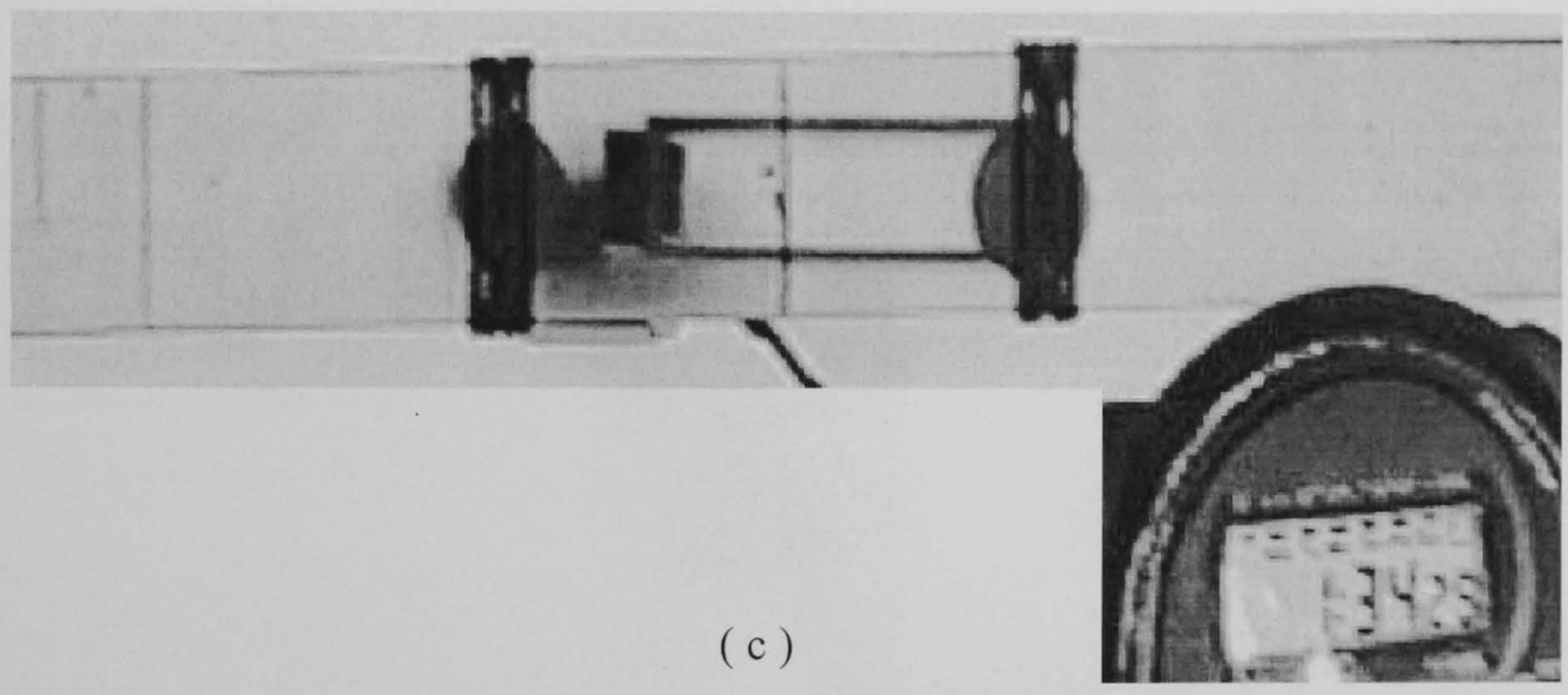

(c)

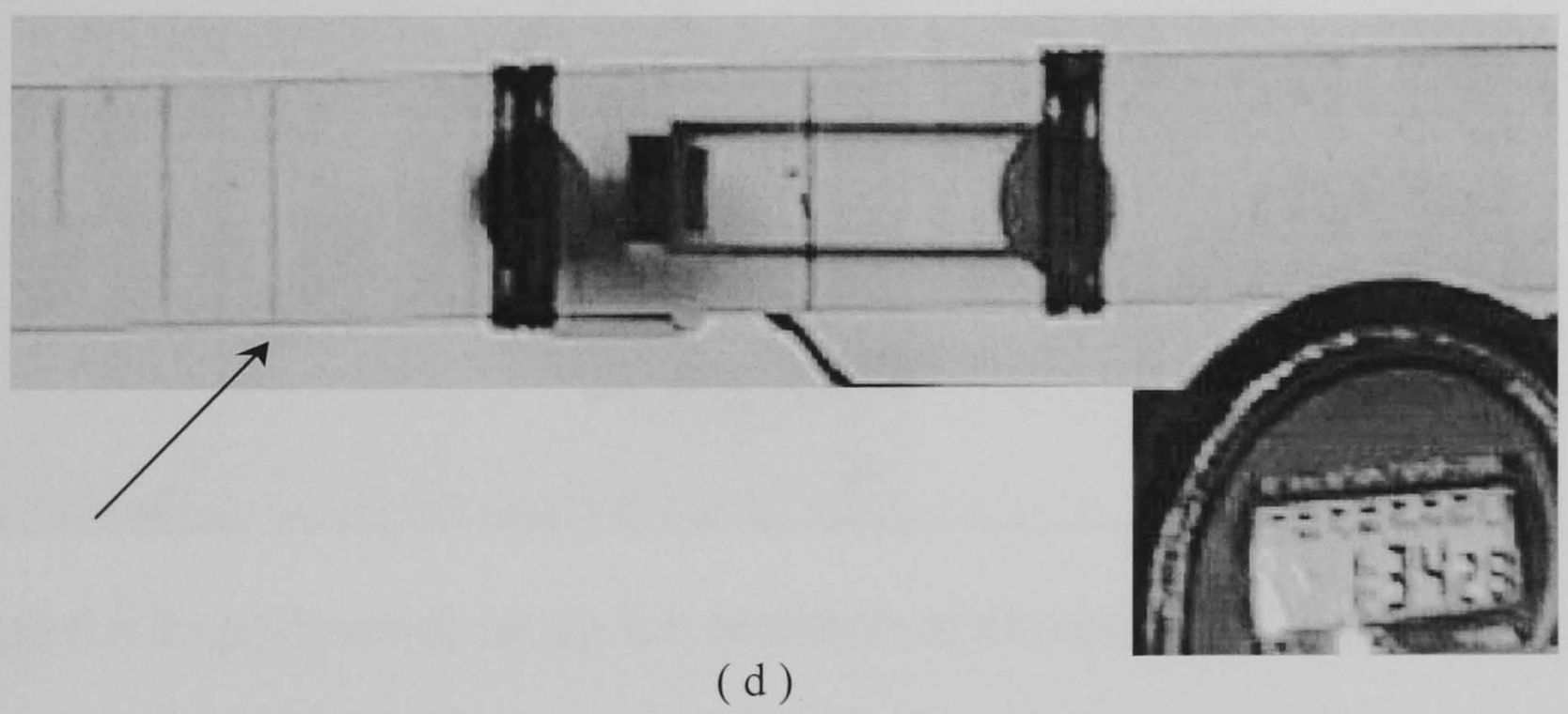

(d)

Figure 6.7 Propagation of Crack 7 outside the extensometer gauge length.

(a) Change of load and strain signal with time.

(b) Change of strain and optical signal with time.

(c) and (d) Video images of the time when the crack passed the sensor. (The difference between time on the x-axis and time shown on the clock in the picture is 0.05s; the arrow indicates the position of the crack.)

0/90 interface, in the usual way. The coupons were 20 mm wide, 180 mm long and the gauge length of the extensometer was 50 mm. Hence the 45° splices were outside the gauge length of the extensometer, the same as the arrangement described in Section 6.2.

The coupons with embedded sensors were cut from the laminate and the holes were drilled so that the sensor was positioned alongside the hole, at a distance of between 3 mm and 6 mm from the hole edge. An example is shown in Figure 6.8. The embedded optical sensor, which runs parallel to the length of the coupon to the right of the hole in Figure 6.8 is not visible at this magnification, but the position of the sensor was delineated on the surface of the coupon with a marker pen.

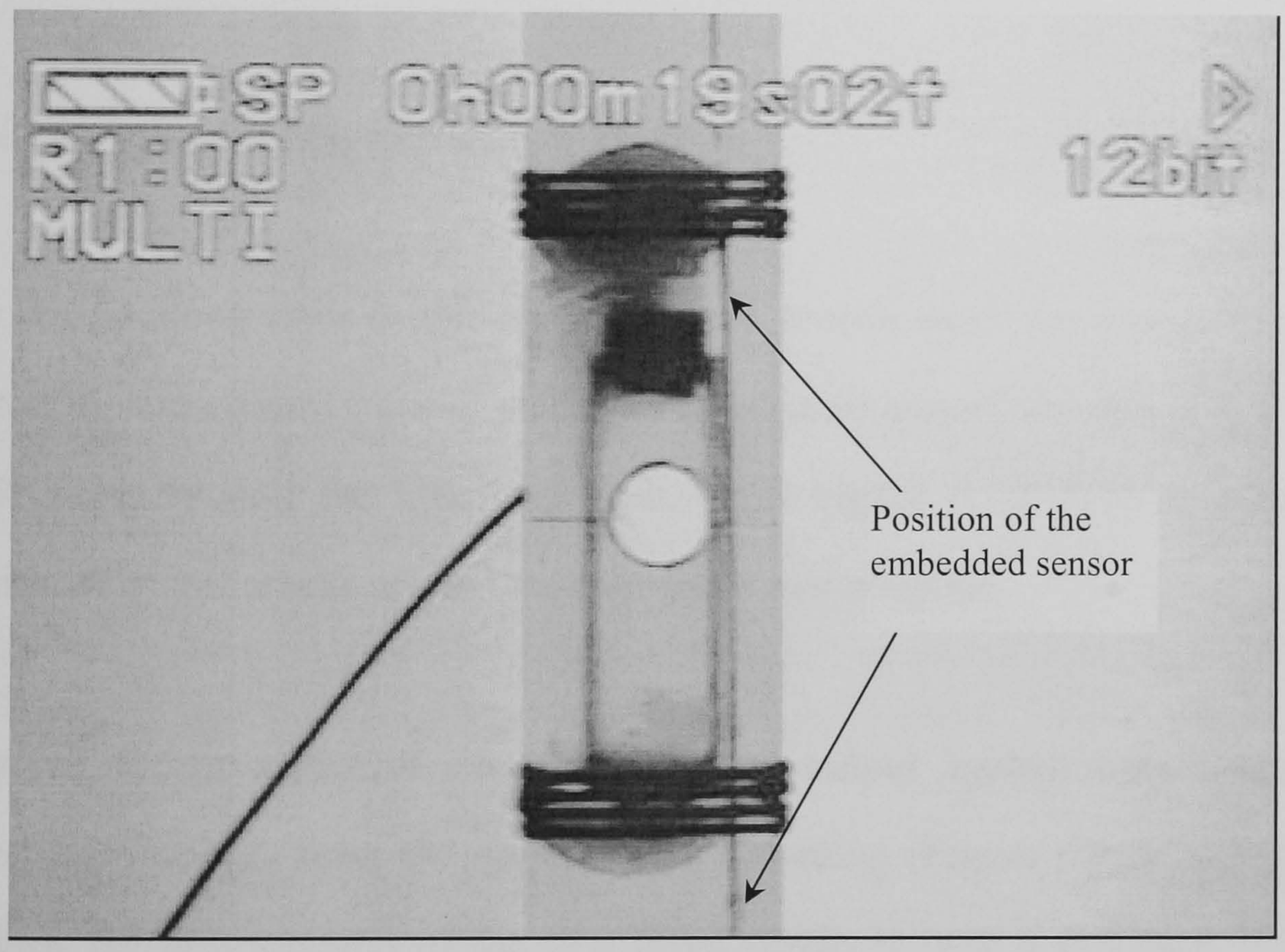

Figure 6.8 Experimental set up for detection of cracks around a circular hole

For these experiments, the VHS video camera was replaced with a digital video camera (Panasonic NV-GX7B) and the photographs were taken from the digitally stored images directly. In addition to better picture quality, the digital camera also allows the time to be printed on the screen directly, so the timer used with the VHS video camera was no longer necessary. The time shown on these digital images is in

the format of hour(h)/minute(m)/second(s)/frame(f). The camera can take and store 50 images per second on the tape, which means that each image is separated by 0.02s. However the time printed on the images contains only 25 frames and two consecutive digital images have the same recorded time (frame number). As a consequence, a crack can grow in two consecutive images but with the same indicated time.

As in the experiments described with the VHS video camera, in these experiments the digital camera and the fatigue machine were started manually. Hence, there is always a small time difference between the time recorded by the camera and the time recorded by the test machine. The coupon was gently tapped in the same way as described in Chapter 4.4.1 to establish the time difference between the digital video camera and the computer datalogger.

6.4.2 Detection of cracks initiating at the hole

When the coupons were loaded in quasi-static tensile load (the testing machine was operated in load control), initial cracks were induced around the hole due to the strain magnification around the hole. Figure 6.9 and Figure 6.10 show examples of the detection of initial cracks around the hole from two coupons.

Figure 6.9 shows a plot of strain and optical output against time (Figure 6.9(a)) together with images from the digital video recording (Figure 6.9(b) to Figure 6.9(d) that show the development of the first three cracks (Crack 8 to Crack 10). Note, in each of Figure (b) to (d), two consecutive images are shown. These are 0.02 seconds apart in time. The strain signal shows a generally linear increase with time as the load increases, whilst the output signal from the sensor is sinusoidal as a result of the optical fringes. The strain output over this time interval during the test (from about 11 seconds to 18 seconds) shows three small step-changes. These increases in strain are subsequently related to the development of cracks with the aid of the images from the digital video recording. The step-change at about 13 seconds corresponds to Crack 8

(Figure 6.9(b)) which developed on the left side of the hole. The step-change at about 15.9 seconds corresponds to the development of Crack 9 (Figure 6.9(c)) which occurred on the right-hand-side of the hole, and the third step-change corresponds to Crack 10 (Figure 6.9(d)) which, like Crack 8, developed on the left side of the hole. It can be seen clearly from the optical output that it is only the crack that develops on the sensor side of the hole, e.g Crack 9, will causes a step-change in the optical response. Cracks 8 and 10, which developed on the side of the hole away from the sensor, do not affect the optical output of the sensor, although the effects of each crack are recorded by the extensometer.

Figure 6.10 shows similar experimental results from another sample; again consecutive images of 0.02 seconds apart are shown in Figure 6.10(b), 6.10(c) and 6.10(e). In this test, the results were obtained from several load/unload cycles of the coupon. Crack 11 and Crack 12 occurred in one tensile loading and there are two strain step-changes corresponding to these two cracks (see Figure 6.10(a)). However a step optical change is only found for Crack 11 (Figure 6.10(a)). Figure 6.10(b) and Figure 6.10(c) from the digital camera show that only Crack 11 has grown on the same side of the hole as the sensor. Figure 6.10(d) shows another, and much clearer, optical change found in a different tension test of the same coupon at higher strains. Unsurprisingly, the crack (Crack 13) had grown on the same side as the embedded optical sensor and had passed it, as shown in Figure 6.10(e).

6.5 Further evidence of crack detection using the polarimetric sensor

The results described in Sections 6.2 and 6.3 showed evidence of crack detection in plain coupons and in Section 6.4, coupons with holes were used to show that cracks are only detected which passed the sensor. In this section, additional evidence is provided of crack detection, this time, of cracks which develop in coupons containing a hole but where the cracks do not develop from the hole. Additionally, the coupons

used here have thicker 0° and 90° plies than the coupons described in Section 6.2 and 6.3.

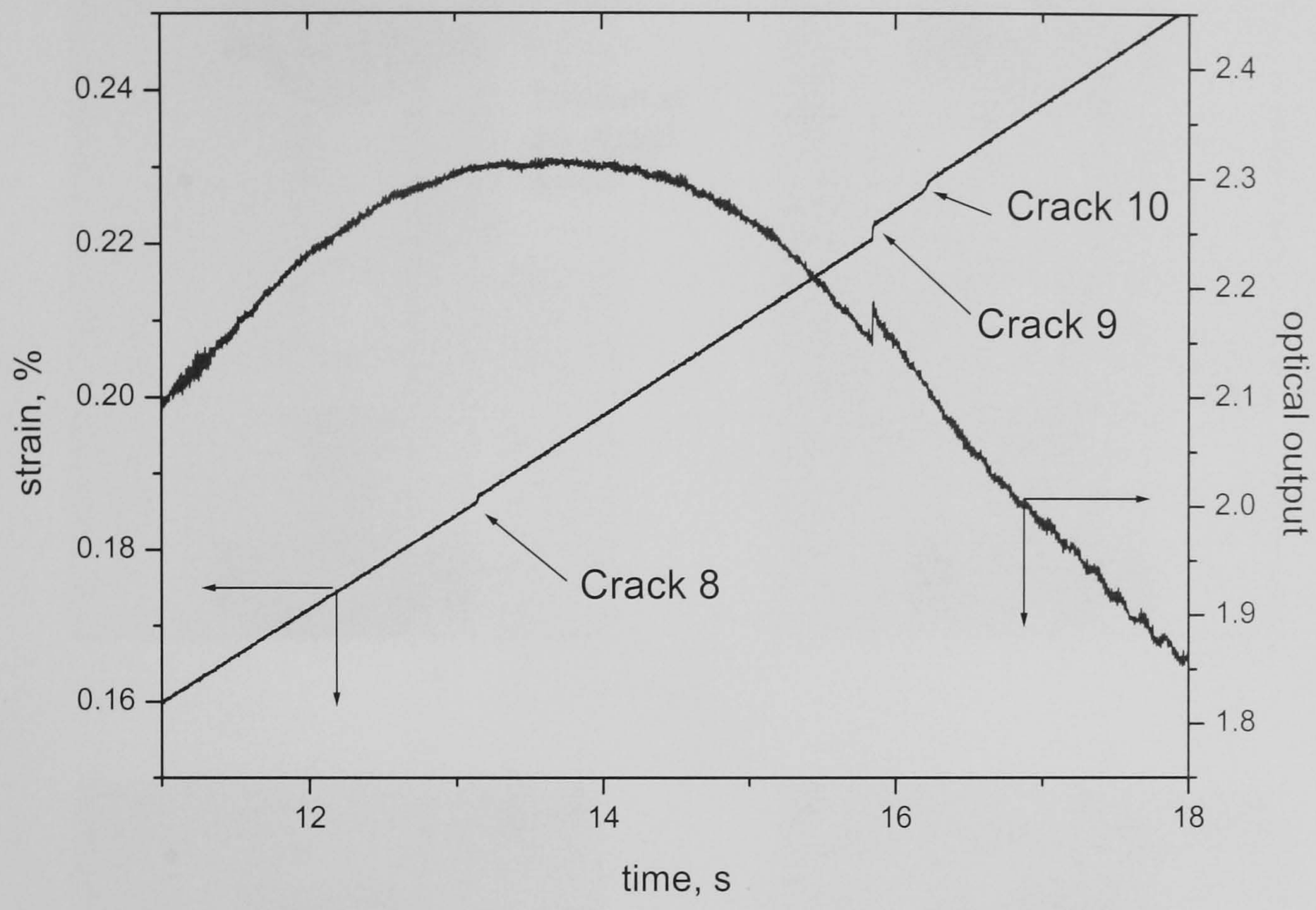

(a)

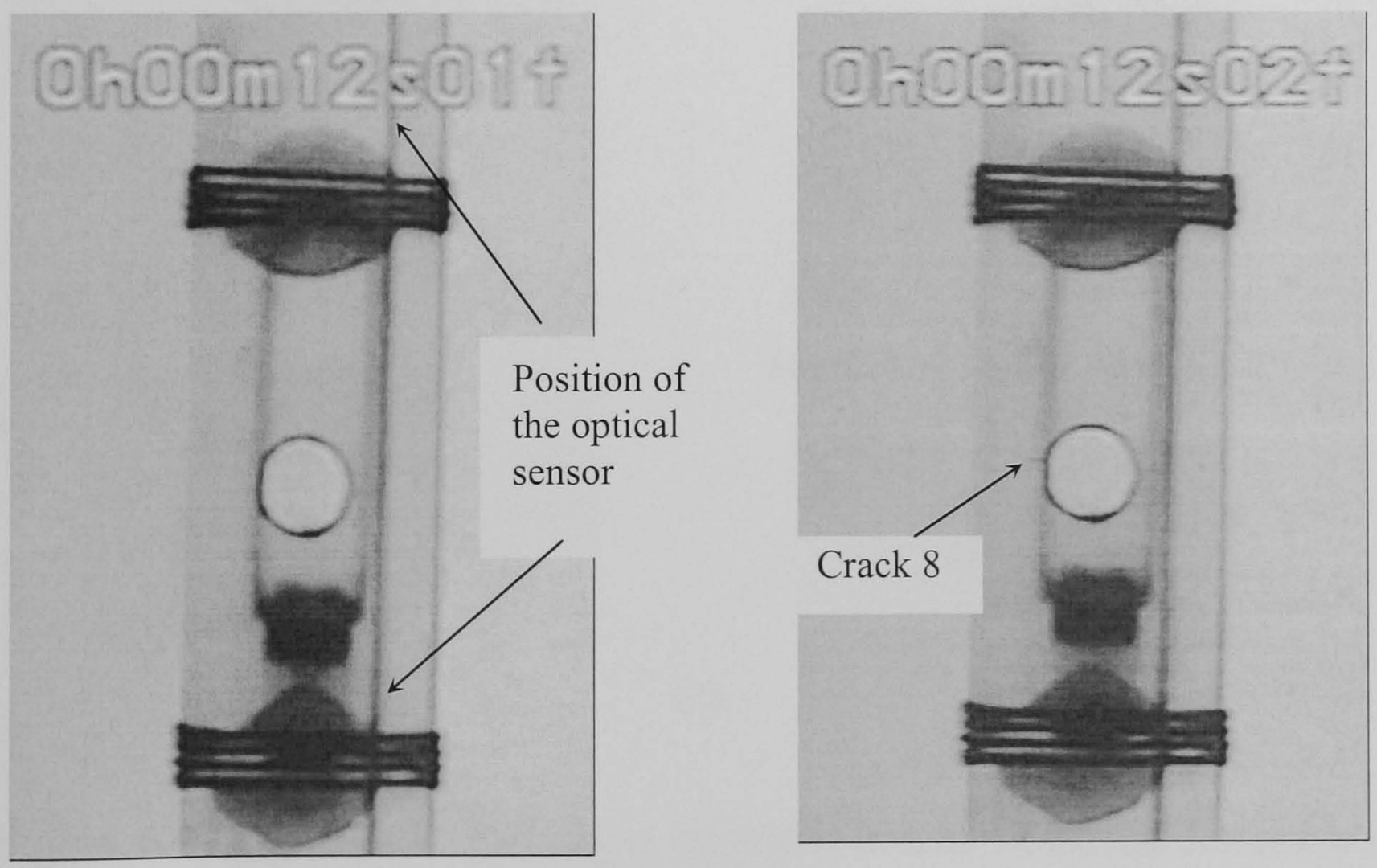

(b)

Figure 6.9 Detection of initial cracks occurred around a circular hole under quasi-static loading in Sample 1.
(a) The responses of strain signal and optical signal when initial cracks occurred around the circular hole.
(b) Video images showing development of Crack 8 around the circular hole.
(c) Video images showing development of Crack 9 around the circular hole.
(d) Video images showing development of Crack 10 around the circular hole.

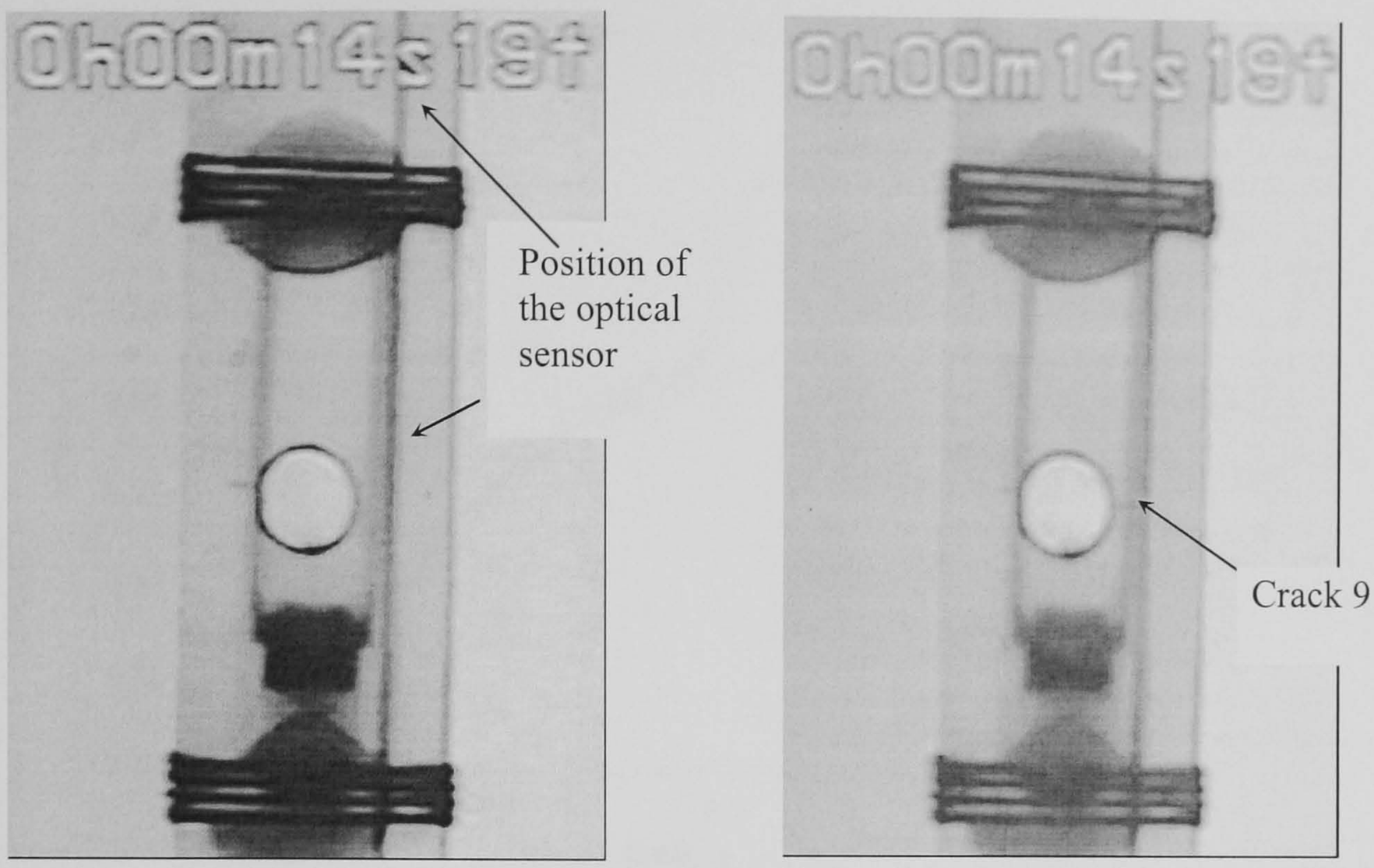

(c)

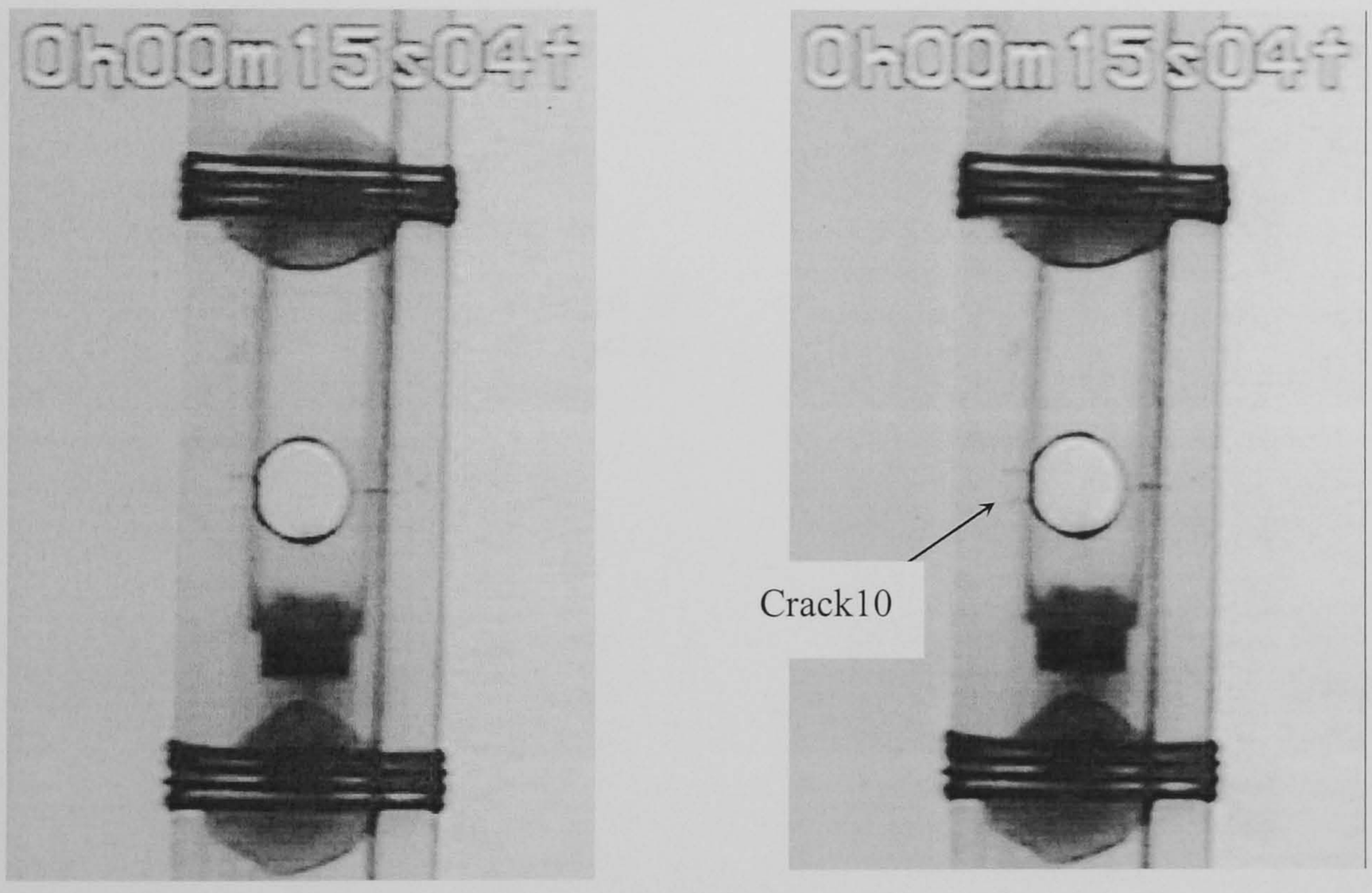

(d).

Figure 6.9 (continued). Detection of initial cracks occurred around a circular hole under quasi-static loading in Sample 1.
(a) The responses of strain signal and optical signal when initial cracks occurred around the circular hole.
(b) Video images showing development of Crack 8 around the circular hole.
(c) Video images showing development of Crack 9 around the circular hole.
(d) Video images showing development of Crack 10 around the circular hole.

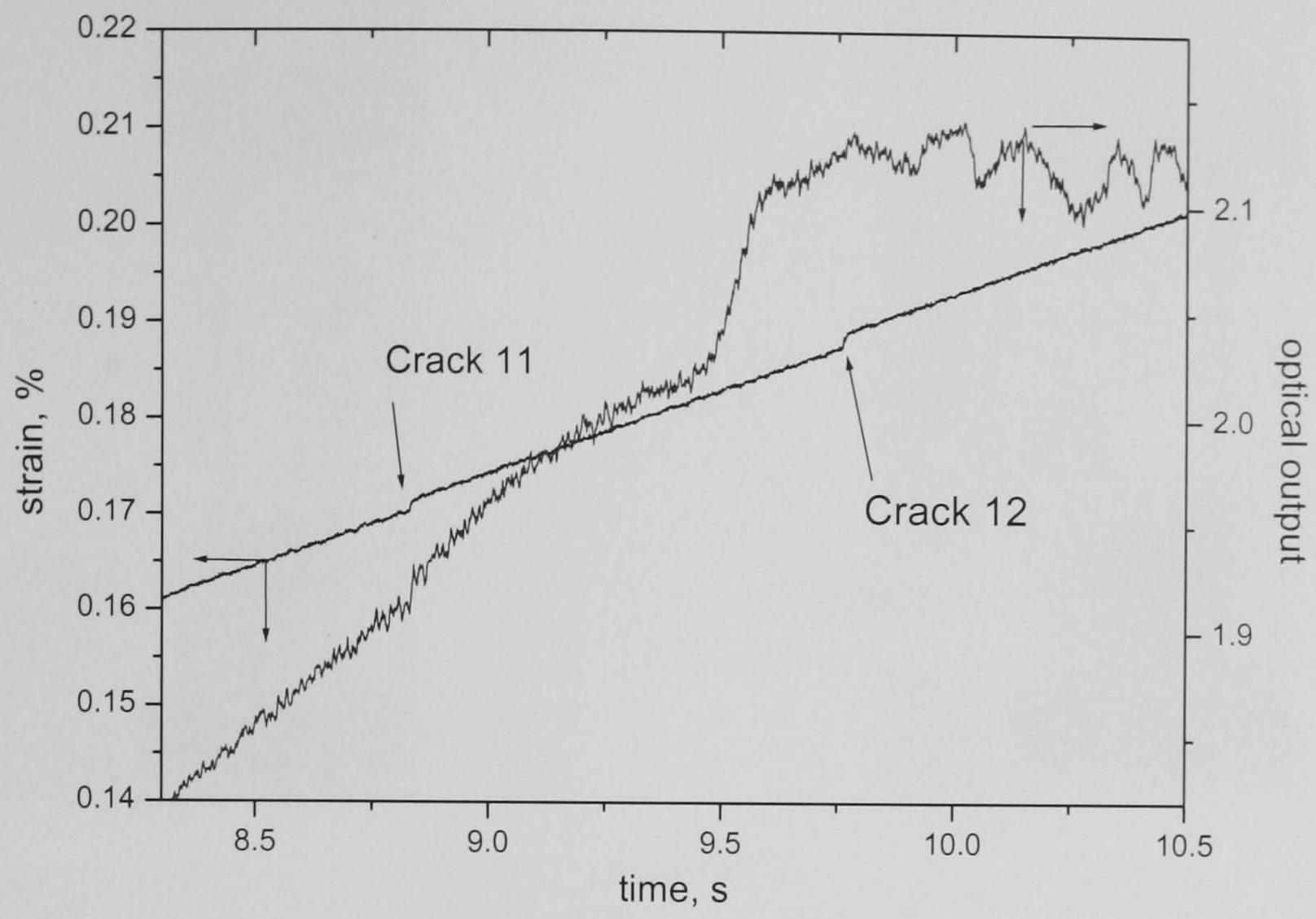

(a)

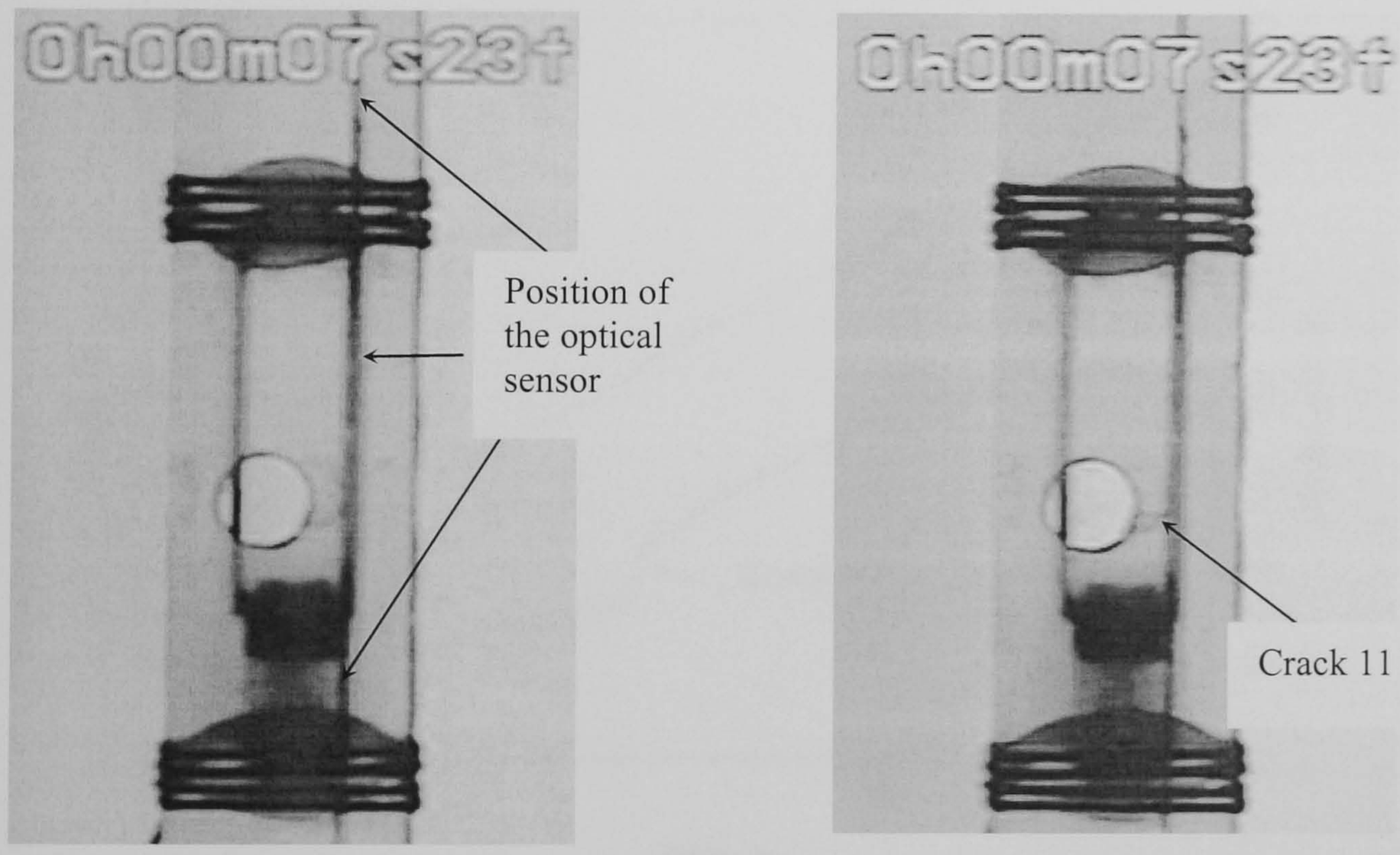

(b)

Figure 6.10 Detection of initial cracks occurred around a circular hole under quasi-static loading in Sample 2.
(a) The responses of strain signal and optical signal when initial Crack 11and Crack 12 occurred around the circular hole.
(b) Video images showing development of Crack 11 around the circular hole.
(c) Video images showing development of Crack 12 around the circular hole.
(d) The responses of strain signal and optical signal when Crack 13 occurred around the circular hole.
(e) Video images showing development of Crack 13 around the circular hole.

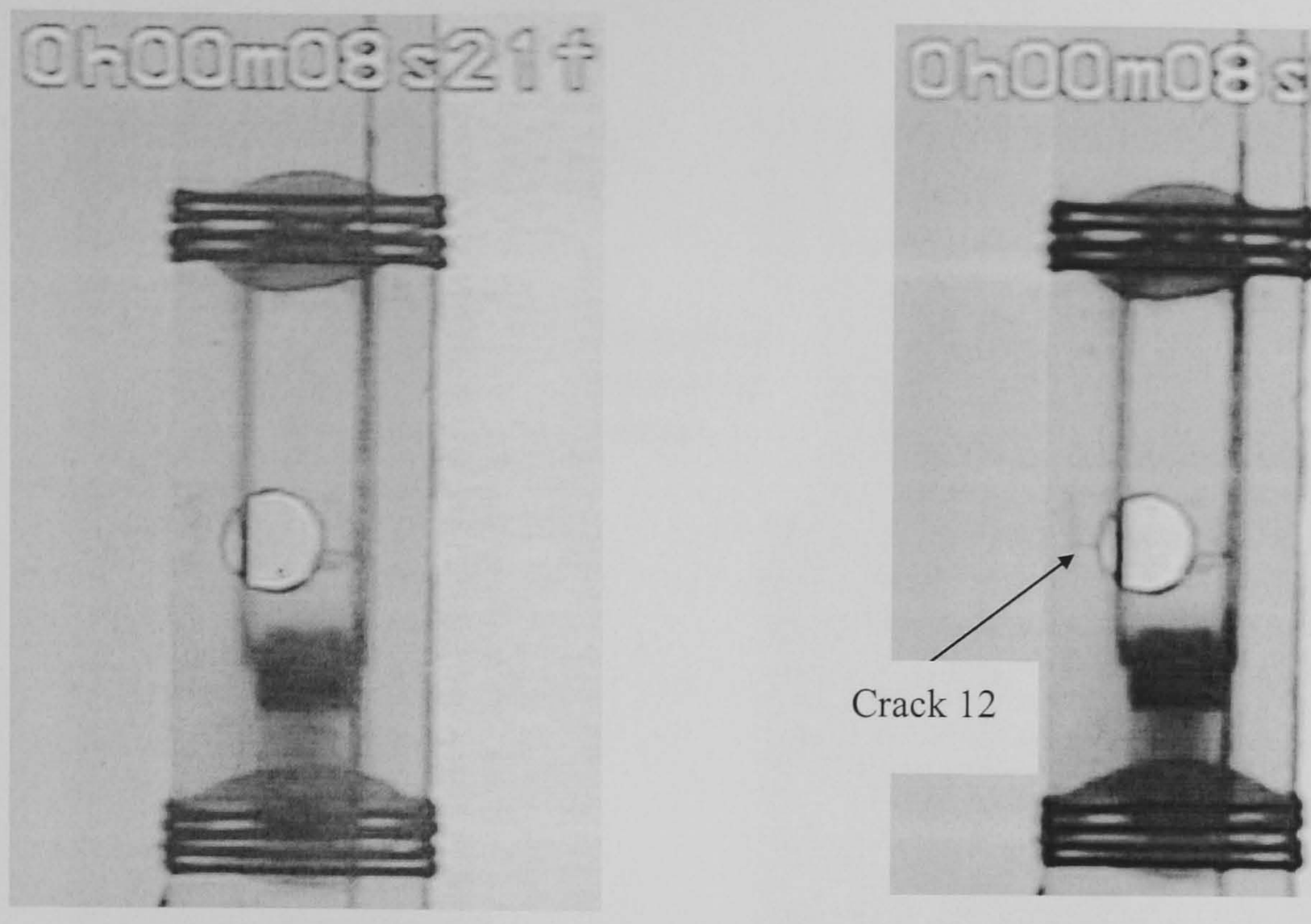

(c)

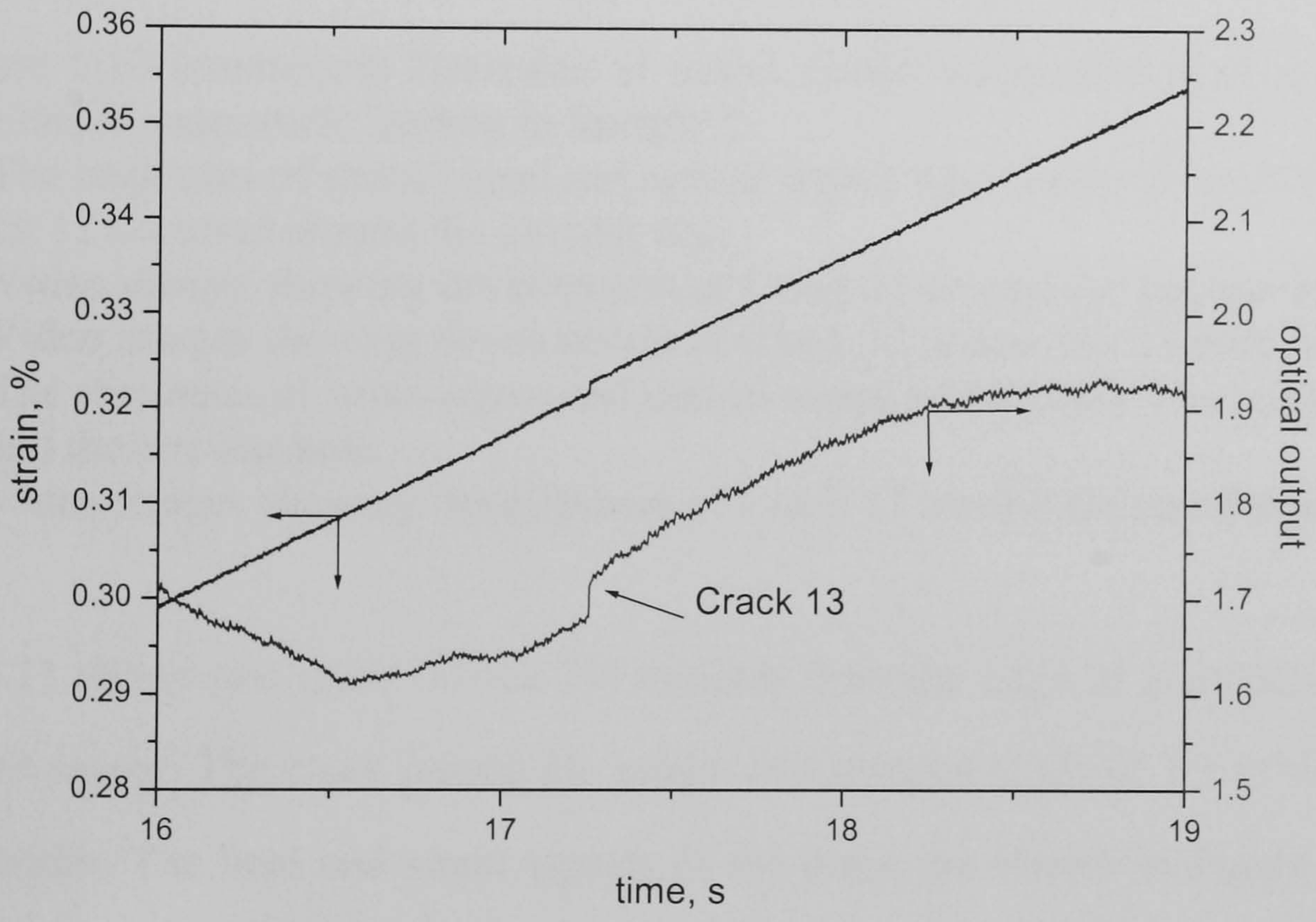

(d)

Figure 6.10 (continued). Detection of initial cracks occurred around a circular hole under quasi-static loading in Sample 2.
(a) The responses of strain signal and optical signal when initial Crack 11 and Crack 12 occurred around the circular hole.
(b) Video images showing development of Crack 11 around the circular hole.
(c) Video images showing development of Crack 12 around the circular hole.
(d) The responses of strain signal and optical signal when Crack 13 occurred around the circular hole.
(e) Video images showing development of Crack13 around the circular hole.

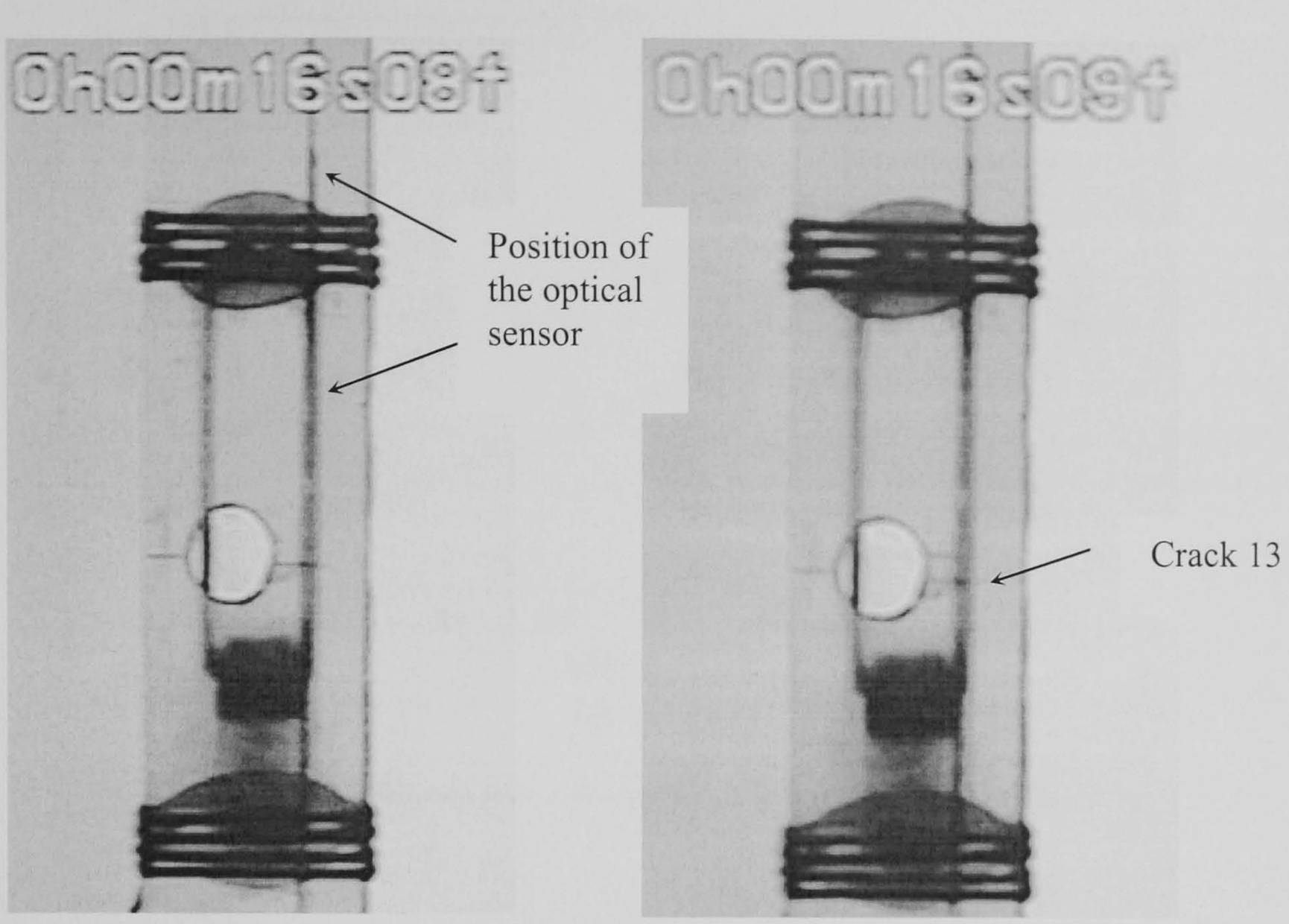

(e)

Figure 6.10 (continued) Detection of initial cracks occurred around a circular hole under quasi-static loading in Sample 2.
(a) The responses of strain signal and optical signal when initial Crack 11 and Crack 12 occurred around the circular hole.
(b) Video images showing development of Crack 11 around the circular hole.
(c) Video images showing development of Crack 12 around the circular hole.
(d) The responses of strain signal and optical signal when Crack 13 occurred around the circular hole.
(e) Video images showing development of Crack 13 around the circular hole.

Figure 6.11 shows one crack (Crack 14) initiates from the edge of a coupon near an embedded sensor. The crack passed the sensor and stopped at about 1/3 of the whole coupon width. The load and strain signals of the crack are shown in Figure 6.11(a). The typical strain step-change and load signal fluctuations discussed in the previous sections are obtained. The graphs of strain and optical signals plotted against time (Figure 6.11(b)) shows that the optical step-change occurs exactly at the time when the strain step-change is induced. The video images of the time of crack development (Figure 6.11(c)) confirm that the change of strain signal and optical signal coincides with the crack development.

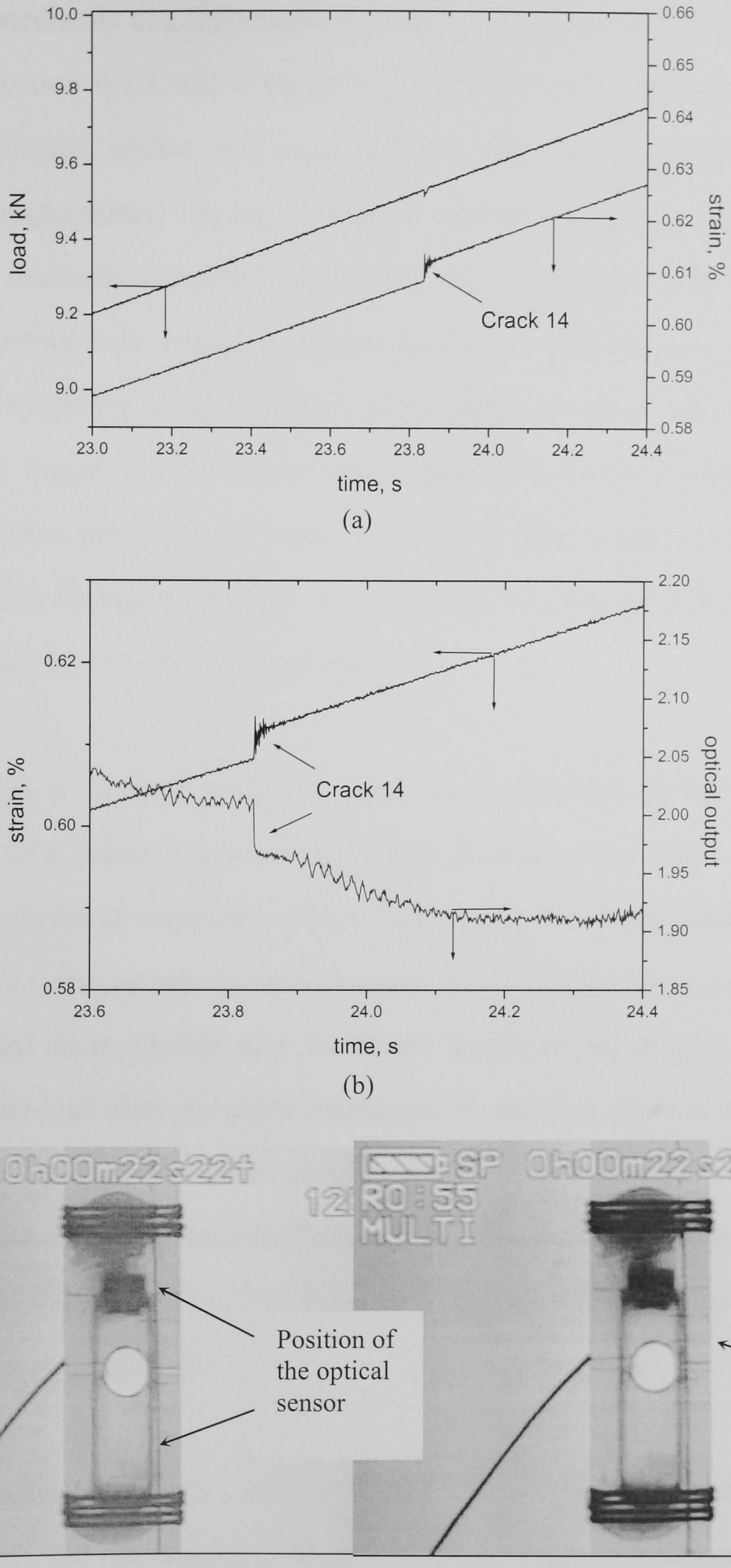

Figure 6.11 The detection of Crack 14.
(a) Load and strain response of the coupon to Crack 1.4
(b) Optical and strain responses to Crack 14.
(c) Video images showing development of Crack 14.

Figure 6.12 shows a transverse crack (Crack 15) that propagated across the width of the coupon immediately at a higher strain. In fact, this is exactly the same condition as described in Section 6.2.1, i.e. a transverse crack that propagates across the whole width of the coupon, within the gauge length of the sensor and within the gauge length of the extensometer. The step-change in strain signal induced by the crack, and the load signal fluctuation generated by the fast response ability of the servo-hydraulic fatigue test machine, are shown in Figure 6.12(a). A step-change in optical signal occurred simultaneously when the step strain change occurred and this is shown in Figure 6.12(b). Figure 6.12(c) shows that a transverse crack developed across the whole width of the coupon when these signals occur. These graphs show clearly that the optical signal change is induced by the crack, or, the transverse crack can be detected by checking the optical signal change.

If Figure 6.12(a) is checked carefully, there are fluctuations of the load and strain signals about 0.5 s before Crack 15 developed. However, the strain signal does not show a step increase as expected, which implies that the crack which gave rise to these signals occurred outside the extensometer gauge length. Hence, the strain signal shows the global strain change over the whole length of the coupon induced by the fluctuation of the load after the crack developed. In addition, there is no optical signal change corresponding to the strain change (Figure 6.12(b)). This indicates that the crack was outside the gauge length of the sensor. Unfortunately, there are no pictures showing the development of this crack because the video camera was focused within the extensometer gauge length.

Some cracks, which were induced at the other side of the coupon, distant from the embedded sensor, did not propagate across the whole width of the coupon and did not pass the sensor. Figure 6.13 shows the occurrence of a crack (Crack 16) of this type.

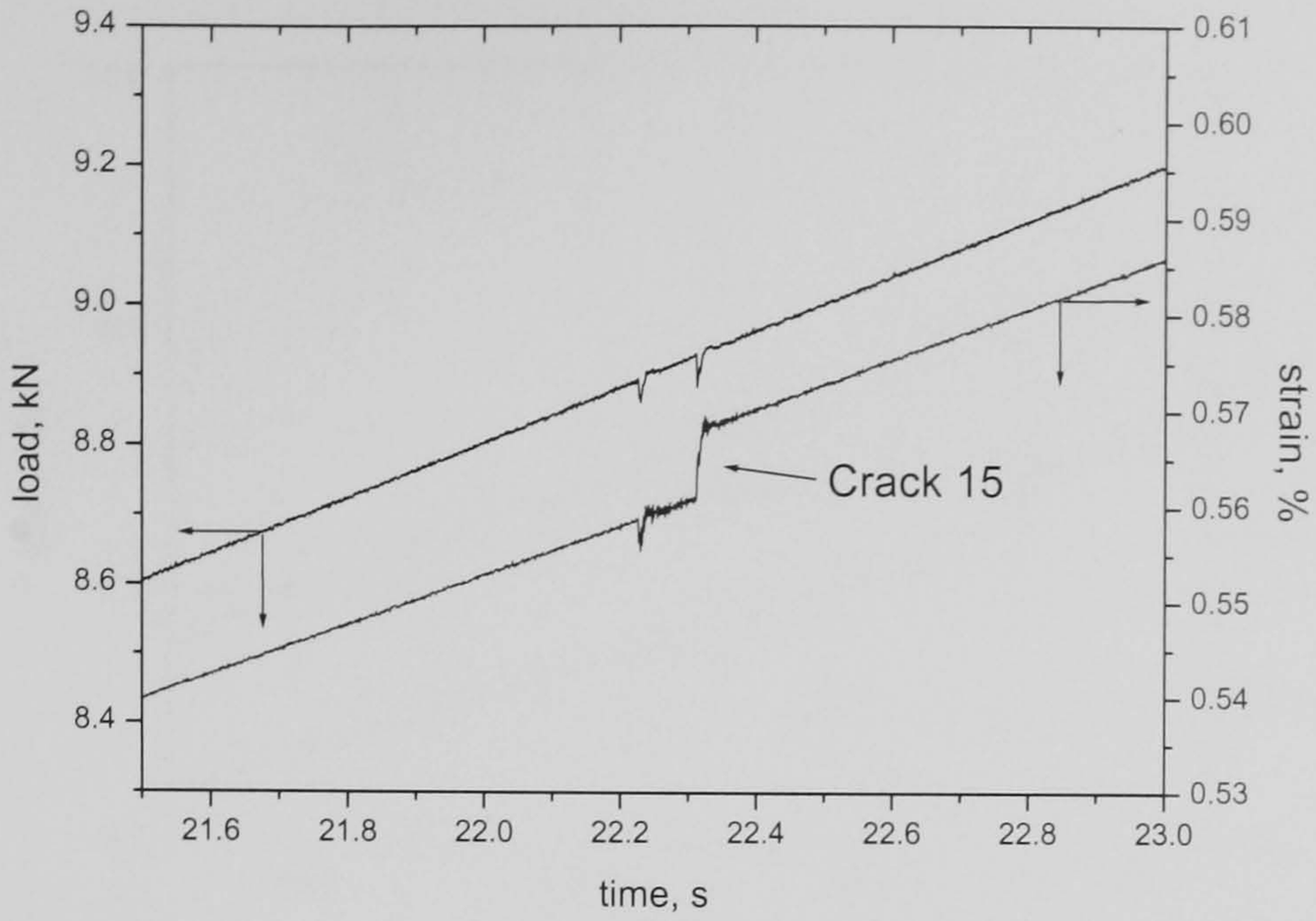

(a)

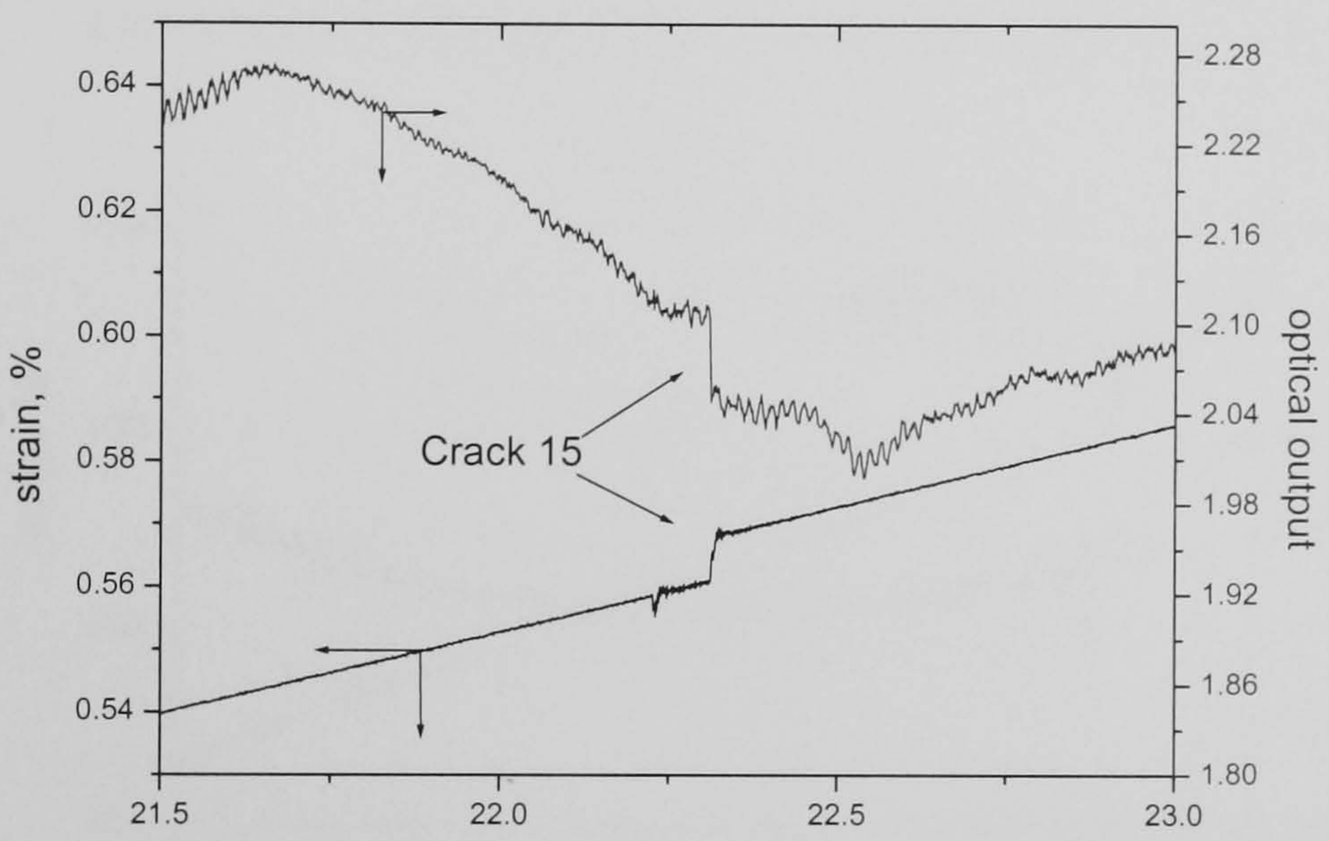

(b)

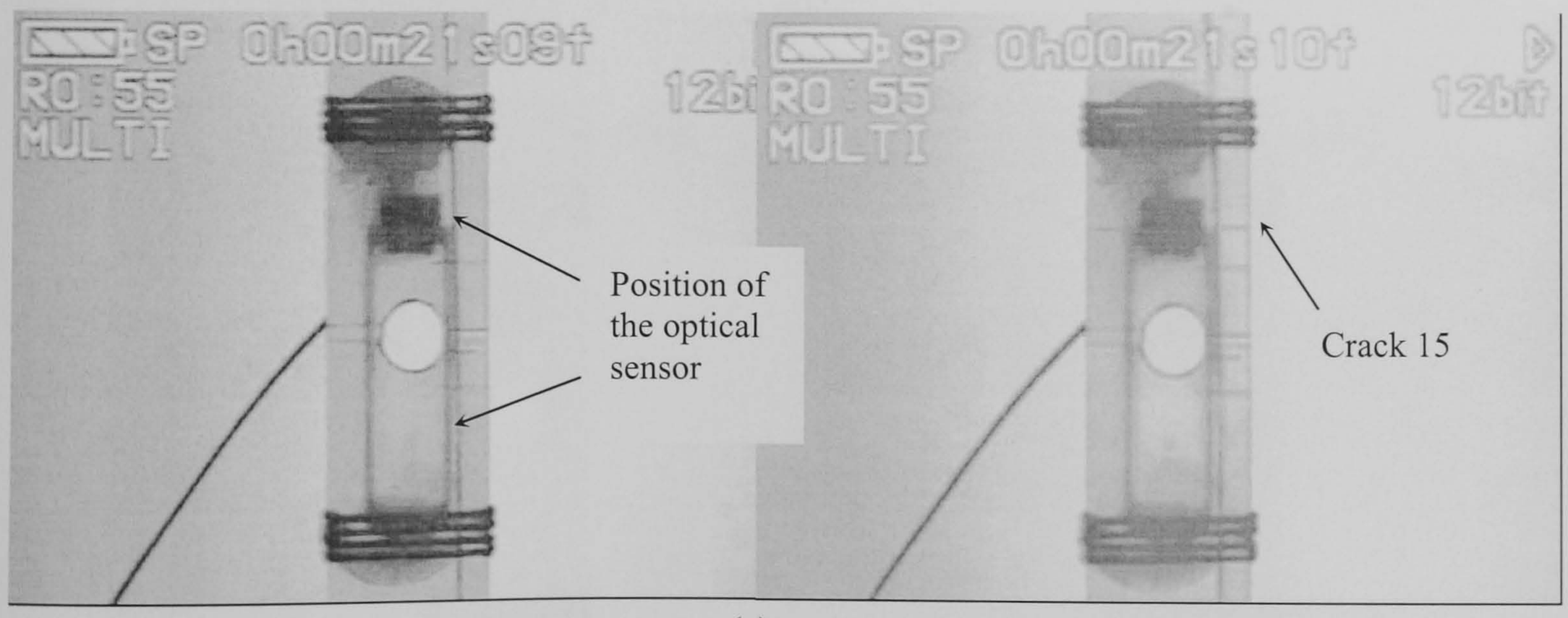

(c)

Figure 6.12 The detection of Crack 15.
(a) Load and strain response of the coupon to Crack 15.
(b) Optical and strain response to Crack 15.
(c) Video images showing development of Crack 15.

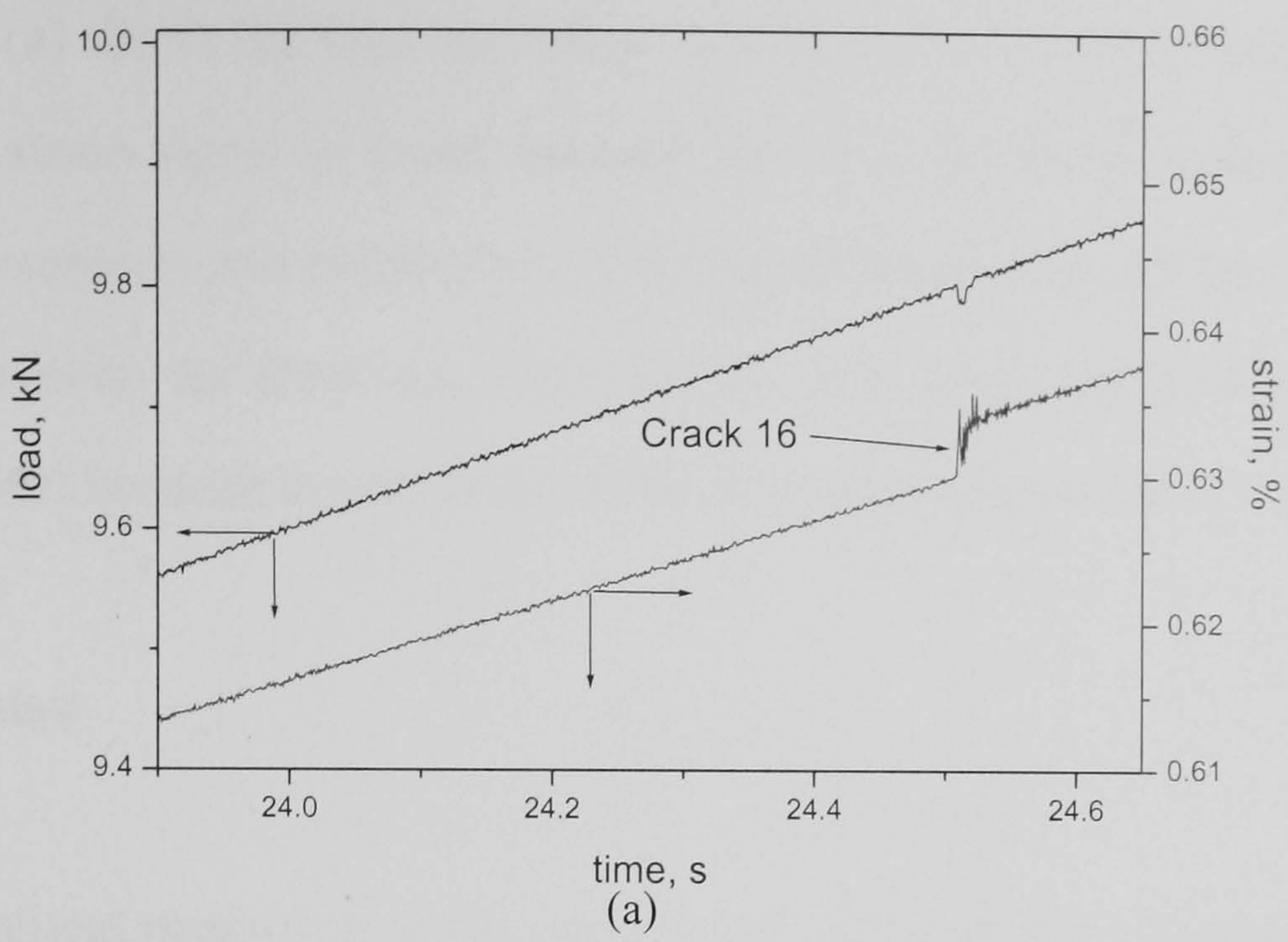

(a)

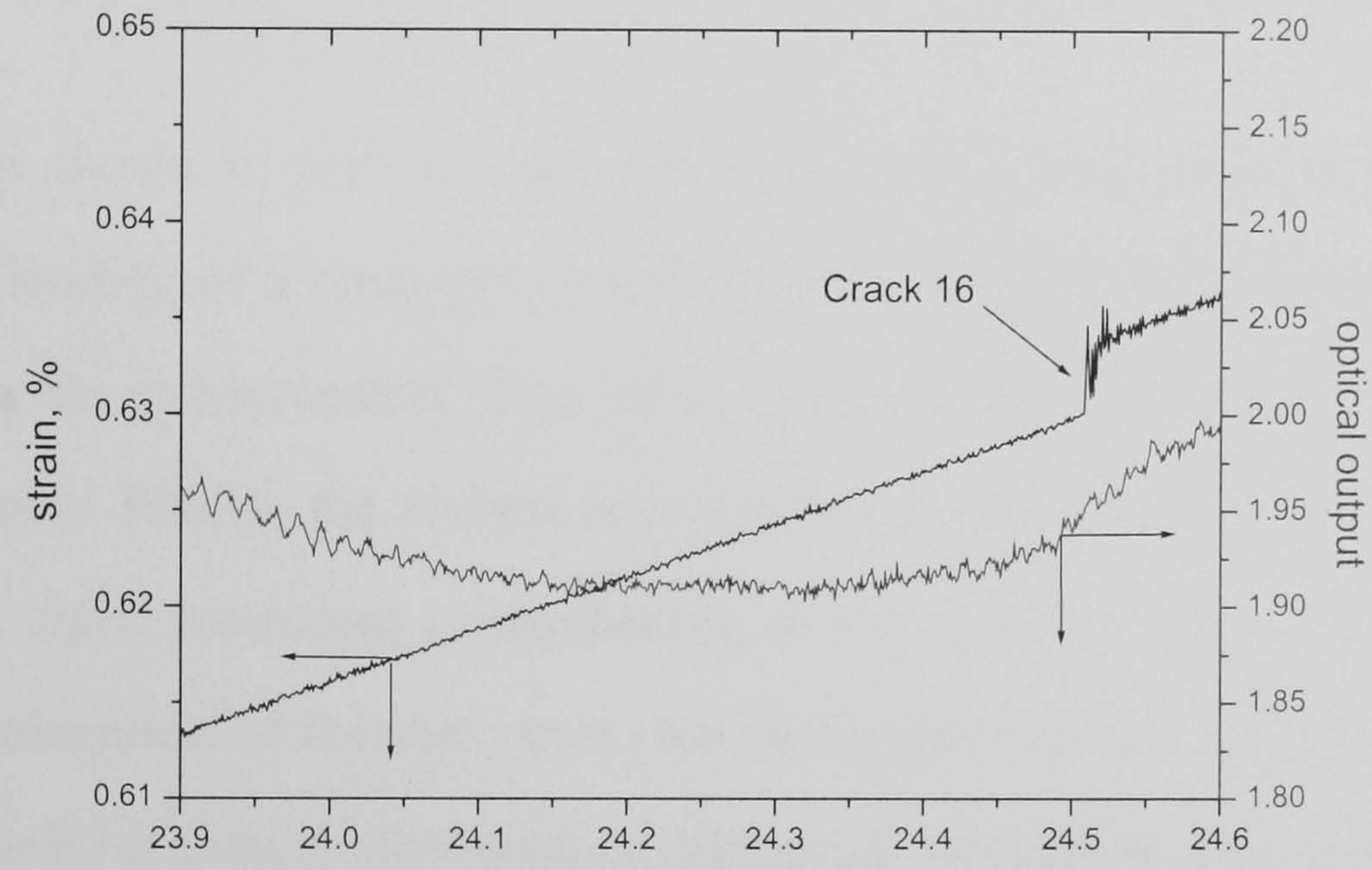

(b)

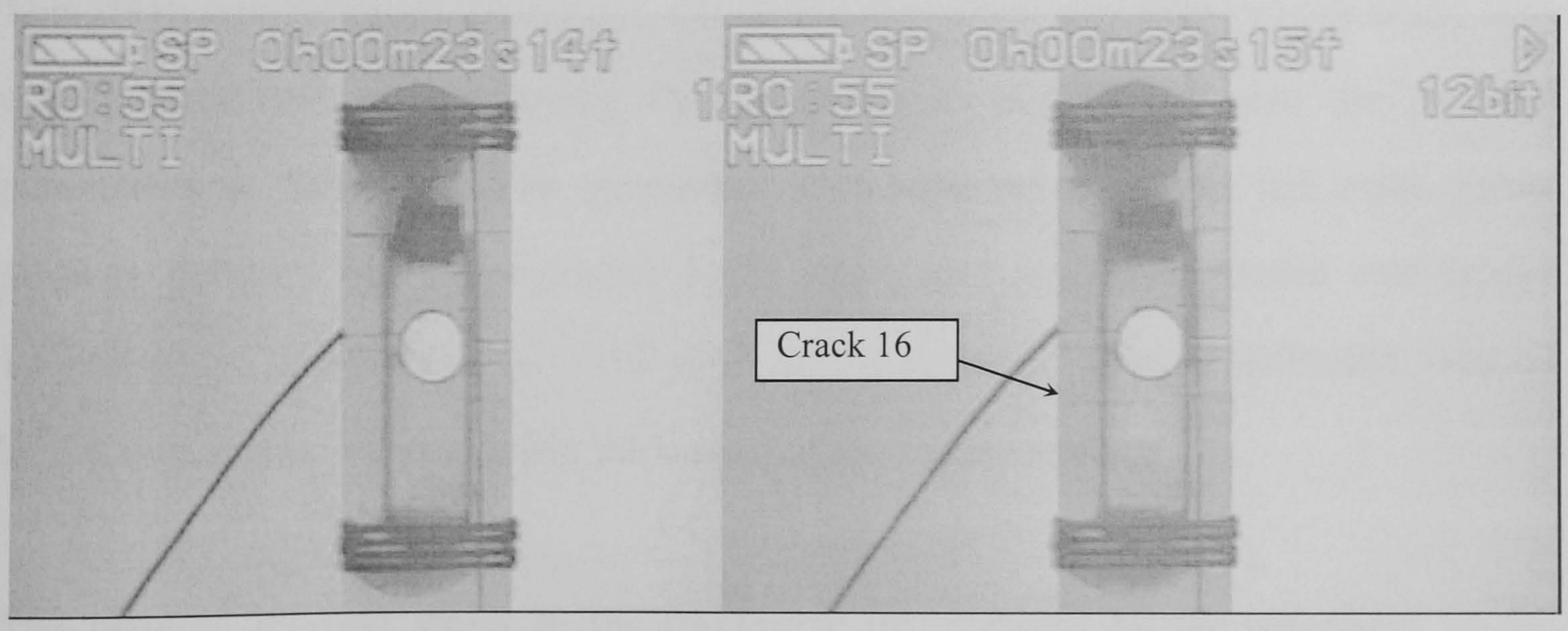

(c)

Figure 6.13 The detection of Crack 16.
(a) Load and strain response of the coupon to Crack 16.
(b) Optical and strain response to Crack 16.
(c) Video images showing development of Crack 16.

Figure 6.13(a) shows the load and strain signals when the crack occurs. There is a step increase in strain signal as usual, because the crack develops within the gauge length of the extensometer and consequent load signal fluctuations are the same as described earlier. However, as expected, there are no corresponding optical step-changes in Figure 6.13(b) because the crack does not propagate pass the sensor (Figure 6.13(c)).

6.6 Discussion

6.6.1 Theoretical prediction of the step-change in the of strain signals

It has been shown in previous sections that when a transverse ply crack develops during the loading of a cross-ply coupon, there is a step-change increase in the strain recorded by the extensometer. Two effects produce the immediate increase in length of the coupon. Firstly, the compressive thermal strain within the 0^0 plies is relaxed around the crack producing a lengthening of the specimen. Secondly, in addition to this local relaxation of thermal strain, the compliance of the specimen increases as a result of crack formation, producing an additional increase in specimen length.

This small elongation of the coupon due to the formation of a matrix crack under load can be predicted by employing the equations in Section 3.6 and the material parameters in Table 6.1. For simplicity, it is assumed here that the crack forms midway between the extensometer knife edges and midway between two cracks 100mm apart. In this case, 2s = 100 mm and the abnormal strain distribution induced by the two cracks will not affect the output of the extensometer.

The residual thermal stress in the transverse ply induced by the mismatch of the thermal expansion coefficients of the 0° and 90° plies is calculated as $\sigma^T = 27.8\ MPa$ by equation 3.31. The extra displacement as a result of the release of the residual thermal stress when a crack forms can be calculated by equation 3.41 and the result is:

Table 6.1 Material properties relevant to the unidirectional laminate (after Barton, 2000)

Property	Value
Longitudinal Young's modulus, E_1(GPa)	39
Transverse Young's modulus, E_2 (GPa)	11
Transverse Young's modulus, E_3 (GPa)	11
Shear modulus, G_{23} (GPa)	4.6
Shear modulus, G_{21} (GPa)	5
Shear modulus, G_{31} (GPa)	5
Poison's ratio, ν_{23}	0.303
Poison's ratio, $\nu_{12}=\nu_{13}=\nu_{21}\cdot E_1/E_2$	0.326
Poison's ratio, ν_{21}	0.092
Parameter, $\Delta\alpha\Delta T$	3.3×10^{-3} *
b, thickness of 0° ply, mm	1
d, half thickness of 90° ply, mm	0.5

*: data from Bassam et al, 1998.

$$\Delta^T = 0.281 \ (\mu m) \tag{6.1}$$

which is independent of the external load applied to the coupon. The extra displacement as a result of the increased compliance of the laminate after formation of a crack is given by equation (3.38). This displacement is a function of stress on the coupon. Inserting the values of the constants, the numerical result is:

$$\Delta^\sigma = 3.81\sigma \ (\mu m) \tag{6.2}$$

where σ is the applied stress (in *MPa*) on the coupon. So the total displacement on the coupon induced by the occurrence of a crack is:

$$\Delta = \Delta^\sigma + \Delta^t = 3.81\sigma + 0.281 \ (mm) \tag{6.3}$$

The displacement is plotted as a function of applied stress in Figure 6.14 together with the experimental results and predicted results for the cracks shown in Figure 6.1(a), Figure 6.4(a) and Figure 6.6(a). The difference between experiment and theory is less than 9%.

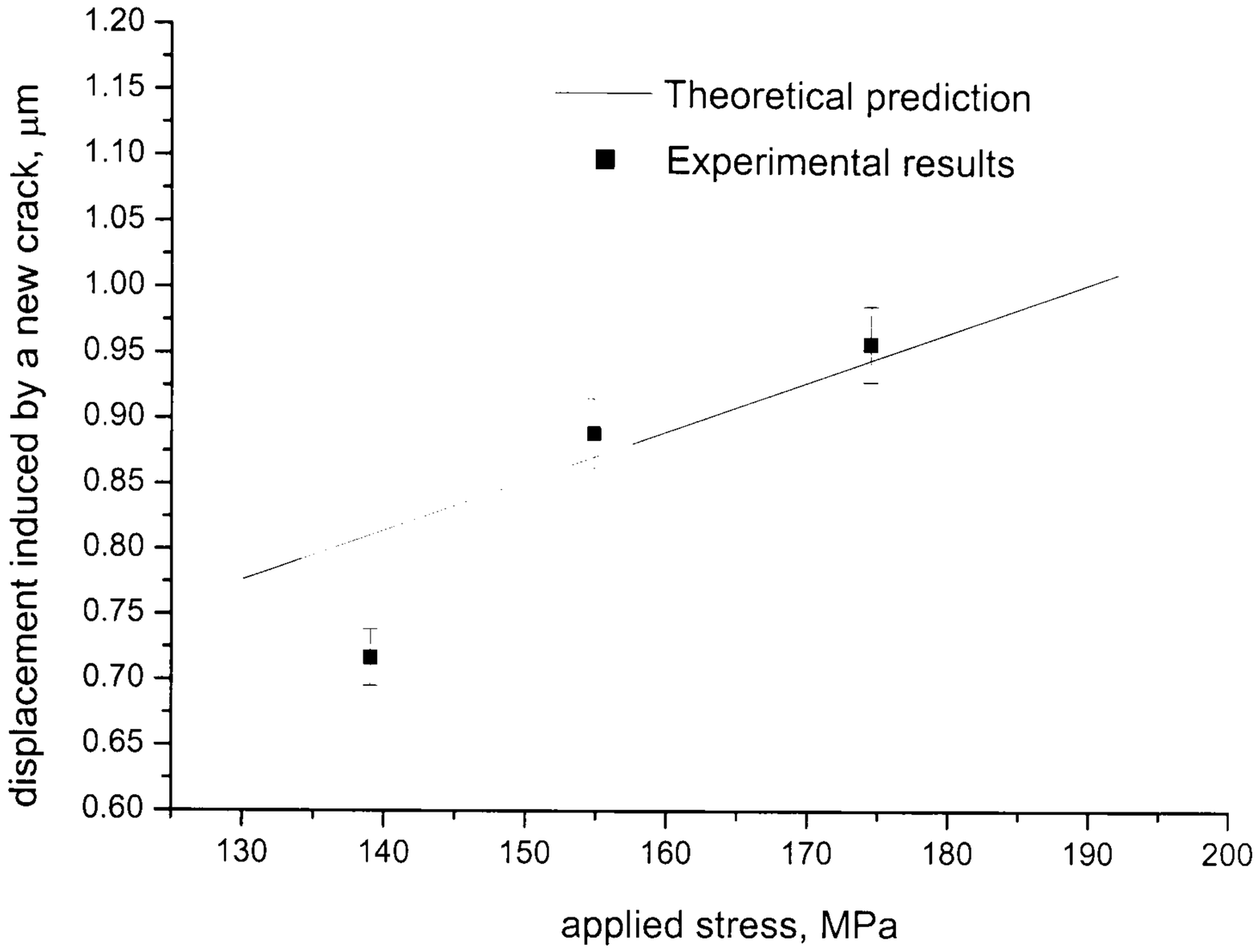

Figure 6.14 Displacement in a coupon induced by a transverse crack

It should be pointed out that although the additional displacements due to crack development can be detected by the extensometer, the resulting change in Young's modulus is too small to be detected. The change of Young's modulus after a crack has propagate across the whole width of a coupon can be predicted using equation (3.34). The predicted change of Young's modulus induced by a single crack is only 0.226% for the laminate with properties and dimensions described above.

6.6.2 The origin of the step- change in the optical signal when a crack passes a sensor

In the present work, it has been shown that the change in the optical signal corresponds to the time when cracks pass the sensor, and this has been confirmed by

the experiments on cracks developing from a hole. It is important to speculate about the origin of this change in the optical signal.

As discussed in the previous section, when a transverse ply crack grows across a laminate as a result of mechanical loading, there is a step-change increase in the strain recorded by the extensometer. If the cracks occur within the extensometer gauge length, these changes in length are recorded by the extensometer as a step-change in strain, as discussed in detail in Section 6.2.1. The servo-hydraulic testing machine was operating under load control, so that when the strain suddenly increased, leading to a drop in load, the servo-hydraulic machine corrected the load to the demand signal. This fluctuation of load on the coupon generates a global strain change on the coupon.

These strain changes have two effects on the sensor. First, when a crack develops, there is a strain magnification in the 0^0 ply, adjacent to the crack because the 90° ply can no longer carry the local load. In these experiments, the polarimetric sensor was positioned close to the 0/90 interface and hence would experience a sudden large local change in strain state as a result of the crack passing the sensor (Arjyal et al, 1998). Secondly, the global strain change in the coupon induced by the load fluctuation also produces a longitudinal strain change in the sensor. Any strain change will contribute to the phase change of the sensor's optical output. However, the experimental results show that only those cracks that pass the sensor will produce a change in the optical output. Cracks that do not pass the sensor or pass the sensor beyond the gauge length of the sensor do not produce a change in the optical output. This means that the step optical signal changes are induced by the complex interaction between the strain field around the matrix crack in the immediate vicinity of the crack tip and the embedded sensor.

The polarimetric sensor is an integrating sensor. This means that any local optical phase changes induced by a local strain change will be carried by the sensor to the output end. As a result, the magnitude of the change in the optical output as a

consequence of the growth of a matrix crack when it passes the sensor depends on the integrated effect of the local strain changes on the path difference between the "fast" and "slow" axes of the sensor. However, there is an added complication: the orientation of the "fast" and "slow" axes with respect to the axes of the composite changes when the sensor is embedded. The interaction between the crack and the sensor is thus a complicated problem. A theoretical prediction for the interaction between the sensor and a crack that passes the sensor is provided in detail in Chapter 10.

6.7 Conclusions

A low cost optical fibre system based on a polarimetric sensor has been used to detect matrix cracks which develop under quasi-static loading in a cross-ply GFRP composite. Unlike previous studies, the transparent nature of the coupons used here makes it possible to determine the moments when cracks pass the sensor. There is a clear one-to-one relationship between a step-change of optical output and the time when the cracks pass the sensor.

It has been shown that the polarimetric sensor can be made either to be sensitive to matrix cracking damage over a particular, short length of the composite or to be sensitive throughout the complete length of the composite. Such a sensor therefore has the potential for detecting damage in large composite structures since the sensor can be very long.

Detection of cracks around a circular hole in a coupon by polarimetric sensors has been carried out. These experiments make it possible to distinguish the effects of cracks that pass the sensor and those that do not pass the sensor on the optical output. The experimental results indicates that these optical signal changes are induced by the

complex interaction between the strain field around the matrix crack in the 90° ply and the sensor embedded in the 0° ply.

Finally, the changes of strain signal when a crack propagates across the whole width of a coupon under load have been predicted successfully using a shear lag model.

Chapter 7. Spectrum analysis of the optical output when cracks occur adjacent to an embedded sensor in cross-ply laminates

7.1 Introduction

It is usual, when discussing the response of an interferometric sensor in a material without damage, to assume that the phase change, and therefore the number of fringes, is linearly proportional to the applied strain. A constant strain rate manifests itself as a sinusoidal optical signal with constant frequency. In real time measurements, if the strain changes rapidly due to any type of damage, the number of fringes per second, or frequency of the sine modulation of the intensity of the optical output, will change discontinuously; this consequence of damage on the optical output of interferometric optical sensors has been noted previously (Kwon et al, 1997; Tsuda et al, 1999). In the present study, it is shown that a band pass FFT (Fast Fourier Transform) filter can be employed to enable crack development to be identified readily from the optical output.

7.2 FFT analysis of the optical output

Fourier's theorem states that a function $f(x)$, of spatial period, λ, can be synthesized as a sum of harmonic functions whose wavelengths are integral submultiples of λ (e.g. λ, $\lambda/2$, $\lambda/3$, etc.) (Hecht, 1970). The Fourier transform is a generalization of the Fourier series. In a strict sense it applies to the class of continuous and aperiodic functions,

but the use of impulse functions permits extending it to discrete signal forms. This makes it possible to perform Fourier transforms on discrete experimental data.

The Fourier transform of a signum function defined as:

$$F(t) = sgn(t) = \begin{cases} -1 & t < 0 \\ +1 & t > 0 \end{cases} \qquad 7.1$$

is (Kraniauskas, 1991)

$$F(j\omega) = -j\frac{2}{\omega} \qquad 7.2$$

The function, and the frequency spectrum of the function after Fourier transform, are shown in Figure 7.1. The figure indicates that the Fourier transform spectrum of the function is composed of a series of frequencies extending from almost zero to infinity with decreasing amplitude.

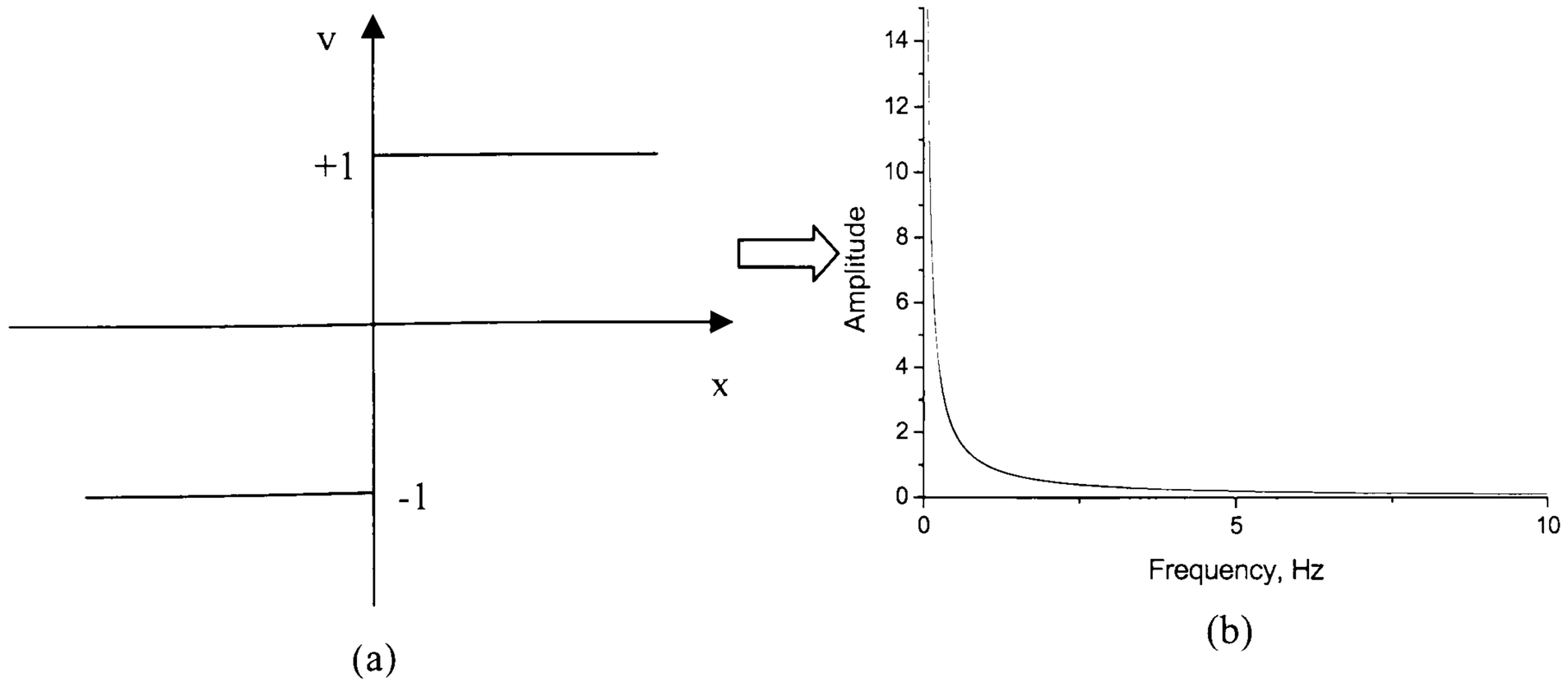

(a) (b)

Figure 7.1 Fourier transform of a signum function.

(a). A signum function;

(b). Frequency spectrum of the signum function after Fourier transform.

As discussed in Chapter 6, the optical response of the polarimetric sensor to a crack that passes the sensor is a step-change in the optical output, e.g. the step-changes in optical signal in Figure 6.1(b), Figure 6.2(b), etc. The Fourier component induced by the step-changes can be explained in the following simplified model. The step-changes in the optical signal when cracks passes the sensor can be taken as the superposition of two functions: a step-change in the optical signal, as shown in Figure 7.2(a) and, a set of regular sine wave optical fringes as shown in Figure 7.2(b). The superposed signal is displayed in Figure 7.2(c) with the inset showing the local magnification of the step change.

The Fourier transform of these functions showing in Figure 7.2 are carried out by the FFT (Fast Fourier Transform) command in Origin® software. The frequency spectrum of the function shown in Figure 7.2(a) after the Fourier transform is shown in Figure 7.3(a). Unsurprisingly, the spectrum is composed of a series of frequencies extending from very low frequencies to infinity, with decreasing amplitude, as predicted in Figure 7.1(b). Theoretically, the frequency spectrum of the sine wave shown in Figure 7.2(b) should be a single spike at the frequency of $1/2\pi$. However, due to the discrete data set used by the software to plot the function, the spectrum is a broadened peak instead of a single spike. As expected from the characteristic linearity of the Fourier transform, the frequency spectrum of the function shown in Figure 7.2(c) is the superposition of frequency spectrums shown in Figure 7.3(a) and 7.3(b), as displayed in Figure 7.3(c).

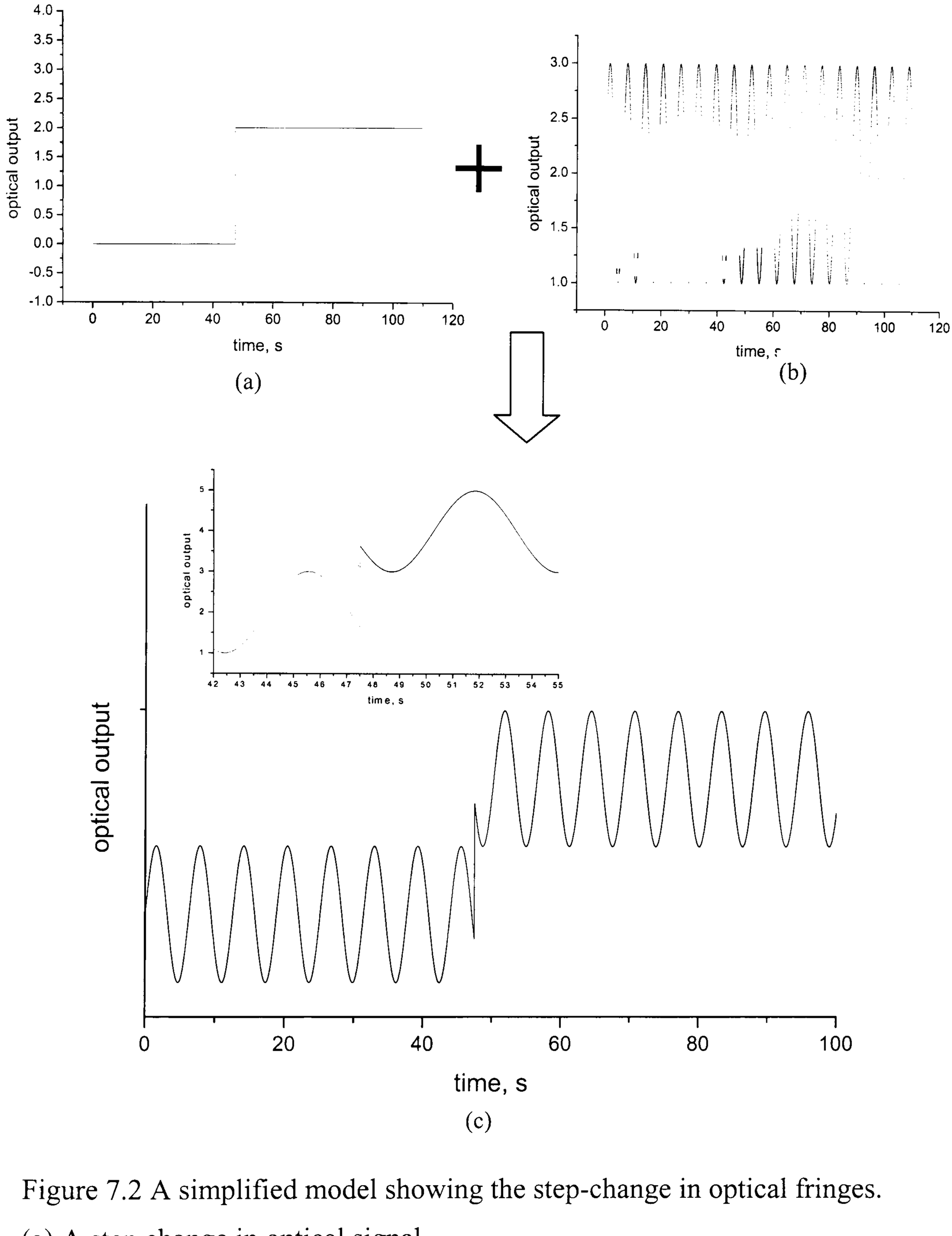

Figure 7.2 A simplified model showing the step-change in optical fringes.

(a) A step change in optical signal.

(b) A set of sine wave optical fringes.

(c) Superposition of (a) and (b), showing a step change in optical fringes.

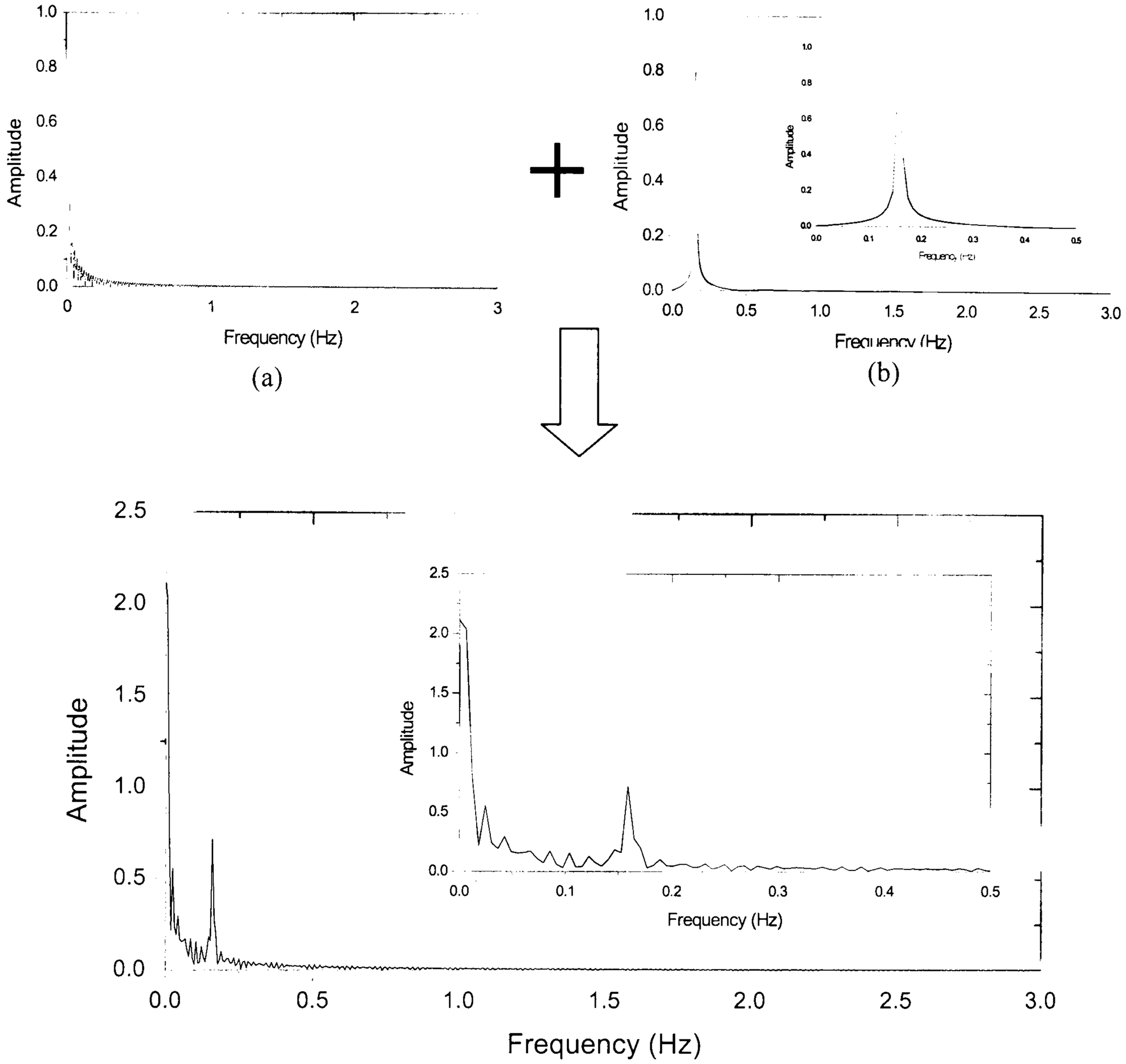

Figure 7.3 FFT analysis of the three functions shown in Figure 7.2.

(a) FFT analysis of the step-change in optical signal shown in Figure 7.2(a).

(b) FFT analysis of the sine wave optical fringes shown in Figure 7.2(b).

(c) FFT analysis of the step-change in optical fringes shown in Figure 7.2(c).

Turning now to the experimental data, in order to identify the optical signature of a transverse crack that passes the sensor, the Fourier transform is carried out on a set of experimental data using the FFT command of the ORIGIN® program. In the first 50 seconds of the under consideration test, no cracks developed. During the time between

140 seconds to 180 seconds of the test, five cracks developed within the sensor gauge length, which were counted by visual observation.

Figure 7.4(a) shows the strain signal and optical signal plotted against time during the first 50 seconds of this experiment. The rate of increasing strain was reduced with

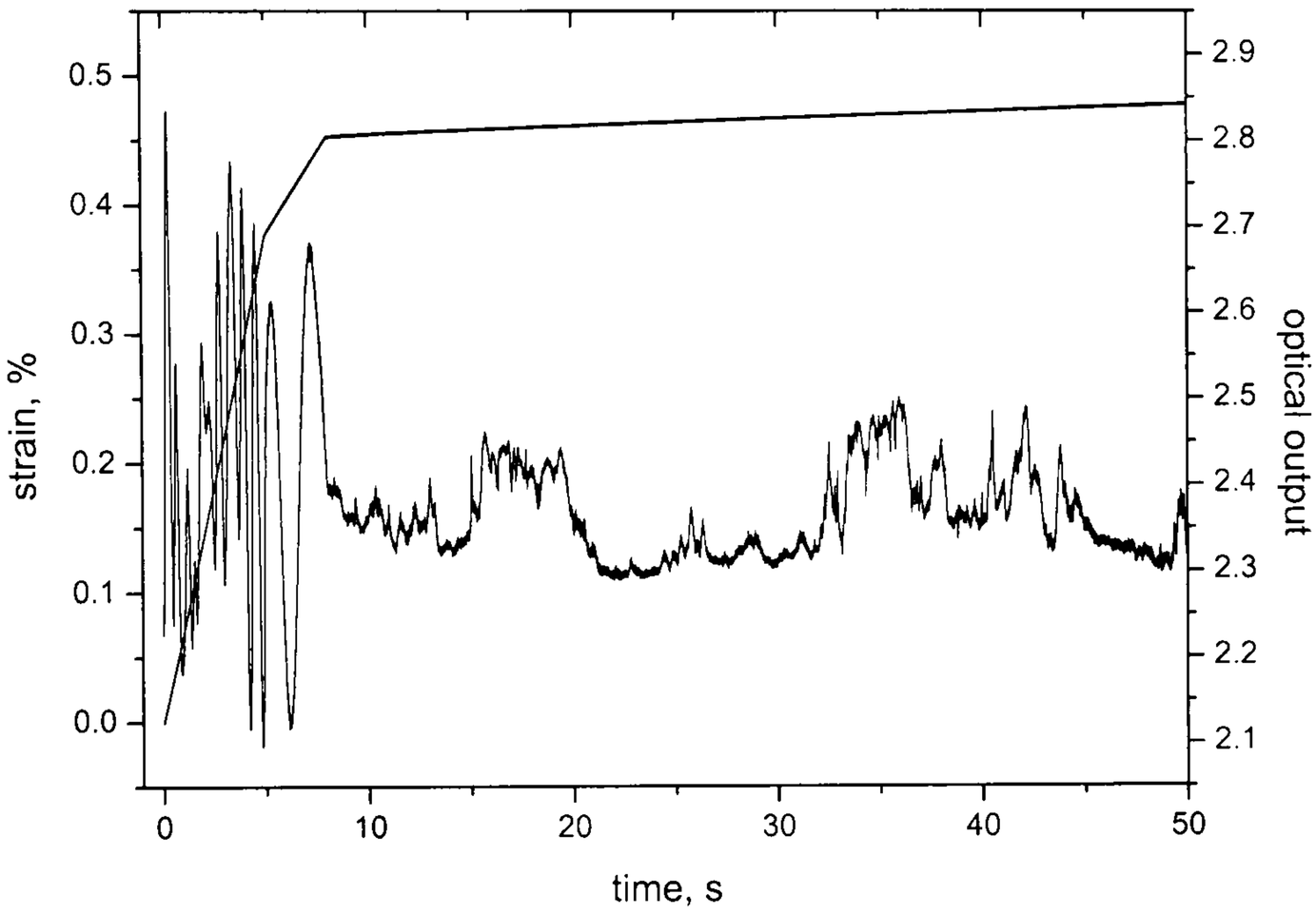

(a)

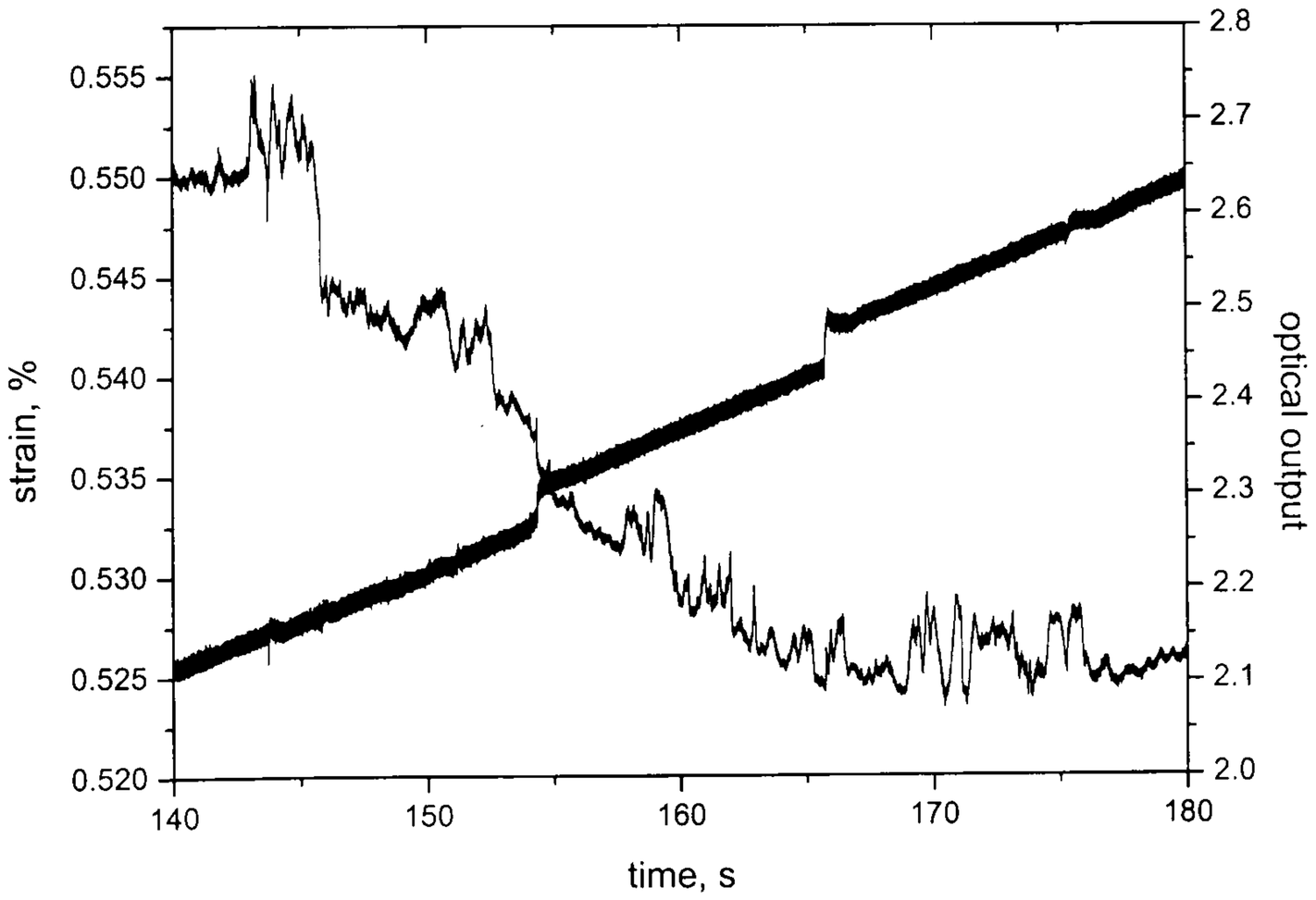

(b)

Figure 7.4 Experimental results from a cross-ply coupon.

(a). Strain and optical signal in the time range of 0 seconds to 50 second when no cracks occurred.

(b). Strain and optical signal in the time range of 140 seconds to 180 second when 5 cracks developed.

time during the test, firstly after 5 seconds and then after 8 seconds, to obtain long time intervals between the development of the transverse cracks. Not surprisingly, the frequency of the optical output reduces at the lower strain rate. Figure 7.4(b) shows the optical and strain responses of the sensor during the time range from 140 seconds to 180 seconds in the same experiment when 5 cracks developed. Due to the small change of the strain signal (about 0.025%) during this period, the phase change of the optical signal is only about π. However, there are some large fluctuations in the strain signal, e.g. at time of 154.3 seconds, 165.7 seconds and 175.3 seconds. These fluctuations suggest that transverse cracks had developed during these 40 seconds, especially the two step-changes at 154.3 seconds and 165.7 seconds which suggest, following Section 6.2, that there were two transverse cracks developed within the extensometer gauge length. The expected corresponding changes in the optical signal are not very clear due to the noisy environment, but as described below, use of the FFT method enables the time when each crack occurred to be determined.

FFT analysis of the optical and strain signals shown in Figure 7.4(a), i.e. when no crack occurred, are presented in Figure 7.5(a) and Figure 7.5(b) respectively. The FFT analysis of optical signal shows peaks at about 20 Hz, 50 Hz, 75 Hz, 100 Hz, 150 Hz, 200 Hz, 320 Hz and a collection of peaks at about 65 Hz. The spectrum also contains strong contributions from low frequencies (< 5 Hz) due to the irregularity of the experimental optical fringes. Compared with the optical spectrum, the FFT analysis of strain spectrum is much cleaner. In Figure 7.5(b), there is only one peak at about 320 Hz despite the contributions of low frequencies. Since the strain signal was recorded by the extensometer and was controlled by the load signal, the peak at 320 Hz may be induced by the testing machine, for example, the vibration of valves that control the hydraulic system. The same peak at 320 Hz is found in the optical spectrum,

indicating that the vibration of the strain signal generates a corresponding vibration with the same frequency in the optical output. The other peaks in the optical spectrum might be induced by the optical system, for example, the laser source, the optical detector, etc.

The results of FFT analysis of the optical and strain signals shown in Figure 7.4(b), i.e. five crack occurred, are displayed in Figure 7.6(a) and Figure 7.6(b) respectively. The optical spectrum and the strain spectrum are almost identical to those shown in Figure

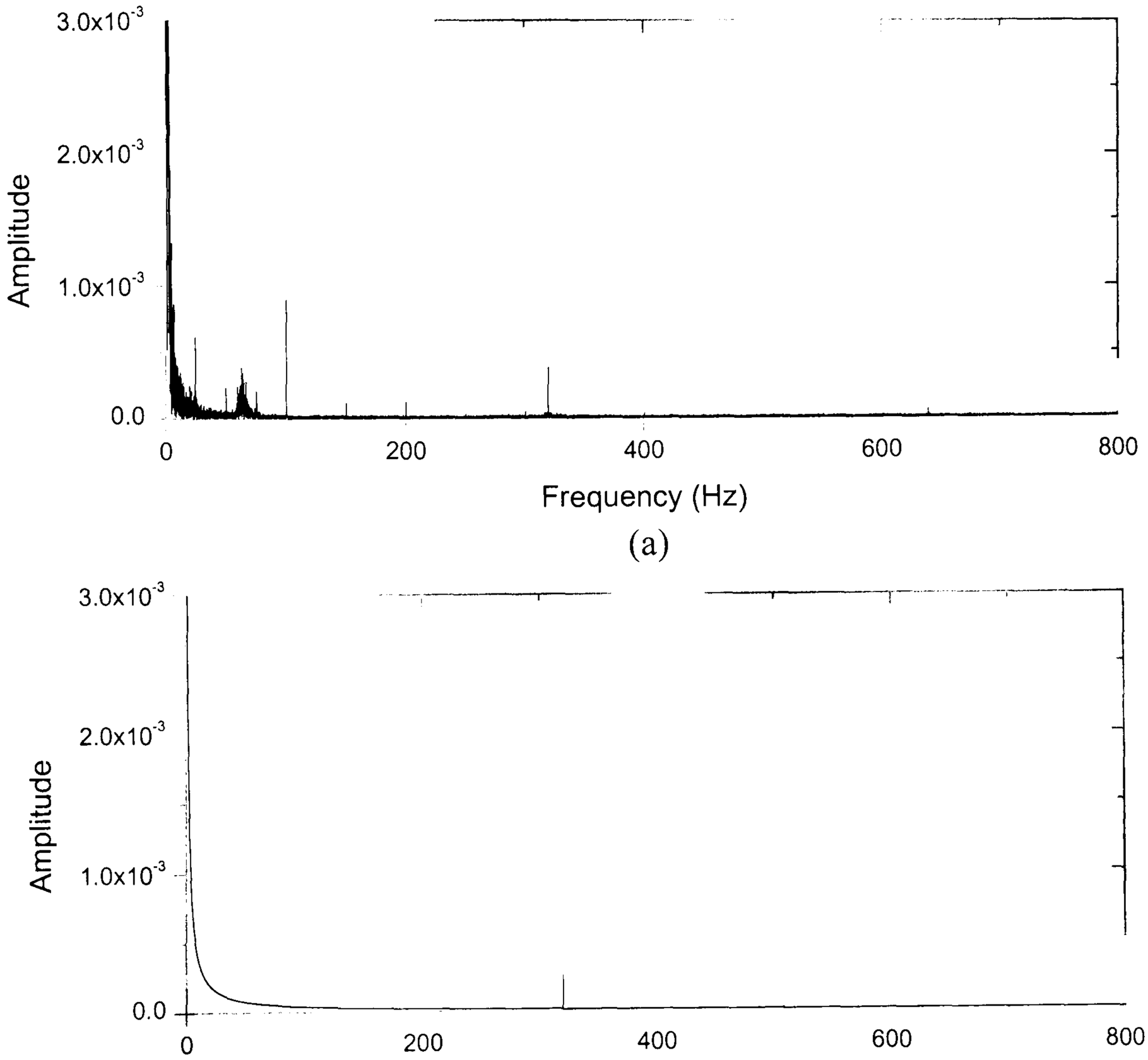

Figure 7.5 FFT analysis of the optical and strain signals shown in Figure 7.4(a).
(a) FFT analysis of the optical signal.
(b) FFT analysis of the strain signal.

7.5, although there are some small changes in the amplitudes of the peaks. This suggests that the step-changes in the optical and strain signals will not generate additional peaks, even at high frequencies. However, as discussed earlier, the Fourier series of step-changes has contributions throughout whole frequency range, including at higher frequencies. The reason why those frequencies cannot be obtained from Figure 7.6 is because the figure provides information about the contributions of different frequencies to the spectrum of the whole time range. The contributions of the step-changes will merge with the original information and cannot be picked out, e.g. the signal to noise ratio is small.

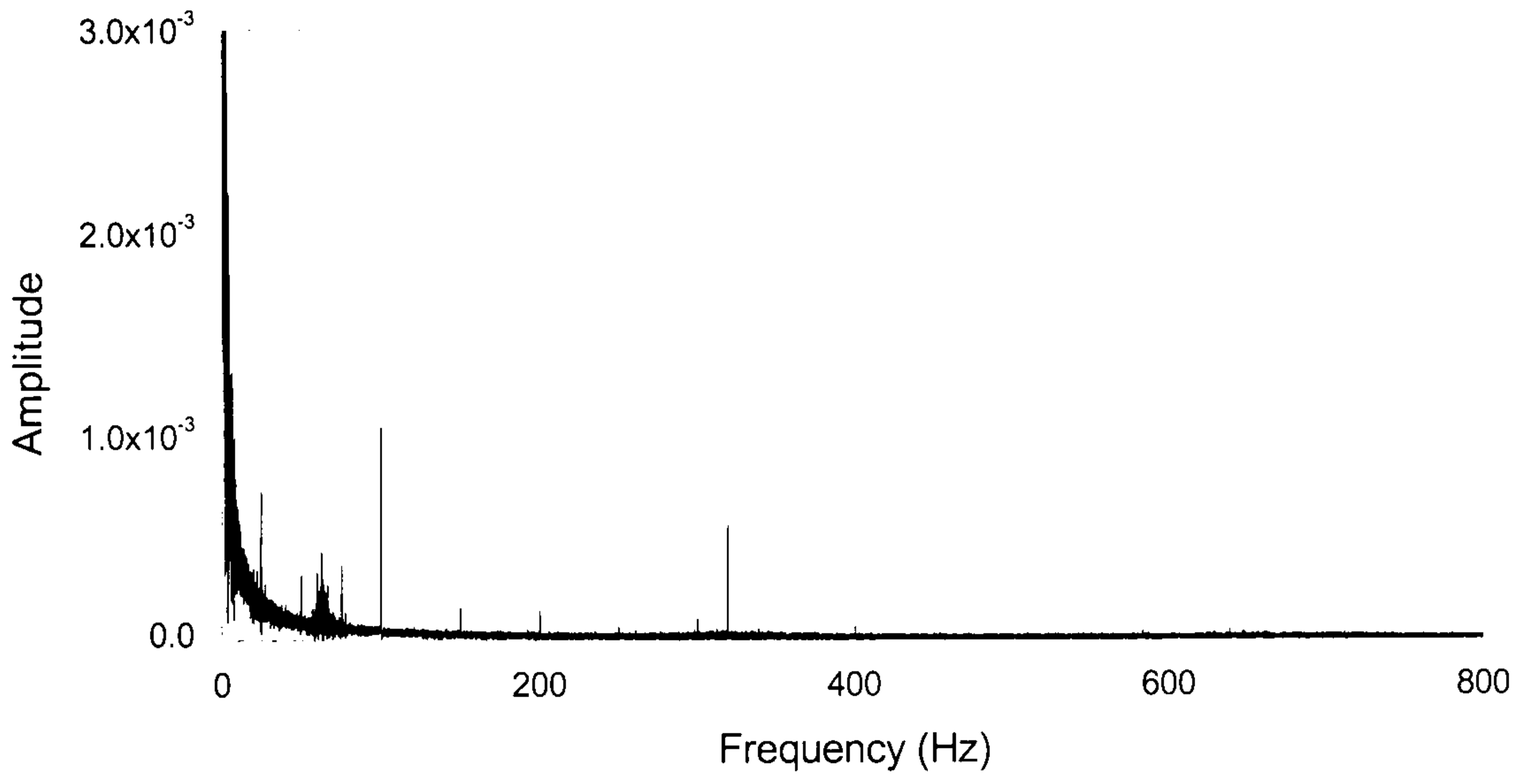

(a)

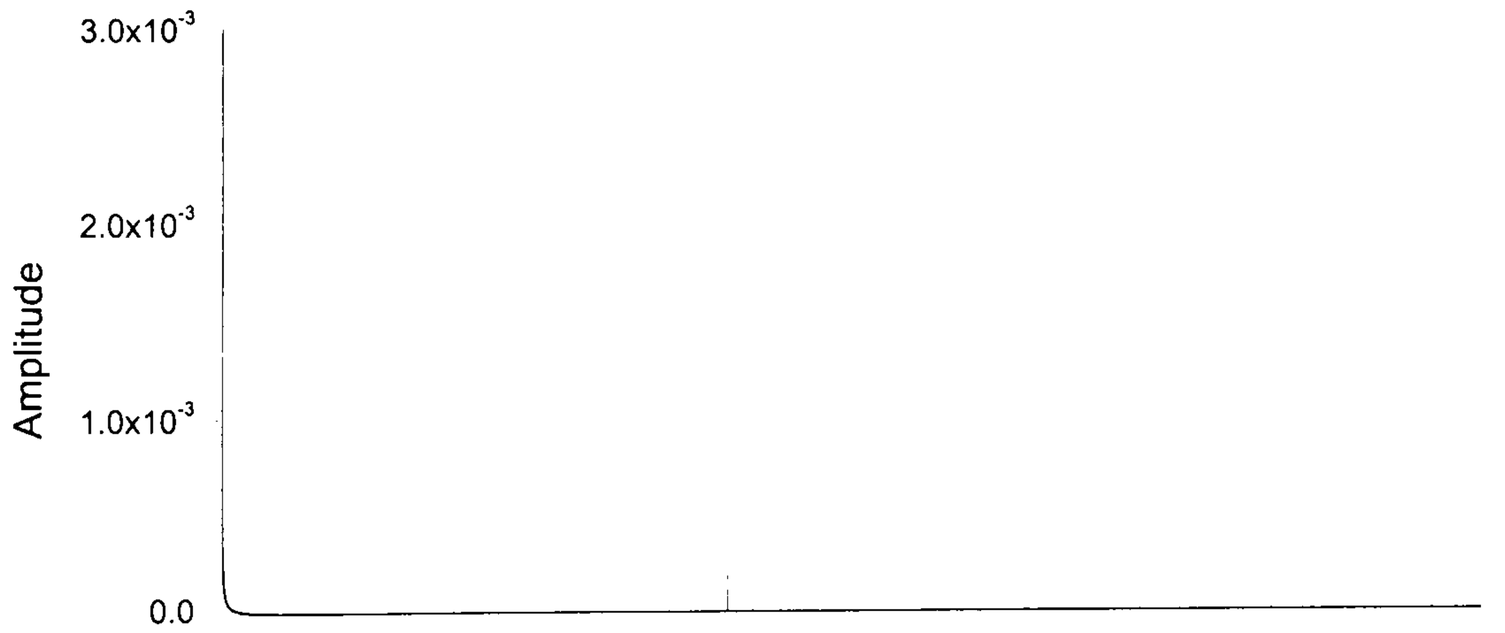

(b)

Figure 7.6 FFT analysis of the optical and strain signals shown in Figure 7.4(b).

(a) FFT analysis of the optical signal.

(b) FFT analysis of the strain signal.

PAGE

MISSING

IN

ORIGINAL

pass FFT filter has been applied to the set of optical data shown in Figure 7.4(b) during the period when 5 cracks passed the sensor and the results are shown in Figure 7.7. It is clear that five peaks emerge: at 143.7 seconds, 145.8 seconds, 154.3 seconds, 165.7 seconds and 175.3 seconds. Careful inspection of the optical signals, which will be shown later, together with fluctuations of the load and strain signals, shows that step-changes can be found at these times, suggesting that the cracks had propagated past the sensor at these particular times. The Fourier filtering process has enabled the contributions of the step-changes to the frequency spectrum to be distinguished from the original information.

The amplitudes shown in Figure 7.7 are the contributions of all the frequencies higher than 50 Hz to the amplitudes of the five peaks. To distinguish the contributions of different frequency components to the spectrum, different band-pass FFT filters have been applied to the set of optical data shown in Figure 7.4(b) and the results are shown in Figure 7.8. The contribution of lower frequencies to the five peaks, for example, frequencies lower than 100 Hz, is relative high. This is shown in Figure 7.8(a) which employ a band pass filter in the range 5 to 50 Hz and Figure 7.8(b) which employ a band pass filter of 50 to 100 Hz. However, due to the existence of other noise frequencies lower than 100 Hz, i.e. the frequencies seen in spectrum of Figure 7.6(a) at 25 Hz, 50 Hz and the band of frequencies around 65 Hz, the five peaks corresponding to the formation of the five cracks are not easily identified. When the band pass filter moves to higher frequencies (100 – 150 Hz, 150 – 200 Hz, 200 – 250 Hz, 250 – 300 Hz), the five peaks are easier to recognise, especially in Figure 7.8(c) and Figure 7.8(d), for which the band pass filter is between 100 Hz and 200 Hz. When the frequencies of the band pass filter are higher than 250 Hz. the

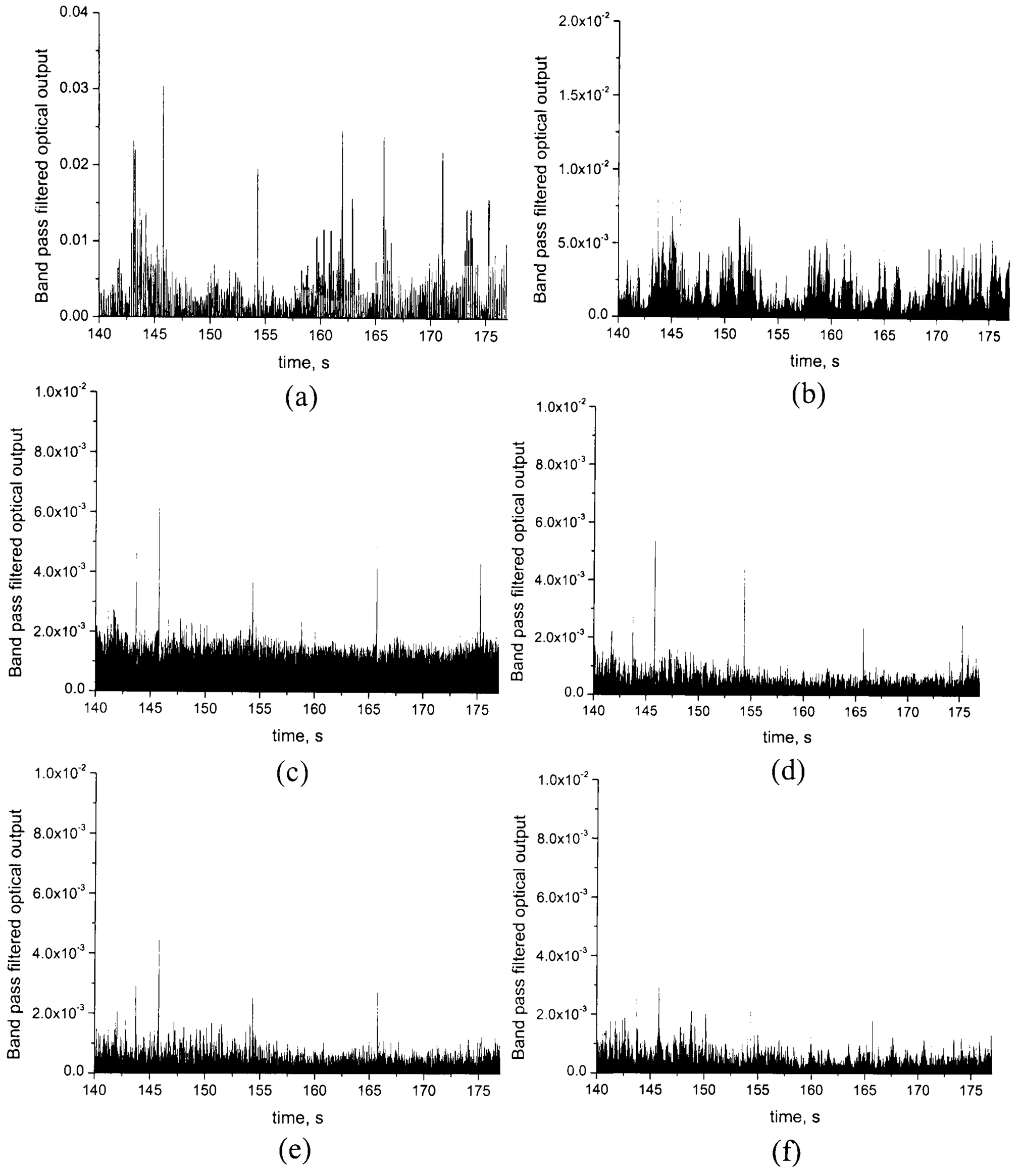

Figure 7.8 Band pass FFT filtered optical signal shown in Figure 7.4(b).

(a). 5 – 50 Hz; (b). 50 – 100 Hz; (c). 100 – 150 Hz;

(d). 150 – 200 Hz; (e). 200 – 250 Hz; (f). 250 – 300 Hz;

amplitudes of the five peaks are reduced to the level of noise and can hardly be picked out, as shown in Figure 7.8(f).

Contributions of different bands of frequencies to the amplitudes of the five peaks shown in Figure 7.8 are plotted in Figure 7.9. In this figure, the amplitude of each of

the five peaks for the different frequency ranges is plotted against the mean value of the frequency range. The figure shows that Fourier transform spectrum of the step-changes in the optical signal is composed of a series of frequencies. The contributions of different frequencies decrease when the band of frequencies analysed is moved to higher values, as predicted in Figure 7.1(b). Note that in Figure 7.9, each data point presents the contribution to the amplitude of the peak by a band of frequencies of 50 Hz wide (45 Hz for the first column of the data).

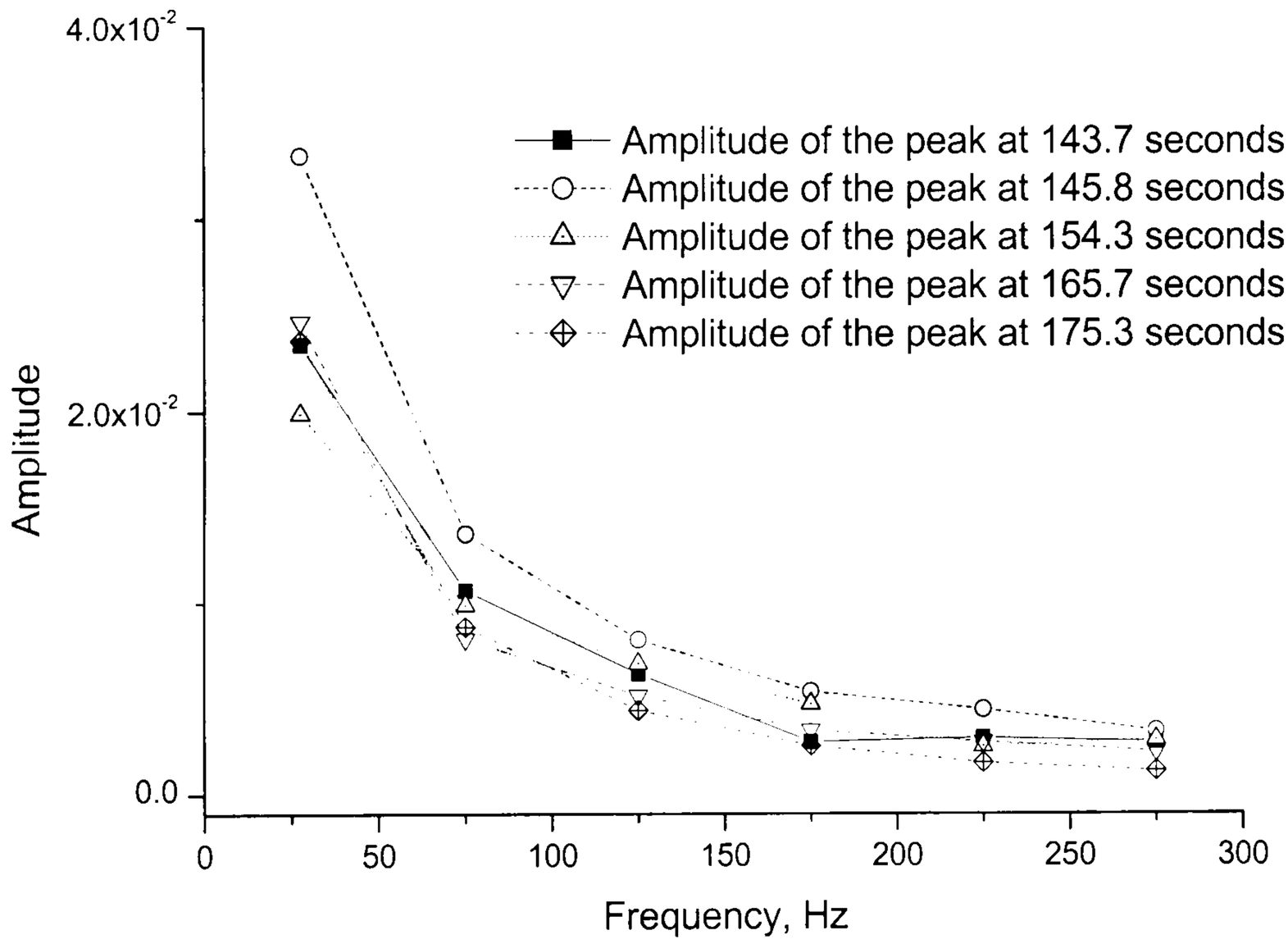

Figure 7.9 Contributions of different frequencies to the five peaks shown in Figure 7.7.

The complete FFT band pass filtered results for the optical output signal shown in Figure 7.4(b) (when 5 cracks have passed the sensor) are shown in Figure 7.10(a). The lower frequency of the band pass filter was chosen to be 100 Hz to block out irrelevant frequencies, and the higher frequency was chosen to be 300 Hz to obtain good signal/noise ratio. The load and strain signals for the cracks, together with the optical output for each crack (labelled A to E) are shown in Figure 7.10 (b) to 7.10(j).

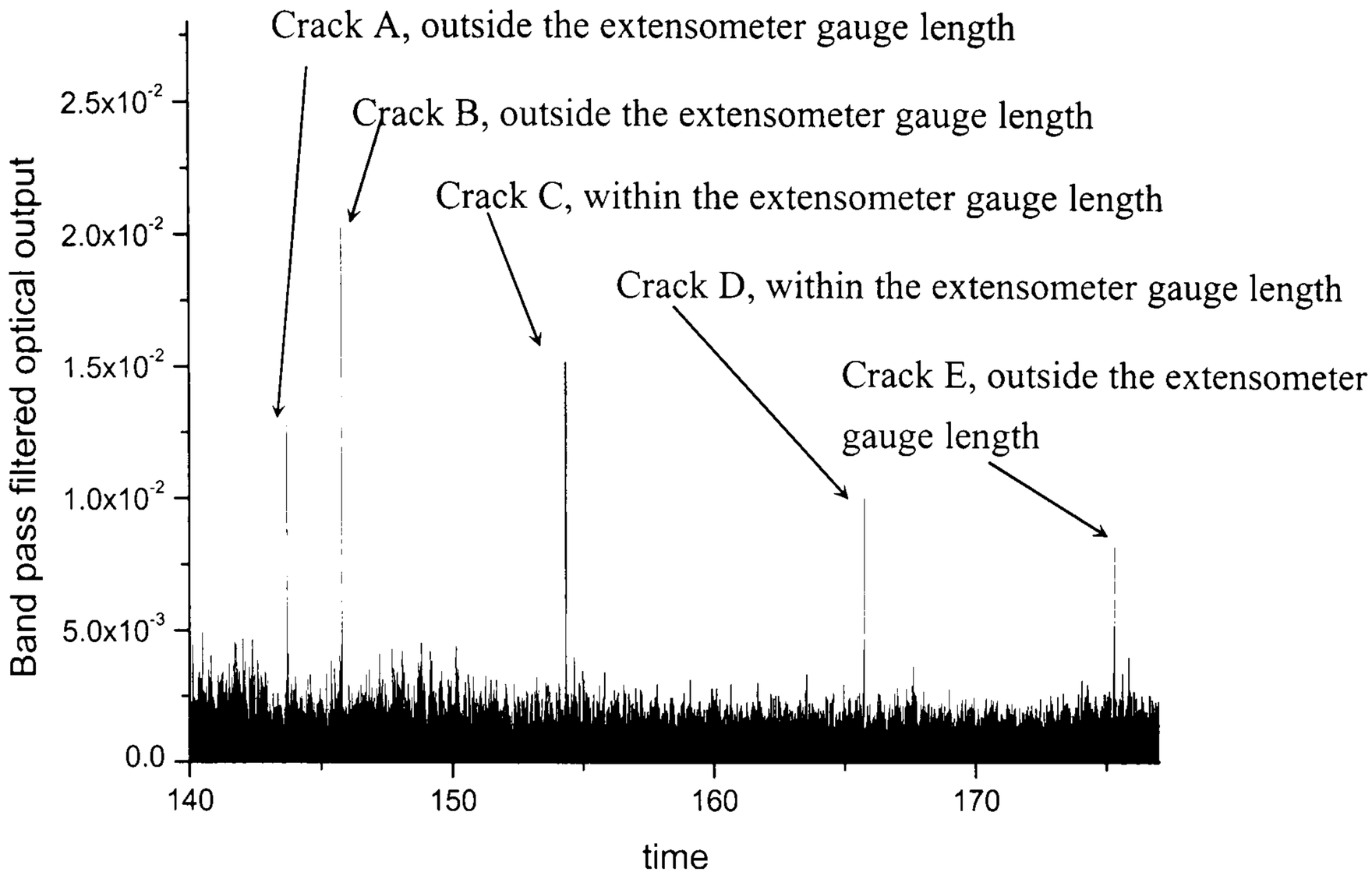

(a)

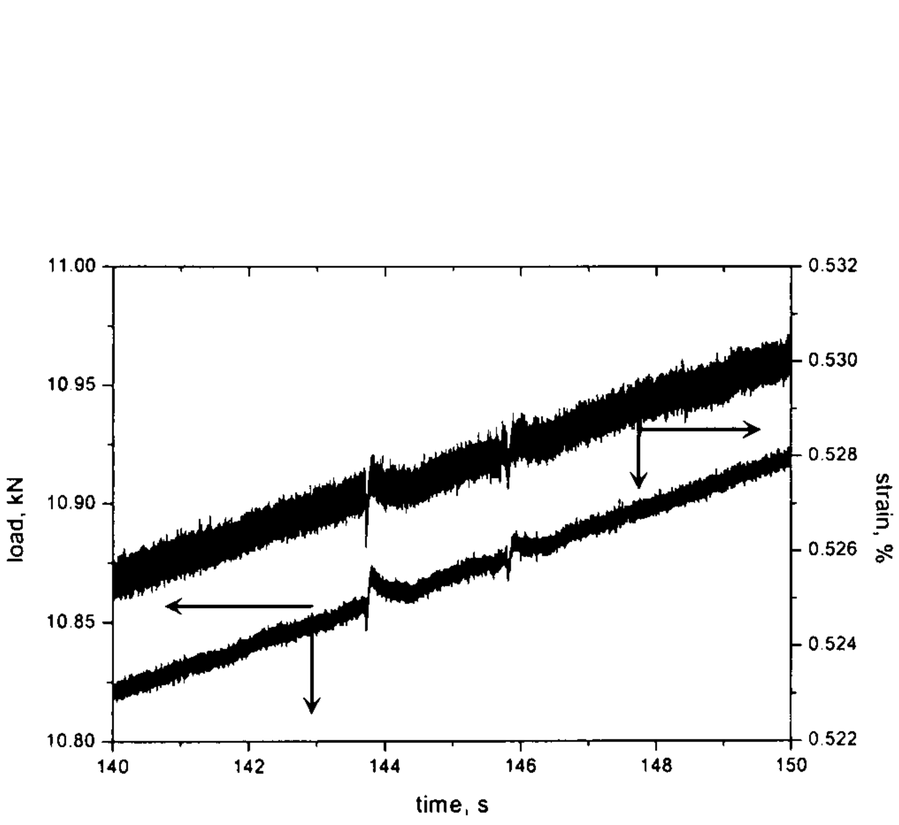

(b)

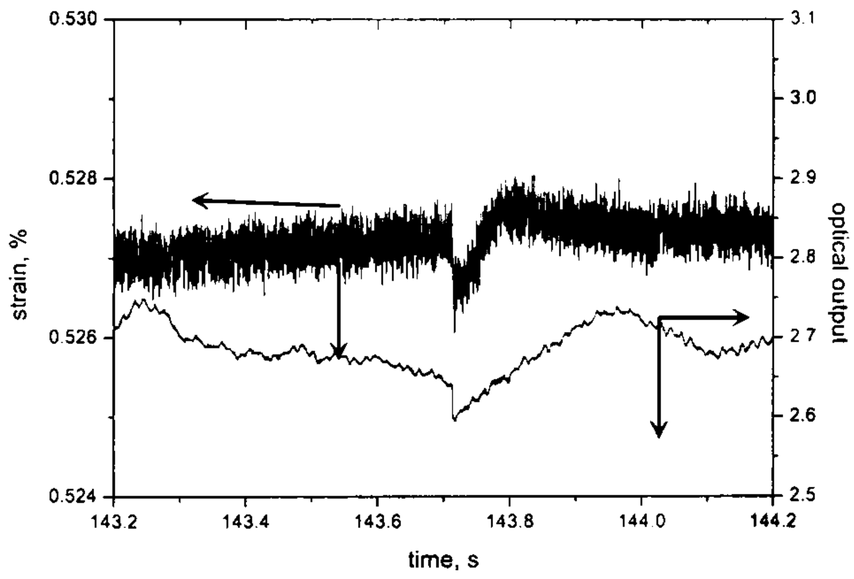

(c)

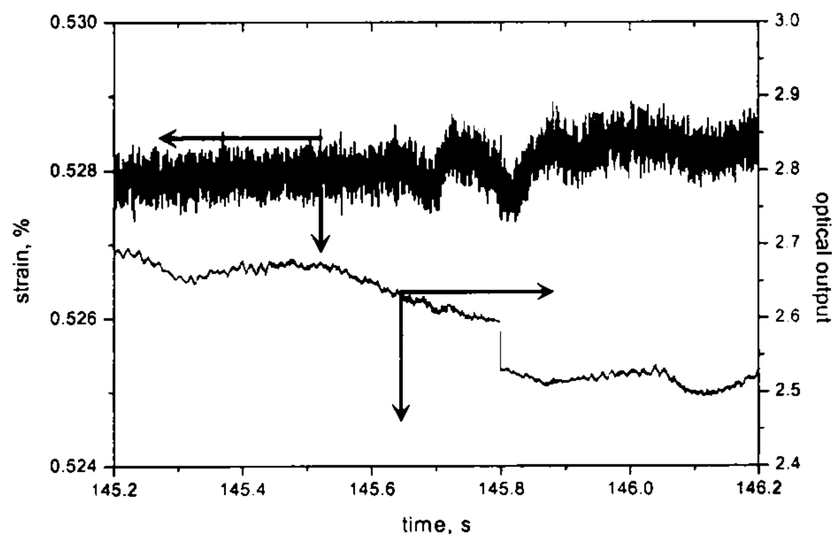

(d)

Figure 7.10 Transverse crack detection by an embedded polarimetric sensor

(a) Band pass filtered optical signal

(b) The load and strain signals of Crack A and Crack B.

(c) The optical and strain signals of Crack A.

(d) The optical and strain signals of Crack B.

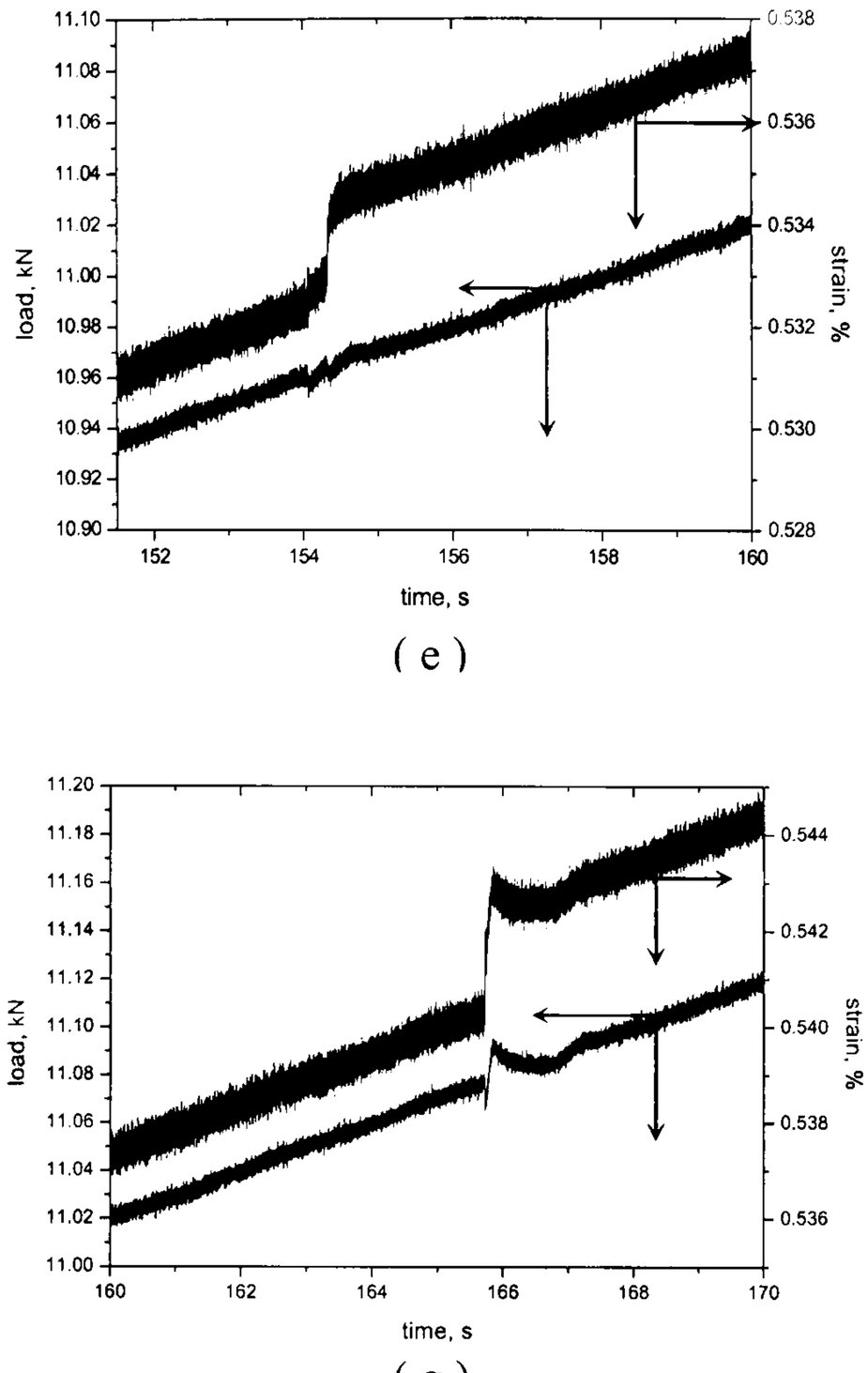

Figure 7.10 (continued) Transverse crack detection by an embedded polarimetric sensor.

(e) The load and strain signals of Crack C;

(f) The optical and strain signals of Crack C;

(g) The load and strain signals of Crack D;

(h) The optical and strain signals of Crack D;

(i) The load and strain signals of Crack E;

(j) The optical and strain signals of Crack E.

It is clear from these figures that there is a one-to-one relationship between the FFT band pass filtered optical signal and the development of matrix cracks. As discussed in Chapter 6, the fluctuations of the load and strain signals when the cracks developed indicate the positions of the crack with respect to the sensor and extensometer gange length. For example, Crack C and Crack D are within extensometer gauge length indicated by the step change of strain signal; whereas Crack A, Crack B and Crack E are outside the extensometer gauge length but within the sensor gauge length.

In order to demonstrate the use of the FFT technique further, the same FFT band pass filter (i.e. having the same upper and lower frequencies) has been applied to the optical output of the crack shown in Figure 6.1 (Crack 1). The result, shown in Figure 7.11, identifies the time of crack formation clearly. Similarly, Figure 7.12 shows the band pass FFT filtered optical signals (again with the same parameters) for Crack 14 and Crack 15 shown in Figure 6.11 and Figure 6.12 (the coupon has a circular hole). The results show that the moments when cracks passed the sensor can again be clearly

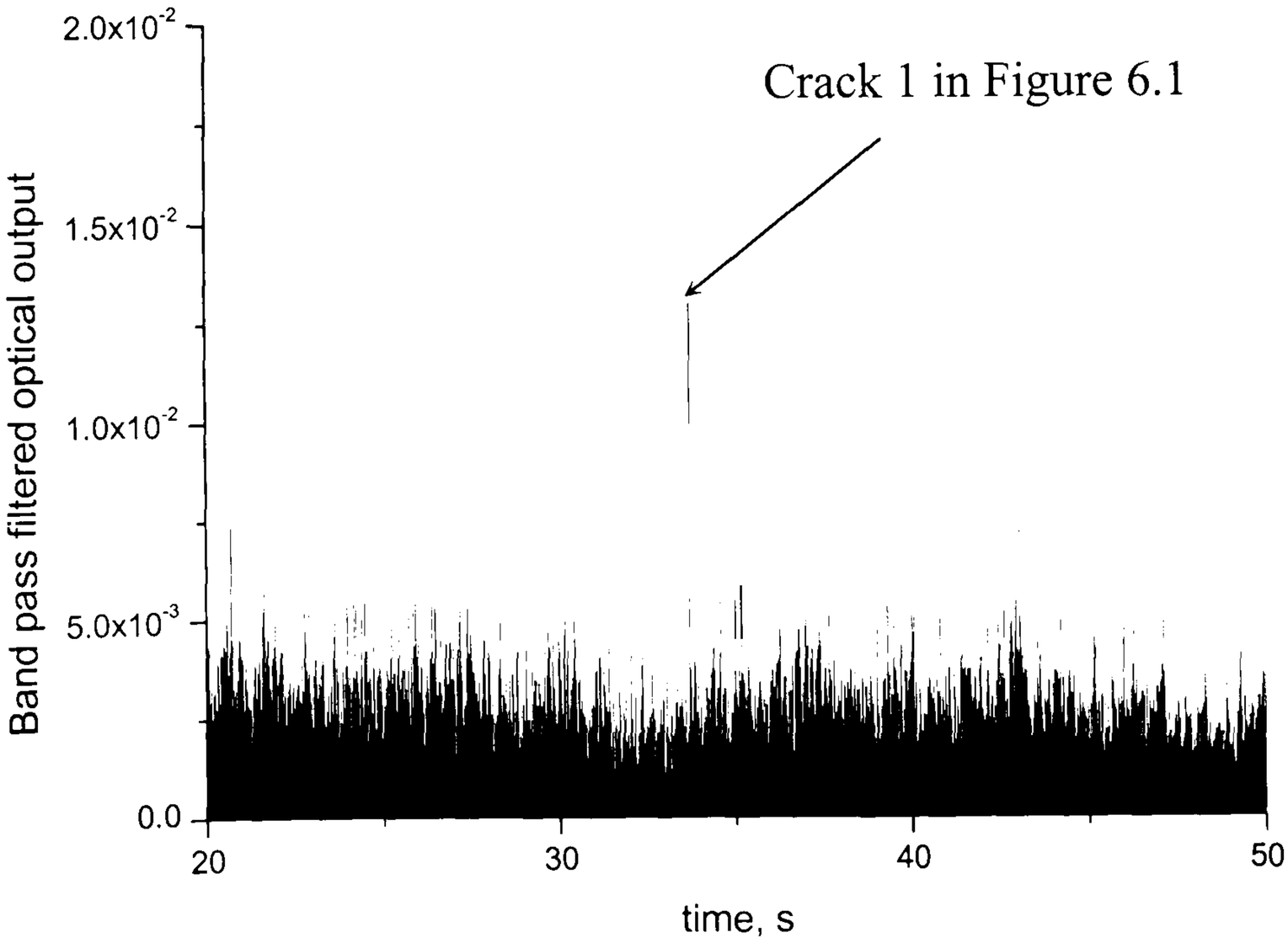

Figure 7.10 FFT band pass analysis of Crack 1 (shown in Figure 6.1)

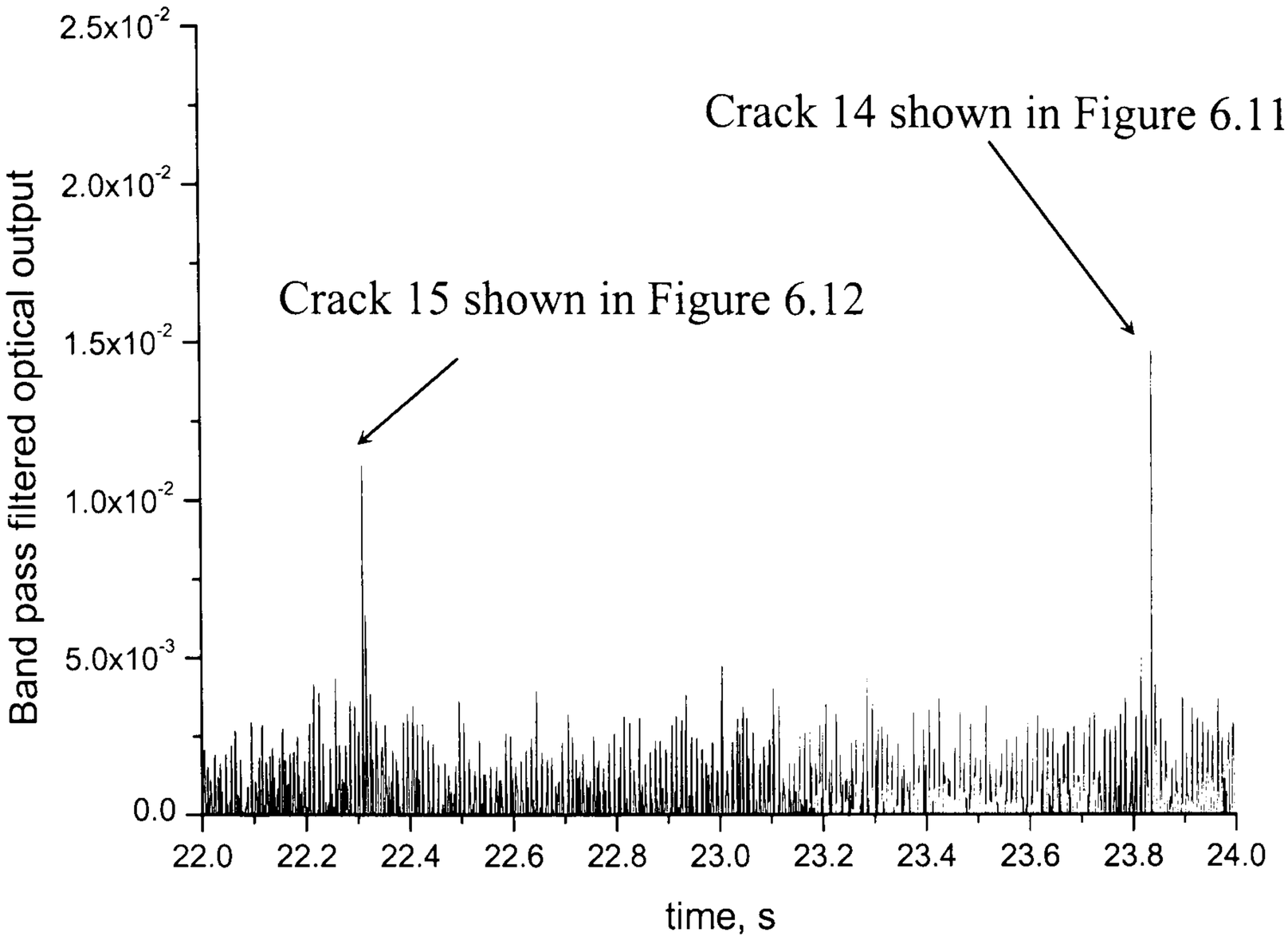

Figure 7.11 FFT band pass analysis of Crack 14 (shown in Figure 6.11) and Crack 15 (shown Figure 6.12).

identified. Hence, it has been shown that , this optical system, together with the FFT technique described, has the potential to detect cracks in composite structures in real time.

7.4 Conclusion

The optical output signals have been analysed using the FFT function in Origin® software. The results show when a crack passes adjacent to an embedded sensor, components of high frequencies emerge in the Fourier spectrum as a consequence of the step-change in the optical signal induced by the crack.

The times when the high frequencies occur can be obtained from a FFT band pass filter analysis and hence the time when cracks occur can be identified. The success of

this technique shows that it should be possible to detect transverse cracks in a composite structure in real time using an embedded polarimetric sensor.

Chapter 8. Detection of matrix cracking damage in double cross-ply laminates under tensile and bending loading

8.1. Introduction

It has been shown that cracks which develop under quasi-static tensile load in a simple cross-ply laminate can be detected by an embedded polarimetric sensor in Chapter 6 and Chapter 7. In this chapter, experiments are carried out to test the polarimetric sensor's ability to detect cracks under more complex conditions.

In this chapter, the results of tests on a laminate with a different lay-up, i.e. (0/90/90/0/90/90/0), are described. Coupons from this laminate have been tested in tensile loading (when cracks develop in both set of 90° plies) and in four-point bending (when cracks develop in the 90° plies put into tension). Detection of cracking is described in tension and four-point bending tests when a polarimetric sensor is located in a 0° ply near the 0/90 interface.

8.2 Crack detection in double cross-ply coupons loaded in simple tension

A laminate with the configuration of (0/90/90/0/90/90/0) was manufactured, as described in Section 4.2, with polarimetric sensors in one of the outer 0° plies, near the 0/90 interface. Coupons cut from the laminate were tested under quasi-static tensile load. The coupons were loaded to increasing higher values of applied load, and unloaded after each test. During loading, transverse cracks were induced in both sets of 90° plies, so that in one set of 90° plies, the cracks passed the sensor in the adjacent 0° ply, and cracks in the other set of 90° plies were separated from the sensor by the central 0° ply and the second set of 90° plies. The results show that only those cracks

which developed in the set of 90° plies adjacent to the sensor could be detected. The following results illustrate these findings.

Figure 8.1 to Figure 8.3 show the development of three cracks and the associated load and optical outputs. Figure 8.1(a) shows the load and optical output for a specimen loaded to a peak load of 10.5 kN in 20 seconds and then unloaded. The step change of optical signal in Figure 8.1(a) at about 19.9 seconds suggests that a crack (Crack 1) has passed the sensor. This is confirmed by Figure 8.1(b) which shows two consecutive pictures of the coupon at this time separated by 0.02s. In the upper picture, the crack has propagated about 1/3 of the way across the coupon, and the crack has passed the sensor in the lower picture. The load signal does not show a distinct fluctuation at this time and this is believed to be because of the step growth of the crack. By contrast, Figure 8.2(a) shows the development of a second crack (Crack 2) which formed after 17.9 seconds and at a higher load than for Crack 1. For Crack 2 in Figure 8.2(a) the load signal fluctuation has no corresponding change in the optical signal, although Figure 8.2(b) and Figure 8.2(c) confirm that this is the time when Crack 2 developed. Part of Figure 8.2(c) has been magnified to show that Crack 2 occurred in almost the same plane as Crack 1, which suggests that Crack 1 and Crack 2 occurred in the two different sets of 90° plies. The results for a third crack, Crack 3, are shown in Figure 8.3. In this case, a step optical change is detected for the crack (see Figure 8.3(a)). Figure 8.3(b) and Figure 8.3(c) show that Crack 3 developed very close to Crack 1 and Crack 2. Subsequent observations made on the coupon after unloading showed that Crack 1 and Crack 3 had developed in the same set of 90° plies and that these 90° plies were the plies adjacent to the 0° ply which contained the embedded sensor.

All of the results on the double cross-ply ply laminate coupon show the same effect, i.e. that cracks in the set of 90° plies adjacent to the sensor can be detected, but cracks

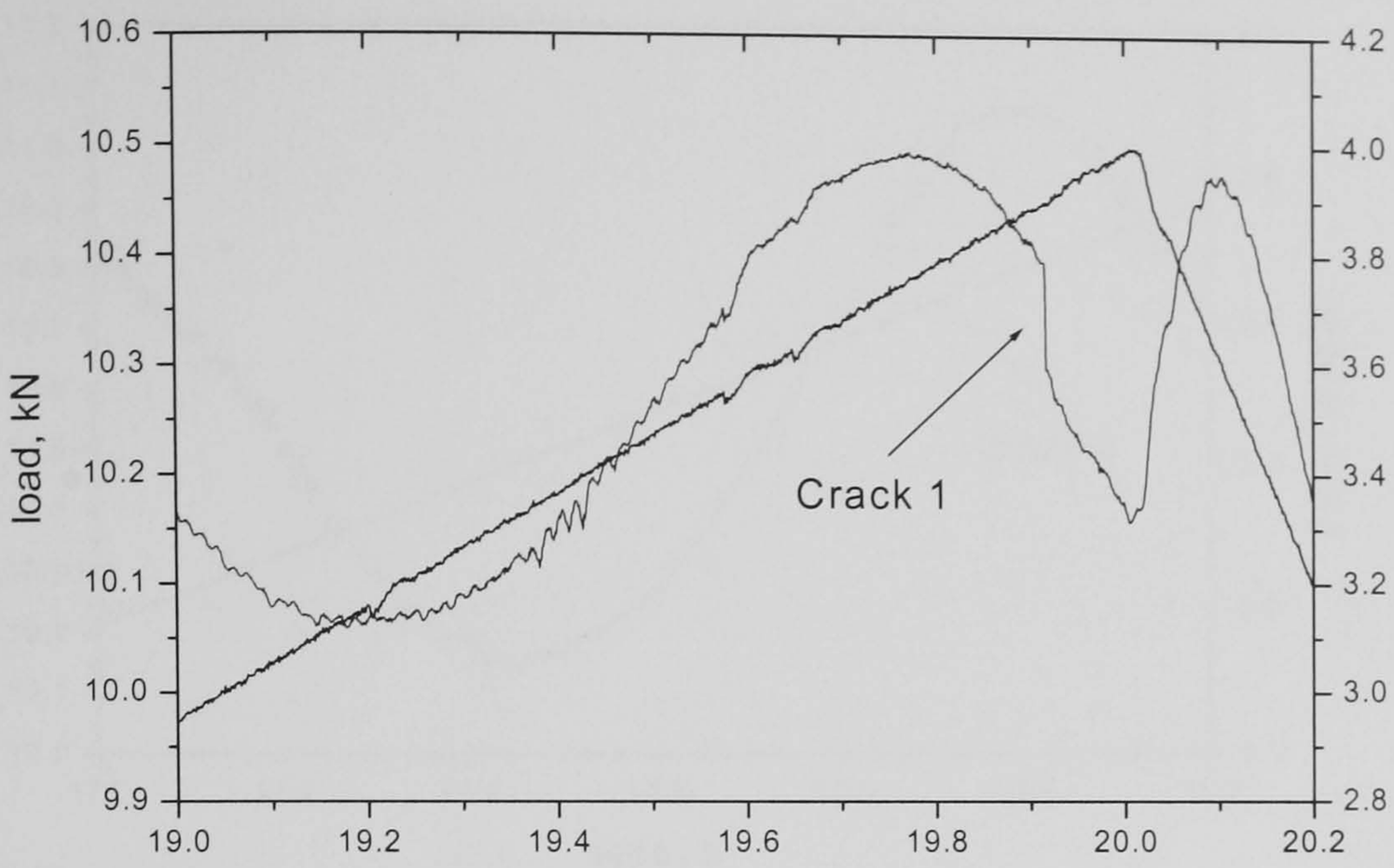

(a)

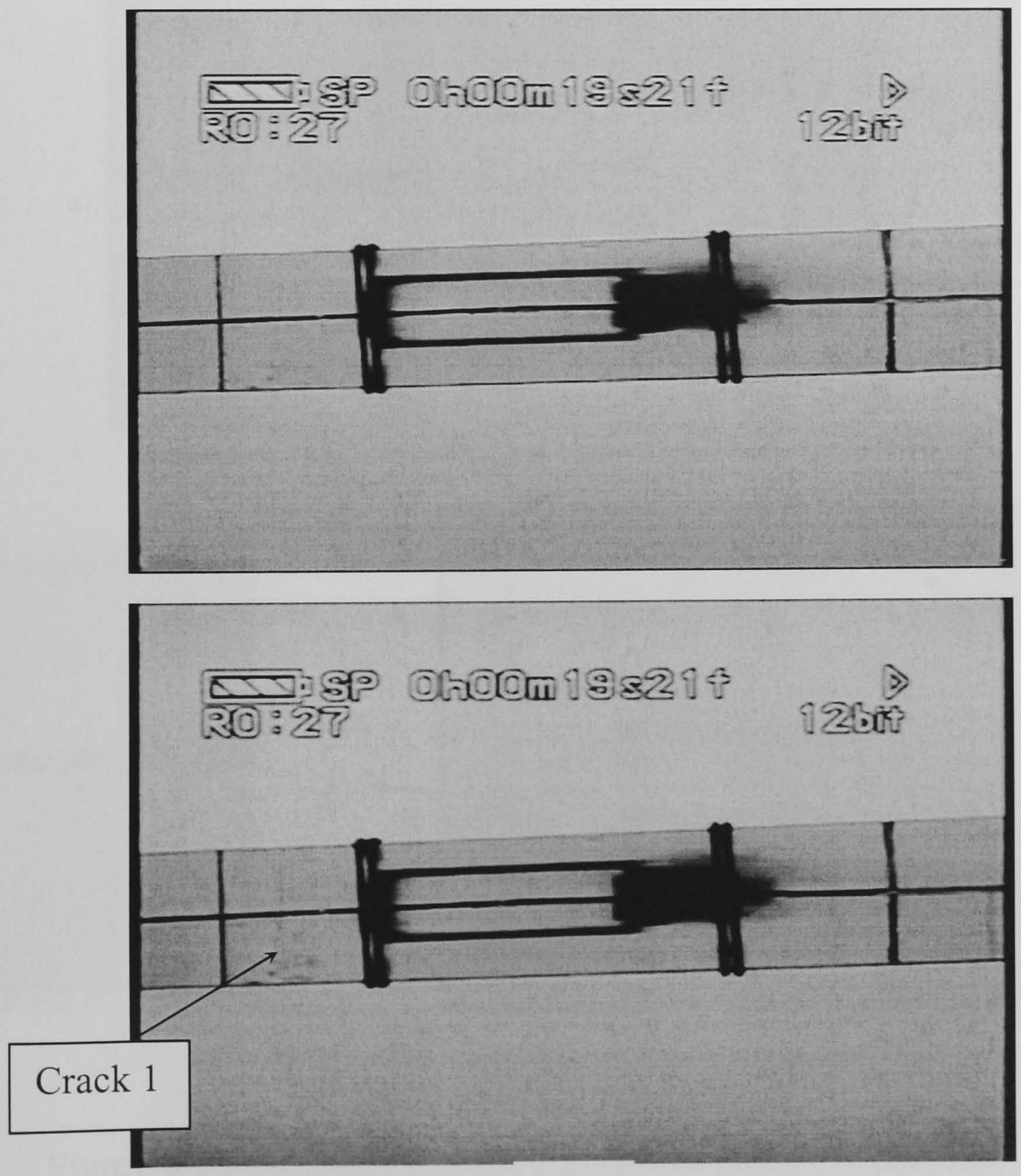

(b)

Figure 8.1 Detection of Crack 1 in double cross-ply coupon.
(a) Optical output and load signal of Crack 1.
(b) Video images showing the propagation of the crack.

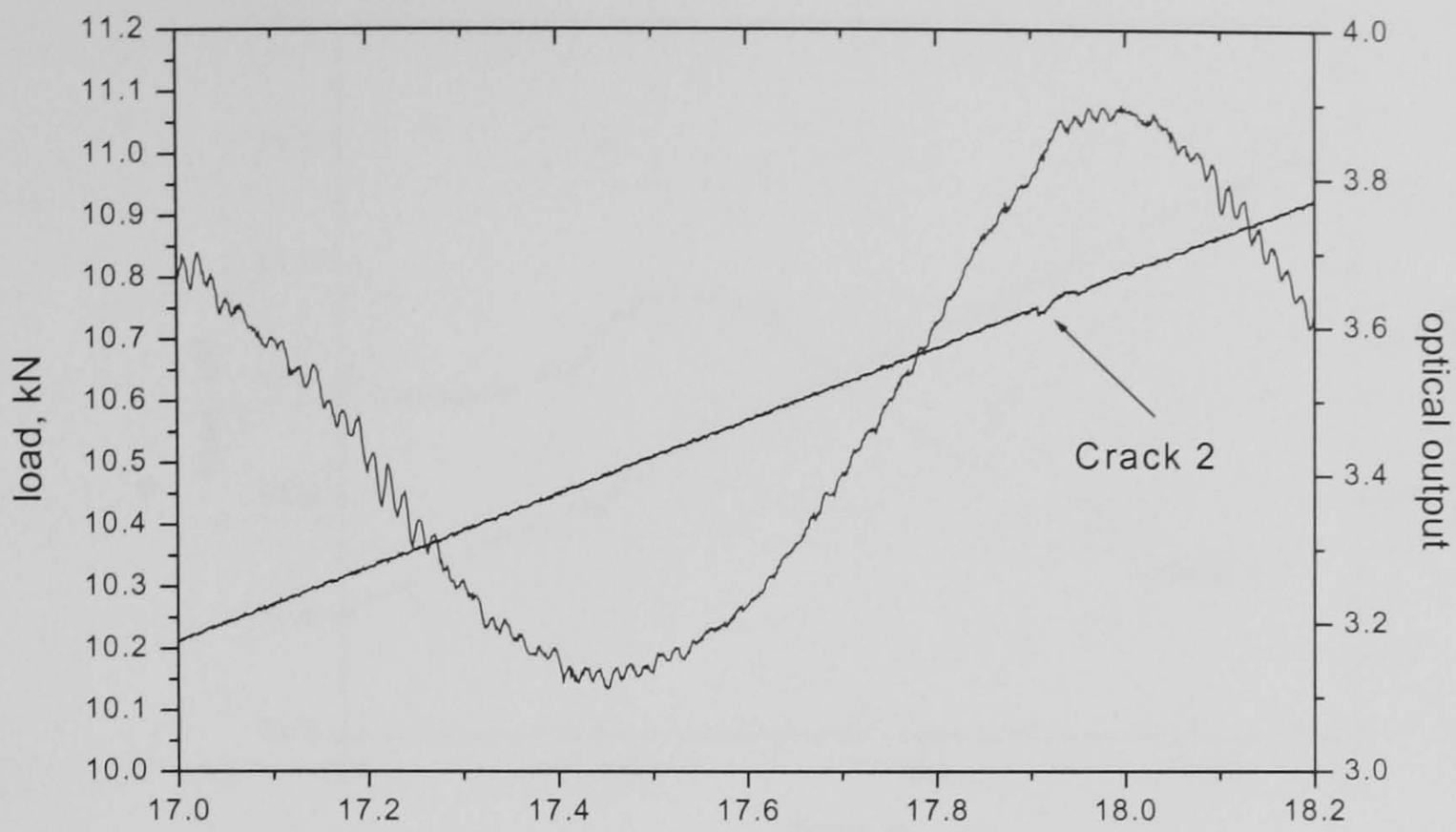

(a)

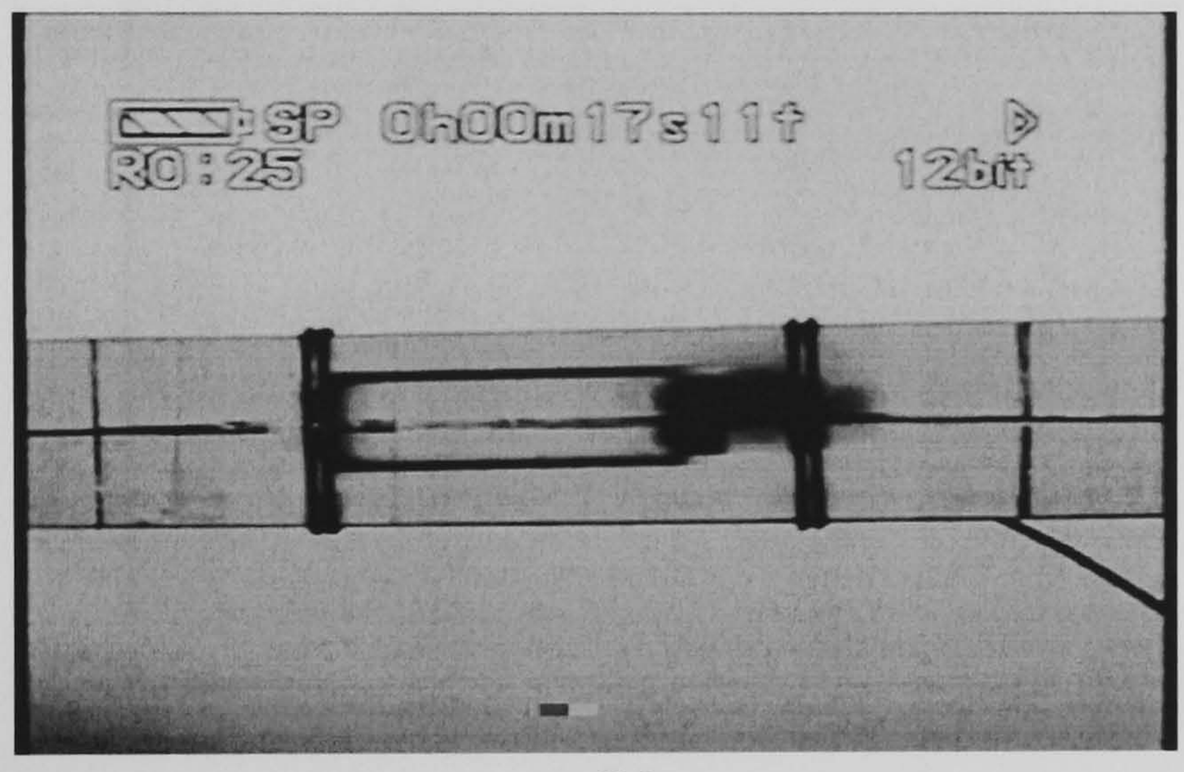

(b)

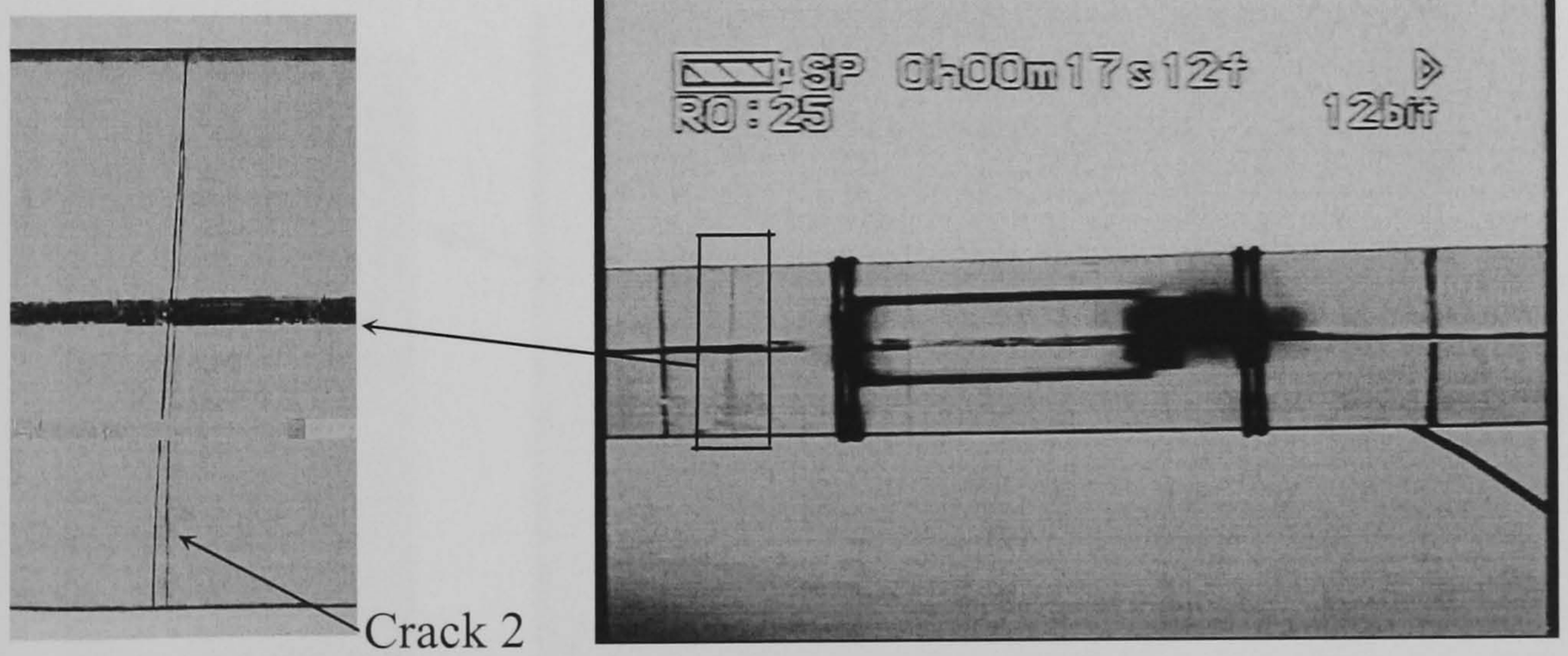

(c)

Figure 8.2 Detection of Crack 2 in double cross-ply coupon.
(a) Optical output and load signal of Crack 2.
(b) Video image showing the moment before Crack 2 occurred.
(c) Video image showing the moment after Crack 2 occurred.

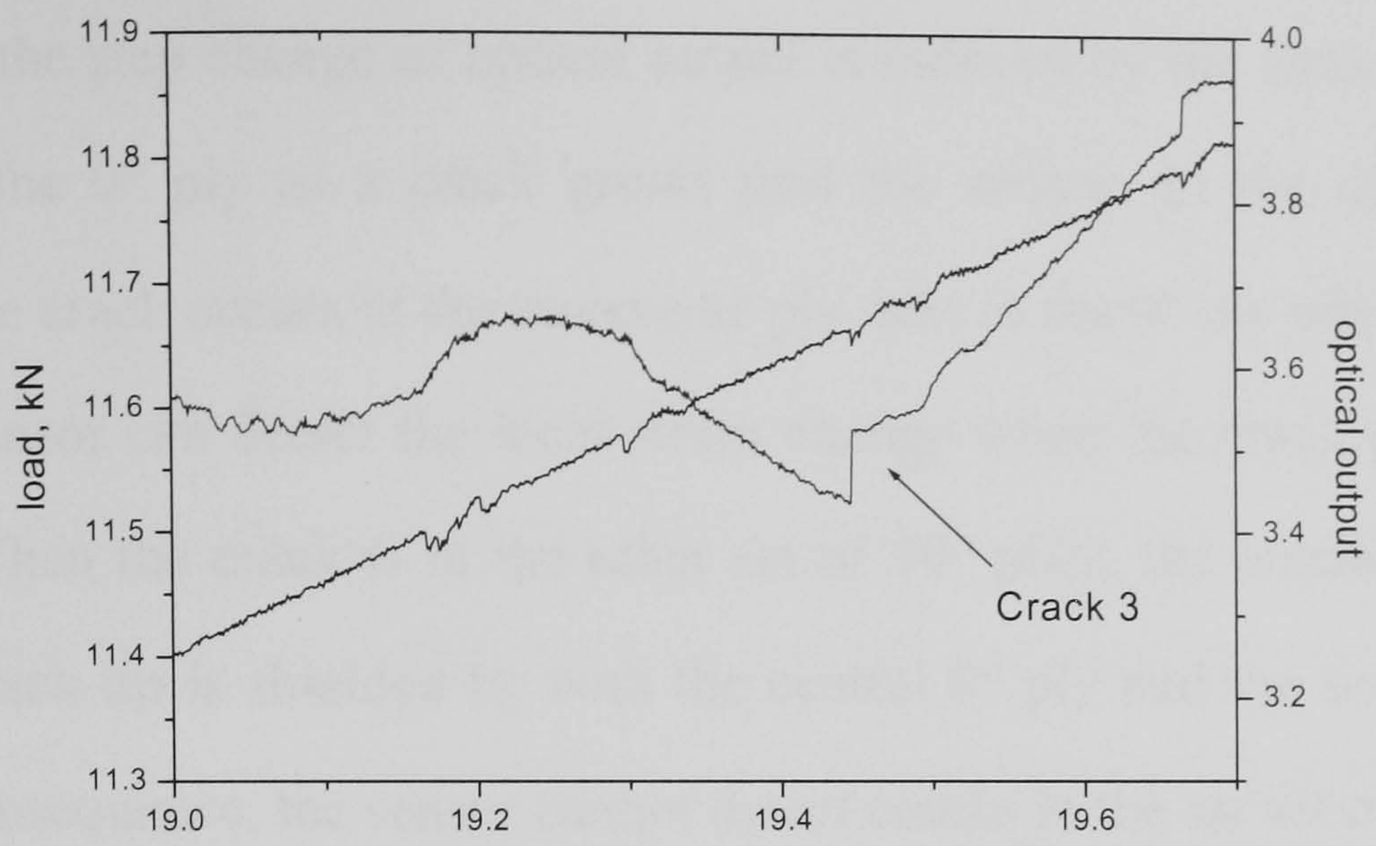

(a)

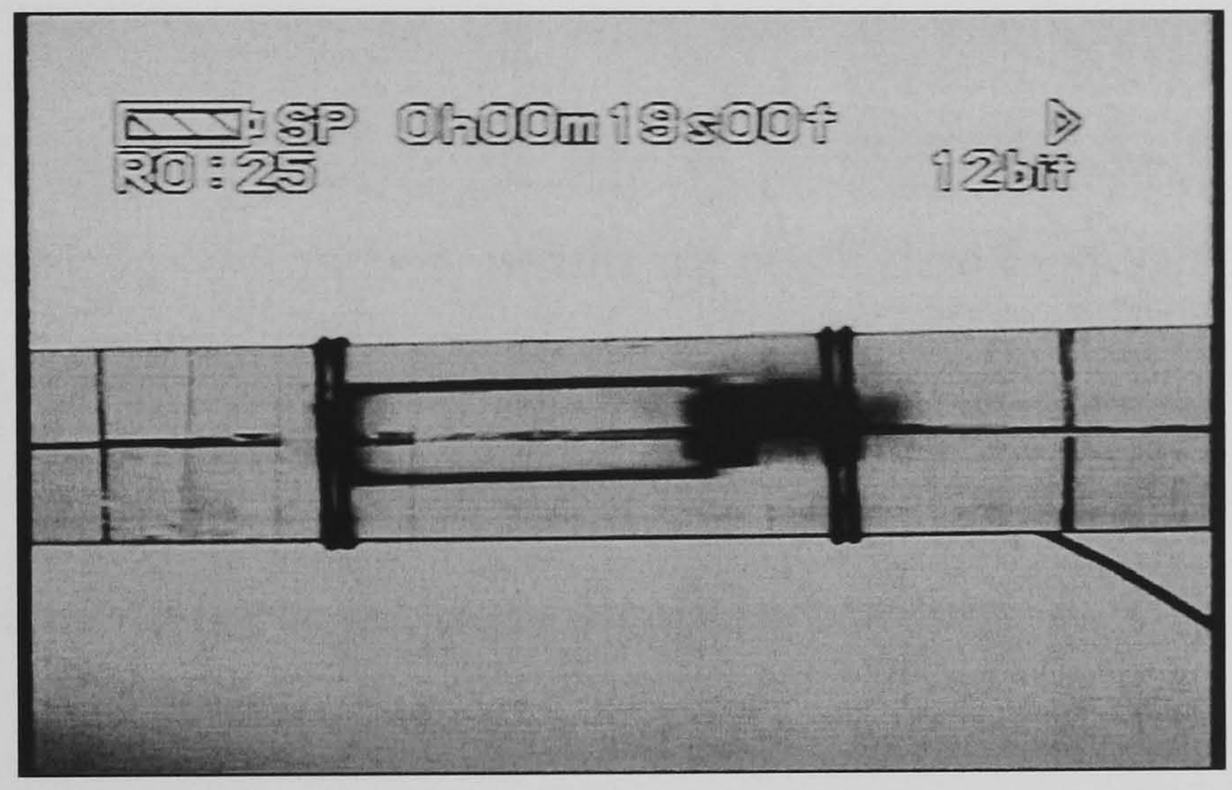

(b)

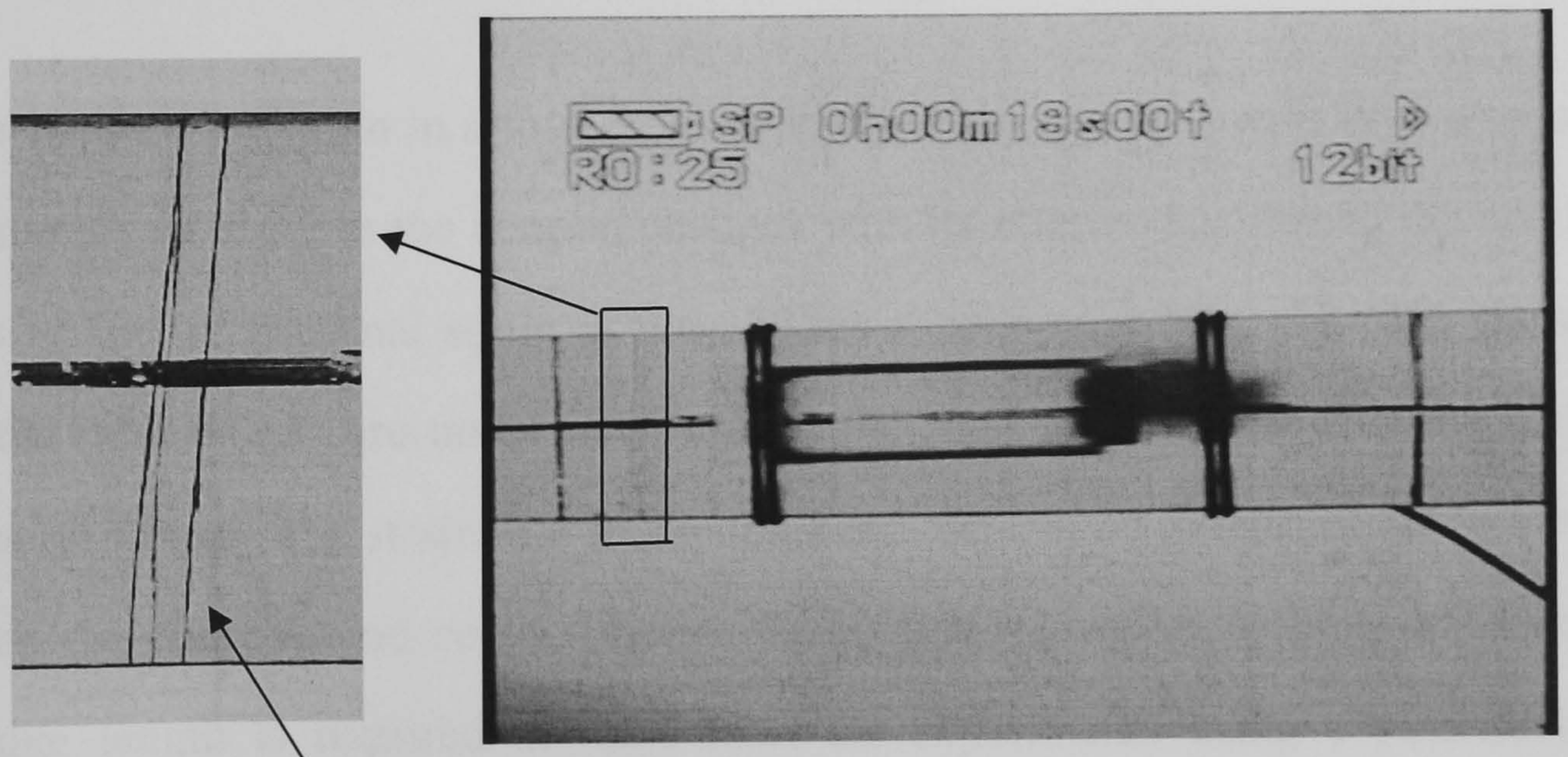

(c)

Figure 8.3 Detection of Crack 3 in double cross-ply coupon.
(a) Optical output and load signal of Crack 3.
(b) Video picture showing the moment before Crack 2 occurred.
(c) Video picture showing the moment after Crack 2 occurred.

in the other set of 90° plies can not be detected. As suggested in Chapter 6, it is believed that the step change of optical output is induced by the strain magnification produced in the 0° ply as a crack grows past the sensor. In the double cross-ply coupons, if the crack occurs in the transverse ply next to the 0° ply with the embedded sensor, the sensor can detect the local strain change when the crack propagates past the sensor. When the crack is in the other set of 90° plies, the enhanced strain field around the crack tip is shielded by both the central 0° ply and the second set of 90° plies. As a consequence, the sensor cannot detect cracks in the far set of 90° plies.

In the following sections, tests on the same laminate configuration in bending are described. Firstly, in Section 8.3, the use of extensometer to measure strains in bending is discussed. In Section 8.4, results on crack detection using the polarimetric sensor in bending are described.

8.3 Use of an extensometer to measure strain in bending

8.3.1 Introduction

The measurement of strain in a four-point bending test is not as simple as in a tensile test. The strain of a ply in the coupon changes with its relative position to the neutral axis, where the longitudinal strain is zero. When a coupon is bent, the plies on one side of the neutral axis are under tension, and the plies on the other side are under compression. Clearly the strain in a four-point bend test can be monitored using strain gauges on the concave and convex faces of a coupon. However, since a reasonably long gauge length is required in these tests for experiments using a polarimetric sensor, together with the possibility of monitoring strain in fatigue tests and continuity with previous testing, an extensometer appears to be a good choice. The conversion of the extensometer reading to a tensile strain reading at the position of the polarimetric sensor requires some analysis to be carried out.

8.3.2. Analysis of the use of an extensometer in a four-point bending test

The experimental set-up of the four-point bending tests has been shown in Figure 4.7 and a part of a coupon, *AA'C'C*, within the constant bending moment region, is shown schematically in Figure 8.4(a). In the figure, if the extensometer is attached to the convex face of the coupon, the two knife edges of the extensometer attach to the surface at point A and A'. If the extensometer is attached to the concave face of the coupon, the two knife edges of the extensometer attach to the surface at point *C* and *C'*.

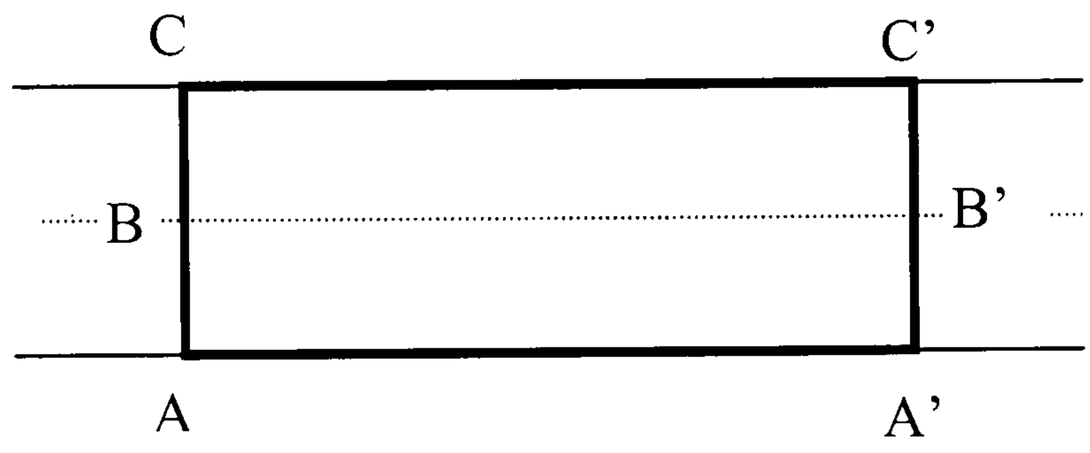

(a)

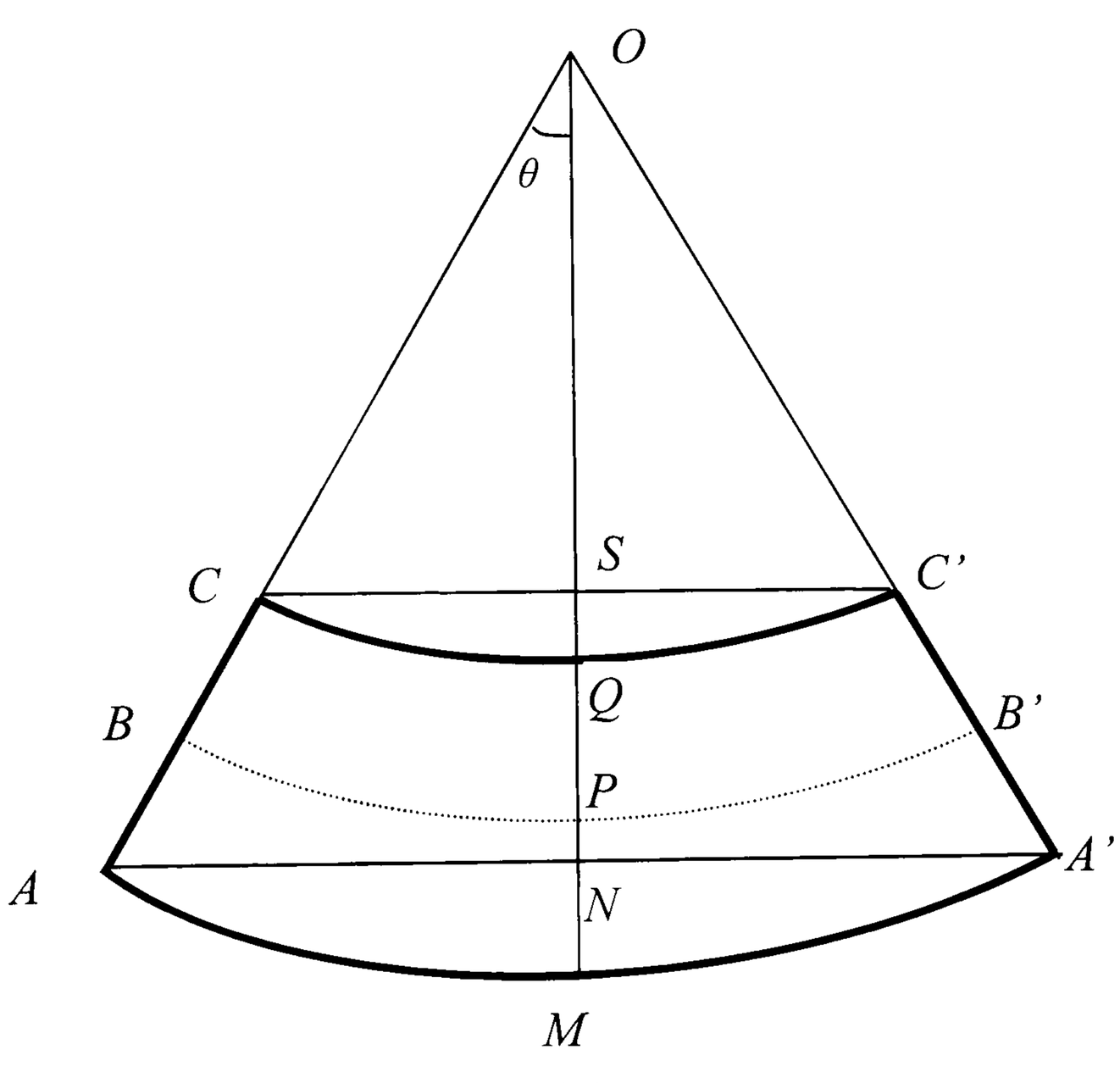

M

(b)

Figure 8.4 The geometry of the extensometer and the coupon.

(a) Part of the coupon with a length of 50 mm before bending.

(b) Part of the coupon with a length of 50 mm after bending.

Before the bending test starts, $AA' = BB' = CC' = 50$ mm, where 50 mm is the gauge length of the extensometer. After bending, *AA'*, *BB'* and *CC'* in Figure 8.4(a) become curves *AMA'*, *BPB'* and *CQC'* in Figure 8.4(b) respectively. The length of *AA'* and *CC'* changes, while *BB'*, which is the neutral axis of the coupon, does not change. The extensometer measures the length of the straight line *AA'* or *CC'* in Figure 8.4(b), depending upon whether the extensometer is fixed below or above the coupon. .

When the extensometer is attached above the neutral axis, then:

$$\theta = \frac{\widehat{BP}}{OB} = \frac{L/2}{R} \tag{8.1}$$

and

$$CS = OC\sin\theta = (OB - BC)\sin\theta = (R - d)\sin\theta = L'/2 \tag{8.2}$$

where *L/2* is half of the gauge length of the extensometer, *L'/2* is half of the new length of the extensometer as a result of the bending, *R* is the radius of curvature of the beam ($R = OB$) and $d = AB = BC$ is half of the thickness of the coupon.

Combining equation (8.1) and (8.2), equation (8.3) is given as:

$$\sin(\frac{L/2}{R}) = \frac{L'/2}{R-d} \tag{8.3}$$

In equation (8.3), *L* is half of the gauge length of the extensometer, (i.e. 25 mm), d can be measured, *L'* can be calculated from the strain signal recorded by the extensometer, so the radius of curvature, *R* can be obtained. The longitudinal strain at any position, *y*, inside the coupon can be calculated (e.g. Meriam, 1978):

$$\varepsilon = -\frac{y}{R} \tag{8.4}$$

where R is the radius of curvature, y is the distance to the neutral axis, and y is measured as positive in the direction of PO in Figure 8.4(b).

Similarly when the extensometer is attached to the convex face of the coupon, the following equation results:

$$\sin(\frac{L/2}{R}) = \frac{AN}{OA} = \frac{L'/2}{R+d} \tag{8.5}$$

Equation 8.3 and 8.5 can also be used to find the flexural modulus of the coupon. In four-point bending, we have:

$$MR = EI_x \tag{8.6}$$

where M is the applied bending moment (which can be calculated from the applied load and dimensions of the coupon), E is the flexural modulus of the coupon, I_x is the 2nd moment of area of the cross-section (which can be calculated) and R is the radius of curvature.

Since R can be obtained from Equation 8.3 or Equation 8.5, depending on where the extensometer is attached, E can be calculated. Due to the characteristics of an extensometer, the flexural modulus of a coupon can be monitored in real time, especially when the flexural modulus reduces with increasing crack density during, for example, fatigue tests. In addition, when a cracked sample is unloaded, the readings from the extensometer can be used to calculate the residual beam curvature due to the cracking. This curvature is a consequence of the relaxation of thermal stress in the vicinity of the matrix cracks (Smith and Ogin, 1999).

8.3.3 Solution of the expressions when an extensometer is used in a four-point bending test

The accurate value of R in Equations (8.3) and (8.5) can be solved using Maple® software, for example, using the ***fsolve*** command. However, the data recorded by the computer controlling the test machine always contains thousands of lines of strain data, which means that thousands of R values will be calculated, and the ***fsolve*** command is not practicable. To obtain *R* values in real time, a combination of Maple®, Excel® and some approximations in the calculation are needed.

With regard to the approximations, the left side of equation (8.3) is expanded first, ignoring powers higher than 3:

$$\sin\left(\frac{L/2}{R}\right) = \frac{L/2}{R} - \frac{(L/2)^3}{6R^3} = \frac{L'/2}{R-d} \tag{8.7}$$

The roots of equation (8.7) are then obtained using Maple® software (see Appendix A). Three roots are obtained, of which only one is reasonable. The conversion of the extensometer reading of strains to the strains at the position of the sensor in the laminate is carried out using Excel® (see Appendix B).

An example of the results is shown in Table 8.1. The first three columns, time (in seconds), load (*kN*) and strain measured by the extensometer (%), are real experimental data obtained from the fatigue machine. *R* is the radius of curvature, and the strain at the position of the sensor, ε_s, is computed in the last column. Only input data and final results are shown in the Table. The complete expressions and other internal functions for the computation are shown in Appendix B.

Similar calculations are carried out for equation 8.5, when the extensometer is attached below the natural axis of the coupon, following the same procedure.

Table 8.1 Conversion of extensometer measurements to sensor strains

Time (s)	Load (kN)	Extensometer strain (%)	Curvature, R (mm)	1/R (mm^{-1})	Longitudinal strain at position of embedded sensor, ε_S, (%)
0.01	4.71E-03	-4.62E-02	3.98E+03	2.51E-04	3.14E-02
0.5	-1.46E-03	-4.66E-02	3.95E+03	2.53E-04	3.16E-02
1.0	-2.67E-03	-5.11E-02	3.61E+03	2.77E-04	3.47E-02
1.5	-9.36E-03	-5.58E-02	3.30E+03	3.03E-04	3.78E-02
2.0	-1.42E-02	-6.08E-02	3.04E+03	3.29E-04	4.12E-02
2.5	-1.95E-02	-6.67E-02	2.78E+03	3.60E-04	4.50E-02
3.0	-2.02E-02	-7.28E-02	2.55E+03	3.93E-04	4.91E-02
3.5	-2.25E-02	-7.92E-02	2.35E+03	4.26E-04	5.33E-02
4.0	-2.69E-02	-8.55E-02	2.18E+03	4.59E-04	5.74E-02
4.5	-3.20E-02	-9.17E-02	2.03E+03	4.92E-04	6.15E-02
5.0	-4.07E-02	-9.81E-02	1.90E+03	5.25E-04	6.56E-02

The ***fsolve*** command in Maple® mentioned above makes it possible to obtain an accurate solution of the equations without the need for the approximation. Though this is not practicable for large amount of data, it is helpful to check the errors introduced using the approximate solution. The comparisons for three strain readings from the extensometer are shown in Table 8.2.

Table 8.2 Error checking of equation (8.7)

Strain readings of the extensometer	L'/2 (mm)	L/2 (mm)	d (mm)	Results calculated using approximation *R*, (mm)	Accurate results calculated by Maple ***(fsolve)*** *R*, (mm)	Error
16%	21	25	1.5	29.99	29.55	1.50%
8%	23	25	1.5	46.08	45.83	0.56%
0.4%	24.9	25	1.5	434.70	434.69	0.002%

In the experimental work, the strain seen by the extensometer is not larger than 8%. Hence the error introduced by the approximation used in equation (8.7) will not be bigger than 0.56%, which is acceptably small.

8.3.4 Position of the extensometer

In the experiments using an extensometer to monitor the strain in bending, the extensometer can be attached to the convex face (lower face of the coupon) or the concave (upper face of the coupon). If the extensometer is attached to the convex face of the coupon, then the relationship between the new half-length of the extensometer and the radius of curvature is given by:

$$L'/2 = (R + d)\sin(\frac{L/2}{R}) \tag{8.8}$$

This function is plotted in Figure 8.5 in which *L'/2* has been converted into strain and *L/2=25mm, d=1.5mm.*

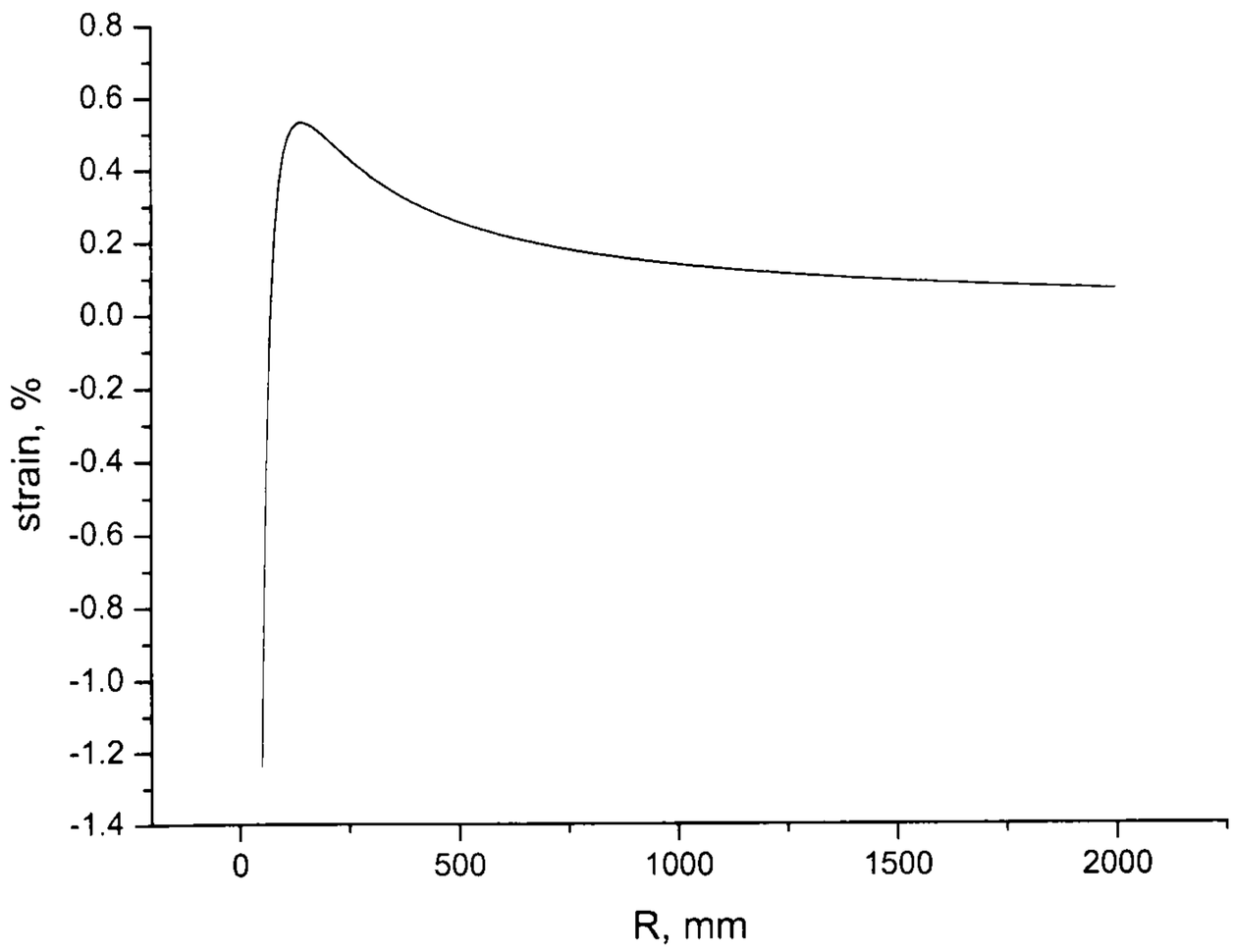

Figure 8.5 Change of strain with *R* when extensometer is attached to the convex face of the coupon.

From Figure 8.5, it is clear that there is no one to one relationship between strain seen by the extensometer and radius of curvature. As the coupon bends, *R* first decreases and the strain increases. When *R* becomes smaller than about 100mm, the strain begins to decrease. As a consequence, one strain output from the extensometer may correspond to two reasonable coupon radii The calculation results from Maple® show

that when the strain output from the extensometer is 0.4% (*L'/2=25.1 mm*), the three roots calculated by Maple® are:

$$\begin{aligned} R_1 &= -1.46881 \quad mm \\ R_2 &= 94.22609 \quad mm \\ R_3 &= 282.24272 \; mm \end{aligned} \tag{8.9}$$

of which two roots are reasonable, 94 mm and 282 mm. The ambiguity suggests that attaching the extensometer to the convex side of the coupon will be problematic if unambiguous strain readings are to be made.

When the extensometer is attached to the concave side of the coupon, the relationship between the recorded strain and radius of curvature is shown in Figure 8.6. The figure shows that for an extensometer attached to the upper surface of the coupon, there is a one-to-one relationship between the extensometer output and the radius of curvature. Calculations carried out using Maple® show that for an extensometer strain of 0.4%, there are two positive roots from the results. However one root (*R=1.469 mm*) is obviously unreasonable.

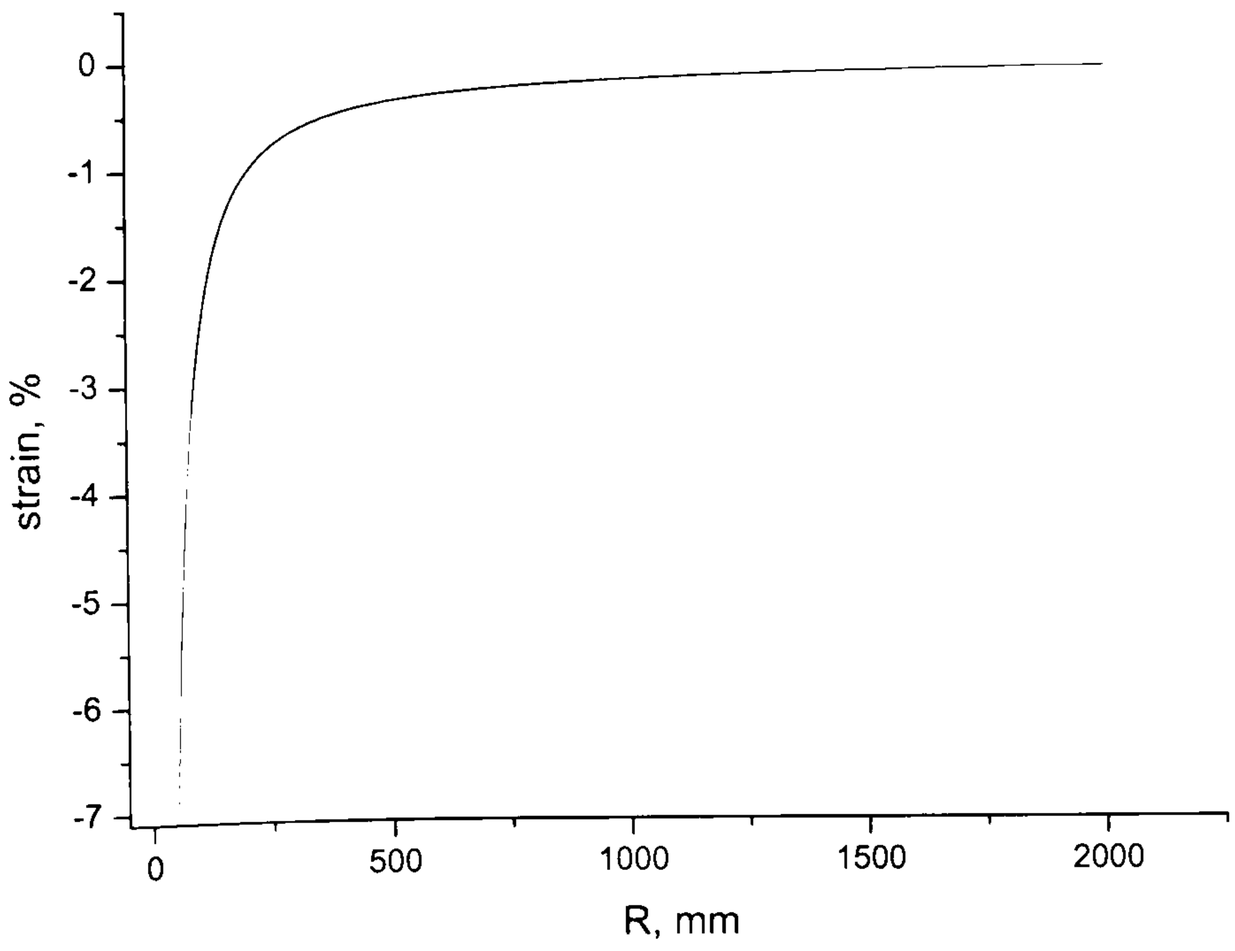

Figure 8.6 Change of strain with *R* when extensometer is attached to the concave face of the coupon.

$$R_1 = -61.16948mm$$
$$R_2 = 1.46905mm \qquad (8.10)$$
$$R_3 = 434.70044mm$$

The physical reason for the difference between the curves shown in Figure 8.5 and Figure 8.6 can be explained using Figure 8.4. Before a four-point bending test starts, what the extensometer measures is the length of *AA'* or *CC'* in Figure 8.4(a), and *AA'=BB'=CC'=L=50mm*, where L is the gauge length of the extensometer. After the bending test has started, what the extensometer measures is the straight line CSC' (extensometer attached to the upper surface) or the straight line *ANA'* (extensometer attaches to lower surface), as shown in Figure 8.4b. The strain signal generated by the extensometer is calculated as:

$$\varepsilon_{convex} = \frac{ANA' - \widehat{BPB'}}{\widehat{BPB'}}$$
$$\varepsilon_{concave} = \frac{CSC' - \widehat{BPB'}}{\widehat{BPB'}} \qquad (8.11)$$

When the extensometer is attached to the convex face of the coupon, *ANA'* first increases and then decreases compared with $\widehat{BPB'}$, so there is a peak in Figure 8.5 and one strain reading may correspond to two reasonable radii of curvature. When the extensometer is attached to the concave face of the coupon, *CSC'* always decreases with decreasing curvature. Hence, there is a one-to-one relationship between strain output and radius of curvature (as shown in Figure 8.6).

In conclusion, this analysis has shown that in the real tests, the extensometer should be attached to the upper surface of the coupon. The experimental arrangement is shown in Figure 8.7. The lower supports are mounted on the actuator of the machine, while the upper supports are connected to the crosshead. Hence, during the text, it is the lower supports (i.e. the outer rollers) which move.

8.3.5 Analysis of the bend test applied to real experimental data

An example of the conversion of the raw data using the extensometer positioned above the specimen (on the concave side) is now given to show the implementation of

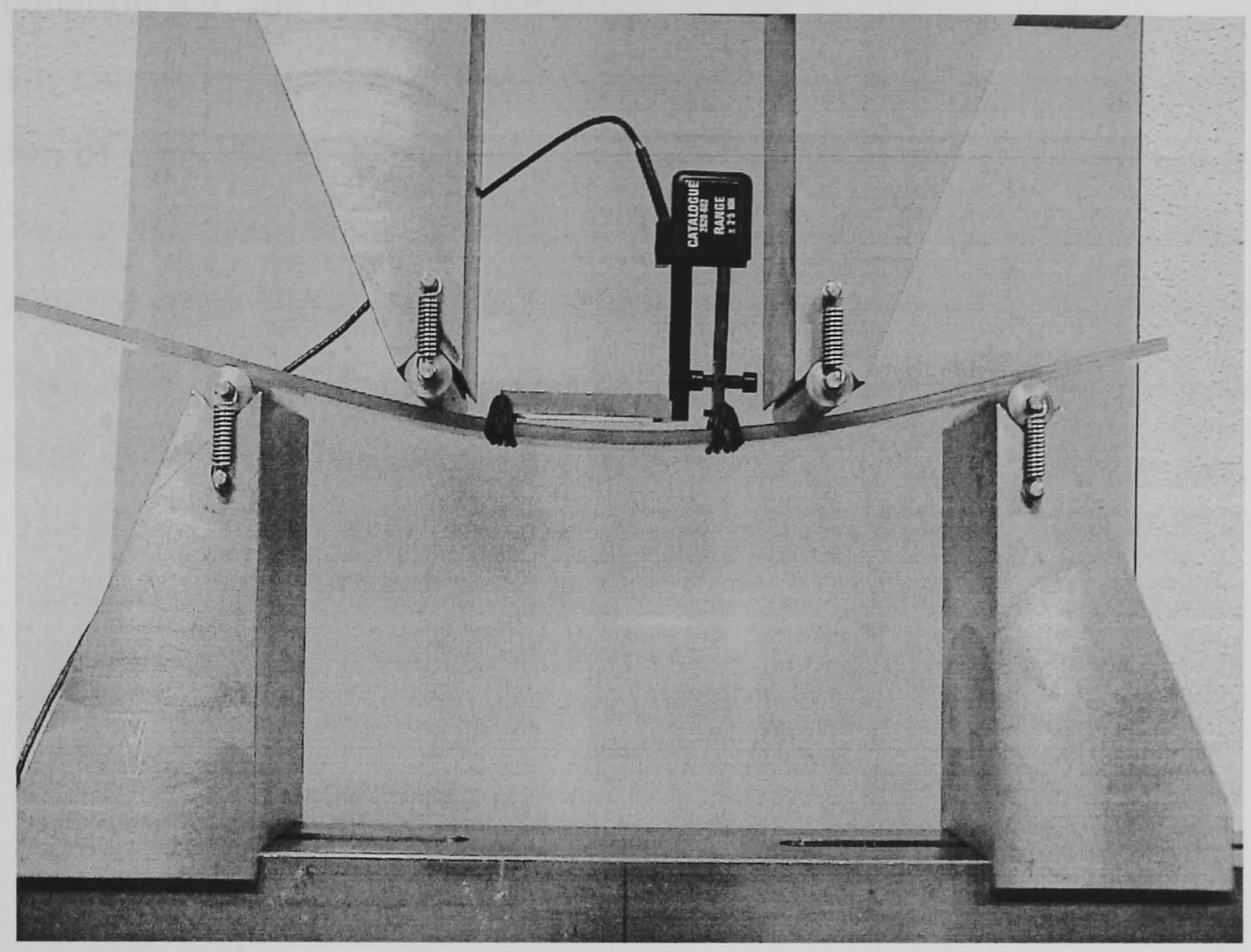

Figure 8.7 Experimental setup of four-point bending test.

the analysis. The fatigue machine was operated in position control mode, and the recorded strain signals and load signals as a function of time in the four-point bending test are shown in Figures 8.8(a) and 8.8(b), respectively. In this test, the lower supports moved 3 mm upward from the unloaded position in a time of 20 seconds, applying (as Figure 8.8(b) shows)a compressive load of 180 *N* to the coupon, and then unloading over a further 5 seconds.

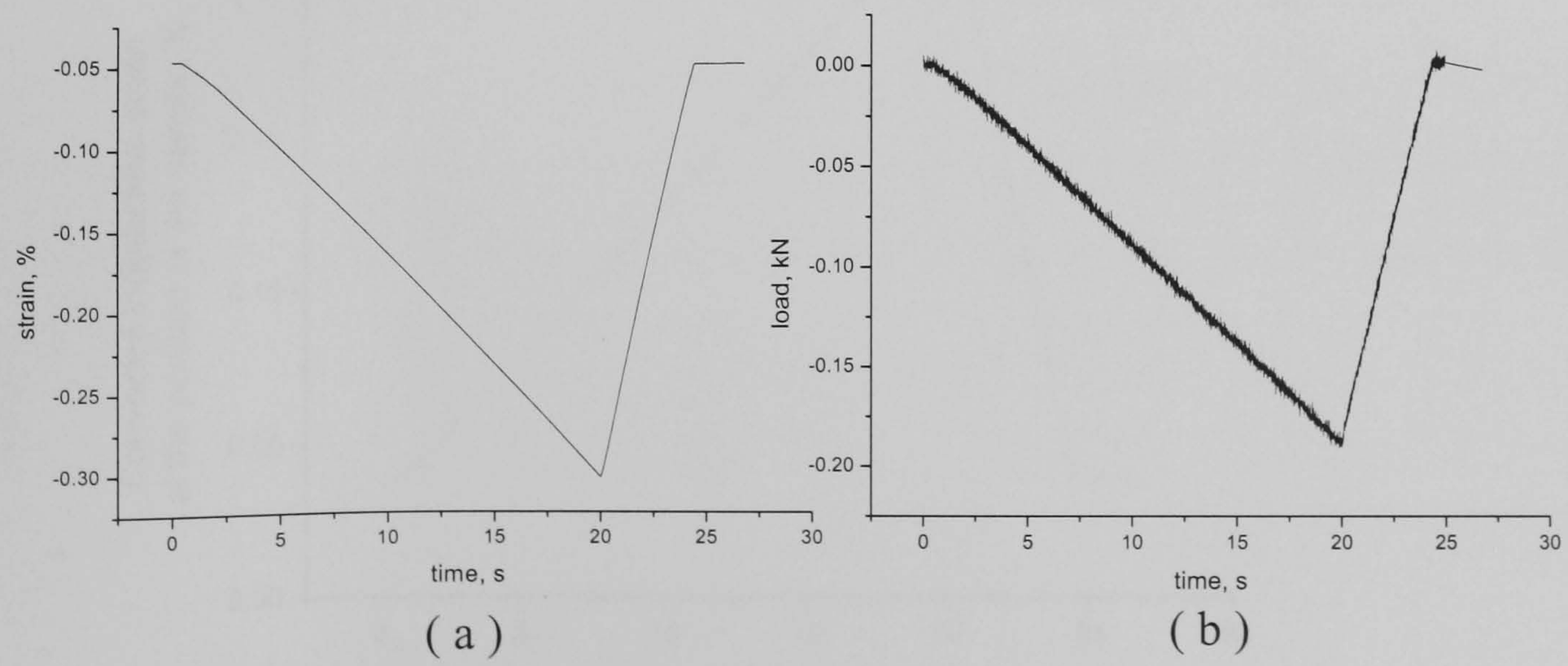

Figure 8.8 Original recorded experimental data during a four-point bending test
(a) Extensometer strain signal as a function of time
(b) Load signal as a function of time

Using equation 8.5, the radius of curvature, R, can be derived as a function of time and this is shown in Figure 8.9. The longitudinal strain at the position of the sensor as a function of time can be calculated using equation (8.4) and this is shown in Figure 8.10. During the test, the extensometer was attached to the upper surface of the coupon, so the strain signals from the extensometer were negative. However, since the sensor itself was below the neutral axis of the coupon, the converted strain signals at the position of the embedded sensor are positive.

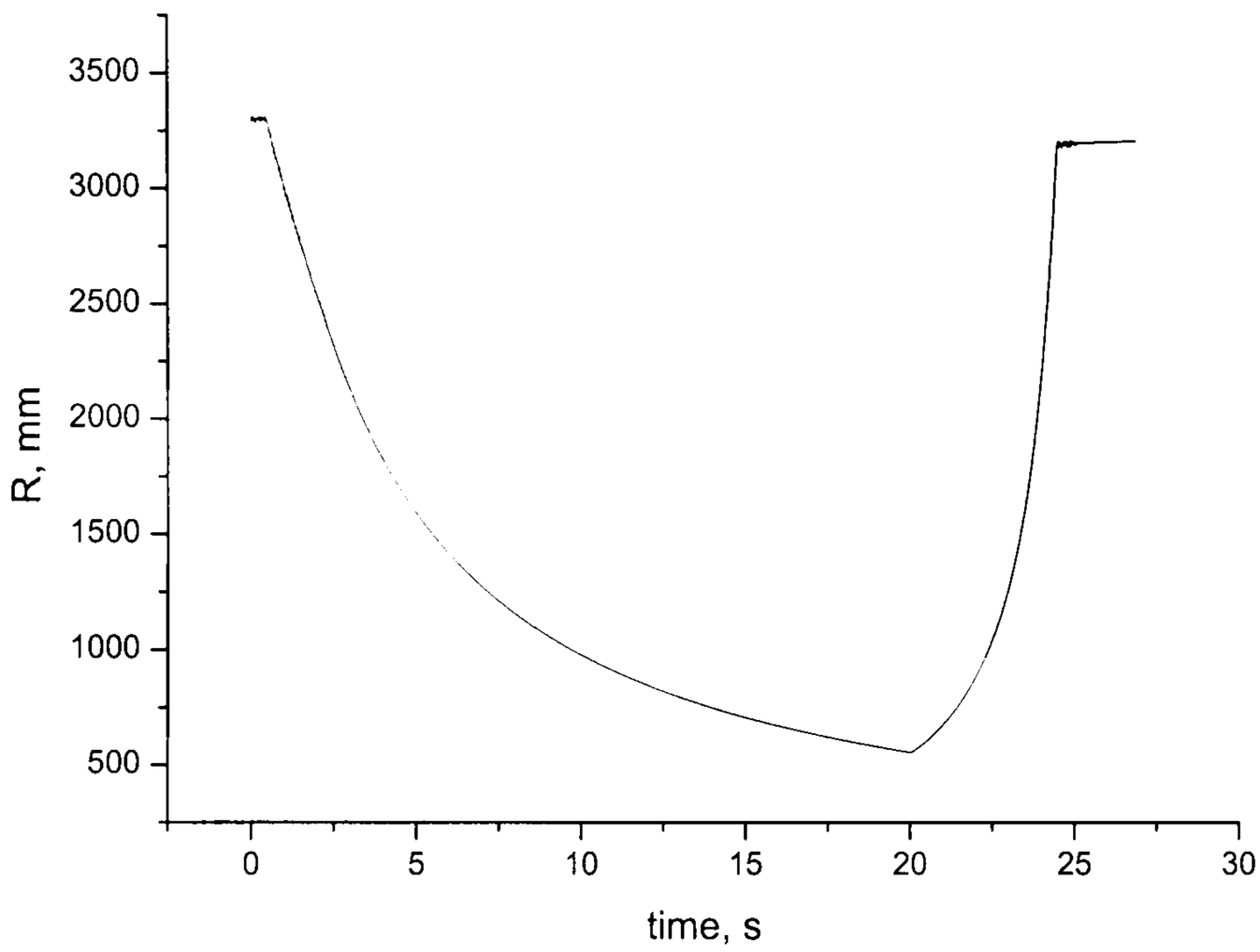

Figure 8.9 Calculated radius of curvature of the coupon as a function of time.

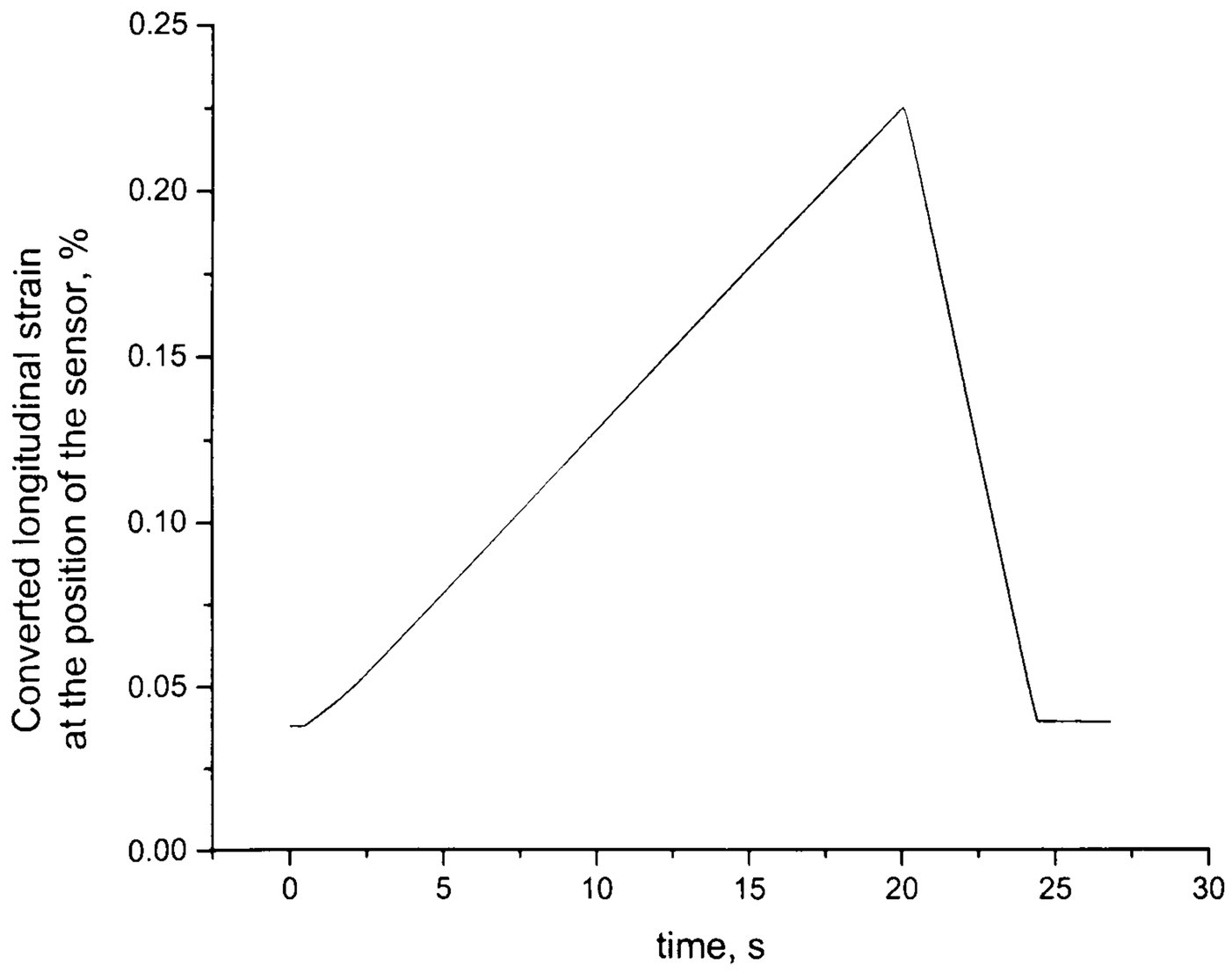

Figure 8.10 Converted longitudinal strain at the position of the embedded sensor as a function of time

The analysis carried out above was used to determine the longitudinal strain at the position of the sensor in the four-point bending tests (see Section 8.4). However, as an aside, the flexural modulus of the coupon can also be derived straightforwardly from this analysis. For a coupon subjected to a bending moment, M, the relationship between the flexural modulus, E, radius of curvature, R, and second moment of area, I_x, is:

$$E \cdot \frac{1}{R} = M \cdot \frac{1}{I_x} \tag{8.12}$$

Differentiation of both sides with respect to time gives:

$$E \cdot \frac{d\frac{1}{R}}{dt} = \frac{1}{I_x} \cdot \frac{dM}{dt} \tag{8.13}$$

A plot of $1/R$ verses time, t, is shown in Figure 8.11. Now, in the test considered here, $d(1/R)/dt$ is the gradient of the straight line in Figure 8.11 and dM/dt can be calculated from the gradient of load-time plot in Figure 8.8(b). The flexural modulus of the coupon can now be determined from equation (8.13) since $M=FL$, where F is half of the load signal in Figure 8.8(b), and L is the distance between the outer roller and inner roller. The measured flexural modulus in bending of the coupons with a lay-up of $(0/90_2/0/90_2/0)$ was found to be 32.5±1.0 GPa. This can be compared with the theoretical prediction of the flexural modulus of the laminate calculated using the method of Smith and Ogin (1999). In this analysis, the modulus is given by:

$$E = \frac{219E_1 + 139E_2}{343} \tag{8.14}$$

When $E_1 = 39$ *GPa* and $E_2 = 11$ *GPa*, then the predicted value is 28.9 *GPa*. The difference between the theoretical value and the experimental value is likely to

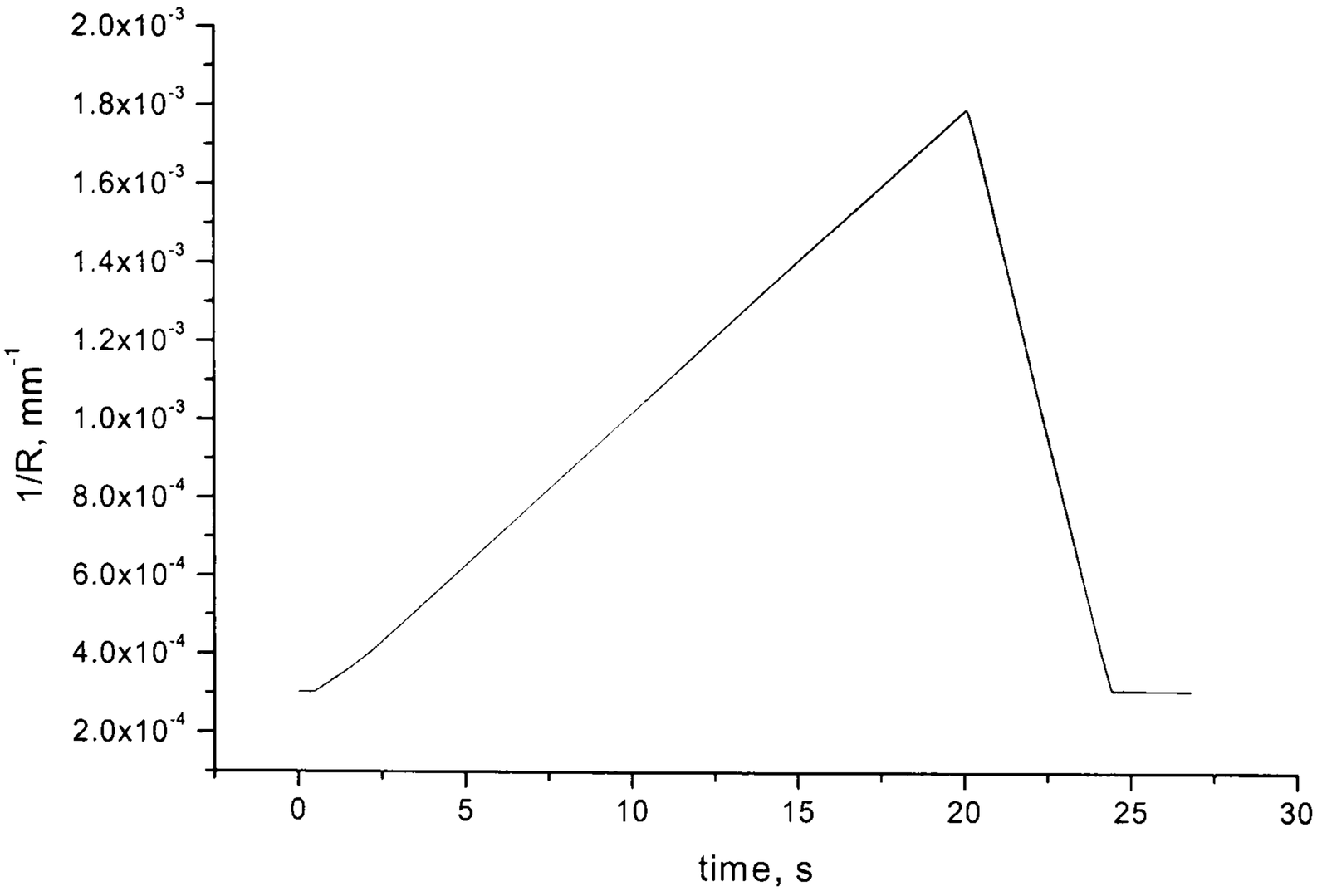

Figure 8.11. Reciprocal of the radius of curvature of the coupon as a function of time under four-point bending

because that the 0° plies and 90° plies do not have the same thickness as assumed in the prediction (the 0° plies are about 10% thicker than the 90° plies).

8.4. Crack detection in four-point bending tests on a double cross-ply laminate

This section describes crack detection experiments using a double cross-ply coupon tested in bending. When coupons cut from the laminate are under four-point bending, cracks develop in the 90° ply which is under tension. Firstly, the response of the embedded polarimetric sensor under bending is discussed.

8.4.1 Basic response of the embedded polarimetric sensor under four-point bending

Sensors were embedded in two positions in the laminate, either in the outer 0° ply near the surface at the 0/90 interface or in the central 0° ply, near a 0/90 interface. During all the tests, the extensometer was attached to the top (i.e. concave) surface of the coupon, as discussed in Section 8.3. In the four-point bending tests, when the sensor was above the neutral axis, the sensor was put into compression. With the

coupon inverted so that the sensor was below the neutral axis, the sensor was, of course, put into tension during loading. As will be seen below, in both circumstances, optical fringes were obtained even though the shapes of the fringes were different.

Figure 8.12 shows the response of the polarimetric sensor to four-point bending tests under quasi-static load. The sensor in the figure was positioned outside of the lower 90° ply. The response of the sensor when the sensor was below the neutral axis is shown in Figure 8.12(a) and Figure 8.12(b). In this case, the sensor is loaded in longitudinal tension. Figure 8.12(a) shows the optical fringes from the sensor when the optical signal is plotted against the strain signal generated by the extensometer. The specimen has been loaded, so that the extensometer strain increases from 0% (no load) to about -1% and then unloaded to 0% extensometer strain again. With the sensor below the neutral axis, the sensor is, of course, loaded in longitudinal tension. About 13 fringes are produced and the fringes are reproducible, with minor variations, for loading and unloading. Figure 8.12(b) shows the optical fringes obtained when the optical output is plotted against the strain at the position of the sensor calculated using the analysis in Section 8.3.3. By inverting the coupon, the same embedded sensor could be tested positioned above the neutral axis i.e. it was now loaded under longitudinal compression. The optical fringes obtained in this case when the optical signals are plotted against the strain from the extensometer are shown in Figure 8.12(c) and when plotted against the strain at the position of the sensor are shown in Figure 8.12(d). The optical fringes are similar to the fringes recorded when the sensor was in tension. For completeness, the same coupon was loaded under simple quasi-static tensile loading, and the fringes as a function of strain are shown in Figure 8.12(e).

The strain in the 0° ply changes with the distance from the neutral axis and so does the strain in the optical core of the embedded sensor. For the sensor shown in Figure 8.12, the sensitivity of the sensor when the sensor was under tension in four-point bending was 250 ± 5 rad/mm; under compression in four-point bending, the value was 214 ± 5 rad/mm; and under quasi-static tensile load the value was 238 ± 5 rad/mm.

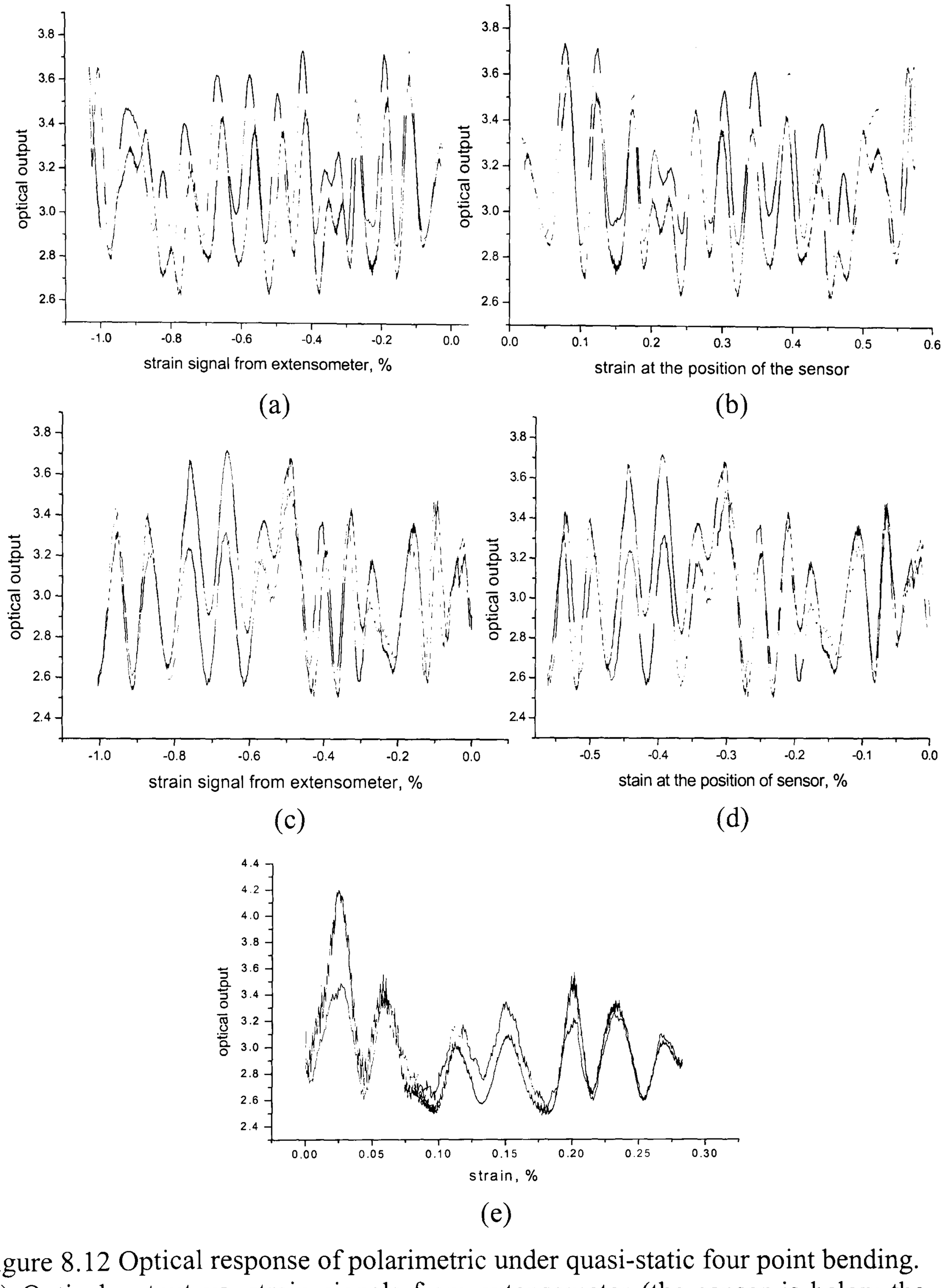

Figure 8.12 Optical response of polarimetric under quasi-static four point bending.
(a) Optical output vs. strain signals from extensometer (the sensor is below the neutral layer).
(b) Optical output vs. strain at the position of the sensor (the sensor is below the neutral layer).
(c) Optical output vs. strain signals from extensometer (the sensor is above the neutral layer).
(d) Optical output vs. strain at the position of the sensor (the sensor is above the neutral layer).
(e) Optical output vs. strain in quasi-static tensile test.

The sensitivities of the sensor are unlikely to be the same when the sensor is loaded in different circumstances, although the precise reason for the differences here is unclear

With regard to crack detection, it was founded experimentally that when tested in bending, the true strain at the position of the sensor had reached 0.6% before any cracks occur for the sensors embedded in the lower set of 0° plies, near the 0/90 interface. This is the upper limitation of the strain to remain the embedded sensor unbroken. Hence, when the sensor is used to detect transverse cracks, as discussed in Section 8.4.2, the sensor is always positioned in the central 0° ply, near the lower 0/90 interface.

Although not used in the crack detection experiments here, it has been demonstrated in further experiments that the polarimetric sensor can be used in fatigue tests in four-point bending. Some results are shown in Figure 8.13. The fatigue machine was controlled using position control mode and the load signal and optical signal for a short fatigue test (duration 10 seconds) are plotted against time in Figure 8.13(a). A magnification of Figure 8.13(a), between 8 seconds and 12 seconds, is shown in figure 8.13(b). The fatigue machine was run at 1 Hz with the actuator moving from the unloaded position of the specimen between 3 mm and 9 mm in compression, with a mean position of 6 mm in compression, and a saw-tooth control waveform. The machine first ramped the position to 6 mm (equivalent to a compressive load of about -0.3 kN) over the first 5 seconds and then cycled the position between 3 mm and 9 mm at 1 Hz for the next 10 seconds, before unloading over the following 5 seconds.

As can be seen in Figure 8.13(a), the frequency of the optical fringes increases dramatically during the cyclic part of the tests. Figure 8.13(b), showing 4 seconds of cycles, indicates that there are approximately $1\frac{1}{4}$ fringes for each 1/2 of the saw-tooth loading cycle and that the fringes are reasonably reproducible. When the optical signals are plotted against the strain at the position of the sensor (rather than against

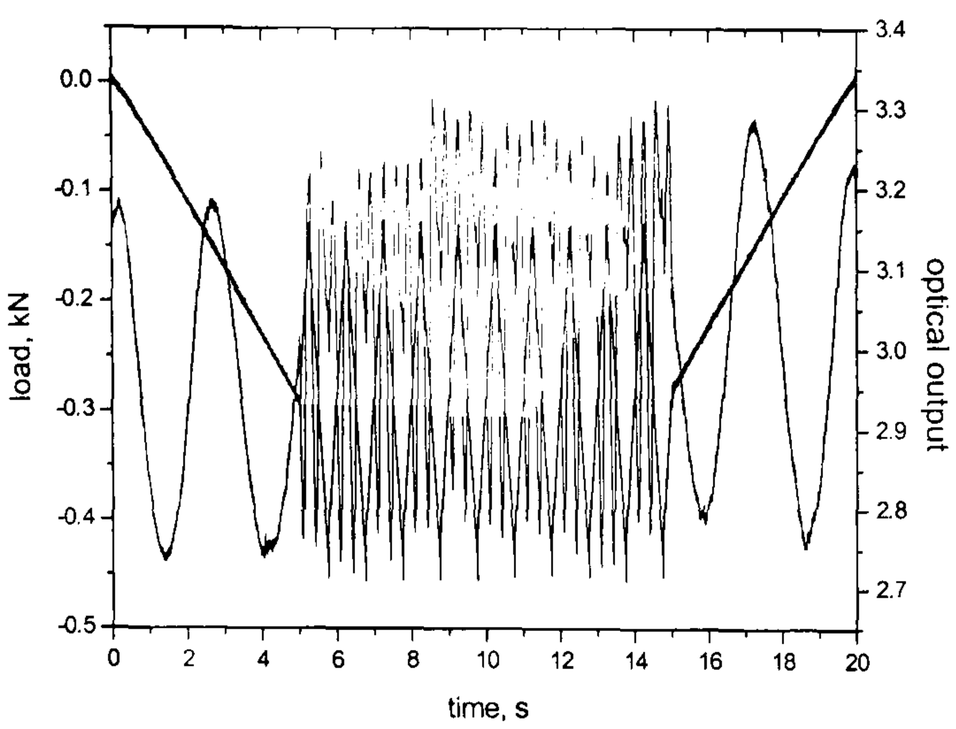

(a)

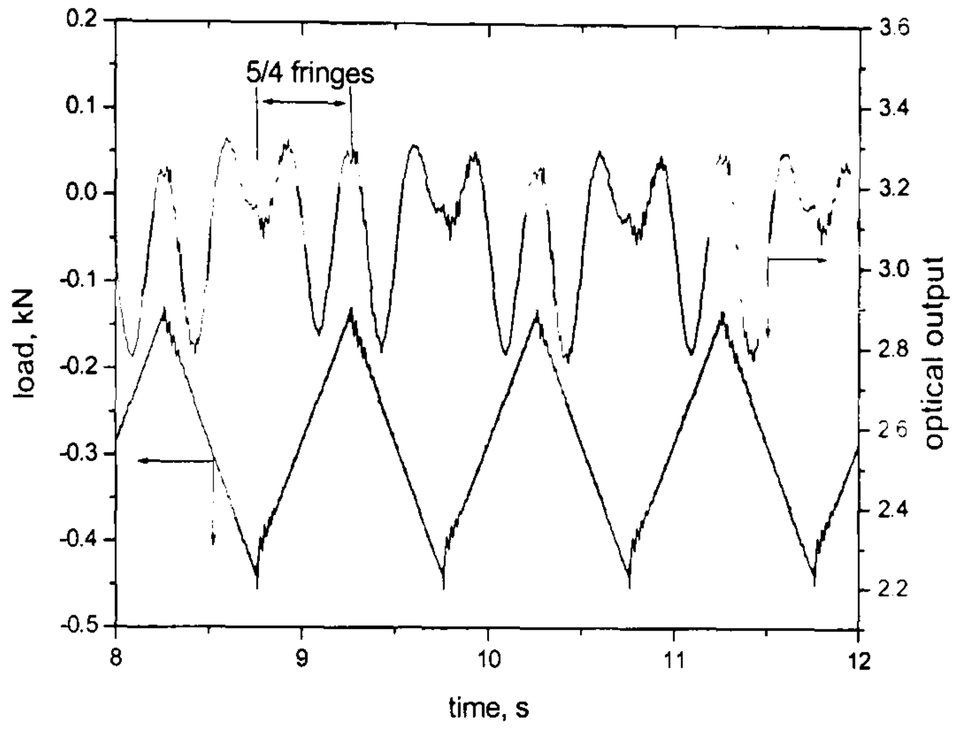

(b)

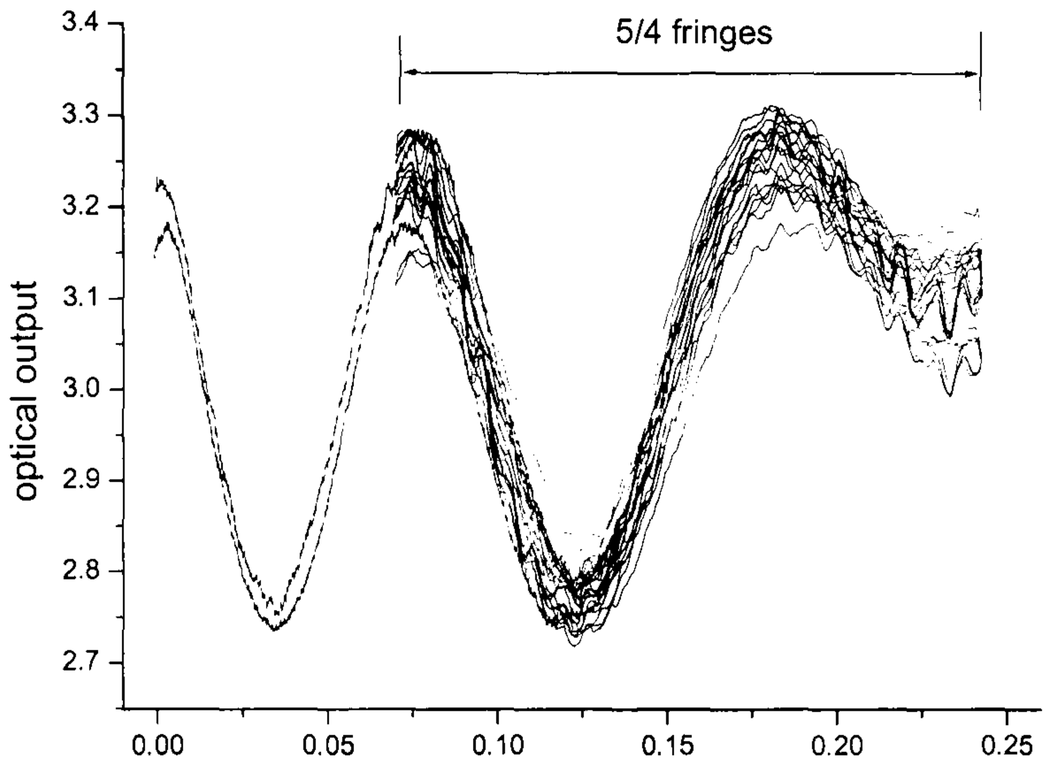

(c)

Figure 8.13 Optical response of polarimetric under fatigue four point bending test.
(a) Optical output vs. time and load signal vs. time in a fatigue four-point bending test.
(b) Optical output vs. time and load signal vs. time in a fatigue four-point bending test (from 8 seconds to 12 seconds).
(c) Optical output vs. strain at the position of the sensor in a fatigue four-point bending test.

time), the expected reproduction of fringes is obtained (see Figure 8.13(c)). These tests demonstrate that the polarimetric sensor could be used to monitor strain changes for four-point bending fatigue tests.

8.4.2. Crack detection in four-point bending using the polarimetric sensor

It was found here in early experiments that under quasi-static four-point bending load, the cracks initiate from one edge of the coupon and propagate slowly across the whole

width of the coupon with increasing load. Additionally, the first cracks always initiate near the rollers. When a crack forms in bending in these coupons, the maximum crack opening would be expected to occur near the outer 0° ply near the 0/90 interface and a smaller crack opening at the inner 0/90 interface, as shown schematically in Figure 8.14.

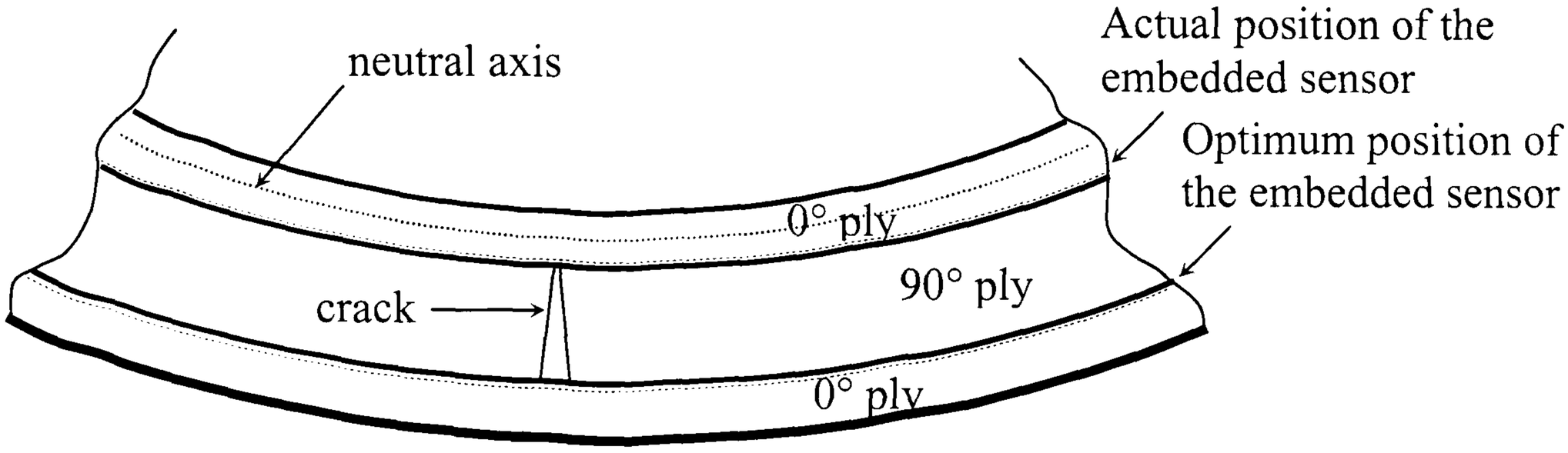

Figure 8.14 A schematic graph showing the difference of change of strain between upper 0/90 interface and lower 0/90 interface

To detect a transverse crack which develops in four-point bending, the optimum position to embed a sensor would therefore be to put the sensor in the 0° ply near the outer 0/90 interface, as shown in Figure 8.14. However, as discussed in Section 8.4.1, the sensor had to be embedded near the inner 0/90 interface to remain unbroken at the strains when the cracks developed (marked as the actual position in Figure 8.14). As a consequence, the step-change in optical signal induced by the crack is expected to be relatively small. Further as explained in Section 8.3.4, to monitor the strain in four-point bending effectively, the extensometer had to be attached to the upper surface of the coupon. Hence the strain fluctuation induced by crack formation is unlikely to be detected, or if detected, is likely to be small.

A typical experimental result when a crack forms is shown in Figure 8.15. Figure 8.15(a) shows a relatively difficult to interpret step-change in optical signal, which occurs at about 24.9 seconds, and is only just greater than the background noise. The strain signal during this time scale is plotted in Figure 8.15(a) as well. Due to the position of the extensometer, which is positioned at the concave face of the coupon,

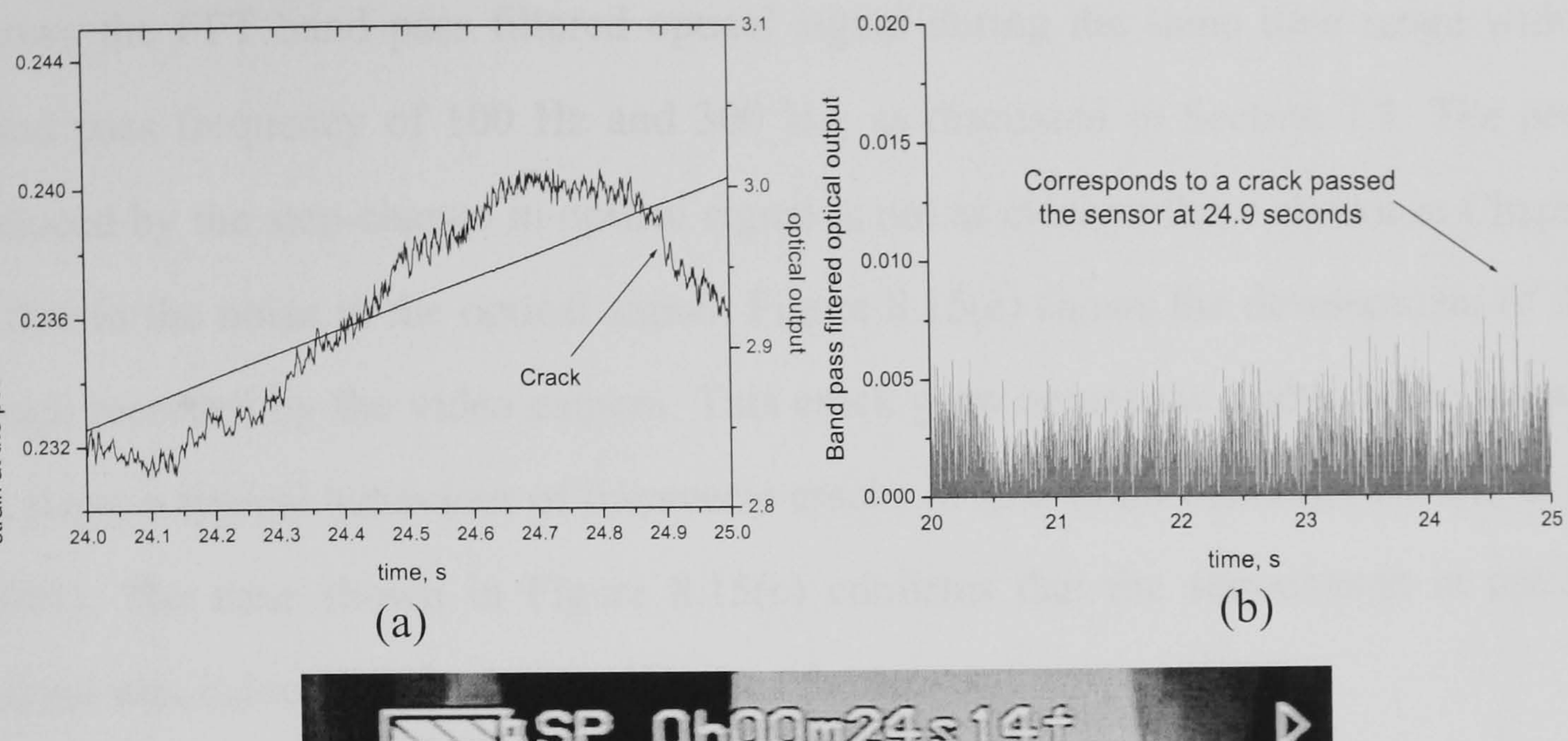

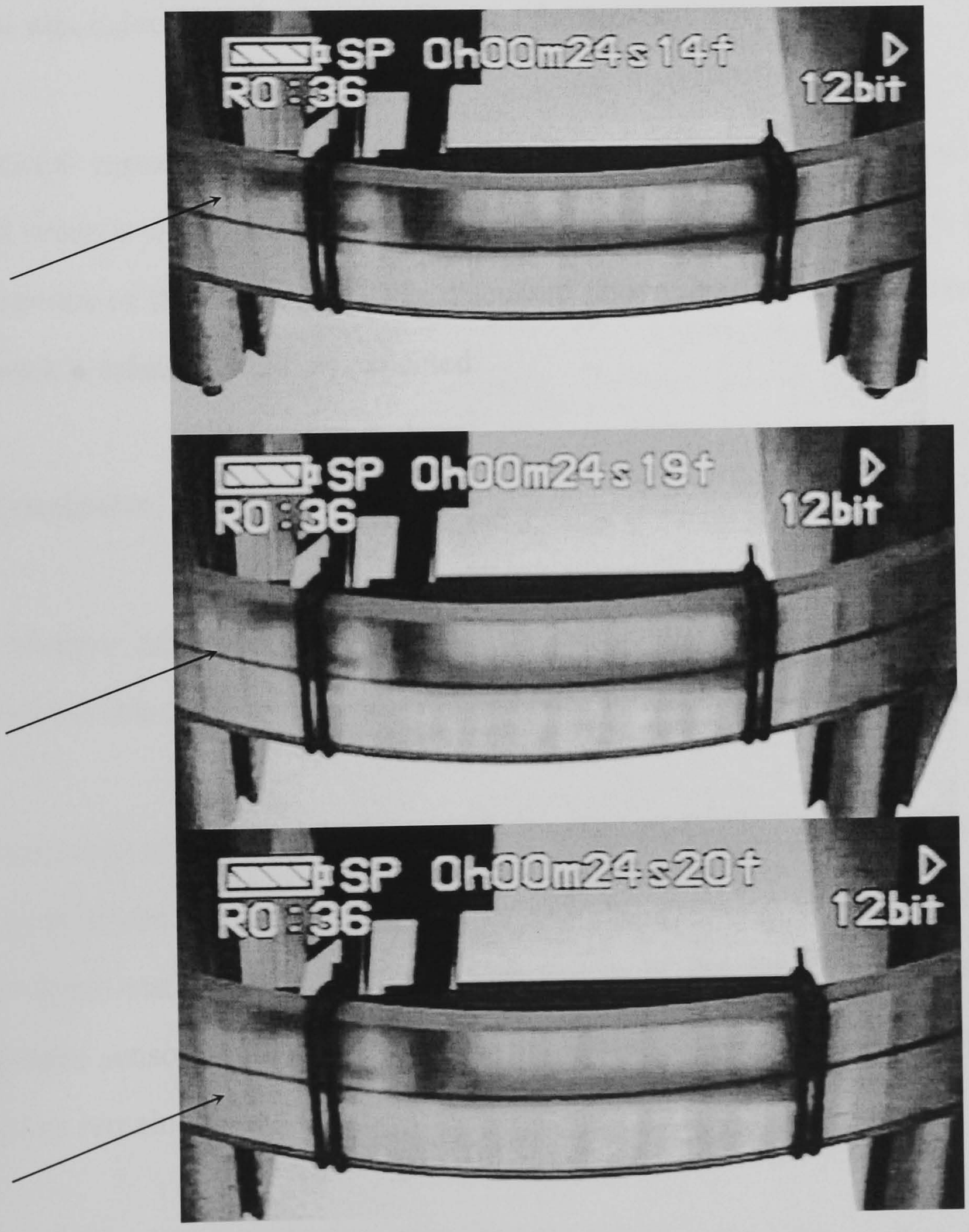

(c)

Figure 8.15 Crack detection in four-point bending with video images. The arrow shows that position of the growing crack

the fluctuations in the strain signal can not be detected in the plot. Figure 8.15(b) shows the FFT band pass filtered optical signal during the same time range with a band pass frequency of 100 Hz and 300 Hz, as discussed in Section 7.3. The peak induced by the step-change in optical signal is not as clear as those shown in Chapter 7 due to the noise in the optical signal. Figure 8.15(c) shows the development of the crack recorded by the video camera. This crack grew across the width of the coupon in steps, a typical behaviour of transverse cracks in four-point bending (Ussorio et al, 2003). The time shown in Figure 8.15(c) confirms that the step-change in optical output was induced when the crack passed the sensor.

Additional experimental data are shown in Figure 8.16. The strain signal and optical signal when a crack occurred are plotted in the Figure. Unsurprisingly, there are no fluctuations of the strain signal, as discussed above, and the step change induced by the crack is relative small, as expected.

8.5 Conclusion

This chapter has described further crack detection experiments using polarimetric sensors but this time with the sensors embedded in a double cross-ply laminate

The necessity of the sensor being adjacent to matrix cracking damage in order for the cracks to be detected has been shown by experiments using double cross-ply coupons under quasi-static tensile loading. Only cracks in the set of 90° plies next to the embedded sensor could be detected by the sensor. Cracks induced in the other set of 90° plies remained undetected.

The same double cross-ply configuration was also used to show that a polarimetric sensor can be employed to monitor strain changes in four-point bending tests, both under quasi-static load and fatigue load.

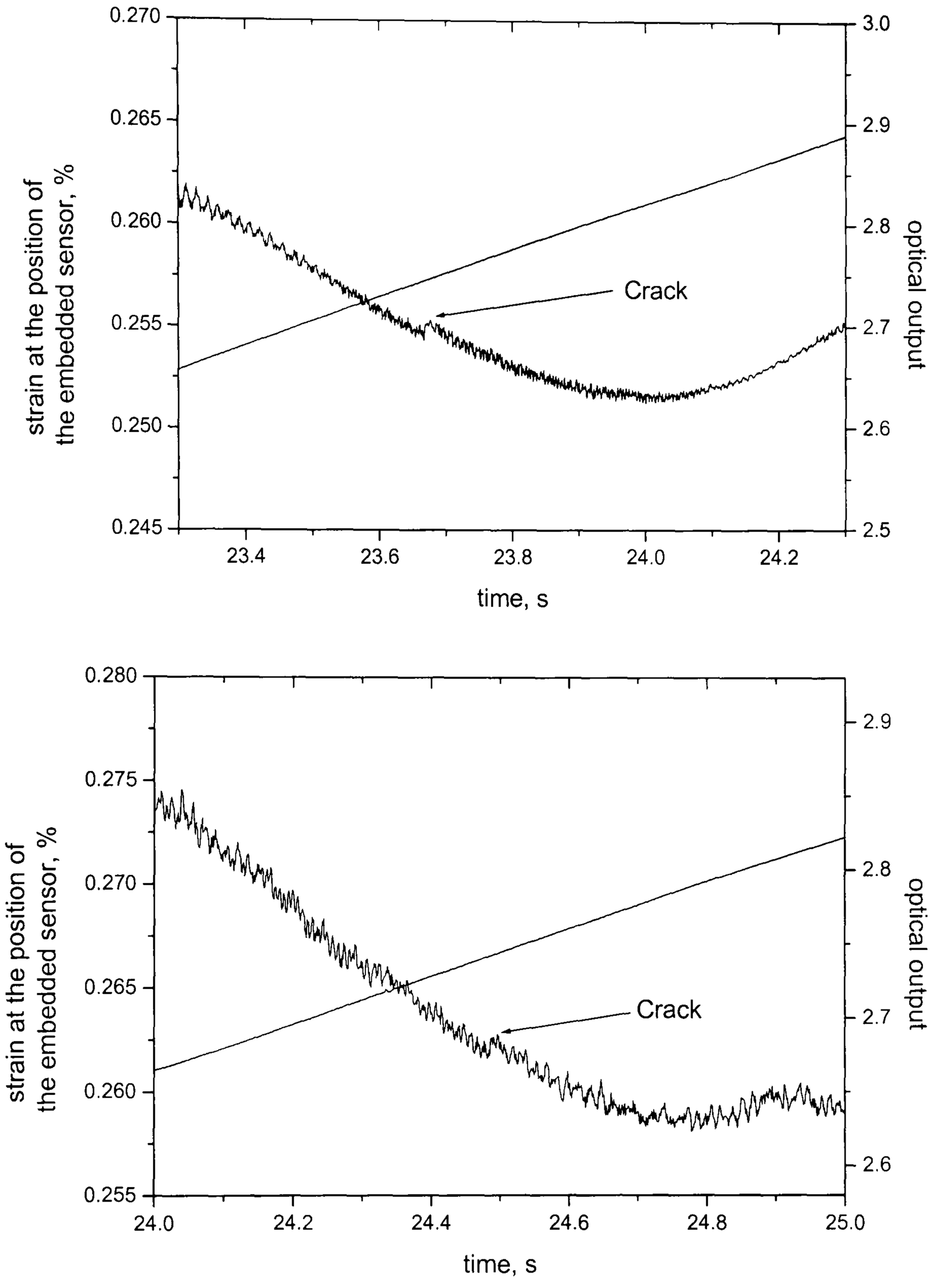

Figure 8.16 Further experimental data of crack detection in four-point bending tests.

Finally, it has been shown that the sensor can be used to detect transverse cracks induced during quasi-static four-point bending tests. In particular the strain at the position of the embedded sensor can be obtained in real time, after a suitable conversion of the strain signal obtained from an extensometer positioned on the upper surface of the coupon (the concave surface during the bending test).

In the next chapter (Chapter 9), the determination of the strain-optical parameters of the sensor will be described, which are needed for the theoretical modelling in Chapter 10.

Chapter 9. Determination of strain-optical parameters of the polarimetric sensor

9.1 Introduction

The ability of the embedded polarimetric sensor to detect cracks has been discussed in detail in Chapter 6, 7 and 8. It has been shown that the sensor can detect the cracks that pass adjacent to the sensor and the sensor has the potential to be used as a real-time sensor for damage detection in engineering applications.

In order to carry out a theoretical treatment of the polarimetric sensor, it is necessary to utilise a suitable theoretical model. Such a model was proposed by Sirkis (Sirkis and Lo, 1994). To use this model to predict the interaction between the polarimetric sensor and a crack passing it, some essential parameters of the model must be obtained first for the type of fibre used in this work.

The model used by Sirkis connects the phase change seen by the sensor to the strain experienced by the optical fibre core:

$$\Delta\varphi = \frac{2\pi}{\lambda}\int_L [K_1\varepsilon_1 + K_2\varepsilon_2 + K_3\varepsilon_3]dL \qquad 9.1$$

where $\Delta\varphi$ is the relative phase change between the two polarisation modes caused by the three-dimensional strain; λ is the wavelength of light in vacuum; ε_1, ε_2 and ε_3 are the three normal strains, where the axis-1 is parallel to the length of the sensor; L is the gauge length of the sensor and K_1, K_2 and K_3 are the dimensionless parameters to be determined which govern the contribution of each component of the normal strains

to $\Delta\varphi$. The K values can be determined experimentally by tension and compression tests of bare sensors. These measurements have been carried out using a modification of the method used by Sirkis (Lo and Sirkis, 1995).

9.2 Tension test of free sensor

The free sensors tested here have had the coating removed, which is also the situation for the embedded sensors. The test methods for the sensors are described in Section

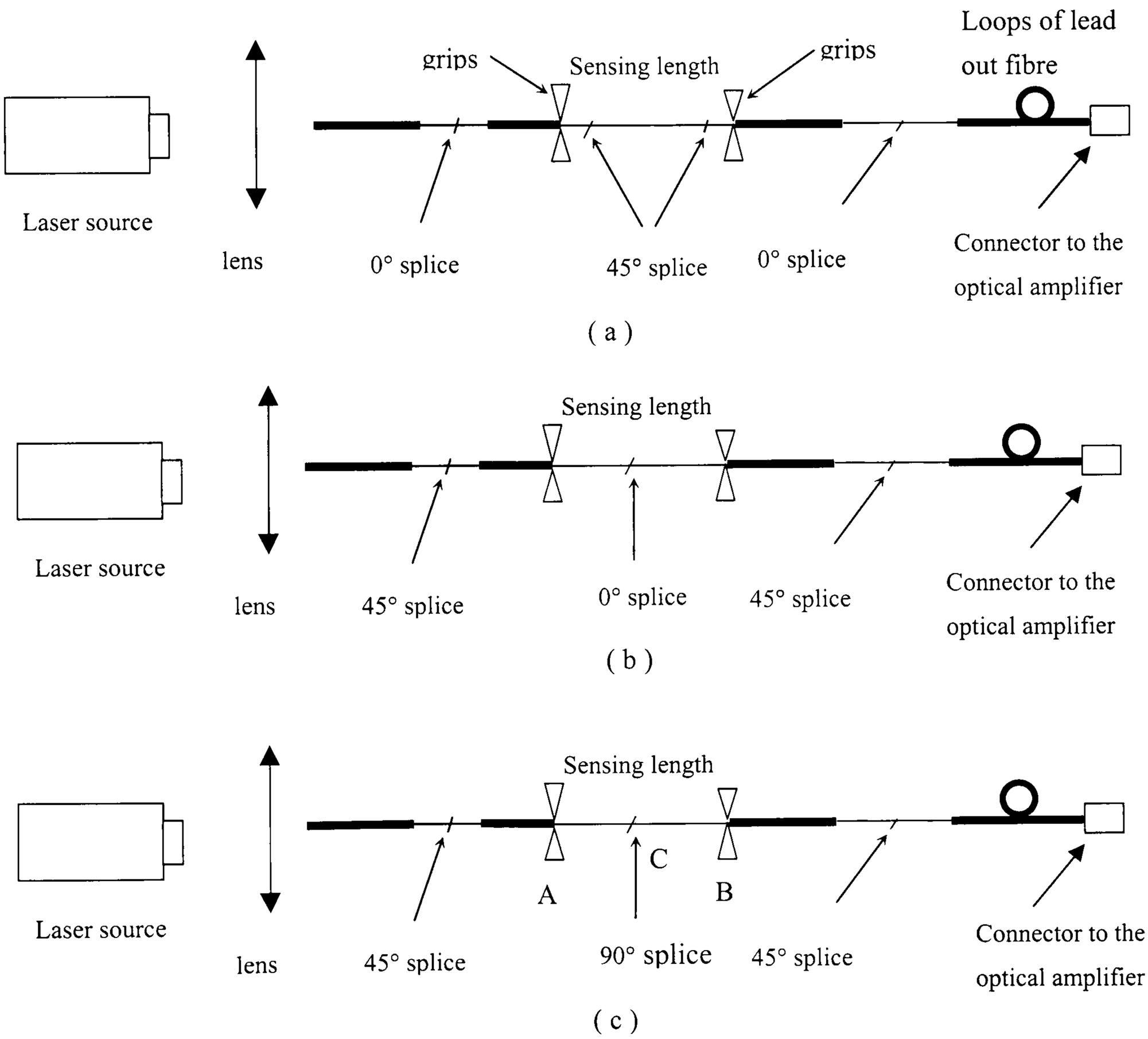

Figure 9.1 Different structures of free sensors

(a) 45° splices inside grips;

(b) 45° splices outside grips, 0° splice inside grips;

(c) 45° splices outside grips, 90° splice inside grips.

4.5.2 and their configurations are shown in Figure 9.1. In the figure, thicker lines represent optical fibres with coatings (inner coating and jacket), thinner lines represent stripped bare fibres (without any coating). Strains were calculated by dividing displacements measured between the two grips by the original fibre length between the grips. These displacements could be measured to an accuracy of 0.02 mm by a micro-screw knob, see Figure 4.10.

The structure of the polarimetric sensor shown in Figure 9.1(a) is the same as the polarimetric sensor embedded in the cross-ply laminates described in Section 6.2. The whole gauge length of the sensor is under strain, which means the gauge length of the sensor is shorter than the total length of the optical fibre under strain. Figure 9.2 shows some typical optical fringes obtained from polarimetric sensors with this type of structure. The fringes are shown as a function of time and although the displacement was controlled manually (and hence the frequency of the fringes is not constant), clear fringes are obtained from the sensors.

The relationship between the longitudinal and transverse strains to the phase difference, $\Delta\varphi$, of the optical output can be obtained from these data.

The longitudinal phase sensitivity of a bare fibre, S_{axial}, is defined as:

$$S_{axial} = \frac{1}{L}\frac{\Delta\varphi}{\Delta\varepsilon_1} \qquad 9.2$$

where L is the gauge length of a sensor, $\Delta\varphi$ is the change of phase and $\Delta\varepsilon_1$ is the longitudinal strain change. The transverse strains of a free sensor are given by:

$$\varepsilon_2 = \varepsilon_3 = -\nu_f \varepsilon_1 \qquad 9.3$$

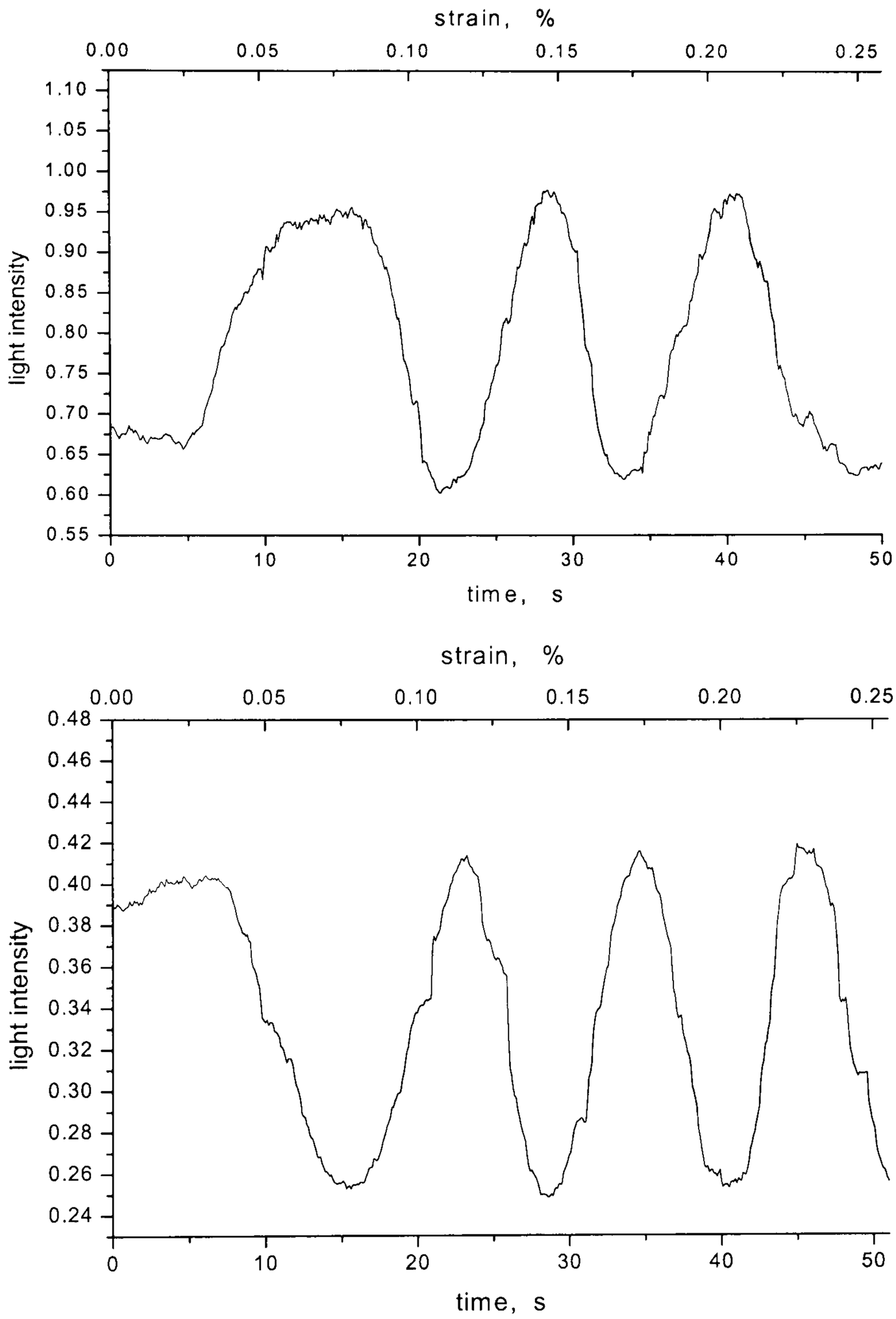

Figure 9.2 Experimental results of free polarimetric sensor with structure shown in Figure 9.1(a).

where ε_2 and ε_3 are transverse strains (as seen by the optical fibre's core), and ν_f is the Poisson's ratio of the optical fibre which is 0.154 . Combining with equation 9.1, the phase difference between the two modes in the core as a result of the applied longitudinal strain is:

$$\Delta\varphi = \frac{2\pi}{\lambda}\int_L [K_1\varepsilon_1 + K_2\varepsilon_2 + K_3\varepsilon_3]dL = \frac{2\pi}{\lambda}L\varepsilon_1(K_1 - \nu_f K_2 - \nu_f K_3) \qquad 9.4$$

Substituting equation 9.4 into equation 9.2, the longitudinal axial strain sensitivity becomes:

$$S_{axial} = \frac{1}{L}\frac{d(\varphi)}{d\varepsilon_1} = \frac{2\pi}{\lambda}(K_1 - \nu_f K_2 - \nu_f K_3) \qquad 9.5.$$

Here, λ, ν_f, K_1, K_2 and K_3 are constants which depend on the laser source and characteristics of the optical fibre. The measured longitudinal strain sensitivity of the sensor was 106 ± 2 rad/mm, where the uncertainty is given by the standard deviation. This result was obtained from 5 experimental measurements. The complete results, showing sensor gauge length and measured sensitivity, are shown in Table 9.1.

Table 9.1 Experimental sensitivities for free sensor with the structure shown in Figure 9.1a

Sensor No.	Gauge length of the sensor (mm)	Longitudinal axial strain sensitivity (rad/mm)
1	120	102.7
2	102	108.7
3	115	105.4
4	117	104.4
5	112	106.8
average	106	
Standard deviation	2	

Figure 9.3 shows an experimental result from a free sensor with the structure shown in Figure 9.1(b) where the 45° splices were outside the grips. Here the sensor's gauge length between the two 45° splices was approximately 1000 mm, much longer than the length over which the strain was applied (approximately 185 mm). Hence only part of the sensor gauge length was subject to external strain, but optical fringes could still be obtained because the phase difference induced by the applied strain within the

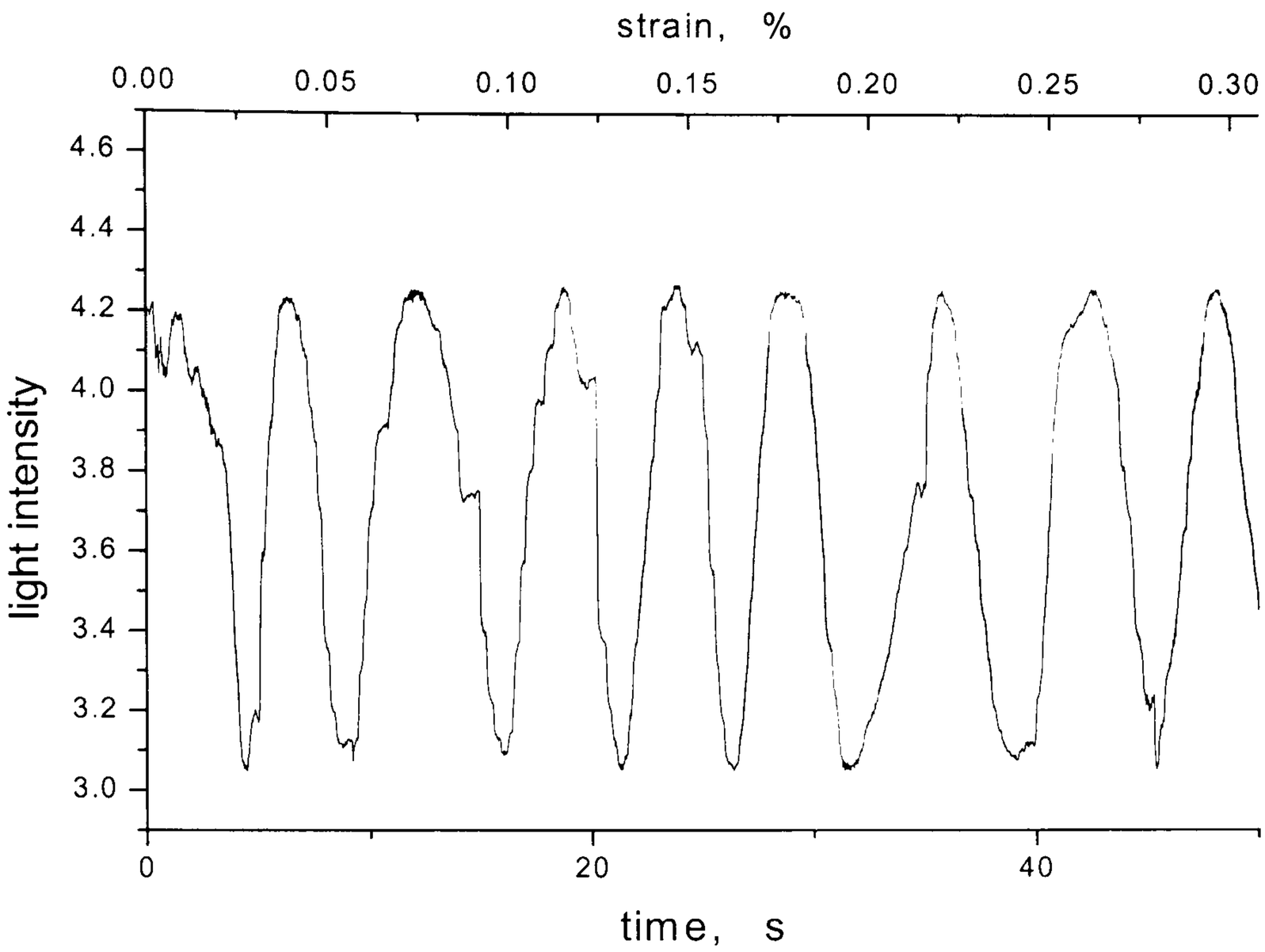

Figure 9.3 Experimental results of free polarimetric sensor with structure shown in Figure 9.1(b).

grips is carried by the sensor unchanged to the second splice where the optical fringes were generated. Typical fringes are shown in Figure 9.3 and the sensitivity of this sensor was measured as 113 ± 2 rad/mm from 5 experiments. The difference between the sensitivities measured in the configurations of Figure 9.1(a) and 9.1(b) might be caused by the abnormal strain state around the grips in the latter case.

The experimental arrangement shown in Figure 9.1(c) is rather unusual and has been used here only to confirm the operation of the sensor. Here, a 90° splice has been situated half-way between the two grips. When this type of sensor is under uni-axial strain, the phase difference between the fast mode and the slow mode induced by the applied strain between the grip A and the central 90° splice (point C in Figure 9.1(c)) is $\Delta\varphi_1$. At the 90° splice, the fast mode and the slow mode are interchanged, meaning that light previously propagating in the fast mode will now propagate in the slow mode and vice versa. After the 90° splice, the phase difference between the fast mode

and the slow mode will be $\Delta\varphi_2$, but since the 90° splice has been positioned centrally between the grips, then $\Delta\varphi_2 = -\Delta\varphi_1$. Hence, the overall phase difference induced by a uniform longitudinal strain should be zero. Typical results for a sensor subject to a strain of about 0.30% in a time of 40 seconds are shown in Figure 9.4. There were no fringes in the optical output, as expected and only noise was recorded. A polarimetric sensor of this structure is called a "self-compensated sensor" (Bock et al, 1989). Any uniform fluctuation of temperature along the sensor length or unwanted fringes from a uniform strain can be cancelled in this way.

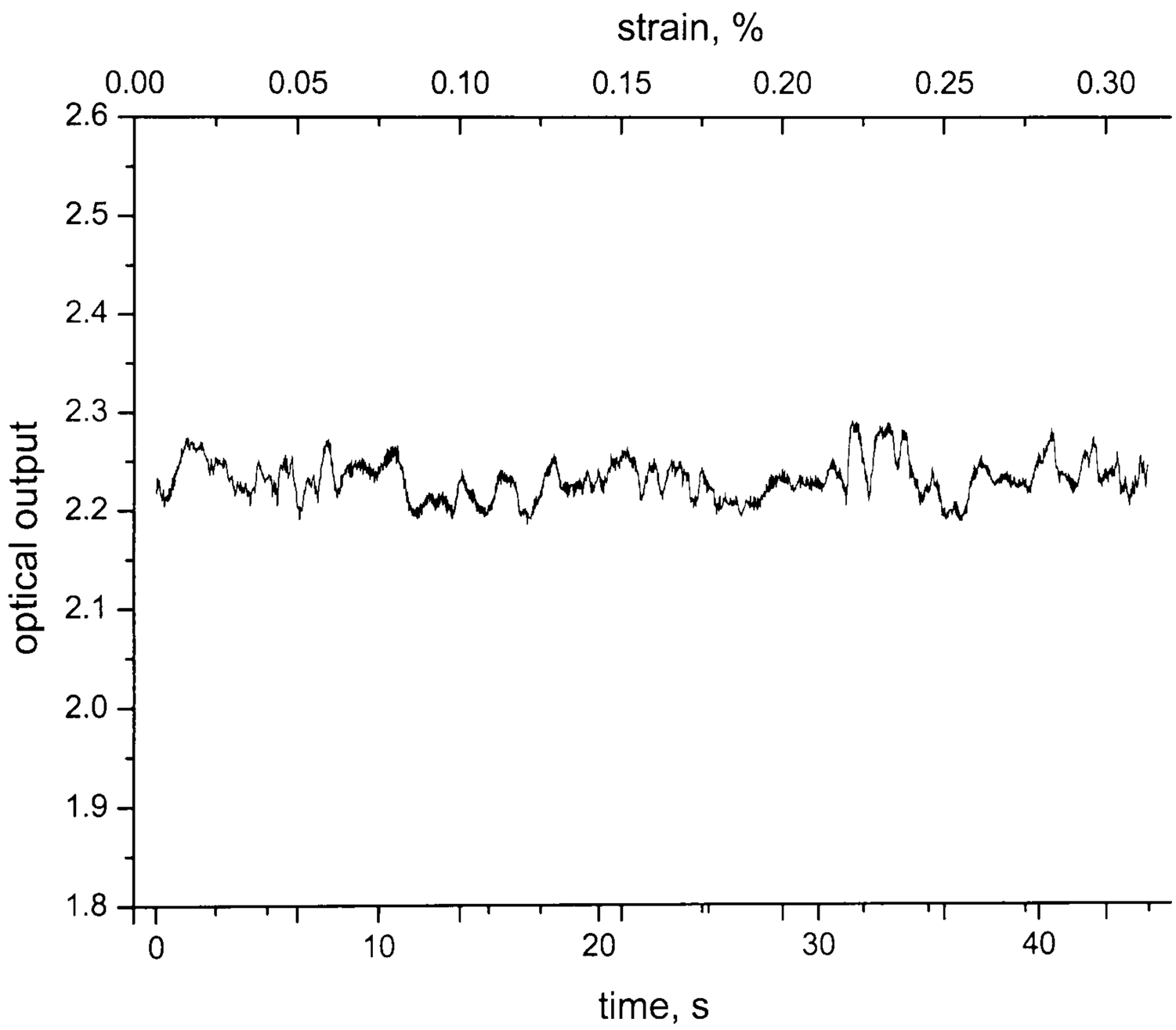

Figure 9.4 Optical output of a "self-compensated sensor" with the structure shown in Figure 9.1(c)

9.3 Transverse compression test of bare polarimetric sensor

To obtain the K values (K_1, K_2 and K_3), three independent equations are required. Equation 9.5 mentioned previously is one valid equation. To calculate the K values,

two more equations are required. The equations can be achieved by transverse compression tests on a bare fibre polarimetric sensor.

When a bare fibre polarimetric sensor is under transverse compression load, the longitudinal strain in the optical core is assumed to be zero (Timoshenko, 1982). The relationship between the strains in the optical fibre and the applied load can be obtained from elasticity solutions for a rod of diameter d, under diametrical compression by an average load P (Timoshenko, 1982), which are:

$$\varepsilon_2^L = \frac{1}{E}\left[(1-\nu^2)\frac{2P}{\pi d} - \nu(1+\nu)(-\frac{6P}{\pi d})\right]$$
$$\varepsilon_3^L = \frac{1}{E}\left[(1-\nu^2)(-\frac{6P}{\pi d}) - \nu(1+\nu)\frac{2P}{\pi d}\right] \qquad 9.6$$

where ${\varepsilon_2}^L$ and ${\varepsilon_3}^L$ are transverse strains (note: ${\varepsilon_2}^L$ is in direction of loading) in the rod, E is the Young's modulus and ν is the Poisson's ratio of the rod. P is load per unit length on the rod and is defined as:

$$P = \frac{F}{L} \qquad 9.7$$

where F is the force on the rod and L is the length of the rod under compression.

When the optical sensor is rotated, as shown schematically in Figure 9.5, the relative orientation of the stress rods to the loading direction will change and hence also the optical axes of the sensor. Consequently, the strain state in the optical core will change with the rotation of the fibre and, for this transverse compression test, sensitivity of the sensor will change with rotation of the sensor.

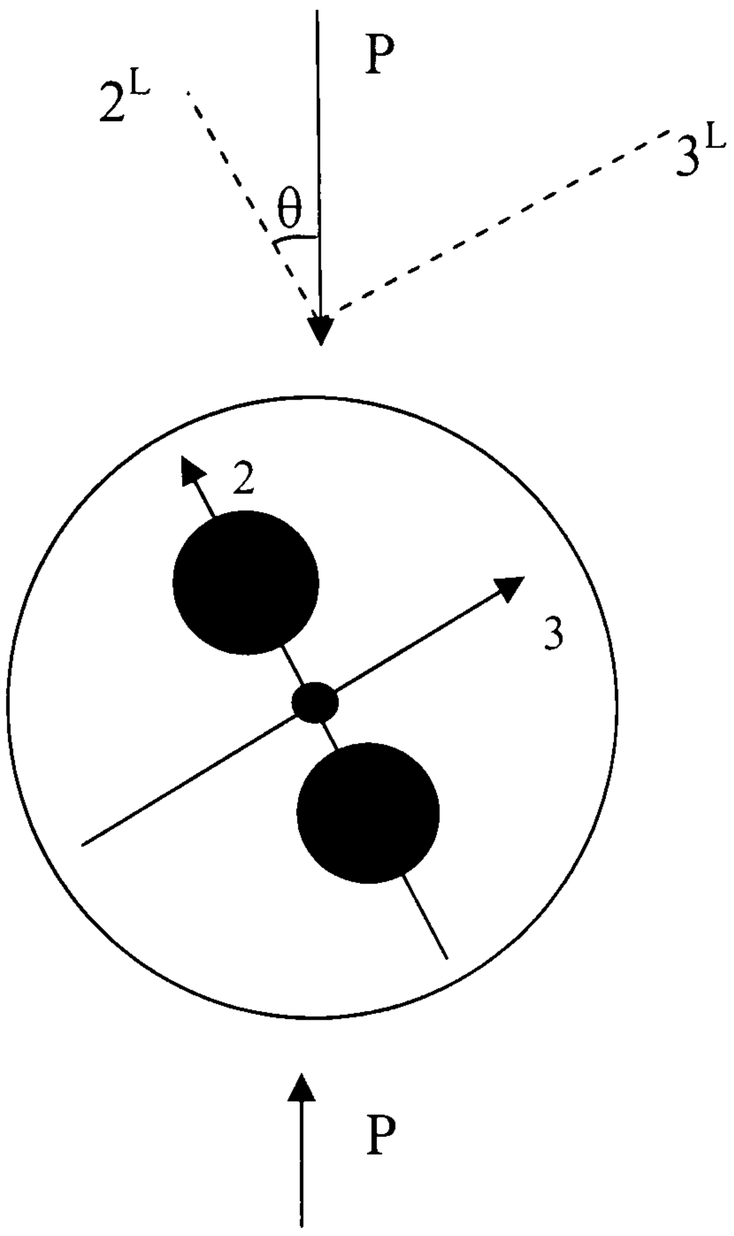

Figure 9.5 A schematic diagram showing the transverse loading direction and the optical axes of the optical sensor.

The experimental arrangement for the transverse compression tests was described in Section 4.5.3. Figure 9.6 shows two optical fringes from the same sensor with different sensitivities under compression. The sensor has been rotated through 30° in Figure 9.6(b) compared to Figure 9.6(a). A clear optical change induced by each step of manual loading can be seen in the two sets of results. Of course the whole fringe is much less regular than that shown in Figure 9.2 or Figure 9.3 due to the manual loading. There were about 10 seconds of unchanging optical signals between the loading and unloading fringes in Figure 9.6, corresponding to a time gap between loading and unloading of the weights (see Section 4.5.3 for experimental details).

The transverse sensitivity of the sensor under compression can be defined as:

$$S_{trans} = \frac{1}{L}\frac{\Delta\varphi}{\Delta P} \qquad 9.8$$

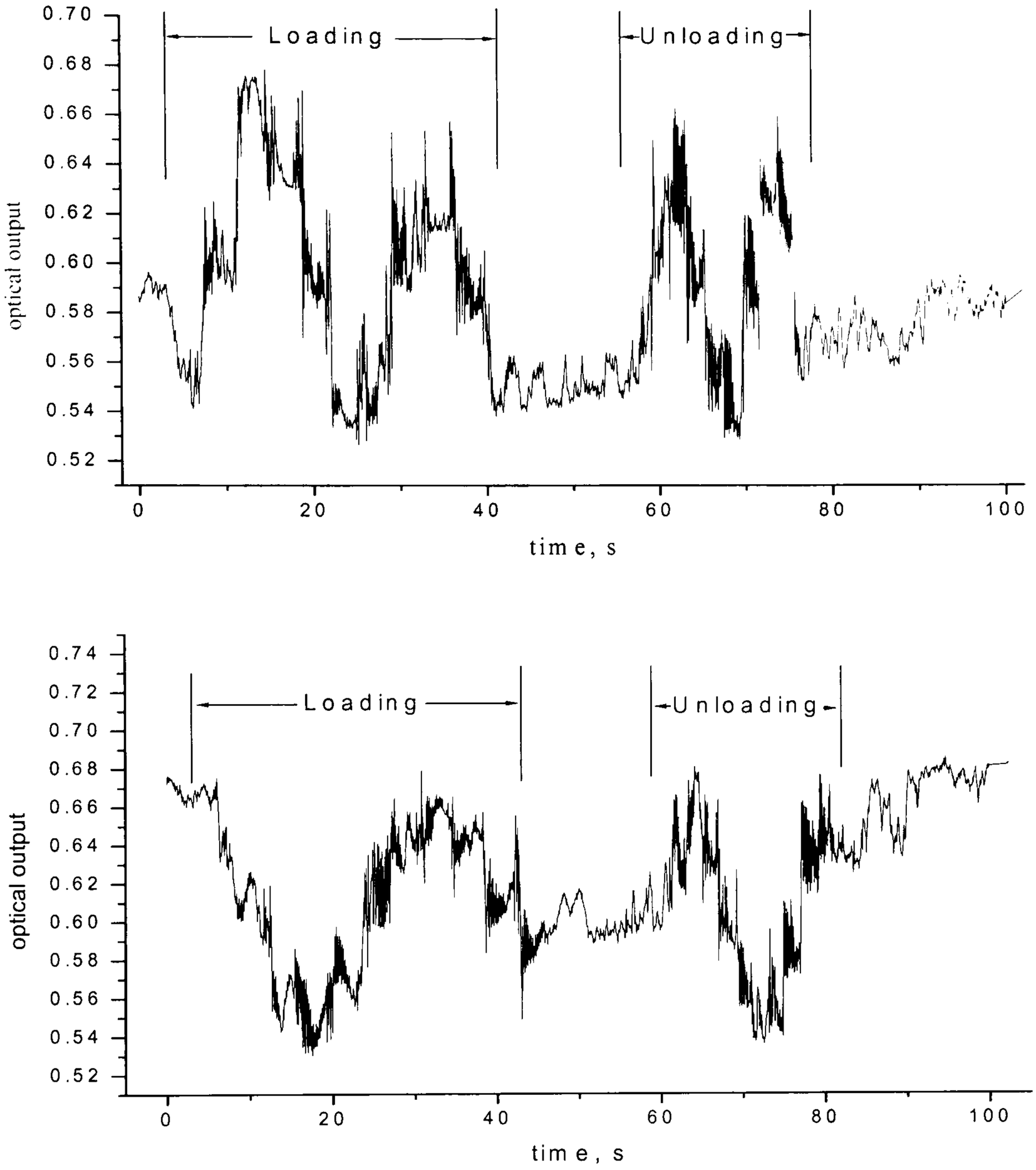

Figure 9.6 Optical fringes of a bare sensor under compression.

where ΔP is the change of load per unit length on the sensor, $\Delta\varphi$ is the phase change induced by ΔP and L is the length of the sensor under transverse compression.

The results showing the change of sensitivity with compression orientation, θ (as shown in Figure 9.5) are plotted in Figure 9.7. The sensitivity as a function of angle θ shows four peaks, which means that the sensor is more sensitive when loaded parallel to the optical axes. This variation in sensitivity with angle is similar to the results from a bow-tie fibre polarimetric sensor tested in transverse compression by Lo and

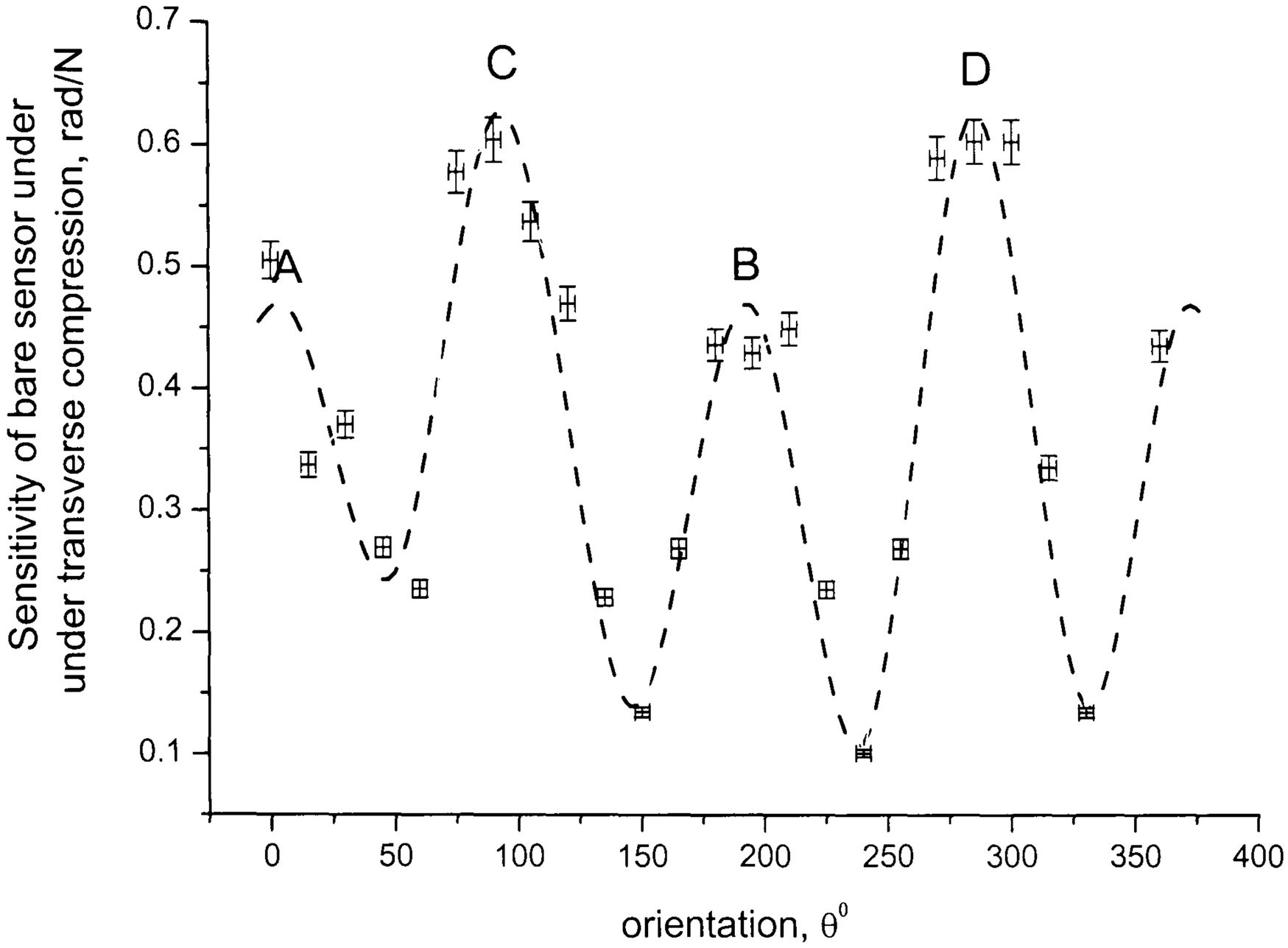

Figure 9.7 Compression sensitivity as a function of orientation.

Sirkis (1995). Peaks labeled A and B correspond to angles of 0 and π. Peaks labeled C and D correspond to angle of $\pi/2$ and $3\pi/2$. The trend of the data is indicated by the dashed line.

9.4 Derivation of the strain-optical parameters, K_1, K_2 and K_3

The results from the compression tests can be used in conjunction with equation 9.5 to find the values of K_1, K_2 and K_3.

If the longitudinal strain is taken as zero for transverse compression tests of the sensor and substitute equation 9.1 into equation 9.8, the transverse sensitivity of the sensor is:

$$S_{trans} = \frac{1}{L}\frac{\Delta\varphi}{\Delta P} = \frac{2\pi}{\lambda}(\varepsilon_2 K_2 + \varepsilon_3 K_3) \qquad 9.9$$

where ε_2 and ε_3 are strains in directions 2 and 3 in optical fibre core, as shown in Figure 9.5.

When the sensor rotates by an angle θ relative to the applied transverse compression load direction and the angle θ (as shown in Figure 9.5) is 0 or π, the strains in the optical axis direction-2 and optical axis direction-3 in the core are:

$$\begin{aligned} \varepsilon_2 &= \varepsilon_2^L \\ \varepsilon_3 &= \varepsilon_3^L \end{aligned} \qquad 9.10$$

When θ is $\pi/2$ or $3\pi/2$, the strains in the optical axis-2 and optical axis-3 in the optical core are:

$$\begin{aligned} \varepsilon_2 &= \varepsilon_3^L \\ \varepsilon_3 &= \varepsilon_2^L \end{aligned} \qquad 9.11$$

Substituting equation 9.10 and 9.11 into equation 9.9, the sensitivity of the sensor under transverse compression at four particular angles can be expressed as:

$$\begin{aligned} S_{trans}^{0,\pi} &= \frac{2\pi}{\lambda}(\varepsilon_2^L K_2 + \varepsilon_3^L K_3) \\ S_{trans}^{\frac{\pi}{2},\frac{3}{2}\pi} &= \frac{2\pi}{\lambda}(\varepsilon_3^L K_2 + \varepsilon_2^L K_3) \end{aligned} \qquad 9.12$$

There are three components of a PANDA fibre, the stress rods, the optical fibre core and the cladding. The materials of the stress rods have the highest thermal expansion coefficients and during the cooling procedure of manufacture, the stress rods contract more than the other parts. Hence, the residual strain in Figure 9.5 in the optical core in the direction-2 is positive (tensile) and the residual strain in the direction-3 is negative (compression). When the optical axis-2 of the optical core is under compression, which means θ in Figure 9.5 is 0 or π, the residual strain in the core in the direction-2 is reduced, and the birefringence (difference in propagation constants between direction-2 and -3) is reduced. Hence, the sensitivity of the sensor is relatively low. This corresponds to the two lower peaks in Figure 9.7, labelled as A and B. When the optical axis-2 of the optical core is under tension, which means θ in Figure 9.5 is $\pi/2$ or $3\pi/2$, the difference in strain in the core between the 2-direction and 3-direction is enhanced, and the sensitivity of the sensor is relatively high. This corresponds to the two higher peaks in Figure 9.7, labelled as C and D.

The material properties of the optical fibre are shown in Table 9.2. The numerical values for the sensitivity at the peaks for angles of 0, π and $\pi/2$, $3\pi/2$ are 0.47 rad/mm and 0.63 rad/mm respectively. Substituting these parameter values into equation 9.5 and equation 9.12, the resulting numerical equations are:

$$\begin{bmatrix} K_1 - 0.154K_2 - 0.154K_3 = 0.01 \\ -4.99K_2 + 2.42K_3 = 0.47 \\ 2.42K_2 - 4.99K_3 = 0.63 \end{bmatrix} \qquad 9.13$$

After solving the equations, the K values of the polarimetric sensor are found to be:

$$\begin{bmatrix} K_1 = -0.055 \\ K_2 = -0.204 \\ K_3 = -0.225 \end{bmatrix} \qquad 9.14$$

Table 9.2 Material properties of an isotropic sensor (after Sirkis, 1993).

Property	Value
Young's modulus, E (GPa)	73.3
Poisson's ratio, ν	0.154
Diameter of the optical fibre, d (μm)	125

The K values found here are compared with the K values for another Bow-tie polarimetric fibre in Table 9.3. It is clear that the parameters for the PANDA fibre are smaller than those for Bow-tie fibre, which is in good agreement with Tsai et al (1991) who found that the PANDA fibre is less sensitive than the Bow-tie fibre. Interestingly, both PANDA and Bow-tie fibres are more sensitive to transverse strain than longitudinal strain (i.e. K_2 and K_3 are both larger than K_1).

Table 9.3 Model parameters for PANDA and Bow-tie fibres.

Fibre	K_1	K_2	K_3
PANDA	-0.055	-0.204	-0.225
Bow-tie	-0.197	-0.714	-0.618

9.5 Conclusion

To treat the behavior of polarimetric sensor theoretically, the strain-optical parameters of the optical fibre used to manufacture the sensor must first be determined. The

determination of K values) has been carried out using tension and compression tests of bare polarimetric sensors.

The sensitivity of a bare polarimetric sensor manufactured from Hi-Bi PANDA fibre has been measured experimentally and it has been shown that optical fringes can be obtained under both tension and compression tests. A phase-strain model available in the literature has been used to determine the characteristic parameters of the optical fibre (the K values) with the aid of tension and compression loading of bare fibre sensors. The results show that PANDA fibre is less sensitive than Bow-Tie fibre.

After the characterisation of the parameters of the sensor model, it is now possible to discuss the sensitivities of embedded sensors and the interaction between the embedded sensor and cracks which pass the sensor in an adjacent ply. These are the topics of the next chapter.

Chapter 10. Theoretical treatment of the interaction between embedded sensors and cracks

10.1 Introduction

As the strain-optical parameters, the K values, have been obtained, it is possible to attempt a theoretical treatment of the behaviour of the sensors. The sensitivities of embedded sensors in undamaged laminates are discussed in Section 10.2. The interaction between the sensor and a crack which passes the sensor in the adjacent ply is predicted using Sirkis' model together with a shear-lag model of the strains associated with matrix cracks, in Section 10.3.

10.2 Sensitivities of embedded polarimetric sensors.

The response of polarimetric sensors embedded in unidirectional and cross-ply laminates under quasi-static tension loading is presented in this section. The response is expected to be different for the two types of laminates because the unidirectional laminates are transversely isotropic whereas the cross-ply laminates are orthotropic.

10.2.1 Response of a polarimetric sensor embedded in a unidirectional laminate under quasi-static tensile load

When a unidirectional coupon is under a quasi-static tensile load leading to a tensile strain ε_1, the strain state in the coupon can be expressed as:

$$\varepsilon_2 = \varepsilon_3 = -\nu_C \varepsilon_1 \qquad 10.1$$

where ε_1 is the longitudinal strain in the coupon, ε_2 and ε_3 are normal strains in the x and y directions, and the ν_C is the Poisson's ratio of the unidirectional 0° ply. The

mechanical properties of the materials used in the experiments are shown in Table 6.1. Substituting the values in Table 6.1 into equations 3.24 and 3.27 to find the strain experienced by the sensor, the following results are obtained:

$$\varepsilon_1^s = 0.02564\sigma_0 = \frac{\varepsilon_0}{E_1} = \varepsilon_1$$
$$\varepsilon_2^s = \varepsilon_3^s = -0.004337\sigma_0 = -0.169\frac{\varepsilon_0}{E_1} = -\nu'\varepsilon_1 \qquad 10.2$$

where ε_1^s is the longitudinal strain (perpendicular to the sensor's optical axes), ε_2^s and ε_3^s are transverse strains in the sensor's optical axes. In equation 10.2, ν' is the effective Poisson's ratio of the embedded sensor and is calculated using equation 3.24 and equation 3.27 to have a value of 0.169. The effective Poisson's ratio of the embedded optical fibre is larger than the Poisson's ratio of the free optical fibre, which is 0.154, because the Poisson's ratio of the surrounding composite is much higher. Hence, the sensitivity of the embedded sensor is expected to be higher than that of the free sensor. The predicted longitudinal sensitivity of the embedded sensor can be derived by substituting equation 10.2 into equation 9.1:

$$S_{axial} = \frac{1}{L}\frac{\Delta\varphi}{\Delta\varepsilon_1} = \frac{2\pi}{\lambda}(K_1 - \nu'K_2 - \nu'K_3) \qquad 10.3$$

Substituting the relevant values, the predicted sensitivity is 170 rad/mm.

Examples of fringes obtained from sensors embedded in unidirectional coupons are shown in Figure 10.1. The sensors' lengths in the figure were 97 mm, 97 mm and 98 mm, respectively, and the experimental result for the longitudinal sensitivity is 136 ± 9 rad/mm. The complete experimental results are shown in Table 10.1.

A number of issues arise from the results on the sensor embedded in unidirectional composites. Firstly, since the transverse Poisson's ratio of the host material

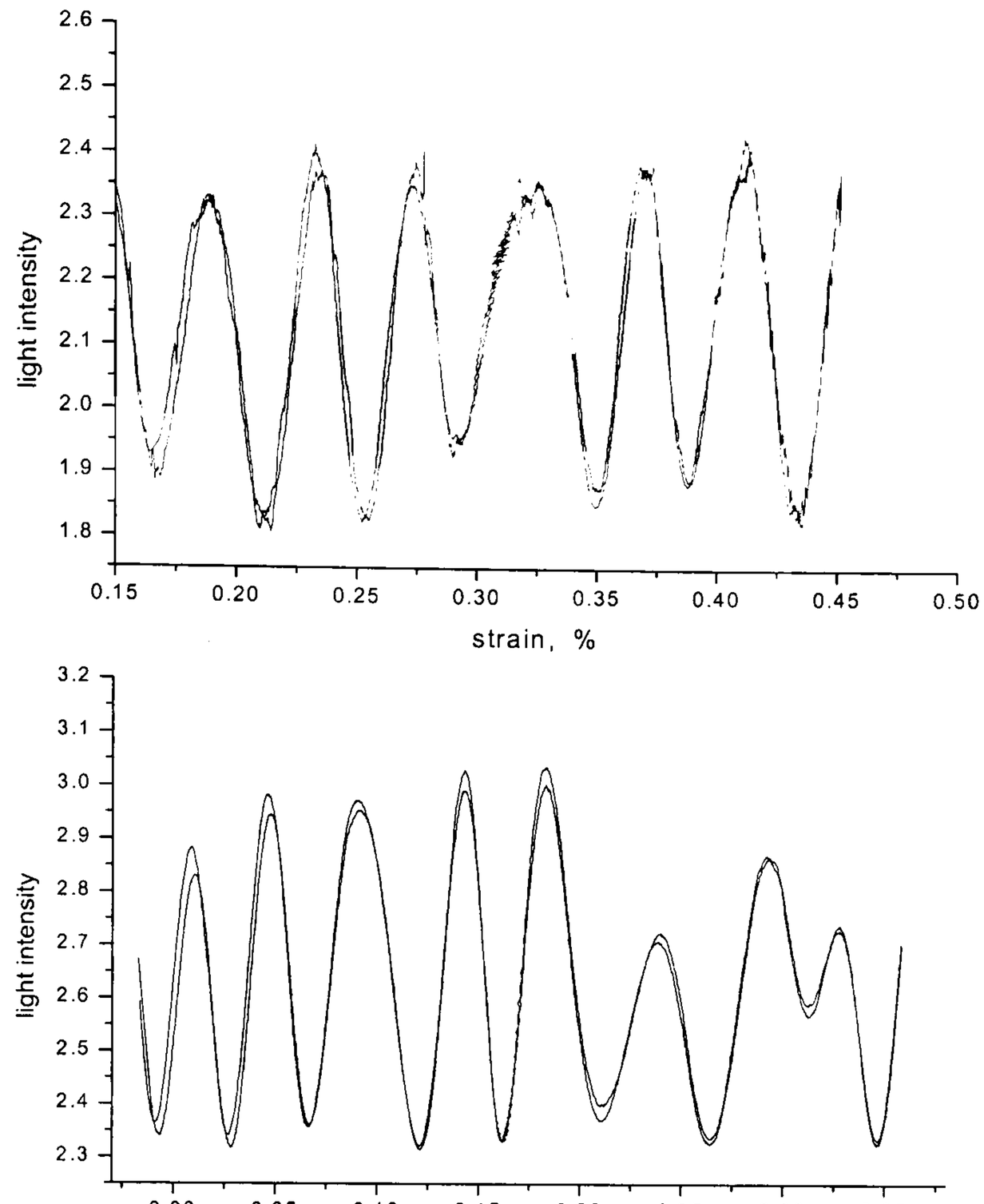

Figure 10.1 Optical fringes from three different polarimetric sensor embedded in unidirectional coupons. The graphs show that loading and unloading fringes are reproducible.

Table 10.1 Experimental data for sensors embedded in unidirectional coupons

No.	1	2	3	4	5	average
Gauge length of embedded sensor, mm	97	97	98	86	89	136 ± 9
Sensitivity of embedded sensor, rad/mm	136.7	120.5	143.6	143.0	134.2	

(ν_{12}=0.326) is bigger than that of the embedded optical fibre (ν_f=0.154), which means the host material is compressing the optical fibre when the host material is under tension. This will increase the Poisson's ratio of the optical fibre and the sensitivity of the sensor (as mentioned above). The predicted and experimentally measured sensitivities are both bigger than that of bare fibre as expected.

Secondly, the experimental sensitivity of the embedded sensor (136 rad/mm) is about 20% less than the predicted values (170 rad/mm). This is likely to be because the theoretical model assumes that the sensor is a cylindrical inclusion embedded in a transversely isotropic host. Therefore, if some part of the host material is less stiff than other parts (for example, if there are resin rich areas around the sensor), the compression effect of the unidirectional composite, which has a higher Poisson's ratio than the sensor, will be reduced. As a consequence, the sensitivity of the embedded sensor will be reduced as well.

Thirdly, the embedded sensors have a larger standard deviation for the experimentally measured sensitivities (9 rad/mm) compared to the free sensors (2 rad/mm). This difference is due to the slight irregularity of the fringe width and spacing for the embedded sensors, as shown in Figure 10.1. Although the fringes are slightly irregular, they are reproducible for both loading and unloading. This suggests that the embedded sensors are sensitive to variations in local transverse strains due to the irregular packing of the structural glass fibres around and the sensor. Such effects cannot be eliminated and lead to larger standard deviations in the sensitivities.

To test the hypothesis that the irregularity of the fringes is due to the influence of the local environment, a sensor still enclosed within its original coatings was embedded into a unidirectional laminate (i.e. the sensor was not stripped to make a bare sensor). The sensor configuration used was similar to that shown in Figure 4.4b, i.e. the 45° splices were outside the coupon but with no necessity to join the fibres with a 0°

splice inside the coupon. The optical fringes from this specimen are shown in Figure 10.2 and are found to be uniform and the widths of the optical fringes are almost identical. Hence, it appears that the abnormal strains around the sensor have been smoothed by the relatively soft silicone inner coating and the nylon outer coating. Of course, any additional strains accompanying damage in a composite would be smoothed as well, and this type of sensor is unlikely to be useful in detecting transverse cracks in a cross-ply laminate. In addition the sensor diameter with inner and outer coatings is approximately 1 mm, which is probably too large for most applications in composite material since the ply thickness is typically 0.125 mm.

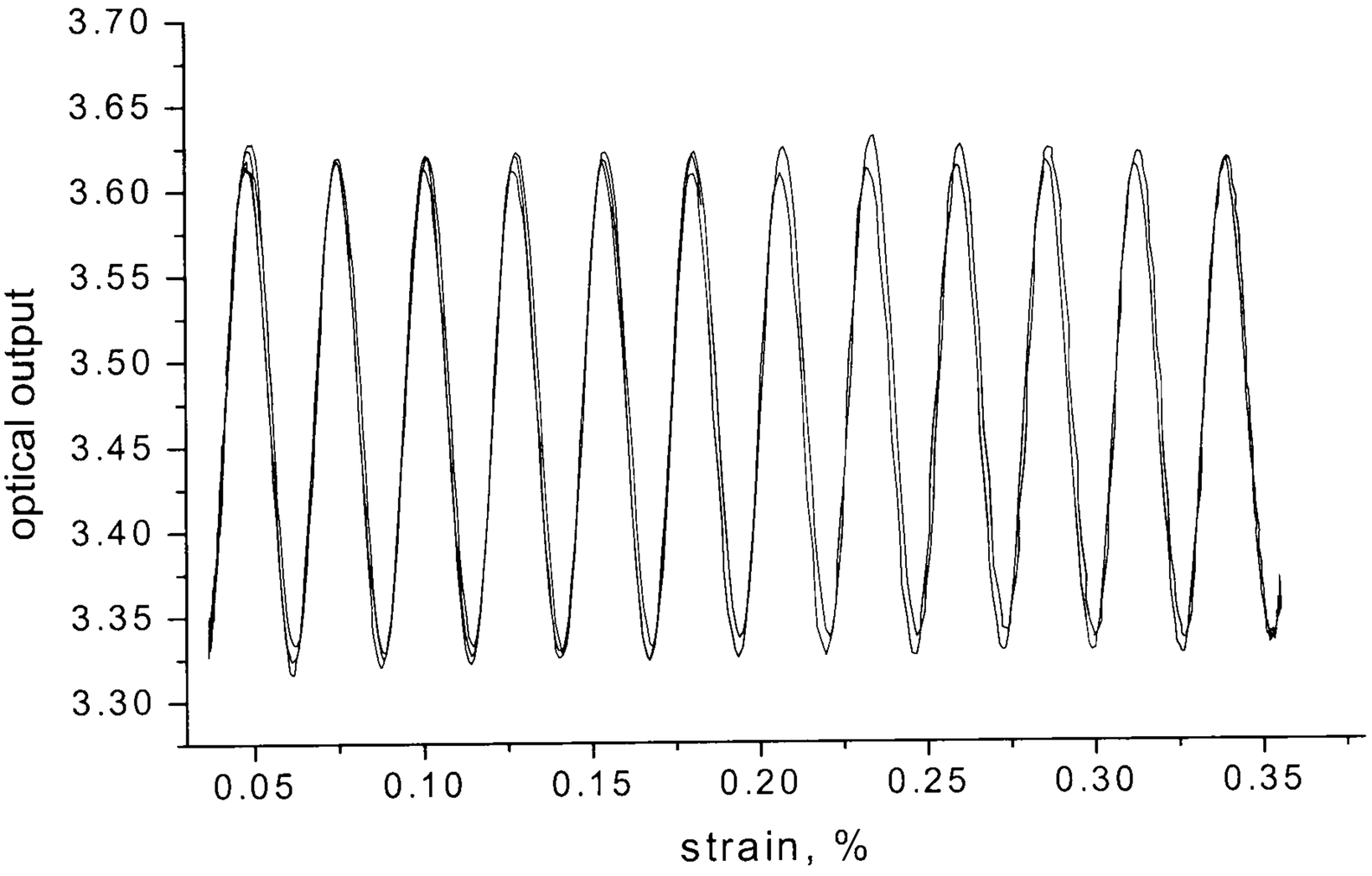

Figure 10.2 Optical fringes from an embedded polarimetric sensor with inner coating and outer coating.

10.2.2 Response of sensors embedded in cross-ply laminates under quasi-static tensile load: the effect of sensor twist

When a polarimetric sensor is embedded in a cross-ply laminate, the strain state around the sensor is more complex. Figure 10.3 shows a set of optical fringes for a sensor embedded in a cross-ply laminate. Compared to a unidirectional laminate

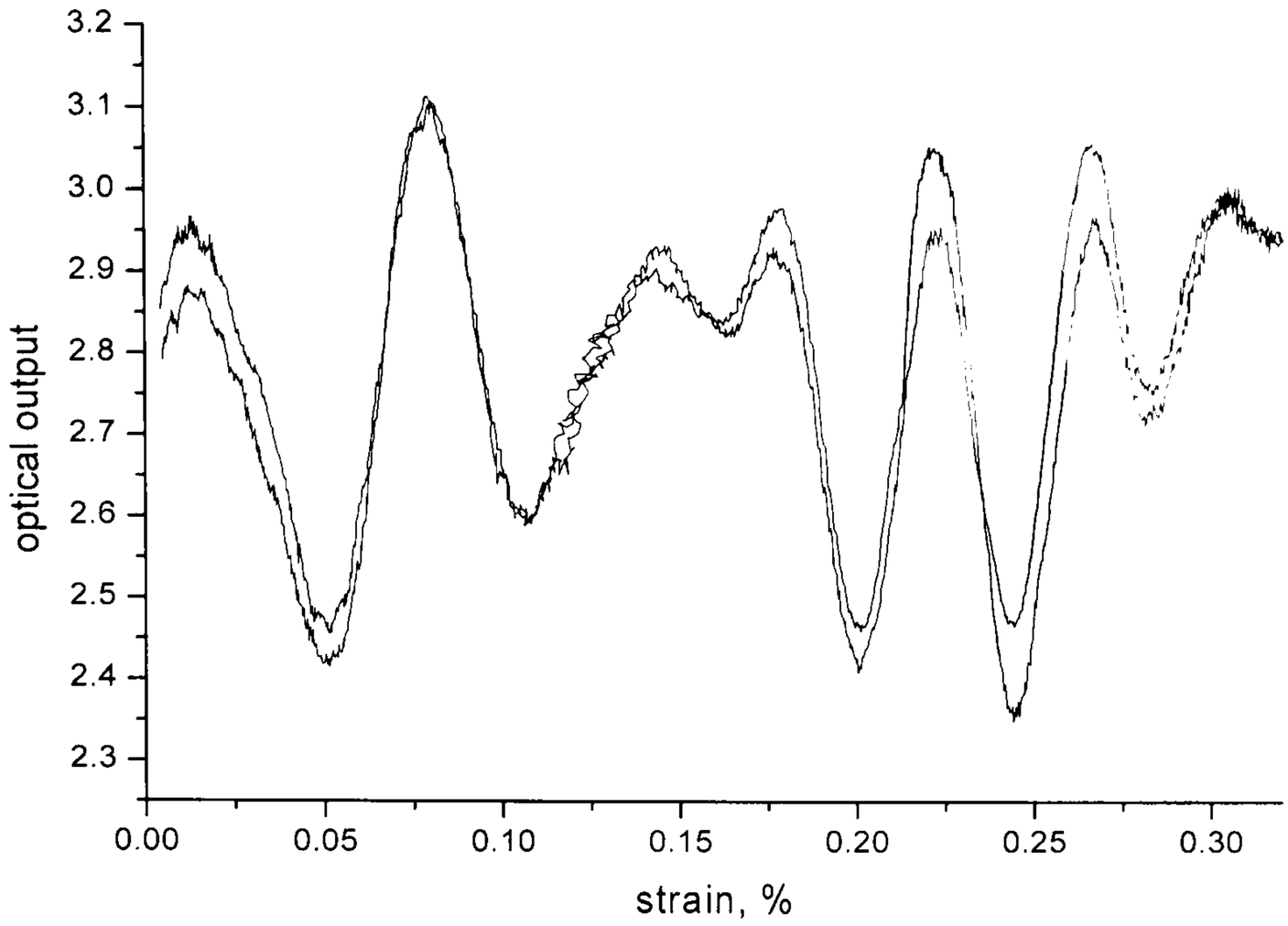

Figure 10.3 A set of optical fringes from a polarimetric sensor embedded in a cross-ply laminate.

which is transversely isotropic, a cross-ply laminate is transversely anisotropic: for a given applied load, the three normal strains in the 0° ply are different and are given according to laminated plate theory (Jones, 1975; Smith et al, 1990; Boniface et al, 1991) by

$$\varepsilon_1 = \sigma \frac{b+d}{bE_1 + dE_2}$$
$$\varepsilon_2 = -\sigma \frac{\nu_{12} E_2 (b+d)^2}{(bE_2 + dE_1)(bE_1 + dE_2)} = -\nu_{12}' \varepsilon_1 \qquad 10.4$$

where the 1 direction is parallel to the fibres in the 0° ply, the 2 direction is across the width of the coupon, and the 3 direction is through the thickness. In equation 10.4, ν_{12}' is the effective Poisson's ratios of the 0° ply, and σ is the average stress on the cross-ply laminate coupon (note that thermal strains are not included here).

Equation 10.4 concerns only strains in the plane of the coupon (i.e. ε_1 and ε_2. However, for thin laminates, the through-thickness strain in the 0° ply will be given by:

$$\varepsilon_3 = -\nu_{13}\varepsilon_1 - \nu_{23}\varepsilon_2 = -\nu_{13}'\varepsilon_1 \qquad 10.5$$

where ε_3 is the through-thickness strain in the 0° ply, ν_{13} and ν_{23} are the two Poisson's ratios of the 0° ply and ν_{13}' is the effective Poisson's ratios of the 0° ply.

When considering the response of a sensor embedded in a 0° ply, there are two sets of axes to consider: the coupon axes and the optical axes of the sensor. The definition of the axes is shown in Figure 10.4. Figure 10.4(a) shows the coupon axes and Figure 10.4(b) shows a cross-section of the coupon with the optical axes 2^s and 3^s shown. It can be seen from Figure 10.4(b) that, in general there will be an angle θ between the optical axes of the sensor and the axes of the coupon. However, this angle is not usually constant along the sensor length, because it was found that the embedded optical fibres have a twist introduced during fabrication. To evaluate the magnitude of the twist, coupons were cut into sections after tests and optical microscope images were taken at different positions along the coupon (i.e. for different z co-ordinates) in order to find the angle θ as a function of z. Figure 10.5 shows a typical result. Micrographs of four sections at various positions along a coupon (10 mm, 34 mm, 64 mm and 86 mm measured from one splice) were taken. The positions of the cross-sections are shown in Figure 10.5(a) and the micrographs are shown in 10.5(b). The angel θ at these positions (30°, -8°, -60° and -100°, respectively) is plotted against position in Figure 10.5(c). Figure 10.5(c) shows that the twist of the sensor is linear along the z-axis, and this was found for all specimens, although the rate of twist was different in different specimens. For the specimen shown in Figure 10.5, the twist rate was 0.03 rad/mm with an overall twist between the splices of 2.5 rad (144°). The overall twist angles of other specimens are shown in Table 10.2.

Of course, because the sensor twists along the z-axis, the response of the sensor to the strains will change from point to point due to the rotation of the sensor axes in a strain field which is not isotropic. As a consequence, the sensitivity of the embedded sensor will change as a function of the initial twist angle and the degree of the twist.

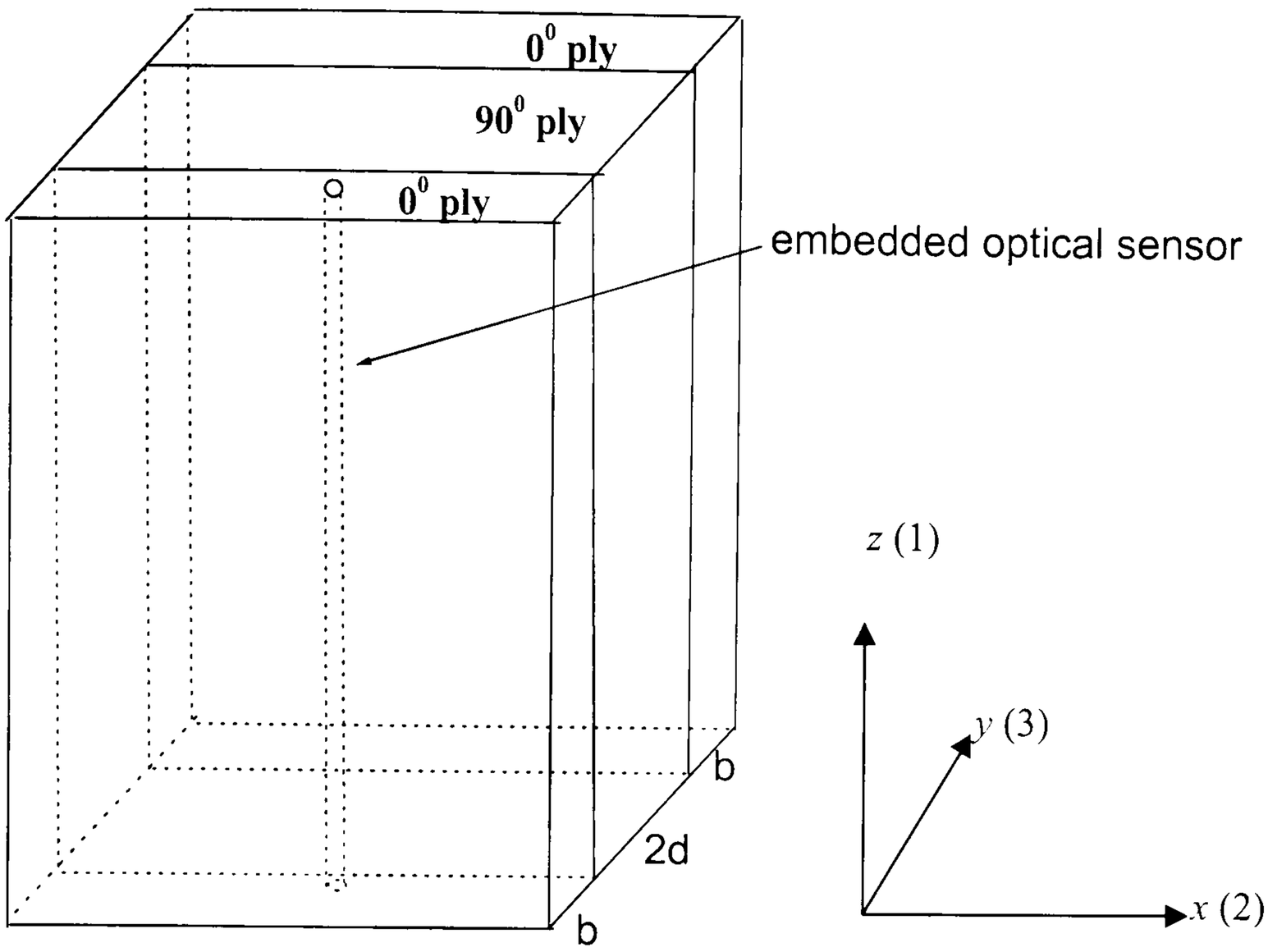

(a)

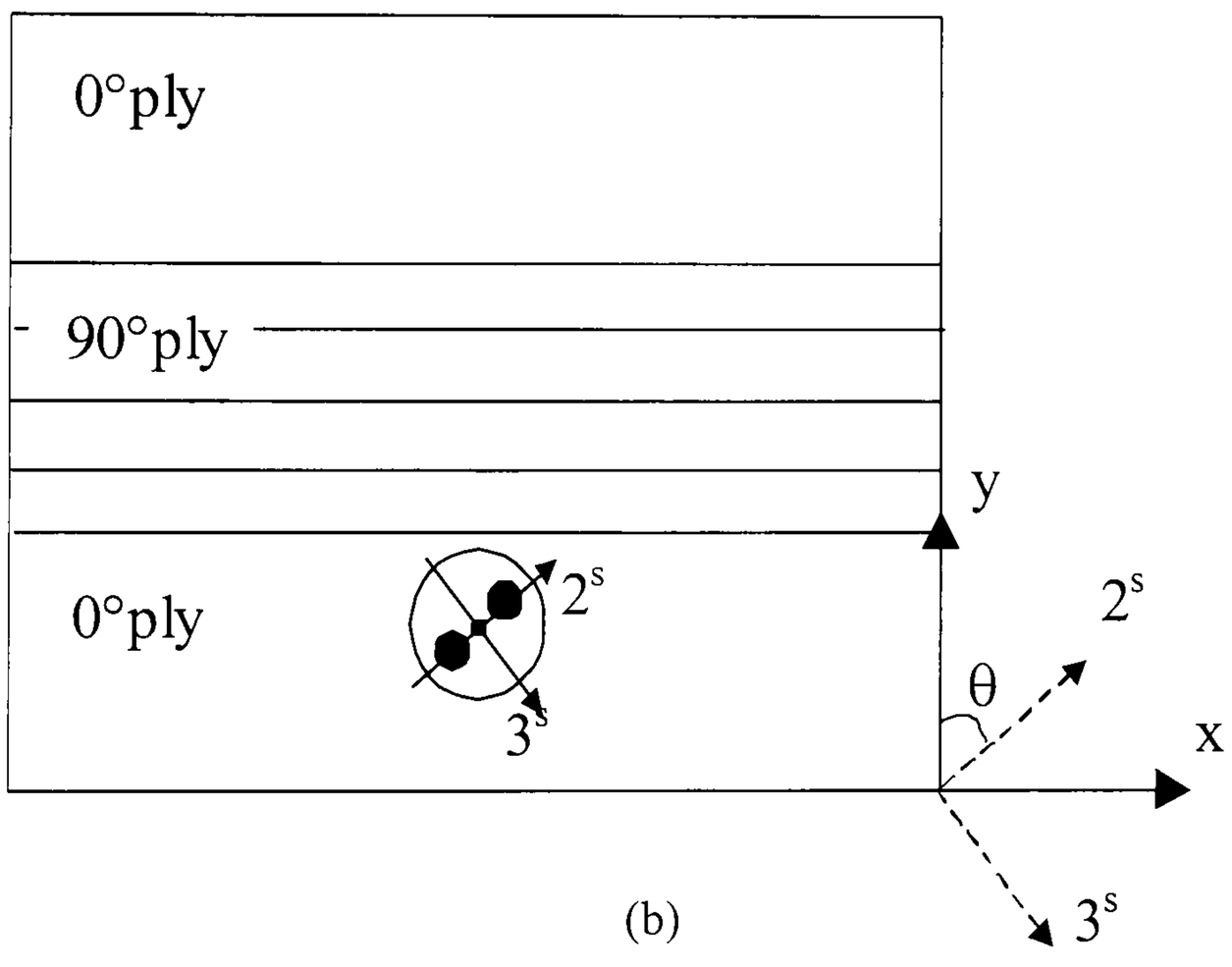

(b)

Figure 10.4 A schematic diagram showing the optical fibre and the crossply laminate axes and polar angle θ.

(a) The axes of the coupon.

(b) A cross-section of a coupon showing the axes of the optical sensor, 2^s and 3^s, in relation to the coupon axes, x, y.

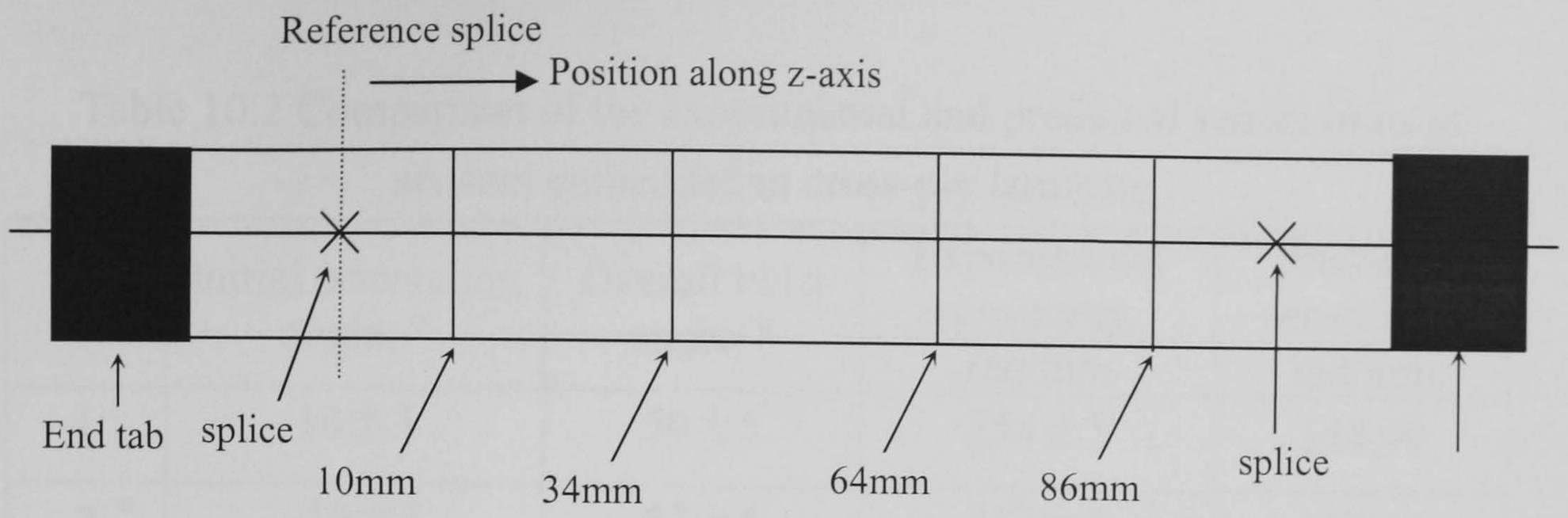

Figure 10.5 Twist of embedded sensor.
(a) Schematic graph showing the *z*-position of cross-section where micrograph were taken.
(b) Optical micrographs at various *z*-positions in the coupon.
(c) The angle θ as a function of *z*-position

Table 10.2 Comparison of the experimental and predicted sensitivities of sensors embedded in cross-ply laminate

No.	Initial orientation angle, °	Overall twist angle, °	Experimental sensitivity, rad/mm	Predicted sensitivity, rad/mm
1	10±3	50±5	254±5	154.99
2	-19±3	52±5	237±5	155.02
3	-29±3	64±5	207±5	154.93
4	-77±3	80±5	149±5	154.20
5	-63±3	124±5	118±5	154.51
6	24±3	144±5	162±5	154.60
7	85±3	168±5	140±5	154.15
8	-19±3	228±5	160±5	154.97
9	30±3	252±5	136±5	154.32
10	-100±3	162±5	148±5	154.60

To define the degree of twist at any position l along the sensor from one splice (reference splice), the orientation of the fiber can be expressed in terms of the angle θ as:

$$\theta_l = \theta_0 + \frac{l}{L_0}\theta \qquad 10.6$$

where θ_l is the orientation of the embedded sensor at position l within the gauge length of the sensor from the reference splice, L_0 is the gauge length of the sensor, θ_0 is the initial orientation of the sensor at the reference splice and θ is the overall twist angle of the sensor at the second splice of the sensor, defined as θ positive for anti-clockwise rotation. l is an arbitrary position within the gauge length of the sensor, such that $0 \le l \le L_0$.

Then the three strains in the optical axis of the sensor core are:

$$\varepsilon_1^s = \varepsilon_1^f$$
$$\varepsilon_2^s = \varepsilon_2^f \cos^2\theta_l + \varepsilon_3^f \sin^2\theta_l = \varepsilon_2^f \cos^2(\theta_0 + \frac{l}{L_0}\theta) + \varepsilon_3^f \sin^2(\theta_0 + \frac{l}{L_0}\theta) \qquad 10.7$$
$$\varepsilon_3^s = \varepsilon_2^f \sin^2\theta_l + \varepsilon_3^f \cos^2\theta_l = \varepsilon_2^f \sin^2(\theta_0 + \frac{l}{L_0}\theta) + \varepsilon_3^f \cos^2(\theta_0 + \frac{l}{L_0}\theta)$$

where $\varepsilon_1^s, \varepsilon_2^s, \varepsilon_3^s$ are the strains in the optical axes of the sensor core in the 1-2 coordinates shown in Figure 10.4, and $\varepsilon_1^f, \varepsilon_2^f, \varepsilon_3^f$ are the three normal strains in the optical sensor in the x-y coordinates shown in Figure 10.4. It should be pointed out that there is an approximation being made here which is to assume that the strains throughout the cross section of the optical fibre are homogenous.

When the sensor is embedded into the 0° ply of a cross-ply laminate, the values of ν_{12}' and ν_{13}' , which are the effective Poisson's ratios of the 0° plies, calculated from equation 10.4, equation 10.5 and Table 6.1 are:

$$\nu_{12}' = 0.176$$
$$\nu_{13}' = 0.273 \qquad 10.8$$

Not surprisingly, equation 10.8 shows that for the 0° ply in a cross-ply laminate $\nu_{12}' \neq \nu_{13}'$. Hence, when the sensor twists within the 0° ply of a cross-ply laminate, the strain field around the sensor changes along its length and the integrated sensitivity of the sensor changes with both the degree of twist and the initial orientation, θ_0, at the reference splice.

However, the effective Poisson's ratios shown in equation 10.8 are not the same as the optical sensor sees, meaning that the strains in the optical fibre are not the same as the

strains in the host composite material at the position of the optical fibre. This is due to the interaction between the host material and the embedded cylinder, as discussed in Section 3.5. It has been shown earlier, that in a unidirectional composite, the effective Poisson's ratio of the sensor embedded in the 0° ply ($v_{12}=v_{13}=0.326$) is 0.169 (equation 10.2), compared to the free sensor value of 0.154. As a first approximation, the Poisson's ratios seen by the embedded sensor can be estimated as a linear interpolation, i.e.:

$$\begin{aligned} \nu_{12}^{s} &= \frac{0.176}{0.326}\times(0.169-0.154)+0.154=0.162 \\ \nu_{13}^{s} &= \frac{0.273}{0.326}\times(0.169-0.154)+0.154=0.167 \end{aligned} \qquad 10.9$$

Hence, the relationship between the strains in the optical fibre and the strains in the host composite at the position of the fibre is:

$$\begin{aligned} \varepsilon_1^f &= \varepsilon_1 \\ \varepsilon_2^f &= -\nu_{12}^{s}\varepsilon_1 \\ \varepsilon_3^f &= -\nu_{13}^{s}\varepsilon_1 \end{aligned} \qquad 10.10$$

The sensitivity of the embedded polarimetric sensor is defined by equation 10.11:

$$S = \frac{1}{L_0}\frac{\Delta\varphi}{\Delta\varepsilon_1} \qquad 10.11$$

Substituting equation 9.1, equation 10.7, equation 10.10, equation 10.4 and equation 10.5 into equation 10.11, gives an expression which can be evaluated using Maple®. Hence, the sensitivity of a polarimetric sensor which twists when embedded in a cross-ply coupon is found to be:

$$
\begin{aligned}
S = -\frac{\pi}{\lambda\theta}[&-2K_1\theta + K_2\nu_{12}^s\cos(\theta_0)\cos^2(\theta)\sin(\theta_0) + K_2\nu_{12}^s\cos^2(\theta_0)\cos(\theta)\sin(\theta)\\
&- K_2\nu_{12}^s\sin^2(\theta_0)\cos(\theta)\sin(\theta) - K_2\nu_{12}^s\sin(\theta_0)\cos(\theta)\sin^2(\theta)\\
&- K_2\nu_{13}^s\cos(\theta_0)\cos^2(\theta)\sin(\theta_0) - K_2\nu_{13}^s\cos^2(\theta_0)\cos(\theta)\sin(\theta)\\
&+ K_2\nu_{13}^s\sin^2(\theta_0)\cos(\theta)\sin(\theta) + K_2\nu_{13}^s\sin^2(\theta_0)\cos(\theta)\sin(\theta)\\
&- K_3\nu_{12}^s\cos(\theta_0)\cos^2(\theta)\sin(\theta_0) - K_3\nu_{12}^s\cos^2(\theta_0)\cos(\theta)\sin(\theta)\\
&+ K_3\nu_{12}^s\sin^2(\theta_0)\cos(\theta)\sin(\theta) + K_3\nu_{12}^s\sin(\theta_0)\cos(\theta)\sin^2(\theta)\\
&+ K_3\nu_{13}^s\cos(\theta_0)\cos^2(\theta)\sin(\theta_0) + K_3\nu_{13}^s\cos^2(\theta_0)\cos(\theta)\sin(\theta)\\
&- K_3\nu_{13}^s\sin^2(\theta_0)\cos(\theta)\sin(\theta) - K_3\nu_{13}^s\sin^2(\theta_0)\cos(\theta)\sin(\theta)\\
&+ K_3\nu_{12}^s\theta + K_3\nu_{13}^{'}\theta + K_2\nu_{12}^s\theta + K_2\nu_{13}^s\theta - K_2\nu_{12}^s\cos(\theta_0)\sin(\theta_0)\\
&+ K_2\nu_{13}^s\cos(\theta_0)\sin(\theta_0) + K_3\nu_{12}^s\cos(\theta_0)\sin(\theta_0) - K_3\nu_{13}^s\cos(\theta_0)\sin(\theta_0)]
\end{aligned}
\qquad 10.12
$$

It should be noted that the theoretical result for the sensitivity is independent of the sensor gauge length, L_0. The details of the calculation carried out using Maple® (i.e. input and output from Maple®) are shown in Appendix C.

The change of sensitivity calculated from equation 10.12 with values from Table 6.1 and taking the initial twist angle θ_0 to be $\theta_0 = 0$, $\theta_0 = \pi/4$, $\theta_0 = \pi/2$ and $\theta_0 = \pi$, are shown in Figure 10.6. The four curves in the figure show that the sensitivity of the embedded sensor changes with the overall twist angle and the initial orientation angle. In each case, there is a relatively big initial fluctuation in sensitivity for small overall twist angles. The fluctuation of the sensitivity reduces with increasing overall twist angle until the sensitivity reaches a constant value. This constant value is insensitive to the initial orientation angle θ_0 and overall twist angle θ.

For real sensors embedded in cross-ply laminate, they not only twist, which means θ in equation 10.12 changes, but the original orientation of the sensors changes as well, which means θ_0 in equation 10.12 changes. Every experimental data point is thus defined by two independent variables: θ (the overall twist) and θ_0 (the initial orientation at the reference splice). The experimental values of the sensitivities of real sensors (with different pairs of θ and θ_0) embedded in cross-ply coupons are plotted

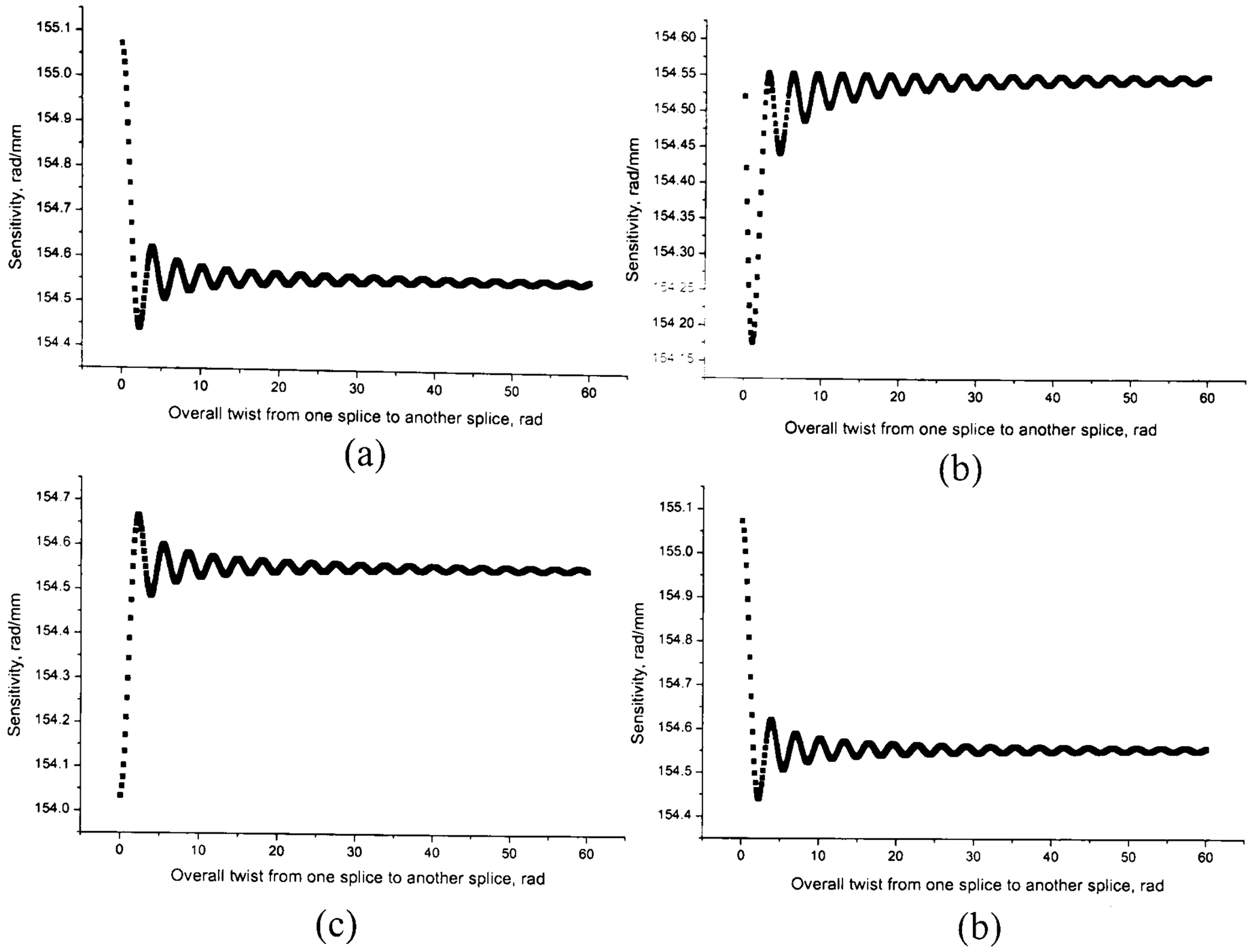

Figure 10.6 Theoretical prediction of the sensitivity of a sensor embedded in a cross-ply coupon.

(a) θ_0=0; (b) θ_0=$\pi/4$; (c) θ_0=$\pi/2$; (d) θ_0=π.

against theoretical predicted value with measured corresponding θ and θ_0 in Figure 10.7. The experimental results are shown in Table 10.2. The trend of the experimentally determined sensitivities follows the trend of predicted values. However, the predicted values do no reflect the wide range of sensitivities measured experimentally.

A number of simplified circumstances can be checked with regard to equation 10.12. Firstly, when a free sensor (i.e. a sensor which has been stripped of inner coating and outer coating and has not been embedded in a composite), is loaded by a tensile load, v_{12}^s and v_{13}^s in equations 10.12 are equal to the Poisson's ratio of the optical fibre, v_f. Figure 10.8 shows the result. During the calculation, the terms containing θ_0 are cancelled. The predicted sensitivity is 106 rad/mm and does not change with initial orientation or with overall twist angle as expected. This value recovers the

experimental value of the longitudinal strain sensitivity used to derive K_1, K_2 and K_3 (see Section 9.4) and is independent of the initial orientation of the sensor.

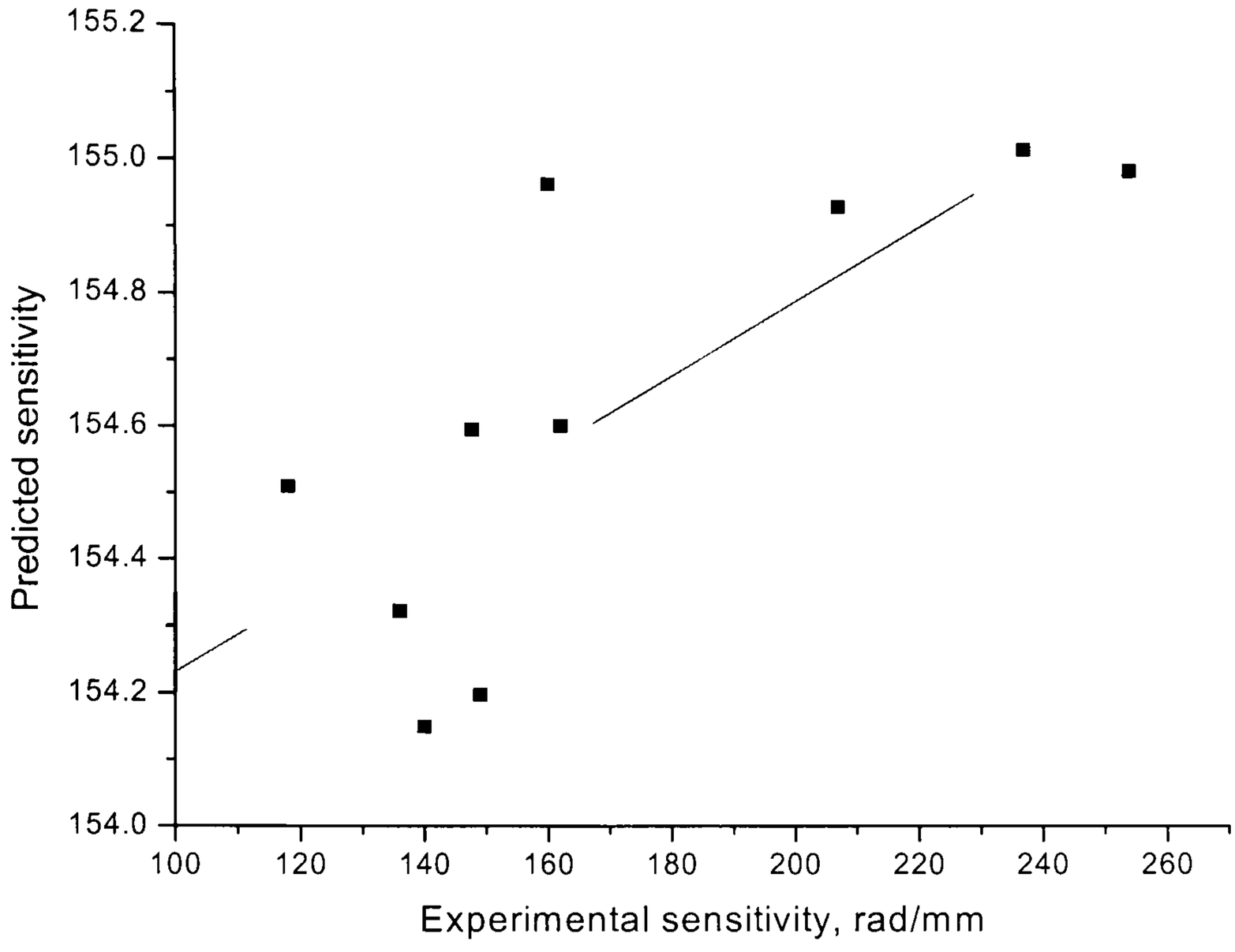

Figure 10.7 Comparison of measured and predicted sensitivities of a polarimetric sensor embedded in cross-ply laminates.

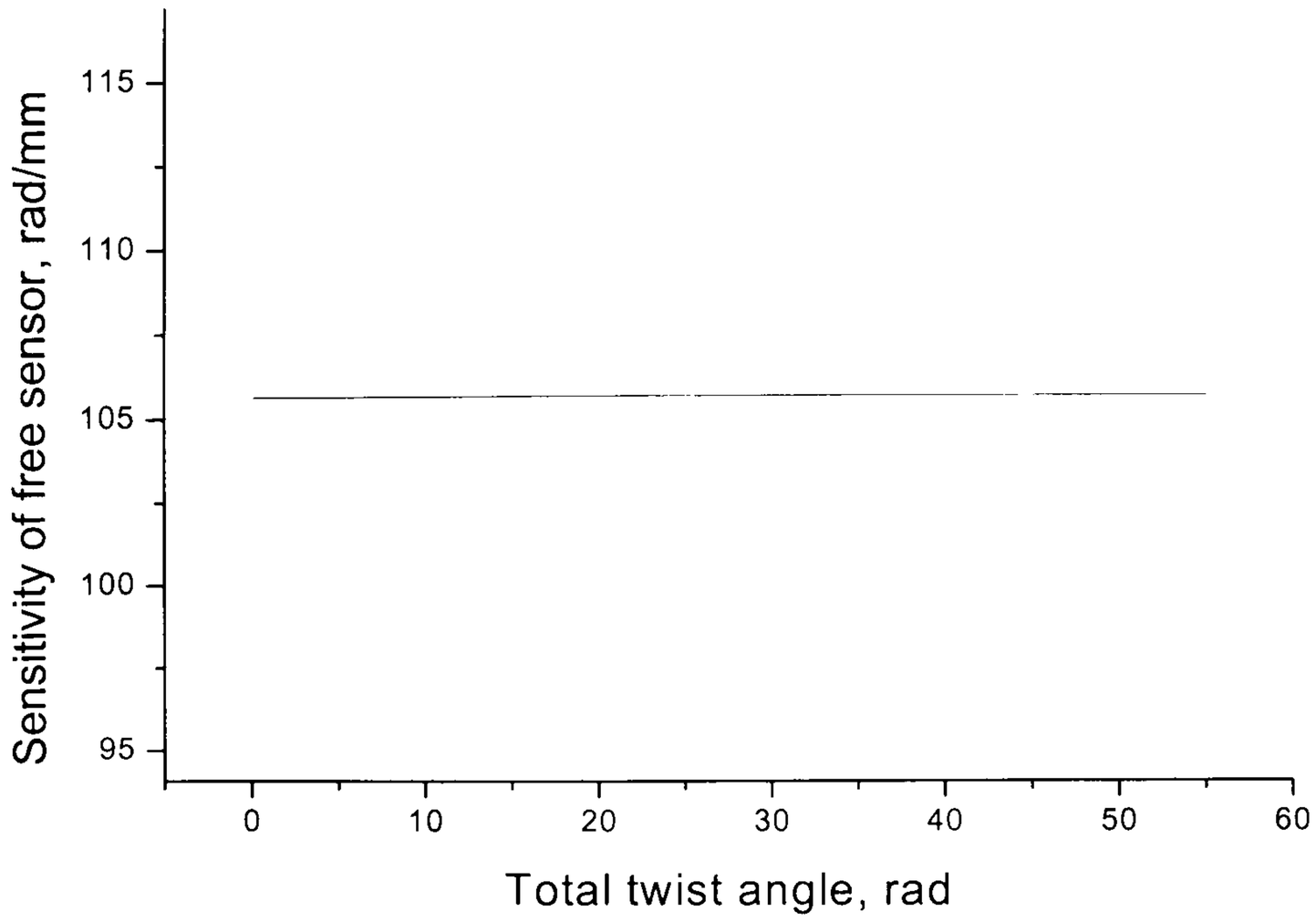

Figure 10.8 Theoretical prediction of the sensitivity of a bare sensor.

Secondly, when a sensor is embedded in a unidirectional coupon, v_{12}^s and v_{13}^s in equation 10.12 are the same as the effective Poisson's ratio, v', in equation 10.2. Again, during the calculation, the items containing θ_0 are cancelled. The sensitivity given by equation 10.12 is plotted in Figure 10.9. The sensitivity remains constant when the sensor twists along the z-axis for different overall twist orientations. The predicted sensitivity is 170 rad/mm, which is in agreement with the prediction in Section 10.2.1.

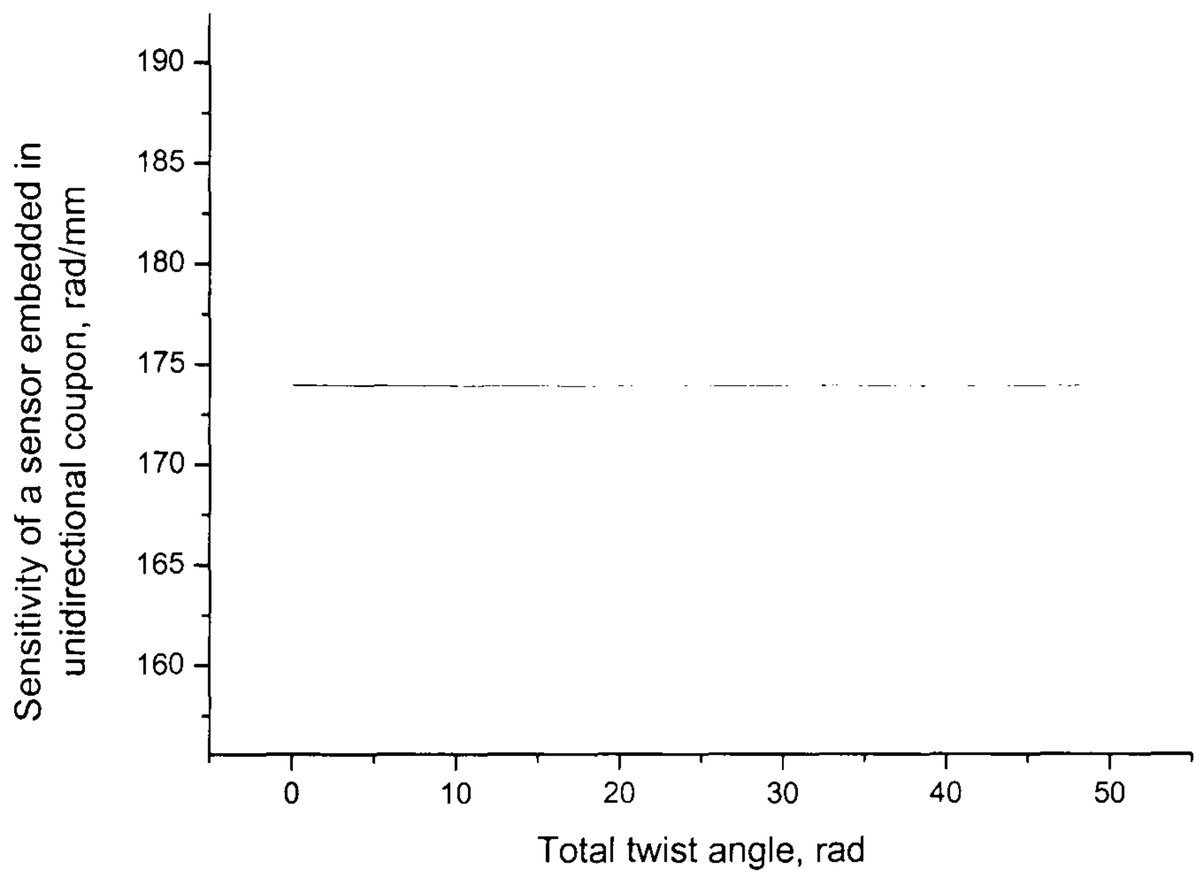

Figure 10.9 Theoretical prediction of the sensitivity of a sensor embedded in a unidirectional coupon

10.3 Interaction between embedded optical sensor and cracks passing the sensor

In the previous section, the sensitivity of a sensor embedded in the 0° ply of a cross-ply laminate for any degree of twist has been investigated. In this section, the change of sensitivity induced by the development of a matrix crack is examined.

10.3.1 Predicted sensitivity changes due to matrix crack development

Assuming that a sensor has an orientation of θ_0 relative to composite axes, as shown in Figure 10.4, then the three normal strains seen by the optical axes of the sensor before a crack occurs are:

$$\begin{aligned}\varepsilon_1^{S_0} &= \varepsilon_1^0 \\ \varepsilon_2^{S_0} &= -\nu_{12}^s \varepsilon_1^0 \cos^2\theta_0 - \nu_{13}^s \varepsilon_1^0 \sin^2\theta_0 \\ \varepsilon_3^{S_0} &= -\nu_{12}^s \varepsilon_1^0 \sin^2\theta_0 - \nu_{13}^s \varepsilon_1^0 \cos^2\theta_0\end{aligned} \qquad 10.13$$

where $\varepsilon_1^{S_0}, \varepsilon_2^{S_0}, \varepsilon_3^{S_0}$ are strains in the optical axes of the sensor before a crack occurs, ε_1^0 is the longitudinal strain in the 0° ply which can be calculated by equation 10.4 and ν_{12}^s, ν_{13}^s are effective Poisson's ratio seen by the sensor which is calculated in equation 10.9. Again there is an approximation here which assumes that the distribution of strains over the cross section of the fibre is homogenous, and the approximation shown in equation 10.9 is still used here. Note that in these calculations, it is assumed that the sensor does not twist along its length (i.e. the overall twist angle $\theta = 0$).

Combining equation 9.1 and equation 10.13, the phase change for a sensor embedded in the coupon subject to a longitudinal strain, $\varepsilon_1{}^0$, before a crack occurs, is:

$$\Delta\varphi_1 = \frac{2\pi}{\lambda}\int_0^{L_0}[K_1\varepsilon_1^0 - K_2(\nu_{12}^s\varepsilon_1^0\cos^2\theta_0 + \nu_{13}^s\varepsilon_1^0\sin^2\theta_0) - K_3(\nu_{12}^s\varepsilon_1^0\sin^2\theta_0 + \nu_{13}^s\varepsilon_1^0\cos^2\theta_0)]dl \qquad 10.14$$

where $\Delta\varphi_1$ is the phase difference induced by a change of strain $\Delta\varepsilon_1{}^0$ and L_0 is the gauge length of the sensor.

To evaluate the phase change as a consequence of crack growth, it is necessary to consider the strain magnification induced in the 0° ply by a crack develops in the 90° ply. When a crack grows completely across the 90° ply of a cross-ply coupon, a strain magnification will occur around the crack where it is constrained at the 0/90 interface. According to Boniface et al (1991), the strains in the 0° ply after a crack is induced are:

$$\varepsilon_1 = \frac{\sigma}{E_1}(1+\frac{d}{b}) - \frac{d}{b}\frac{\sigma}{E_1}\frac{E_2}{E_0}(1-e^{-\lambda y}) = \varepsilon_1^0 + \frac{d}{b}\frac{\sigma}{E_1}\frac{E_2}{E_0}e^{-\lambda y}$$

$$\varepsilon_2 = -\frac{\nu_{12}E_2(b+d)^2}{(bE_2+dE_1)(bE_1+dE_2)}\{1-[1-\frac{bE_1+dE_2}{E_1(b+d)}]e^{-\lambda y}\} \qquad 10.15$$

$$= \varepsilon_2^0 + \frac{\nu_{12}E_2(b+d)^2}{(bE_2+dE_1)(bE_1+dE_2)}[1-\frac{bE_1+dE_2}{E_1(b+d)}]e^{-\lambda y}$$

where ε_1, and ε_2 are normal strains in the 0° ply after a crack is induced, ε_1^0, and ε_2^0 are normal strains in the 0° ply before a crack is induced which can be calculated from equation 10.4, and y is the distance from the crack in the longitudinal direction. The quantity λ is given by:

$$\lambda^2 = \frac{3G_{23}(b+d)E_0}{d^2bE_1E_2} \qquad 10.16$$

For thin laminates, the through-thickness strain in the 0° ply will be given by:

$$\varepsilon_3 = -\nu_{13}\varepsilon_1 - \nu_{23}\varepsilon_2 \qquad 10.17$$

where ε_3 is the through-thickness strain in the 0° ply after a transverse has been induced, ν_{13} and ν_{23} are the two Poisson's ratios of the 0° ply (it should be noted that these expressions again ignore the thermal strains in the laminate).

Assuming that all the strain magnifications around the crack tip in the host composite are transferred to the embedded optical fibre and the Poisson's ratio seen by the sensor are the same as those shown in equation (10.9), then the strains in the optical fiber are:

$$\varepsilon_1^f = \varepsilon_1$$

$$\varepsilon_2^f = -\nu_{12}^s \varepsilon_1 = -\nu_{12}^s \cdot (-\frac{\varepsilon_2}{\nu_{12}^{'}}) = \frac{\nu_{12}^s}{\nu_{12}^{'}} \varepsilon_2 \qquad 10.18$$

$$\varepsilon_3^f = -\nu_{13}^s \varepsilon_1 = -\nu_{13}^s \cdot (-\frac{\varepsilon_3}{\nu_{13}^{'}}) = \frac{\nu_{13}^s}{\nu_{13}^{'}} \varepsilon_3$$

where $\varepsilon_1^f, \varepsilon_1^f, \varepsilon_1^f$ are three normal strains in the optical fibre, ν_{12}^s, ν_{13}^s are Poisson's ratio seen by the embedded sensor, and $\nu_{12}^{'}, \nu_{13}^{'}$ are effective Poisson's ratio of the 0° ply.

When the optical axis has an initial orientation of θ_0 to the composite axis, as shown in Figure 10.4(b), the three normal strains in the optical axis, which change with the initial orientation, can be expressed as:

$$\varepsilon_1^s = \varepsilon_1^f$$
$$\varepsilon_2^s = \varepsilon_2^f \cos^2\theta_0 + \varepsilon_3^f \sin^2\theta_0 \qquad 10.19$$
$$\varepsilon_3^s = \varepsilon_2^f \sin^2\theta_0 + \varepsilon_3^f \cos^2\theta_0$$

where $\varepsilon_1^s, \varepsilon_2^s, \varepsilon_3^s$ are the strains in the optical axes of the sensor core in the 1-2 coordinate shown in Figure 10.4, and $\varepsilon_1^f, \varepsilon_2^f, \varepsilon_3^f$ are the three normal strains in the optical sensor in the x-y coordinate shown in Figure 10.4.

Now, considering the phase change when a crack develops, suppose that a single crack is present in the coupon at a distance L_1 from one splice and L_2 from the second splice (i.e. $L_1+L_2=L_0$). Then, the new phase change if the specimen is loaded to the same average stress is:

$$\Delta\varphi_2 = \frac{2\pi}{\lambda} \int_0^{L_1} (K_1\varepsilon_1^s + K_2\varepsilon_2^s + K_3\varepsilon_3^s)dl + \int_0^{L_2} (K_1\varepsilon_1^s + K_2\varepsilon_2^s + K_3\varepsilon_3^s)dl \qquad 10.20$$

where $\Delta\varphi_2$ is the new phase difference after a single crack has formed.

It is now possible to write the expression for the phase change induced when a crack develops. If a single crack develops when the coupon is under load, the phase change induced by the crack is:

$$\Delta(\Delta\varphi) = \Delta\varphi_2 - \Delta\varphi_1 \qquad 10.21$$

and this phase change can be evaluated as a function of the sensor orientation by substituting equation 10.20 and equation 10.14 into equation 10.21. The calculations have been carried out using Maple and the details are shown in Appendix D. Again, various conditions can be investigated.

Suppose that the sensor has a gauge length of 100 mm and the crack passes midway between the two splices, so that $L_1=L_2=L_0/2=50\ mm$. Using the values in Table 6.1, the optical phase change induced by a crack passing the sensor is plotted in Figure 10.10 as a function of the initial orientation of the sensor axes (note that the overall twist angle is assumed to be zero). It is shown clearly in the figure that when a crack

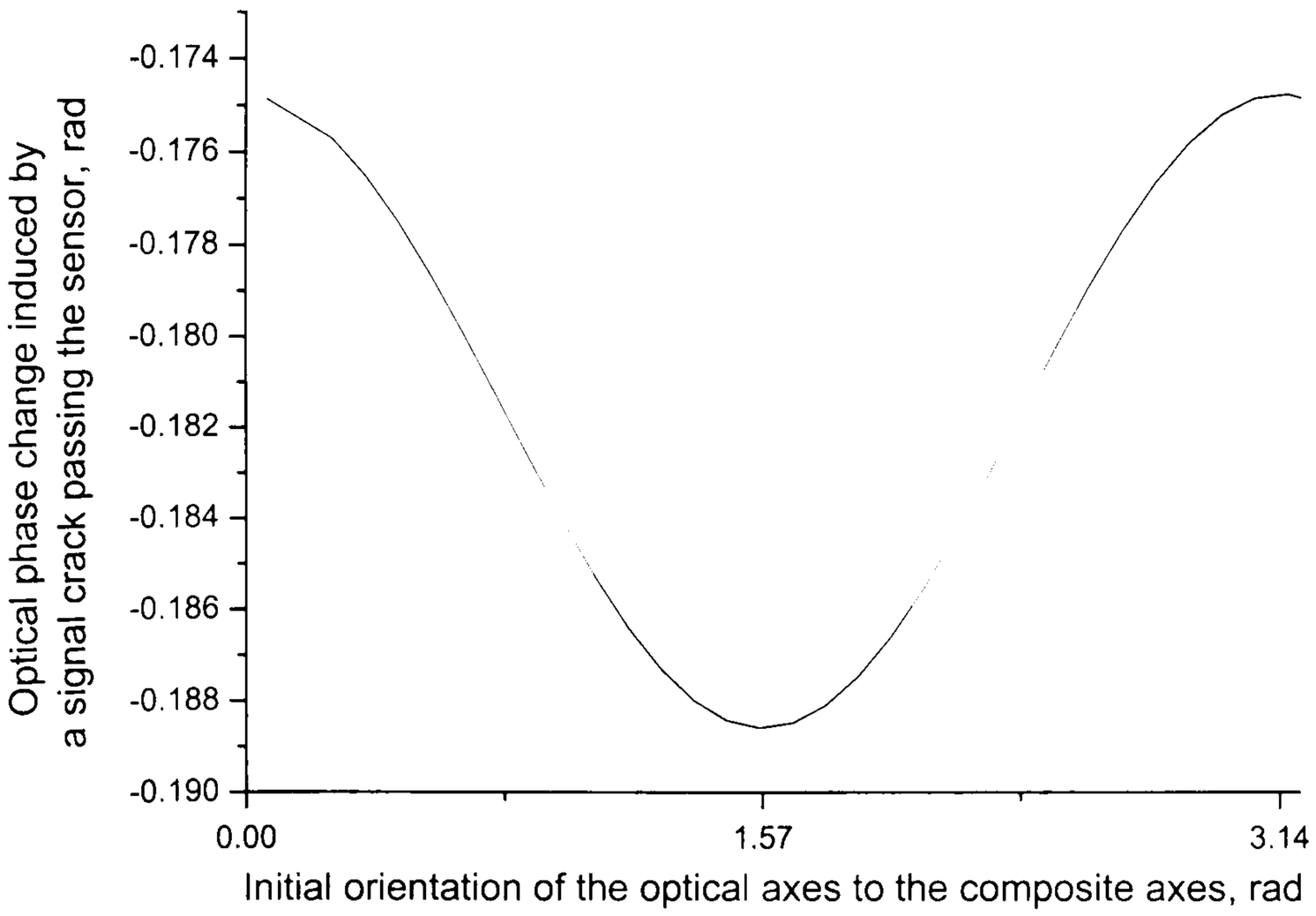

Figure 10.10 Predicted optical changes induced by a crack passing an embedded sensor

passes, there is always a reduction of optical output phase predicted for all initial orientations, although the magnitude of the reduction varies with the initial orientation of the optical axes.

Once a transverse crack has developed during the loading period of a quasi-static test, its effect on the sensor persists. When the coupon is reloaded, the cracks induced in previous tests will affect the present optical output, which suggests that the sensitivity of the sensor during reloading tests will reduce. An example of the experimentally measured change in the sensitivity of the sensor with increasing numbers of cracks is shown in Figure 10.11. Initially, the sensitivity of the sensor is 170 rad/mm. After five cracks have formed, the sensitivity has dropped to about 164 rad/mm and a further reduction to 153 rad/mm occurs after 12 cracks have formed. Hence, this discussion explains qualitatively why such a reduction occurs. However, one major problem remains. An analysis of the direction of the step-change of the optical output for individual crack shows that a complete explanation has not yet been achieved.

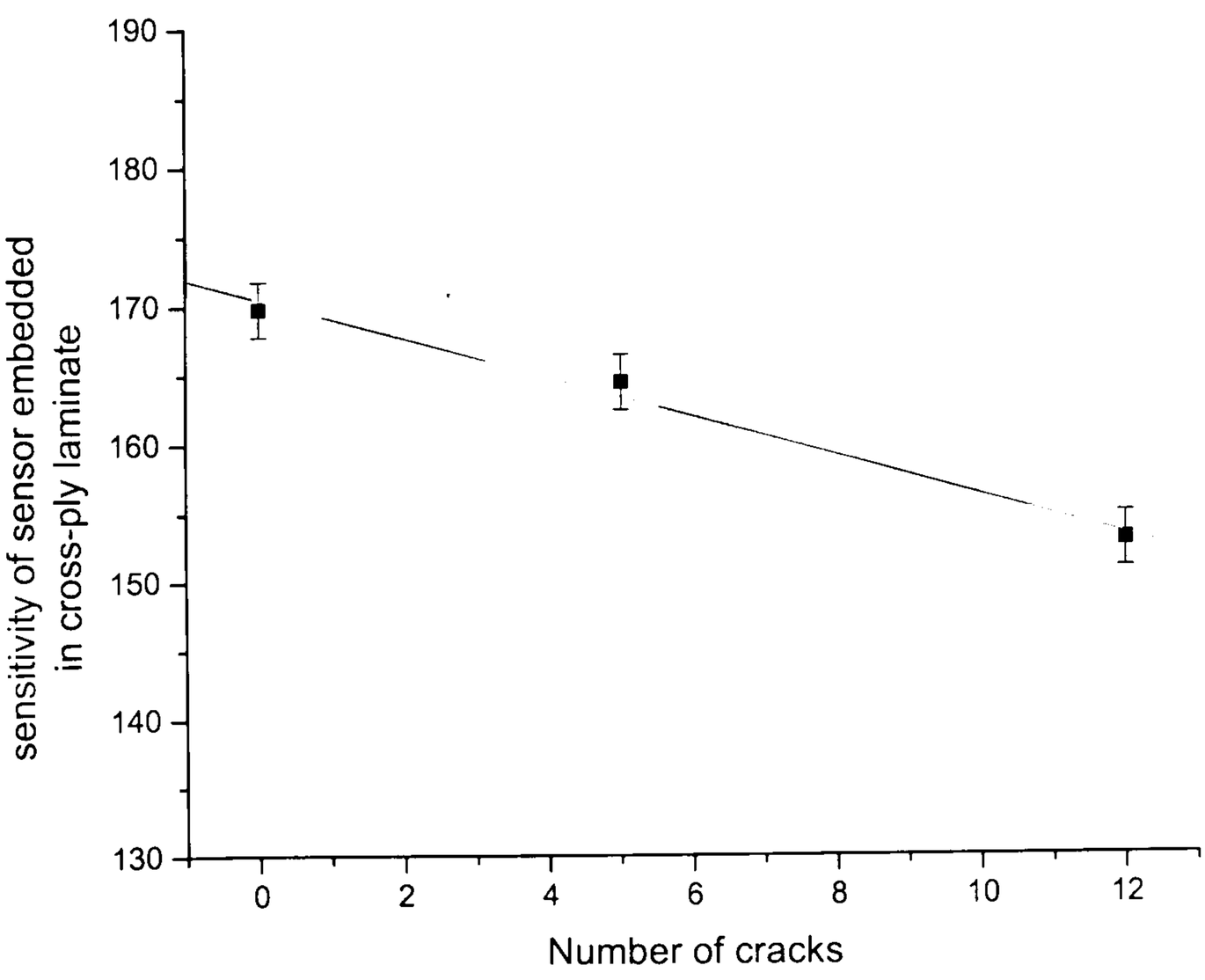

Figure 10.11 Experimental results showing the change of sensitivities with number of cracks passing the sensor

10.3.2. The direction of optical output changes during crack formation

When the optical signal changes induced by passing cracks are checked carefully, it is found that in some cases, the optical output intensity increases and in some cases it decreases. Table 10.3 shows the results for ten samples. For each sample, the number of cracks analysed is shown, together with the measured variation of the distance of the core of the sensor to the 0/90 interface. For example, in Sample 1, nine cracks form and the distance varies between 62.5 and 80 μm (determined by sectioning and polishing). Also shown is the variation in the orientation of the optical axes of the sensor with the composite axes for the cracks. However, the most important columns for this discussion are those showing the "jump direction" and "agreement". The "jump direction of optical change" is explained by Figure 10.12. When the optical fringe is increasing in intensity and the optical change when a crack forms also increases (Figure 10.12(a)), or when an optical fringe is decreasing in intensity and

Table 10.3 Experimental results of optical signal change direction

Sample No.	Distance of optical core to 0/90 interface, μm	Orientation between optical axes and composite axes, °	Jump direction of optical changes, up/down	Agreement between optical change and optical fringe, yes/no
1	62.5 -- 80	13 -- 34	5/4	7/2
2	85.5 -- 86.5	85 -- 127	2/3	3/2
3	72.5 -- 77.5	-19 -- 37	8/11	11/8
4	65.5 – 108.5	-53 -- 42	1/3	3/1
5	62.5 – 67.5	0 -- 84	2/0	1/1
6	67.5 –- 132.5	-105 -- -71	4/1	4/1
7	62.5 –- 64.5	-100 -- -110	0/2	1/1
8	75.7 –- 113.1	-71 -- -76	3/4	7/0
9	72.5 – 92.5	-17 -- 22	3/2	5/0
10	67.5 – 75.5	-23 -- 17	2/2	2/2

the optical change decreases (Figure 10.12(b)), the optical change is said to follow the fringes. Otherwise, the optical change does not follow the fringes (Figure 10.12(c) and Figure 10.12(d)). Overall, 72 % of the optical step-changes follow the fringes. although 28 % of the changes do not follow the fringes. Interestingly, whether the optical change follows the fringes or not, the overall effect on the sensor sensitivity is to decrease the sensitivity as discussed earlier. The analysis in Section 10.3.2 has dealt with this aspect of the change and the sensitivity of the sensor would be expected to decrease. However, the prediction of whether the optical change will follow the fringe or not, is much more difficult and this question has been addressed as follows.

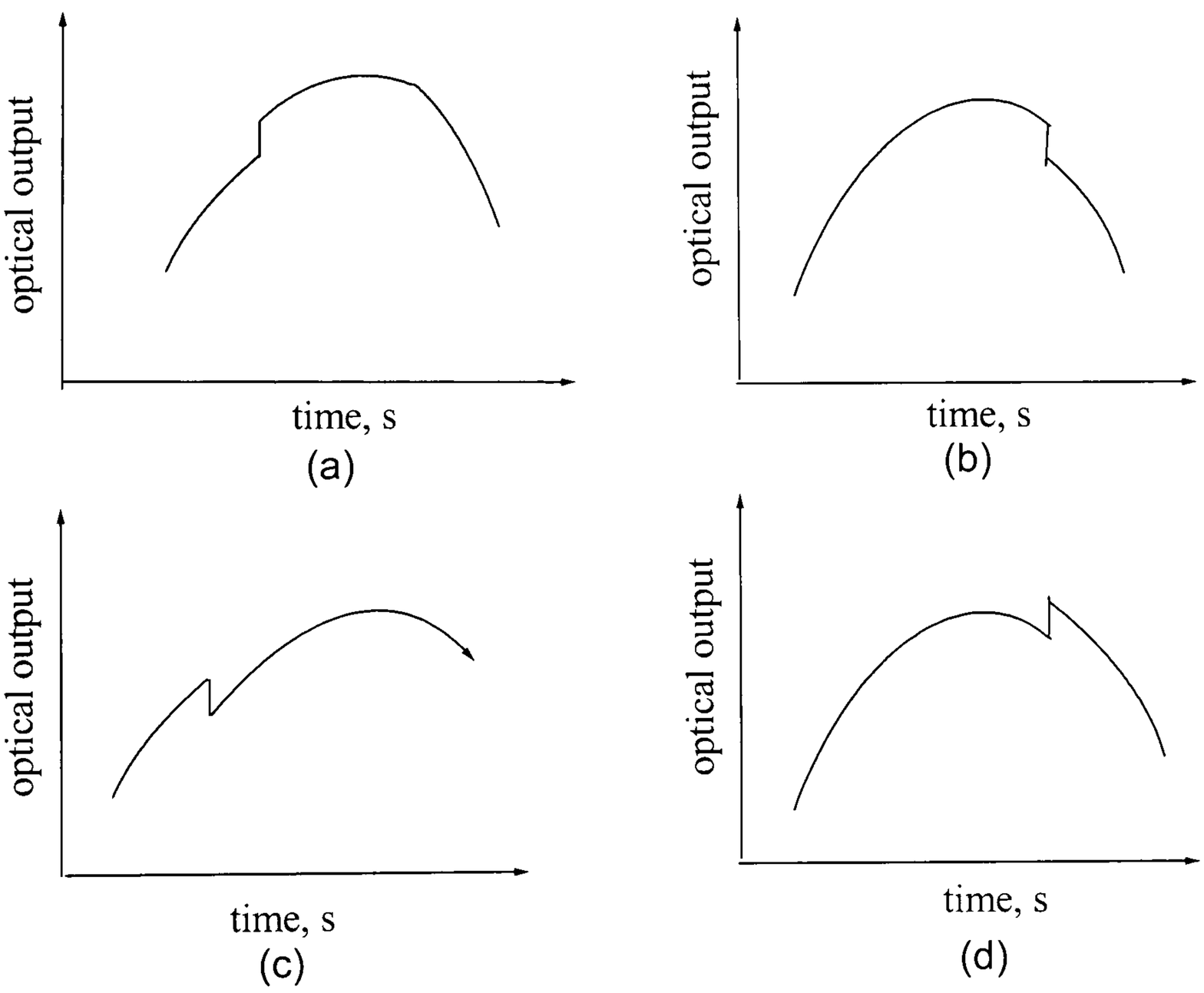

Figure 10.12 Schematic of the terminology of optical changes

The reason for the optical signal change is that when a transverse crack passes the embedded sensor, the abnormal strain field around the crack changes the optical refractive indices of the optical axes in the sensor core. The change of the refractive indices affects the velocity of the optical waves propagating in the optical axes in the sensor core, and after interference at the second splice, the consequence is an

alteration of the optical output of the sensor. The two variables which might be expected to affect whether the optical change follows the fringe or not are the relative orientation of the optical axes to the axes of the composite and the distance of the sensor from the 0/90 interface (since Arjyal et al (1998) have shown that the strain field around the crack tip changes rapidly with distance from the 0/90 interface).

To investigate the effect of these two parameters, a large number of optical changes were examined in relation to the cracks which caused them. Use of the video recording enabled each crack to be determined and sectioning the coupons enabled both the sensor axes' orientation and the distance of the sensor from the 0/90 interface to be identified for each crack. The experimental data are listed in Table 10.3. The results shown in the table suggest that the orientation of the optical axes to the composite axes, and the distances of the sensor from the 0/90 interface are not the parameters which affect the direction of the optical output changes. It appears from the results that the optical change direction for cracks having similar sensor orientation and sensor distance can either follow, or not follow the fringe direction. Hence it has been concluded that further work be required to understand this particular result.

10.4 Conclusion

In this chapter, a number of aspects of the behaviours of the polarimetric sensor have been treated analytically.

Firstly, the longitudinal sensitivity of a polarimetric sensor embedded in a unidirectional laminate has been measured under quasi-static tensile loading. The measured sensitivity is in reasonable agreement with the sensitivity predicted using the phase-strain model for a polarimetric sensor with the parameters determined from the tests of the free sensor.

Secondly, a model has been developed for the sensitivity of a polarimetric sensor embedded in a cross-ply laminate. This model includes the effect of the initial orientation of the optical axes of the sensor at the reference splice relative to the composite axes and the overall twist angle of the sensor between the two splices. A parametric study has shown that the sensitivity of the embedded sensor is affected by the initial orientation of the sensor for small overall twist angles. When the overall twist angle of the embedded sensor increases, the sensitivity of the sensor reaches a constant value and is independent of the initial orientations. Although the trend of the predicted sensitivities is in agreement with the experimental results, the range of the sensitivities predicted is significantly smaller than the range found experimentally.

Finally, with regard to damage detection, the problem of the interaction between an embedded sensor in the 0° ply and a crack that grows in the 90° ply within the gauge length of the sensor has been treated using a simple shear-lag model in conjunction with the phase-strain model. The analysis shows that when a crack passes, there will always be a reduction in the sensitivity of the embedded sensor. The experimental results show that the sensitivity does indeed decrease with increasing numbers of cracks in a linear fashion. However, although the trend of the reduction in sensitivity is predicted by the analytical model, it has not been possible to explain why the step-change in the optical output sometimes follows the fringe direction and sometimes does not.

In the next chapter, Chapter 11, the conclusions of the thesis will be presented together with suggestions for further work.

Chapter 11. Conclusions and further work

11.1 Conclusions

The material system used in the experiment here is an E-glass/epoxy laminate with a polarimetric sensor embedded in the 0° ply near 0/90 interface. The transparent nature of the GFRP composite makes it easy to observe and record the propagation of transverse cracks in relation to the position of the embedded sensors. Furthermore, the explanation of the response of the load, strain and optical signals to crack formation is easier due to the well-documented understanding of crack behaviour in a cross-ply laminate.

The basic responses of polarimetric sensors of different types and under different embedding conditions (free sensor, sensor embedded in unidirectional laminate, sensor embedded in cross-ply laminate) have been obtained. True optical fringes can only be obtained by bending the lead-out optical fibre properly. Experiments of polarimetric sensors under different loading conditions (tensile loading, compression loading, fatigue tests) have been carried out. The polarisation state of polarised light in the fibre core has been analysed and shown to be understood.

The temperature response of a polarimetric sensor has been tested and the results show that the sensor is not very sensitive to the temperature and not suitable to use as a temperature sensor, especially for short lengths. However this means that when the sensor with a length of 0.1 m is employed to detect cracks in a laminate in a temperature-controlled lab, any thermal effects can be neglected

Different types of damage detection tests (transverse cracks in cross-ply coupons with and without circular holes) have been carried out. The experimental results show that there is a clear one to one relationship between the step-change of the optical output and the instant that the cracks pass the sensor. Such a sensor could therefore form the basis of a simple system for real time damage monitoring.

Detection of cracks around a circular hole in a coupon by polarimetric sensors makes it possible to distinguish the effects of the cracks that pass the sensor and cracks that do not pass the sensor on the optical output of the sensor when a crack is developed. The experimental results confirm that when a crack passes the sensor, there will be a step optical signal change. When a crack occurs without passing the embedded sensor, no optical change can be obtained. This indicates that the step optical signal changes are induced by the complex interaction between the strain field around the matrix crack in the immediate vicinity of the crack tip and the embedded sensor.

It has been shown that the polarimetric sensor can be made sensitive to matrix cracking damage over a particular, short length of the composite (with 2×45° splices embedded in the composite structure) or to be sensitive throughout the complete length of the composite (with 2×45° splices outside the composite structure). Such a sensor therefore has the potential for detecting damage in large composite structures since the sensing length can be very long.

In addition, the optical output signals have been analysed using the FFT function in Origin® software. The results show when a crack passes adjacent to an embedded sensor, components of high frequencies emerge in the Fourier series that represent the

step-optical change induced by the crack. The times that the characteristic frequency occurs can be obtained by the band pass FFT analysis; hence, the time that cracks occur can be identified. This makes it possible to detect transverse cracks in a composite structure in real time by an embedded polarimetric sensor in engineering applications.

Further crack detection experiments using polarimetric sensors in double cross-ply coupons tested in tension have confirmed that when a crack grows in a 90° ply adjacent to the sensor, there are step-changes in the optical signal. When a crack develops without passing adjacent to the embedded sensor, no optical change is found.

It has been shown that a polarimetric sensor can be employed to monitor strain change in four-point bending tests, both under quasi-static load and fatigue load. In addition, the sensor can be used to detect transverse cracks induced in quasi-static four-point bending tests as well.

To determine the strain-optical parameters of the optical fibre utilised in the present work, the sensitivity of a bare fibre polarimetric sensor made of the Hi-Bi PANDA fibre has been measured experimentally and it has been shown that optical fringes can be obtained both under tension and diametric compression tests of the bare sensor. A phase-strain model available in the literature has been used to determine the characteristic parameters of the optical fibre (the K values). The results show that the PANDA fibre used lower strain sensitivity than Bow-Tie fibre.

After the strain-optical parameters of the sensor have been obtained, it has been possible to discuss the sensitivities of an embedded sensors and the interaction

between the embedded sensor and cracks which pass the sensor in an adjacent ply. Firstly, the longitudinal sensitivity of a polarimetric sensor embedded in a unidirectional laminate has been measured under quasi-static tensile loading. The measured sensitivity is in reasonable agreement with the sensitivity predicted using the phase-strain model for a polarimetric sensor with the K values determined from the tests carried out here on free sensors.

Secondly, a model has been developed for the sensitivity of a polarimetric sensor embedded in a cross-ply laminate including the effect of the initial orientation of the optical axes of the sensor at the reference splice relative to the composite axes and the total twist angle of the sensor up to the second splice. A brief parametric study has shown that the sensitivities of the embedded sensor are affected by the initial orientations of sensor at small overall twist angles. When the overall twist angle of the embedded sensor increases, the sensitivity of the sensor reaches a constant value and is independent of the initial orientation. The trend of the predicted sensitivities is in reasonable agreement with the experimental results.

Finally, with regard to damage detection, the problem of the interaction between an embedded sensor in the 0° ply and a crack that grows in the 90° ply within the gauge length of the sensor has been treated using a simple shear-lag model in conjunction with the phase-strain model. The analysis shows that when a crack passes, there will always be a reduction in the sensitivity of the sensor. The experimental results show that the sensitivity does indeed decrease with increasing numbers of cracks. However, although the reduction in sensitivity is predicted by the analytical model, it has not been possible to explain why the step-change in the optical output sometimes follows the fringe direction and sometimes does not.

11.2 Further work

This work has shown that matrix crack can be detected in transparent GFRP coupons with the cross-ply lay-up. On the experimental side, the first step of further work would be to show that such cracks can be detected in off-axis plies, e.g. $(0/\pm 45°)_s$. Secondly, it is important to show that cracks can be detected in other composite systems, particularly CFRP. Finally, a complete engineering package should be demonstrated, using the FFT filter method to detect matrix cracking without the need to store large amounts of data.

On the theoretical side, the theory developed here to predict the step-change in the optical signal when a crack passes is incomplete. An analytical solution of the problem may not be possible, given the complexity of the stress state around the core of a Hi-Bi fibre, and it may well be necessary to attempt to model the problem numerically.

References

Akhavan F., Watkins S. E. and Chandrashekhara K. "Measurement and analysis of impact-induced strain using extrinsic Fabry-Perot fibre optic sensors". Smart Materials and Structures, 1998; 7; pp. 745-751.

Ansari F. and Wang J. "Rate sensitivity of high birefringent fibre optic sensors under large dynamic loads", Journal of Lightwave Technology, 1995; 10; pp.1992-1997.

Araujo F. M., Ferreiro L. A. and Santos J. L. "Temperature and strain insensitive bending measurements with D-type fibre Bragg gratings", Measurement Science and Technology, 2001; 12; pp. 829-833.

Arjyal B. P., Galiotis C., Ogin S. L. and Whattingham. R. D. "Residual strain and Young's modulus determination in cross-ply composite using an embedded aramid fibre strain sensor", Composites Part A, 1998; 29A; pp. 1363-1369.

Arjyal B. P., Galiotis C., Ogin S. L. and Whattingham. R. D., "Monitoring local strains in cracked cross-ply composites using an embedded fibre strain sensor", Journal of Material Science, June, 1998; Vol. 33, Num. 11; pp. 2745-2750.

Asundi A., Cheng H.K. and Toh S.L. "Effect of input polarization angle on force sensitivity of embedded single mode poarimetric sensors", Proceedings SPIE International Society of Optical Engineering. 1996; Vol 2872; pp. 79-86.

Badcock R. A. and Fernando G. F., "An intensity-based optical fibre sensor for fatigue damage detection in advanced fibre-reinforced composites", Smart Materials and Structures. 1995; 4; pp. 223-230.

Bailey J. E., Curtis P. T. and Parvize A. "On the transverse cracking and longitudinal splitting behaviour of glass and carbon fibre reinforced epoxy cross ply laminates and the effect of Poisson and thermally generated strain", Proc. R. Soc. London, A. 366, 1979; pp.599-623.

Baillie P. W. R. and Hale K. F. "Optical Fibre Sensing of Acoustic Emission in Fibre Reinforced Composites", North American Conference on Smart Structures and Materials, 1995.

Barry G. G. and Huang L. "Fibre optic sensor array for multi-dimensional strain measurement", Smart Materials and Structure, 1998; 7; pp. 159-165.

Barton E. N., Ogin S. L., Thorne A. M. and Reed G. T. "Detectiong transverse cracks in composite materials", Proceedings of the Applied Optics and Opto-electronics Conference, UK, 2000.

Barton E. N. "Detection of matrix cracking in a GFRP laminate using a fibre optic sensor". Ph. D. Thesis, 2000.

Barton E. N., Ogin S. L., Thorne A. M. and Reed. G. T. "Use of a polarimetric sensor to detect the fatigue crack growth of matrix cracks in a cross-ply composite laminate". 13th International Conference on Composite Materials, Beijing, 2001.

Bassam F., Boniface L., Jones K. and Ogin S. L., "On the behaviour of the residual strain produced by matrix cracking in cross-ply laminates", Composites Part A, 1998; 29A; pp. 1425-1432.

Bocherens E.,.Bourasseau S. and Dewynter M. V. "Damage detection in a radome sandwich material with embedded fibre optic sensors", Smart Materials and Structures, 2001; 9; pp. 310-315.

Bock W. J. "Multiplexing of fibre-optic sensors for stress measurements in civil engineering applications", Proceedings of SPIE, 1998; 3414; pp. 86-92.

Bock W. J. and Wolinski T. R. "High-pressure fibre optic sensor based on polarization-rotated reflection in optical fibre sensors", Proceedings in physics. 1989; 44; pp. 464-469.

Bock W. J., Domanski A. W. and. Wolinski T. R. "Influence of high hydrostatic pressure on beat length highly birefringent single-mode bow tie fibres", Applied Optics, 1990; Vol. 29, No.24; pp. 3484-3488.

Born M., and Wolf E. "Principles of optics". Pergamon Press, 1970.

Boniface L., Ogin, S. L. and Smith P. A. "Strain energy release rates and the fatigue growth of matrix cracks in model arrays in composite laminates", Proce. R. Soc. Lond. A, 1991; pp. 427-444.

Boniface L., Smith P. A. and Bader M. G. "Transverse ply cracking in cross-ply CFRP laminates-initiation or propagation controlled?", Journal of Composite Materials, 1997; Vol. 31, No.11; pp. 1080-1111.

Butter C. D.and Hocker G. B. " Fibre optics strain gauge", Applied Optics, 1978; Vol. 17, No. 18; pp. 2867-2869.

Chang C. and Sirkis J. S. "Design of fire optic sensor systems for low velocity impact detection", Smart Materials and Structures. 1998; 7; pp. 166-177.

Chu P. L. and Wong D. "Phase sensitivity of polarization-maintaining optical fibre used as temperature sensor", Journal of Lightwave Technology, 1986; Vol. LT-4. No.1; pp. 41-49.

Chu P. L. and Sammut R. A. "Analytical method for calculation of stresses and material birefringence in polarization-maintaining optical fibre", Journal of Lightwave Technology, 1984; Vol. LT-2, No.5; pp. 650-662.

Crocker L. E., Ogin S. L. and Smith P. A. "Intro-laminar fracture in angle-ply laminates". Composites Part A, 1997; 28A; 839-846.

Dakin J. and Culshaw B. "Optic fibre sensors: vol 1, Principles and components", Norwood, MA; London : Artech House, 1988.

Dasgupta A., Wan Y. and Sirkis J.S. "Prediction of resin pocket geometry for stress analysis of optical fibres embedded in laminated composites", Smart Materials and Structures. 1992; 1; pp. 101-107.

Domanski A. W., Tomasz R. W. and Bock W. J. "Polarimetric fibre optics sensors: state of the art and future", SPIE, 1997; Vol. 2341; pp. 21-28.

Domanski A.W., Karpierz M. and Sierakowski M. "Polarimetric optical sensor with compensated birefringence for dynamic strain measurement", Proceedings of SPIE, 1997; vol 3189; pp. 83-85.

Ecke W., Latka I. and Willsch R. "Fibre optic sensor network for spacecraft health monitoring", Measurement Science and Technology, 2001; 12; pp. 974-980.

Fan N. Y., Huang S. and Measures R. M. "Localized long gage fibre optic strain sensors", Smart Materials and Structures, 1998; 7; pp. 257-264.

Fernandez A, Berghmans F and Brichard B. "Multi-component force sensor based on multiplexed fibre Bragg grating strain sensors", Measure Science and Technology. 2001; 12; pp. 810-813.

Garcia-Ramos F J, Ortix-Canavate J, Ruiz-Altisent M and Diez J, "Development and implementation of an on-line impact sensor for firmness sensing of fruits", Journal of Food Engineering, 2003; 58; pp. 53-57:

Garret K. W. and Bailey J. E., "Multiple transverse fracture in 90° cross-ply laminates of a glass fibre-reinforced polyester", Journal of Materials Science, 1997; 12: pp. 157-168.

Gaumont E., Chakari A. and Meyrueis P. "Minimisation of thermal effects on the polarisation in a polarimetric sensor using a single-mode fibre optic". Proceedings SPIE, The International Society for Optical Engineering. 1998; 3483; pp. 184-188.

George A. "Use of smart technologies in Bridge Construction", The 13th International Conference on Composite Materials, Beijing, June, 2001.

Graham D. and Michel L. "Arbitrary strain transfer from a host an embedded firbre-optic sensor", Smart Materials and Structures, 2000; 9; pp. 492-497.

Green A K, Mzaidman and Shafir E. "Infrastructure development for incorporating fibre-optic sensors in composite materials", Smart Materials and Structures, 2000; 9; pp.316-321.

Guemes J. A., Menendze J. M. and Frovel M. "Experimental analysis of buckling in aircraft skin panels by fibre optic sensors". Smart Materials and Structures 2001; 10; pp. 490-496.

Guild F.G., Ogin S.L. and Smith P.L. "Modelling of 90° Ply Cracking in Cross Ply Laminates, Including Three-Dimentional Effect", Journal of Composite Materials, 1993; 27; pp. 646-667.

Gunther W., Percy N. and Kalinowski H. J. "A fibre optic Bragg grating strain sensor for monitoring ventilatory movements", Measurement Science and Technology, 2001; 12; pp. 805-809.

Hadjiprocopiou M. "Fibre optic sensors for smart structures", Ph.D. Thesis, 2000.

Hadjiprocopiou M, Reed G.T., Garden H., Thorne A.M. and Hollawey L. "Experimental results and finite element modelling of an embedded polarimetric sensor", Composite, 1995; 265; pp. 775-783.

Hale K.F. "An optical-fibre fatigue crack-detection and monitoring system", Smart Materials and Structure, 1992; 1; pp. 156-161.

Hecht E. "Theory and problems of optics", McGraw-Hill Book Company. 1975

Henrik D. S. "Demonstration of twisted polarimetric optical fibre sensor embedded in carbon-epoxy composite", The 2nd European Conference on Smart Structures and Materials, Glasgow, 1994.

Hong C., Bang H., Kang H. and Kim C. "Real-time damage detection for smart composite materials using optical fibre sensors", The 13th International Conference on Composite Materials, Beijing, 2001.

Insang L., Yuan L. and Ansari F. "Fibre-optic crack-tip opering displacement sensor for concrete", Cement and Concrete Composites, 1997; 19; pp. 59-68.

Ito T., "Thermal hysteresis of phase retardation in polarization maintaining optical fibres", Journal of Lightwave Technology. 1994; Vol. 12, No.8; pp. 1343-1347.

Johns R. C. "A new calculus for the treatment of optic systems", J. Optv. Oc Am. 1941; Vol. 31, No.7; pp. 483-493.

Johnson F. J., Cross W. M. and Boyles D. A. ""Complete" system monitoring of polymer matrix composites". Composites Part A: applied science and manufacturing, 2000; 31; pp. 959-968.

Kalamkarow A. L., MacDonald D.O. and Fitzgerald S.B. "Reliability assessment of pultruded FRP reinforcements with embedded fibre optic sensors", Composite Structures 2000; 50; pp. 69-78.

Kang H.. K., Park J. W. and Ryu C. Y. "Development of fibre optic ingress-egress methods for smart composite structures", Smart Materials and Structures, 2000; 9; pp. 149-156.

Kollar L. P. and Steenkiste R. J. "Calculation of the Stresses and Strains in Embedded Fibre Optic Sensors", Journal of Composite Materials, 1998; 3218; pp. 1647-1679.

Kraniauskas P. "Transforms in signals and systems"; Addison-Wesley Publishing Company, 1991.

Kwon B., Kim C. G. and Hong C. S. "Simultaneous Sensing of the Strain and Points of Failure in Composite Beams with an Embedded Fibre Optic Michelson Sensor", Composites Science and Technology, 1997; 57; pp. 1639-1651.

Lee D. C., Lee J. J. and Kwon I. B. "Monitoring of fatigue damage of composite structures by using embedded intensity-based optical fibre sensors", Smart Materials and Structures. 2001; 10; pp. 285-292.

Lee M. L., Park J. S. and Lee W. L. "A polarimetric current sensor using an orthogonally polarized dual-frequency fibre laser", Metal. Science Technol. 1998; 9; pp. 952-959.

Lee S. T., Aneeshkumar B., Radhakrishnan P., Vallabhan C.P.G and Nampoori V.P.N. "A microbent fibre optic pH sensor", Optics Communications, 2002; 205; pp. 253-256

Levin K. and Jarlas R. "Vulnerability of embedded EFPI sensors to low energy impacts", Smart Materials and Structures. 1997; 6; pp. 369-382.

Liu K., and Measures R. M. "Analysis of macro-strain transfer and complete strain state measurement with embedded fibre-optic sensors", Smart Materials and Structures 1993; 2; pp. 66-70.

Lo Y. I., Sirkis J. S. and Ritchie K. T. "A study of the optomechanical response of a diametrically loaded high-birefringent optical fibre", Smart Materials and Structure, 1995; 4; pp. 327-333.

Lunia A, Kakkattukuzhy M. and Chandrashekhara. K. "Aerodynamic testing of a smart composite wing using fibre-optic strain sensing and neural network", Smart Materials and Structures. 2000; 9; pp. 767-773.

Ma J. and Asundi A. "Structural health monitoring using a fibre optic polarimetric sensor and a fibre optic curvature sensor-static and dynamic test", Smart Materials and Structures, 2001; 10; pp. 181-188.

Ma J. and Tang. W. "Second-order sensitivity effect on optical fibre polarimetric temperature sensor and strain sensor"; Applied Optics, 1997; Vol.36, No.34; pp. 9010-9013.

Ma J., Tang W. and Wen Z. "Dual-wavelength optical fibre polarimetric sensor for simultaneous measurement of strain and temperature", Acta Optica Sinica, 1998; Vol.18, No.3; pp. 361-364.

McKenzie I.,.Jones R. and Marshall I.H. "Optical fibre sensors for health monitoring of bonded repair systems", Composite Structures, 2000; 50; pp. 405-416.

Meriam J.L. "Engineering Mechanics". 1987

Murukeshan V.M., Chan P.Y. and Ong L. S. "Effects of different parameters on the performance of a fibre polarimetric sensor for smart structure applications", Sensors and Actuators, 2000; 80; pp. 249-255.

Murukeshan V. M., Chan P.Y. and Ong L. S. "On-line health monitoring of smart composite structures using fibre polarimetric sensor", Smart Materials and Structures. 1999; 8; pp. 544-548.

Murukeshan V. M., Chan P.Y. and Ong L. S. "Towards realization of a smart polarimetric sensor", Proceedings SPIE, The International Society for Optical Engineering. 1999; 3670; pp. 54-64.

Norbert F., Markus S. and Wojetk J. "Dynamic pressure sensing with a fibre optic polarimetric pressure transducer with two-wavelength passive quadrature readout". Applied optics, 1998; Vol 37, No. 4; pp. 663-671.

Ogin, S.L., Smith, P.A. and Beaumont, P.W.R. "Matrix cracking and stiffness reduction during the fatigue of a 0/90s GFRP laminate", Composite Science and Technology, 1985; 22; pp. 23-31.

Okabe. Y, Yashiro. S, Kosaka. T and Takeda N. "Detection of transverse cracks in CFRP composites using embedded fibre Bragg grating sensor", Smart Materials and Structures, 2000; 9; pp. 832-838.

Pak Y. E. "Longitudinal shear transfer in fibre optic sensors", Smart Materials and Structures, 1992; 1; pp. 57-62.

Park J. M., Lee S. I., Kwon O. Y., "Comparison of non-destructive microfailure evaluation of fibre-optic Bragg grating and acoustic emission piezoelectric sensors using fragmentation test", Composite: Part A, 2003; 34; pp. 203-216.

Parvizi A., Garrett K. W. and Bailey J. E. "Constrained cracking in glass fibre-reinforced epoxy cross-ply laminates", Journal of Materials Science, 1978; 13; pp. 195-201.

Passy R., Gama A.L. and Gisin N. "Pressure dependence of polarization mode dispersion in Hi-Bi fibres", Journal of Lightwave Technology. 1992; Vol.10, No.11; pp. 1527-1531.

Rashleigh, S.C. "Magnetic-field sensing with a single-mode fibre", Optical Letters. 1981; 6; pp. 19-21.

Rashleigh S. C. "Origins and control of polarization effects in single-mode fibres". Journal of Lightwave Technology. 1983; Vol. Lt-1, No.2; pp. 245-276.

Rasmussen J. C. and Scholl B. "Fibre optic polarimetric temperature sensor with high sensitivity", Proceedings SPIE The International Society for Optical Engineering. 1997; 3121; pp. 249-258.

Rippert L., Wevers M. and Huffel S. V. "Optical and Acoustic Damage Detection in Laminated CFRP Composite Materials", Composites Science and Technology, 2000: 60; pp. 2713-2724.

Sammut R. A. and Chu P. L. "Axial stress and its effect on relative strength of polarization-maintaining fibres and perform", Journal of Lightwave Technology, 1985; Vol. LT-3, No.2; pp. 283-287.

Sergey A. G., Anatoly N. M. and Alexander S. P. "Spectral signal processing in intrinsic interferometric sensors based on birefringent polarization maintaining optical fibres", Journal of Lightwave Technology, 1995; Vol.13, No. 7; pp. 1231-1236.

Senior J. M, "Optical Fibre Communications, Principles and Practice", Second edition, Prentice hall, 1992.

Simpon J. and Stolen R. "A single-polarization fibre", Journal of Lightwave Technology, 1983; LT-1, No. 2; pp. 370-374.

Sirkis J. S. "Optical and mechanical isotropies in embedded fibre optic sensors", Smart Materials and Structure, 1993; 2; pp. 255-259.

Sirkis J. S. "Unified approach to phase-strain-temperature models for smart structure interferometric optical fibre sensors: Part 1, Development, Part 2, Application". Optical Engineering. 1993; 324; pp. 752-773.

Sirkis J. S. and.Lo Y.L. "Phase-strain model for polarimetric strain sensor based on fictitious residual strains", Journal of Intelligent Materials Systems and Structures, 1994; 5; pp. 494-500.

Smith P. A. and Wood J. R. "Poisson's ratio as a damage parameter in the static tensile loading of simple cross-ply laminates", Composite Science and Technology,

1990; 38; pp.85-93.

Spillman W B, Sirkis J S. and Gardiner P.T. "Smart materials and structures: what are they?", Smart Materials and Structures. 1996; 5; pp. 247-254.

Studer M., Peters K., and Botsis J., "Method for dtermination of crack bridging parameters using long optical fibre Bragg grating sensors", Composite: Part B, 2003; 43; pp. 347-359.

Sung D., Kim C. and Hong C., "Simultaneous monitoring of impact locations and damage s in composite laminates using piezoceramic sensors", The 13th International Conference on Composite Materials, Beijing, 2001.

Tennyson R C, Mufti A A. and Rizkalla.S. "Structural health monitoring of innovative bridges in Canada with fibre optic sensors", Smart Materials and Structures, 2001; 10; pp. 560-573.

Takehito F. "Recent R&D of smart composites in Japan", The 13th International Conference on Composites Materials, Beijing, 2001.

Tsuda H., Takahashi J. and Urabe K. "Damage monitoring of carbon fibre-reinforced plastics with Michelson interferometric fibre-optic sensors", Journal of Materials Science, 1999; 34; pp. 4163-4172.

Varnham M. P. and Payne D. N. "Coiled-birefringent-fibre Polarizers", Optics Letters, 1984; 94; pp.306-308.

Varnham M. P., Payne D. N. and Barlow A. J. "Analytic Solution for the birefringence produced by thermal stress in polarization-maintiaining optical fibres", Journal of Lightwave Technology. 1983; Vol. Lt-1, No. 2; pp. 332-339.

Wood K., Brown T. and Rogowski R. "Fibre optic sensors for health monitoring of morphing airfriames: I. Bragg grating strain and temperature sensor", Smart Materials and Structures, 2000; 9; pp. 163-169.

Wong D. and Poole R. "Temperature independent birefringent fibre", International Journal of optoelectronics, 1993; 82; pp. 179-186.

Wang G., Pran K., Sagvolden G. "Ship hull structure monitoring using fibre optic sensors", Smart Materials and Structure, 2001; 10; pp. 472-478.

Yoji I., Yashiro S. and Kosaka T. "Detection of transverse cracks in CFRP

composites using embedded fibre Bragg gratiing sensors", Smart Materials and Structures, 2000; 9; pp. 832-838.

Yuan L. and Zhou L. "Sensitivity coefficient evaluation of an embedded fibre-optic strain sensor", Sensors and Actuators A, 1998; 69; pp. 5-11.

Zhang B., Wang D. and Du S. "An investigation of a fibre optic sensor in the composite cure process", Smart Materials and Structures. 1999; 8; pp. 515-518.

Smith P.A. and Ogin S.L. "On transverse matrix cracking in cross-ply laminates loaded in simple bending", Composites: Part A, 1999; 30; pp. 1003-1008.

Appendix A. Application of extensometer in four point bending experiments-Input and output from MAPLE

When an extensometer is used in four-point bending tests, some analysis needs to be carried out to convert the strain signal provided by the extensometer attached to the specimen surface to the strain at the position of the embedded sensor.

As shown in Section 8.3, when the extensometer is attached to the top (concave) surface of the coupon in four-point bending tests, the following equation exists:

$$\sin(\frac{L/2}{R}) = \frac{L'/2}{R-d}$$

A1

When the extensometer was attached to the bottom surface of the coupon in four-point bending tests, the following equation exist:

$$\sin(\frac{L/2}{R}) = \frac{L'/2}{R+d}$$

A2

In both equations, *L/2* is half of the gauge length of the extensometer, *L'/2* is half of the new length of the extensometer as a result of the bending, *R* is the radius of curvature of the beam and *d* half the thickness of the coupon.

The accurate value of R in Equations (A1) and (A2) can be solved using Maple® software, for example, the ***fsolve*** command. However, the data recorded by the computer controlling the fatigue machine always contain thousands of lines of strain data, which means that thousands of R values should be calculated, and using the

fsolve command is not practicable. To obtain R values in real time, Maple®, Excel® and some approximation in calculation should be used.

Extending the left side of equation A1 and equation A2, and ignoring the orders higher than 3, the following equations can be obtained:

$$\frac{L/2}{R}-\frac{(L/2)^3}{6R^3}=\frac{L'/2}{R-d} \qquad \text{A3}$$

$$\frac{L/2}{R}-\frac{(L/2)^3}{6R^3}=\frac{L'/2}{R+d} \qquad \text{A4}$$

The roots of Equation A3 and Equation A4 were calculated using Maple® and compared with accurate results computing with ***fsolve*** commands. The input commands and output results from Maple®, including additional explanations, are shown below:

```
> restart;
```

Solution of equation A3 and equation A4

```
> equationA1 :=sin(a/R)=b/(R-d);
```

$$equationA1 := \sin\left(\frac{a}{R}\right)=\frac{b}{R-d}$$

```
> equationA2 :=sin(a/R)=b/(R+d);
```

$$equationA2 := \sin\left(\frac{a}{R}\right)=\frac{b}{R+d}$$

```
> equationA3 :=a/R-a^3/6/R^3=b/(R-d);
```

$$equationA3 := \frac{a}{R}-\frac{a^3}{6\,R^3}=\frac{b}{R-d}$$

```
> equationA4 :=a/R-a^3/6/R^3=b/(R+d);
```

$$equationA4 := \frac{a}{R}-\frac{a^3}{6\,R^3}=\frac{b}{R+d}$$

```
> solve(equationA3, {R});
```

$$\{R = \left((12\,a^2\,d - 30\,d\,a\,b + 18\,d\,b^2 - 8\,d^3 \right.$$

$$- 2\sqrt{81\,b^2\,d^2 + 2\,a^3\,b - 108\,a\,b\,d^2 - 2\,a^4 + 24\,a^2\,d^2 - 72\,d^4}\;a$$

$$\left. + 2\sqrt{81\,b^2\,d^2 + 2\,a^3\,b - 108\,a\,b\,d^2 - 2\,a^4 + 24\,a^2\,d^2 - 72\,d^4}\;b \right)^{(1/3)} / (6\,(-a+b)) - ($$

$$-a^2 + a\,b - 2\,d^2) \Big/ (3\,(-a+b)\,(12\,a^2\,d - 30\,d\,a\,b + 18\,d\,b^2 - 8\,d^3$$

$$- 2\sqrt{81\,b^2\,d^2 + 2\,a^3\,b - 108\,a\,b\,d^2 - 2\,a^4 + 24\,a^2\,d^2 - 72\,d^4}\;a$$

$$\left. + 2\sqrt{81\,b^2\,d^2 + 2\,a^3\,b - 108\,a\,b\,d^2 - 2\,a^4 + 24\,a^2\,d^2 - 72\,d^4}\;b \right)^{(1/3)}) - \frac{d}{3\,(-a+b)} \Bigg)$$

$$a\}, \{R = \left(- (12\,a^2\,d - 30\,d\,a\,b + 18\,d\,b^2 - 8\,d^3 \right.$$

$$- 2\sqrt{81\,b^2\,d^2 + 2\,a^3\,b - 108\,a\,b\,d^2 - 2\,a^4 + 24\,a^2\,d^2 - 72\,d^4}\;a$$

$$\left. + 2\sqrt{81\,b^2\,d^2 + 2\,a^3\,b - 108\,a\,b\,d^2 - 2\,a^4 + 24\,a^2\,d^2 - 72\,d^4}\;b \right)^{(1/3)} / (12\,(-a+b))$$

$$+ (-a^2 + a\,b - 2\,d^2) \Big/ (6\,(-a+b)\,(12\,a^2\,d - 30\,d\,a\,b + 18\,d\,b^2 - 8\,d^3$$

$$- 2\sqrt{81\,b^2\,d^2 + 2\,a^3\,b - 108\,a\,b\,d^2 - 2\,a^4 + 24\,a^2\,d^2 - 72\,d^4}\;a$$

$$\left. + 2\sqrt{81\,b^2\,d^2 + 2\,a^3\,b - 108\,a\,b\,d^2 - 2\,a^4 + 24\,a^2\,d^2 - 72\,d^4}\;b \right)^{(1/3)}) - \frac{d}{3\,(-a+b)}$$

$$+ \frac{1}{2}\,I\sqrt{3}\,((12\,a^2\,d - 30\,d\,a\,b + 18\,d\,b^2 - 8\,d^3$$

$$- 2\sqrt{81\,b^2\,d^2 + 2\,a^3\,b - 108\,a\,b\,d^2 - 2\,a^4 + 24\,a^2\,d^2 - 72\,d^4}\;a$$

$$\left. + 2\sqrt{81\,b^2\,d^2 + 2\,a^3\,b - 108\,a\,b\,d^2 - 2\,a^4 + 24\,a^2\,d^2 - 72\,d^4}\;b \right)^{(1/3)} / (6\,(-a+b)) + ($$

$$-a^2 + a\,b - 2\,d^2) \Big/ (3\,(-a+b)\,(12\,a^2\,d - 30\,d\,a\,b + 18\,d\,b^2 - 8\,d^3$$

$$- 2\sqrt{81\,b^2\,d^2 + 2\,a^3\,b - 108\,a\,b\,d^2 - 2\,a^4 + 24\,a^2\,d^2 - 72\,d^4}\;a$$

$$\left. + 2\sqrt{81\,b^2\,d^2 + 2\,a^3\,b - 108\,a\,b\,d^2 - 2\,a^4 + 24\,a^2\,d^2 - 72\,d^4}\;b \right)^{(1/3)})) \Bigg) a\}, \{R = \left(-$$

$$(12\,a^2\,d - 30\,d\,a\,b + 18\,d\,b^2 - 8\,d^3$$

$$- 2\sqrt{81\,b^2\,d^2 + 2\,a^3\,b - 108\,a\,b\,d^2 - 2\,a^4 + 24\,a^2\,d^2 - 72\,d^4}\;a$$

$$\left. + 2\sqrt{81\,b^2\,d^2 + 2\,a^3\,b - 108\,a\,b\,d^2 - 2\,a^4 + 24\,a^2\,d^2 - 72\,d^4}\;b \right)^{(1/3)} / (12\,(-a+b))$$

$$+ (-a^2 + a\,b - 2\,d^2) \Big/ (6\,(-a+b)\,(12\,a^2\,d - 30\,d\,a\,b + 18\,d\,b^2 - 8\,d^3$$

$$- 2\sqrt{81\,b^2\,d^2 + 2\,a^3\,b - 108\,a\,b\,d^2 - 2\,a^4 + 24\,a^2\,d^2 - 72\,d^4}\;a$$

$$\left. + 2\sqrt{81\,b^2\,d^2 + 2\,a^3\,b - 108\,a\,b\,d^2 - 2\,a^4 + 24\,a^2\,d^2 - 72\,d^4}\;b \right)^{(1/3)}) - \frac{d}{3\,(-a+b)}$$

$$- \frac{1}{2}\,I\sqrt{3}\,((12\,a^2\,d - 30\,d\,a\,b + 18\,d\,b^2 - 8\,d^3$$

$$-2\sqrt{81\,b^2\,d^2+2\,a^3\,b-108\,a\,b\,d^2-2\,a^4+24\,a^2\,d^2-72\,d^4}\;a$$
$$+2\sqrt{81\,b^2\,d^2+2\,a^3\,b-108\,a\,b\,d^2-2\,a^4+24\,a^2\,d^2-72\,d^4}\;b)^{(1/3)}/(6\,(-a+b))+($$
$$-a^2+a\,b-2\,d^2)\,/\,(3\,(-a+b)\,(12\,a^2\,d-30\,d\,a\,b+18\,d\,b^2-8\,d^3$$
$$-2\sqrt{81\,b^2\,d^2+2\,a^3\,b-108\,a\,b\,d^2-2\,a^4+24\,a^2\,d^2-72\,d^4}\;a$$
$$+2\sqrt{81\,b^2\,d^2+2\,a^3\,b-108\,a\,b\,d^2-2\,a^4+24\,a^2\,d^2-72\,d^4}\;b)^{(1/3)}))\Bigg)a\}$$

```
> solve(equationA4, {R});
```

$$\{R=\Bigg((-12\,a^2\,d+30\,d\,a\,b-18\,d\,b^2+8\,d^3$$
$$-2\sqrt{81\,b^2\,d^2+2\,a^3\,b-108\,a\,b\,d^2-2\,a^4+24\,a^2\,d^2-72\,d^4}\;a$$
$$+2\sqrt{81\,b^2\,d^2+2\,a^3\,b-108\,a\,b\,d^2-2\,a^4+24\,a^2\,d^2-72\,d^4}\;b)^{(1/3)}/(6\,(-a+b))-($$
$$-a^2+a\,b-2\,d^2)\,/\,(3\,(-a+b)\,(-12\,a^2\,d+30\,d\,a\,b-18\,d\,b^2+8\,d^3$$
$$-2\sqrt{81\,b^2\,d^2+2\,a^3\,b-108\,a\,b\,d^2-2\,a^4+24\,a^2\,d^2-72\,d^4}\;a$$
$$+2\sqrt{81\,b^2\,d^2+2\,a^3\,b-108\,a\,b\,d^2-2\,a^4+24\,a^2\,d^2-72\,d^4}\;b)^{(1/3)}+\frac{d}{3\,(-a+b)}\Bigg)$$
$$a\},\{R=\Bigg(-(-12\,a^2\,d+30\,d\,a\,b-18\,d\,b^2+8\,d^3$$
$$-2\sqrt{81\,b^2\,d^2+2\,a^3\,b-108\,a\,b\,d^2-2\,a^4+24\,a^2\,d^2-72\,d^4}\;a$$
$$+2\sqrt{81\,b^2\,d^2+2\,a^3\,b-108\,a\,b\,d^2-2\,a^4+24\,a^2\,d^2-72\,d^4}\;b)^{(1/3)}/(12\,(-a+b))$$
$$+(-a^2+a\,b-2\,d^2)\,/\,(6\,(-a+b)\,(-12\,a^2\,d+30\,d\,a\,b-18\,d\,b^2+8\,d^3$$
$$-2\sqrt{81\,b^2\,d^2+2\,a^3\,b-108\,a\,b\,d^2-2\,a^4+24\,a^2\,d^2-72\,d^4}\;a$$
$$+2\sqrt{81\,b^2\,d^2+2\,a^3\,b-108\,a\,b\,d^2-2\,a^4+24\,a^2\,d^2-72\,d^4}\;b)^{(1/3)}+\frac{d}{3\,(-a+b)}$$
$$+\frac{1}{2}\,I\sqrt{3}\,((-12\,a^2\,d+30\,d\,a\,b-18\,d\,b^2+8\,d^3$$
$$-2\sqrt{81\,b^2\,d^2+2\,a^3\,b-108\,a\,b\,d^2-2\,a^4+24\,a^2\,d^2-72\,d^4}\;a$$
$$+2\sqrt{81\,b^2\,d^2+2\,a^3\,b-108\,a\,b\,d^2-2\,a^4+24\,a^2\,d^2-72\,d^4}\;b)^{(1/3)}/(6\,(-a+b))+($$
$$-a^2+a\,b-2\,d^2)\,/\,(3\,(-a+b)\,(-12\,a^2\,d+30\,d\,a\,b-18\,d\,b^2+8\,d^3$$
$$-2\sqrt{81\,b^2\,d^2+2\,a^3\,b-108\,a\,b\,d^2-2\,a^4+24\,a^2\,d^2-72\,d^4}\;a$$
$$+2\sqrt{81\,b^2\,d^2+2\,a^3\,b-108\,a\,b\,d^2-2\,a^4+24\,a^2\,d^2-72\,d^4}\;b)^{(1/3)}))\Bigg)a\},\{R=\Bigg(-$$
$$(-12\,a^2\,d+30\,d\,a\,b-18\,d\,b^2+8\,d^3$$
$$-2\sqrt{81\,b^2\,d^2+2\,a^3\,b-108\,a\,b\,d^2-2\,a^4+24\,a^2\,d^2-72\,d^4}\;a$$
$$+2\sqrt{81\,b^2\,d^2+2\,a^3\,b-108\,a\,b\,d^2-2\,a^4+24\,a^2\,d^2-72\,d^4}\;b)^{(1/3)}/(12\,(-a+b))$$
$$+(-a^2+a\,b-2\,d^2)\,/\,(6\,(-a+b)\,(-12\,a^2\,d+30\,d\,a\,b-18\,d\,b^2+8\,d^3$$

$$-2\sqrt{81\,b^2\,d^2+2\,a^3\,b-108\,a\,b\,d^2-2\,a^4+24\,a^2\,d^2-72\,d^4}\;a$$

$$+2\sqrt{81\,b^2\,d^2+2\,a^3\,b-108\,a\,b\,d^2-2\,a^4+24\,a^2\,d^2-72\,d^4}\;b)^{(1/3)})+\frac{d}{3\,(-a+b)}$$

$$-\frac{1}{2}\,I\sqrt{3}\,((-12\,a^2\,d+30\,d\,a\,b-18\,d\,b^2+8\,d^3$$

$$-2\sqrt{81\,b^2\,d^2+2\,a^3\,b-108\,a\,b\,d^2-2\,a^4+24\,a^2\,d^2-72\,d^4}\;a$$

$$+2\sqrt{81\,b^2\,d^2+2\,a^3\,b-108\,a\,b\,d^2-2\,a^4+24\,a^2\,d^2-72\,d^4}\;b)^{(1/3)}/(6\,(-a+b))+($$

$$-a^2+a\,b-2\,d^2)\,/\,(3\,(-a+b)\,(-12\,a^2\,d+30\,d\,a\,b-18\,d\,b^2+8\,d^3$$

$$-2\sqrt{81\,b^2\,d^2+2\,a^3\,b-108\,a\,b\,d^2-2\,a^4+24\,a^2\,d^2-72\,d^4}\;a$$

$$+2\sqrt{81\,b^2\,d^2+2\,a^3\,b-108\,a\,b\,d^2-2\,a^4+24\,a^2\,d^2-72\,d^4}\;b)^{(1/3)}))\Big)\,a\}$$

Error Check

Let a=25mm, b=21mm, d=1.5mm

```
> a :=25;
> b :=21;
> d :=1.5;
```

$$a := 25$$

$$b := 21$$

$$d := 1.5$$

```
> fsolve(equationA1,{R});
```

$$\{R = 29.55167703\}$$

```
> solve(equationA3,{R});
```

$$\{R = -22.09338681\},\ \{R = 1.473644088\},\ \{R = 29.99474272\}$$

The error of equationA3 is 1.50%.

Let a=25mm, b=23mm, d=1.5mm

```
> a :=25;
> b :=23;
> d :=1.5;
```

$$a := 25$$

$$b := 23$$

$$d := 1.5$$

```
> fsolve(equationA1,{R});
```

$$\{R = 45.82696308\}$$

```
> solve(equationA3,{R});
```

$$\{R = -28.80584644\},\ \{R = 1.471274963\},\ \{R = 46.08457147\}$$

The error of equationA3 is 0.56%.

Let a=25mm, b=24.9mm, d=1.5mm

```
>a :=25;
>b :=24.9;
>d :=1.5;
```

$$a := 25$$

$$b := 24.9$$

$$d := 1.5$$

```
>fsolve(equationA3,{R});
```

$$\{R = 434.6917525\}$$

```
>solve(equationA3,{R});
```

$$\{R = -61.16948195\}, \{R = 1.469045191\}, \{R = 434.7004368\}$$

The error of equation2 is 0.00199%.

Position of the extensometer

```
>a :=25; b :=25.1; d :=1.5;
```

$$a := 25$$

$$b := 25.1$$

$$d := 1.5$$

```
>solve(equationA4, {R});
```

$$\{R = -1.468811647\}, \{R = 94.22609186\}, \{R = 282.2427198\}$$

```
>a :=25; b :=24.9; d :=1.5;
```

$$a := 25$$

$$b := 24.9$$

$$d := 1.5$$

```
>solve(equationA3, {R});
```

$$\{R = -61.16948195\}, \{R = 1.469045191\}, \{R = 434.7004368\}$$

Appendix B. Application of extensometer in four point bending experiments-Functions in Excel®

As shown in Appendix A, the conversion of the strain signal from the extensometer to the strain signal at the position of the embedded sensor, some complex calculations needs to be carried out. These calculations are done by the help of Excel®.

The first ten lines for a computation of a real set of data from Excel® are displayed in Table B.1.

The first three columns are real experimental data obtained from the fatigue test machine. b is calculated from the strain signal from the extensometer. d is half thickness of the coupon. R is the radius of the beam and the strain at the position of the sensor is computed in the last column. The other columns are internal functions for the computation. These computations are complex number computations and the formulas of the internal functions are listed at below:

Table B.1. The computations carried out by Excel

Time	Load kN	Strain 1 %	b	d	A	B	C	D	E	1	2	3	4	5	6	7	R	1/R	strain at position of sensor
0	-8.2E-04	-1.1E-03	24.99	1.8	4.99	-45.(	1.7(	-6.3(	-2.7	132	13	5.E+04	-1(	10	3.9	7944	1.6E+05	6.3E-06	7.9E-04
0.02	5.5E-04	-1.5E-03	24.99	1.8	4.99	-45.(	1.7(	-6.3(	-3.7	979	97	4.E+04	-7(	78	2.0(	5872	1.2E+05	8.5E-06	1.1E-03
0.04	3.6E-04	-1.3E-03	24.99	1.8	4.99	-45.(	1.7(	-6.3(	-3.2	115	11	5.E+04	-9(	92	-2.(	6915	1.4E+05	7.2E-06	9.0E-04
0.06	4.5E-04	-1.3E-03	24.99	1.8	4.99	-45.(	1.7(	-6.3(	-3.3	111	11	4.E+04	-8(	89	4.7	6681	1.3E+05	7.5E-06	9.4E-04
0.08	2.1E-03	-1.8E-03	24.99	1.8	4.99	-45.'	1.7(	-6.3(	-4.5	812	81	3.E+04	-6(	64	-2.1	4866	9.7E+04	1.0E-05	1.3E-03
0.1	-7.5E-05	-2.4E-03	24.99	1.8	5.00	-45.'	1.7(	-6.3(	-5.8	630	63	3.E+04	-5(	50	4.0	3774	7.5E+04	1.3E-05	1.7E-03
0.12	-1.9E-03	-2.7E-03	24.99	1.8	5.00	-45.'	1.7(	-6.34	-6.7	553	55	2.E+04	-4(	44	1.8	3314	6.6E+04	1.5E-05	1.9E-03
0.14	-1.7E-03	-2.7E-03	24.99	1.8	5.00	-45.'	1.7(	-6.34	-6.8	540	54	2.E+04	-4(	43	8.9	3237	6.5E+04	1.5E-05	1.9E-03
0.16	-4.0E-03	-2.8E-03	24.99	1.8	5.00	-45.'	1.7(	-6.34	-7.0	528	52	2.E+04	-4(	42	9.9	3166	6.3E+04	1.6E-05	2.0E-03

```
b=COMPLEX(25*(1+C2/100),0,"i")
A=IMSQRT(-2*25^4+2*25^3*$D$2+24*25^2*E2^2-108*25*$D$2*E2^2-
72*E2^4+81*$D$2^2*E2^2)
B=IMSUM(E2*7500-750*E2*$D$2+18*E2*$D$2*$D$2-
8*E2^3,IMPRODUCT((2*$D$2-50),F2))
C=IMPOWER(G2,1/3)
D=COMPLEX(-625+25*$D$2-2*E2*E2,0,"i")
```

E=COMPLEX(-25+D2,0,"i")

1= IMDIV(H2,-0.48*J2)

2=IMDIV(25*I2,IMPRODUCT(6*J2,H2))

3=-25*E2/3/J2

4=IMPRODUCT(COMPLEX(-0.08,0,"i"),K2)

5=IMPRODUCT(COMPLEX(0.08,0,"i"),L2)

6=IMSUM(O2,N2)

7=IMPRODUCT(COMPLEX(0,-25*3^0.5/2,"i"),P2)

R=IMREAL(IMSUM(K2,L2,M2,Q2))

1/R=1/R

Strain at the position of the sensor=1.25/R

Appendix C. The change of sensitivities of optical fibre embedded in cross-ply laminates -- Input and output from Maple®

The calculations of equations in Section 10.2 are carried out using Maple®. Detailed analysis can be found in Section 10.2, only the input commands and output results, including instructive texts from Maple®, are recorded here:

```
> restart;
```

The three normal strains in the optical fibre:

```
> strain20 :=-v12*strain10;
```

$$strain20 := -v12\ strain10$$

```
> strain30 :=-v13*strain10;
```

$$strain30 := -v13\ strain10$$

The three normal strains in the optical axis of the core:

```
> strain1 :=strain10;
```

$$strain1 := strain10$$

```
> strain2 :=
strain20*cos(theta0+theta/L0*l)^2+strain30*sin(theta0+the
ta/L0*l)^2;
```

$$strain2 := -v12\ strain10 \cos\left(\theta 0 + \frac{\theta\, l}{L0}\right)^2 - v13\ strain10 \sin\left(\theta 0 + \frac{\theta\, l}{L0}\right)^2$$

```
> strain3
:=strain20*sin(theta0+theta/L0*l)^2+strain30*cos(theta0+t
heta/L0*l)^2;
```

$$strain3 := -v12\ strain10 \sin\left(\theta 0 + \frac{\theta\, l}{L0}\right)^2 - v13\ strain10 \cos\left(\theta 0 + \frac{\theta\, l}{L0}\right)^2$$

Sensitivity of the optical sensor:

```
> Integration :=k1*strain1+k2*strain2+k3*strain3;
```

$$Integration := k1\ strain10 + k2\left(-v12\ strain10 \cos\left(\theta 0 + \frac{\theta\, l}{L0}\right)^2 - v13\ strain10 \sin\left(\theta 0 + \frac{\theta\, l}{L0}\right)^2\right) + k3\left(-v12\ strain10 \sin\left(\theta 0 + \frac{\theta\, l}{L0}\right)^2 - v13\ strain10 \cos\left(\theta 0 + \frac{\theta\, l}{L0}\right)^2\right)$$

```
> phase_change :=2*pi/lamda*int(Integration, l=0..L0);
```

$$phase\_change := \pi\ strain10\ L0\ (k2\ v12\cos(\theta0)\sin(\theta0) - k2\ v13\cos(\theta0)\sin(\theta0)$$
$$- k3\ v12\cos(\theta0)\sin(\theta0) + k3\ v13\cos(\theta0)\sin(\theta0)$$
$$+ k2\ v13\cos(\theta0)^2\cos(\theta)\sin(\theta) - k2\ v13\sin(\theta0)\sin(\theta)^2\cos(\theta0)$$
$$+ k3\ v12\cos(\theta0)\cos(\theta)^2\sin(\theta0) + k3\ v12\cos(\theta0)^2\cos(\theta)\sin(\theta)$$
$$- k3\ v12\sin(\theta0)^2\sin(\theta)\cos(\theta) - k3\ v12\sin(\theta0)\sin(\theta)^2\cos(\theta0)$$
$$- k3\ v13\cos(\theta0)\cos(\theta)^2\sin(\theta0) - k3\ v13\cos(\theta0)^2\cos(\theta)\sin(\theta)$$
$$- k2\ v13\sin(\theta0)^2\sin(\theta)\cos(\theta) + k3\ v13\sin(\theta0)^2\sin(\theta)\cos(\theta)$$
$$+ k3\ v13\sin(\theta0)\sin(\theta)^2\cos(\theta0) - k2\ v12\cos(\theta0)\cos(\theta)^2\sin(\theta0)$$
$$- k2\ v12\cos(\theta0)^2\cos(\theta)\sin(\theta) + k2\ v12\sin(\theta0)^2\sin(\theta)\cos(\theta)$$
$$+ k2\ v12\sin(\theta0)\sin(\theta)^2\cos(\theta0) + k2\ v13\cos(\theta0)\cos(\theta)^2\sin(\theta0) - k2\ v12\ \theta$$
$$+ 2\ k1\ \theta - k2\ v13\ \theta - k3\ v13\ \theta - k3\ v12\ \theta)/(lamda\ \theta)$$

```
> sensitivity :=phase_change/strain1/L0;
```

$$sensitivity := \pi\ (k2\ v12\cos(\theta0)\sin(\theta0) - k2\ v13\cos(\theta0)\sin(\theta0)$$
$$- k3\ v12\cos(\theta0)\sin(\theta0) + k3\ v13\cos(\theta0)\sin(\theta0)$$
$$+ k2\ v13\cos(\theta0)^2\cos(\theta)\sin(\theta) - k2\ v13\sin(\theta0)\sin(\theta)^2\cos(\theta0)$$
$$+ k3\ v12\cos(\theta0)\cos(\theta)^2\sin(\theta0) + k3\ v12\cos(\theta0)^2\cos(\theta)\sin(\theta)$$
$$- k3\ v12\sin(\theta0)^2\sin(\theta)\cos(\theta) - k3\ v12\sin(\theta0)\sin(\theta)^2\cos(\theta0)$$
$$- k3\ v13\cos(\theta0)\cos(\theta)^2\sin(\theta0) - k3\ v13\cos(\theta0)^2\cos(\theta)\sin(\theta)$$
$$- k2\ v13\sin(\theta0)^2\sin(\theta)\cos(\theta) + k3\ v13\sin(\theta0)^2\sin(\theta)\cos(\theta)$$
$$+ k3\ v13\sin(\theta0)\sin(\theta)^2\cos(\theta0) - k2\ v12\cos(\theta0)\cos(\theta)^2\sin(\theta0)$$
$$- k2\ v12\cos(\theta0)^2\cos(\theta)\sin(\theta) + k2\ v12\sin(\theta0)^2\sin(\theta)\cos(\theta)$$
$$+ k2\ v12\sin(\theta0)\sin(\theta)^2\cos(\theta0) + k2\ v13\cos(\theta0)\cos(\theta)^2\sin(\theta0) - k2\ v12\ \theta$$
$$+ 2\ k1\ \theta - k2\ v13\ \theta - k3\ v13\ \theta - k3\ v12\ \theta)/(lamda\ \theta)$$

When a free sensor is under tension;

```
> k1  :=-0.055;
```

$$k1 := -0.055$$

```
> k2  :=-.204;
```

$$k2 := -0.204$$

```
> k3  :=-.225;
```

$$k3 := -0.225$$

```
> lamda  :=0.000633;
```

$$lamda := 0.000633$$

```
> v12  :=0.154;
```

$$v12 := 0.154$$

```
> v13  :=0.154;
```

$$v13 := 0.154$$

```
> eval(sensitivity);
```

$$34.96366509\ \pi$$

```
> simplify(%);
```

$$34.96366509\,\pi$$

When a sensor is embedded in an unidirectional laminate:

```
> v12  :=0.169;
```

$$v12 := 0.169$$

```
> v13  :=0.169;
```

$$v13 := 0.169$$

```
> v13  :=  .169;
```

$$v13 := 0.169$$

```
> eval(sensitivity);
```

$$55.29541864\,\pi$$

```
> simplify(%);
```

$$55.29541864\,\pi$$

When a sensor is embedded in a cross-ply coupon:

```
> E0  :=(b*E1+d*E2)/(b+d);
```

$$E0 := \frac{b\,E1 + d\,E2}{b + d}$$

```
> strain_1  :=stress/E0;
```

$$strain\_1 := \frac{stress\,(b + d)}{b\,E1 + d\,E2}$$

```
> strain_2  :=-
stress*V12*E2*(b+d)^2/(b*E2+d*E1)/(b*E1+d*E2);
```

$$strain\_2 := -\frac{stress\ V12\ E2\,(b + d)^2}{(b\,E2 + d\,E1)\,(b\,E1 + d\,E2)}$$

```
> strain_3  :=-V13*strain_1-V23*strain_2;
```

$$strain\_3 := -\frac{V13\ stress\,(b + d)}{b\,E1 + d\,E2} + \frac{V23\ stress\ V12\ E2\,(b + d)^2}{(b\,E2 + d\,E1)\,(b\,E1 + d\,E2)}$$

```
> v12  :=-strain_2/strain_1;
```

$$v12 := \frac{V12\ E2\,(b + d)}{b\,E2 + d\,E1}$$

```
> v13  :=-strain_3/strain_1;
```

$$v13 := -\frac{\left(-\frac{V13\ stress\,(b + d)}{b\,E1 + d\,E2} + \frac{V23\ stress\ V12\ E2\,(b + d)^2}{(b\,E2 + d\,E1)\,(b\,E1 + d\,E2)}\right)(b\,E1 + d\,E2)}{stress\,(b + d)}$$

```
> b  :=1.0;
```

$$b := 1.0$$

```
> d  :=0.5;
```

$$d := 0.5$$

```
> V12  :=0.326;
```

$$V12 := 0.326$$

```
> V13  :=.326;
```

$$V13 := 0.326$$

```
> V23  :=0.303;
```

$$V23 := 0.303$$

```
> E1  :=39*10^9;
> E2  :=11*10^9;
```

$$E1 := 39000000000$$

$$E2 := 11000000000$$

```
> eval(v12);
```

$$0.1763606557$$

```
> eval(v13);
```

$$0.2725627215$$

The actual Poisson's ratio seen by the sensor are:

```
> v12  :=0.162;
```

$$v12 := 0.162$$

```
> v13  :=0.167;
```

$$v13 := 0.167$$

```
> simplify(sensitivity);
```

$$0.3000000000\ 10^{-9}\ \pi\ (0.1639863086\ 10^{12}\ \theta + 0.1105845182\ 10^{10}\ \cos(\theta 0)\ \cos(\theta)^2\ \sin(\theta 0) + 0.1105845182\ 10^{10}\ \cos(\theta 0)^2\ \cos(\theta)\ \sin(\theta) - 0.552922591\ 10^{9}\ \sin(\theta)\ \cos(\theta) - 0.1105845182\ 10^{10}\ \cos(\theta 0)\ \sin(\theta 0))/\theta$$

```
> theta0  :=0;
```

$$\theta 0 := 0$$

```
> simplify(sensitivity);
```

$$\frac{0.3000000000\ 10^{-9}\ \pi\ (0.1639863086\ 10^{12}\ \theta + 0.552922591\ 10^{9}\ \sin(\theta)\ \cos(\theta))}{\theta}$$

```
> limit(sensitivity, theta=0);
```

$$49.36176935\ \pi$$

```
> limit(sensitivity, theta=infinity);
```

$$49.19589258\ \pi$$

Appendix D The interaction between a sensor embedded in cross-ply laminate and a transverse crack past in adjacent 0° ply-- Input and output from Maple®

The calculations of equations in Section 10.3.1 are carried out using Maple®. Detailed analysis can be found in Section 10.3.1, only the input commands and output results, including instructive texts from Maple®, are recorded here:

> restart;

For a cross-ply laminate, the three normal strains in the 0 ply are:

```
> E0  :=(b*E1+d*E2)/(b+d);
```

$$E0 := \frac{b\,E1 + d\,E2}{b + d}$$

```
> strain1_c :=stress/E0;
```

$$strain1\_c := \frac{stress\,(b + d)}{b\,E1 + d\,E2}$$

```
> strain2_c :=-v12*strain10;
```

$$strain2\_c := -v12\,strain10$$

```
> strain3_c :=-v13*strain10;
```

$$strain3\_c := -v13\,strain10$$

When the sensor is embedded in a cross-ply laminate, the normal strains in the optical axis are:

```
> strain10 :=stress/E0;
```

$$strain10 := \frac{stress\,(b + d)}{b\,E1 + d\,E2}$$

```
> strain20 :=-v12s*strain10;
```

$$strain20 := -\frac{v12s\,stress\,(b + d)}{b\,E1 + d\,E2}$$

```
> strain30 :=-v13s*strain10;
```

$$strain30 := -\frac{v13s\,stress\,(b + d)}{b\,E1 + d\,E2}$$

When the sensor has an orientation of theta before a crack forms:

```
> strain1 :=strain10;
```

$$strain1 := \frac{stress\,(b + d)}{b\,E1 + d\,E2}$$

```
> strain2 :=
strain20*cos(theta0)^2+strain30*sin(theta0)^2;
```

$$strain2 := -\frac{v12s\ stress\ (b+d)\cos(\theta 0)^2}{b\ E1 + d\ E2} - \frac{v13s\ stress\ (b+d)\sin(\theta 0)^2}{b\ E1 + d\ E2}$$

```
> strain3 :=strain20*sin(theta0)^2+strain30*cos(theta0)^2;
```

$$strain3 := -\frac{v12s\ stress\ (b+d)\sin(\theta 0)^2}{b\ E1 + d\ E2} - \frac{v13s\ stress\ (b+d)\cos(\theta 0)^2}{b\ E1 + d\ E2}$$

```
> integration :=k1*strain1+k2*strain2+k3*strain3;
```

$$integration := \frac{k1\ stress\ (b+d)}{b\ E1 + d\ E2}$$
$$+ k2\left(-\frac{v12s\ stress\ (b+d)\cos(\theta 0)^2}{b\ E1 + d\ E2} - \frac{v13s\ stress\ (b+d)\sin(\theta 0)^2}{b\ E1 + d\ E2}\right)$$
$$+ k3\left(-\frac{v12s\ stress\ (b+d)\sin(\theta 0)^2}{b\ E1 + d\ E2} - \frac{v13s\ stress\ (b+d)\cos(\theta 0)^2}{b\ E1 + d\ E2}\right)$$

```
> phase_before_crack :=2*pi/lamad_optics*int(integration,
l=0..L0);
```

$$phase\_before\_crack := 2\pi\left(\frac{k1\ stress\ (b+d)\ L0}{b\ E1 + d\ E2}\right.$$
$$+ k2\left(-\frac{v12s\ stress\ (b+d)\cos(\theta 0)^2}{b\ E1 + d\ E2} - \frac{v13s\ stress\ (b+d)\sin(\theta 0)^2}{b\ E1 + d\ E2}\right) L0$$
$$\left. + k3\left(-\frac{v12s\ stress\ (b+d)\sin(\theta 0)^2}{b\ E1 + d\ E2} - \frac{v13s\ stress\ (b+d)\cos(\theta 0)^2}{b\ E1 + d\ E2}\right) L0\right) /$$
$$lamad\_optics$$

When there is a crack occurs at an orientation of theta with distances of L1 and L2 to the two splices, the three normal strains in the host composite are:

```
> strain_10 :=strain1_c+stress*d/b*E2/E0*exp(-lamad*y)/E1;
```

$$strain\_10 := \frac{stress\ (b+d)}{b\ E1 + d\ E2} + \frac{stress\ d\ E2\ (b+d)\ \mathbf{e}^{(-lamad\ y)}}{b\ (b\ E1 + d\ E2)\ E1}$$

```
> strain_20
:=strain2_c+stress*V12*E2*(b+d)^2/(b*E2+d*E1)/(b*E1+d*E2)
*(1-(b*E1+d*E2)/E1/(b+d))*exp(-lamad*y);
```

$$strain\_20 := -\frac{v12\ stress\ (b+d)}{b\ E1 + d\ E2} + \frac{stress\ V12\ E2\ (b+d)^2\left(1 - \frac{b\ E1 + d\ E2}{E1\ (b+d)}\right)\mathbf{e}^{(-lamad\ y)}}{(b\ E2 + d\ E1)(b\ E1 + d\ E2)}$$

```
> strain_30 :=-V13*strain_10-V23*strain_20;
```

$$strain\_30 := -V13\left(\frac{stress\ (b+d)}{b\ E1 + d\ E2} + \frac{stress\ d\ E2\ (b+d)\ \mathbf{e}^{(-lamad\ y)}}{b\ (b\ E1 + d\ E2)\ E1}\right) -$$
$$V23\left(-\frac{v12\ stress\ (b+d)}{b\ E1 + d\ E2} + \frac{stress\ V12\ E2\ (b+d)^2\left(1 - \frac{b\ E1 + d\ E2}{E1\ (b+d)}\right)\mathbf{e}^{(-lamad\ y)}}{(b\ E2 + d\ E1)(b\ E1 + d\ E2)}\right)$$

The strains seen by the optical fibre in x-y coordinate are:

```
> strain_1f :=strain_10;
```

$$strain\_1f := \frac{stress\ (b+d)}{b\ E1 + d\ E2} + \frac{stress\ d\ E2\ (b+d)\ \mathbf{e}^{(-lamad\ y)}}{b\ (b\ E1 + d\ E2)\ E1}$$

```
> strain_2f :=v12s/v12*strain_20;
```

$$strain\_2f := \frac{v12s\left(-\frac{v12\ stress\ (b+d)}{b\ E1 + d\ E2} + \frac{stress\ V12\ E2\ (b+d)^2\left(1 - \frac{b\ E1 + d\ E2}{E1\ (b+d)}\right)\mathbf{e}^{(-lamad\ y)}}{(b\ E2 + d\ E1)\ (b\ E1 + d\ E2)}\right)}{v12}$$

```
> strain_3f :=v13s/v13*strain_30;
```

$$strain\_3f := v13s\left(-V13\left(\frac{stress\ (b+d)}{b\ E1 + d\ E2} + \frac{stress\ d\ E2\ (b+d)\ \mathbf{e}^{(-lamad\ y)}}{b\ (b\ E1 + d\ E2)\ E1}\right) - V23\left(-\frac{v12\ stress\ (b+d)}{b\ E1 + d\ E2} + \frac{stress\ V12\ E2\ (b+d)^2\left(1 - \frac{b\ E1 + d\ E2}{E1\ (b+d)}\right)\mathbf{e}^{(-lamad\ y)}}{(b\ E2 + d\ E1)\ (b\ E1 + d\ E2)}\right)\right) / v13$$

The three normal in the optical axis of the sensor are:

```
> strain_1 :=strain_1f;
```

$$strain\_1 := \frac{stress\ (b+d)}{b\ E1 + d\ E2} + \frac{stress\ d\ E2\ (b+d)\ \mathbf{e}^{(-lamad\ y)}}{b\ (b\ E1 + d\ E2)\ E1}$$

```
> strain_2
:=strain_2f*cos(theta0)^2+strain_3f*sin(theta0)^2;
```

$$strain\_2 := v12s\left(-\frac{v12\ stress\ (b+d)}{b\ E1 + d\ E2} + \frac{stress\ V12\ E2\ (b+d)^2\left(1 - \frac{b\ E1 + d\ E2}{E1\ (b+d)}\right)\mathbf{e}^{(-lamad\ y)}}{(b\ E2 + d\ E1)\ (b\ E1 + d\ E2)}\right)\cos(\theta 0)^2/v12 + v13s\left(-V13\left(\frac{stress\ (b+d)}{b\ E1 + d\ E2} + \frac{stress\ d\ E2\ (b+d)\ \mathbf{e}^{(-lamad\ y)}}{b\ (b\ E1 + d\ E2)\ E1}\right) - V23\left(-\frac{v12\ stress\ (b+d)}{b\ E1 + d\ E2} + \frac{stress\ V12\ E2\ (b+d)^2\left(1 - \frac{b\ E1 + d\ E2}{E1\ (b+d)}\right)\mathbf{e}^{(-lamad\ y)}}{(b\ E2 + d\ E1)\ (b\ E1 + d\ E2)}\right)\right)\sin(\theta 0)^2/v13$$

```
> strain_3
:=strain_2f*sin(theta0)^2+strain_3f*cos(theta0)^2;
```

$$strain\_3 := v12s \left(-\frac{v12\ stress\ (b+d)}{b\ E1 + d\ E2} + \frac{stress\ V12\ E2\ (b+d)^2 \left(1 - \frac{b\ E1 + d\ E2}{E1\ (b+d)}\right) \mathbf{e}^{(-lamad\ y)}}{(b\ E2 + d\ E1)(b\ E1 + d\ E2)} \right)$$

$$\sin(\theta 0)^2/v12 + v13s \left(-V13 \left(\frac{stress\ (b+d)}{b\ E1 + d\ E2} + \frac{stress\ d\ E2\ (b+d)\ \mathbf{e}^{(-lamad\ y)}}{b\ (b\ E1 + d\ E2)\ E1} \right) - V23 \left(-\frac{v12\ stress\ (b+d)}{b\ E1 + d\ E2} + \frac{stress\ V12\ E2\ (b+d)^2 \left(1 - \frac{b\ E1 + d\ E2}{E1\ (b+d)}\right) \mathbf{e}^{(-lamad\ y)}}{(b\ E2 + d\ E1)(b\ E1 + d\ E2)} \right) \right)$$

$$\cos(\theta 0)^2/v13$$

```
>integration_crack :=k1*strain_1+k2*strain_2+k3*strain_3;
```

$$integration\_crack := k1 \left(\frac{stress\ (b+d)}{b\ E1 + d\ E2} + \frac{stress\ d\ E2\ (b+d)\ \mathbf{e}^{(-lamad\ y)}}{b\ (b\ E1 + d\ E2)\ E1} \right) + k2 \left(v12s \left(-\frac{v12\ stress\ (b+d)}{b\ E1 + d\ E2} + \frac{stress\ V12\ E2\ (b+d)^2 \left(1 - \frac{b\ E1 + d\ E2}{E1\ (b+d)}\right) \mathbf{e}^{(-lamad\ y)}}{(b\ E2 + d\ E1)(b\ E1 + d\ E2)} \right) \right.$$

$$\cos(\theta 0)^2/v12 + v13s \left(-V13 \left(\frac{stress\ (b+d)}{b\ E1 + d\ E2} + \frac{stress\ d\ E2\ (b+d)\ \mathbf{e}^{(-lamad\ y)}}{b\ (b\ E1 + d\ E2)\ E1} \right) - V23 \left(-\frac{v12\ stress\ (b+d)}{b\ E1 + d\ E2} + \frac{stress\ V12\ E2\ (b+d)^2 \left(1 - \frac{b\ E1 + d\ E2}{E1\ (b+d)}\right) \mathbf{e}^{(-lamad\ y)}}{(b\ E2 + d\ E1)(b\ E1 + d\ E2)} \right) \right)$$

$$\left. \sin(\theta 0)^2/v13 \right) + k3 \left(v12s \left(-\frac{v12\ stress\ (b+d)}{b\ E1 + d\ E2} + \frac{stress\ V12\ E2\ (b+d)^2 \left(1 - \frac{b\ E1 + d\ E2}{E1\ (b+d)}\right) \mathbf{e}^{(-lamad\ y)}}{(b\ E2 + d\ E1)(b\ E1 + d\ E2)} \right) \right.$$

$$\sin(\theta 0)^2/v12 + v13s \left(-V13 \left(\frac{stress\ (b+d)}{b\ E1 + d\ E2} + \frac{stress\ d\ E2\ (b+d)\ \mathbf{e}^{(-lamad\ y)}}{b\ (b\ E1 + d\ E2)\ E1} \right) - V23 \left(-\frac{v12\ stress\ (b+d)}{b\ E1 + d\ E2} + \frac{stress\ V12\ E2\ (b+d)^2 \left(1 - \frac{b\ E1 + d\ E2}{E1\ (b+d)}\right) \mathbf{e}^{(-lamad\ y)}}{(b\ E2 + d\ E1)(b\ E1 + d\ E2)} \right) \right)$$

$$\left. \left. \cos(\theta 0)^2/v13 \right) \right)$$

```
>phase_after_crack
:=2*pi/lamad_optics*(int(integration_crack,
y=0..L1)+int(integration_crack, y=0..L2));
```

$$
\begin{aligned}
phase\_after\_crack :=\ & 2\,\pi\,(-(k1\ v12\ v13\ d\ E2^2\ \mathbf{e}^{(-lamad\ L1)}\ b \\
& + k1\ v12\ v13\ d^2\ E2\ \mathbf{e}^{(-lamad\ L1)}\ E1 + k2\ v12s\ \cos(\theta 0)^2\ v13\ b^2\ v12\ L1\ E1\ lamad\ E2 \\
& + k2\ v12s\ \cos(\theta 0)^2\ v13\ b\ v12\ L1\ E1^2\ lamad\ d \\
& + k2\ v12s\ \cos(\theta 0)^2\ v13\ b\ V12\ E2\ d\ \mathbf{e}^{(-lamad\ L1)}\ E1 \\
& - k2\ v12s\ \cos(\theta 0)^2\ v13\ b\ V12\ E2^2\ d\ \mathbf{e}^{(-lamad\ L1)} \\
& + k2\ v13s\ \sin(\theta 0)^2\ v12\ V13\ L1\ b^2\ E1\ lamad\ E2 \\
& + k2\ v13s\ \sin(\theta 0)^2\ v12\ V13\ L1\ b\ E1^2\ lamad\ d \\
& - k2\ v13s\ \sin(\theta 0)^2\ v12\ V13\ d\ E2^2\ \mathbf{e}^{(-lamad\ L1)}\ b \\
& - k2\ v13s\ \sin(\theta 0)^2\ v12\ V13\ d^2\ E2\ \mathbf{e}^{(-lamad\ L1)}\ E1 \\
& - k2\ v13s\ \sin(\theta 0)^2\ v12^2\ V23\ b^2\ L1\ E1\ lamad\ E2 \\
& - k2\ v13s\ \sin(\theta 0)^2\ v12^2\ V23\ b\ L1\ E1^2\ lamad\ d \\
& - k2\ v13s\ \sin(\theta 0)^2\ v12\ V23\ b\ V12\ E2\ d\ \mathbf{e}^{(-lamad\ L1)}\ E1 \\
& + k2\ v13s\ \sin(\theta 0)^2\ v12\ V23\ b\ V12\ E2^2\ d\ \mathbf{e}^{(-lamad\ L1)} \\
& + k3\ v12s\ \sin(\theta 0)^2\ v13\ b^2\ v12\ L1\ E1\ lamad\ E2 \\
& + k3\ v12s\ \sin(\theta 0)^2\ v13\ b\ v12\ L1\ E1^2\ lamad\ d \\
& + k3\ v12s\ \sin(\theta 0)^2\ v13\ b\ V12\ E2\ d\ \mathbf{e}^{(-lamad\ L1)}\ E1 \\
& - k3\ v12s\ \sin(\theta 0)^2\ v13\ b\ V12\ E2^2\ d\ \mathbf{e}^{(-lamad\ L1)} \\
& + k3\ v13s\ \cos(\theta 0)^2\ v12\ V13\ L1\ b^2\ E1\ lamad\ E2 \\
& + k3\ v13s\ \cos(\theta 0)^2\ v12\ V13\ L1\ b\ E1^2\ lamad\ d \\
& - k3\ v13s\ \cos(\theta 0)^2\ v12\ V13\ d\ E2^2\ \mathbf{e}^{(-lamad\ L1)}\ b \\
& - k3\ v13s\ \cos(\theta 0)^2\ v12\ V13\ d^2\ E2\ \mathbf{e}^{(-lamad\ L1)}\ E1 \\
& - k3\ v13s\ \cos(\theta 0)^2\ v12^2\ V23\ b^2\ L1\ E1\ lamad\ E2 \\
& - k3\ v13s\ \cos(\theta 0)^2\ v12^2\ V23\ b\ L1\ E1^2\ lamad\ d \\
& - k3\ v13s\ \cos(\theta 0)^2\ v12\ V23\ b\ V12\ E2\ d\ \mathbf{e}^{(-lamad\ L1)}\ E1 \\
& + k3\ v13s\ \cos(\theta 0)^2\ v12\ V23\ b\ V12\ E2^2\ d\ \mathbf{e}^{(-lamad\ L1)} \\
& - k1\ v12\ v13\ L1\ b^2\ E1\ lamad\ E2 - k1\ v12\ v13\ L1\ b\ E1^2\ lamad\ d \\
& - k1\ v12\ v13\ d^2\ E2\ E1 + k3\ v13s\ \cos(\theta 0)^2\ v12\ V13\ d^2\ E2\ E1 \\
& + k3\ v13s\ \cos(\theta 0)^2\ v12\ V23\ b\ V12\ E2\ d\ E1 \\
& - k3\ v13s\ \cos(\theta 0)^2\ v12\ V23\ b\ V12\ E2^2\ d - k2\ v12s\ \cos(\theta 0)^2\ v13\ b\ V12\ E2\ d\ E1 \\
& + k2\ v12s\ \cos(\theta 0)^2\ v13\ b\ V12\ E2^2\ d + k2\ v13s\ \sin(\theta 0)^2\ v12\ V13\ d\ E2^2\ b \\
& + k2\ v13s\ \sin(\theta 0)^2\ v12\ V13\ d^2\ E2\ E1 + k2\ v13s\ \sin(\theta 0)^2\ v12\ V23\ b\ V12\ E2\ d\ E1 \\
& - k2\ v13s\ \sin(\theta 0)^2\ v12\ V23\ b\ V12\ E2^2\ d - k1\ v12\ v13\ d\ E2^2\ b \\
& - k3\ v12s\ \sin(\theta 0)^2\ v13\ b\ V12\ E2\ d\ E1 + k3\ v12s\ \sin(\theta 0)^2\ v13\ b\ V12\ E2^2\ d \\
& + k3\ v13s\ \cos(\theta 0)^2\ v12\ V13\ d\ E2^2\ b)\ stress\ (b+d)/(b\ v13\ lamad\ E1\ (b\ E1 + d\ E2) \\
& (b\ E2 + d\ E1)\ v12) - (k1\ v12\ v13\ d\ E2^2\ \mathbf{e}^{(-lamad\ L2)}\ b \\
& + k1\ v12\ v13\ d^2\ E2\ \mathbf{e}^{(-lamad\ L2)}\ E1 + k2\ v12s\ \cos(\theta 0)^2\ v13\ b^2\ v12\ L2\ E1\ lamad\ E2
\end{aligned}
$$

$$+ k2\ v12s\ \cos(\theta 0)^2\ v13\ b\ v12\ L2\ E1^2\ lamad\ d$$
$$+ k2\ v12s\ \cos(\theta 0)^2\ v13\ b\ V12\ E2\ d\ \mathbf{e}^{(-lamad\ L2)}\ E1$$
$$- k2\ v12s\ \cos(\theta 0)^2\ v13\ b\ V12\ E2^2\ d\ \mathbf{e}^{(-lamad\ L2)}$$
$$+ k2\ v13s\ \sin(\theta 0)^2\ v12\ V13\ L2\ b^2\ E1\ lamad\ E2$$
$$+ k2\ v13s\ \sin(\theta 0)^2\ v12\ V13\ L2\ b\ E1^2\ lamad\ d$$
$$- k2\ v13s\ \sin(\theta 0)^2\ v12\ V13\ d\ E2^2\ \mathbf{e}^{(-lamad\ L2)}\ b$$
$$- k2\ v13s\ \sin(\theta 0)^2\ v12\ V13\ d^2\ E2\ \mathbf{e}^{(-lamad\ L2)}\ E1$$
$$- k2\ v13s\ \sin(\theta 0)^2\ v12^2\ V23\ b^2\ L2\ E1\ lamad\ E2$$
$$- k2\ v13s\ \sin(\theta 0)^2\ v12^2\ V23\ b\ L2\ E1^2\ lamad\ d$$
$$- k2\ v13s\ \sin(\theta 0)^2\ v12\ V23\ b\ V12\ E2\ d\ \mathbf{e}^{(-lamad\ L2)}\ E1$$
$$+ k2\ v13s\ \sin(\theta 0)^2\ v12\ V23\ b\ V12\ E2^2\ d\ \mathbf{e}^{(-lamad\ L2)}$$
$$+ k3\ v12s\ \sin(\theta 0)^2\ v13\ b^2\ v12\ L2\ E1\ lamad\ E2$$
$$+ k3\ v12s\ \sin(\theta 0)^2\ v13\ b\ v12\ L2\ E1^2\ lamad\ d$$
$$+ k3\ v12s\ \sin(\theta 0)^2\ v13\ b\ V12\ E2\ d\ \mathbf{e}^{(-lamad\ L2)}\ E1$$
$$- k3\ v12s\ \sin(\theta 0)^2\ v13\ b\ V12\ E2^2\ d\ \mathbf{e}^{(-lamad\ L2)}$$
$$+ k3\ v13s\ \cos(\theta 0)^2\ v12\ V13\ L2\ b^2\ E1\ lamad\ E2$$
$$+ k3\ v13s\ \cos(\theta 0)^2\ v12\ V13\ L2\ b\ E1^2\ lamad\ d$$
$$- k3\ v13s\ \cos(\theta 0)^2\ v12\ V13\ d\ E2^2\ \mathbf{e}^{(-lamad\ L2)}\ b$$
$$- k3\ v13s\ \cos(\theta 0)^2\ v12\ V13\ d^2\ E2\ \mathbf{e}^{(-lamad\ L2)}\ E1$$
$$- k3\ v13s\ \cos(\theta 0)^2\ v12^2\ V23\ b^2\ L2\ E1\ lamad\ E2$$
$$- k3\ v13s\ \cos(\theta 0)^2\ v12^2\ V23\ b\ L2\ E1^2\ lamad\ d$$
$$- k3\ v13s\ \cos(\theta 0)^2\ v12\ V23\ b\ V12\ E2\ d\ \mathbf{e}^{(-lamad\ L2)}\ E1$$
$$+ k3\ v13s\ \cos(\theta 0)^2\ v12\ V23\ b\ V12\ E2^2\ d\ \mathbf{e}^{(-lamad\ L2)}$$
$$- k1\ v12\ v13\ L2\ b^2\ E1\ lamad\ E2 - k1\ v12\ v13\ L2\ b\ E1^2\ lamad\ d$$
$$- k1\ v12\ v13\ d^2\ E2\ E1 + k3\ v13s\ \cos(\theta 0)^2\ v12\ V13\ d^2\ E2\ E1$$
$$+ k3\ v13s\ \cos(\theta 0)^2\ v12\ V23\ b\ V12\ E2\ d\ E1$$
$$- k3\ v13s\ \cos(\theta 0)^2\ v12\ V23\ b\ V12\ E2^2\ d - k2\ v12s\ \cos(\theta 0)^2\ v13\ b\ V12\ E2\ d\ E1$$
$$+ k2\ v12s\ \cos(\theta 0)^2\ v13\ b\ V12\ E2^2\ d + k2\ v13s\ \sin(\theta 0)^2\ v12\ V13\ d\ E2^2\ b$$
$$+ k2\ v13s\ \sin(\theta 0)^2\ v12\ V13\ d^2\ E2\ E1 + k2\ v13s\ \sin(\theta 0)^2\ v12\ V23\ b\ V12\ E2\ d\ E1$$
$$- k2\ v13s\ \sin(\theta 0)^2\ v12\ V23\ b\ V12\ E2^2\ d - k1\ v12\ v13\ d\ E2^2\ b$$
$$- k3\ v12s\ \sin(\theta 0)^2\ v13\ b\ V12\ E2\ d\ E1 + k3\ v12s\ \sin(\theta 0)^2\ v13\ b\ V12\ E2^2\ d$$
$$+ k3\ v13s\ \cos(\theta 0)^2\ v12\ V13\ d\ E2^2\ b)\ stress\ (b + d)/(b\ v13\ lamad\ E1\ (b\ E1 + d\ E2)$$
$$(b\ E2 + d\ E1)\ v12))/lamad\_optics$$

```
>phasechange :=phase_after_crack-phase_before_crack;
```

$$
\begin{aligned}
phasechange := 2\,\pi\,(&-(k1\ v12\ v13\ d\ E2^2\ \mathbf{e}^{(-lamad\ L1)}\ b + k1\ v12\ v13\ d^2\ E2\ \mathbf{e}^{(-lamad\ L1)}\ E1 \\
&+ k2\ v12s\ \cos(\theta 0)^2\ v13\ b^2\ v12\ L1\ E1\ lamad\ E2 \\
&+ k2\ v12s\ \cos(\theta 0)^2\ v13\ b\ v12\ L1\ E1^2\ lamad\ d \\
&+ k2\ v12s\ \cos(\theta 0)^2\ v13\ b\ V12\ E2\ d\ \mathbf{e}^{(-lamad\ L1)}\ E1 \\
&- k2\ v12s\ \cos(\theta 0)^2\ v13\ b\ V12\ E2^2\ d\ \mathbf{e}^{(-lamad\ L1)} \\
&+ k2\ v13s\ \sin(\theta 0)^2\ v12\ V13\ L1\ b^2\ E1\ lamad\ E2 \\
&+ k2\ v13s\ \sin(\theta 0)^2\ v12\ V13\ L1\ b\ E1^2\ lamad\ d \\
&- k2\ v13s\ \sin(\theta 0)^2\ v12\ V13\ d\ E2^2\ \mathbf{e}^{(-lamad\ L1)}\ b \\
&- k2\ v13s\ \sin(\theta 0)^2\ v12\ V13\ d^2\ E2\ \mathbf{e}^{(-lamad\ L1)}\ E1 \\
&- k2\ v13s\ \sin(\theta 0)^2\ v12^2\ V23\ b^2\ L1\ E1\ lamad\ E2 \\
&- k2\ v13s\ \sin(\theta 0)^2\ v12^2\ V23\ b\ L1\ E1^2\ lamad\ d \\
&- k2\ v13s\ \sin(\theta 0)^2\ v12\ V23\ b\ V12\ E2\ d\ \mathbf{e}^{(-lamad\ L1)}\ E1 \\
&+ k2\ v13s\ \sin(\theta 0)^2\ v12\ V23\ b\ V12\ E2^2\ d\ \mathbf{e}^{(-lamad\ L1)} \\
&+ k3\ v12s\ \sin(\theta 0)^2\ v13\ b^2\ v12\ L1\ E1\ lamad\ E2 \\
&+ k3\ v12s\ \sin(\theta 0)^2\ v13\ b\ v12\ L1\ E1^2\ lamad\ d \\
&+ k3\ v12s\ \sin(\theta 0)^2\ v13\ b\ V12\ E2\ d\ \mathbf{e}^{(-lamad\ L1)}\ E1 \\
&- k3\ v12s\ \sin(\theta 0)^2\ v13\ b\ V12\ E2^2\ d\ \mathbf{e}^{(-lamad\ L1)} \\
&+ k3\ v13s\ \cos(\theta 0)^2\ v12\ V13\ L1\ b^2\ E1\ lamad\ E2 \\
&+ k3\ v13s\ \cos(\theta 0)^2\ v12\ V13\ L1\ b\ E1^2\ lamad\ d \\
&- k3\ v13s\ \cos(\theta 0)^2\ v12\ V13\ d\ E2^2\ \mathbf{e}^{(-lamad\ L1)}\ b \\
&- k3\ v13s\ \cos(\theta 0)^2\ v12\ V13\ d^2\ E2\ \mathbf{e}^{(-lamad\ L1)}\ E1 \\
&- k3\ v13s\ \cos(\theta 0)^2\ v12^2\ V23\ b^2\ L1\ E1\ lamad\ E2 \\
&- k3\ v13s\ \cos(\theta 0)^2\ v12^2\ V23\ b\ L1\ E1^2\ lamad\ d \\
&- k3\ v13s\ \cos(\theta 0)^2\ v12\ V23\ b\ V12\ E2\ d\ \mathbf{e}^{(-lamad\ L1)}\ E1 \\
&+ k3\ v13s\ \cos(\theta 0)^2\ v12\ V23\ b\ V12\ E2^2\ d\ \mathbf{e}^{(-lamad\ L1)} \\
&- k1\ v12\ v13\ L1\ b^2\ E1\ lamad\ E2 - k1\ v12\ v13\ L1\ b\ E1^2\ lamad\ d \\
&- k1\ v12\ v13\ d^2\ E2\ E1 + k3\ v13s\ \cos(\theta 0)^2\ v12\ V13\ d^2\ E2\ E1 \\
&+ k3\ v13s\ \cos(\theta 0)^2\ v12\ V23\ b\ V12\ E2\ d\ E1 \\
&- k3\ v13s\ \cos(\theta 0)^2\ v12\ V23\ b\ V12\ E2^2\ d - k2\ v12s\ \cos(\theta 0)^2\ v13\ b\ V12\ E2\ d\ E1 \\
&+ k2\ v12s\ \cos(\theta 0)^2\ v13\ b\ V12\ E2^2\ d + k2\ v13s\ \sin(\theta 0)^2\ v12\ V13\ d\ E2^2\ b \\
&+ k2\ v13s\ \sin(\theta 0)^2\ v12\ V13\ d^2\ E2\ E1 + k2\ v13s\ \sin(\theta 0)^2\ v12\ V23\ b\ V12\ E2\ d\ E1 \\
&- k2\ v13s\ \sin(\theta 0)^2\ v12\ V23\ b\ V12\ E2^2\ d - k1\ v12\ v13\ d\ E2^2\ b \\
&- k3\ v12s\ \sin(\theta 0)^2\ v13\ b\ V12\ E2\ d\ E1 + k3\ v12s\ \sin(\theta 0)^2\ v13\ b\ V12\ E2^2\ d \\
&+ k3\ v13s\ \cos(\theta 0)^2\ v12\ V13\ d\ E2^2\ b)\ stress\ (b+d)/(b\ v13\ lamad\ E1\ (b\ E1 + d\ E2) \\
&(b\ E2 + d\ E1)\ v12) - (k1\ v12\ v13\ d\ E2^2\ \mathbf{e}^{(-lamad\ L2)}\ b \\
&+ k1\ v12\ v13\ d^2\ E2\ \mathbf{e}^{(-lamad\ L2)}\ E1 + k2\ v12s\ \cos(\theta 0)^2\ v13\ b^2\ v12\ L2\ E1\ lamad\ E2
\end{aligned}
$$

$$+ k2\ v12s\ \cos(\theta 0)^2\ v13\ b\ v12\ L2\ E1^2\ lamad\ d$$
$$+ k2\ v12s\ \cos(\theta 0)^2\ v13\ b\ V12\ E2\ d\ \mathbf{e}^{(-lamad\ L2)}\ E1$$
$$- k2\ v12s\ \cos(\theta 0)^2\ v13\ b\ V12\ E2^2\ d\ \mathbf{e}^{(-lamad\ L2)}$$
$$+ k2\ v13s\ \sin(\theta 0)^2\ v12\ V13\ L2\ b^2\ E1\ lamad\ E2$$
$$+ k2\ v13s\ \sin(\theta 0)^2\ v12\ V13\ L2\ b\ E1^2\ lamad\ d$$
$$- k2\ v13s\ \sin(\theta 0)^2\ v12\ V13\ d\ E2^2\ \mathbf{e}^{(-lamad\ L2)}\ b$$
$$- k2\ v13s\ \sin(\theta 0)^2\ v12\ V13\ d^2\ E2\ \mathbf{e}^{(-lamad\ L2)}\ E1$$
$$- k2\ v13s\ \sin(\theta 0)^2\ v12^2\ V23\ b^2\ L2\ E1\ lamad\ E2$$
$$- k2\ v13s\ \sin(\theta 0)^2\ v12^2\ V23\ b\ L2\ E1^2\ lamad\ d$$
$$- k2\ v13s\ \sin(\theta 0)^2\ v12\ V23\ b\ V12\ E2\ d\ \mathbf{e}^{(-lamad\ L2)}\ E1$$
$$+ k2\ v13s\ \sin(\theta 0)^2\ v12\ V23\ b\ V12\ E2^2\ d\ \mathbf{e}^{(-lamad\ L2)}$$
$$+ k3\ v12s\ \sin(\theta 0)^2\ v13\ b^2\ v12\ L2\ E1\ lamad\ E2$$
$$+ k3\ v12s\ \sin(\theta 0)^2\ v13\ b\ v12\ L2\ E1^2\ lamad\ d$$
$$+ k3\ v12s\ \sin(\theta 0)^2\ v13\ b\ V12\ E2\ d\ \mathbf{e}^{(-lamad\ L2)}\ E1$$
$$- k3\ v12s\ \sin(\theta 0)^2\ v13\ b\ V12\ E2^2\ d\ \mathbf{e}^{(-lamad\ L2)}$$
$$+ k3\ v13s\ \cos(\theta 0)^2\ v12\ V13\ L2\ b^2\ E1\ lamad\ E2$$
$$+ k3\ v13s\ \cos(\theta 0)^2\ v12\ V13\ L2\ b\ E1^2\ lamad\ d$$
$$- k3\ v13s\ \cos(\theta 0)^2\ v12\ V13\ d\ E2^2\ \mathbf{e}^{(-lamad\ L2)}\ b$$
$$- k3\ v13s\ \cos(\theta 0)^2\ v12\ V13\ d^2\ E2\ \mathbf{e}^{(-lamad\ L2)}\ E1$$
$$- k3\ v13s\ \cos(\theta 0)^2\ v12^2\ V23\ b^2\ L2\ E1\ lamad\ E2$$
$$- k3\ v13s\ \cos(\theta 0)^2\ v12^2\ V23\ b\ L2\ E1^2\ lamad\ d$$
$$- k3\ v13s\ \cos(\theta 0)^2\ v12\ V23\ b\ V12\ E2\ d\ \mathbf{e}^{(-lamad\ L2)}\ E1$$
$$+ k3\ v13s\ \cos(\theta 0)^2\ v12\ V23\ b\ V12\ E2^2\ d\ \mathbf{e}^{(-lamad\ L2)}$$
$$- k1\ v12\ v13\ L2\ b^2\ E1\ lamad\ E2 - k1\ v12\ v13\ L2\ b\ E1^2\ lamad\ d$$
$$- k1\ v12\ v13\ d^2\ E2\ E1 + k3\ v13s\ \cos(\theta 0)^2\ v12\ V13\ d^2\ E2\ E1$$
$$+ k3\ v13s\ \cos(\theta 0)^2\ v12\ V23\ b\ V12\ E2\ d\ E1$$
$$- k3\ v13s\ \cos(\theta 0)^2\ v12\ V23\ b\ V12\ E2^2\ d - k2\ v12s\ \cos(\theta 0)^2\ v13\ b\ V12\ E2\ d\ E1$$
$$+ k2\ v12s\ \cos(\theta 0)^2\ v13\ b\ V12\ E2^2\ d + k2\ v13s\ \sin(\theta 0)^2\ v12\ V13\ d\ E2^2\ b$$
$$+ k2\ v13s\ \sin(\theta 0)^2\ v12\ V13\ d^2\ E2\ E1 + k2\ v13s\ \sin(\theta 0)^2\ v12\ V23\ b\ V12\ E2\ d\ E1$$
$$- k2\ v13s\ \sin(\theta 0)^2\ v12\ V23\ b\ V12\ E2^2\ d - k1\ v12\ v13\ d\ E2^2\ b$$
$$- k3\ v12s\ \sin(\theta 0)^2\ v13\ b\ V12\ E2\ d\ E1 + k3\ v12s\ \sin(\theta 0)^2\ v13\ b\ V12\ E2^2\ d$$
$$+ k3\ v13s\ \cos(\theta 0)^2\ v12\ V13\ d\ E2^2\ b)\ stress\ (b + d)/(b\ v13\ lamad\ E1\ (b\ E1 + d\ E2)$$

$$(b\,E2 + d\,E1)\,v12))/lamad\_optics - 2\,\pi\left(\frac{k1\ stress\ (b+d)\,L0}{b\,E1 + d\,E2}\right.$$
$$+ k2\left(-\frac{v12s\ stress\ (b+d)\cos(\theta 0)^2}{b\,E1 + d\,E2} - \frac{v13s\ stress\ (b+d)\sin(\theta 0)^2}{b\,E1 + d\,E2}\right)L0$$
$$\left.+ k3\left(-\frac{v12s\ stress\ (b+d)\sin(\theta 0)^2}{b\,E1 + d\,E2} - \frac{v13s\ stress\ (b+d)\cos(\theta 0)^2}{b\,E1 + d\,E2}\right)L0\right)/$$
$$lamad\_optics$$

V12, V13 and V23 are Poisson's ratio of a unidirectional laminate; v12 are v13 are effective Poisson's ratio of the 0 ply in a cross-ply laminate; v12s and v13s are Poisson's ratio seen by the optical core in optical axis.

```
> b :=1.0;
```
$$b := 1.0$$
```
> d :=0.5;
```
$$d := 0.5$$
```
> v12 :=0.176;
```
$$v12 := 0.176$$
```
> v13 :=0.273;
```
$$v13 := 0.273$$
```
> v12s :=0.162;
```
$$v12s := 0.162$$
```
> v13s :=0.167;
```
$$v13s := 0.167$$
```
> V12 :=0.326;
```
$$V12 := 0.326$$
```
> V13 :=0.326;
```
$$V13 := 0.326$$
```
> V23 :=0.303;
```
$$V23 := 0.303$$
```
> k1 :=-0.055;
```
$$k1 := -0.055$$
```
> k2 :=-.204;
```
$$k2 := -0.204$$
```
> k3 :=-.225;
```
$$k3 := -0.225$$
```
> lamad_optics :=0.000633;
```
$$lamad\_optics := 0.000633$$
```
> lamad :=2.495;
```
$$lamad := 2.495$$
```
> stress :=9.56*10^3/61.74/10^(-6);
```
$$stress := 0.1548428895\ 10^{9}$$

```
> E1  :=39*10^9;
> E2  :=11*10^9;
```

$$E1 := 39000000000$$

$$E2 := 11000000000$$

```
> simplify(%);
```

$$11000000000$$

Assuming that the crack occurs at the middle of the coupon:

```
> L0  :=100;
```

$$L0 := 100$$

```
> L1  :=50;
```

$$L1 := 50$$

```
> L2  :=50;
```

$$L2 := 50$$

```
> simplify(phasechange);
```

$$0.01381491312\ \pi \cos(\theta 0)^2 - 0.1886457820\ \pi$$

Varification of the model:

```
> theta0  :=0;
```

$$\theta 0 := 0$$

```
> eval(phasechange);
```

$$-0.17483088\ \pi$$

```
> theta0  :=3.1415926/2;
```

$$\theta 0 := 1.570796300$$

```
> eval(phasechange);
```

$$-0.18864580\ \pi$$